$\{M_{72}Fe_{30}\}$ (M=Mo, W) Polyoxometalates: Electrocatalysis, Proton Conductivity, Gelation and Mechanochemistry

A THESIS

Submitted in partial fulfilment of the

requirements for the award of the degree

of
DOCTOR OF PHILOSOPHY

by

KOLLI HEMA KUMARI
(16CHPH38)

School of Chemistry
University of Hyderabad
Hyderabad - 500046, India.

May 2023

DEDICATED TO MY MOTHER,

TEACHERS AND

FAMILY

CONTENTS

Chapter 1. Polyoxometalate Based Materials for Electrocatalysis and Proton Conduction: Introduction and Motivation of the Thesis Work

Chapter 2. Nano-Blackberries of $\{W_{72}Fe_{30}\}$ and $\{Mo_{72}Fe_{30}\}$: Electrocatalytic Water Reduction

Chapter 3. Solid Nanoblackberries Exhibiting Super Proton Conductivity Fabricated as Proton Transport Membranes

Chapter 4. Giant Polyoxometalate $\{W_{72}Fe_{30}\}$ in the form of Gel and Xerogel: Rheology and Proton Conduction

Chapter 5. Mechanochemical and Aerial KI Oxidation Mediated by a Giant $\{Mo_{72}Fe_{30}\}$ Polyoxometalate

Chapter 6. Concluding Remarks and Future Scope

DECLARATION

I, Kolli Hema Kumari, hereby declare that the matter embodied in the thesis '$\{M_{72}Fe_{30}\}$ *(M=Mo, W) Polyoxometalates: Electrocatalysis, Proton Conductivity, Gelation and Mechanochemistry*' is the result of my investigation carried out in School of Chemistry, University of Hyderabad, Hyderabad, India, during the period of May 2017 to May 2023, under the supervision of **Prof. Samar K. Das**.

In keeping with the general practice of reporting scientific observation, due acknowledgements have been made wherever the work described is based on the findings of other investigations. Any omission, which might have occurred by oversight or error, is regretted. This research work is free from plagiarism. I hereby agree that my thesis can be deposited in Shodhganaga / NFLIBNET. A report on plagiarism statistics from the library, University of Hyderabad, is enclosed.

S.K.Das

Prof. Samar K. Das

(Thesis supervisor)

22/05/2023

Prof. Samar K. Das
School of Chemistry
University of Hyderabad.
Hyderabad-500 046., INDIA.
skdas@uohyd.ac.in

K. Hema Kumari
22/5/2023.

Kolli Hema Kumari

(16CHPH38)

प्रतिष्ठित संस्थान
INSTITUTION OF EMINENCE

CERTIFICATE

This is to certify that the work described in this thesis entitled '*$\{M_{72}Fe_{30}\}$ (M=Mo, W) Polyoxometalates: Electrocatalysis, Proton Conductivity, Gelation and Mechanochemistry*' submitted on 25/5/2023, has been carried out by **Kolli Hema Kumari**, bearing registration number 16CHPH38 (Date of joining: May 29, 2017), in partial fulfilment of the requirements for the award of Doctor of Philosophy in the School of Chemistry, University of Hyderabad, is a bonafide work carried out by her under my supervision and guidance. This thesis is free from plagiarism and has not been submitted previously in part or in full, to this or any other University or Institution for the award of any degree or diploma.

Parts of this thesis has been published in the following publications.

1. Kolli, H. K.; Jana, D.; Das, S. K. *Inorg. Chem.* **2021**, *60*, 15569–15582. **(Chapter 2)**

The student has made presentation in the following conferences.

Oral presentation

1. Chemfest 2022 (Annual in-house symposium) at School of Chemistry. UoH.

Poster presentation

1. Chemfest 2022 (Annual in-house symposium) at School of Chemistry. UoH.
2. International conference on modern trends in inorganic chemistry (MTIC-XVIII).

The student has passed the following courses towards fulfilment of course work

S.No.	Course	Title	Credits	Pass/Fail
1.	CY-801	Research Proposal	3	Pass
2.	CY-802	Chemistry Pedagogy	3	Pass
3.	CY-805	Instrumental Methods - A	3	Pass
4.	CY-402	Organic Chemistry	3	Pass

Ashwini Nangia

Dean
School of Chemistry,
University of Hyderabad,
Hyderabad – 500046, India.

Dean
SCHOOL OF CHEMISTRY
University of Hyderabad
Hyderabad-500 046

S.K.Das

Prof. Samar K. Das 22/05/2023
(Thesis supervisor)

Prof. Samar K. Das
School of Chemistry
University of Hyderabad
Hyderabad-500 046., INDIA.
skdas@uohyd.ac.in

ACKNOWLEDGEMENTS

I would like to express my deepest gratitude to acknowledge all those who had helped and supported me during my research work.

I convey my profound gratitude and sincere thanks to my thesis supervisor ***Dr. Samar K. Das****, for his invaluable guidance, constant encouragement, and the support he gave me in carrying my research work. His positive approach in every aspect was admirable and inspiring. He has always been approachable, helpful, completely supportive, and cooperative. I will forever be grateful for giving the opportunity to be a part of his research family. I thank* ***Prof. Ashwini Nangia****, Dean, School of Chemistry, and all the former Deans of the School of Chemistry for providing the facilities needed for my research work. I extend my heartfelt thanks to my Doctoral Committee members,* ***Prof. Samudranil Pal*** *and* ***Prof. Tushar Jana****, and all the School of Chemistry faculty members for their co-operation on various occasions.*

I sincerely thank all the non-teaching staff and instrument operators of School of Chemistry for their help and assistance on various occasions. I specially thank to Mr. Durga Prasad, Mr. Sunil, Mr. Mahesh, Mr. Venkata Ramana, Mrs. Ayesha, Mr. Gupta, Mr. Dilip, Mr. Abraham, Mr. Vijay Bhaskar, Mr. Naik, Smt. Geeta, Mr. David Raju and Mr. Venkey anna, Mr. Durgesh, Mr. Mahinder, Mr. Turabuddin. Kalyan, Santosh.

I am sincerely thankful to all my colleagues in School of Chemistry for fruitful scientific and social discussions and making my research life productive. I wish to thank DST-INSPIRE for fellowship, DST-SERB, UOH-IOE and UGC for providing required instruments, chemicals and facilities.

At this time, I recall with deep respect to my teachers Dr. Ashok Kumar, Dr. Madhu, Dr. Kishore Babu, Dr. Gopi, Dr. Divya Jyothi, Dr. Ramgopal Rao, kiranmay mam, Ratna Kumar Sir, Srinivas sir, Radha mam for their perpetual inspiration and it was their encouragement, which paved me as a researcher. Also, I like to pay my respectful regards to all my teachers at various stages of my academic life.

I'm extremely grateful to my lab seniors, Rajendar anna, Vinod anna, Pinki di, Sateesh anna, Suresh anna, Thulasi akka, Subha da, Tanmaya, Chandani di, Joycee di, Pinki di, and Mousami di. I wish to thank my friends Ms. Chandani Singh and Ms. Joycy N. Haokip and a special thanks to my colleagues Debu Jana and Athira Ravi for their endless support not only in my research work and also as mentors like an own brother and sister. I would like to thank my juniors Parvathy, Gopika, Rameswari, Florence, Laxmi Priya, Sarbani and Shalini for their love. A special token of thanks to the M.Sc. project student Prasenjit maity and NRC project students Nikitha and Jay for their contribution to some of the projects. My special thanks to Karthik for helping me in all the administration works and for creating a joyful environment in lab. I am thankful to my friend and research collaborator Dr. Anupam Das for his continuous support in everything in my research journey.

I am also lucky enough to have the support of many School of Chemistry seniors, specially, Dr. Anil Kumar who has helped me a lot in my research life, , Dr. Suryanarayana, Dr. Majji Shankar, *Dr. Balasubhramani, Dr. Tiru, Dr. Ravinder, Dr. Chaitanya, Dr. Swapna, Dr. Divya Madhuri, Dr. Radhika, Dr. Dhanashekar, Dr. Krishna, Dr. Mahesh, Dr. Annadhasan, Dr Subham Dutt, Manas, Dr. Harilal, Dr. Ankit Srivastava, Dr. Anjana, Dr. Sateesh, Dr. Senthilnathan, Dr. Surendhar Reddy and Dr. Anif Pasha for their help and guidance at different stages of the journey. I thank my friends Jyothi, Mamina, Somnath Das, Ravi Jada, Ravi Ketavath, Vinay, Vinod, Navaneeta, Santosh, Ranadeep, Ramnaidu, Somratan, Smriti, Suman, Kamala Lakshmi, Ali, Parvathy, Anjaneyulu, Anju, Hemanth, Prasanaatha, Shanthi, Kalyani, Keerthi, Saradhamani Mondal, Sneha Banarje, Suman Chaudry, Shashikant, Anu, Ritesh, Isha, Ishwaq, Jaladhara, Irfan, Bhuvana for their help and encouragement during these years.*

I would like to specially thank my best friends Amala and Varalakshmi for always being on my side in this beautiful journey of my life. I would like to acknowledge my degree friend Mr. Chinna Rao for his valuable chemistry discussions. I would like to thank all my M.Sc. classmates for their beautiful companion in Andhra University. I am thankful to all my ITC PSPD Bhadrachalam colleagues for being a part of this wonderful learning process, especially Dr. Patnaik Sir, Achyutha Rao sir, Sateesh Sir, Prasad Reddy Sir, Azar Sir and Suresh Sir.

Looking back finally I thank to my parents, Ashok Kumar and Saroja whom I adore most for their love, blessing and confidence on me in building the platform of my life. Also, I express my love to my brother, Rakesh Kumar, for his immeasurable affection and support. I am always thankful to my husband, Soma Sundar who has encouraged me and supported me in all the ways to complete my Ph.D. research journey and I am very lucky to have him in my life.

My sincere apologies if I have missed anyone, but I wish to extend my heartful gratitude to everyone who has been involved in my life and helped me in one way or another.

Hema Kumari

University of Hyderabad,
May, 2023

SYNOPSIS

of the Thesis Entitled

$\{M_{72}Fe_{30}\}$ (M=Mo, W) Polyoxometalates: Electrocatalysis, Proton Conductivity, Gelation and Mechanochemistry

To be submitted to the
University of Hyderabad

For the degree of
DOCTOR OF PHILOSOPHY

by

KOLLI HEMA KUMARI
(16CHPH38)

School of Chemistry
University of Hyderabad
Hyderabad - 500046, India.

May 2023

The doctoral thesis entitled as "**$\{M_{72}Fe_{30}\}$ (M=Mo, W) Polyoxometalates: Electrocatalysis, Proton Conductivity, Gelation and Mechanochemistry**" contains five chapters: four working chapters and one chapter on general introduction on literature and motivation of the work. The chapters are as follow: (1) Polyoxometalate Based Materials for Electrocatalysis and Proton Conduction: Introduction and Motivation of the Thesis Work, (2) Nano-blackberries of $\{W_{72}Fe_{33}\}$ and $\{Mo_{72}Fe_{30}\}$: Electrocatalytic Water Reduction, (3) Solid Nano-blackberries Exhibiting Super Proton Conductivity Fabricated as Proton Transport Membrane, (4) Giant Polyoxometalate $\{W_{72}Fe_{30}\}$ in the form of Gel and Xerogel: Rheology and Proton Conduction and (5) Mechanochemical and Aerial KI Oxidation Mediated by a Giant $\{Mo_{72}Fe_{30}\}$ Polyoxometalate.

The First Chapter which is the introduction chapter of this thesis includes discussion about water splitting, which is basically two half-cell reactions, viz. hydrogen evolution reaction (HER) and Oxygen evolution reaction (OER) catalysis. It also explains about the fuel cells, and materials to be developed to use as proton conductors and HER electrocatalysts. The motivation of this thesis work is discussed in the end of this chapter. All other chapters are divided into the following parts: (a) Overview (brief overview of the work), (b) Introduction (literature survey relevant to the study), (c) Experimental section (including materials and methods employed for the study), (d) Results and discussion, (e) Conclusion and (f) References. The compounds in the thesis work are characterized by FT-IR spectral analysis, powder X-Ray diffraction (PXRD), Raman spectroscopy, thermogravimetric analysis (TGA), UV-Visible diffused reflectance spectroscopy (DRS), field emission scanning electron microscopy (FESEM), dynamic light scattering (DLS) analysis, high resolution transmittance electron microscopy (HRTEM), inductively coupled plasmon optical emission spectroscopy (ICP-OES) and N_2 & water sorption analysis. Gas chromatography (GC) is used to detect the hydrogen gas evolved during HER catalysis (**Chapter 2**). The electrochemical studies were carried out in both aqueous and non-aqueous media in heterogeneous mode with the help of three-electrode setup. Proton conductivity studies of $\{W_{72}Fe_{30}\}$ samples were performed using a two electrode setup, whereas the proton conductivity studies of $\{W_{72}Fe_{30}\}$@polymer membranes were performed with the help of four electrode setup.

Chapter 1

Polyoxometalate Based Materials for Electrocatalysis and Proton Conduction: Introduction and Motivation of the Thesis Work

Polyoxometalates (POMs) are one of the most unique class of functional materials whose story dates back to around two and half centuries, when these were first synthesized. Since then, the research works on POMs have been increased in an exponential rate. Specifically, Keplerates (a sub-class of POMs) have more than 130 research articles on $\{Mo_{72}Fe_{30}\}$ and $\{W_{72}Fe_{30}\}$ cluster containing compounds. Though these clusters are explored for many applications from last few years, their electrochemical functional nature has not been much explored. Having a closer look into their physical and chemical properties, it is expected that they have huge potential towards electrochemical water splitting to produce molecular hydrogen and oxygen. This class of compounds has also potential to show proton conductivity in the solid state. Current chapter describes the evolution of POMs, mainly, Keplerates of $\{W_{72}Fe_{30}\}$ and $\{Mo_{72}Fe_{30}\}$ cluster containing compounds and their diverse applications. We have described, how these clusters are useful in electrocatalytic hydrogen evolution reaction and we have also presented their ability to act as solid-state proton conducting materials (crucial for fuel cells for efficient energy conversion) and proton conduction mechanism. Lastly, we have given a brief overview on water splitting and proton conduction and finally we have mentioned the motivation of the thesis work.

Chapter 2

Nano-blackberries of $\{W_{72}Fe_{30}\}$ and $\{Mo_{72}Fe_{30}\}$: Electrocatalytic Water Reduction

The *reversible* self-assembly of $\{Mo_{72}Fe_{30}\}$ cluster into nano-blackberries in the dilute solution of the relevant crystalline compound $[Mo_{72}Fe_{30}O_{252}(CH_3COO)_{12}\{Mo_2O_7(H_2O)\}_2\{H_2Mo_2O_8(H_2O)\}(H_2O)_{91}]\cdot 150H_2O$ (**$\{Mo_{72}Fe_{30}\}_{cryst}$**) was demonstrated by Liu, Müller and their coworkers as a landmark discovery in the area of polyoxometalate chemistry. We have described, in the present work, how these nano-objects, $\{M_{72}Fe_{30}\}$ (M = W and Mo) of ~2.5 nm can be self-assembled into nano-blackberries *irreversibly* leading to their solid state isolation as nanomaterials, $Fe_3[W_{72}Fe_{30}O_{252}(CH_3COO)_2(OH)_{25}(H_2O)_{103}]\cdot 180H_2O$ (**$\{W_{72}Fe_{30}\}_{NM}$**) and $Na_2[Mo_{72}Fe_{30}O_{252}(CH_3COO)_4(OH)_{16}(H_2O)_{108}]\cdot 180H_2O$ (**$\{Mo_{72}Fe_{30}\}_{NM}$**), respectively (NM stands for nanomaterial). The formulations of these one-pot synthesized nano-blackberries of

$\{W_{72}Fe_{30}\}_{NM}$ and **$\{Mo_{72}Fe_{30}\}_{NM}$** have been established by spectral analysis including Raman spectroscopy, elemental analysis including ICP metal analysis, volumetric analysis (for iron), microscopy techniques and DLS studies. The thermal stability of the tungsten nano-blackberries, **$\{W_{72}Fe_{30}\}_{NM}$** is quite higher than that of its molybdenum analogue **$\{Mo_{72}Fe_{30}\}_{NM}$**. This might be due to the extra three ferric (Fe^{3+}) ions per $\{W_{72}Fe_{30}\}$ cluster in **$\{W_{72}Fe_{30}\}_{NM}$**, that are not part of the $\{W_{72}Fe_{30}\}$ cluster cage but are placed between two adjacent clusters (*i.e.*, each cluster has six surrounding $0.5Fe^{3+}$) to form this self-assembly. The isolated blackberries behave like an inorganic acid, water suspension of which shows the pH values of 3.9 for **$\{W_{72}Fe_{30}\}_{NM}$** and 3.7 for **$\{Mo_{72}Fe_{30}\}_{NM}$** because of the deprotonation of the hydroxyl groups in them. We have demonstrated, for the first time, a meaningful application of these inexpensive and easily synthesized nano-blackberries by showing that it can act as an electrocatalyst for hydrogen evolution reaction (HER) by reducing water. We have performed detailed kinetic studies for the electrocatalytic water reduction catalyzed by **$\{W_{72}Fe_{30}\}_{NM}$** and **$\{Mo_{72}Fe_{30}\}_{NM}$** in a comparative study. The relevant turnover frequencies (TOFs) of **$\{W_{72}Fe_{30}\}_{NM}$** and **$\{Mo_{72}Fe_{30}\}_{NM}$** ($\sim 0.72 s^{-1}$ and $\sim 0.45 s^{-1}$, respectively), the overpotential values of **$\{W_{72}Fe_{30}\}_{NM}$** and **$\{Mo_{72}Fe_{30}\}_{NM}$** (527 mV and 767 mV, respectively) and the relative stability issues of the catalysts indicate that **$\{W_{72}Fe_{30}\}_{NM}$** is reasonably superior to **$\{Mo_{72}Fe_{30}\}_{NM}$**. We have described a rationale of why **$\{W_{72}Fe_{30}\}_{NM}$** performs better than **$\{Mo_{72}Fe_{30}\}_{NM}$** in terms of catalytic activity and stability.

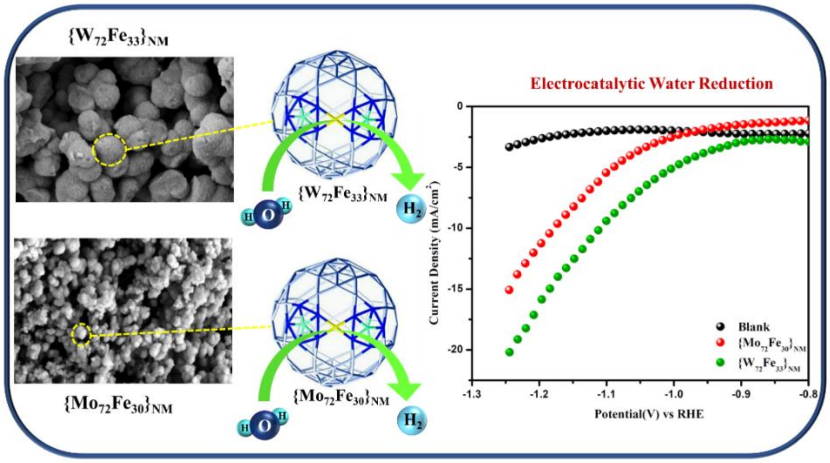

Figure 1. Schematic representation of **$\{W_{72}Fe_{30}\}_{NM}$** and **$\{Mo_{72}Fe_{30}\}_{NM}$**, and their FESEM images showing their nanoblackberry type of morphology and their corresponding electrocatalytic water reduction reaction to produce hydrogen.

Chapter 3

Solid Nano-blackberries Exhibiting Super Proton Conductivity Fabricated as Proton Transport Membrane

The crystalline $\{Mo_{72}Fe_{30}\}$ and $\{W_{72}Fe_{30}\}$ Keplerates, a versatile polyoxometalate system, were first synthesized in Bielefeld, Germany by Müller's research group. Subsequently, Liu, Müller and their co-workers demonstrated the formation of nanoblackberries of $\{Mo_{72}Fe_{30}\}$ and $\{W_{72}Fe_{30}\}$ in respective aqueous solutions. We have recently isolated these nanoblackberries in the solid state in the form of amorphous substances. In this work, we have shown that the isolated tungsten blackberries, $Fe_3[W_{72}Fe_{30}O_{252}(CH_3COO)_2(OH)_{25}(H_2O)_{103}]\cdot 180H_2O$ (**$\{W_{72}Fe_{30}\}_{NB}$**) exhibit highest proton conductivity among polyoxometalates (POMs) and MOFs: 3.30×10^{-1} S cm^{-1} at 80 °C and RH 98%. A vehicular mechanism is expected to operate in this proton conduction through the metal-oxide based solid electrolyte **$\{W_{72}Fe_{30}\}_{NB}$** with an activation energy = 1.95 eV. But this solid electrolyte, as such, cannot form a free-standing film which is essential for its use as proton exchange membrane (PEM) in the fuel cell. We have thus used this POM-based solid electrolyte of highest proton conductivity among POMs and MOFs as nanofiller in an organic polymer, poly [2,2′-(m-phenylene)- 5,5′-benzimidazole] (m-PBI) to fabricate the POM-based polymer composite membrane, **50%$\{W_{72}Fe_{30}\}$@m-PBI** (50% tungsten blackberries loading by weight). We have also prepared phosphoric acid (PA) doped $\{W_{72}Fe_{30}\}$@m-PBI membranes using two different loading levels of $\{W_{72}Fe_{30}\}$ by weight: **2.5%$\{W_{72}Fe_{30}\}$+PA@m-PBI** and **5.0%$\{W_{72}Fe_{30}\}$+PA@m-PBI** for their use as PEM at a higher temperature, at 160 °C. We have performed detailed proton conductivity studies of these polymer composite membranes along with their thermo-mechanical properties. In summary, we have demonstrated that the vesicle-like nanoblackberries, that are reversibly formed in a dilute aqueous solution of a giant polyoxometalate (POM) cluster $\{W_{72}Fe_{30}\}$ containing compound, can be assembled irreversibly to nanoblackberries (without empty interior) that are isolated in solid state in gram quantities exhibiting super proton conductivity and fabricated to the flexible mixed matrix PEM of highest proton conducting efficiency.

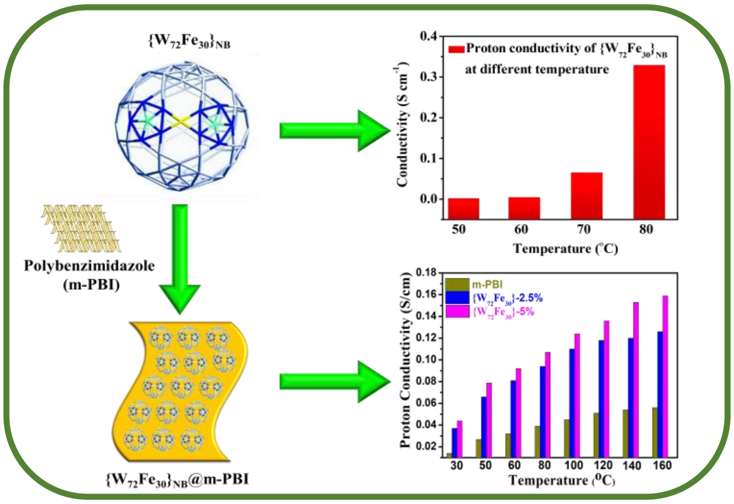

Figure 2. Graphical representation of **$\{W_{72}Fe_{30}\}_{NB}$** and its proton conductivity studies, and its fabrication into **$\{W_{72}Fe_{30}\}_{NB}$@polymer** mixed matrix membranes.

Chapter 4

Giant Polyoxometalate $\{W_{72}Fe_{30}\}$ in the form of Gel and Xerogel: Rheology and Proton Conduction

Polyoxometalate (POM) gel is quite well-known, but mostly with organic molecules. Pure inorganic POM gel is hardly known. When an aqueous solution of sodium tungstate is mixed with an aqueous solution of ferric chloride, an immediate precipitation is observed to be formed ─ the resulting suspension on stirring at room temperature for three hours followed by its centrifugation results in the formation of straw-color gel. The resulting gel has been characterized by rheological studies indicating that this is a soft gel. Linear visco elastic (LVE) region for the 24 hours data of this gel spans from 0.1 – 2.5%, when the storage modulus (G′) is 2674 Pa. The relevant yield stress (σ_y) value is found to be 82 Pa. As expected, when we apply more strain, the storage modulus gets decreased. Dehydration of this gel at room temperature brings about the corresponding xerogel, characterization of which confirms that the xerogel is a $\{W_{72}Fe_{30}\}$ type giant Keplerate-based POM compound $[Fe(H_2O)_6]_{14}[W_{72}Fe_{30}O_{252}(H_2O)_{72}(OH)_{60}]\cdot166H_2O$ (**$\{W_{72}Fe_{30}\}_{XG}$**) and the basic building unit of the gel must be $\{W_{72}Fe_{30}\}$ cluster unit. The xerogel is characterized with 60 hydroxyl groups per formula unit and these hydroxyl groups are acidic in nature. Interestingly, the title xerogel, **$\{W_{72}Fe_{30}\}_{XG}$**, an inexpensive metal-oxide-based material, exhibits proton conduction in the solid state. The material shows super proton conductivity of 6.99×10^{-2} S cm^{-1} at 80 ^{0}C and 98% relative humidity. The activation energy (*Ea*) for the proton conduction is found to be 0.2 eV indicating that the Grotthuss mechanism is involved in the proton conduction.

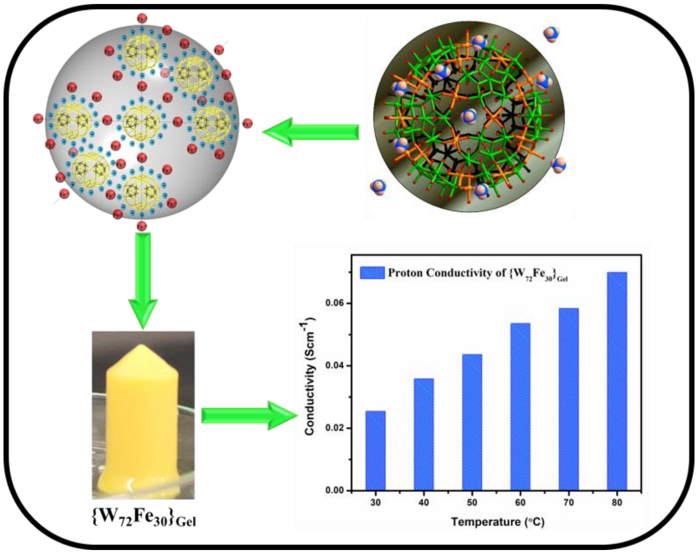

Figure 3. Schematic representation of $\mathbf{\{W_{72}Fe_{30}\}_{XG}}$ formation and its proton conductivity studies.

Chapter 5

Mechanochemical and Aerial KI Oxidation Mediated by a Giant $\{Mo_{72}Fe_{30}\}$ Polyoxometalate

The giant polyoxometalate cluster of the Keplerate compound $[Mo_{72}Fe_{30}O_{252}(CH_3COO)_{12}\{Mo_2O_7(H_2O)\}_2\{H_2Mo_2O_8(H_2O)\}(H_2O)_{91}]\cdot150\ H_2O$ ($\mathbf{\{Mo_{72}Fe_{30}\}_{cryst}}$) is known to be characterized with 72 cage Mo^{VI}-centers and 30 high spin Fe^{III} centers. When this yellow colored Keplerate compound is grinded with KI (potassium iodide) solid in a mortar pestle in solid state, the color of the solid mixture becomes olive green, which turns back into yellow-orange, when this green-color solid mixture is exposed to air for few hours. It turns out that KI gets oxidized by $\mathbf{\{Mo_{72}Fe_{30}\}_{cryst}}$ in solid state with the formation of iodine (I_2) in the solid reaction mixture and in turn, the $\{Mo_{72}Fe_{30}\}$ cluster get reduced with the formation of $\{Mo_{72}Fe_{30}\}^{15-}$, retaining the $\{Mo_{72}Fe_{30}\}$ cluster cage without any destruction. When this green-colored reduced solid reaction mixture is exposed to air, the aerial oxygen oxidizes the reduced $\{Mo_{72}Fe_{30}\}^{15-}$ cluster regenerating the parent oxidized state of $\{Mo_{72}Fe_{30}\}$ resulting in the formation of potassium superoxide (KO_2) in the orange-yellow solid reaction mixture. The molecular iodine (I_2) formed in the solid reaction mixture is extracted with chloroform ($CHCl_3$). Thus the overall reaction cycle can be described as a mechanochemical aerial KI oxidation mediated by the Keplerate $\mathbf{\{Mo_{72}Fe_{30}\}_{cryst}}$.

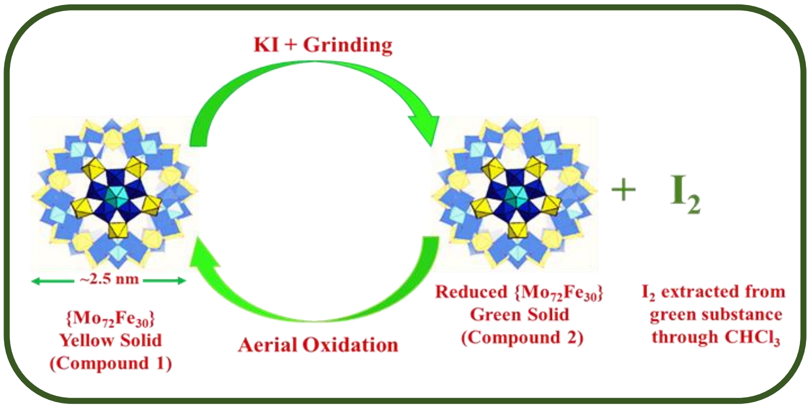

Figure 4. Schematic representation of **{$Mo_{72}Fe_{30}$}** exhibiting mechanochemical solid state redox reaction.

Summary and Future Scope

The summary and future scopes of the work, carried out in this thesis, are discussed after the working chapters. This thesis aims to show the isolation of Keplerate compounds into amorphous form by self-assembling process and application of these Keplerate materials as a heterogeneous electrocatalyst for hydrogen evolution reaction catalysis and proton conduction. The future scope of this work includes further development of Keplerate materials like $Mo_{75}V_{20}$, Mo_{102}, $Mo_{72}V_{30}$, $Mo_{72}Cr_{30}$, $W_{72}Mo_{60}$, $W_{72}V_{30}$ which are less explored for electrochemical properties towards water reduction and water oxidation reactions. Also, Keplerates have an oxygen rich surface which are easily accessible to form extensive hydrogen bonding with water for proton conduction. Furthermore, formation of amorphous forms of these types of Keplerate compounds which show water insoluble nature can be utilized for the proton conductivity studies. POM (Keplerate)@polymer based mixed matrix membranes needs to be studied more as it has a good potential as a proton exchange membrane for fuel cells.

CHAPTER 1

Polyoxometalate Based Materials for Electrocatalysis and Proton Conduction: Introduction and Motivation of the Thesis Work

Chapter 1

Overview

Polyoxometalates (POMs) are one of the most unique class of functional materials whose story dates back to around two and half centuries, when these were first synthesized. Since then, the research works on POMs have been increased in an exponential rate. Specifically, Keplerates (a sub-class of POMs) have more than 130 research articles on $\{Mo_{72}Fe_{30}\}$ and $\{W_{72}Fe_{30}\}$ cluster containing compounds. Though these clusters are explored for many applications from last few years, their electrochemical functional nature has not been much explored. Having a closer look into their physical and chemical properties, it is expected that they have huge potential towards electrochemical water splitting to produce molecular hydrogen and oxygen. This class of compounds has also potential to show proton conductivity in the solid state. Current chapter describes the evolution of POMs, mainly, Keplerates of $\{W_{72}Fe_{30}\}$ and $\{Mo_{72}Fe_{30}\}$ cluster containing compounds and their diverse applications. We have described, how these clusters are useful in electrocatalytic hydrogen evolution reaction and we have also presented their ability to act as solid-state proton conducting materials (crucial for fuel cells for efficient energy conversion) and proton conduction mechanism. Lastly, we have given a brief overview on water splitting and proton conduction and finally we have mentioned the motivation of the thesis work.

1.1. Introduction

In the process of reaching an advance stage of social and cultural development, during last five decades, the energy demand has increased tremendously. It also increased the consumption of fossil fuels exponentially, thereby it becomes environmental concerns. When we look into the last few years' reports, the primary energy demand has been increased by 5.8% in 2021.[1] Though, the major renewable energy sources like solar energy, wind energy, biomass, hydroelectric, nuclear energy and geothermal energy are being used in the energy related sectors, but still to reach the energy demand, the electricity production from the fossil fuels is continued to increase.[2]

Carbon and energy intensity are the two major components which builds the relation between energy consumption and emissions. As per the reports of international energy outlook 2021, there is an increase in CO_2 emission and greenhouse gases emission as the fossil fuel consumption has been increased by 25% from the last few years (Figure 1.1-1.2).[3-6] According to the bp statistical review world energy 2022, the CO_2 emission has been increased to 5.7% in 2021 due to the energy use in industrial sector, usage of methane and also emissions from flaring.[1,7]

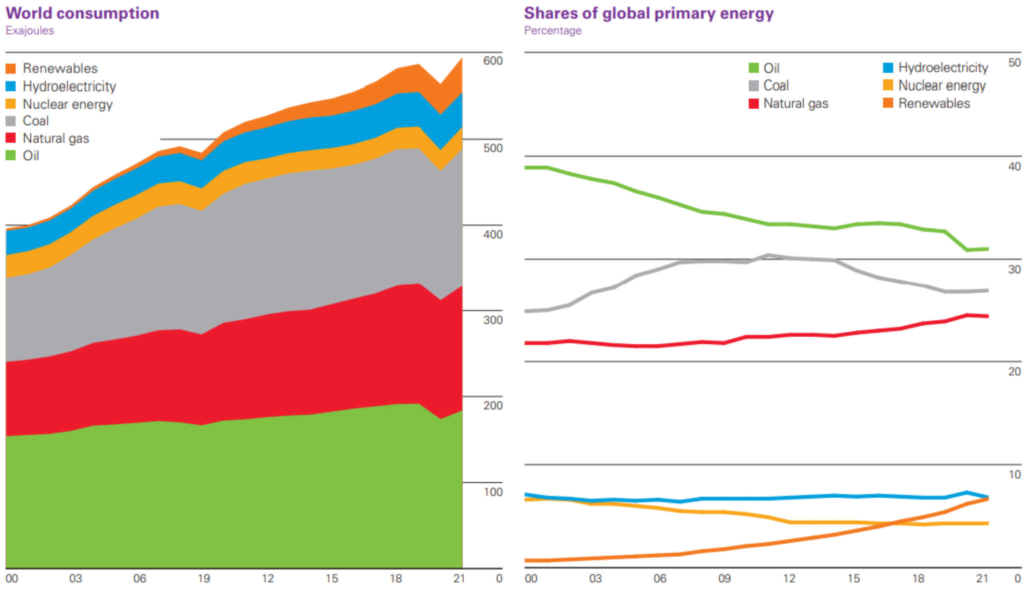

Figure 1.1. Global primary energy consumption of the world.[1]

Oil, natural gas and industrial use of petroleum are going to increase in the coming years to attain the energy demand all over the world. Now it is essential to focus on energy transition to carbon free energy sources to achieve a clean energy and strong climate. To contain adverse effects of fossil fuel consumption, it is necessary to move towards the clean energy especially to renewable energy sources i.e., wind, solar, biofuels and green energy. According to the U.S. EIA Annual Energy Outlook 2022 and World Energy Transition outlook 2022, the solar energy is playing the crucial role as its share in energy production would be increased from 7% in 2020 to 29% in 2050.[3,8] But, despite of its fast growth, it still needs to long way to reach the production capacity suitable for industrial purposes. In this point of view, we have to consider two concerns in the energy production i.e., we have to produce green energy in efficient way to reach the high production level at low cost including its storage.

The highly efficient green energy production has been achieved through the fuel cells and still the research is continuing to increase its efficiency to 100%. The energy storage technologies involve hydrogen, batteries, superconductivity, pumped hydro, supercapacitors and compressed air etc.[9-12] Among these, the best energy storage and energy carrier is hydrogen.[13] It can fully compensate the place of fossil fuels in the energy production and its transportation is an easy task from the production site. In fuel cell, the conversion of chemical energy to electrical energy, the only wastage is water as a steam which is harmless to the environment.[14-15]

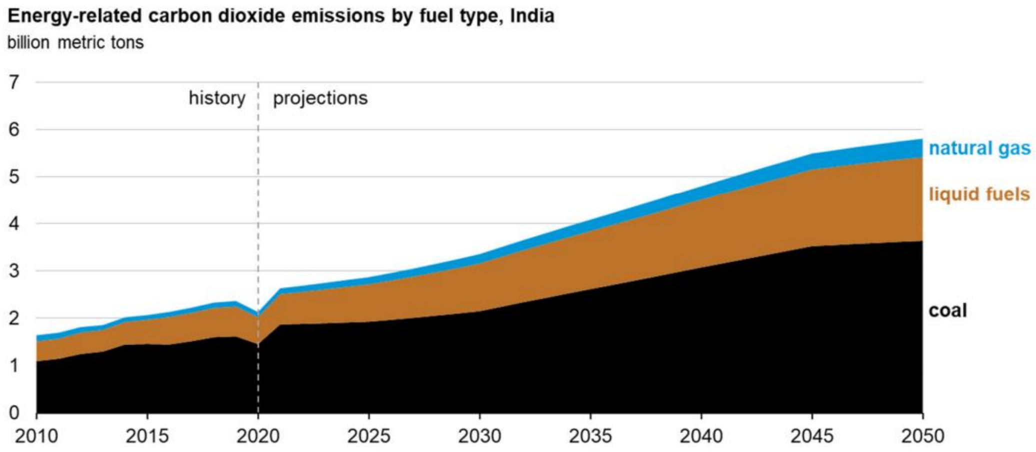

Figure 1.2. Carbon dioxide emission by different fuel sources in india.[3]

One of the best ways to produce hydrogen in the clean energy form without any waste, is water splitting. Splitting of water molecules into hydrogen and oxygen can be achieved by choosing the relevant energy sources that can break the bond between hydrogen and oxygen in the water molecule. Some of the processes which are being used for the water splitting are photochemical, electrochemical and thermochemical processes etc. Among these processes, the electrochemical water splitting is worth mentioning. The water splitting through electrocatalysis can be taken place as mentioned below in two half-reactions, i.e., oxygen evolution reaction (OER) and hydrogen evolution reaction (HER).

$$2H_2O \leftrightarrow 2H_2 + O_2 \qquad E_0 = -\ 1.23\text{ V vs. NHE} \qquad \textbf{(1)}$$

$$2H_2O \leftrightarrow O_2 + 4H^+ + 4\,e^- \qquad E = -\ 1.23\text{ V vs. NHE (OER)} \qquad \textbf{(2)}$$

$$4H^+ + 4e^- \leftrightarrow 2H_2 \qquad E = 0.0\text{ V vs. NHE (HER)} \qquad \textbf{(3)}$$

On the other hand, the fuel cells are the most efficient device compared to others in the conversion of chemical energy to electrical energy. In the process of generating the green energy without the usage of fossil fuels, both the steps, namely water splitting and proton conduction play a major role.[16] In the fuel cell, at the anode the hydrogen molecules are getting oxidized and at the cathode oxygen is getting reduced.[17-21] Especially, at the anode the oxidation of hydrogen molecules is taking place along with

1. Electrons flow in the outer circuit.
2. Protons flow from anode to cathode through the proton conducting polyelectrolyte membrane (PEM) on which the fuel cell efficiency is completely dependent.

In the current chapter, the discussion will be divided into two parts: (1) POM as electrochemical HER catalyst and (2) POM as proton conducting material.

1.2. Polyoxometalates: Keplerate structure and its importance in electrochemical water splitting and proton conductivity studies

1.2.1. History and Structural description of POM

Polyoxometalates are a unique class of anionic metal oxide clusters, that are formed when metal oxides polyhedral units self-assemble in specific reaction conditions. The commonly found metals (addenda atoms) in POMs are transition metals, mostly belongs to V and VI group, in their higher oxidation states and these metals are connected with bridging oxo group (O^{2-} state). In the formation of polyoxometalates, reaction conditions like pH, temperature and concentration have a vital role. In the specific reaction conditions, the metal-oxo anions of these transition metals of group V and VI (W, Mo, V, Nb, Ta etc.) undergoes polycondensation through protonation to form a polyoxometalate.

Though the first crystallographic structural analysis of POM was achieved in 1933 by Keggin ($(H_5O_2)_3[PW_{12}O_{40}]$),[22-41] their story dates back to 19th Century. Based on the available literature, Berzelius discovered the formation of phosphomolybdic acid $[PMo_{12}O_{40}]^{3-}$ (yellow precipitate) from ammonium molybdate and phosphoric acid in 1826 without any crystal structure.[42] Before Keggin, many research groups have attempted to find the structure of this POM. Among them, Pauling was the one who could make an assumption that the basic units of POM clusters are in octahedral geometry, which was later supported by Keggin.[42-43] In 1960's M. T. Pope developed synthetic methods and characterization techniques for POMs. He also attempted and succeeded in NMR spectra-assisted POM structural analysis, and published his findings.[44-47] On the other hand, while studying the formation and degradation of POMs, in 1963, Souchay found that the formation of polyoxometalates involve condensation reactions.[48] All these studies helped in gaining deep insights in to their structural diversity along with their range of physical and chemical properties. As a result, POM field has seen major improvements in 20th century.[49] Various research groups have been working on this field including our group and made it as an interesting field by exploring its properties and applications. The timeline of major developments in POM chemistry and contribution of various researchers are tabulated and presented in Figure 1.3.[42-45,48,50-127]

Year	Research Group	Year	Research Group
1778	Scheele	1960	M. T. Pope
1826	Berzelius	1963	Souchay
1848	Swanberg and Struve	1968 and 1974	Evans and Tsigdinos
1862	Marignac	1976	Fuchs and Hartl
1893	Werner	1982	Kozhevinikov, Fuchs and Knopnadel
1908	Miolati and Pizzighelli	1991	Muller
1912	Laue	1995	Hill
1913	Bragg	1998	Gouzerh, Neumann and Proust
1917	Rosenheim and Jaenicki	2002	S. K. Das, Hansenknof and Gouzerh
1929	Pauling	2007	Cronin
1933	Keggin	2011	S. Roy
1937	Anderson	2013	Patzke
1948	Evans	2014	Tinanbo Liu and Proust
1950	Lindquist	2016	Kortz

Figure 1.3. Timeline showing the development of POMs along with scientists involved in it.

Previous literatures showed that POMs can be broadly classified into two groups, namely, isopolyanions and heteropolyanions on the basis of their composition and structure. In isopolyanions $[M_mO_y]^{p-}$, only one type of transition metal is coordinated with the oxygen atom. Whereas, heteropoly anions consist of a common molecular formula $[X_xM_mO_y]^{q-}$ where $x \leq m$ and M is a V or VI group transition metal from the periodic table and X is a heteroatom (Phosphates, silicates and borates etc.) which is also coordinated with the oxygen atom.[71-72, 128-132]

In the class of isopolyanions, Lindquist, is the well-known POM among them, which is discovered in the year 1950. Whereas, heteropoly anions' class has Keggin, Silverton, Waugh, Dawson, Strandberg and Anderson kind of major POM sub-classes (Figure 1.4). Also, there is one more class of polyoxometalates which are formed due to the condensation of molybdates /

tungstates in a solution under reduced conditions and have large number of atoms with icosahedral symmetry. These are known as Keplerates with giant structures. The present thesis work mainly deals with Keplerate type of POMs; hence we have discussed only about Keplerates in details.

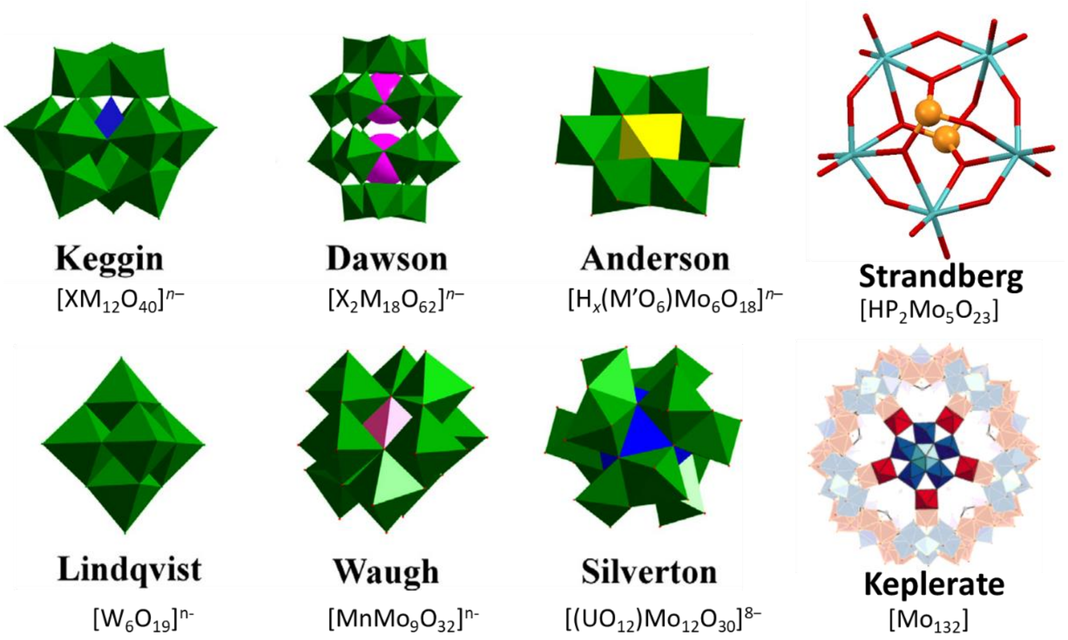

Keggin $[XM_{12}O_{40}]^{n-}$

Dawson $[X_2M_{18}O_{62}]^{n-}$

Anderson $[H_x(M'O_6)Mo_6O_{18}]^{n-}$

Strandberg $[HP_2Mo_5O_{23}]$

Lindqvist $[W_6O_{19}]^{n-}$

Waugh $[MnMo_9O_{32}]^{n-}$

Silverton $[(UO_{12})Mo_{12}O_{30}]^{8-}$

Keplerate $[Mo_{132}]$

Figure 1.4. Structural representations of diverse polyoxometalates.[133-135]

1.2.2. Molybdenum Blue and Molybdenum Brown ─ reduced POM clusters

As mentioned in previous sections, Scheele and Berzelius pioneered the field of POMs. They were the first ones who identified and studied a naturally available bluish amorphous molybdenum blue (as it is normally called).[50-51] Initially they formulated it as $Mo_3O_8.nH_2O$ and later changed to $Mo_5O_{14}.nH_2O$. Later in 1995-1999, it was revealed that molybdenum blue consists of huge clusters with torus shape i.e., Mo_{154} and Mo_{176} type clusters along with hedgehog shaped cluster Mo_{368}.[136] In the journey to studying POM clusters, Müller and Group could isolate a few crystals from the molybdenum blue solution after adding hydroxylamine (a reducing agent) to it and with the help of crystal structure studies, they showed the Mo_{154} wheel structure with 14 NO ligands. Though they could produce crystals of the sample enough for structural studies, they could not isolate the complete crystalline phase of it.[137,138]

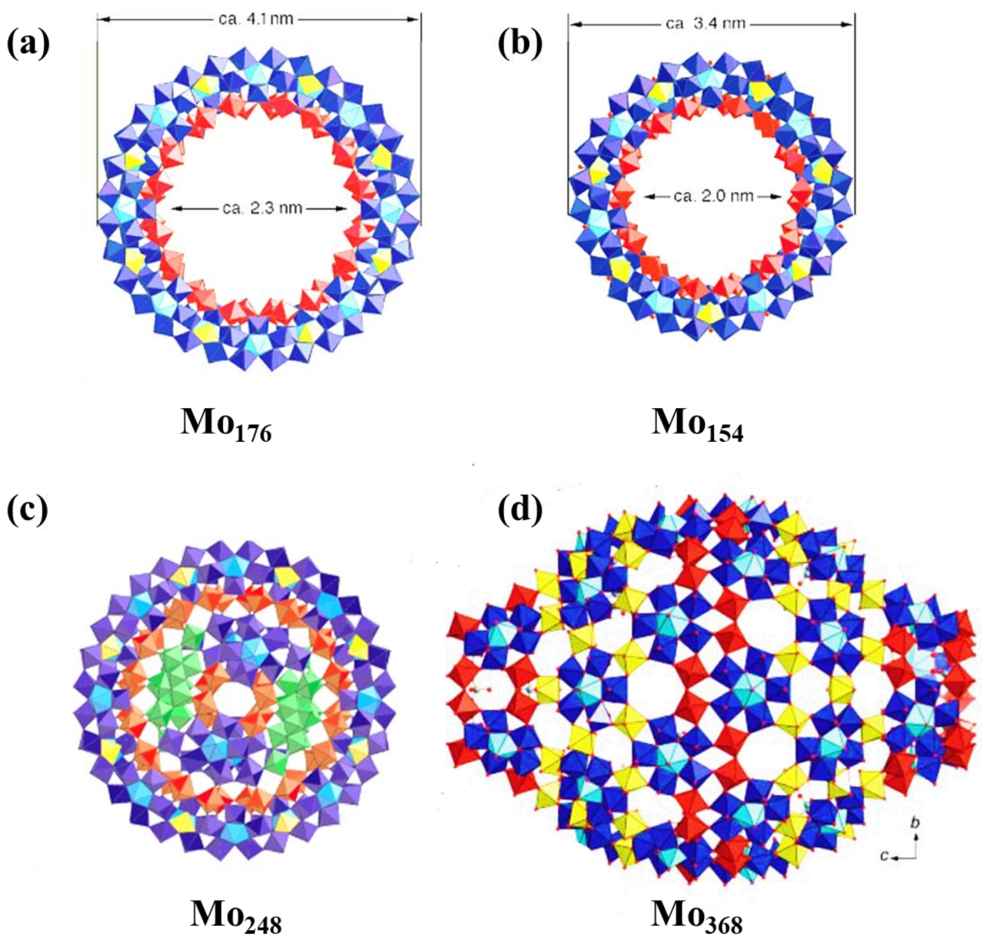

Figure 1.5. Polyhedral representations of (a) $\{Mo_{176}\}$, (b) $\{Mo_{154}\}$, (c) $\{Mo_{248}\}$ and (d) $\{Mo_{368}\}$.[139, 141-142]

In later investigations, they replaced these 14 $\{MoNO\}^{3+}$ units with 14 $\{MoO\}^{4+}$ in Mo_{154} and achieved the pure crystal it with high yield which assisted in determining the complete formula of it. Thorough structural studies revealed that, $\{Mo_{154}\}$ consists of 14 pentagonal bipyramids $\{MoO_7\}$ units and 140 octahedra $\{MoO_6\}$ units which were arranged in a ring-shaped structure. Similarly, Mo_{176} (wheel shaped cluster) was isolated by varying the experimental conditions *viz.* increasing the concentration of molybdates and lowering the pH.[139-140] and a bulky Mo_{248} cluster was also synthesized from acidic aqueous molybdate solution by employing ascorbic acid (a reducing agent).[141] Researchers also developed a lemon – shaped cluster $\{Mo_{368}\}$ with a formula $[H_{16}Mo_{368}O_{1032}(H_2O)_{240}(SO_4)_{48}]^{48-}$. Synthesis of this cluster was carried out in an acidic solution containing H_2SO_4 which facilitated incorporation of sulphate anions (48 sulphate anions on the inner sphere of the cluster) inside the cluster framework which was assumed to be the driving force behind shape of the cluster from wheel to lemon-shape.[142-144] These wheel type of clusters (Figure

1.5) found to be having good applications in various fields including electrochemistry and electronic and magnetic properties driven fields etc. Their nano structures with cavities have a benefit in host-guest chemistry. In later stages Müller and group fine-tuned the art of producing and modifying giant POM clusters by altering reaction conditions. One of such interesting examples was synthesizing a spherical ball shaped Mo_{132} cluster. The cluster was produced from giant wheel shaped clusters in presence acetic acid, and increased amount of reducing agent along with altering the pH of the solution.[145] Discovery of this Mo_{132} giant spherical cluster contributed significantly to the progress of POM chemistry. These clusters not only have been exhibiting many potential applications in various fields including nanoscience, they also opened doors for a new branch of POM chemistry like Keplerates.

1.2.3. Keplerates

Keplerates are polyoxometalate with large number of atoms and giant structures formed by condensation of molybdates in a solution under reduced conditions with icosahedral symmetry. They are composed of two basic building units, namely pentagons and linkers and the sphere also consist of twenty evenly distributed hexagonal pores on the surface. The pore-diameter and cavity size of the Keplerates depend on the nature of the linker, whether it is mononuclear or binuclear. General formula for the Keplerate is $[M_{72}M`_{30}]$ where M is Mo or W containing clusters and M` is the linker either a mononuclear or dinuclear.[146] As mentioned earlier, in 1998 Müller and group synthesized Mo_{132} and it was termed as an inorganic super fullerene based on its topology. This was unambiguously characterized by single crystal X-ray crystallography and accordingly it was formulated as $(NH_4)_{42}[Mo^{VI}_{72}Mo^{V}_{60}O_{372}(CH_3COO)_{30}(H_2O)_{72}]$. ca. $300H_2O$. ca. $10CH_3COONH_4$. There are 12 pentagonal units $\{Mo^{VI}(Mo^{VI}_5O_{21})\}$ and 30 binuclear linkers $\{Mo^{V}_2O_4\}$.[145] In this kind of Keplerate structures each pentagon $\{M^{VI}(M^{VI})_5\}$ consists of pentagonal bipyramidal MoO_7 central unit sharing the five edges with MoO_6 octahedra and all these 12 pentagonal units link together with the help of 30 linkers to form a complete spherical cluster. As depicted in Molecular formula of Mo_{132}, there are additional bidentate ligands (CH_3COO) present in the cluster which coordinates to linkers in different ways. Presence of this kind of ligands affects the total charge of the system, size of the cavity and hydrophilic or hydrophobic nature of the surface of the cluster compared to other clusters.

After the synthesis of Mo$_{132}$, Müller and his group has realized that the synthesis of Keplerates with combination of different linkers is possible and in later studies they started replacing these binuclear linkers {Mo$^{V}_{2}$O$_{4}$} with mononuclear linkers like M\` = Fe$^{3+}$, Cr$^{3+}$ and VO$^{2+}$ which led to formation of smaller Keplerates like [M$^{VI}_{72}$M\`$^{V}_{30}$].[147] One such example was Mo$_{72}$Fe$_{30}$ Keplerate which was a combination of 12 Mo(Mo)$_{5}$ pentagonal units and 30 Fe^{3+} mononuclear linkers.[147]

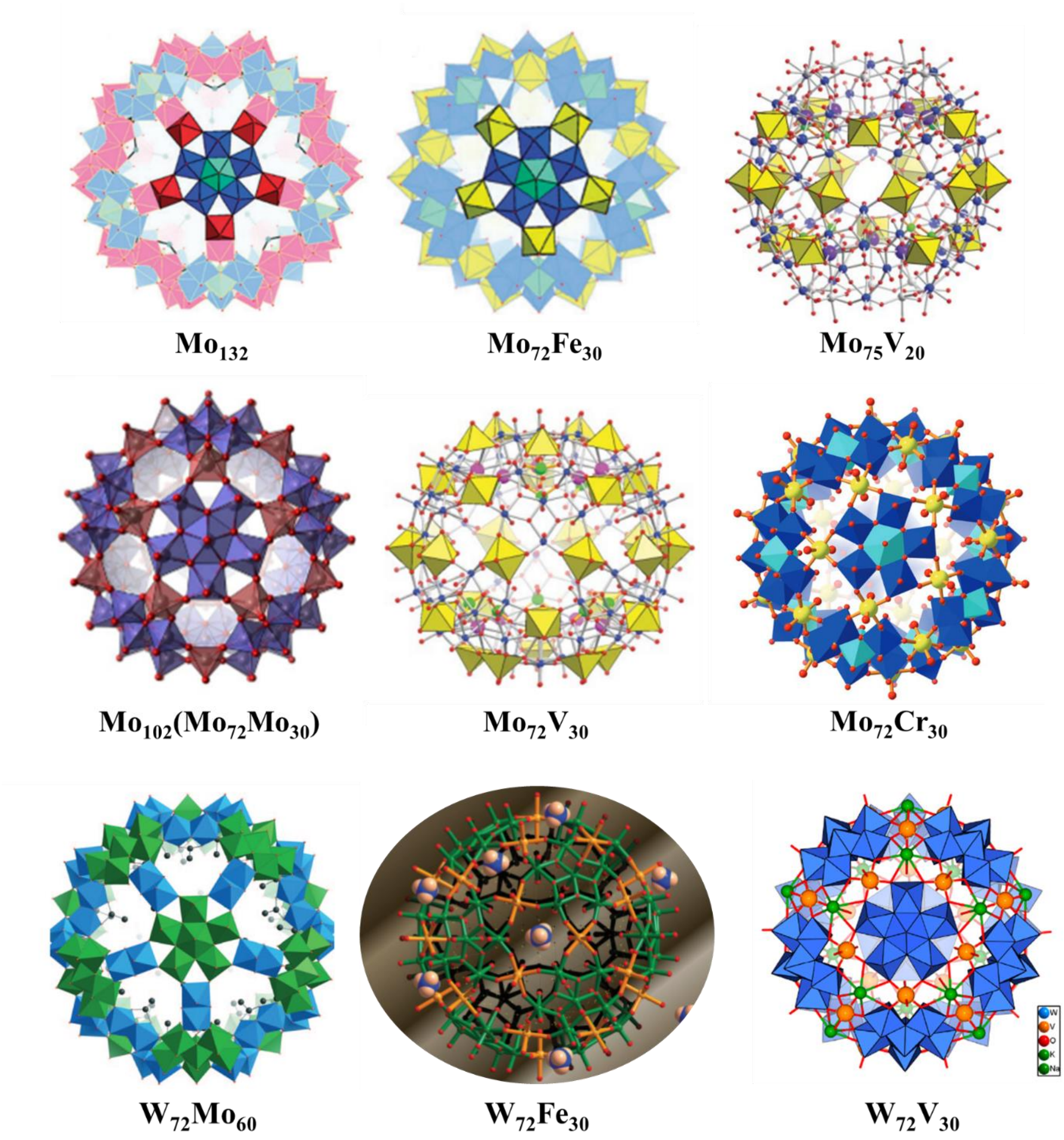

Mo$_{132}$ **Mo$_{72}$Fe$_{30}$** **Mo$_{75}$V$_{20}$**

Mo$_{102}$(Mo$_{72}$Mo$_{30}$) **Mo$_{72}$V$_{30}$** **Mo$_{72}$Cr$_{30}$**

W$_{72}$Mo$_{60}$ **W$_{72}$Fe$_{30}$** **W$_{72}$V$_{30}$**

Figure 1.6. Types of Keplerates reported till date.[145, 147-153]

Consecutively they published a work related to the concept of building blocks in which they reported $Mo_{75}V_{20}$ cluster.[148] Later they synthesized the Mo_{102} ($Mo_{72}Mo_{30}$) in which MoO^{3-} group is linker and they also reported $Mo_{72}V_{30}$ and $Mo_{72}Cr_{30}$ in which $V^{IV}O$ and Cr^{III} are taken as linkers respectively.[148-150] They also generated a pentagonal unit with W i.e., W(W_5) which is assembled with Mo ($W_{72}Mo_{60}$) and Fe ($W_{72}Fe_{30}$).[151-152] Similarly, Wang group also grabbed opportunity and synthesized $W_{72}V_{30}$ cluster.[153] All these Keplerate containing compounds (Figure 1.6) are found to have unique chemical, magnetic and electronic properties which can be used in the real time applications. The pores of these giant clusters have a receptor property; thus the spherical surface chemistry of this cluster opens a new way for supramolecular chemistry. There are huge number of reports related to their magnetic properties and catalytic behavior of the cluster in different reaction conditions.[147-153]

Work presented in this thesis mainly focuses on $\{Mo_{72}Fe_{30}\}$ and $\{W_{72}Fe_{30}\}$ cluster containing compounds.

1.2.4. $\{Mo_{72}Fe_{30}\}$ Keplerate

The $\{Mo_{72}Fe_{30}\}$ Keplerate compound was synthesized by Müller and his group in 1999.[147] Initially, though they had hard time synthesizing a spherical object from pentagons $\{Mo(Mo)_5\}$ later they have constructed giant molecular spheres of different sizes by varying the linkers. They could separate a yellow colored crystalline compound $\{Mo_{72}Fe_{30}\}$ by reaction of $FeCl_3$ with Mo_{132} cluster anion with high yield and formulated it as $[Mo_{72}Fe_{30}O_{252}(CH_3COO)_{12}\{Mo_2O_7(H_2O)\}_2\{H_2Mo_2O_8(H_2O)\}(H_2O)_{91}]\cdot 150H_2O$. The structural analysis of $\{Mo_{72}Fe_{30}\}$ revealed that, the 12 pentagonal units are in the form of $\{Mo(Mo)_5\}$ and the 60 $\{Mo^V{}_2\}$ linkers were successfully replaced by 30 Fe^{III} linkers. The closer look into the structural arrangement of this cluster also revealed that, the central pentagonal bipyramidal MoO_7 group linked to the five MoO_6 octahedra by edge sharing and these 12 pentagonal units $[(Mo)Mo_5O_{21}(H_2O)_6]^{6-}$ connected to 30 Fe^{III} linkers $\{Fe^{III}O_5(H_2O)\}^{3+}$ to get the overall structure of the cluster i.e., icosahedral symmetry with 102 metal atoms and ligands (Figure 1.7). Müller group had also tried to study the stability of this cluster and in 2000 they published a report which has proved that the $\{Mo_{72}Fe_{30}\}$ Keplerate is more stable than the Keggin POM; they have incorporated the Keggin POM inside the $\{Mo_{72}Fe_{30}\}$ cluster without any structural changes in the ball structure.[154] The importance of this cluster was shown by many research groups by publishing ample number of research articles till date. In 2014, the Müller's group has also synthesized a completely amorphous form of this cluster containing compound, following a similar synthetic procedure used for ferrimolybdite.[155] In 2016, our group published

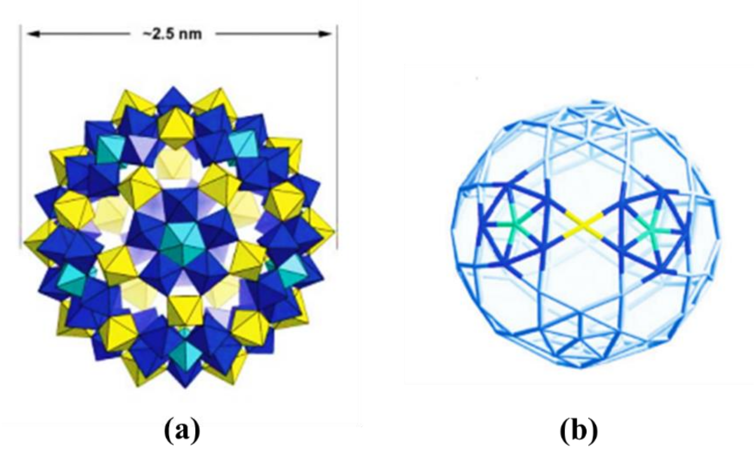

Figure 1.7. (a) Polyhedral and (b) Ball and stick representation of $\{Mo_{72}Fe_{30}\}$.[147]

an article on amorphous $\{Mo_{72}Fe_{30}\}$ ($Na_2[Mo_{72}Fe_{30}O_{252}(CH_3COO)_4(OH)_{16}(H_2O)_{108}]\cdot 180H_2O$) with an optimized synthetic procedure.[156] Later this compound also acquired an immense interest in many applicative fields.

1.2.5. $\{W_{72}Fe_{30}\}$ Keplerate

As stated earlier, Müller and group for the first time introduced $\{(W)(W)_5\}$ pentagonal units in to polyoxotungstates.[151] In 2009 they reported a $\{W_{72}Mo_{60}\}$ spherical Keplerate with $\{(W)(W)_5\}$ pentagons and Mo dinuclear linkers and in 2010 they reported the same pentagons linked with the Fe^{III} ions and forming a Keplerate formulated as $[Na_6(NH_4)_{20}\{Fe(H_2O)_6\}_2][\{W^{VI}_6O_{21}(SO_4)\}_{12}\{Fe(H_2O)\}_{30}(SO_4)_{13}(H_2O)_{34}]\cdot 200H_2O$ (Figure 1.8).[152] They synthesized it by treating the acidic sodium tungstate solution with ferrous sulphate which led to formation of yellow-colored crystals of $\{W_{72}Fe_{30}\}$. It is a cluster with icosahedral symmetry.

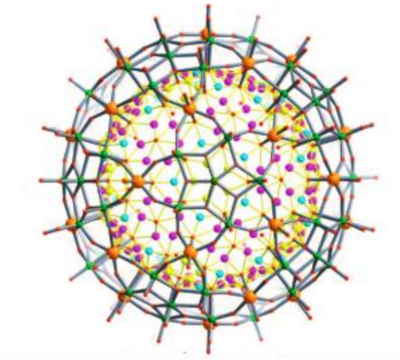

Figure 1.8. Ball and stick representation of $\{W_{72}Fe_{30}\}$.[152]

It consist of 12 $\{W^{VI}{}_6O_{21}(SO_4)\}$ pentagonal units, 30 Fe^{III} linkers $\{(Fe(H_2O))_{30}\}$ and it has 20 crown ether type $\{Fe_3W_3O_6\}$ pores which are hydrogen bonded with 20 NH_4^+ ions. It also has 25 SO_4^{2-} ligands inside the cavity of the cluster. This crystalline compound $\{W_{72}Fe_{30}\}$ is less explored in the application studies. Recently, our group published a report on amorphous $\{W_{72}Fe_{30}\}$ Keplerate compound with high yield which will be discussed in detail in the second chapter of this thesis.[157]

1.3. $\{Mo_{72}Fe_{30}\}$ and $\{W_{72}Fe_{30}\}$ related compounds and their applications

1.3.1. $\{Mo_{72}Fe_{30}\}$ and $\{W_{72}Fe_{30}\}$ clusters importance as Catalysts

$\{Mo_{72}Fe_{30}\}$ type giant Keplerate cluster containing compound $([Mo_{72}Fe_{30}O_{252}(CH_3COO)_{12}\{Mo_2O_7(H_2O)\}_2\{H_2Mo_2O_8(H_2O)\}(H_2O)_{91}]\cdot 150\ H_2O$ (which is 2.5 nm size) has been well explored in last few years. Thorough search on Scifinder, it was revealed that more than 126 research articles were published including their property studies and application in different fields; the relevant search results were summarized in Table 1.1. These $\{Mo_{72}Fe_{30}\}$ clusters were found to be magnetically active, owing to the presence 150 unpaired electrons per cluster contributed by 30 Fe(III) high spin centers and these properties were well exploited by various research groups.[158-165] Many research groups also worked on exploring its catalytic activity for example, selective oxidation of anthracene (H_2O_2 as an oxidant), isolation of carbon nanotubes with the help of chemical vapour deposition process, aerobic synthesis of benzimidazoles, epoxidation of olefins (H_2O_2 as an oxidant) and the selective oxidation of methanol are worth mentioning. [166-169] Photocatalytic activity of the compound $\{Mo_{72}Fe_{30}\}$ is also been well explored. Researchers from University of Birjand have shown that the both crystalline and amorphous forms of the compound $\{Mo_{72}Fe_{30}\}$ exhibit the photocatalytic degradation of organic dyes and conversion of H_2O_2 to H_2O and O_2.[170-172] There are numerous research groups who have been working on the bio-medical applications of this $\{Mo_{72}Fe_{30}\}$ cluster containing compound. $\{Mo_{72}Fe_{30}\}$ has been combined with biologically active substances like vitamin B_1 and insulin to improve the drug delivery process. $\{Mo_{72}Fe_{30}\}$ was also employed to study its ability to deliver antitumor drugs like doxorubicin.[173-174] Interestingly, when the $\{Mo_{72}Fe_{30}\}$ cluster is combined with tetracycline, it has exhibited the antibacterial activity.[175]

On the other hand, $\{W_{72}Fe_{30}\}$ is less explored compared to $\{Mo_{72}Fe_{30}\}$ cluster. To the best of our knowledge, till date, there is only one report found in literature related to the catalytic activity in which it catalyzes the selective oxidation of sulfides to sulfones in the presence of H_2O_2.[175]

This thesis primarily focuses more on the properties and applications of this $\{W_{72}Fe_{30}\}$ cluster containing compound.

Table 1.1. $\{Mo_{72}Fe_{30}\}$ and $\{W_{72}Fe_{30}\}$ compounds and related applications

S.No.	Compound	Application	Ref
1	Amorphous $\{Mo_{72}Fe_{30}\}$	Heterogeneous catalyst for condensation of various aromatic 1,2-diamines and aldehydes in green method.	172
2	Crystalline and Amorphous $\{Mo_{72}Fe_{30}\}$	Visible-light driven photocatalyst for conversion of H_2O_2 to H_2O and O_2.	171
3	Chitosan and $\{Mo_{72}Fe_{30}\}$	Electrocatalytic reduction of ClO_3^-, BrO_3^-, and IO_3^-.	176
4	$\{Mo_{72}Fe_{30}\}$ with Vitamin B_1	Thermodynamic interactions between $\{Mo_{72}Fe_{30}\}$ and Vitamin B_1 for drug delivery.	177
5	Amorphous $\{Mo_{72}Fe_{30}\}$	Photocatalytic degradation of organic dyes (Rhodamine B).	170
6	Amorphous $\{Mo_{72}Fe_{30}\}$	Association of $\{Mo_{72}Fe_{30}\}$ with vitamin B_1 and insulin for drug delivery.	173
7	Melem and $\{Mo_{72}Fe_{30}\}$	Photocatalytic activity toward hydrogen peroxide (H_2O_2) dismutation under visible-light irradiation.	178
8	$\{Mo_{72}Fe_{30}\}$ with Albumin	Stabilization of $\{Mo_{72}Fe_{30}\}$ by albumin for targeted drug delivery.	179

9	$\{PMo_{12}O_{40}@Mo_{72}Fe_{30}\}_n$	Photochemical water oxidation.	115
10	$\{Mo_{72}Fe_{30}\}$	$\{Mo_{72}Fe_{30}\}$ used as an anode material for Lithium-ion batteries.	180
11	POM@$(DOX)_{12}$	Binding of the antitumor drug doxorubicin (DOX) with the nanocluster polyoxometalate (POM) $\{Mo_{72}Fe_{30}\}$ for drug delivery.	174
12	$\{Mo_{72}Fe_{30}\}@TC_{12.5}$	Response of $\{Mo_{72}Fe_{30}\}$ towards the antibacterial activity along with the Tetracycline (TC).	175
13	Magnetic surfactant (MagSurf), $(C_{18})_2C_2N^+[FeCl_4]^-$, and POM, $\{Mo_{72}Fe_{30}\}$	POM/MagSurf serves as magnetic transporting vehicles to anchor and deliver a protein molecule, myoglobin (Mb).	181
14	Crystalline $\{Mo_{72}Fe_{30}\}$	Electrochemical behavior of $\{Mo_{72}Fe_{30}\}$ and aggregated $\{Mo_{72}Fe_{30}\}$.	182
15	$BW_{12} \subset Mo_{72}Fe_{30}$	Catalytic activity of Keggin encapsulated $Mo_{72}Fe_{30}$ in the oxidation of sulfides into sulfoxides or sulfones and oxidative desulfurization of dibenzothiophene with hydrogen peroxide.	183
16	Crystalline $\{Mo_{72}Fe_{30}\}$	Electrical conductivity at room temperature.	184
17	Metronidazole+$\{Mo_{72}Fe_{30}\}$	Wound dressing in rat model.	185
18	$PMo_{12} \subset Mo_{72}Fe_{30}$, $SiMo_{12} \subset Mo_{72}Fe_{30}$ and $BW_{12} \subset Mo_{72}Fe_{30}$	Study of catalytic efficiency in the epoxidation of olefins with hydrogen peroxide.	186
19	$H_xPMo_{12}O_{40} \subset H_4Mo_{72}Fe_{30}(CH_3COO)_{15}O_{254}$	Catalyst for epoxidation of alkenes in the presence of H_2O_2 as a green oxidant with a selectivity of 99%.	167
20	Crystalline $\{Mo_{72}Fe_{30}\}$	Isolation of Carbon nanotubes (CNTs) using chemical vapour deposition process catalysed by $\{Mo_{72}Fe_{30}\}$.	168
21	HDS-MoFeO from $\{Mo_{72}Fe_{30}\}$	Catalytic activity for selective oxidation of methanol.	169

22	$\{Mo_{72}Fe_{30}\}$+Doxorubicin	Targeted drug delivery as an antitumor medicine.	187
23	Crystalline $\{Mo_{72}Fe_{30}\}$	Preparation of bio-inspired $FeMo_2S_4$ microsphere via the one-step sulfuration of Keplerate-type polyoxometalate $\{Mo_{72}Fe_{30}\}$.	188
24	Crystalline $\{W_{72}Fe_{30}\}$	Catalyst for Selective oxidation of sulfides to sulfones in the presence of H_2O_2.	189
25	Crystalline $\{W_{72}Fe_{30}\}$	Effective electrocatalyst for the cathodic activation of O_2 in H_2O leading to the oxidation of light alkanes and alkenes.	190, 191

Despite of their applicability found in other fields, there are a few reports found reporting electrocatalytic activity of these giant inorganic clusters $\{Mo_{72}Fe_{30}\}$ and $\{W_{72}Fe_{30}\}$. Initially, Xiang Feng and his group have reported the electrochemical behavior of the $\{Mo_{72}Fe_{30}\}$ and their aggregates in aqueous solution. They have compared the simple cyclic voltammogram of the both $\{Mo_{72}Fe_{30}\}$ and its aggregations. Interestingly, the electrochemical behavior of both of them is same. In the same report they have additionally explained the major driving force of the self-assembly of this cluster.[182]

In 2009, Jingcheng Hao and coworkers fabricated composite films of $\{Mo_{72}Fe_{30}\}$ + Chitosan for the electrocatalytic reduction of ClO_3^-, BrO_3^- and IO_3^- in an acidic aqueous solution and the experimental results revealed the electrocatalytic activity followed the order of $IO_3^- > BrO_3^- > ClO_3^-$.[176] On the other hand, in 2017 Soumyajit Roy's group has taken a step forward to demonstrate the photochemical water oxidation to produce oxygen with the help of $\{PMo_{12}O_{40}@Mo_{72}Fe_{30}\}_n$ in which Keggin type POM is encapsulated inside the Keplerate $\{Mo_{72}Fe_{30}\}$. This catalyst was found to be very much stable under photochemical reaction conditions and it exhibited reasonably good turnover frequency (24.11 min^{-1}).[115]

$\{W_{72}Fe_{30}\}$ giant cluster has recently been recognized as an effective electrocatalyst for the cathodic activation of O_2 in aqueous medium for the oxidation of alkanes to alkenes at room temperature.[190] On the basis of above report, Neumann's group used this giant Keplerate $\{W_{72}Fe_{30}\}$ as electrocatalyst for arene hydroxylation, alkyl C-H bond activation, dealkylation of alkylamines and alkylsulphides including desaturation reactions. [191]

The reports in literature dealing with electrocatalytic activity of these cluster containing compounds, prompted us to think of exploring their applicability towards an unexplored area of $\{Mo_{72}Fe_{30}\}$ and $\{W_{72}Fe_{30}\}$ assisted electro catalytic water splitting. In one of their reports, Müller group showed that two electron reduced species of crystalline $\{Mo_{72}Fe_{30}\}$, in which the free electrons can be delocalized over 72 molybdenum ions on the surface of the $\{Mo_{72}Fe_{30}\}$ cage by maintaining the structure intact.[192] Hence we believe that $\{Mo_{72}Fe_{30}\}$ and $\{W_{72}Fe_{30}\}$ have a great potential to act as a heterogeneous electrocatalyst towards water reduction to produce molecular hydrogen (**Chapter-2**).

1.3.2. Keplerates as Proton Conductors

Proton conduction plays a crucial role in effective functioning of Fuel cells. Generally, a fuel cell has two chambers, namely, cathodic chamber and anodic chamber which are physically separated by a polyelectrolyte proton conducting membrane and are connected by external connector including a output device as illustrated in Figure 1.9. Anodic chamber oxidizes H_2/fuel to H^+/proton, whereas in cathodic chamber oxygen is reduced to water. The electrical energy is provided by electrons flow in the outer circuit and the protons from anodic chamber are transformed to cathodic chamber via proton conducting membrane which helps in the conversion of O_2 to H_2O. The fuel cell functions successfully only if the protons are allowed to transfer efficiently from anodic chamber to cathodic chamber. If they are not being efficiently scavenged and H^+ concentration increases at the anodic chamber, the functionality of the fuel cell will come to stall. In other words, the performance and efficiency of a fuel cell vastly depend on the efficiency of the proton conducting membrane separating its anodic and cathodic chambers.[19,20,193]

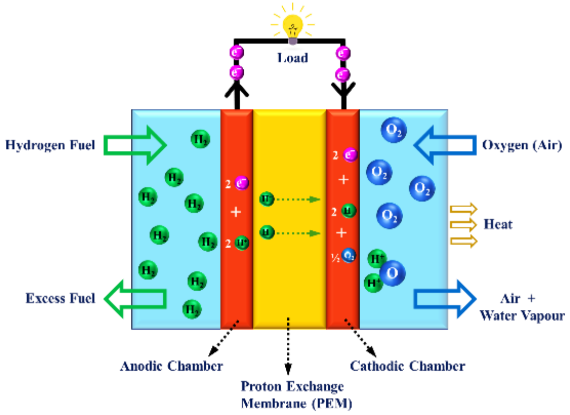

Figure 1.9. Schematic representation of proton exchange membrane fuel cell (PEMFC).

As we know that water is one of the good proton conductors, hence initial research was conducted in water and protic acid solutions (aqueous) to know the mechanism of proton conduction. Earlier, it was reported that the proton transports through water following Grotthuss proton hopping mechanism. Here proton transported through rotation of the water molecules which requires a less activation energy and shows high efficiency at a temperature below 100 ºC.[16,194] At elevated temperatures (temperatures above 100 ºC) the proton transport takes place through vehicular mechanism where the proton or proton source travels *via* proton conduction channel which requires a high activation energy compared to Grotthuss mechanism, due to which vehicular mechanism is efficient at higher temperature.[18]

Initially all the studies were carried out on proton conduction in water and acidic aqueous solutions which are considered as proton conducting materials. Despite of their good conduction properties their practical applications were limited. To widen the usability of proton conducting materials, researchers started moving towards the development of solid-state proton conductors.[20,193] In the search for potential solid state proton conducting systems, they found metal-oxides as suitable candidates for this purpose. Owing to the availability of wide range of structural information, the study of the proton transport mechanism through metal oxides became easy. However, these metal oxides and hydroxides came up with their own limitations like high activation energy requirement due to its rigid structure and lack of labile protons and they follow the vehicular mechanism.[195] Later the organic polymers like Nafion attracted the lime-light as an efficient proton conductor It was discovered in 1960 and has been a well-known and commercially available proton conductor. It contains a self-repeating unit of sulfonated tetrafluoroethylene and it is not only highly hydrophilic in nature but also very stable under harsh chemical environments and exhibits super-protonic conducting properties till the temperature of 100 ºC. As it is a polymer, it has been widely used as a proton conducting membrane in fuel cell.[196] However, it is also having a few drawbacks like (1) non-crystalline nature and lacks a predictable long-range structure which makes it difficult to relate its structure, function and its proton conductivity. (2) Manufacturing cost of Nafion is very high. (3) Nafion follows the Grotthuss mechanism for water assisted proton transport. Its proton conductivity decreases rapidly near 100 ºC as its hydrophilicity decreases.

Later MOFs came up as a link between organic polymers and metal oxides which combines the benefits of both materials.[193] From the last few years POMs are also being considered as good proton conducting materials because of their stable crystal structures and POMs can be easily converted to composites by reacting with the organic and inorganic motifs.[197-198] These also can be the replacement for Nafion and another proton conducting organic polymer.[199-200]

There are many reports where the POMs showing a good proton conducting properties (details summarized in Table 1.2). Like other POMs, Keplerate also penetrating the field as suitable proton conducting candidate, owing to their metal oxide nature with large number of hydroxyl groups. In their recent work Supriya and group measured proton conductivity of crystalline $\{Mo_{72}Fe_{30}\}$ which showed a proton conductivity of 1.85×10^{-3} at a temperature of 330 K. The required activation energy was 0.2 eV, which clearly indicates that it follows the Grotthuss proton hopping mechanism.[197] Thus, giant spherical clusters $\{Mo_{72}Fe_{30}\}$ and $\{W_{72}Fe_{30}\}$ have a high chance of having proton conduction property as they consist of large number of mobile protons generated from the acidic Fe(III)-OH_2 centers and lattice water molecules. Besides, it can be easily anticipated that the Grotthuss mechanism involved in proton conduction as the mobile protons from the Fe(III)-OH_2 forms a hydrogen bonding with lattice water molecules and forming H_3O^+-H_2O system which helps in the migration of protons to achieve high conductivity values.

In this thesis, proton conductivity studies of $\{W_{72}Fe_{30}\}$ cluster containing compound and its real time application of making a proton exchange membrane are presented in chapters 3 and 4 respectively. The scope of the thesis is extended to study the solid-state mechanochemical property of $\{Mo_{72}Fe_{30}\}$ that involves grinding of $\{Mo_{72}Fe_{30}\}$ crystalline solid and KI in solid state producing reduced $\{Mo_{72}Fe_{30}\}$ and molecular iodine. This is discussed in the last working chapter of this thesis.

Table 1.2. Table of various reported POM based proton conductors and their conductivity

SI.No.	**Compound**	**Conductivity ($S\ cm^{-1}$)**	**Activation Energy (eV)**	**Conditions**	**Reference**
1	$\{Mo_{72}Fe_{30}\}$	1.85×10^{-3}	0.24	<330K, 50% RH	197
2	Mo_{240}	1.03×10^{-1}	0.24	80 ºC, 98% RH	198
3	$HImMo_{132}$	4.98×10^{-2}	0.51	60 ºC, 98% RH	199
4	$HMeIm\text{-}Mo_{132}$	2.1×10^{-2}	0.44	60 ºC, 98% RH	199
5	$NbO_2(OH)PW_{12}$	7.25×10^{-3}	0.39	77 ºC, 98% RH	200
6	$H_{14}[Na_6(H_2O)_{12}]_4[K_{42}Ge_8W_{72}O_{272}(H_2O)_{60}]\cdot$solvent	6.8×10^{-2}	0.52	85 ºC, 98% RH	201

7	7	$[Cu_{12}(BTC)_8(H_2O)_{12}][H_3PW_{12}O_{40}]nH_2O$	4.76 x 10^{-5}	0.41	90 ºC, 70% RH	202
8	9	$K_{11}Eu[P_5W_{30}O_{110}K]\cdot 30H_2O$	1.0 x 10^{-2}	0.26	368K, 90% RH	203
9	10	$K_5H_6Eu[P_5W_{30}O_{110}K]\cdot 0.032PAA3000\cdot 30H_2O$	1.2 x 10^{-2}	0.48	368K, 90% RH	203
10	13	$K_8H_4[Bi(H_2O)P_5W_{30}O_{110}]\bullet 0.03PAA5000\bullet 19H_2O$	8.5 x 10^{-3}	0.16	368K, 75% RH	204
11	14	$K_{13.0}H_{1.0}[Na(H_2O)P_5W_{30}O_{110}]\cdot 0.03PAA5000\cdot 20H_2O$	1.7 x 10^{-3}	0.40	338K, 75% RH	205
12	17	$[La_{10}Ni_{48}W_{140}Sb_{16}P_{12}O_{568}(OH)_{24}(H_2O)_{20}]^{86-}$	2.05 x 10^{-2}	0.22	295K, 100% RH	206
13	19	$H_5PW_{10}V_2O_{40}\cdot 15H_2O$	1.27 x 10^{-2}	0.263	18 ºC, 80% RH	207
14	21	$H_2[Cu_2OL_3(H_2O)_2][Ce(L)(H_2O)_3(PW_{11}O_{39})]\cdot 17H_2O$	3.175 x 10^{-4}	0.456	85 ºC, 98% RH	208
15	22	$((TEAH)_7K_2H_9\{P_2W_{18}\}\subset\{Mo_{24}Fe_{12}\}\cdot 116H_2O)$	5.9 x 10^{-3}	0.28	368K, 90% RH	209
16	23	$((TEAH)_{14}Na_{10}K_8H_8\{P_5W_{30}\}_2\subset\{Mo_{22}Fe_8\}\cdot 50H_2O)$	1.7 x 10^{-2}	0.31	368K, 90% RH	209
17	24	$[Cu(H_2bibb)_2(H_2O)_3(\alpha P_2W_{18}O_{62})]\cdot 10.5H_2O$	2.52 x 10^{-4}	0.42	85 ºC, 98% RH	210
18	27	$H_3PW_{12}O_{40}\cdot 29H_2O$	1.7 x 10^{-1}	0.14	25 ºC, 80±5% RH	211
19		$NaH_{15}\{[P_2W_{15}Nb_3O_{62}]_2(4PBA)_2((4PBA)_2O)\}\cdot 53H_2O$	1.59 x 10^{-1}	0.66	90 ºC, 98% RH	212
20		$H_{14}[Na_6(H_2O)_{12}]_4[K_{42}Ge_8W_{72}O_{272}(H_2O)_{60}]\cdot solvent$	6.8 x 10^{-2}	0.52	85 ºC, 98% RH	201

21	$\{Na_7[(nBu)_4N]_{17}\}[Zn(P_3Mo_6O_{29})_2]_2\cdot$solvent	1.04×10^{-2}	0.22	80 ^{o}C, 75% RH	213
22	$H_{13}(HIm)_4K_2Na_4(H_2O)_9[Sb^{III}{}_9Sb^{V}Sm_3O_{14}{}^{-}(H_2O)_3][(SbW_9O_{33})_3(PW_9O_{34})]\cdot 26H_2O$	1.64×10^{-2}	0.54	85 ^{o}C, 98% RH	214
23	$(H_2bimb)_3[Zn_3(H_6P_4Mo_6O_{31})_2]$	4.54×10^{-3}	0.46	85 ^{o}C, 98% RH	215
24	$H[Ce(H_2O)_4]_2[Mn^{V1}{}_3O_{38}]\cdot 9NMP\cdot 17H_2O$	4.68×10^{-3}	0.45	61 ^{o}C, 97% RH	216
25	$H[La(H_2O)_4]_2[Mn^{V1}{}_3O_{38}]\cdot 9NMP\cdot 17H_2O$	3.46×10^{-3}	0.48	61 ^{o}C, 97% RH	216
26	$\{(NH_4)_{13}[Mo_{28}{}^{V}Mo_{126}{}^{VI}O_{456}H_{34}(H_2O)_{70}]Cl_{17}(ClO_4)_{14}\cdot mH_2O$ $(m\approx 240)\}_n$ (3D-$\{Mo_{154}\}_n$)	1.1×10^{-2}	0.264	22 ^{o}C, 100% RH	217
27	$C_{108}H_{36}Cu_{24}N_{48}O_{116}PMo_4V_8$	8.03×10^{-3}	0.96	343K, 98% RH	218
28	$((TEAH)_7K_2H_9\{P_2W_{18}\}\subset\{Mo_{24}Fe_{12}\}\cdot 116H_2O)$	5.9×10^{-3}	0.28	368K, 90% RH	209
29	(TMA)KNa-$Mo_{16}S_{16}Se_8$	1.2×10^{-2}	0.77	55 ^{o}C, 97% RH	219
30	$H_3PMo_{12}O_{40}\cdot$29H2O	1.8×10^{-1}	0.16	25 ^{o}C, 80±5% RH	211

1.4. Motivation of the work

In the wake of modern world's need for sustainable energy storage and effective energy conversion systems, generating water splitting catalysts for green hydrogen production and highly efficient solid state proton conducting material are found to be vital. In water splitting, both the HER and OER have their own significance and they also come with their own drawbacks which needs to be addressed. In the journey towards fabricating efficient materials for said purpose, our group previously reported the complete amorphous compound of $\{Mo_{72}Fe_{30}\}$ and measured its stability at different temperatures. Similarly, part of the work, presented in this thesis, mainly deals with designing and producing a complete amorphous compound of $\{W_{72}Fe_{30}\}$ and its role in electrocatalytic water splitting reaction along with the $\{Mo_{72}Fe_{30}\}$ cluster containing compound (**chapter 2**). In following section of the thesis (**chapter 3**), proton conductivity studies on$\{W_{72}Fe_{30}\}$ cluster containing compound have presented along with its incorporation as a nanofiller in to a polymer membrane for proton conductivity applications. In next chapter (**chapter 4**) of the thesis, the scope of the work extended to synthesizing a complete inorganic gel out of $\{W_{72}Fe_{30}\}$ cluster containing compound. Formed gel's strength and elasticity were measured by rheology studies and it was utilized as a proton conducting gel material for further studies. On the other hand, there were few reports related to solid state transformation of POM containing compounds. This made us to study the solid-state transformation of $\{Mo_{72}Fe_{30}\}$ cluster containing compound and its catalytic activity towards the conversion of KI to I_2 at room temperature (**chapter 5**). Since, in the present thesis work, I have synthesized a different form of $\{W_{72}Fe_{30}\}$ cluster containing compounds and studied extensively to understand their electrocatalytic behavior towards the water splitting and proton conduction and I strongly believe that knowledge added to the field through this work would be significant and help others positively in moving a step closer to which are important to construct sustainable energy storage and effective energy conversion systems.

1.5. References

1 BP Statistical Review of World Energy, **2022**.

2 Qazi, A.; Hussain, F.; Rahim, N. A.; Hardaker, G.; Alghazzawi, D.; Shaban, K.; Haruna, K. Towards Sustainable Energy: A Systematic Review of Renewable Energy Sources, Technologies, and Public Opinions. *IEEE Access*. **2019**, *7*, 63837-63851.

3 US EIA. International Energy Outlook 2021 (IEO2021). US EIA. Annual Energy Outlook **2022**, *IEO2022*.

4 Ranasinghe, R.; Ruane, A.C.; Vautard, R.; Arnell, N.; Coppola, E.; Cruz, F.A.; Dessai, S.; Islam, A. S.; Rahimi, M.; Ruiz Carrascal, D.; Sillmann, J.; Sylla, M. B.; Tebaldi, C.; Wang, W.; Zaaboul, R. Climate Change Information for Regional Impact and for Risk Assessment (Chapter 12), **2021**, 1767–1926.

5 Crippa, M.; Guizzardi, D.; Muntean, M.; Schaaf, E.; Solazzo, E.; Monforti-Ferrario, F.; Olivier, J.G.J.; Vignati, E. *Fossil CO_2 emissions of all world countries - 2020 Report*; 2020.

6 Aiguo, D. Increasing drought under global warming in observations and models. Nature climate change. **2013**, *3*, 52-58.

7 Global Energy Review 2021. Assessing the effects of economic recoveries on global energy demand and CO_2 emissions in 2021. *International Energy Agency*, **2021**, 1-32.

8 World Energy Transitions Outlook 2022. *International Renewable Energy Agency (IRENA 2022)*, **2022**.

9 Turner, J. A. A Realizable Renewable Energy Future. *Science*, **1999**, *285*, 687-689.

10 Dyatkin, B.; Presser, V.; Heon, M.; Lukatskaya, M. R.; Beidaghi, M.; Gogotsi, Y. Development of a Green Supercapacitor Composed Entirely of Environmentally Friendly Materials. *ChemSusChem*, **2013**, *6*, 2269-2280.

11 Ma, T.; Yang, H.; Lu, L. Development of hybrid battery–supercapacitor energy storage for remote area renewable energy systems. *Applied Energy*, **2015**, *153*, 56-62.

12 Akram, U.; Khalid, M.; Shafiq, S. An Innovative Hybrid Wind-Solar and Battery-Supercapacitor Microgrid System Development and Optimization. *IEEE Access*, **2017**, *5*, 2169-3536.

13 Moller, K. T.; Jensen, T. R.; Akiba, E.; Li. H. W. Hydrogen - A sustainable energy carrier. *Progress in Natural Science: Materials International*. **2017**, *27*, 34-40.

14 Carmo, M.; Fritz, D. L.; Mergel, J.; Stolten, D. A comprehensive review on PEM water electrolysis. International Journal of Hydrogen Energy. **2013**, *38*, 4901-4934.

15 Kumar, S. S.; Himabindu, V. Hydrogen production by PEM water electrolysis – A review. *Materials Science for Energy Technologies*. **2019**, *2*, 442–454.

16 Kreuer, K. D.; Proton Conductivity: Materials and Applications. *Chem. Mater.* **1996,** *8*, 610-641.

17 Meng, Q.; Cai, K.; Chen, Y.; Chen, L. Research progress on conducting polymer based supercapacitor electrode materials. *Nano Energy*. **2017**, *36*, 268-285.

18 Belousov, V. V. Next-Generation Electrochemical Energy Materials for Intermediate Temperature Molten Oxide Fuel Cells and Ion Transport Molten Oxide Membranes. *Acc. Chem. Res.* **2017**, *50*, 273-280.

19 Robert, C. L.; Valle, K.; Pereira, F.; Sanchez, C. Design and properties of functional hybrid organic–inorganic membranes for fuel cells. *Chem. Soc. Rev.*, **2011**, *40*, 961-1005.

20 Scofield, M. E.; Liu, H.; Wong, S. S. A concise guide to sustainable PEMFCs: recent advances in improving both oxygen reduction catalysts and proton exchange membranes. *Chem. Soc. Rev.*, **2015**, *44*, 5836-5860.

21 Molmen, L.; Eiler, K.; Fast, L.; Leisner, P.; Pellicer, E. Recent advances in catalyst materials for proton exchange membrane fuel cells. *APL Mater*. **2021**, *9*, 040702.

22 Yamase, T. Photo- and Electrochromism of Polyoxometalates and Related Materials. *Chem Rev.*, **1998**, *98*, 307-325.

23 Blazevic, A.; Rompel, A. The Anderson-Evans Polyoxometalate: From Inorganic Building Blocks via Hybrid Organic-Inorganic Structures to Tomorrows ―BioPOM.‖ Coord. Chem. Rev., **2016**, *307*, 42-64.

24 Pope, M. T.; Sadakane, M.; Kortz, U. Celebrating Polyoxometalate Chemistry. *Eur J Inorg Chem.*, **2019**, *3*, 340-342.

25 Miras, H. N.; Yan, J.; Long, D. L.; Cronin, L. Engineering Polyoxometalates with Emergent Properties. Chem Soc Rev., **2012**, *41*, 7403-7430.

26 Long, D. L.; Tsunashima, R.; Cronin, L. Polyoxometalates: Building Blocks for Functional Nanoscale Systems. *Angew Chemie - Int Ed.* **2010**, *49*, 1736-1758.

27 Long, D. L.; Burkholder, E.; Cronin, L. Polyoxometalate Clusters, Nanostructures and Materials: From Self Assembly to Designer Materials and Devices. *Chem Soc Rev.*, **2007**, *36*, 105-121.

28 Katsoulis, D. E. A Survey of Applications of Polyoxometalates. *Chem Rev.*, **1998**, *98*, 359-387.

29 Izzet, G.; Volatron, F.; Proust, A. Tailor–made Covalent Organic-Inorganic Polyoxometalate Hybrids: Versatile Platforms for the Elaboration of Functional Molecular Architectures. *Chem Rec.*, **2017**, *17*, 250-266.

30 Casan-Pastor, N.; Gomez-Romero, P. Polyoxometalates: from Inorganic Chemistry to Materials Science. *Front. Biosci. (Landmark Ed)*, **2004**, *9*, 1759–1770.

31 Li, D.; Ma, P.; Niu, J.; Wang, J. Recent advances in transition-metal-containing Keggin-type polyoxometalate-based coordination polymers. *Coord Chem Rev.*, **2019**, *392*, 49-80.

32 Proust, A.; Matt, B.; Villanneau, R.; Guillemot, G.; Gouzerh, P.; Izzet, G. Functionalization and Post-Functionalization: A Step Towards Polyoxometalate-Based Materials. *Chem Soc Rev.*, **2012**, *41*, 7605-7622.

33 Cui, F.-Y.; Ma, X.-Y.; Li, C.; Dong, T.; Gao, Y.-Z.; Han, Z.-G.; Chi, Y.-N.; Hu, C.-W. Two New Organic-Inorganic Hybrid Compounds Based on Metal-Pyrazine Coordination Polymers and Keggin Polyoxometalates: Effect of Metal Ions on the Structure. *J. Solid State Chem.*, **2010**, *183*, 2925-2931.

34 Bu, Y.; Liu, R.; Zhen, M.; Li, F.; Sun, Z.; Xu, L. A Hybrid Compound Containing Polyoxoanions and Organic Dye Cations with Visible-Light Photocatalytic H2 Evolution Activity. *Inorg Chem. Commun.*, **2015**, *62*, 34-36.

35 Li, M. X.; Zhang, Y.; Zhu, Z. M.; Su, F.; Zhang, L. C.; Sang, X. J. Synthesis, Characterization and Electrocatalytic Properties of two New Open Wells-Dawson-type Tungstosilicates. *J. Coord. Chem.*, **2020**, *73*, 2437-2449.

36 Walsh, J. J.; Bond, A. M.; Forster, R. J.; Keyes, T. E. Hybrid Polyoxometalate Materials for Photo(electro-) Chemical Applications. *Coord. Chem. Rev.*, **2016**, *306*, 217-234.

37 Hajizadeh, F.; Zonoz, F. M.; Duval, S.; Maleki, B.; Amiri, A. Synthesis and Investigation of two New Crystalline Organic Inorganic Nano-Hybrids Based on Wells-Dawson Vanadotungstates and 1H-1, 2, 4-triazole as Electro- and Photocatalysts. *J. Mol. Struct.*, **2021**, *1224*, 129003-129013.

38 Niu, J.-Q.; Zhao, Q.; Xin, X.; Zhang, Y.-Q.; Hu, N.; Ma, Y.-Y.; Han, Z.-G. Krebs-type Polyoxometalate-based Crystalline Materials: Synthesis, Characterization and Catalytic Performance. *J. Coord. Chem.*, **2020**, *73*, 2391-2401.

39 Ye, J. J.; Wu, C. De. Immobilization of Polyoxometalates in Crystalline Solids for Highly Efficient Heterogeneous Catalysis. *Dalton Trans.*, **2016**, *45*, 10101-10112.

40 Lefebvre, F. Polyoxometalates Encapsulated in Inorganic Materials: Applications in Catalysis. *New and Future Developments in Catalysis: Hybrid Materials, Composits, and Organocatalysts, Elsevier*, **2013**, 265-288.

41 Keggin, J. F. Structure of the Crystals of 12-Phosphotungstic Acid. *Nature*, **1933**, *132*, 351.

42 Berzelius, J. Beitrag zur näheren Kenntniss des Molybdäns, *Annalen der Physik*, **1826**, *82*, 369-392.

43 Pauling, L. The Principles Determining the Structure of Complex Ionic Crystals *J. Am. Chem. Soc.*, **1929**, *51*, 4, 1010-1026.

44 Pope, M.; Varga, G. Proton Magnetic Resonance of Aqueous Metatungstate Ion: Evidence for Two Central Hydrogen Atoms. *Chem. Commun.*, **1966**, 653-654.

45 So, H.; Pope, M. Origin of some charge-transfer spectra. Oxo compounds of vanadium, molybdenum, tungsten, and niobium including heteropoly anions and heteropoly blues. *Inorg. Chem.*, **1972**, *11*, 1441 - 1443.

46 Leparulo-Loftus, M. A.; Pope, M. Vanadium-51 NMR spectroscopy of tungstovanadate polyanions. Chemical shift and line-width patterns for the identification of stereoisomers. *Inorg. Chem.*, **1987**, *26*, 2112 - 2120.

47 Mbomekalle, I.; Keita, B.; Lu, Y. W.; Nadjo, L.; Contant, R.; Belai, N.; Pope, M. Synthesis and Electrochemistry of the Monolacunary Dawson-Type Tungstoarsenate $[H_4AsW_{17}O_{61}]^{11-}$ and Some First-Row Transition-Metal Ion Derivatives. *Eur. J. Inorg. Chem.*, **2004**, *2004*, 4132 - 4139.

48 Souchay, P. Polyanions et polycations; Monographies de chimie mineerale; *GaithierVillars*, Paris, **1963**.

49 Varga, G.; Papaconstantinou, E.; Pope, M. Heteropoly blues. IV. Spectroscopic and magnetic properties of some reduced polytungstates. *Inorg. Chem.*, **1970**, *9*, 662-667.

50 Scheele, C. W. Hermbstädt DSF, Sämtliche Physische und Chemische Werke. *ed. Martin Sändig, Niederwalluf/Wiesbaden*, **1971**, 185.

51 Gouzerh, P.; Che, M. From Scheele and Berzelius to Murller. Polyoxometalates (POMs) Revisited and the "Missing Llink" Between the Bottom up and top Down Approaches. *Actual. Chim.*, **2006**, *298*, 9–22.

52 Svanberg, L.; Struve, H. Atomgewichte der einfachen Körper. *Justus Liebigs Ann. Chem.*, **1848**, *68*, 209–218.

53 Marignac, J.-C. G. d. *Ann. Chim. Phys.*, **1864**, *4*, 1.

54 Struve, H. Ueber verschiedene Doppelsalze der Molybdänsäure und Wolframsäure. *Journal für Praktische Chemie*, **1854**, *61*, 449-470.

55 Werner, A. Beitrag zur Konstitution anorganischer Verbindungen. *Z. Anorg. Chem.*, **1893**, *3*, 267-330.

56 Miolati, A.; Pizzighelli, R. Zur Kenntnis der komplexen Säuren I. 1. Über die Leitfähigkeit von molybdänsäurehaltigen Gemischen. *Journal für Praktische Chemie*, **1908**, *77*, 417-456.

57 Rosenheim, V. A.; Jaenicke, V. J. The Knowledge of Iso-and Hetero-Poly Acids XV Announcement-Crital Experiments on the Constitution of Hetero-Poly Acids. *Z. Für Anorg. Allg. Chem*, **1917**, *100*, 304-354.

58 Lindqvist, I.; The structure of the tetramolybdate ion. *ARKIV FOR KEMI*, **1950**, *2*, 349-355.

59 Friedrich, W.; Knipping, P.; Laue, M.; Sitzungsber. K. Bayer. *Akad. Wiss. Math. Phys. Kl.*, **1912**, 303–322.

60 Laue, M. Phys. Z., **1913**, *14*, 1075–1079. (d) Bragg, W. H. X-rays and Crystals. *Nature*, **1912**, *90*, 219.

61 Fuchs, J.; Knopnadel, I. Crystal Structure of Disodium Tetramethylammonium Octamolybdate Dihydrate ($Na_2[N(CH_3)_4]_2Mo_8O_{26}.2H_2O$) and the relation between molybdenum-oxygen distance and bond order in polymolybdates. *Z. Kristallogr. Kristallgeom. Kristallphys. Kristallchem.*, **1982**, *158*, 165-180.

62 Anderson, J. S. Constitution of the Poly-acids. *Nature*, **1937**, *140*, 850.

63 Evans, H. T. The Crystal Structures of Ammonium and Potassium Molybdotellurates. *J. Am. Chem. Soc.*, **1948**, *70*, 1291–1292.

64 Evans, H. T. Refined molecular structure of the heptamolybdate and hexamolybdotellurate ions. *J. Am. Chem. Soc.*, **1968**, *90*, 3275–3276.

65 Evans, H. T. The Molecular Structure of the Hexamolybdotellurate ion in the Crystal Complex with Telluric acid $(NH_4)_6[TeMo_6O_{24}].Te(OH)_6.7H_2O$. *Acta Crystallogr., Sect. B: Struct. Crystallogr. Cryst. Chem.*, **1974**, *30*, 2095–2112.

66 Fuchs, J.; Hartl, H. Anion Structure of Tetrabutylammonium Octamolybdate $[N(C_4H_9)_4]_4 Mo_8O_{26}]$. *Angew. Chem., Int. Ed. Engl.*, **1976**, *15*, 375–376.

67 Gouzerh, P.; Proust, A. Main-Group Element, Organic, and Organometallic Derivatives of Polyoxometalates. *Chem. Rev.*, **1998**, *98*, 77–111.

68 Song, Y.-F.; Long, D.-L.; Cronin, L. *Angew. Chem., Int. Ed.*, **2007**, *46*, 3900–3904.

69 Song, Y.-F.; Long, D.-L.; Kelly, S. E.; Cronin, L. Sorting the Assemblies of Unsymmetrically Covalently Functionalized Mn-Anderson Polyoxometalate Clusters with Mass Spectrometry. *Inorg. Chem.*, **2008**, *47*, 9137–9139.

70 Hasenknopf, B.; Delmont, R.; Herson, P.; Gouzerh, P. Anderson-Type Heteropolymolybdates Containing Tris(alkoxo) Ligands: Synthesis and Structural Characterization. *Eur. J. Inorg. Chem.*, **2002**, *2002*, 1081–1087.

71 Kozhevnikov, I. Catalysis by Polyoxometalates; Catalysis for Fine Chemical Synthesis. *Wiley & Sons*, **2002**, *2*, 216.

72 Hill, C. L. Introduction: Polyoxometalates Multicomponent Molecular Vehicles to Probe Fundamental Issues and Practical Problems. *Chem. Rev.*, **1998**, *98*, 1-2.

73 Tsigdinos, G. A.; Hallada, C. J. Molybdovanadophosphoric acids and their salts. I. Investigation of methods of preparation and characterization. *Inorg. Chem.*, **1968**, *7*, 437-441

74 Kozhevnikov, I. V.; Matveev, K. I. Heteropolyacids in Catalysis. *Russ. Chem. Rev.*, **1982**, *51*, 1075-1088.

75 Kozhevnikov, I. V.; Matveev, K. I. Homogeneous catalysts based on heteropoly acids (review). *Appl. Catal.*, **1983**, *5*, 135-150.

76 Kozhevnikov, I. V. Advances in Catalysis by Heteropolyacids. *Russ. Chem. Rev.*, **1987**, *56*, 811-825.

77 Kozhevnikov, I. V. Heteropoly Acids and Related Compounds as Catalysts for Fine Chemical Synthesis. *Catal. Rev.*, **1995**, *37*, 311-352.

78 Kozhevnikov, I. V. Sustainable heterogeneous acid catalysis by heteropoly acids. *J. Mol. Catal. A: Chem.*, **2007**, *262*, 86-92.

79 Hill, C. L.; Prosser-McCartha, C. M. Homogeneous catalysis by transition metal oxygen anion clusters. *Coord. Chem. Rev.*, **1995**, *143*, 407- 455.

80 Grigoriev, V. A.; Hill, C. L.; Weinstock, I. A. Role of Cation Size in the Energy of Electron Transfer to 1:1 Polyoxometalate Ion Pairs $\{(M^+)(X^{n+}VW_{11}O_{40})\}^{(8-n)-}$ (M = Li, Na, K). *J. Am. Chem. Soc.*, **2000**, *122*, 3544 - 3545.

81 Geletii, Y. V.; Atalla, R. H.; Bailey, A. J.; Delannoy, L.; Hill, C. L.; Weinstock, I. A. Oxidation catalysis by polyoxometalates: fundamental electron-transfer phenomena. *In Proceedings of the 13th International Symposium on Homogenous Catalysis*, **2002**, 165.

82 Hill, C. L. Progress and challenges in polyoxometalate-based catalysis and catalytic materials chemistry. *J. Mol. Cat. A: Chem.*, **2007**, *262*, 2-6.

83 Pope, M. T.; Müller, A. Polyoxometalate Chemistry: An Old Field with New Dimensions in Several Disciplines. *Angew. Chem. Int. Ed.*, **1991**, *30*, 34-48.

84 Pope, M. T.; Müller, A. Introduction to polyoxometalate chemistry: from topology via self-assembly to applications, *Springer Netherlands*, **2001**, 1-6.

85 Müller, A.; Roy, S. En route from the mystery of molybdenum blue via related manipulatable building blocks to aspects of materials science. *Coord. Chem. Rev.*, **2003**, *245*, 153-166.

86 Nicoara, A.; Patrut, A.; Margineanu, D.; Müller, A. Electrochemical investigation of molecular growth of the $\{Mo_{57}V_6\}$ polyoxometalate cluster. *Electrochem. Comm.*, **2003**, *5*, 511-518.

87 Gouzerh, P.; Che, M. Polyoxometalates (POMs) revisited and the “missing link” between the bottom up and top down approaches. *l'actualité chimique*, **2006**, *298*, 9-22.

88 Weinstock, I. A.; Müller, A. Oxo-Metalate Building Blocks: Conceptual Competitors for Tetravalent Carbon? *Isr. J. Chem.*, **2011**, *51*, 176-178.

89 Hallada, C. J.; Tsigdinos, G.; Hudson, B. S. Molybdovanadophosphoric acids and their salts. II. Investigation of solution properties *J. Phys. Chem. A*, **1968**, *72*, 4304-4307.

90 Tsigdinos, G. A.; Hallada, C. J. Solution properties of 12-heteropoly acids of molybdenum. *Inorg. Chem.*, **1970**, *9*, 2488-2492.

91 Tsigdinos, G. A.; Hallada, C. J. Synthesis and electrochemical properties of heteropolymolybdates. *J. Less Com. Metals*, **1974**, *36*, 79-93.

92 Tsigdinos, G. A.; Moh, G. H. Aspects of molybdenum and related chemistry. *Berlin: Springer*. **1978**, *76*, 1-64.

93 Neumann, R.; Dahan, M. Molecular Oxygen Activation by a Ruthenium-Substituted "Sandwich" Type Polyoxometalate, *J. Am. Chem. Soc.*, **1998**, *120*, 11969-11976.

94 Khenkin, A. M.; Weiner, L.; Wang, Y.; Neumann, R. Electron and Oxygen Transfer in Polyoxometalate, $H_5PV_2Mo_{10}O_{40}$, Catalyzed Oxidation of Aromatic and Alkyl Aromatic Compounds: Evidence for Aerobic Mars−van Krevelen-Type Reactions in the Liquid Homogeneous Phase. *J. Am. Chem. Soc.*, **2001**, *123*, 8531-8542.

95 Hirao, H.; Kumar, D.; Chen, H.; Neumann, R.; Shaik, S. The Electronic Structure of Reduced Phosphovanadomolybdates and the Implications on Their Use in Catalytic Oxidation Initiated by Electron Transfer. *J. Phys. Chem. C,* **2007**, *111*, 7711-7719.

96 Khenkin, A. M.; Leitus, G.; Neumann, R. Electron Transfer−Oxygen Transfer Oxygenation of Sulfides Catalyzed by the $H_5PV_2Mo_{10}O_{40}$ Polyoxometalate. *J. Am. Chem. Soc.,* **2010**, *132*, 11446-11448.

97 Efremenko, I.; Neumann, R. Protonation of Phosphovanadomolybdates $H_{3+x}PV_xMo_{12-x}O_{40}$: Computational Insight into Reactivity. *J. Phys. Chem. A,* **2011**, *115*, 4811-4826.

98 Efremenko, I.; Neumann, R. Computational Insight into the Initial Steps of the Mars–van Krevelen Mechanism: Electron Transfer and Surface Defects in the Reduction of Polyoxometalates. *J. Am. Chem. Soc.,* **2012**, *134*, 20669-20680.

99 Haider, A.; Ibrahim, M.; Bassil, B. S.; Carey, A.M.; Nguyen Viet, A.; Xing, X.; Ayass, W. W.; Miñambres, J. F.; Liu, R.; Zhang, G.; Keita, B.; Mereacre, V.; Powell, Introduction 15 A. K.; Balinski, K.; N'Diaye, A. T.; Kuepper, K.; Chen, H.-Y.; Stimming, U.; Kortz, U. Mixed-Valent Mn16-Containing Heteropolyanions: Tuning of Oxidation State and Associated Physicochemical Properties. *Inorg. Chem*., **2016**, *55*, 2755-2764.

100 Wang, K.-Y.; Bassil, B. S.; Carey, A. M.; Mougharbel, A. S.; Kortz, U. Reinvestigation of Dilacunary 19-Tungsto-2-arsenate(III) $[As^{III}_2W_{19}O_{67}(H_2O)]^{14-}$ Including ^{183}W NMR Study in Solution. *Eur. J. Inorg. Chem.*, **2017**, *2017*, 4210–4213.

101 Bassil, B. S.; Haider, A.; Ibrahim, M.; Mougharbel, A. S.; Bhattacharya, S.; Christian, J. H.; Bindra, J. K.; Dalal, N. S.; Wang, M.; Zhang, G.; Keita, B.; Rutkowska, I. A.; Kulesza, P. J.; Kortz, U. 15-Copper(ii)-containing 36-tungsto-4-silicates(iv) $[Cu_{15}O_2(OH)_{10}X(A\text{-}\alpha\text{-}SiW_9O_{34})_4]^{25-}$ (X = Cl, Br): synthesis, structure, magnetic properties, and electrocatalytic CO_2 reduction. Dalton Trans. 2018, 47, 12439–12448.

102 Douvas, A. M.; Tsikrizis, D.; Tselios, C.; Kennou, S.; Haider, A.; Mougharbel, A. S.; Kortz, U.; Palilis, L. C.; Hiskia, A.; Coutsolelos, A. G.; Vasilopoulou, M.; Argitis, P. Multi-electron reduction of Wells–Dawson polyoxometalate films onto metallic, semiconducting and dielectric substrates. *Phys. Chem. Chem. Phys.*, **2019**, *21*, 427-437.

103 Ma, T.; Yang, P.; Dammann, I.; Lin, Z.; Mougharbel, A. S.; Li, M.-X.; Adăscăliţei, F.; Mitea, R.; Silvestru, C.; Thorstenson, C.; Ullrich, M. S.; Cseh, K.; Jakupec, M. A.; Keppler, B. K.; Donalisio, M.; Cavalli, R.; Lembo, D.; Kortz, U. Tetra-(p-tolyl)antimony(III)-Containing Heteropolytungstates, $[\{(p\text{-tolyl})Sb^{III}\}_4(A\text{-}\alpha\text{-}XW_9O_{34})_2]^{n-}$ (X = P, As, or Ge): Synthesis, Structure, and Study of Antibacterial and Antitumor Activity. *Inorg. Chem.*, **2020**, *59*, 2978-2987.

104 Zhan, C.; Zheng, Q.; Long, D. -L.; Vilà-Nadal, L.; Cronin, L. Controlling the Reactivity of the $[P_8W_{48}O_{184}]^{40-}$ Inorganic Ring and Its Assembly into POMZite Inorganic Frameworks with Silver Ions. *Angew. Chem. Int. Ed.*, **2019**, *131*, 17442-17446.

105 Chen, J.-J.; Symes, M. D.; Cronin, L. Highly reduced and protonated aqueous solutions of $[P_2W_{18}O_{62}]^{6-}$ for on-demand hydrogen generation and energy storage. *Nature Chem.*, **2018**, *10*, 1042-1047.

106 Duros, V.; Grizou, J.; Xuan, W.; Hosni, Z.; Long, D. -L.; Miras, H. N.; Cronin, L. Human versus Robots in the Discovery and Crystallization of Gigantic Polyoxometalates. *Angew. Chem. Int. Ed.*, **2017**, *56*, 10815-10820.

107 Zang, H.-Y.; Chen, J.-J.; Long, D.-L.; Cronin, L.; Miras, H. Assembly of inorganic $[Mo_2S_2O_2]^{2+}$ panels connected by selenite anions to nanoscale chalcogenide–polyoxometalate clusters. *N. Chem. Sci.*, **2016**, *7*, 3798-3804.

108 Sartzi, C.; Miras, H. N. ; Vilà-Nadal, L.; Long, D.-L. ; Cronin, L. Trapping the δ Isomer of the Polyoxometalate-Based Keggin Cluster with a Tripodal Ligand. *Angew. Chem. Int. Ed.*, **2015**, *54*, 15488-15492.

109 Luo, J.; Zhang, B.; Yvon, C.; Hutin, M.; Gerislioglu, S.; Wesdemiotis, C.; Cronin, L.; Liu, T. Self-Assembly of Polyoxometalate–Peptide Hybrids in Solution: Elucidating the Contributions of Multiple Possible Driving Forces. *Eur. J. Inorg. Chem.*, **2019**, *2019*, 380-386.

110 Zhou, J.; Hu, J.; Li, M.; Li, H.; Wang, W.; Liu, Y.; Winans, R. E.; Li, T.; Liu, T.; Yin, P. Hydrogen bonding directed co-assembly of polyoxometalates and polymers to core–shell nanoparticles. *Mater. Chem. Front*, **2018**, *2*, 2070-2075.

111 Zhang, B.; Song, J.; Hu, L.; Hill, C. L.; Liu, T. Self-Assembly of Polyoxovanadate-Containing Fluorosurfactants. *Langmuir*, **2016**, *32*, 12856-12861.

112 Zhou, J.; Yin, P.; Chen, X.; Hu, L.; Liu, T. Temperature- and salt-responsive polyoxometalate–poly(N-isopropylacrylamide) hybrid macromolecules in aqueous solution. *Chem. Comm.*, **2015**, *51*, 15982-15985.

113 Rachel, A.; Scullion, A.; Surman, J.; Xu, F.; Mathieson, J. S.; Long, D.-L.; Haso, F.; Liu, T.; Cronin, L. Exploring the Symmetry, Structure, and Self-Assembly Mechanism of a Gigantic Seven-Fold Symmetric $\{Pd_{84}\}$ Wheel. *Angew. Chem. Int. Ed.*, **2014**, *126*, 10196-10201.

114 Barman, S.; Sreejith, S.; Garai, S.; Pochamoni, R.; Roy, S. Selective Photocatalytic Carbon Dioxide Reduction by a Reduced Molybdenum-Based Polyoxometalate Catalyst. *ChemPhotoChem*, **2019**, *3*, 93-100. ; Barman, S.; Das, S.; Sreejith, S. S.; Garai, S.; Pochamoni, R.; Roy, S. Selective light driven reduction of CO2 to HCOOH in water using a $\{MoV_9\}_n$ (n = 1332–3600) based soft-oxometalate (SOM). *Chem. Commun.*, **2018**, *54*, 2369-2372.

115 Das, S.; Roy, S. Photochemical Water Oxidation Using $\{PMo_{12}O_{40}@Mo_{72}Fe_{30}\}_n$ Based Soft Oxometalate. *J. Mol. Eng. Mater.*, **2017**, *5*, 1750001.

116 Roy, S. Soft-oxometalates beyond crystalline polyoxometalates: formation, structure and properties. *CrystEngComm*., **2014**, *16*, 4667-4676.

117 Roy, S. Soft oxometalates"(SOMs): a very short introduction. *Comments on Inorg. Chem.* **2011**, *32*, 113-126.

118 Lubin, N.; Robin, G.; Triana, C. A.; Bernhard, S.; Kim, K.; Patzke, G. R. Pathways towards true catalysts: computational modelling and structural transformations of Zn-polyoxotungstates. *Dalton Trans*., **2019**, *48*,13293-13304.

119 Joaquín, S.-L.; Song, F.; Patzke, G. R.; Galan-Mascaros, J. R. Photoinduced oxygen evolution catalysis promoted by polyoxometalate salts of cationic photosensitizers. *Front. Chem.* **2018**, *6*, 302.

120 Car, P.-E.; Patzke, G. R. The Fascination of Polyoxometalate Chemistry. *Inorganics*, **2015**, *3*,511-515.

121 von Allmen, K.; Car, P.-E.; Blacque, O.; Fox, T.; Müller, R.; Patzke, G. R. Structure and Properties of New Gallium-containing Polyoxotungstates with Hexanuclear and Tetranuclear Cores. *Zeitschrift für Anorganische und Allgemeine Chemie*, **2014** *640*,781-789.

122 Lubin, N.; Bernhard, S.; Stephen, W.; Patzke, G. R. Trilacunary Keggin-Type POMs as Versatile Building Blocks for Lanthanoid Silicotungstates. *Eur. J. Inorg. Chem.*, **2013**, 1681-1692.

123 Shivaiah, V,; Narasimha Reddy, P. V.; Cronin, L.; Das, S. K. A novel polyoxometalate chain formed from heteropolyanion building blocks and rare earth metal ion linkers: $[La(H_2O)_7Al(OH)_6Mo_6O_{18}]_n\cdot 4nH_2O$. *J. Chem. Soc. Dalton Trans.*, **2002**, 3781-3782.

124 Shivaiah, V.; Nagaraju, M.; Das, S. K. Formation of a Spiral-Shaped Inorganic−Organic Hybrid Chain, $[Cu^{II}(2,2'\text{-bipy})(H_2O)_2Al(OH)_6Mo_6O_{18}]_n^{n-}$: Influence of Intra- and Interchain Supramolecular Interactions. *Inorg. Chem.*, **2003**, *42*, 6604-6606.

125 Shivaiah, V.; Das, S. K. Inclusion of a Cu^{2+} Ion by a Large-Cavity Crown Ether Dibenzo-24-Crown-8 through Supramolecular Interactions. *Inorg. Chem.*, **2005**, *44*, 7313-7315

126 Arumuganathan, T.; Das, S. K. Discrete Polyoxovanadate Cluster into an Organic Free Metal-Oxide-Based Material: Syntheses, Crystal Structures, and Magnetic Properties of a New Series of Lanthanide Linked-POV Compounds $[\{Ln(H_2O)_6\}_2 As_8V_{14}O_{42}(SO_3)]\cdot 8H_2O$ (Ln = La^{3+}, Sm^{3+}, and Ce^{3+}). *Inorg. Chem.*, **2009**, *48*, 496-507.

127 Chatterjee, T.; Kumar, N. T.; Das, S. K. A planar anthracene–imidazolium/ anthracene–benzimidazolium cation system in a spherical polyoxometalate matrix: Synthesis, crystallography and spectroscopy. *Polyhedron*, **2017**, *127*, 68-83.

128 Pope, M. T. Heteropoly and Isopoly Oxometalates, *Springer–Verlag: Berlin*, **1983.**

129 Misono, M. Acidic and catalytic properties of heteropoly compounds. *Mat. Chem. Phy.*, **1987**, *17*, 103-120.

130 Okuhara, T.; Mizuno, N.; Misono, M. Catalytic Chemistry of Heteropoly Compounds. *Adv. Cat.*, **1996**, *41*, 113-252

131 Mizuno, N.; Misono, M. Heteropolyanions in catalysis. *J. Mol. Cat.*, **1994**, *86*, 319-342.

132 Maksimov, G. Advances in the synthesis of polyoxometalates and in the study of heteropolyacids. Russ. Chem. Rev., **1995**, *64*, 445-461.

133 Hutin, M.; Rosnes, M. H.; Long, D.; Cronin, L. 2.10-Polyoxometalates: Synthesis and Structure–From Building Blocks to Emergent Materials. Comprehensive Inorganic Chemistry II, pp.241-269. *Comprehensive Inorganic Chemistry II: From Elements to Applications*, **2013**, *2*, 241−269.

134 Du, D. Y.; Yan, L. K.; Su, Z. M.; Li, S. L.; Lan, Y. Q.; Wang, E. B. Chiral polyoxometalate-based materials: From design syntheses to functional applications. *Coordination Chemistry Reviews*, **2013**, *257*, 702−717.

135 Omwoma, S.; Gore, C. T.; Ji, Y.; Hu, C.; Song, Y. F. Environmentally benign polyoxometalate materials. *Coordination Chemistry Reviews*, **2015**, *286*, 17−29.

136 Müller, A.; Gouzerh, P. From linking of metal-oxide building blocks in a dynamic library to giant clusters with unique properties and towards adaptive chemistry. *Chem. Soc. Rev.* **2012**, *41*, 7431-7463.

137 Müller, A.; Krickemeyer, E.; Meyer, J.; Bögge, H.; Peters, F.; Plass, W.; Diemann, E.; Dillinger, S.; Nonnenbruch, F.; Randerath, M.; Menke, C. $[Mo_{154}(NO)_{14}O_{420}(OH)_{28}(H_2O)_{70}]^{(25\pm5)-}$: A Water-Soluble Big Wheel with More than 700 Atoms and a Relative Molecular Mass of About 24000. *Angew. Chem.-Int. Edit. Engl.* **1995**, *34*, 2122-2124.

138 Müller, A.; Serain, C. Soluble molybdenum blues "des pudels kern". *Acc. Chem. Res.* **2000**, *33*, 2-10.

139 Müller, A.; Krickemeyer, E.; Bögge, H.; Schmidtmann, M.; Beugholt, C.; Kögerler, P.; Lu, C. Formation of a Ring-Shaped Reduced "Metal Oxide" with the Simple Composition $[(MoO_3)_{176}(H_2O)_{80}H_{32}]$. *Angew. Chem., Int. Ed.*, **1998**, *37*, No. 9.

140 Jiang, C. C.; Wei, Y. G.; Liu, Q.; Zhang, S. W.; Shao, M. C.; Tang, Y. Q. Self-assembly of a novel nanoscale giant cluster:$[Mo_{176}O_{496}(OH)_{32}(H_2O)_{80}]$. *Chem. Commun.*, **1998**, *18*, 1937–1938.

141 Müller, A.; Shah, S. Q.; Bögge, H.; Schmidtmann, M. Molecular growth from a Mo_{176} to a Mo_{248} cluster. *Nature*, **1999**, *397*, 48-50.

142 Müller, A.; Beckmann, E.; Bögge, H.; Schmidtmann, M.; Dress, A. Inorganic Chemistry Goes Protein Size: A Mo_{368} Nano-Hedgehog Initiating Nanochemistry by Symmetry Breaking. *Angew. Chem., Int. Ed.*, **2002**, *41*, 1162–1167.

143 Müller, A.; Botar, B.; Das, S. K.; Bögge, H.; Schmidtmann, M.; Merca, A. On the complex hedgehog-shaped cluster species containing 368 Mo atoms: simple preparation method, new spectral details and information about the unique formation. *Polyhedron*, **2004**, *23*, 2381–2385.

144 Schaefer, H. E.; Nanoscience: the science of the small in physics, engineering, chemistry, biology and medicine. *Springer Science & Business Media.* **2010**.

145 Müller, A.; Krickemeyer, E.; Bögge, H.; Schmidtmann, M.; Peters, F. Organizational forms of matter: an inorganic super fullerene and keplerate based on molybdenum oxide. *Angew. Chem. Int. Ed.* **1998**, *37*, 3359–3363.

146 Schäffer, C.; Todea, A. M.; Gouzerh, P.; Müller, A. Spontaneous self-assembly of a giant spherical metal-oxide Keplerate: addition of one building block induces "immediate" formation of the complementary one from a constitutional dynamic library. *Chem. Commun.* **2012**, *48*, 350-352.

147 Müller, A.; Sarkar, S.; Shah, S. Q. N.; Bögge, H.; Schmidtmann, M.; Sarkar, S.; Kögerler, P.; Hauptfleisch, B.; Trautwein, A. X.; Schünemann, V. Archimedean synthesis and magic numbers:"sizing" giant molybdenum-oxide-based molecular spheres of the keplerate type. *Angew. Chem.-Int. Edit.* **1999**, *38*, 3238-3241.

148 Koegerler, P.; Tsukerblat, B.; Mueller, A. Structure-related frustrated magnetism of nanosized polyoxometalates: aesthetics and properties in harmony. *Dalton Trans.*, **2010**, *39*, 21–36.

149 Melgar, D.; Bandeira, N. A.; Bo, C. Electronic structure studies on the whole keplerate family: predicting new members. *Chem. Eur. J.* **2017**, *23*, 5338 –5344.

150 Todea, A. M.; Merca, A.; Bögge, H.; van Slageren, J.; Dressel, M.; Engelhardt, L.; Luban, M.; Glaser, T.; Henry, M.; Mueller, A. Extending the $\{(Mo)Mo_5\}_{12}M_{30}$ capsule Keplerate sequence: a $\{Cr_{30}\}$ cluster of S= 3/2 metal centers with a $\{Na(H_2O)_{12}\}$ encapsulate. *Angew. Chem. Int. Ed.* **2007**, *46*, 6106–6110.

151 Schäffer, C.; Merca, A.; Bögge, H.; Todea, A. M.; Kistler, M. L.; Liu, T.; Thouvenot, R.; Gouzerh, P.; Müller, A. Unprecedented and differently applicable pentagonal units in a dynamic library: a keplerate of the type $\{(W)W_5\}_{12}\{Mo_2\}_{30}$. *Angew. Chem.* **2009**, *121*, 155 –159.

152 Todea, A. M.; Merca, A.; Bögge, H.; Glaser, T.; Pigga, J. M.; Langston, M. L.; Liu, T.; Prozorov, R.; Luban, M.; Schröder, C.; Casey, W. H. Porous capsules $\{(M)M_5\}_{12}Fe^{III}_{30}(M=Mo^{VI}, W^{VI})$: sphere surface supramolecular chemistry with 20 ammonium ions, related solution properties, and tuning of magnetic exchange interactions. *Angew. Chem. Int. Ed.* **2010**, *49*, 514 –519.

153 Li, Y.; Li, Y. G.; Zhang, Z. M.; Wu, Q.; Wang, E. B. A new polyoxotungstate-based $\{W_{72}V_{30}\}$ spherical cage. *Inorganic Chemistry Communications*, **2009**, *12*, 864–867.

154 Müller, A.; Das, S.; Kögerler, P.; Bögge, H.; Schmidtmann, M.; Trautwein, A.; Schünemann, V.; Krickemeyer, E.; Preetz, W., A New Type of Supramolecular Compound: Molybdenum-Oxide-Based Composites Consisting of Magnetic Nanocapsules with Encapsulated Keggin-Ion Electron Reservoirs Cross-Linked to a Two-Dimensional Network. *Angew. Chem. Int. Ed. Engl.* **2000**, *39*, 3413-3417.

155 Kuepper, K.; Neumann, M.; Al-Karawi, A. J. M.; Ghosh, A.; Walleck, S.; Glaser, T.; Gouzerh, P.; Müller, A. Immediate formation/ precipitation of icosahedrally structured iron-molybdenum mixed oxides from solutions upon mixing simple iron(III) and molybdate salts. *J. Cluster Sci.* **2014**, *25*, 301−311.

156 Mekala, R.; Supriya, S.; Das, S. K. Isolation of Blackberry-Shaped Nanoparticles of a Giant $\{Mo_{72}Fe_{30}\}$ Cluster and Their Transformation to a Crystalline Nanoferric Molybdate. *Inorg. Chem.* **2016**, *55*, 12504−12507.

157 Kolli, H. K.; Jana, D.; Das, S. K. Nanoblackberries of $\{W_{72}Fe_{33}\}$ and $\{Mo_{72}Fe_{30}\}$: electrocatalytic water reduction. *Inorg. Chem.* **2021**, *60*, 15569–15582.

158 Jung, J. K.; Procissi, D.; Vincent, R.; Suh, B. J.; Borsa, F.; Kogerler, P.; Schroder, C.; Luban, M. Proton NMR in the giant paramagnetic molecule $\{Mo_{72}Fe_{30}\}$. *Journal of Applied Physics*, **2002,** *91*, 7388-7390.

159 Kuepper, K.; Derks, C.; Taubitz, C.; Prinz, M.; Joly, L.; Kappler, J. P.; Postnikov, A.; Yang, W.; Kuznetsova, T. V.; Wiedwald, U.; Ziemann, P.; Neumann, M. Electronic structure and soft-X-ray-induced photoreduction studies of iron-based magnetic polyoxometalates of type $\{(M)M_5\}_{12}Fe^{III}_{30}(M = Mo^{VI}, W^{VI})$. *Dalton Trans.*, **2013**, *42*, 7924–7935.

160 Garlea, V. O.; Nagler, S. E.; Zarestky, J. L.; Stassis, C.; Vaknin, D.; Kögerler, P.; McMorrow, D. F.; Niedermayer, C.; Tennant, A.; Lake, B.; Qiu, Y.; Exler, M.; Schnack, J.; Luban, M. Probing spin frustration in high-symmetry magnetic nanomolecules by inelastic neutron scattering. *Physical Review B*, **2006**, *73*, 024414.

161 Lago, J.; Micotti, E.; Corti, M. Low-energy spin dynamics in the giant Keplerate molecule $Mo_{72}Fe_{30}$%: A muon spin relaxation and ^{1}H NMR investigation. *Physical Review B*, **2007**, *76*, 064432.

162 Schröder, C. Multiple nearest-neighbor exchange model for the frustrated magnetic molecules $\{Mo_{72}Fe_{30}\}$ and $\{Mo_{72}Cr_{30}\}$. *Physical Review B*, **2008**, *77*, 224409.

163 Neuscamman, E.; Chan, G. K. Correlator product state study of molecular magnetism in the giant Keplerate $Mo_{72}Fe_{30}$. *Physical Review B*, **2012**, *86*, 064402.

164 Schröder, C. Competing Spin Phases in Geometrically Frustrated Magnetic Molecules. *PRL*. **2005**, *94*, 017205.

165 Liu, T.; Imber, B.; Diemann, E.; Liu, G.; Cokleski, K.; Li, H.; Chen, Z.; Müller, A. Deprotonations and Charges of Well-Defined $\{Mo_{72}Fe_{30}\}$ Nanoacids Simply Stepwise Tuned by pH Allow Control/Variation of Related Self-Assembly Processes. *J. Am. Chem. Soc.* **2006**, *128*, 15914-15920.

166 Ostroushko, A. A.; Tonkushina, M. O.; Korotaev, V. Y.; Prokofeva, A. V.; Kutyashev, B.; Vazhenin, V. A.; Danilova,I. G.; Menshikov, S. Y. Stability of the $Mo_{72}Fe_{30}$ Polyoxometalate Buckyball in Solution. *Russian Journal of Inorganic Chemistry*, **2012**, *57*, 1210–1213.

167 Fareghi-Alamdari, R.; Hafshejani, S. M.; Taghiyar, H.; Yadollahi, B.; Farsani, M. R. Recyclable, Green and Efficient Epoxidation of Olefins in Water with Hydrogen Peroxide Catalyzed by Polyoxometalate Nanocapsule. *Catalysis Communications*, **2016**, *78*, 64-67.

168 Goss. K.; Kamra, A.; Spudat, C.; Meyer, C.; Kögerler, P.; Schneider, C. M. CVD growth of carbon nanotubes using molecular nanoclusters as catalyst. *Phys. Status Solidi B*, **2009**, *246*, 2494–2497.

169 Shimoda, K.; Ishikawa, S.; Tashiro, M.; Kumaki, M.; Hiyoshi, N.; Ueda, W. Synthesis of High Dimensionally Structured Mo–Fe Mixed Metal Oxide and Its Catalytic Activity for Selective Oxidation of Methanol. *Inorg. Chem.* **2020**, *59*, 5252–5255.

170 Garazhian, Z.; Rezaeifard, A.; Jafarpour, M.; Farrokhi, A. $\{Mo_{72}Fe_{30}\}$ Nanoclusters for the Visible-Light-Driven Photocatalytic Degradation of Organic Dyes. *ACS Appl. Nano Mater*. **2020**, *3*, 648−657.

171 Mokhtari, R.; Rezaeifard, A.; Jafarpour, M.; Farrokhi, A. Visible-light driven catalase-like activity of blackberry-shaped $\{Mo_{72}Fe_{30}\}$ nanovesicles: combined kinetic and mechanistic studies. *Catal. Sci. Technol*., **2018**, *8*, 4645-4656.

172 Garazhian, Z.; Rezaeifard, A.; Jafarpour, M. A nanoscopic icosahedral $\{Mo_{72}Fe_{30}\}$ cluster catalyzes the aerobic synthesis of benzimidazoles. *RSC Adv.*, **2019**, *9*, 34854-34861.

173 Ostroushko, A. A.; Gagarin, I. D.; Tonkushina, M. O.; Grzhegorzhevskii, K. V.; Danilova, I. G.; Gette, I. F.; Kim, G. A. Iontophoretic transport of associates based on porous Keplerate-type cluster polyoxometalate $Mo_{72}Fe_{30}$ and containing biologically active substances. *Russian Journal of Physical Chemistry A*, **2017**, *91*, 1811-1815.

174 Tonkushina, M. O.; Grzhegorzhevskii, K. V.; Ermoshin, A. A.; Tugbaeva, A. S.; Kim, G. A.; Taniya, O. S.; Gagarin, I. D.; Ostroushko, A. A. The Electrostatic-Mediated Formation of a Coordination Complex: the Trapping and Release of an Antitumor Drug with an Anthracycline Core from $\{Mo_{72}Fe_{30}\}$-Based Ensembles. *ChemistrySelect*, **2022**, *7*, e202203684.

175 Grzhegorzhevskii, K.; Tonkushina, M.; Gushchin, P.; Gagarin, I.; Ermoshin, A.; Belova, K.; Prokofyeva, A.; Ostroushko, A.; Novikov, A. Association of Keplerate-Type Polyoxometalate $\{Mo_{72}Fe_{30}\}$ with Tetracycline: Nature of Binding Sites and Antimicrobial Action. *Inorganics*, **2023**, *11*, 9.

176 Fan, D.; Hao, J. Fabrication and electrocatalytic properties of chitosan and Keplerate-type polyoxometalate $\{Mo_{72}Fe_{30}\}$ hybrid films. *J. Phys. Chem. B*, **2009**, *113*, 7513-7516.

177 Tonkushina, M. O.; Belozerova, K. A.; Gagarin, I. D.; Adamova, L. V.; Terziyan, T. V.; Russkikh, O. V.; Ostroushko, A. A. Thermodynamics of the interaction between Keplerate-type polyoxometalate {$Mo_{72}Fe_{30}$} and vitamin B1. *Thermochimica Acta*, **2022**, *711*, 179201.

178 Nikookar, M.; Rezaeifard, A.; Grzhegorzhevskii, K.V.; Jafarpour, M.; Khani, R. Melem Nanorectangular Prism-Modified {$Mo_{72}Fe_{30}$} Nanocapsule as a Visible-Light-Assisted Photocatalyst for Catalase-Like Activity. *ACS Appl. Nano Mater.* **2022**, *5*, 7917-7931.

179 Tonkushina, M. O.; Gagarin, I. D.; Russkikh, O. V.; Belozerova, K. A.; Ostroushko, A. A. Destruction of polyoxometalate {$Mo_{72}Fe_{30}$} as a transport agent in blood simulating media, its stabilization by albumin. *Fiziko-Khimicheskie Aspekty Izucheniya Klasterov, Nanostruktur i Nanomaterialov*, **2020**, *12*, 885-892.

180 Huang, S. C.; Lin, C. C.; Hsu, C. T.; Guo, C. H.; Chen, T. Y.; Liao, Y. F.; Chen, H. Y.; Keplerate-type polyoxometalate {Mo72Fe30} nanoparticle anodes for high-energy lithium-ion batteries. Journal of Materials Chemistry A, 2020, 8, 21623-21633.

181 Zhao, W.; Cui, J.; Hao, J.; Van Horn, J. D. Co-assemblies of polyoxometalate {$Mo_{72}Fe_{30}$}/double-tailed magnetic-surfactant for magnetic-driven anchorage and enrichment of protein. *Journal of colloid and interface science*, **2019**, *536*, 88-97.

182 Jia, X.; Yu, S.; Ma, Y.; Li, P.; Ren, H. Self-Association Study from Electrochemical Behaviours of {Mo_{154}} and {$Mo_{72}Fe_{30}$} in Aqueous Solution. *Asian Journal of Chemistry*, **2010**, *22*, 8033-8040.

183 Taghiyar, H.; Yadollahi, B. Keggin polyoxometalates encapsulated in molybdenum-iron-type Keplerate nanoball as efficient and cost-effective catalysts in the oxidative desulfurization of sulfides. *Science of the Total Environment*, **2020**, *708*, 134860.

184 Ostroushko, A. A.; Grzhegorzhevskii, K. V. Electric conductivity of nanocluster polyoxomolybdates in the solid state and solutions. *Russian Journal of Physical Chemistry A*, **2014**, *88*,1008-1011.

185 Taghiyar, H.; Yadollahi, B.; Moshtaghian, S. J. Talebi, A.; Kajani, A.A., PMMA nanofibers containing Keplerate-type polyoxometalate and metronidazole: Preparation and wound-healing effect in a rat model. *Journal of Drug Delivery Science and Technology*, **2022**, *69*, 103140.

186 Taghiyar, H.; Yadollahi, B. New perspective to catalytic epoxidation of olefins by Keplerate containing Keggin polyoxometalates. *Polyhedron*, **2018**, *156*, 98-104.

187 Gubarev, Yu. A.; Lebedeva, N. Sh.; Tonkushina, M. O.; Gagarin, I. D.; Golub, A. Ya.; Ostroushko, A. A. Interaction of iron-containing nanocluster polyoxometalate with doxorubicin. *Fiziko-Khimicheskie Aspekty Izucheniya Klasterov, Nanostruktur i Nanomaterialov*, **2021**, *13*, 841-851.

188 Tian, Z. Y.; Han, X. Q.; Du, J.; Li, Z. B.; Ma, Y. Y.; Han, Z. G. Bio-inspired $FeMo_2S_4$ microspheres as bifunctional electrocatalysts for boosting hydrogen oxidation/evolution reactions in alkaline solution. *ACS Appl. Mater. Interfaces*, **2023**, *15*, 11853-11865.

189 Haddadi, H.; Korani, E. M.; Hafshejani, S. M.; Farsani, M. R. Highly selective oxidation of sulfides to sulfones by H_2O_2 catalyzed by porous capsules. *Journal of Cluster Science*, **2015**, *26*, 1913-1922.

190 Bugnola, M.; Carmieli, R.; Neumann, R. Aerobic Electrochemical Oxygenation of Light Hydrocarbons Catalyzed by an Iron–Tungsten Oxide Molecular Capsule. *ACS Catal.* **2018**, *8*, 3232-3236.

191 Bugnola, M.; Shen, K.; Haviv, E.; Neumann, R. Reductive electrochemical activation of molecular oxygen catalyzed by an iron-tungstate oxide capsule: reactivity studies consistent with compound I type oxidants. *ACS Catalysis*, **2020**, *10*, 4227-4237.

192 Todea, A. M.; Szakacs, J.; Konar, S.; Bogge, H.; Crans, D. C.; Glaser, T.; Rousseliere, H.; Thouvenot, R.; Gouzerh, P.; Müller, A. Reduced Molybenum-Oxide-Based Core–Shell Hybrids: “Blue” Electrons Are Delocalized on the Shell. *Chem. Eur. J.* **2011**, *17*, 6635 – 6642.

193 Ramaswamy, P.; Wong, N. E.; Shimizu, G. K. MOFs as proton conductors–challenges and opportunities. *Chem. Soc. Rev.*, **2014**, *43*, 5913-5932.

194 Grancha, T.; Ferrando-Soria, J.; Cano, J.; Amorós, P.; Seoane, B.; Gascon, J.; Bazaga-García, M.; Losilla, E. R.; Cabeza, A.; Armentano, D.; Pardo, E. Insights into the dynamics of grotthuss mechanism in a proton-conducting chiral bio MOF. *Chem. Mater.* **2016**, *28*, 4608-4615.

195 Wang, H.; Chen, L.; Yang, H.; Wang, M.; Yang, L.; Du, H.; Cao, C.; Ren, Y.; Wu, Y.; Pan, F.; Jiang, Z. Brønsted acid mediated covalent organic framework membranes for efficient molecular separation. ***J. Mater. Chem. A***, **2019**, *7*, 20317-20324.

196 Dang, J.; Zhao, L.; Zhang, J.; Liu, J.; Wang, J. Imidazole microcapsules toward enhanced phosphoric acid loading of polymer electrolyte membrane for anhydrous proton conduction. *Journal of Membrane Science*, **2018**, *545*, 88-98.

197 Tandekar, K.; Singh, C.; Supriya, S. Proton Conductivity in $\{Mo_{72}Fe_{30}\}$-Type Keplerate. *Eur. J. Inorg. Chem.* **2021**, 734–739.

198 Lin, J.; Li, N.; Yang, S.; Jia, M.; Liu, J.; Li, X. M.; An, L.; Tian, Q.; Dong, L. Z.; Lan, Y. Q. Self-Assembly of Giant Mo_{240} Hollow Opening Dodecahedra. *J. Am. Chem. Soc.* **2020**, *142*, 13982–13988.

199 Liu, W. J.; Dong, L. Z.; Li, R. H.; Chen, Y. J.; Sun, S. N.; Li, S. L.; Lan, Y. Q. Different Protonic Species on Affecting Proton-Conductivity in Hollow Sphere-Like Polyoxometalates. *ACS Appl. Mater. Interfaces* **2019**, *11*, 7030–7036.

200 Wang, Y. D.; Wang, J. X.; Wei, M. J.; Liu, B. L.; Zang, H. Y.; Tan, H. Q.; Wang, Y. H.; Li, Y. G. Niobium Oxyhydroxide-Polyoxometalate Composite as an Efficient Proton-Conducting Solid Electrolyte. *ChemElectroChem* **2018**, *5*, 1–6.

201 Li, Z.; Lin, L. D.; Yu, H.; Li, X. X.; Zheng, S. T. All-Inorganic Ionic Porous Material Based on Giant Spherical Polyoxometalates Containing Core-Shell $K_6@K_{36}$-Water Cage. *Angew. Chem.* **2018**, *130*, 16003 –16007.

202 Liu, Y.; Yang, X.; Miao, J.; Tang, Q.; Liu, S.; Shi, Z.; Liu, S. Polyoxometalate-functionalized metal–organic frameworks with improved water retention and uniform proton-conducting pathways in three orthogonal directions. *Chem. Commun.*, **2014**, *50*, 10023-10026.

203 Iwano, T.; Shitamatsu, K.; Ogiwara, N.; Okuno, M.; Kikukawa, Y.; Ikemoto, S.; Shirai, S.; Muratsugu, S.; Waddell, P. G.; Errington, R. J.; Sadakane, M.; Uchida, S. Ultrahigh Proton Conduction via Extended Hydrogen-Bonding Network in a Preyssler-Type Polyoxometalate-Based Framework Functionalized with a Lanthanide Ion. *ACS Appl. Mater. Interfaces* **2021**, *13*, 19138-19147.

204 Iwano, T.; Miyazawa, S.; Osuga, R.; Konda, J. N.; Honjo, K.; Kitao, T.; Uemura, T.; Uchida, S. Confinement of poly(allylamine) in Preyssler-type polyoxometalate and potassium ion framework for enhanced proton conductivity. *Communications Chemistry*, **2019**, *2*, 1-8.

205 Niinomi, K.; Miyazawa, S.; Hibino, M.; Mizuno, N.; Uchida, S. High Proton Conduction in Crystalline Composites Based on Preyssler-Type Polyoxometalates and Polymers under Nonhumidified or Humidified Conditions. *Inorg. Chem.* **2017**, *56*, 15187-15193.

206 Li, S. R.; Wang, H. Y.; Su, H. F.; Chen, H. J.; Du, M. H.; Long, L. S.; Kong, X. J.; Zheng, L. S. A Giant 3d-4f Polyoxometalate Super-Tetrahedron with High Proton Conductivity. *Small Methods* **2020**, *5*, 2000777.

207 Wu, X.; Wu, Q. A typical solid high-protonic conductor: A kind of vanadium-substituted heteropoly acid $H_5PW_{10}V_2O_{40}\cdot 15H_2O$. *Materials Letters* **2021**, *302*, article No.130372.

208 Zhang, R. T.; Xiao, H. P.; Li, Z.; Wang, M.; Xie, Y. F.; Ye, Y. D.; Li, X. X.; Zheng, S. T. Two highly stable inorganic–organic hybrid 3D frameworks based on Cu–Ln incorporated polyoxometalates for selective dye removal and proton conduction. *CrystEngComm*, **2021**, *23*, 2973-2981.

209 Zhu, M.; Iwano, T.; Tan, M.; Akutsu, D.; Uchida, S.; Chen, G.; Fang, X. Macrocyclic Polyoxometalates: Selective Polyanion Binding and Ultrahigh Proton Conduction. *Angew. Chem. Int. Ed.* **2022**, *61*, 1-5.

210 Li, D.; Tan, X. L.; Chen, L. L.; Liu, X. Y.; Li, Y. M.; Dang, D. B.; Bai, Y. Four Dawson POM-based inorganic-organic supramolecular compounds for proton conduction, electrochemical and photocatalytic activity. *Journal of Solid State Chemistry*, **2022**, *305*, article No.122694.

211 Nakamura, O.; Kodama, T.; Ogino, I.; Miyake, Y. High-Conductivity Solid Proton Conductors: Dodecamolybdophosphoric Acid and Dodecatungstophosphoric Acid Crystals. *CHEMISTRY LETTERS*, **1979**, 17-18.

212 Li, S.; Zhao, Y.; Knoll, S.; Liu, R.; Li, G.; Peng, Q.; Qiu, P.; He, D.; Streb, C.; Chen, X. High Proton-Conductivity in Covalently Linked Polyoxometalate-Organoboronic Acid-Polymers. *Angew. Chem. Int. Ed.* **2021**, *60*, 16953 –16957.

213 Gao, Q.; Wang, X. L.; Xu, J.; Bu, X. H. The First Demonstration of the Gyroid in a Polyoxometalate-Based Open Framework with High Proton Conductivity. *Chem. Eur. J.* **2016**, *22*, 9082-9086.

214 Xiao, H. P.; Zhang, R. T.; Li, Z.; Xie, Y. F.; Wang, M.; Ye, Y. D.; Sun, C.; Sun, Y. Q.; Li, X. X.; Zheng, S. T. Organoamine-Directed Assembly of 5p−4f Heterometallic Cluster Substituted Polyoxometalates: Luminescence and Proton Conduction Properties. *Inorg. Chem.* **2021**, *60*, 13718-13726.

215 Wang, X.; Mao, W.; Song, Y.; Meng, F.; Hu, X.; Liu, B.; Su, Z. Hourglass-Type Polyoxometalate-Based Crystalline Material as an Efficient Proton-Conducting Solid Electrolyte. *Inorg. Chem.* **2021**, *60*, 18912-18917.

216 Wang, J. X.; Wang, Y. D.; Wei, M. J.; Tan, H. Q.; Wang, Y. H.; Zang, H. Y.; Li, Y. G. Inorganic open framework based on lanthanide ions and polyoxometalates with high proton conductivity. *Inorg. Chem. Front.*, **2018**, *5*, 1213-1217.

217 Wang, H. Y.; Li, S. R.; Wang, X.; Long, L. S.; Kong, X. J.; Zheng, L. S. Enhanced proton conductivity of Mo_{154}-based porous inorganic framework. *Sci China Chem* **2021**, *64*, 959-963.

218 Xin, Y.; Zhou, Y.; Dong, L.; Wei, P.; Zou, X.; Zhang, F.; Li, G. One-pot self-assembly synthesis of $H_{3+x}PMo_{12-x}V_xO_{40}@[Cu_6O(TZI)_3(H_2O)_9(NO_3)_n]\cdot(H_2O)_{15}$ for enhanced proton conduction materials. *New J. Chem.*, **2022**, *46*, 3909-3915.

219 Zang, H. Y.; Chen, J. J.; Long, D. L.; Cronin, L.; Miras, H. N. Assembly of Thiometalate-Based $\{Mo_{16}\}$ and $\{Mo_{36}\}$ Composite Clusters Combining $[Mo_2O_2S_2]^{2+}$ Cations and Selenite Anions. *Adv. Mater.* **2013**, *25*, 6245-6249.

CHAPTER 2

Nano-Blackberries of $\{W_{72}Fe_{30}\}$ and $\{Mo_{72}Fe_{30}\}$: Electrocatalytic Water Reduction

---

Overview

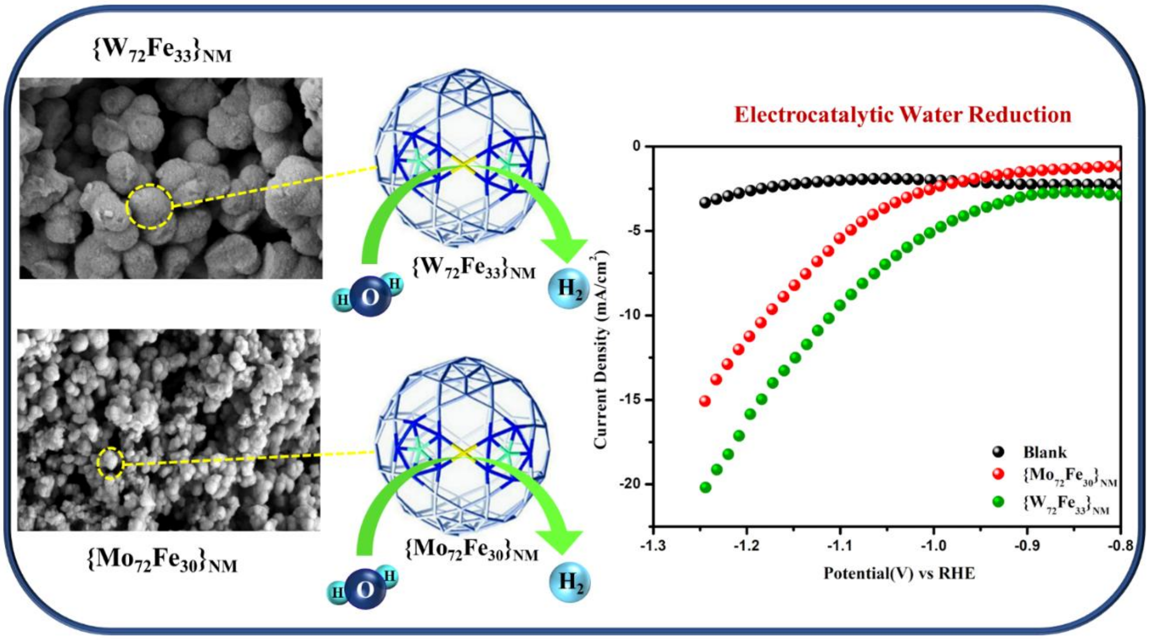

The *reversible* self-assembly of $\{Mo_{72}Fe_{30}\}$ cluster into nano-blackberries in the dilute solution of the relevant crystalline compound $[Mo_{72}Fe_{30}O_{252}(CH_3COO)_{12}\{Mo_2O_7(H_2O)\}_2\{H_2Mo_2O_8(H_2O)\}(H_2O)_{91}]\cdot150H_2O$ (**$\{Mo_{72}Fe_{30}\}_{cryst}$**) was demonstrated by Liu, Müller and their coworkers as a landmark discovery in the area of polyoxometalate chemistry. We have described, in the present work, how these nano-objects, $\{M_{72}Fe_{30}\}$ (M = W and Mo) of ~2.5 nm can be self-assembled into nano-blackberries *irreversibly* leading to their solid state isolation as nanomaterials, $Fe_3[W_{72}Fe_{30}O_{252}(CH_3COO)_2(OH)_{25}(H_2O)_{103}]\cdot180H_2O$ (**$\{W_{72}Fe_{30}\}_{NM}$**) and $Na_2[Mo_{72}Fe_{30}O_{252}(CH_3COO)_4(OH)_{16}(H_2O)_{108}]\cdot180H_2O$ (**$\{Mo_{72}Fe_{30}\}_{NM}$**), respectively (NM stands for nanomaterial). The formulations of these one-pot synthesized nano-blackberries of **$\{W_{72}Fe_{30}\}_{NM}$** and **$\{Mo_{72}Fe_{30}\}_{NM}$** have been established by spectral analysis including Raman spectroscopy, elemental analysis including ICP metal analysis, volumetric analysis (for iron), microscopy techniques and DLS studies. The thermal stability of the tungsten nano-blackberries, **$\{W_{72}Fe_{30}\}_{NM}$** is quite higher than that of its molybdenum analogue **$\{Mo_{72}Fe_{30}\}_{NM}$**. This might due to the extra three ferric (Fe^{3+}) ions per $\{W_{72}Fe_{30}\}$ cluster in **$\{W_{72}Fe_{30}\}_{NM}$**, that are not part of the $\{W_{72}Fe_{30}\}$ cluster cage but are placed between two adjacent clusters (*i.e.*, each cluster has six surrounding $0.5Fe^{3+}$) to form this self-assembly. The isolated blackberries behave like an inorganic acid, water suspension of which shows the pH values of 3.9 for **$\{W_{72}Fe_{30}\}_{NM}$** and 3.7 for **$\{Mo_{72}Fe_{30}\}_{NM}$** because of the deprotonation of the hydroxyl groups in them. We have demonstrated, for the first time, a meaningful application of these inexpensive and easily synthesized nano-blackberries by showing that it can act as an electrocatalyst for hydrogen evolution reaction (HER) by reducing water. We have performed detailed kinetic studies for the electrocatalytic water reduction catalyzed by {$\mathbf{W_{72}Fe_{30}}$}$_{\mathbf{NM}}$ and {$\mathbf{Mo_{72}Fe_{30}}$}$_{\mathbf{NM}}$ in a comparative study. The relevant turnover frequencies (TOFs) of {$\mathbf{W_{72}Fe_{30}}$}$_{\mathbf{NM}}$ and {$\mathbf{Mo_{72}Fe_{30}}$}$_{\mathbf{NM}}$ (~0.72 s^{-1} and ~0.45 s^{-1}, respectively), the overpotential values of {$\mathbf{W_{72}Fe_{30}}$}$_{\mathbf{NM}}$ and {$\mathbf{Mo_{72}Fe_{30}}$}$_{\mathbf{NM}}$ (527 mV and 767 mV, respectively) and the relative stability issues of the catalysts indicate that {$\mathbf{W_{72}Fe_{30}}$}$_{\mathbf{NM}}$ is reasonably superior to {$\mathbf{Mo_{72}Fe_{30}}$}$_{\mathbf{NM}}$. We have described a rationale of why {$\mathbf{W_{72}Fe_{30}}$}$_{\mathbf{NM}}$ performs better than {$\mathbf{Mo_{72}Fe_{30}}$}$_{\mathbf{NM}}$ in terms of catalytic activity and stability.

2.1 Introduction

{$Mo_{72}Fe_{30}$}–type giant spherical polyoxometalate (POM) cluster (popularly known as Keplerate) containing compound $[Mo_{72}Fe_{30}O_{252}(CH_3COO)_{12}\{Mo_2O_7(H_2O)\}_2\{H_2Mo_2O_8(H_2O)\}(H_2O)_{91}]\cdot150H_2O$ **{$Mo_{72}Fe_{30}$}$_{\mathbf{cryst}}$**, isolated as a single crystalline material more than a decade ago, has been recognized as a wonder molecule. More than 135 original research articles have been published till today (source: Scifinder, ACS) based on, only this compound. The concerned {$Mo_{72}Fe_{30}$} cluster cage is constructed by 12 pentagonal $[(Mo)Mo_5O_{21}(H_2O)_6]^{6-}$ units, that are linked by 30 $\{Fe^{III}O_5(H_2O)\}^{3+}$ linkers (Figure 2.1).[1] Since this compound **{$Mo_{72}Fe_{30}$}$_{\mathbf{cryst}}$**, having 30 Fe(III) centers, has been characterized as a high spin system with 150 unpaired electrons per cluster, a major portion of its publications covers works related to its versatile magnetism.[2-9] Its catalytic activities are also reported in recent time. Among {$Mo_{72}Fe_{30}$} cluster based catalysis, selective oxidation of anthracene (H_2O_2 as an oxidant), epoxidation of olefins (H_2O_2 as an oxidant), isolation of carbon nanotubes (using chemical vapour deposition process) are worth mentioning.[10-12] Reversible self-assembly of this giant nano-sized object, {$Mo_{72}Fe_{30}$} in the dilute aqueous solution of the relevant compound **{$Mo_{72}Fe_{30}$}$_{\mathbf{cryst}}$**, demonstrated by Liu– and Müller–group, has been proved to be the breakthrough research in the area of polyoxometalate chemistry. Liu, Müller and their co-workers showed that, in an aqueous solution, **{$Mo_{72}Fe_{30}$}$_{\mathbf{cryst}}$** cluster acts as a weak inorganic acid that gets deprotonated to different extents, depending on the pH of the concerned aqueous solution and the cluster surface charge densities, and self-assemble to form blackberry-type nano-vesicles of different sizes.[9,13-15] The reversible formation of these blackberries (spherical sized assemblies) was proven by dynamic light scattering (DLS) studies of the concerned dilute solution of **$\{Mo_{72}Fe_{30}\}_{cryst}$** and HR-TEM studies (by drop-casting this solution onto a freshly glow discharged carbon-coated TEM grid).[9] Until then, this kind assemblies (so called nano-blackberries) were never isolated as a solid material. In the meantime, Müller and co-workers synthesized $\{Mo_{72}Fe_{30}\}$ compound as an amorphous substance.[16] We, then, for the first time, described this amorphous material of $\{Mo_{72}Fe_{30}\}$ as the assemblies of nano-sized blackberry type globules by FESEM and HR-TEM microscopic studies and formulated this molybdenum nano-blackberry compound as $Na_2[Mo_{72}Fe_{30}O_{252}(CH_3COO)_4(OH)_{16}(H_2O)_{108}]\cdot180H_2O$ (**$\{Mo_{72}Fe_{30}\}_{NM}$**) from various spectroscopic studies including Raman spectroscopy and elemental analysis.[17]

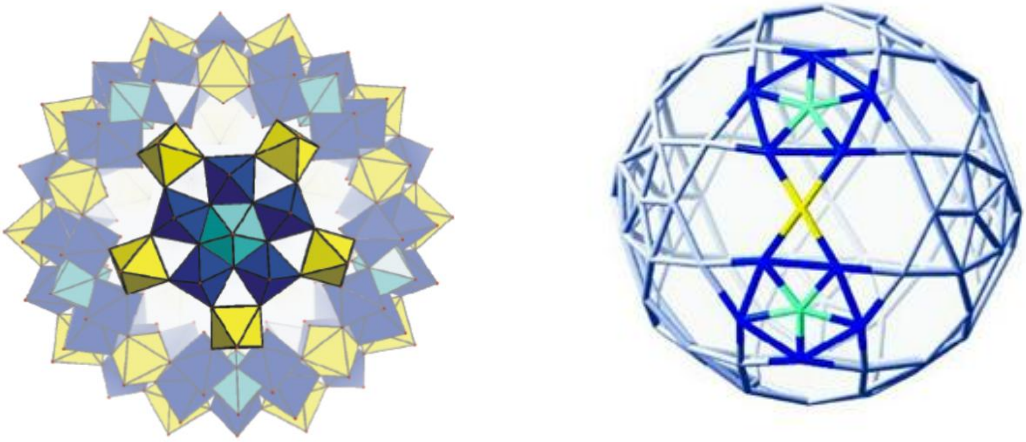

Figure 2.1. (a) Polyhedral representation of $\{Mo_{72}Fe_{30}\}$ cluster-based compound structure; (b) Stick representation of $\{Mo_{72}Fe_{30}\}$ cluster containing compound (reprinted with permission from ref 17, copyright 2016, American Chemical Society).

The isolated nano-blackberries, **$\{Mo_{72}Fe_{30}\}_{NM}$** are insoluble in water, whereas **$\{Mo_{72}Fe_{30}\}_{cryst}$** crystals are moderately water soluble. In this work, we have made an attempt to understand the *irreversible* solid state synthesis of these nano-blackberry type assemblies as an insoluble and amorphous nanomaterial *versus* their *reversible* formation in dilute solution of the soluble crystalline compound **$\{Mo_{72}Fe_{30}\}_{cryst}$** (Appendix 2, Section A2.19). The amorphous nanomaterial **$\{Mo_{72}Fe_{30}\}_{NM}$** (or nano-blackberries) can be synthesized instantaneously in gram quantities, but the synthesis of crystalline compound, **$\{Mo_{72}Fe_{30}\}_{cryst}$** is not only time consuming but also with low yields. We were, thus, very keen to investigate, whether such inexpensive and instantly isolated nanomaterial[17] finds some meaningful applications. In the meantime, Rezaeifard, Jafarpour and their co-workers from Catalysis Research Laboratory of University of

Birjand have shown that this amorphous nanomaterial **$\{Mo_{72}Fe_{30}\}_{NM}$** is quite superior to crystalline **$\{Mo_{72}Fe_{30}\}_{cryst}$** as far as photocatalytic performances toward degradation of organic dyes and catalase like activity including an aerobic synthesis of benzimidazoles are concerned.[18-20] Recently, Supriya and co-workers have performed the proton conductivity studies on **$\{Mo_{72}Fe_{30}\}_{cryst}$** and they have even extended their studies to know the photochromism properties of **$\{Mo_{72}Fe_{30}\}$**-type Keplerate.[21,22] Last several years, we have been working on electrocatalytic water splitting,[23,24] an important and contemporary research goal at the moment worldwide (energy crisis issue on our planet Earth). Since this amorphous substance, $Na_2[Mo_{72}Fe_{30}O_{252}(CH_3COO)_4(OH)_{16}(H_2O)_{108}]\cdot180H_2O$ (**$\{Mo_{72}Fe_{30}\}_{NM}$**) is water insoluble having 16 hydroxyl groups per $(Mo_{72}Fe_{30}\}$ cluster in contrast to its crystalline analogue, $[Mo_{72}Fe_{30}O_{252}(CH_3COO)_{12}\{Mo_2O_7(H_2O)\}_2\{H_2Mo_2O_8(H_2O)\}(H_2O)_{91}]\cdot150H_2O$ **($\{Mo_{72}Fe_{30}\}_{cryst}$)** and Müller group established that guest-free $\{Mo_{72}Fe_{30}\}$ cluster cage can be reduced by two electrons that get delocalized over 72 Mo ions on the cage surface retaining its structural integrity,[25] the substance **$\{Mo_{72}Fe_{30}\}_{NM}$** has potential to act as a heterogeneous electrocatalyst for water reduction to yield molecular hydrogen. We have truly shown in this work that the nanomaterial, **$\{Mo_{72}Fe_{30}\}_{NM}$** acts as a heterogeneous electrocatalyst for hydrogen evolution reaction (HER) by reducing water. However, the major drawback of this isolated molybdenum "nano-blackberries" compound **$\{Mo_{72}Fe_{30}\}_{NM}$** is that it is a kinetically labile substance, which transforms to ferric molybdate with time in a solid to solid transformation.[17,26] We thus intended to synthesize the tungsten analogue of **$\{Mo_{72}Fe_{30}\}_{NM}$**, because tungsten systems are generally kinetically sluggish in comparison to molybdenum system. We could synthesize the nano-blackberries of its tungsten analogue by mixing sodium tungstate with ferric chloride and acetic acid in an aqueous solution; but a careful chemical analysis of this tungsten "nano-blackberries" compound confirms that it is **$\{W_{72}Fe_{30}\}_{NM}$** (with extra three iron ions per cluster compared to its molybdenum analogue) instead of **$\{W_{72}Fe_{30}\}_{NM}$**. These three extra ferric ions per $\{W_{72}Fe_{30}\}$ cluster in compound **$\{W_{72}Fe_{30}\}_{NM}$** play a crucial role in offering an enormous amount of rigidity / thermal stability to **$\{W_{72}Fe_{30}\}_{NM}$** (vide infra). A crystalline **$\{W_{72}Fe_{30}\}_{cryst}$** compound having $\{W_{72}Fe_{30}\}$ cluster cage with sulfate ligand has been reported: $[Na_6(NH_4)_{20}\{Fe(H_2O)_6\}_2][\{W^{VI}{}_6O_{21}(SO_4)\}_{12}\{Fe(H_2O)\}_{30}(SO_4)_{13}(H_2O)_{34}]\cdot200H_2O$ (**$\{W_{72}Fe_{30}\}_{cryst}$**), which is highly water soluble in comparison to the solubility of crystalline **$\{Mo_{72}Fe_{30}\}_{cryst}$**.[1,27] This crystalline **$\{W_{72}Fe_{30}\}_{cryst}$** compound includes two $\{Fe(H_2O)_6\}^{3+}$ cations per $\{W_{72}Fe_{30}\}$ cluster anion.

The discovery of reversible formation of nano-blackberries (vesicles) *via* self-assembly of giant $\{Mo_{72}Fe_{30}\}$ clusters in the dilute aqueous solution of compound $[Mo_{72}Fe_{30}O_{252}(CH_3COO)_{12}\{Mo_2O_7(H_2O)\}_2\{H_2Mo_2O_8(H_2O)\}(H_2O)_{91}]\cdot 150H_2O$ (**$\{Mo_{72}Fe_{30}\}_{cryst}$**) was remarkable from fundamental understanding (of how metal oxide based giant cluster self-assemble to nano-vesicles) point of view. It would have been even more versatile and significant if these black-berries could have been isolated in solid-state to check, whether these nano-blackberries find some useful applications. We reported the solid-state isolation of these nano-blackberries **$\{Mo_{72}Fe_{30}\}_{NM}$** as an amorphous nano-material as a preliminary communication,[17] but without any application. In the present contribution, we not only have reported an important application, *i.e.*, electrocatalytic water reduction to molecular hydrogen, catalyzed by this material **$\{Mo_{72}Fe_{30}\}_{NM}$** (nano-blackberries) but also we have succeeded to isolate its tungsten analogue **$\{W_{72}Fe_{30}\}_{NM}$**. We have shown that the tungsten “nano-blackberries” material is much more superior to its molybdenum analogue **$\{Mo_{72}Fe_{30}\}_{NM}$** as far as electrocatalytic water reduction performance and stability issues are concerned. We have given a rationale describing the driving force for this irreversible solid-state isolation of these nano-blackberries, that are known to be formed reversibly in dilute solution in the case of **$\{Mo_{72}Fe_{30}\}_{cryst}$**. The tungsten “nano-blackberries” compound **$\{W_{72}Fe_{30}\}_{NM}$** has been formulated as $Fe_3[W_{72}Fe_{30}O_{252}(CH_3COO)_2(OH)_{25}(H_2O)_{103}]\cdot 180H_2O$ (**$\{W_{72}Fe_{30}\}_{NM}$**), which unlike **$\{Mo_{72}Fe_{30}\}_{NM}$** does not contain sodium ion but contains three extra ferric ions per $\{W_{72}Fe_{30}\}$ cluster as shown in the Figure 2.2. The novelty of **$\{W_{72}Fe_{30}\}_{NM}$** over **$\{Mo_{72}Fe_{30}\}_{NM}$** is that the tungsten analogue is kinetically stable and it does not disintegrate even at 200^{o}C to $Fe_2(WO_4)_3$ unlike **$\{Mo_{72}Fe_{30}\}_{NM}$**, a kinetically labile substance, which on heating at 60-70^{o}C degrades to $Fe_2(MoO_4)_3$.[17,28] In this work, we have reported the synthesis and characterization of **$\{W_{72}Fe_{30}\}_{NM}$** nano-blackberries. We have also described electrocatalytic hydrogen evaluation reaction (HER) by water reduction, catalyzed by **$\{W_{72}Fe_{30}\}_{NM}$** and **$\{Mo_{72}Fe_{30}\}_{NM}$** in a comparison mode with detailed kinetic studies.

2.2. Experimental Section

2.2.1. Materials

All the chemicals were used as received without any further purification. Sodium molybdate dihydrate ($Na_2MoO_4 \cdot 2H_2O$), sodium tungstate ($Na_2WO_4 \cdot 2H_2O$) and acetic acid – 100% were purchased from SRL chemicals. Ferric chloride hexa hydrate ($FeCl_3 \cdot 6H_2O$) was purchased from Sigma Aldrich Chemicals.

2.2.2. Synthesis

2.2.2.1. Synthesis of $Na_2[Mo_{72}Fe_{30}O_{252}(CH_3COO)_4(OH)_{16}(H_2O)_{108}] \cdot 180H_2O$ ({$Mo_{72}Fe_{30}$}$_{NM}$)

An aqueous solution (25 mL) of $Na_2MoO_4 \cdot 2H_2O$ (3 g, 12.3 mmol) was acidified with 25 mL of acetic acid; under vigorous stirring condition, another aqueous solution (5 mL) of $FeCl_3 \cdot 6H_2O$ (2.09 g, 7.7 mmol) was added to it. Instantaneously yellow colored precipitation was observed; the reaction mixture was stirred for an hour at room temperature and the resulting precipitate was filtered off and washed with water thoroughly and dried the compound at room temperature. Yield: 2.6 g.

2.2.2.2. Synthesis of $Fe_3[W_{72}Fe_{30}O_{252}(CH_3COO)_2(OH)_{25}(H_2O)_{103}] \cdot 180H_2O$ ({$W_{72}Fe_{30}$}$_{NM}$)

An aqueous solution (25 mL) of $Na_2WO_4 \cdot 2H_2O$ (4 g, 12.12 mmol) was acidified with 5 mL of acetic acid; under vigorous stirring condition, another aqueous solution (5 mL) of $FeCl_3 \cdot 6H_2O$ (3.402 g, 12.58 mmol) was added to it. Instantaneously, a yellow-colored precipitation was observed; the reaction mixture was stirred for an hour at room temperature and the resulting precipitate was filtered off and washed with water thoroughly and dried at room temperature. Yield: 2.3 g.

2.2.3. Methods

The instrumental details of the all the experiments are provided in appendix 1.

2.2.3.1. Electrochemical Studies

We have performed most of the electrochemical studies with the help of an electrochemical cell with three-electrode system which has Ag/AgCl (3M) as reference electrode, glassy carbon as the working electrode and Pt-wire as the counter-electrode. The electrolyte used was aqueous solution of 0.1 M Na_2SO_4 at pH 2.5. The electrochemical measurements were carried out in a heterogeneous manner for the insoluble compounds by taking the sample and preparing a homogenous suspension. The sample is prepared by taking 8.0 mg of amorphous compounds that are insoluble in water and 2.0 mg of carbon black powder in a 2.0 mL of ethanol and water mixture (3:2) solution. After sonicating the suspension mixture for 30 minutes, we added 20 µL of 5 weight% nafion to the sonicated suspension and then the mixture was sonicated for further 30 minutes to get complete homogeneous suspension / ink. On the glassy carbon electrode which is having a geometrical area of 0.07 (cm^2), 10 µL of the sample mixture / homogeneous suspension ink was coated and this way 40 µg of the sample was actually coated on the surface of the working electrode and the same amount of sample was used for whole electrochemical measurements except bulk electrolysis. In the case of bulk electrolysis, fluorine doped tin oxide (FTO) glass substrate was used as a working electrode instead of glassy carbon electrode and the counter electrode is Pt-wire with high surface area. Measurements were carried out at room temperature and the IR-Lamp was used to dry the sample mixture which was coated on the surface of the glassy carbon electrode (working electrode). Ag/AgCl electrode was used as a reference electrode and all the electrode potentials in the measurements were transformed to RHE scale with the help of the following relation. E (NHE) = E (Ag/AgCl) + 0.204 + 0.059 pH. Usually, the cyclic voltametric measurements were carried out at a scan rate of 100 mVs^{-1} and iR corrections were manually fixed after finishing all the measurements. With the help of galvanostatic polarization curve, the Tafel plots were plotted and a home-made set-up was used to carry out the bulk electrolysis from which we calculated the Faradic efficiency of the compounds and we quantified the amount of hydrogen evolved in the bulk electrolysis.

2.3 Results and Discussion

2.3.1. Reversible formation in dilute solution *versus* irreversible isolation of aggregated nano-blackberries

Liu and Müller group established that the deprotonation of the iron-coordinated water molecules on the surface of the $\{Mo_{72}Fe_{30}\}$ cluster (Figure 2.1.) of the crystalline compound $[Mo_{72}Fe_{30}O_{252}(CH_3COO)_{12}\{Mo_2O_7(H_2O)\}_2\{H_2Mo_2O_8(H_2O)\}(H_2O)_{91}]\cdot150H_2O$ (**$\{Mo_{72}Fe_{30}\}_{cryst}$**) in a dilute aqueous solution [resulting in the generation of the charge density (OH^-) on the cluster surface and formation of H_3O^+ ions around the clusters] is essential for the $\{Mo_{72}Fe_{30}\}$ clusters to self-assemble into blackberry-like supramolecular structures (nano-sized vesicles) with counter cations (H_3O^+) placed between the $\{Mo_{72}Fe_{30}\}$ cluster units.[9] They also showed that the rate of aggregation of {$Mo_{72}Fe_{30}$} cluster entities into nano-blackberries is directly dependent on the concentration of the {$Mo_{72}Fe_{30}$} clusters, meaning that, more the concentration of the {$Mo_{72}Fe_{30}$} clusters, more is their aggregation. Even though, formation of these nano-blackberries has been demonstrated in an aqueous solution of **{$Mo_{72}Fe_{30}$}$_{\mathbf{cryst}}$**, one cannot expect to isolate these blackberries as a solid-state material from the aqueous solution of **{$Mo_{72}Fe_{30}$}$_{\mathbf{cryst}}$** because of their reversible formation and the limited solubility (0.5−1.0 mg/mL) of **{$Mo_{72}Fe_{30}$}$_{\mathbf{cryst}}$** in an aqueous solution. In order to have more concentration of these cluster entities to be self-assembled in an aqueous solution, one has to generate a large excess amount of {$Mo_{72}Fe_{30}$} clusters in an aqueous solution, which is only possible by a direct *in situ* synthesis, in which the formation of a huge amount of {$Mo_{72}Fe_{30}$} cluster entities are possible. In the present study, the synthesis of aggregated nano-blackberries of $Na_2[Mo_{72}Fe_{30}O_{252}(CH_3COO)_4(OH)_{16}(H_2O)_{108}]\cdot180H_2O$ (**{$Mo_{72}Fe_{30}$}$_{\mathbf{NM}}$**) includes the anticipated concentration of the {$Mo_{72}Fe_{30}$}- cluster species is 50 mg/mL. This high concentration of the cluster species with small negative charge, for example, $[Mo_{72}Fe_{30}O_{252}(CH_3COO)_4(OH)_{16}(H_2O)_{108}]^{2-}$ in an aqueous solution, not surprisingly, leads to its isolation as a sodium salt; but this does not guarantee the self-assembly of this cluster anion to nano-blackberries.

2.3.2. Formation of {$Mo_{72}Fe_{30}$}$_{\mathbf{NM}}$

The formation of these nano-blackberries *via* self-assembly of {$Mo_{72}Fe_{30}$}-cluster species leading to the solid-state isolation of **{$Mo_{72}Fe_{30}$}$_{\mathbf{NM}}$** can be explained by understanding the formation of the {$Mo_{72}Fe_{30}$} cluster species in the present aqueous synthesis. The addition of $FeCl_3\cdot6H_2O$ (which is nothing but $[Fe(H_2O)_6]Cl_3$) into an aqueous solution of sodium molybdate in the presence of acetic acid results in the isolation of **{$Mo_{72}Fe_{30}$}$_{\mathbf{NM}}$** instantaneously, whereby the pH of the solid-solution suspension turns out to be around 2.0. This pH drop (below 4.0) is due to the formation of HCl acid, one of the hydrolyzed products of $FeCl_3\cdot6H_2O$. Even though the ultimate hydrolyzed products of $FeCl_3\cdot6H_2O$ are Fe_2O_3 and HCl ($2FeCl_3 + 3H_2O \rightarrow Fe_2O_3 + HCl$), the formation of intermediate species of mononuclear-, di-nuclear- and multi-nuclear iron complexes with hydroxide (OH^-) and chloride (Cl^-) ligands are known to be detected by ESI spectroscopy.[29] It is already established that the basic building blocks of the {$Mo_{72}Fe_{30}$} cluster of crystalline compound $[Mo_{72}Fe_{30}O_{252}(CH_3COO)_{12}\{Mo_2O_7(H_2O)\}_2$ $\{H_2Mo_2O_8(H_2O)\}(H_2O)_{91}]\cdot150H_2O$

(**{$Mo_{72}Fe_{30}$}$_{cryst}$**) are 12 pentagonal $[(Mo)Mo_5O_{21}(H_2O)_6]^{6-}$ units, that are connected by 30 $\{Fe^{III}O_5(H_2O)\}^{3+}$ linkers to construct the icosahedral $\{Mo_{72}Fe_{30}\}$ nano-object $[Mo_{72}Fe_{30}O_{252}(CH_3COO)_{12}\{Mo_2O_7(H_2O)\}_2\{H_2Mo_2O_8(H_2O)\}(H_2O)_{91}]$ of compound **{$Mo_{72}Fe_{30}$}$_{cryst}$**.[1] In this compound, +90 charges of 30 Fe(III) ions are counterbalanced by −72 charges of twelve pentagons $[(Mo)Mo_5O_{21}(H_2O)_6]^{6-}$, −12 charges of twelve acetate anions and −6 charges of three molybdenum dimers (each having −2 charge), encapsulated in the cavity of the $\{Mo_{72}Fe_{30}\}$ cluster. The crystalline compound **{$Mo_{72}Fe_{30}$}$_{cryst}$** was synthesized from relatively larger icosahedral cluster $\{Mo_{132}\}$ containing compound having 30 molybdenum dimers, each having an acetate ligand.[1] Thus twelve acetate anions and three molybdenum dimers, present in compound **{$Mo_{72}Fe_{30}$}$_{cryst}$**, have come from its precursor $\{Mo_{132}\}$ compound. The twelve pentagonal units, 12 $[(Mo)Mo_5O_{21}(H_2O)_6]^{6-}$ remain intact from $\{Mo_{132}\}$ to **{$Mo_{72}Fe_{30}$}$_{cryst}$**. On the other hand, molybdenum nano-blackberries **{$Mo_{72}Fe_{30}$}$_{NM}$** has been formulated as $Na_2[Mo_{72}Fe_{30}O_{252}(CH_3COO)_4(OH)_{16}(H_2O)_{108}]\cdot 180H_2O$ based on elemental analysis and spectroscopic studies. In contrast to synthesis of crystalline **{$Mo_{72}Fe_{30}$}$_{cryst}$**, the nano-blackberries **{$Mo_{72}Fe_{30}$}$_{NM}$** are synthesized instantaneously from the aqueous solution of sodium molybdate and ferric chloride in the presence of acetic acid. During the addition of $[Fe(H_2O)_6]Cl_3$ ($FeCl_3\cdot 6H_2O$) to the Na_2MoO_4 solution, $\{Fe(H_2O)_6\}^{3+}$ induces MoO_4^{2-} to form the pentagon $[(Mo)Mo_5O_{21}(H_2O)_6]^{6-}$ (eqn. 1) in an acidic aqueous solution as shown below.

$$6\,MoO_4^{2-} + 6H^+ + 3H_2O \rightarrow [(Mo)Mo_5O_{21}(H_2O)_6]^{6-} \qquad (1)$$

Since the spherical / icosahedral cluster (to be formed) in the isolated material needs 12 pentagonal units, 12 such pentagonal units assemble with $30\{Fe(H_2O)_6\}^{3+}$ mononuclear species (as linker) to form the nanosized cluster $[Mo_{72}Fe_{30}O_{252}(CH_3COO)_4(OH)_{16}(H_2O)_{108}]^{2-}$ in the isolated nanomaterial (Mo nano-blackberries) as shown below in the balanced equation (eqn. 2).

$$30\{Fe(H_2O)_6\}^{3+} + 12[(Mo)Mo_5O_{21}(H_2O)_6]^{6-} + 4\ CH_3COOH \rightarrow Mo_{72}Fe_{30}O_{252}(CH_3COO)_4(OH)_{16}(H_2O)_{108}]^{2-} + 20H^+ + 128\ H_2O \qquad (2)$$

The precipitation of nano-blackberries, **{$Mo_{72}Fe_{30}$}$_{NM}$**, *via* this reaction (eqn. 2) with the generation of twenty protons per cluster formation, explains the pH drop in the reaction mixture. This also accounts for the number of acetate ligands per cluster of nano-blackberries (**{$Mo_{72}Fe_{30}$}$_{NM}$**), which is only four, considerably less than that (twelve acetate anions) per cluster of crystalline **{$Mo_{72}Fe_{30}$}$_{cryst}$**. Because of this low pH value of the resulting reaction mixture, the acetic acid would not be deprotonated easily to act as the ligand to balance the rest +16 charges (positive charges of 30 Fe^{3+} centers − negative charges of 12 pentagons = +90−72 = +18; four acetate ligands and two sodium cations are experimentally found, thus rest charges = +18 + 2−4 = 16) during the formation of {$Mo_{72}Fe_{30}$} cluster. In this situation, some of the iron coordinated water molecules deprotonate to form hydroxyl anions or that are formed by partial hydrolysis of $FeCl_3 \cdot 6H_2O$ used in this synthesis to counterbalance the excess positive charges of iron centers (+16 in the case of {$Mo_{72}Fe_{30}$} cluster) resulting in the cluster anion, $[Mo_{72}Fe_{30}O_{252}(CH_3COO)_4(OH)_{16}(H_2O)_{108}]^{2-}$ that self-assemble into **{$Mo_{72}Fe_{30}$}$_{NM}$** nano-blackberries and the resulting nano-blackberries further aggregate leading to the solid state isolation of aggregated nano-blackberries (Figure A2.6a-c, Appendix 2).

2.3.3. Formation of {$W_{72}Fe_{30}$}$_{NM}$

The formation of tungsten analogue of this molybdenum nano-blackberry material is even more interesting. We followed identical synthetic procedure for tungsten nano-blackberries as that of molybdenum compound except we used sodium tungstate instead of sodium molybdate and we have used some more amount to $FeCl_3 \cdot 6H_2O$ in this case (12.58 mmol instead of 7.77 mmol). As expected, we could obtain the ‘tungsten nano-blackberries’ compound $Fe_3[W_{72}Fe_{30}O_{252}(CH_3COO)_2(OH)_{25}(H_2O)_{103}] \cdot 180H_2O$ (**{$W_{72}Fe_{30}$}$_{NM}$**) instantaneously as an amorphous nano-material, consisting of aggregated nano-blackberries of {$W_{72}Fe_{30}$}. The compound is characterized by elemental and spectral analysis including microscopic studies (FESEM and HR-TEM). This time, the {$W_{72}Fe_{30}$} cluster is more anionic (with −9 charges) than the Mo-analogue one. The relevant balanced chemical equations for this synthesis can be described as follows (eqns. 3 and 4).

$$6WO_4^{2-} + 6H^+ + 3H_2O \rightarrow [(W)W_5O_{21}(H_2O)_6]^{6-} \qquad (3)$$

$$30\{Fe(H_2O)_6\}^{3+} + 12[(W)W_5O_{21}(H_2O)_6]^{6-} + 2\ CH_3COOH \rightarrow$$
$$[W_{72}Fe_{30}O_{252}(CH_3COO)_2(OH)_{25}(H_2O)_{103}]^{9-} + 27H^+ + 124\ H_2O \qquad (4)$$

As shown in eqn. 4, the reaction mixture, in which the tungsten ‘nano-blackberry’ compound gets precipitated instantaneously, would be acidic (27 protons are generated per {$W_{72}Fe_{30}$} cluster formation) and indeed the measured pH value of the solid-solution suspension, in which the precipitation of **{$W_{72}Fe_{30}$}$_{NM}$** occurs immediately after mixing of ferric chloride solution to acidified sodium tungstate solution, is 1.35, which is even lower than that of solid-solution suspension of **{$Mo_{72}Fe_{30}$}$_{NM}$**. This does not allow acetic acid, present in the reaction mixture, much to be deprotonated ─ thus only two acetate anions are present per $\{W_{72}Fe_{30}\}$ cluster anion of **$\{W_{72}Fe_{30}\}_{NM}$**. Accordingly there are more hydroxyl anions (25 OH^{-} anions), present per $\{W_{72}Fe_{30}\}$ cluster in compound **$\{W_{72}Fe_{30}\}_{NM}$**. Thus the negative charge density on the $\{W_{72}Fe_{30}\}$ cluster surface of **$\{W_{72}Fe_{30}\}_{NM}$** is much more than that on $\{Mo_{72}Fe_{30}\}$ cluster surface in **$\{Mo_{72}Fe_{30}\}_{NM}$**. This makes difference in terms of their self-assembly processes. In the self-assembly in **$\{Mo_{72}Fe_{30}\}_{NM}$**, the H_3O^+ ions are placed between $\{Mo_{72}Fe_{30}\}$ clusters, whereas in the self-assembly in the case of **$\{W_{72}Fe_{30}\}_{NM}$**, the Fe^{3+} ions are placed between $\{W_{72}Fe_{30}\}$ clusters, according to Liu−Müller model of H_3O^+ ions placed between $\{Mo_{72}Fe_{30}\}$ clusters in the reversible self-assembly in the dilute solution of **$\{Mo_{72}Fe_{30}\}_{cryst}$**. The repetitive and careful analyses of tungsten 'nano-blackberry' compound shows 33 iron atoms per formula unit. We have thus formulated tungsten nano-blackberries as $Fe_3[W_{72}Fe_{30}O_{252}(CH_3COO)_2(OH)_{25}(H_2O)_{103}] \cdot 180H_2O$ (**$\{W_{72}Fe_{30}\}_{NM}$**), keeping in mind that in the self-assembly leading to the formation of nano-blackberries, each $\{W_{72}Fe_{30}\}$ cluster is surrounded by six 0.5 Fe^{3+} ions from six directions along three orthogonal axes, each linking two adjacent $\{W_{72}Fe_{30}\}$clusters *via* Fe−OH−Fe−OH−Fe bonds as proposed in Figure 2.2, where two Fe−OH entities are from two different adjacent $\{W_{72}Fe_{30}\}$ clusters. This linking offers the isolated material $Fe_3[W_{72}Fe_{30}O_{252}(CH_3COO)_2(OH)_{25}(H_2O)_{103}] \cdot 180H_2O$ (**$\{W_{72}Fe_{30}\}_{NM}$**) an enormous

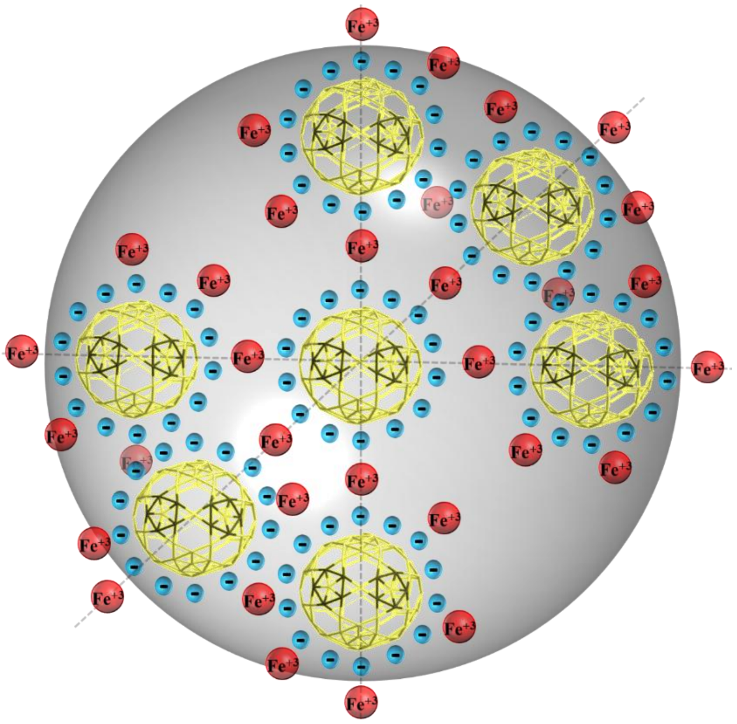

Figure 2.2. Schematic representation of compound **$\{W_{72}Fe_{30}\}_{NM}$** in which six $0.5Fe^{3+}$ cations surrounding each cluster from six sides in three axes.

stability and robustness. This is evidenced by the fact that this material **{$W_{72}Fe_{30}$}$_{NM}$**, even after heating in the aerial condition at 200^{0}C, remains intact (Appendix 2, Figure A2.2e) without its collapsing. On the other hand, the molybdenum nano-blackberries, $Na_2[Mo_{72}Fe_{30}O_{252}(CH_3COO)_4(OH)_{16}(H_2O)_{108}]\cdot 180H_2O$ (**{$Mo_{72}Fe_{30}$}$_{NM}$**), upon heating at 60-70^{0}C, undergoes solid to solid transformation resulting in the formation of $Fe_2(MoO_4)_3$ (Appendix 2, Figure A2.2b).[17] Thus the nano-material **{$Mo_{72}Fe_{30}$}$_{NM}$** (molybdenum nano-blackberries), is a kinetically labile product but its tungsten analogue is not. Accordingly, the aqueous suspension of tungsten nano-blackberries, (**{$W_{72}Fe_{30}$}$_{NM}$**) is extremely stable; tungsten nano-blackberry compound remains intact even after its reflux for several hours. On the other hand, one hour reflux of the aqueous suspension of **{$Mo_{72}Fe_{30}$}$_{NM}$** (molybdenum nano-blackberries) results in the transformation from nano-blackberries to ferric molybdate.

Now we wish to give a rationale of why these instantaneously formed clusters $[Mo_{72}Fe_{30}O_{252}(CH_3COO)_4(OH)_{16}(H_2O)_{108}]^{2-}$ and $[W_{72}Fe_{30}O_{252}(CH_3COO)_2(OH)_{25}(H_2O)_{103}]^{9-}$ self-assemble irreversibly leading to the isolation of aggregated-nano-blackberries $Na_2[Mo_{72}Fe_{30}O_{252}(CH_3COO)_4(OH)_{16}(H_2O)_{108}]\cdot 180H_2O$ (**{$Mo_{72}Fe_{30}$}$_{NM}$**) and $Fe_3[W_{72}Fe_{30}O_{252}(CH_3COO)_2(OH)_{25}(H_2O)_{103}]\cdot 180H_2O$ (**{$W_{72}Fe_{30}$}$_{NM}$**), respectively in our direct synthesis in contrast to the reversible self-assembly of the {$Mo_{72}Fe_{30}$} cluster in the dilute solution of crystalline $[Mo_{72}Fe_{30}O_{252}(CH_3COO)_{12}\{Mo_2O_7(H_2O)\}_2\{H_2Mo_2O_8(H_2O)\}(H_2O)_{91}]\cdot 150H_2O$ (**{$Mo_{72}Fe_{30}$}$_{cryst}$**). Electrostatic intermolecular interaction would likely change when the supramolecular structures (globules / nano-blackberries) transit from solution to solid state. In the present study, the driving force for the solidification of the nano-blackberries (solid-state isolation) is two-fold assemblies / aggregations: (i) first, the assemblies of {$Mo_{72}Fe_{30}$} and {$W_{72}Fe_{30}$} clusters into nano-sized blackberries / globules as described by Liu and Müller[9] and (ii) aggregations of these nano-blackberries to macro-porous material as shown in Figure A2.6a-c (Appendix 2) and Figure 2.3.(a-c), respectively. Thus, the second-generation aggregation leading to the aggregated nano-blackberries is the driving force for their solid-state isolation. Electrostatic inter-blackberries interactions occur to form aggregated nano-blackberries considering Liu-Müller model of placing H_3O^+ ions in between the negatively charged nano-blackberries leading to their solid-state isolation. The experimental and convincing evidence for this electrostatic interaction of using H_3O^+ ions in between individual negatively charged nano-blackberries resulting in aggregated nano-blackberries can be obtained simply by suspending aggregated nano-blakberries, $\mathbf{\{Mo_{72}Fe_{30}\}_{NM}}$ and $\mathbf{\{W_{72}Fe_{30}\}_{NM}}$ separately in neutral water, when the pH value drops down from 7.0 to 3.7 for $\mathbf{\{Mo_{72}Fe_{30}\}_{NM}}$ and 7.0 to 3.9 for $\mathbf{\{W_{72}Fe_{30}\}_{NM}}$. This clearly indicates that the inter-nano-blackberries interactions, responsible for solid state isolation, involves deprotonation of hydroxyl groups of an individual nano-blackberry $[Mo_{72}Fe_{30}O_{252}(CH_3COO)_4(OH)_{16}(H_2O)_{108}]^{2-}$ and $[W_{72}Fe_{30}O_{252}(CH_3COO)_2(OH)_{25}(H_2O)_{103}]^{9-}$ followed by placing the resulting H_3O^+ ions in between the nano-blackberries.

2.3.4. Zeta potential measurement of $\{W_{72}Fe_{30}\}_{NM}$ and $\{Mo_{72}Fe_{30}\}_{NM}$

The mean Zeta-potential (ζ) values of the nano-suspensions of $\mathbf{\{W_{72}Fe_{30}\}_{NM}}$ and $\mathbf{\{Mo_{72}Fe_{30}\}_{NM}}$, respectively, are −34.6 mV and −16.1 mV (Appendix 2, Section A2.11). These values are consistent with the fact that nano-suspension of $\mathbf{\{W_{72}Fe_{30}\}_{NM}}$ does not disintegrate to ferric tungstate (ever after heating for several hours) and that of $\mathbf{\{Mo_{72}Fe_{30}\}_{NM}}$, upon heating at a moderate temperature, collapses to ferric molybdate. Zeta potential (ζ) determination of a nano-suspension is an important technique to estimate the surface charge, thereby to understand the physical stability of the concerned nano-particles in the suspension. A nano-suspension having a ζ value, that is not in the range of −30 mV to +30 mV, is generally considered to have the better physical colloidal stability because of sufficient repulsive forces between the nano-particles of the nano-suspension.

2.3.5. FESEM and HR-TEM analysis of $\{W_{72}Fe_{30}\}_{NM}$

The sizes of nano-blackberries of $\mathbf{\{W_{72}Fe_{30}\}_{NM}}$ are in the range of 300 – 350 nm as shown in their FESEM images in Figure 2.3.a, 2.3.b and 2.3.c. The analysis of high resolution transmission electron microscopy (HR-TEM) images of $\mathbf{\{W_{72}Fe_{30}\}_{NM}}$ is consistent with its FESEM studies as shown in Figure 2.3.d and 2.3.e. The selective area electron diffraction (SAED) of compound $\mathbf{\{W_{72}Fe_{30}\}_{NM}}$ does not show any diffraction as seen in the Figure 2.3.f which completely supports its amorphous nature. As shown in Figure 2.3.a-c, this amorphous material is nothing but aggregated nano-blackberries showing surface porosity. We have thus performed the gas adsorption studies for the compound $\mathbf{\{W_{72}Fe_{30}\}_{NM}}$ and we have found that the BET surface area is 5.345 m^2g^{-1} (Appendix 2, section A2.13). The average pore volume and average pore width of the material $\mathbf{\{W_{72}Fe_{30}\}_{NM}}$ are 0.0117 cc/g and 43.95 Å (around 4 nm), respectively. The nature of adsorption isotherm (Fig. A2.17, Appendix 2) for this material indicates that it is a type III macro-porous material.

The sizes of nano-blackberries of **{$Mo_{72}Fe_{30}$}$_{NM}$** are in the range of 70 – 100 nm (Appendix 2, Figure A2.6). The size difference of the resulting self-assemblies / nano-blackberries in going from molybdenum to tungsten may be due to the difference in charge densities of the building units $[Mo_{72}Fe_{30}O_{252}(CH_3COO)_4(OH)_{16}(H_2O)_{108}]^{2-}$ {$Mo_{72}Fe_{30}$} having 16 OH^- groups and $[W_{72}Fe_{30}O_{252}(CH_3COO)_2(OH)_{25}(H_2O)_{103}]^{9-}$ {$W_{72}Fe_{30}$} having 25 hydroxyl groups. The surface of the tungsten cluster unit {$W_{72}Fe_{30}$} has more negative charge densities than that of molybdenum cluster unit {$Mo_{72}Fe_{30}$} and thus a {$W_{72}Fe_{30}$} cluster unit fetches more positive ions (Fe^{3+}, in the case of tungsten nano-blackberries) around it and each of these surrounding Fe^{3+} ions would attract {$W_{72}Fe_{30}$} cluster unit around it and so on. This way, a solid sphere kind of arrangement or nano- blackberry would be formed as shown in Figure 2.2.

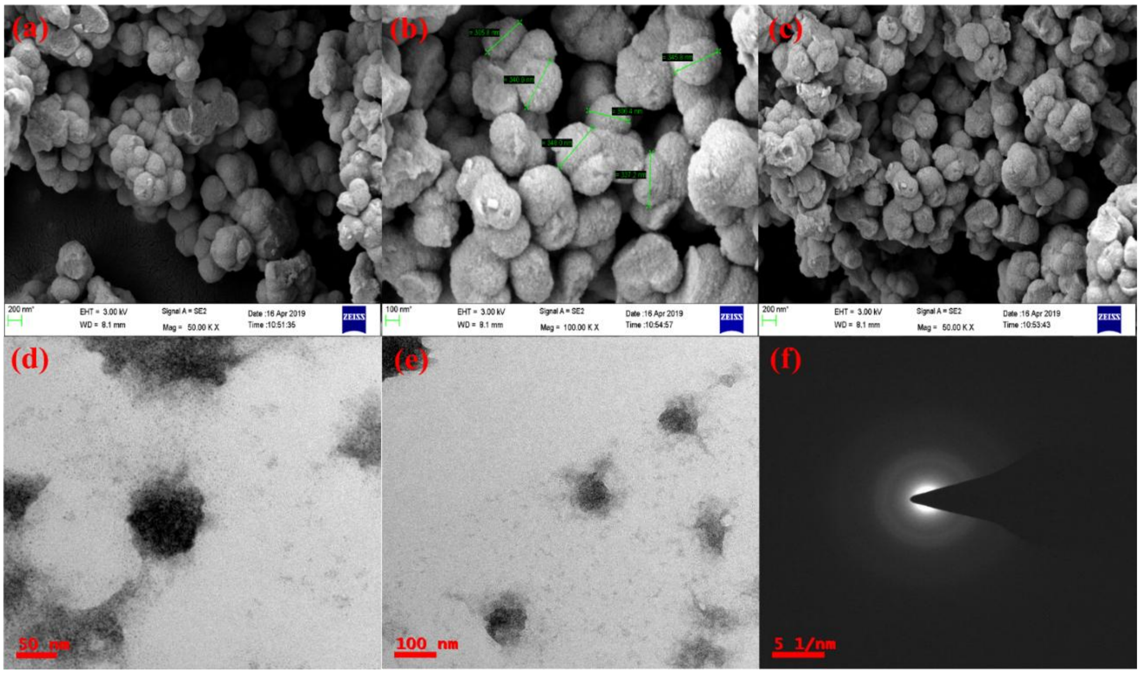

Figure 2.3. (a-c) FESEM images of the compound $Fe_3[W_{72}Fe_{30}O_{252}(CH_3COO)_2(OH)_{25}(H_2O)_{103}]\cdot 180H_2O$ at different resolutions; (d,e) HR-TEM images of the cluster **{$W_{72}Fe_{30}$}$_{NM}$** containing compound; (f) SAED pattern of the cluster **{$W_{72}Fe_{30}$}$_{NM}$** containing compound.

The situation of the irreversible formation of this solid nano-blackberry can be compared with the hydration of a small cation with high charge density (e.g., Li^+ ion), whereby the surrounding water ligands would make a spherical arrangement around the small cation, as demonstrated in Figure 2.2, where the central {$W_{72}Fe_{30}$} cluster with high negative charge density is spherically surrounded by the Fe^{3+} ions. The difference between these isolated nano-blackberries, formed *irreversibly* in a direct one-pot synthesis and the blackberries, formed *reversibly* from a dilute aqueous solution of $[Mo_{72}Fe_{30}O_{252}(CH_3COO)_{12}\{Mo_2O_7(H_2O)\}_2\{H_2Mo_2O_8(H_2O)\}(H_2O)_{91}]\cdot150H_2O$ (**$\{Mo_{72}Fe_{30}\}_{cryst}$**) is that the later are nano-vesicles (hollow / empty space inside) and the former are solid nano-blackberries (inside space is filled, as shown in the formation of these blackberries in Figure 2.2).

2.3.6. DLS measurement of $\{W_{72}Fe_{30}\}_{NM}$ and $\{Mo_{72}Fe_{30}\}_{NM}$

The Zeta (ζ) potential value (−16.1 mV) of the 'molybdenum nano-blackberries' compound, **$\{Mo_{72}Fe_{30}\}_{NM}$** indicates that these nano-blackberries (70 −100 nm) would further aggregate in its aqueous suspension and indeed an aqueous suspension of molybdenum nano-blackberries (70 −100 nm) undergo further aggregation to form bigger supramolecular assemblies (with a hydrodynamic radius of ~510 nm), as found in the DLS studies (Figure A2.16, Appendix 2). On the other hand, 'tungsten nano-blackberries' (size distribution: 300 – 350 nm) in compound, **$\{W_{72}Fe_{30}\}_{NM}$** in its aqueous suspension does not aggregate further as indicated in the DLS studies hydrodynamic radius: ~400 nm (Figure A2.15, Appendix 2), which is consistent with its Zeta (ζ) potential value of −34 mV.

2.3.7. Magnetic Moment measurements of $\{W_{72}Fe_{30}\}_{NM}$

We have performed the room temperature magnetic moment measurements for the both compounds **$\{Mo_{72}Fe_{30}\}_{NM}$** and **$\{W_{72}Fe_{30}\}_{NM}$**; the resultant magnetic moment values are 10.19 BM and 9.47 BM respectively. Even though these values are comparable, the room temperature magnetic moment of **$\{W_{72}Fe_{30}\}_{NM}$** is little less than that of **$\{Mo_{72}Fe_{30}\}_{NM}$**. This may be due to the presence of extra three Fe^{3+} ions per formula unit of **$\{W_{72}Fe_{30}\}_{NM}$**, proposed to be placed in between the nano-blackberries to make the assembly. This may add some contribution from extra-antiferromagnetic coupling interactions which is not present in **$\{Mo_{72}Fe_{30}\}_{NM}$**.

2.3.8 Structural analysis $Fe_3[W_{72}Fe_{30}O_{252}(CH_3COO)_2(OH)_{25}(H_2O)_{103}]\cdot180H_2O$ ($\{W_{72}Fe_{30}\}_{NM}$)

2.3.8.1. Raman Spectroscopy

In our preliminary communication,[17] we reported synthesis of molybdenum nano-blackberry compound $Na_2[Mo_{72}Fe_{30}O_{252}(CH_3COO)_4(OH)_{16}(H_2O)_{108}]\cdot180H_2O$ (**$\{Mo_{72}Fe_{30}\}_{NM}$**), as an amorphous nanomaterial, characterized by IR- and Raman-spectral analyses, thermogravimetric studies, microscopic studies and elemental (C & H) analyses including metal content analyses (ICP-OES). Since the {$Mo_{72}Fe_{30}$} cluster, in crystalline compound $[Mo_{72}Fe_{30}O_{252}(CH_3COO)_{12}\{Mo_2O_7(H_2O)\}_2\{H_2Mo_2O_8(H_2O)\}(H_2O)_{91}]\cdot150H_2O$ (**{$Mo_{72}Fe_{30}$}$_{cryst}$**), has characteristic Raman signal for the {$Mo_{72}Fe_{30}$}cluster cage, it helped us to characterize the identical {$Mo_{72}Fe_{30}$}cluster cage in the amorphous molybdenum nano-blackberry substance **{$Mo_{72}Fe_{30}$}$_{NM}$**. Even

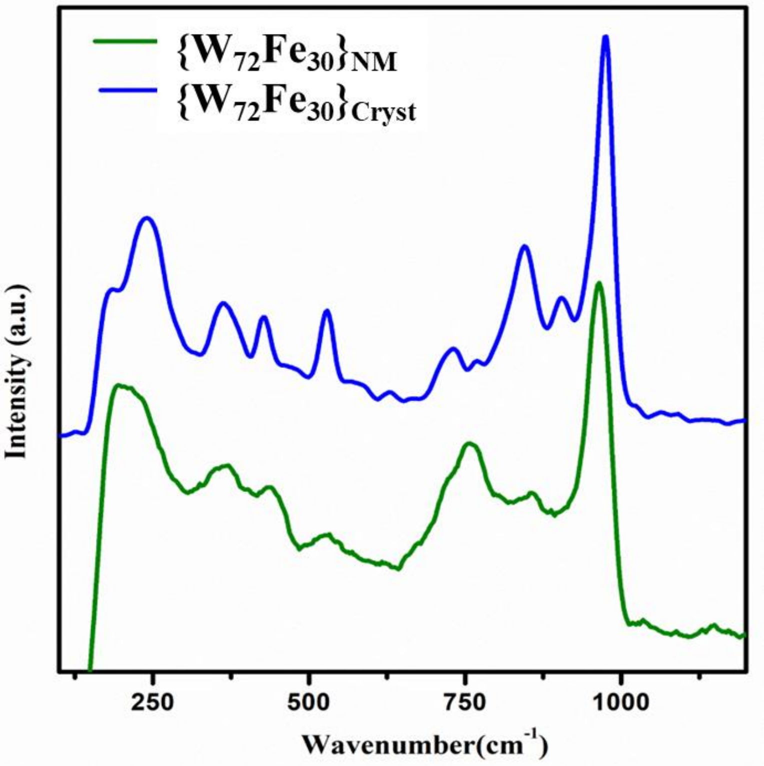

Figure 2.4. Raman spectrum of the cluster **{$W_{72}Fe_{30}$}$_{NM}$** which is compared with that of **{$W_{72}Fe_{30}$}$_{cryst}$**

though, there is no crystalline analogue of tungsten nano-blackberry compound **{$W_{72}Fe_{30}$}$_{NM}$** with acetate ligand, a {$W_{72}Fe_{30}$}cluster cage containing crystalline compound with sulfate ligand, $[Na_6(NH_4)_{20}\{Fe(H_2O)_6\}_2][\{W^{VI}_6O_{21}(SO_4)\}_{12}\{Fe(H_2O)\}_{30}(SO_4)_{13}(H_2O)_{34}]\cdot200H_2O$ is known with its single crystal structure. Its Raman signal (using 632 nm laser excitation) is comparable to that of amorphous tungsten nano-blackberry compound **{$W_{72}Fe_{30}$}$_{NM}$** in the present work (showing the Raman bands at 965 (W=O), 856, 756, 528, 437, 364 and 202 cm^{-1}) as shown in the Figure 2.4.; this conforms that the cluster cage {$W_{72}Fe_{30}$} remains same in crystalline compound $[Na_6(NH_4)_{20}\{Fe(H_2O)_6\}_2]$ $[\{W^{VI}_6O_{21}(SO_4)\}_{12}\{Fe(H_2O)\}_{30}(SO_4)_{13}(H_2O)_{34}]\cdot200H_2O$ (**{$W_{72}Fe_{30}$}$_{cryst}$**) as well as in the amorphous material **{$W_{72}Fe_{30}$}$_{NM}$** compound of the present study. We have formulated this amorphous nano-material as $Fe_3[W_{72}Fe_{30}O_{252}(CH_3COO)_2(OH)_{25}(H_2O)_{103}]\cdot180H_2O$ (**{$W_{72}Fe_{30}$}$_{NM}$**) based on elemental analysis / ICP metal analysis, diverse spectroscopic studies, microscopic techniques, thermogravimetry, powder X-ray diffraction (PXRD) studies and titrimetric analysis of iron.

2.3.8.2. IR analysis of $\{Mo_{72}Fe_{30}\}_{NM}$ and $\{W_{72}Fe_{30}\}_{NM}$

The IR spectra of **$\{Mo_{72}Fe_{30}\}_{NM}$** and **$\{W_{72}Fe_{30}\}_{NM}$** are quite comparable (Figure 2.5. except the fact that the intensity of acetate peaks of the compound **$\{W_{72}Fe_{30}\}_{NM}$** is rather smaller than that of the acetate peaks of **$\{Mo_{72}Fe_{30}\}_{NM}$**. This is consistent with their elemental analysis (Appendix 2, Figures A2.11 and A2.12). There are two acetate anions per formula unit of **$\{W_{72}Fe_{30}\}_{NM}$** and four acetate anions per formula unit of **$\{Mo_{72}Fe_{30}\}_{NM}$**.

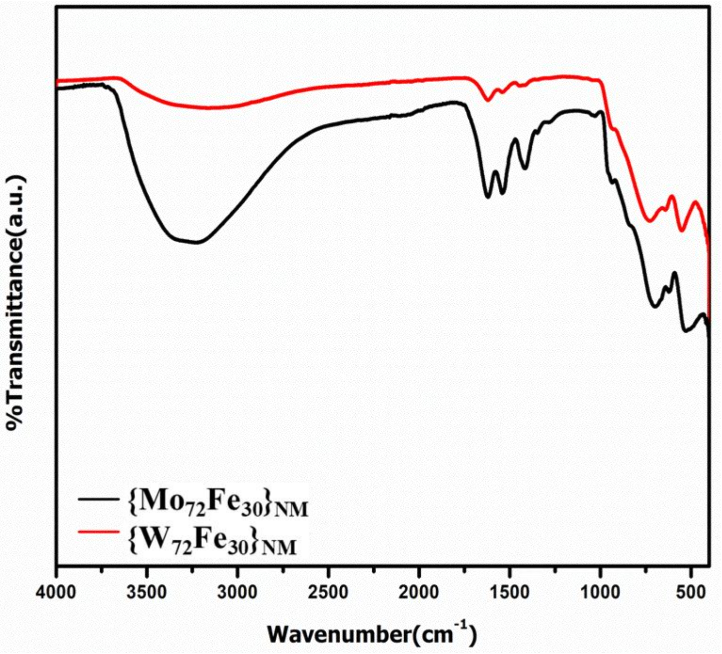

Figure 2.5. FT-IR spectrum of **$\{W_{72}Fe_{30}\}_{NM}$** cluster containing compound $Fe_3[W_{72}Fe_{30}O_{252}(CH_3COO)_2(OH)_{25}(H_2O)_{103}]\cdot180H_2O$, compared with that of the compound **$\{Mo_{72}Fe_{30}\}_{NM}$**.

2.3.8.3 Thermo gravimetric analysis- GCMS of $\{W_{72}Fe_{30}\}_{NM}$ and $\{Mo_{72}Fe_{30}\}_{NM}$

TGA plot of the compound **$\{Mo_{72}Fe_{30}\}_{NM}$** clearly shows that below and around 100 ºC temperature, it loses the water molecules as shown in Figure A2.3 and it is thermally less stable when compared to **$\{W_{72}Fe_{30}\}_{NM}$** compound as shown in the Figure 4c. We have also carried out the TGA-GCMS analysis for the compound **$\{W_{72}Fe_{30}\}_{NM}$** to conform the presence of acetate ligands in the cluster and we have obtained a clear mass spectrum of the compound **$\{W_{72}Fe_{30}\}_{NM}$** as shown in the Figure A2.4. As shown in the thermogravimetric analysis (TGA) plot of **$\{W_{72}Fe_{30}\}_{NM}$** (Figure A2.4c), acetate anions come out (in the form of acetic acid) after 600°C (GC mass, Figure A2.4, Appendix 2).

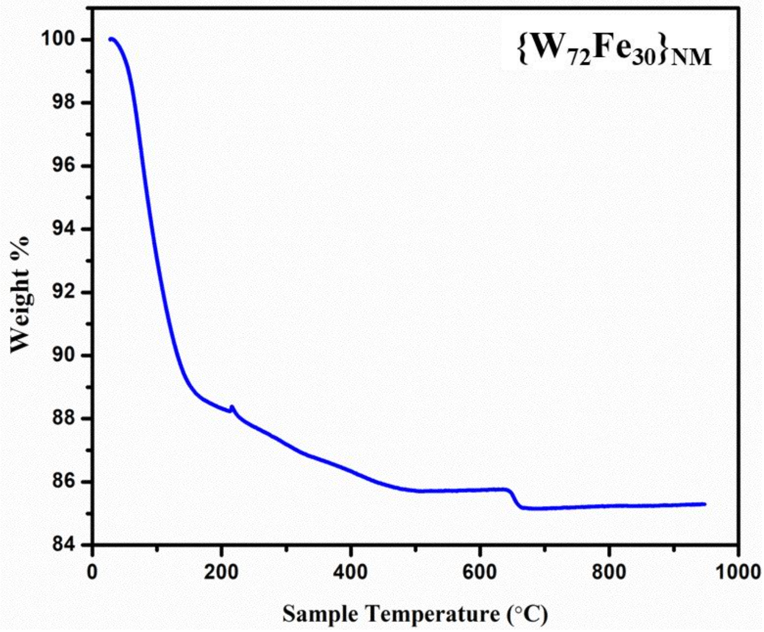

Figure 2.6. Thermogravimetric plot of the amorphous compound **{$W_{72}Fe_{30}$}$_{NM}$**.

2.3.8.4 PXRD pattern of {$Mo_{72}Fe_{30}$}$_{NM}$ and {$W_{72}Fe_{30}$}$_{NM}$

The PXRD pattern of the as synthesized {$Mo_{72}Fe_{30}$} cluster showing broad peak (Appendix 2 Figure A2.2a) clearly indicates that is amorphous in nature. The molybdenum nano-blackberries, $Na_2[Mo_{72}Fe_{30}O_{252}(CH_3COO)_4(OH)_{16}(H_2O)_{108}]\cdot180\ H_2O$ (**{$Mo_{72}Fe_{30}$}$_{NM}$**), upon heating in oven at 70^0C for 42 hrs, undergoes solid to solid transformation resulting in the formation of $Fe_2(MoO_4)_3$ as we have shown in the PXRD (Appendix 2 Figure A2.2b); it shows sharp peaks which is completely in crystalline state. We have also refluxed the compound **{$Mo_{72}Fe_{30}$}$_{NM}$** in 50mL water at 100^0C for one hour, it has been transformed to crystalline form of ferric molybdate as shown in Appendix 2 Figure A2.2c. When we have heated the compound **{$W_{72}Fe_{30}$}$_{NM}$** in muffle furnace at 200^0C for 2 hrs, the compound remains intact without transforming to ferric tungstate as shown in the PXRD pattern (Appendix 2 Figure A2.2e) it exhibits a broad peak as before in Figure A2.2d which indicates that **{$W_{72}Fe_{30}$}$_{NM}$** is still in amorphous nature. Even, when the compound **{$W_{72}Fe_{30}$}$_{NM}$** was refluxed in 50mL water at 100^0C for six hours, it remained intact as it is showing the broad peak in PXRD (Figure A2.2f). The powder X-Ray diffraction (PXRD) plot of the as synthesized **{$W_{72}Fe_{30}$}$_{NM}$** compound shows a broad feature (Figure A2.4d), which clearly establishes that it is amorphous in nature. This is consistent with the selective area electron diffraction (SAED) of compound **{$W_{72}Fe_{30}$}$_{NM}$**, which did not show any diffraction (Figure A2.3f) in its HR-TEM studies.

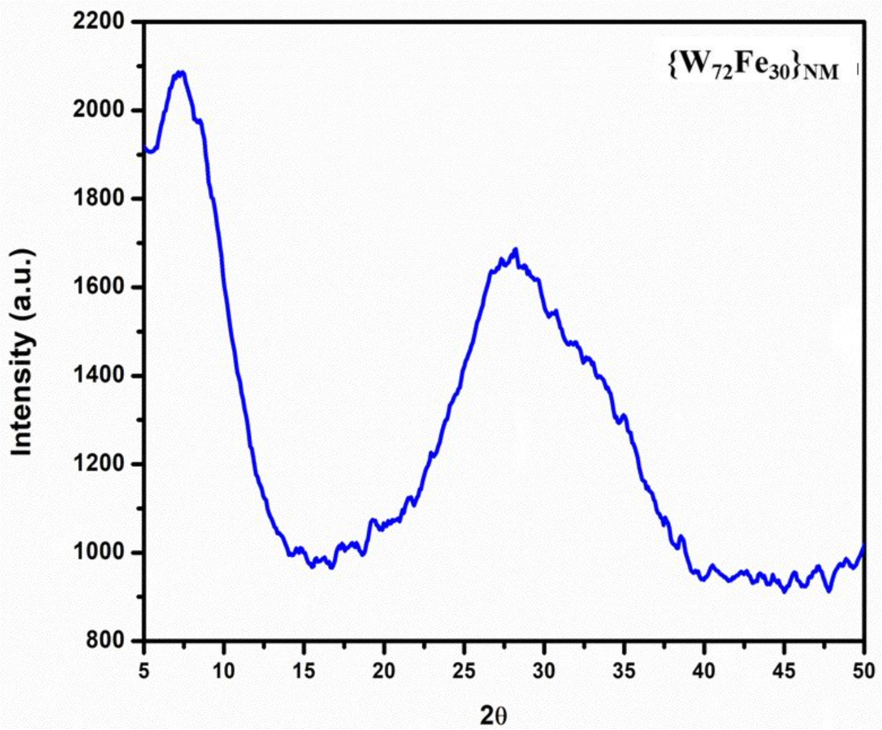

Figure 2.7. PXRD pattern of compound **{$W_{72}Fe_{30}$}$_{NM}$**.

2.3.9. Controlled Experiment

Both the compounds, **{$Mo_{72}Fe_{30}$}$_{NM}$** and **{$W_{72}Fe_{30}$}$_{NM}$** are synthesized under identical conditions, but there is a big difference in their cation contents; **{$Mo_{72}Fe_{30}$}$_{NM}$** is characterized with two sodium cations per {$Mo_{72}Fe_{30}$} cluster per formula unit,[17] whereas, **{$W_{72}Fe_{30}$}$_{NM}$** has three Fe^{3+} cations per {$W_{72}Fe_{30}$} cluster, thereby 33 Fe(III) ions per formula unit. We have confirmed this iron content not only from its ICP metal analyses (ICP-OES data, Appendix 2, Figure A2.9) but also from quantitative titrimetric estimation of iron (Appendix 2, Section A2.20). Likewise, the acetate content (two acetate ligands per formula unit) in $Fe_3[W_{72}Fe_{30}O_{252}(CH_3COO)_2(OH)_{25}(H_2O)_{103}]\cdot180H_2O$ (**{$W_{72}Fe_{30}$}$_{NM}$**) is found out from elemental analyses and TGA studies. We have already mentioned that the iron(III) cations of compound **{$W_{72}Fe_{30}$}$_{NM}$** take part in the self-assembly by linking {$W_{72}Fe_{30}$} cluster units (Figure 2.2) to result in the formation of tungsten nano-blackberries (Figure 2.3.). This linking of {$W_{72}Fe_{30}$} cluster units by Fe^{3+} cations offers enormous stability to the resulting **{$W_{72}Fe_{30}$}$_{NM}$** nano-blackberries compound. In principle, if our assumption that, these Fe^{3+} cations act as linkers to assemble {$W_{72}Fe_{30}$} cluster units to result in the **{$W_{72}Fe_{30}$}$_{NM}$** nano-blackberries as shown in Figure 2.2 is correct, then we should be able to isolate this “nano-blackberries” compound **{$W_{72}Fe_{30}$}$_{NM}$** (beside its direct synthesis) from its crystalline analogue,

$[Na_6(NH_4)_{20}$ $[\{Fe(H_2O)_6\}_2][\{W^{VI}{}_6O_{21}(SO_4)\}_{12}\{Fe(H_2O)\}_{30}$ $(SO_4)_{13}(H_2O)_{34}]\cdot 200H_2O$ (**{W$_{72}$Fe$_{30}$}$_{cryst}$**) because it has same {$W_{72}Fe_{30}$}discrete units and the crystalline compound is highly water soluble unlike **{Mo$_{72}$Fe$_{30}$}$_{cryst}$**. Practically, when we dissolve 0.4 gm of **{W$_{72}$Fe$_{30}$}$_{cryst}$** in 20.00 mL water acidified with 25.0 mL of glacial acetic acid and to it, if we add 0.2 gm of $FeCl_3\cdot 6H_2O$ dissolved in 5.0 mL of water under stirring, a small amount of precipitation formation is observed after 15 minutes. The resulting insoluble precipitate, after its washing (with water) and drying (at room temperature), shows micro-blackberries in its FESEM image (Figures A2.28, Appendix 2). The main difference between these blackberries (obtained from **{W$_{72}$Fe$_{30}$}$_{cryst}$**, sulfate ligated) and **{W$_{72}$Fe$_{30}$}$_{NM}$** blackberries (obtained in direct synthesis) is two folds: these are low yield micro-sized blackberries in contrast to high yield nano-sized blackberries of direct synthesis. Moreover, as expected, these blackberries are characterized with both acetate and sulfate ligands (see IR spectrum Figure A2.29, Appendix 2). The underlying chemistry of this partial transformation of sulfate ligated crystalline {$W_{72}Fe_{30}$} compound $[Na_6(NH_4)_{20}\{Fe(H_2O)_6\}_2][\{W^{VI}{}_6O_{21}(SO_4)\}_{12}\{Fe(H_2O)\}_{30}$ $(SO_4)_{13}(H_2O)_{34}]\cdot 200H_2O$ (**{W$_{72}$Fe$_{30}$}$_{cryst}$**) to amorphous micro-blackberries includes replacement of sulfate ligands by water and acetate anion forming a cluster of relatively less anionic charges and some surface charge densities as shown in the following tentative formula: $[\{W^{VI}{}_6O_{21}(H_2O)_6\}_{12}\{Fe(H_2O)\}_{30}(SO_4)_2(CH_3COO)_2(OH)_3(H_2O)_{19}]^{9-}$, which can be self-assembled by three Fe^{3+} cations (present in the concerned solution, excess ferric chloride added) to form micro-globules as shown in Figure A2.28 (Appendix 2). This experiment clearly proves that tungsten nano-blackberries compound **{W$_{72}$Fe$_{30}$}$_{NM}$** is formed by the self-assembly of {$W_{72}Fe_{30}$} having hydroxyl ligands, whereupon the Fe^{3+} cations are placed in between the {$W_{72}Fe_{30}$} clusters as linkers.

We could not isolate the molybdenum nano-blackberries compound **{Mo$_{72}$Fe$_{30}$}$_{NM}$** (other than its direct synthesis) from its crystalline analogue $[Mo_{72}Fe_{30}O_{252}(CH_3COO)_{12}\{Mo_2O_7(H_2O)\}_2$ $\{H_2Mo_2O_8(H_2O)\}(H_2O)_{91}]\cdot 150H_2O$ (**{Mo$_{72}$Fe$_{30}$}$_{cryst}$**) because of its limited solubility in an aqueous medium. We attempted to covert **{Mo$_{72}$Fe$_{30}$}$_{cryst}$** to {**Mo$_{72}$Fe$_{30}$}$_{NM}$** by performing similar experiment as that of obtaining tungsten micro-blackberries from sulfate ligated crystalline compound **{W$_{72}$Fe$_{30}$}$_{cryst}$**, but we could not succeed, instead, we always ended up with obtaining starting compound **{Mo$_{72}$Fe$_{30}$}$_{cryst}$** (Figure A2.28, Appendix 2).

2.3.10. EDX analysis of $\{\mathbf{W_{72}Fe_{30}}\}_{\mathbf{NM}}$

Energy dispersive X-ray (EDX) spectroscopy was performed for the $\{\mathbf{W_{72}Fe_{30}}\}_{\mathbf{NM}}$ compound to find out the surface composition of tungsten nano-blackberries. Figure A2.7 (Appendix 2) shows the image of the selected surface area of $\{\mathbf{W_{72}Fe_{30}}\}_{\mathbf{NM}}$ including its EDX plot and histogram of the elemental composition. The relevant EDX- elemental mapping analyses have been provided with Appendix 2 (Figure A2.8).

The number of 25 hydroxyl (OH^-) anions as ligands in the formula of $\{\mathbf{W_{72}Fe_{30}}\}_{\mathbf{NM}}$ compound, *i.e.*, $Fe_3[W_{72}Fe_{30}O_{252}(CH_3COO)_2(OH)_{25}(H_2O)_{103}]\cdot 180H_2O$ ($\{\mathbf{W_{72}Fe_{30}}\}_{\mathbf{NM}}$) has been deduced from repeated CHN elemental analysis, ICP metal analysis and quantitative titrimetric iron analysis and by understanding the formation of $\{W_{72}Fe_{30}\}$ cluster in compound $\{\mathbf{W_{72}Fe_{30}}\}_{\mathbf{NM}}$. It is known that $\{W_{72}Fe_{30}\}$ cluster is formed by 12 $[(W)W_5O_{21}(H_2O)_6]^{6-}$ pentagons and 30 $[Fe^{III}]^{3+}$ linkers,[27] resulting in +18 charges that has to be counter-balanced by −18 charges. From CHN and TGA analyses we found two acetate anions and from ICP-OES metal analyses, we found that there are 72 tungsten ions and 33 iron ions per formula unit of the compound (Appendix 2, Section A2.5, A2.9 and A2.10). Quantitative titrimetric iron analyses also support 33 iron ions per formula unit (Appendix 2, Section A2.20). Raman spectroscopy has clearly indicated the presence of $\{W_{72}Fe_{30}\}$ cluster in compound $\{\mathbf{W_{72}Fe_{30}}\}_{\mathbf{NM}}$. These three extra iron ions act as cations per formula. Thus, if there are three Fe^{3+} ions and two acetate anions, we need −25 charges to compensate the resulting +25 charges (+18 + 9 – 2 = +25). Therefore, we have used 25 OH^- as monodentate ligands per formula unit. We have already explained about the source of OH^- anions in the pertinent aqueous synthesis mixture in the section of irreversible formation of nano-blackberries (*vide supra*). On a par with molybdenum system, as established by Liu and his co-workers, the concentration of $\{W_{72}Fe_{30}\}$ cluster units and the rate of their aggregation into nano-blackberries have a direct relationship between them, namely, the aggregation is faster when the concentration of cluster is higher; [9,13,30,31] as this is a spontaneous assembly process and the $\{W_{72}Fe_{30}\}$cluster is formed instantaneously in a large amount, the concerned system does not get enough time to arrange the $\{W_{72}Fe_{30}\}$ clusters in an order fashion to get the crystalline product, instead the clusters, with large negative charge density on the clusters surfaces,[17] assemble *via* Fe^{3+} cations to result in the formation of nano-blackberries of enormous stability. In contrast to the solution phase assembly of $\{Mo_{72}Fe_{30}\}$ clusters in a dilute aqueous solution of $\{\mathbf{Mo_{72}Fe_{30}}\}_{\mathbf{cryst}}$, the formation of isolated nano-blackberries in the solid state includes two folds assemblies / aggregations. First the nano-blackberries are formed by the assembly of $\{W_{72}Fe_{30}\}$ clusters with the particle size ranging from 300 nm to 350 nm. The second fold aggregation involves some kind of fusion among the nano-blackberries (Figure 2.3. a-c).

2.3.11. $\{\mathbf{W_{72}Fe_{30}}\}_{\mathbf{NM}}$ *versus* $\{\mathbf{W_{72}Fe_{30}}\}_{\mathbf{cryst}}$

The dilute solution of known crystalline $\{W_{72}Fe_{30}\}$ cluster containing compound $[Na_6(NH_4)_{20}\{Fe(H_2O)_6\}_2][\{W^{VI}_6O_{21}(SO_4)\}_{12}\{Fe(H_2O)\}_{30}(SO_4)_{13}(H_2O)_{34}]\cdot 200H_2O$ (**$\{W_{72}Fe_{30}\}_{cryst}$**) was subjected to laser light-scattering studies by Liu and Müller and their co-workers to investigate, whether the relevant $\{W_{72}Fe_{30}\}$ cluster (with sulphate ligands) self-assembles into nano-blackberry-type structures, which is unlikely because of the electrostatic repulsion caused by the resulting high negative charge (−32) of the macroion, $[\{W^{VI}_6O_{21}(SO_4)\}_{12}\ \{Fe(H_2O)\}_{30}(SO_4)_{13}(H_2O)_{34}]^{32-}$ (when 20 ammonium cations are released from the $\{W_{72}Fe_{30}\}$ cluster pores).[27] However, they demonstrated the formation of supramolecular structures in an aqueous dilute solution of **$\{W_{72}Fe_{30}\}_{cryst}$** at pH 4.6, with an average hydrodynamic radius (R_h) of approximately 31 nm. Liu and Müller explained this unexpected observation by demonstrating a lower charge (*e.g.*, −12) of the macroion in the dilute solution of **$\{W_{72}Fe_{30}\}_{cryst}$** at pH 4.6, as if, 20 NH_4^+ ions are not released from the pores of the relevant $\{W_{72}Fe_{30}\}$ cluster in this condition.[27] This clearly indicates that the macroion $[\{W^{VI}_6O_{21}(SO_4)\}_{12}\{Fe(H_2O)\}_{30}(SO_4)_{13}(H_2O)_{34}(NH_4)_{20}]^{12-}$ undergoes self-assembly into nano-blackberries in the dilute aqueous solution of **$\{W_{72}Fe_{30}\}_{cryst}$** at pH 4.6 and at this pH, 20 NH_4^+ ions remain intact on 20 pores of the $\{W_{72}Fe_{30}\}$ cluster to maintain the charge of the cluster of −12. In the present study, we have shown that the macroion $[W_{72}Fe_{30}O_{252}(CH_3COO)_2(OH)_{25}(H_2O)_{103}]^{9-}$ undergoes assembly using three Fe^{3+} cations as the linkers per macroion leading to the solid-state isolation of tungsten nano-blackberry compound $Fe_3[W_{72}Fe_{30}O_{252}(CH_3COO)_2(OH)_{25}(H_2O)_{103}]\cdot 180H_2O$ (**$\{W_{72}Fe_{30}\}_{NM}$**). We have also shown that the addition of ferric chloride and acetic acid to an aqueous solution of **$\{W_{72}Fe_{30}\}_{cryst}$** results in the formation and solid-state isolation of micro-blackberries of probable composition $Fe_3[\{W^{VI}_6O_{21}(H_2O)_6\}_{12}\{Fe(H_2O)\}_{30}(SO_4)_2(CH_3COO)_2(OH)_3(H_2O)_{19}]\cdot xH_2O$.

2.4. Electrocatalytic Water Reduction to Molecular Hydrogen

The electrocatalytic performances of **$\{Mo_{72}Fe_{30}\}_{NM}$** and **$\{W_{72}Fe_{30}\}_{NM}$** toward hydrogen evolution reaction (HER) by water reduction have been studied by cyclic voltammograms (CVs) and linear sweep voltammograms (LSVs) in the acidic electrolyte (0.1M Na_2SO_4 at pH 2.5) with three electrode configuration. As shown in Figure 2.8.a, **$\{W_{72}Fe_{30}\}_{NM}$** exhibits better performance for HER, compared to **$\{Mo_{72}Fe_{30}\}_{NM}$** since **$\{W_{72}Fe_{30}\}_{NM}$** shows greater catalytic current density than **$\{Mo_{72}Fe_{30}\}_{NM}$**. CVs of **$\{Mo_{72}Fe_{30}\}_{NM}$** and **$\{W_{72}Fe_{30}\}_{NM}$** were also recorded (Figure 2.8.b) at a scan rate 100 mV s^{-1} in 0.1M Na_2SO_4 at pH 2.5 to check the electrocatalytic activity for HER. As expected, the CV of **$\{W_{72}Fe_{30}\}_{NM}$** shows lower onset potential and greater catalytic current density, compared to those of **$\{Mo_{72}Fe_{30}\}_{NM}$**. In polyoxometalate, a trend was observed that with increasing in electronegativity (χ) of the polyatom the redox potential decreases.[32]As the χ of tungsten (2.36) is greater than χ of molybdenum (2.16), **$\{W_{72}Fe_{30}\}_{NM}$** shows better electrocatalytic performance than **$\{Mo_{72}Fe_{30}\}_{NM}$**. The another reason for better electrocatalytic activity of **$\{W_{72}Fe_{30}\}_{NM}$** than **$\{Mo_{72}Fe_{30}\}_{NM}$** is the labile nature of **$\{Mo_{72}Fe_{30}\}_{NM}$** as compared to **$\{W_{72}Fe_{30}\}_{NM}$** (*vide supra).* Catalytic stability of a catalyst is very crucial for the practical application. The catalytic stability of **$\{Mo_{72}Fe_{30}\}_{NM}$** and **$\{W_{72}Fe_{30}\}_{NM}$** for HER in acidic medium (0.1M Na_2SO_4 at pH 2.5) were investigated by chronoamperometric measurements at an onset potential −1.0V for 2h. As shown in Figures 2.8.c and 2.8.d, a stable current density (−0.73 mA cm^{-2}) was achieved for a period of 2h by **$\{Mo_{72}Fe_{30}\}_{NM}$** and also a stable current density (−1.02 mA cm^{-2}) was achieved for a period of 2h by **$\{W_{72}Fe_{30}\}_{NM}$**. A negligible change of current density in each case was observed due to the continuous evolution of hydrogen bubbles from electrode surface. The evolved H_2 gas was analyzed by gas chromatography (Appendix 2, Section A2.15). A very negligible leaching of both catalysts into the electrolytic solution during the chronoamperometric measurement was observed, which are confirmed by ICP-OES analysis of electrolytic solution, obtained at the end of the chronoamperometric measurement (Appendix 2 A2.18).

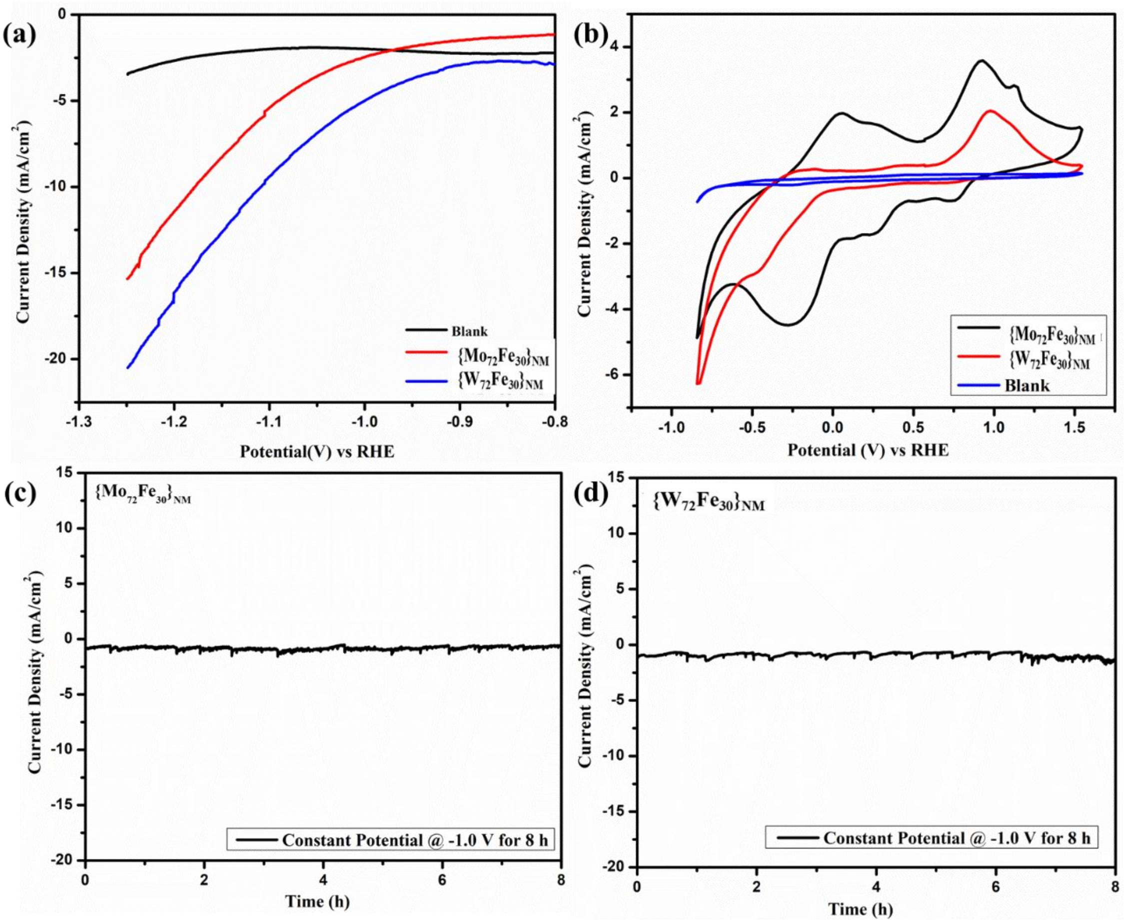

Figure 2.8. (a) LSV curves of blank, **$\{Mo_{72}Fe_{30}\}_{NM}$** and **$\{W_{72}Fe_{30}\}_{NM}$** in 0.1M Na_2SO_4 (pH 2.5) at a scan rate 10 mV s^{-1}. (b) CV curves of blank, **$\{Mo_{72}Fe_{30}\}_{NM}$** and **$\{W_{72}Fe_{30}\}_{NM}$** in 0.1M Na_2SO_4 (pH 2.5) at a scan rate 100 mV s^{-1}. (c) Chronoamperometric plot of **$\{Mo_{72}Fe_{30}\}_{NM}$** at potential −1.0V for 2h. (d) Chronoamperometric plot of **$\{W_{72}Fe_{30}\}_{NM}$** at potential −1.0V for 2h.

Tafel equation is of fundamental importance in electrochemical kinetics and it relates the rate of electrochemical reaction (electric current) to the applied electrochemical potential *via* a linear correlation, $\eta = a + b \log i$ (where i = current density, b = Tafel slope, η = overpotential and a = constant).[33] A low value of overpotential and Tafel slope corresponds to better electrocatalytic performance for HER. Tafel plots of **$\{Mo_{72}Fe_{30}\}_{NM}$** and **$\{W_{72}Fe_{30}\}_{NM}$** were obtained by performing galvanostatic polarization in 0.1M Na_2SO_4 at pH 2.5. In case of **$\{Mo_{72}Fe_{30}\}_{NM}$**, an overpotential of 767 mV is required to attain a current density of 1 mV cm^{-2} (Figure 2.9a). Similarly,

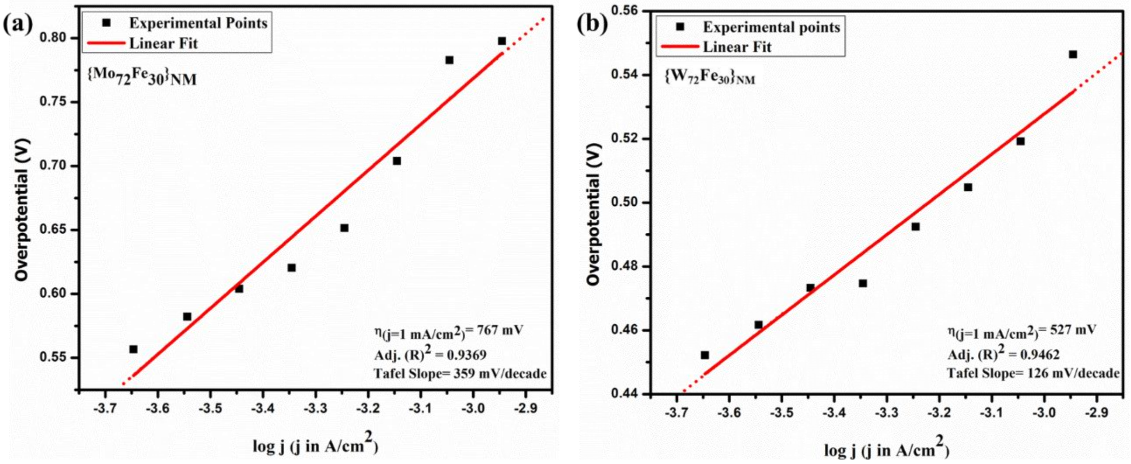

Figure 2.9. (a) Tafel plot of **$\{Mo_{72}Fe_{30}\}_{NM}$** in 0.1M Na_2SO_4 at pH 2.5. (b) Tafel plot of **$\{W_{72}Fe_{30}\}_{NM}$** in 0.1M Na_2SO_4 at pH 2.5.

the overpotential requirement for **$\{W_{72}Fe_{30}\}_{NM}$** is found to be 527 mV cm^{-2} which was lower than that of **$\{Mo_{72}Fe_{30}\}_{NM}$** by 240 mV (Figure 2.9.b). This clearly indicates that **$\{W_{72}Fe_{33}\}_{NM}$** is better electrocatalyst for HER, compared to that of **$\{Mo_{72}Fe_{30}\}_{NM}$**. As shown in Figures 2.9.a & b, the Tafel slope of **$\{W_{72}Fe_{30}\}_{NM}$** was lower than that of **$\{Mo_{72}Fe_{30}\}_{NM}$** by 233 mV/decade. This also indicates that **$\{W_{72}Fe_{30}\}_{NM}$** is superior electrocatalyst to **$\{Mo_{72}Fe_{30}\}_{NM}$** for HER. The extra overpotential is required for **$\{Mo_{72}Fe_{30}\}_{NM}$** to attain a current density of 1 mVcm^{-2} as compared to **$\{W_{72}Fe_{30}\}_{NM}$** because **$\{Mo_{72}Fe_{30}\}_{NM}$** is structurally labile than **$\{W_{72}Fe_{30}\}_{NM}$**.

2.4.1. Calculation of Turnover Frequency (TOF) for H$_2$ evolution

Turn over frequency (TOF) was calculated for both **$\{Mo_{72}Fe_{30}\}_{NM}$** and **$\{W_{72}Fe_{30}\}_{NM}$** using the formula TOF = I/Q, where I is the constant current (in A) obtained from chronoamperometric measurement and Q is the charge (in A s) obtained from the reduction peak in the CV, recorded under noncatalytic conditions (Appendix 2, Section A2.16).[34] The TOF values for **$\{Mo_{72}Fe_{30}\}_{NM}$** and **$\{W_{72}Fe_{30}\}_{NM}$** are 0.45 s^{-1} and 0.72 s^{-1} respectively. From the TOF values also, it is evident that **$\{W_{72}Fe_{30}\}_{NM}$** is more efficient electrocatalyst to produce more hydrogen gas per second than **$\{Mo_{72}Fe_{30}\}_{NM}$** does per second.

2.4.2. Calculation of Faradaic Efficiency

Faradaic efficiencies of **$\{Mo_{72}Fe_{30}\}_{NM}$** and **$\{W_{72}Fe_{30}\}_{NM}$** have been calculated from the amount of evolved hydrogen gas under chronoamperometric measurement using homemade setup (Appendix 2, Section A2.14). Faradaic efficiencies of **$\{Mo_{72}Fe_{30}\}_{NM}$** and **$\{W_{72}Fe_{30}\}_{NM}$** are found to be 56% and 72% respectively. The Faradaic efficiency of

56% for molybdenum blackberry compound **{$Mo_{72}Fe_{30}$}$_{NM}$** is directly consistent with its kinetic lability of its solid to solid conversion to ferric molybdate.[17] Even though, the thermal stability of tungsten analogue, **{$W_{72}Fe_{30}$}$_{NM}$** is enormous, its stability in the electrochemical cell (0.1M sodium sulfate electrolyte at pH 2.5) is diminished as shown by its Faradaic efficiency of 72%.

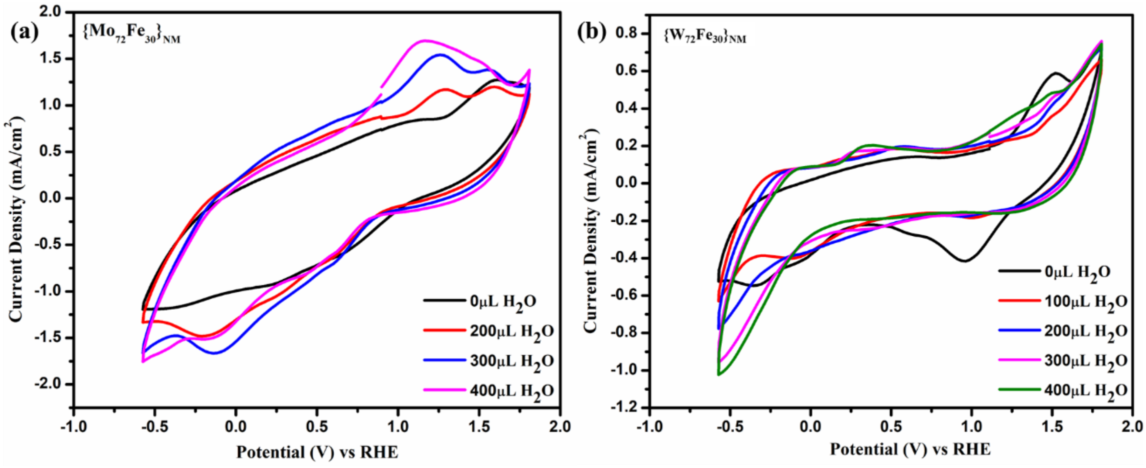

Figure 2.10. (a) Cyclic voltammograms of **{$Mo_{72}Fe_{30}$}$_{NM}$** in THF (tetrabutylammonium perchlorate has been used as an electrolyte) with sequential additions of 0 µL, 200 µL, 300 µL, 400 µL water. (b) Cyclic voltammograms of **{$W_{72}Fe_{30}$}$_{NM}$** in THF (tetrabutylammonium perchlorate was used as electrolyte) with sequential additions of 0 µL, 100 µL, 200 µL, 400 µL water.

Since all the electrochemical HER measurements have been performed in an acidic medium (0.1M Na_2SO_4 at pH 2.5), there are two possibility to produce hydrogen gas: (i) water reduction and (ii) proton reduction. In order to confirm that it is water reduction (and not proton reduction), CVs of **{$Mo_{72}Fe_{30}$}$_{NM}$** were performed in tetrahydrofuran (THF) medium using tetrabutylammonium perchlorate as supporting electrolyte with sequential addition of water (Figure 7a). It has been observed that the catalytic current for HER increases with sequential addition of water. Similar experiment was performed with **{$W_{72}Fe_{30}$}$_{NM}$** and same results are observed (Figure 2.10.b). From these experiments, it is confirmed that the hydrogen gas is produced by both **{$Mo_{72}Fe_{30}$}$_{NM}$** and **{$W_{72}Fe_{30}$}$_{NM}$** due to water reduction. We wanted to find out the functional site for water reduction, especially for **{$W_{72}Fe_{30}$}$_{NM}$** (kinetically stable compound), whether it is tungsten or iron center. We performed some controlled experiments using **{$W_{72}Fe_{30}$}$_{NM}$** and ferric chloride (see Appendix 2, section A2.22, Figure A2.32) and found out that it is the iron center (not the tungsten center) that acts as the functional site for water reduction.

To explain a reaction including concerned half reactions where both protons and electrons are involved with regard to the relevant mechanism, the proton-coupled electron transfer (PCET) has to be considered,[35] because all HER measurements in the present study were performed in an acidic medium. As shown in Figures 2.11.a & b, a successive increase of catalytic current is observed with increase in pH of electrolyte for both **{$Mo_{72}Fe_{30}$}$_{NM}$** and **{$W_{72}Fe_{30}$}$_{NM}$**. In case of **{$Mo_{72}Fe_{30}$}$_{NM}$**, a linear plot of potential *versus* pH has been constructed from the CVs in different pH values where required potentials have been obtained at a fixed current density of -2.1 $mAcm^{-2}$ (Figure 2.11.c). The slope, obtained from potential *versus* pH plot for **{$Mo_{72}Fe_{30}$}$_{NM}$**, is found to be −373 mV/pH. Similarly, in case of **{$W_{72}Fe_{30}$}$_{NM}$**, a linear plot of potential *versus* pH was

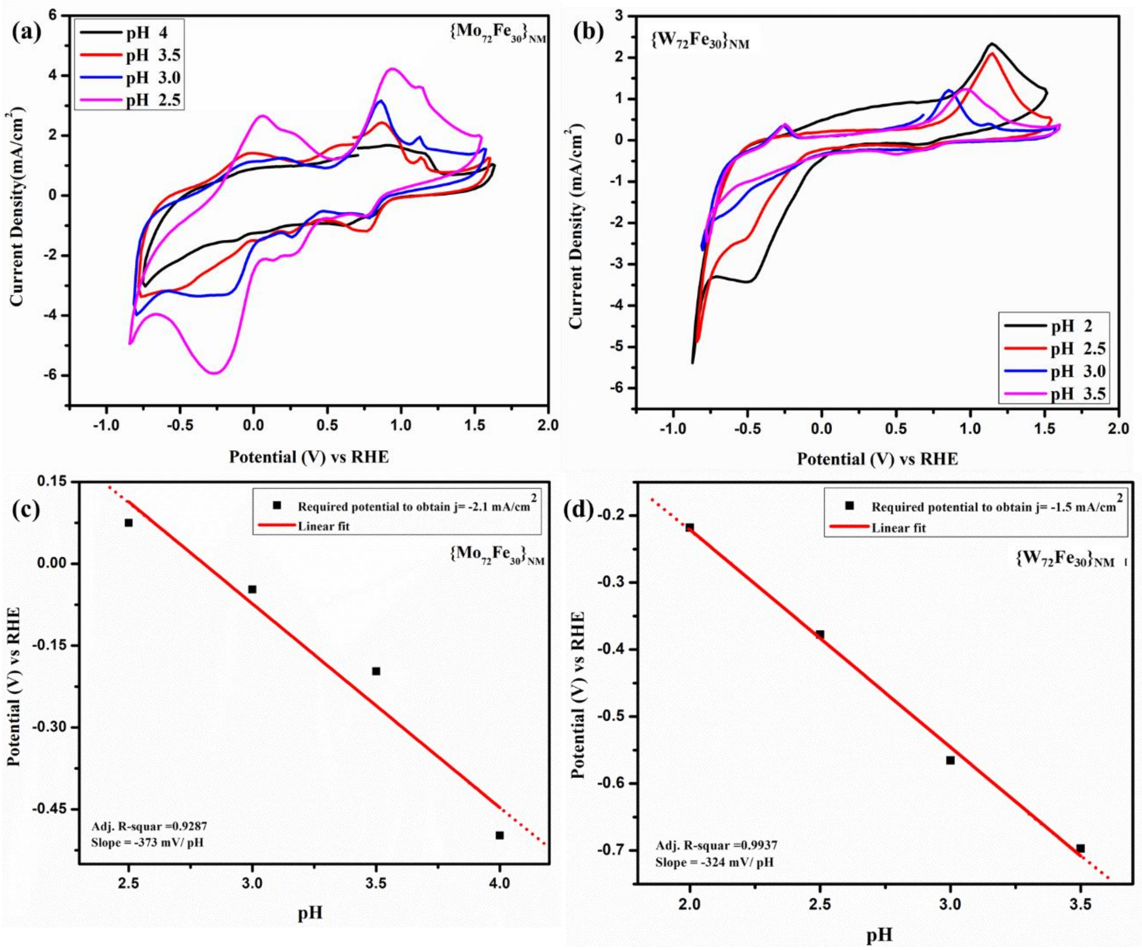

Figure 2.11. (a) Cyclic voltammograms of **{$Mo_{72}Fe_{30}$}$_{NM}$** in 0.1M Na_2SO_4 at pH 4.0, pH 3.5, pH 3.0, pH 2.5. (b) Cyclic voltammograms of **{$W_{72}Fe_{30}$}$_{NM}$** in 0.1M Na_2SO_4 at pH 3.5, pH 3.0, pH 2.5, pH 2.0. (c) Potential *versus* pH plot of **{$Mo_{72}Fe_{30}$}$_{NM}$** (at j = -2.1 mA cm^{-2}) and (d) potential *versus* pH plot of **{$W_{72}Fe_{30}$}$_{NM}$** (at j = -1.5 mA cm^{-2}).

constructed from the CVs in different pH values, where required potentials were obtained at a fixed current density of -1.5 mA cm^{-2} (Figure 2.11.d). The slope, obtained from the plot of potential *versus* pH in this case (**{$W_{72}Fe_{30}$}$_{NM}$**) is observed to be -324 mV/pH. Müller and his co-workers reported that guest-free {$Mo_{72}Fe_{30}$}-type polyoxometalate (POM) cluster is involved in electrochemical reduction by two electrons.[25] It has been found from the concerned slope value that **{$Mo_{72}Fe_{30}$}$_{NM}$** involves proton-coupled electron transfer in HER with thirteen protons and two electrons ($13H^+$-$2e^-$) (Appendix 2, Section A2.17). Similarly, **{$W_{72}Fe_{30}$}$_{NM}$** involves proton-coupled electron transfer in water reduction with eleven protons and two electrons ($11H^+$-$2e^-$) (Appendix 2, Section A2.17). Thus, a large number of protons are involved in the present proton-coupled electron transfer pathways because such type of POM clusters contains a large number of metal centers in their highest oxidation states on which electrons can be delocalized to accumulate a good number of protons.

The crystalline water soluble analogues $Mo_{72}Fe_{30}O_{252}(CH_3COO)_{12}\{Mo_2O_7(H_2O)\}_2\{H_2Mo_2O_8(H_2O)\}(H_2O)_{91}]\cdot150H_2O$ (**{$Mo_{72}Fe_{30}$}$_{cryst}$**) and $[Na_6(NH_4)_{20}\{Fe(H_2O)_6\}_2][\{W^{VI}_6O_{21}(SO_4)\}_{12}\{Fe(H_2O)\}_{30}(SO_4)_{13}(H_2O)_{34}]\cdot200H_2O$ (**{$W_{72}Fe_{30}$}$_{cryst}$**) are known to be catalysts, in general. We thus attempted to perform homogeneous electrocatalytic water reduction by using the crystalline substances, **{$Mo_{72}Fe_{30}$}$_{cryst}$** and **{$W_{72}Fe_{30}$}$_{cryst}$** as catalysts in the same aqueous medium condition, which we used for heterogeneous electrocatalysis of water using amorphous nano-blackberry materials **{$Mo_{72}Fe_{30}$}$_{NM}$** and **{$W_{72}Fe_{30}$}$_{NM}$** as catalysts. But our attempts to perform homogeneous electrocatalysis of water using **{$Mo_{72}Fe_{30}$}$_{cryst}$** and **{$W_{72}Fe_{30}$}$_{cryst}$** as catalysts were without success. When we performed electrocatalysis in an aqueous solution of the crystalline compound, **{$Mo_{72}Fe_{30}$}$_{cryst}$** or **{$W_{72}Fe_{30}$}$_{cryst}$**, it does not act as a true electrocatalyst because it gets electrochemically deposited on the working electrode which we proved by doing controlled experiments (see Appendix 2, section A2.21, Figures A2.30 and A2.31). This restricts us to compare the electrocatalysis of our nano-blackberries **{$Mo_{72}Fe_{30}$}$_{NM}$** and **{$W_{72}Fe_{30}$}$_{NM}$** with that of their crystalline analogues **{$Mo_{72}Fe_{30}$}$_{cryst}$** and **{$W_{72}Fe_{30}$}$_{cryst}$**.

2.5. Conclusions

We have demonstrated that the fundamental concept of Liu and Müller of reversible formation of self-assemblies / nano-blackberries of {$Mo_{72}Fe_{30}$} clusters in the dilute aqueous solution of the crystalline compound $[Mo_{72}Fe_{30}O_{252}(CH_3COO)_{12}\{Mo_2O_7(H_2O)\}_2\{H_2Mo_2O_8(H_2O)\}(H_2O)_{91}]\cdot150H_2O$ (**{$Mo_{72}Fe_{30}$}$_{cryst}$**) can be materialized by isolating such nano-blackberries in the solid state. We have not only isolated molybdenum nano-blackberries,[17] but also we have isolated and characterized tungsten nano-blackberries **{$W_{72}Fe_{30}$}$_{NM}$** focusing a new light of assembling {$W_{72}Fe_{30}$} clusters through Fe^{3+} ions.

For the first time we have shown a meaningful application of these nano-blackberries in the direction of generating sustainable energy.

We have successfully synthesized the nano-blackberries of tungsten analogue $Fe_3[W_{72}Fe_{30}O_{252}(CH_3COO)_2(OH)_{25}(H_2O)_{103}]\cdot180H_2O$ (**$\{W_{72}Fe_{30}\}_{NM}$**) by mixing low cost chemicals, sodium tungstate, ferric chloride and acetic acid in an aqueous solution. The self-assembled nano-blackberries of (**$\{W_{72}Fe_{30}\}_{NM}$**) has been characterized by diverse spectral studies including FT-IR, Raman spectroscopy, elemental analysis including ICP metal analysis and CHN analysis, volumetric analysis (for iron), microscopy techniques, DLS and Zeta potential measurements. We have found that extra three iron ions, that are present per $\{W_{72}Fe_{30}\}$ cluster in the compound **$\{W_{72}Fe_{30}\}_{NM}$** as linker of assembly, offer an enormous amount of rigidity / thermal stability of compound **$\{W_{72}Fe_{30}\}_{NM}$** when compared to its molybdenum analogue $Na_2[Mo_{72}Fe_{30}O_{252}(CH_3COO)_4(OH)_{16}(H_2O)_{108}]\cdot180H_2O$ (**$\{Mo_{72}Fe_{30}\}_{NM}$**), a kinetically labile substance, which on heating at 60-70^{o}C degrades to $Fe_2(MoO_4)_3$. We have explored the electrocatalytic activity of the compounds **$\{Mo_{72}Fe_{30}\}_{NM}$** and **$\{W_{72}Fe_{30}\}_{NM}$** for hydrogen evolution reaction (HER) by water reduction. In a comparative kinetic study, the relevant turnover frequencies (TOFs) of **$\{W_{72}Fe_{30}\}_{NM}$** and **$\{Mo_{72}Fe_{30}\}_{NM}$** (~$0.72s^{-1}$ and ~$0.45s^{-1}$, respectively) and the overpotential values of **$\{W_{72}Fe_{30}\}_{NM}$** and **$\{Mo_{72}Fe_{30}\}_{NM}$** (527 mV and 767 mV, respectively) show that **$\{W_{72}Fe_{30}\}_{NM}$** performs better than **$\{Mo_{72}Fe_{30}\}_{NM}$** in terms of their catalytic activity.

2.6. References

1. Müller, A.; Sarkar, S.; Shah, S. Q. N.; Bogge, H.; Schmidtmann, M.; Sarkar, Sh.; Kögerler, P.; Hauptfleisch, B.; Trautwein, A. X.; Schunemann, V. Archimedean synthesis and magic numbers: ″sizing″ giant molybdenum-oxide-based molecular spheres of the Keplerate type. *Angew. Chem. Int. Ed.* **1999,** *38*, 3238-3241.
2. Jung, J. K.; Procissi, D.; Vincent, R.; Suh, B. J.; Borsa, F.; Kogerler, P.; Schroder, C.; Luban, M. Proton NMR in the giant paramagnetic molecule $\{Mo_{72}Fe_{30}\}$. *Journal of Applied Physics,* **2002,** *91*, 7388-7390.
3. Kuepper, K.; Derks, C.; Taubitz, C.; Prinz, M.; Joly, L.; Kappler, J. P.; Postnikov, A.; Yang, W.; Kuznetsova, T. V.; Wiedwald, U.; Ziemann, P.; Neumann, M. Electronic structure and soft-X-ray-induced photoreduction studies of iron-based magnetic polyoxometalates of type $\{(M)M_5\}_{12}Fe^{III}_{30}(M = Mo^{VI}, W^{VI})$. *Dalton Trans.*, **2013**, *42*, 7924–7935.

4. Garlea, V. O.; Nagler, S. E.; Zarestky, J. L.; Stassis, C.; Vaknin, D.; Kögerler, P.; McMorrow, D. F.; Niedermayer, C.; Tennant, A.; Lake, B.; Qiu, Y.; Exler, M.; Schnack, J.; Luban, M. Probing spin frustration in high-symmetry magnetic nanomolecules by inelastic neutron scattering. *Physical Review B,* **2006**, *73,* 024414.
5. Lago, J.; Micotti, E.; Corti, M. Low-energy spin dynamics in the giant Keplerate molecule $Mo_{72}Fe_{30}$%: A muon spin relaxation and ^{1}H NMR investigation. *Physical Review B*, **2007**, *76*, 064432.
6. Schröder, C. Multiple nearest-neighbor exchange model for the frustrated magnetic molecules {$Mo_{72}Fe_{30}$} and {$Mo_{72}Cr_{30}$}. *Physical Review B,* **2008**, *77*, 224409.
7. Neuscamman, E.; Chan, G. K. Correlator product state study of molecular magnetism in the giant Keplerate $Mo_{72}Fe_{30}$. *Physical Review B,* **2012**, *86*, 064402.
8. Schröder, C. Competing Spin Phases in Geometrically Frustrated Magnetic Molecules. *PRL*. **2005**, *94*, 017205.
9. Liu, T.; Imber, B.; Diemann, E.; Liu, G.; Cokleski, K.; Li, H.; Chen, Z.; Müller, A. Deprotonations and Charges of Well-Defined {$Mo_{72}Fe_{30}$} Nanoacids Simply Stepwise Tuned by pH Allow Control/Variation of Related Self-Assembly Processes. *J. Am. Chem. Soc*. **2006**, *128*, 15914-15920.
10. Ostroushko, A. A.; Tonkushina, M. O.; Korotaev, V. Y.; Prokofeva, A. V.; Kutyashev, B.; Vazhenin, V. A.; Danilova,I. G.; Menshikov, S. Y. Stability of the $Mo_{72}Fe_{30}$ Polyoxometalate Buckyball in Solution. *Russian Journal of Inorganic Chemistry,* **2012**, *57*, 1210–1213.
11. Fareghi-Alamdari, R.; Hafshejani, S. M.; Taghiyar, H.; Yadollahi, B.; Farsani, M. R. Recyclable, Green and Efficient Epoxidation of Olefins in Water with Hydrogen Peroxide Catalyzed by Polyoxometalate Nanocapsule. *Catalysis Communications,* **2016**, *78*, 64-67.
12. Goss. K.; Kamra, A.; Spudat, C.; Meyer, C.; Kögerler, P.; Schneider, C. M. CVD growth of carbon nanotubes using molecular nanoclusters as catalyst. *Phys. Status Solidi B*, **2009**, *246*, 2494–2497.
13. Liu, T. Supramolecular Structures of Polyoxomolybdate-Based Giant Molecules in Aqueous Solution. *J. Am. Chem. Soc.* **2002**, *124*, 10942-10943.
14. Mishra, P. P.; Pigga, J.; Liu, T. Membranes Based on “Keplerate”-Type Polyoxometalates: Slow, Passive Cation Transportation and Creation of Water Microenvironment. *J. Am. Chem. Soc.* **2008**, *130*, 1548-1549.
15. Zhang, J.; Li, D.; Liu, G.; Glover, K, J.; Liu, Tianbo. Lag Periods During the Self-Assembly of {$Mo_{72}Fe_{30}$} Macroions: Connection to the Virus Capsid Formation Process. *J. Am. Chem. Soc*. **2009**, *131*, 15152-15159.

16. Kuepper, K.; Neumann, M.; Al-Karawi, A. J. M.; Ghosh, A.; Walleck, S.; Glaser, T.; Gouzerh, P.; Müller, M. Immediate Formation/Precipitation of Icosahedrally Structured Iron–Molybdenum Mixed Oxides from Solutions Upon Mixing Simple Iron(III) and Molybdate Salts. *J. Clust. Sci*. **2014**, *25*, 301–311.
17. Mekala, R.; Supriya, S.; Das, S. K. Isolation of Blackberry-Shaped Nanoparticles of a Giant {$Mo_{72}Fe_{30}$} Cluster and Their Transformation to a Crystalline Nanoferric Molybdate. *Inorg. Chem.* **2016**, *55*, 12504−12507.
18. Garazhian, Z.; Rezaeifard, A.; Jafarpour, M.; Farrokhi, A. {$Mo_{72}Fe_{30}$} Nanoclusters for the Visible-Light-Driven Photocatalytic Degradation of Organic Dyes. *ACS Appl. Nano Mater*. **2020**, *3*, 648−657.
19. Mokhtari, R.; Rezaeifard, A.; Jafarpour, M.; Farrokhi, A. Visible-light driven catalase-like activity of blackberry-shaped {$Mo_{72}Fe_{30}$} nanovesicles: combined kinetic and mechanistic studies. *Catal. Sci. Technol*., **2018**, *8*, 4645-4656.
20. Garazhian, Z.; Rezaeifard, A.; Jafarpour, M. A nanoscopic icosahedral {$Mo_{72}Fe_{30}$} cluster catalyzes the aerobic synthesis of benzimidazoles. *RSC Adv.*, **2019**, *9*, 34854-34861.
21. Tandekar, K.; Singh, C.; Supriya, S. Proton Conductivity in {$Mo_{72}Fe_{30}$}-Type Keplerate. *Eur. J. Inorg. Chem.* **2021**, *8*, 734 –739.
22. Tandekar, K.; Mishra, N. K.; Supriya, S. Solvent mediated reversible solid state photochromism of {$Mo_{72}Fe_{30}$} Keplerate. *Dalton Trans.* **2021**, *50*, 6146–6151.
23. Mukhopadhyay, S.; Debgupta, J.; Singh, C.; Kar, A.; Das, S. K. A Keggin Polyoxometalate Shows Water Oxidation Activity at Neutral pH: POM@ZIF-8, an Efficient and Robust Electrocatalyst. *Angew. Chem. Int. Ed.* **2018**, *57*, 1918 –1923.
24. Mukhopadhyay, S.; Basu, O.; Kar, A.; Das, S. K. Efficient Electrocatalytic Water Oxidation by Fe(salen)−MOF Composite: Effect of Modified Microenvironment. *Inorg. Chem.* **2020**, *59*, 472−483.
25. Todea, A. M.; Szakacs, J.; Konar, S.; Bogge, H.; Crans, D. C.; Glaser, T.; Rousseliere, H.; Thouvenot, R.; Gouzerh, P.; Müller, A. Reduced Molybenum-Oxide-Based Core–Shell Hybrids: “Blue” Electrons Are Delocalized on the Shell. *Chem. Eur. J.* **2011**, *17*, 6635 – 6642.
26. Kerr, P. F.; Thomas, A. W.; Langer, A. M. The nature and synthesis of ferrimolybdite. *The American Mineralogist*, **1963**, *48*, 14-32.
27. Todea, A. M.; Merca, A.; Bogge, H.; Glaser, T.; Pigga, J. M.; Langston, M. L. K.; Liu, T.; Prozorov, R.; Luban, M.; Schroder, C.; Casey, W. H.; Müller, A. Porous Capsules {$(M)M_5$}$12Fe^{III}_{30}$ ($M=Mo^{VI}$, W^{VI}): Sphere Surface Supramolecular Chemistry with 20 Ammonium Ions, Related Solution Properties, and Tuning of Magnetic Exchange Interactions. *Angew. Chem. Int. Ed.* **2010**, *49*, 514 –519.

28. Mekala, R.; Supriya, S.; Das, S. K. Fate of a Giant $\{Mo_{72}Fe_{30}\}$-Type Polyoxometalate Cluster in an Aqueous Solution at Higher Temperature: Understanding Related Keplerate Chemistry, from Molecule to Material. *Inorg. Chem.* **2013**, *52*, 9708−9710.
29. Hellman, H.; Laitinen, R. S.; Kaila, L.; Jalonen, J.; Hietapelto, V.; Jokela, J.; Sarpola, A.; Ramo, J. Identification of hydrolysis products of $FeCl_3.6H_2O$ by ESI-MS. *J. Mass Spectrom.* **2006**, *41*, 1421–1429.
30. Liu, T. An Unusually Slow Self-Assembly of Inorganic Ions in Dilute Aqueous Solution. *J. Am. Chem. Soc.* **2003**, *125*, 312−313.
31. Liu, G.; Cai, Y.; Liu, T. Automatic and Subsequent Dissolution and Precipitation Process in Inorganic Macroionic Solutions. *J. Am. Chem. Soc.* **2004**, *126*, 16690−16691.
32. Friedl, J.; Holland-Cunz, M. V.; Cording, F.; Pfanschilling, F. L.; Wills, C.; McFarlane, W.; Schricker, B.; Fleck, R.; Wolfschmidt, H.; Stimming, U. Asymmetric polyoxometalate electrolytes for advanced redox flow batteries. *Energy Environ. Sci.,* **2018**, *11*, 3010-3018.
33. Fang, Y. H.; Liu, Z. P. Tafel Kinetics of Electrocatalytic Reactions: From Experiment to First-Principles. *ACS Catal.* **2014**, *4*, 4364−4376.
34. Mahmood, J.; Li, F.; Jung, S. M.; Okyay, M. S.; Ahmad, I.; Kim, S. J.; Park, N.; Jeong, H. Y.; Baek, J. B. An efficient and pH-universal ruthenium-based catalyst for the hydrogen evolution reaction. *Nature Nanotechnology*, **2017**, *12*, 441-447.
35. Weinberg, D. R.; Gagliardi, C. J.; Hull, J. F.; Murphy, C. F.; Kent, C. A.; Westlake, B. C.; Paul, A.; Ess, D. H.; McCafferty, D. G.; Meyer, T. J. Proton-Coupled Electron Transfer. *Chem. Rev.* **2012**, *112*, 4016−4093.

CHAPTER 3

Solid Nanoblackberries Exhibiting Super Proton Conductivity Fabricated as Proton Transport Membranes

Overview:

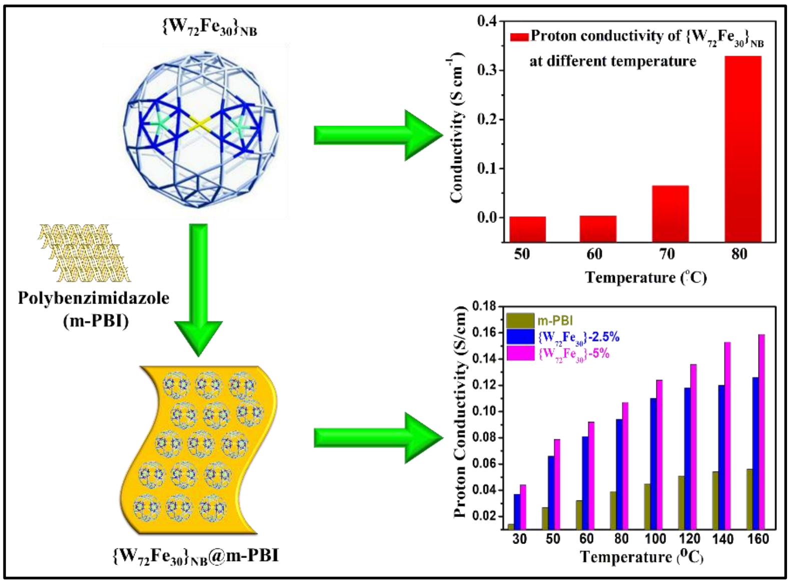

The crystalline $\{Mo_{72}Fe_{30}\}$ and $\{W_{72}Fe_{30}\}$ Keplerates, a versatile polyoxometalate system, were first synthesized in Bielefeld, Germany by Müller’s research group. Subsequently, Liu, Müller and their co-workers demonstrated the formation of nanoblackberries of $\{Mo_{72}Fe_{30}\}$ and $\{W_{72}Fe_{30}\}$ in respective aqueous solutions. We have recently isolated these nanoblackberries in the solid state in the form of amorphous substances. In this work, we have shown that the isolated tungsten blackberries, $Fe_3[W_{72}Fe_{30}O_{252}(CH_3COO)_2(OH)_{25}(H_2O)_{103}]\cdot 180H_2O$ (**$\{W_{72}Fe_{30}\}_{NB}$**) exhibit highest proton conductivity among polyoxometalates (POMs) and MOFs: 3.30×10^{-1} S cm^{-1} at 80 °C and RH 98%. A vehicular mechanism is expected to operate in this proton conduction through the metal-oxide based solid electrolyte **$\{W_{72}Fe_{30}\}_{NB}$** with an activation energy = 1.95 eV. But this solid electrolyte, as such, cannot form a free-standing film which is essential for its use as proton exchange membrane (PEM) in the fuel cell. We have thus used this POM-based solid electrolyte of highest proton conductivity among POMs and MOFs as nanofiller in an organic polymer, poly [2,2′-(m-phenylene)- 5,5′-benzimidazole] (m-PBI) to fabricate the POM-based polymer composite membrane, **50%$\{W_{72}Fe_{30}\}$@m-PBI** (50% tungsten blackberries loading by weight). We have also prepared phosphoric acid (PA) doped $\{W_{72}Fe_{30}\}$@m-PBI membranes using two different loading levels of $\{W_{72}Fe_{30}\}$ by weight: **2.5%$\{W_{72}Fe_{30}\}$+PA@m-PBI** and **5.0%$\{W_{72}Fe_{30}\}$+PA@m-PBI** for their use as PEM at a higher temperature, at 160 °C. We have performed detailed proton conductivity studies of these polymer composite membranes along with their thermo-mechanical properties. In summary, we have demonstrated that the vesicle-like nanoblackberries, that are reversibly formed in a dilute aqueous solution of a giant polyoxometalate (POM) cluster $\{W_{72}Fe_{30}\}$ containing compound, can be assembled irreversibly to nanoblackberries (without empty interior) that are isolated in solid state in gram quantities exhibiting super proton conductivity and fabricated to the flexible mixed matrix PEM of highest proton conducting efficiency.

3.1 Introduction

There is a lot to talk about $\{M_{72}Fe_{30}\}$ Keplerates (M = Mo and W), a versatile polyoxometalate (POM) system, discovered by Müller and his co-workers.[1-2] The $\{M_{72}Fe_{30}\}$ Keplerate is a giant icosahedral POM object (nano-sized cluster made up of 12 $\{M_6O_{21}(H_2O)\}^{6-}$ pentagonal shaped-building units linked by 30 $\{Fe^{III}\}$ linkers), which has made a distinctive mark in contemporary chemical science because of its versatile applications including magnetism,[3-9] catalysis[10-12] and more importantly because of its propensity of undergoing self-aggregation to form vesicle-like super-assemblies.[13] Liu and his group used this giant icosahedral POM system, particularly $\{Mo_{72}Fe_{30}\}$ and made a landmark in discovery of $\{Mo_{72}Fe_{30}\}$-blackberry-like nano-vesicles.[13-16] These nano-blackberries were demonstrated to be formed reversibly in a dilute aqueous solution of crystalline $(Mo_{72}Fe_{30}\}$ compound, $[Mo_{72}Fe_{30}O_{252}(CH_3COO)_{12}\{Mo_2O_7(H_2O)\}_2\{H_2Mo_2O_8(H_2O)\}(H_2O)_{91}]\cdot 150H_2O$ (**$\{Mo_{72}Fe_{30}\}_{cryst}$**).[10,13] These $\{Mo_{72}Fe_{30}\}$-black-berries are single-layer, vesicle-like-supramolecular structures having sizes ranging from tens to hundreds of nanometres, as established by DLS and microscopy studies of dilute solution of **$\{Mo_{72}Fe_{30}\}_{cryst}$** (by drop-casting the relevant dilute aqueous solution onto a freshly glow discharged carbon-coated TEM grid).[13]

These nano-vesicles, having cavities that are filled by millions of water molecules, could not be isolated as a solid substance (other than drop-casting on the grids) because of their reversible formation and the condition of dilute aqueous solution. We could isolate $\{M_{72}Fe_{30}\}$-nanoblackberries (M = Mo and W) as an amorphous solid-substance in an instantaneous one-pot synthesis involving an aqueous solution of sodium-molybdate / -tungstate, ferric chloride and acetic acid.[17,18] The amorphous nature of the isolated nano-material is not surprising because there is no long-range ordered packing of $\{Mo_{72}Fe_{30}\}$-building units on the resulting blackberry surface, as discussed by Liu and co-workers in the context of reversible formation of these nanoblackberries in a dilute aqueous solution of **$\{Mo_{72}Fe_{30}\}_{cryst}$**.[10,13,15] The solid $\{M_{72}Fe_{30}\}$-nanoblackberries (M = Mo and W), we isolated, are not vesicle-like, rather these are like nanoglobules having interior completely filled with same composition as that of the surface of the blackberry. Solid molybdenum nano-blackberries, $Na_2[Mo_{72}Fe_{30}O_{252}(CH_3COO)_4(OH)_{16}(H_2O)_{108}] \cdot 180H_2O$ (**$\{Mo_{72}Fe_{30}\}_{NB}$**), are not thermally stable; at moderate temperature it decomposes to ferric molybdate.[18,19] On the other hand, the isolated solid tungsten-nanoblackberries, $Fe_3[W_{72}Fe_{30}O_{252}(CH_3COO)_2(OH)_{25}(H_2O)_{103}] \cdot 180H_2O$ (**$\{W_{72}Fe_{30}\}_{NB}$**) are enormously stable even at higher temperatures.[17] This tungsten nanoblackberry material is the subject of this work.

The vesicle-like blackberries, formed in dilute aqueous solution, have limitation as far as their practical applications are concerned, because these are formed reversibly in an aqueous solution and cannot be isolated as a solid material.[13-16] Despite this limitation, Liu and his group have demonstrated a remarkable application of these $\{Mo_{72}Fe_{30}\}$-nanovesicles in solution, in which the blackberry shell behaves like a membrane allowing passive transportation of small cations through the shell. This is because, these nanoblackberries are permeable unlike the constituent individual $\{Mo_{72}Fe_{30}\}$-cluster.[15] The permeability of these nanoblackberry-like vesicles' shell is due to the fact that the individual $\{Mo_{72}Fe_{30}\}$-clusters do not touch each other (electrostatic repulsions!) but assembled via hydronium (H_3O^+) ions placed between the $\{Mo_{72}Fe_{30}\}$-clusters during the formation of these nanoblackberries resulting in the formation of channels on the surface of the blackberries.[15] If the shell of the $\{Mo_{72}Fe_{30}\}$-nanovesicles, composed of $\{Mo_{72}Fe_{30}\}$-clusters (2.5 nm building objects) and hydronium ions, can transport small cations, our isolated solid nano-blackberries **$\{W_{72}Fe_{30}\}_{NB}$** having similar $\{W_{72}Fe_{30}\}$-building units and Fe^{3+} cations, in principle, should have potential to behave like a membrane material for transporting small cations. We have chosen, in the present work, the smallest cation, proton (H^+) to be transported through this membrane-like material, namely, solid (isolated) tungsten-nanoblackberries **$\{W_{72}Fe_{30}\}_{NB}$**. Why have we chosen the passage of proton through this material!? Proton transport through proton exchange membrane (PEM) is a crucial event in a fuel cell, an electrochemical energy conversion device converting directly the chemical energy into electrical energy in the context of today's high demand of achieving sustainable / renewable energy.[20,21] In a typical fuel cell, molecular hydrogen gets oxidized (to proton) in the anode and oxygen gets reduced (to water) in the cathode, while proton gets transported from anode to cathode (through a PEM) and current (electrical energy) flows in the outer circuit.[22,23] The efficiency of a fuel cell is largely dependent on the effectiveness of proton conduction through the PEM.[24,25] Thus, achieving efficient proton-conducting materials have become important goal in the contemporary sustainable energy research. Nafion membrane, a perfluorosulfonic acid polymer, developed by Dupont, is often used as PEM in the fuel cell. Even though Nafion has shown reasonable performance in the PEM fuel cell but its commercial use is limited by its high cost and its considerably poor performance at low humidity and at higher temperatures.[26] In recent years, metal organic framework (MOF) and polyoxometalate (POM) based compounds have been evolved extensively as proton conducting materials.[25,27-36] We have reported a MOF system that exhibits highest proton conductivity among MOF containing compounds; we made it possible by applying defect engineering to the concerned MOF system.[36] In this work, we have demonstrated that the most inexpensive and instantaneously synthesized tungsten nano-blackberries **$\{W_{72}Fe_{30}\}_{NB}$** exhibit highest proton conductivity of 3.30×10^{-1} S cm^{-1} at 80°C (relative humidity 98%), which is not only highest among POMs but also highest among MOF containing compounds. We are talking about a POM system of maximum proton conductivity, which can be synthesized in gram quantities within few minutes in a simple aqueous synthesis. But a POM compound cannot be used as an electrolyte material for proton conduction in a fuel cell unless it is fabricated as a free-standing film (membrane). We have thus used this solid electrolyte of highest proton conductivity among POMs and MOFs as nanofiller with a polymer, poly [2,2′-(m-phenylene)-5,5′-benzimidazole] (m-PBI) to fabricate a POM-based inorganic-organic composite membrane system, $\{W_{72}Fe_{30}\}$@m-PBI. We could load maximum 50% (by weight) $\{W_{72}Fe_{30}\}$ into the m-PBI polymer i.e., we could achieve **50%$\{W_{72}Fe_{30}\}$@m-PBI** composite membrane which shows proton conductivity of 5.70×10^{-2} S cm^{-1} at 80 °C and RH 98%. The obtained activation energy (E_a) of this composite is found to be 0.18 eV indicating that the proton transport is taking place following Grotthuss mechanism in the case inorganic-organic composite membrane unlike that in solid electrolyte **$\{W_{72}Fe_{30}\}_{NB}$** (activation energy = 1.95 eV indicating vehicular mechanism for proton conduction). We have also fabricated phosphoric acid (PA) doped $\{W_{72}Fe_{30}\}$@m-PBI membranes using two different loading levels of $\{W_{72}Fe_{30}\}$ by weight: **2.5% $\{W_{72}Fe_{30}\}$+PA@m-PBI** and **5.0% $\{W_{72}Fe_{30}\}$+PA@m-PBI** for their use as PEM at a higher temperature, e.g., 160 °C. While, m-PBI polymer membrane itself shows proton conductivity value of 0.056 S cm^{-1} at 160 °C under anhydrous condition, the obtained proton conductivity values of the **2.5%$\{W_{72}Fe_{30}\}$+PA@m-PBI** and **5.0%$\{W_{72}Fe_{30}\}$+PA@m-PBI** membranes are 0.126 S cm^{-1} and 0.159 S cm^{-1}, respectively at 160 °C under anhydrous condition. The obtained E_a values for **2.5%$\{W_{72}Fe_{30}\}$+PA@m-PBI and 5.0%$\{W_{72}Fe_{30}\}$+PA@m-PBI** membranes are in the range of 0.13-0.14 eV. To our knowledge, this is the first report of a polyoxometalate (POM)-based compound exhibiting highest proton conductivity not only among POMs but also among MOFs. Likewise, it is a rare paradigm of fabricating a giant POM cluster containing electrolyte into the flexible POM-polymer composite membranes with excellent proton conduction efficiency.

3.2. EXPERIMENTAL SECTION

3.2.1. Materials

3,3',4,4'-tetraaminobiphenyl (TAB), Isophthalic acid (IPA) polyphosphoric acid (115%) (PPA), Sodium tungstate ($Na_2WO_4.2H_2O$) and glacial acetic acid were purchased from SRL chemicals and ferric chloride ($FeCl_3{\cdot}6H_2O$) from Sigma Aldrich, India. Ortho phosphoric acid (85%) were purchased from Merck India. Sulphuric acid (98%), N, N-Dimethyl-acetamide (DMAc) and ethanol (EtOH) were purchased from Finar Chemicals. All the chemicals were used as received without any further purification. DDI water was used throughout the project.

3.2.2. Synthesis

3.2.2.1. Synthesis of $Fe_3[W_{72}Fe_{30}O_{252}(CH_3COO)_2(OH)_{25}(H_2O)_{103}]{\cdot}$ 180 H_2O ($\{W_{72}Fe_{30}\}_{NB}$)

Synthesis of $Fe_3[W_{72}Fe_{30}O_{252}(CH_3COO)_2(OH)_{25}(H_2O)_{103}]{\cdot}$ 180 H_2O ($\{W_{72}Fe_{30}\}_{NB}$) was adapted from our earlier report.[17] An aqueous solution of $Na_2WO_4.2H_2O$ was acidified with acetic acid and another aqueous solution of $FeCl_3.6H_2O$ was added to it. The resultant mixture was stirred for 1 h at room temperature. The obtained yellow precipitate was filtered off and thoroughly washed with water to remove the unreacted starting materials. Finally, the compound is dried properly at room temperature and used for further studies.

3.2.2.2. Synthesis of poly [2,2′-(m-phenylene)-5,5′-benzimidazole]

Synthesis of poly [2,2′-(m-phenylene)-5,5′-benzimidazole] (m-PBI) has been performed by following our earlier literature reported procedure.[37,38]

3.2.3. Methods

The instrumental details of the all the experiments are provided in appendix 1.

3.2.4. Fabrication strategy of $\{W_{72}Fe_{30}\}$@m-PBI Mixed Matrix Membranes

Solution casting method has been utilized to fabricate the **$\{W_{72}Fe_{30}\}$@m-PBI** mixed matrix membranes (MMMs) with the loading of **2.5 wt%** and **5 wt%** and **50 wt%** (with respect to m-PBI polymer wt%) **$\{W_{72}Fe_{30}\}$** polyoxometalates homogeneous dispersion in dimethyl acetamide (DMAc) to 2 wt % **m-PBI** solution in DMAc, and the final **m-PBI** concentration in solution was 1 wt %. Then the entire solution was stirred vigorously for 24 h to form a homogeneous dispersion of the polyoxometalates into the PBI matrix, followed by casting the resulted solution in a glass Petri dish inside a heating oven at 80 °C for 12 h to slowly evaporate the solvent. The transparent yellow-coloured membranes, namely **2.5%$\{W_{72}Fe_{30}\}$@m-PBI**, **5%$\{W_{72}Fe_{30}\}$@m-PBI** and **50%$\{W_{72}Fe_{30}\}$@m-PBI** are then peeled off gently from the petri dish and dried further at 80 °C for 24 h to remove the trapped moisture and solvents inside the MMMs. The membrane fabrication procedure is schematically represented in Scheme 3.1**.**

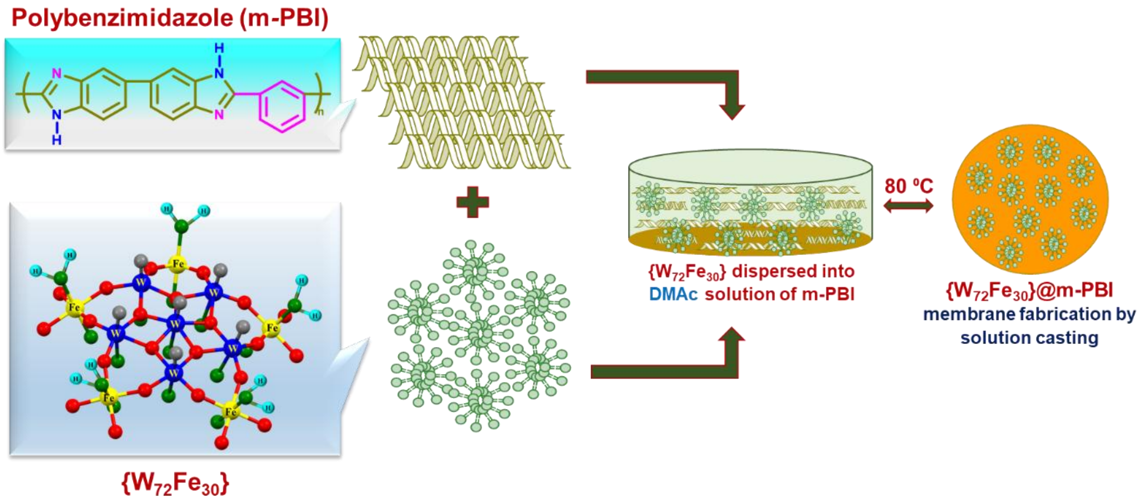

Scheme 3.1. Schematic representation of the fabrication of $\{W_{72}Fe_{33}\}$@m-PBI MMMs.

3.2.5. Phosphoric Acid (PA) loading on the 2.5%$\{W_{72}Fe_{30}\}$@m-PBI, 5%$\{W_{72}Fe_{30}\}$@m-PBI membranes

2.5%$\{W_{72}Fe_{30}\}$@m-PBI, **5%$\{W_{72}Fe_{30}\}$@m-PBI** membranes were dried properly at 100 °C for 24 h and then these were immersed in PA solution (85%) for 5 days to obtain PA loaded MMMs that are effectively proton exchange membranes (PEMs). These membranes were then removed from the PA container and soaked with tissue papers to wipe out loosely bound surface PA. Finally, the PA doped MMMs were stored in zip-lock airtight covers for their characterizations and proton conduction performance.

3.3 Results and Discussions

3.3.1. Origin of proton conductivity

We have already mentioned that the tungsten nano-blackberries-compound $Fe_3[W_{72}Fe_{30}O_{252}(CH_3COO)_2(OH)_{25}(H_2O)_{103}]\cdot 180H_2O$ (**$\{W_{72}Fe_{30}\}_{NB}$**), that can be obtained in an instantaneous aqueous synthesis just by mixing an aqueous ferric chloride solution to an acidified (acetic acid) sodium tungstate solution, is the aggregation of nano-assemblies, each of the nano-assembly (nanoblackberry) being formed by $[W_{72}Fe_{30}O_{252}(CH_3COO)_2(OH)_{25}(H_2O)_{103}]^{9-}$ cluster anions (icosahedral building units) and Fe^{3+} cations (linkers) using Coulombic type (attractive) interaction. There are 25 hydroxyl groups per formula unit of the nanoblackberries-compound. Each hydroxyl group (OH^-) is attached with a Fe^{3+} center of icosahedral $\{W_{72}Fe_{30}\}$ cage making the cluster surface negatively charged because of deprotonation of these hydroxyl groups (Fe^{3+} center is a strong Lewis acid!). Therefore, each nanoblackberry can be described as a spherical assembly, in which each negatively charged icosahedral $\{W_{72}Fe_{30}\}$ cluster is linked by Fe^{3+} center from its six sides in three dimensions along with its deprotonated iron(III)-coordinated hydroxyl groups so that each cluster in the nanoblackberry is surrounded by free protons as shown in Figure 3.1**.**

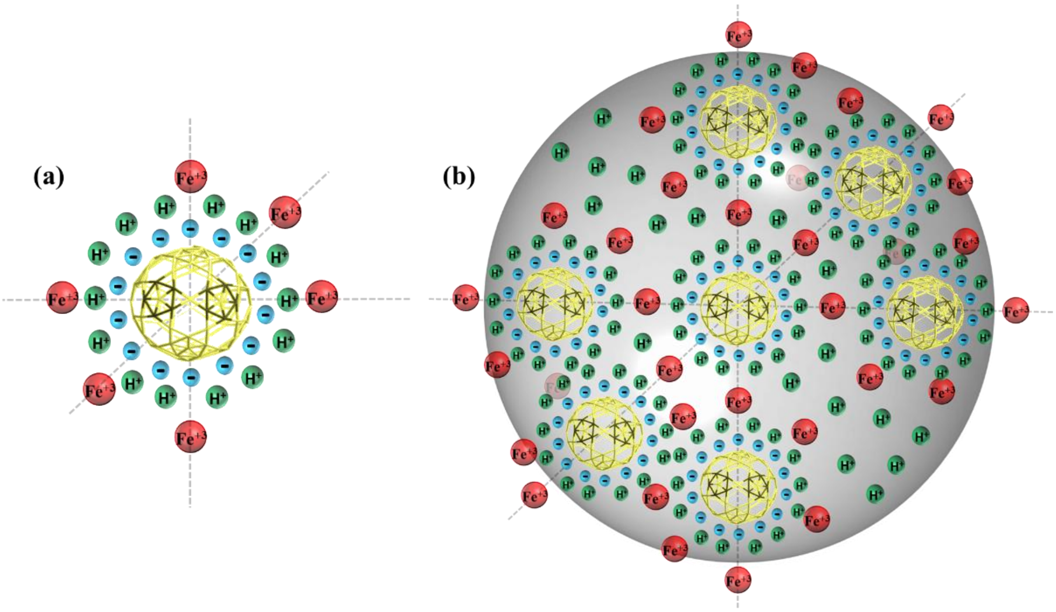

Figure 3.1. a) Structure of **$\{W_{72}Fe_{30}\}_{NB}$** individual cluster. (b) Structure of self-assembly of the cluster $\{W_{72}Fe_{30}\}$.

These protons, that, as if, are floating around the cluster as well as in the linking region, in principle can freely move inside the nanoblackberries and make the overall material proton conductive. Indeed, when this nanoblackberries-material is suspended in neutral water, the pH of the resulting suspension drops down from 7.0 to 3.4. Thus, the isolated tungsten nanoblackberries-compound behaves like an inorganic acid and can be used as an inexpensive metal-oxide based proton conductive material. The overall composition of the vesicle-like nanoblackberries (formed reversibly in a dilute aqueous solution of crystalline **$\{M_{72}Fe_{30}\}_{cryst}$**) and present isolated solid globule like nano-blackberries is more or less similar: in both cases, the basic unit is $\{M_{72}Fe_{30}\}$ icosahedral cluster. But in a vesicle-nanoblackberry, the whole interior is filled by millions of solvent water molecules along with a deprotonated surface, in which the resulting hydronium ions act as connectors, responsible for the formation of self-assembly / nanoblackberry; on the other hand, in the present isolated solid nanoblackberries, the whole interior has same composition as that of the surface and the nano-assembly is formed by Fe^{3+} ion linkers (instead of hydronium ions) and deprotonated $[W_{72}Fe_{30}O_{252}(CH_3COO)_2(OH)_{25}(H_2O)_{103}]^{9-}$ anions — the hydroxyl protons are freely available to move across the whole solid material, making the isolated solid tungsten nano-blackberries highest (super) proton conductor in solid state among polyoxometalates (POMs) as well as among MOFs.

3.3.2. POMs as proton conducting materials

It is well-established that the POMs are excellent candidates as proton conducting materials because of their high proton affinity, thereby their water retaining ability and the presence of oxygen rich surfaces providing hydrogen hopping sites and sufficient hydrophilicity.[39] But POM's water solubility restricts their direct use in proton conducting devices (e.g., fuel cells). One way to overcome this solubility problem is to immobilize the POM in a porous material.[40-41] Another approach is to synthesize an organic-inorganic hybrid compound (adduct of organic ligand cation, generally by protonation and POM anion).[42-43] The most successful means to achieve a water insoluble and stable proton conductive POM is to obtain high-nuclear POM clusters[43-44] and framework material, in which the basic building unit is the proton conductive POM cluster.[43] We have introduced, in the present work, the self-assembly process of a giant POM cluster unit $\{W_{72}Fe_{30}\}$ (vide supra), that leads to stable and water-insoluble inexpensive metal-oxide based material (nano-blackberries) of highest proton conductivity.

Miyake and co-workers first reported proton conductivities of acid salts of Keggin POMs, $H_3PMo_{12}O_{40}\cdot29H_2O$ and $H_3PW_{12}O_{40}\cdot29H_2O$—the respective values are 1.8×10^{-1} S cm^{-1} and 1.7×10^{-1} S cm^{-1} at room temperature.[45] But, because of their higher water solubility, their proton conductivity could not be measured at higher temperatures and at slightly higher humidity. Martinelli and co-workers have recently used an anhydrous form of imidazolium substituted tungsten analogue, i.e., $(imid)_3PW_{12}O_{40}\cdot 4H_2O$ and reported the proton conductivity value of 0.8×10^{-6} S cm^{-1} at 322 K.[46] After 12-tungstophosphoric acid, the next highest proton conductivity value is 1.59×10^{-1} S cm^{-1} at 90^0C and 98% relative humidity shown by the covalently linked polyoxometalate-organoboronic acid-polymers, reported by Chen, Streb and Li and their co-workers.[47] Zheng group reported an interesting POM compound, $\{K_{42}Ge_8W_{72}O_{272}(H_2O)_{60}\}$ having highest-nuclearity alkali-metal-water cluster, that exhibits the proton conductivity value of 6.8×10^{-2} S cm^{-1} at 98% RH and 85^0C.[48] Khashab and her group have described an interesting host-guest system, namely a strong Lewis acid guest within the Lewis base POM support, exhibits shows an exceptional proton conductivity of 4.5×10^{-2} S cm^{-1} at 85^0C (70% RH).[49]

3.3.3. MOFs as proton conducting materials

In recent time, metal organic framework (MOF) containing compounds have received considerable attention and popularity being used as proton conducting materials. The notable proton conductive values are 1.27×10^{-1} S cm^{-1} at 80°C under 100% RH (sulfonic acid rich flexible MOF),[50] 1.49×10^{-1} S cm^{-1} under 80°C under 98% RH (polycarboxylate-templated coordination polymers),[51] 1.64×10^{-1} S cm^{-1} at 80 °C under 98% RH (UiO-66-NH_2, PSM 1)[52] and 1.82 S cm^{-1} at 70 °C under 90% RH (MIL-101-SO_3H).[53] The highest proton conductivity value among MOFs, so far, is found to be 2.6×10^{-1} S cm^{-1} at 80 °C under 98% RH (defect engineering in MOF-808).[54] With regard to the above-mentioned super proton conductivity values of POMs and MOFs, the title compound $Fe_3[W_{72}Fe_{30}O_{252}(CH_3COO)_2(OH)_{25}(H_2O)_{103}]\cdot 180H_2O$**$\{W_{72}Fe_{30}\}_{NB}$** in the present work, exhibits the proton conductivity of 3.30×10^{-1} S cm^{-1} at 80 °C (RH 98%), the highest proton conductivity value among those of POMs and MOFs, reported so far. In addition, this metal-oxide based nano-material can be synthesized instantaneously in a gram quantity from an aqueous solution. The title compound **$\{W_{72}Fe_{30}\}_{NB}$**, which was reported in the context of electrocatalytic hydrogen evolution reaction (HER), has been characterized by PXRD analysis, Raman spectroscopy, TGA analysis, FT-IR spectroscopy, FESEM, water sorption analysis (Appendix3, Section A3.2-A3.6), that are compared and matched with relevant reported data.[17] The primary objective of this work is to explore the proton transportation properties of this inexpensive instantly synthesized material followed by its fabrication with a organic polymer to make mixed matrix proton-exchange membranes suitable for fuel cell applications.

3.4. Proton conductivity measurement and data analysis

Temperature-dependent proton conductivities of **$\{W_{72}Fe_{30}\}_{NB}$** were measured using two-electrode setup attached in parallel mode by alternating current (ac) impedance spectroscopy. The amorphous powdered samples of **$\{W_{72}Fe_{30}\}_{NB}$** were sandwiched between two carbon papers and pelletized with pressure of 5-ton cm^{-2} for 3 min. After putting the pellet inside the two-electrode cell setup, that whole electrode setup was employed into a home-made giant conical flask setup (Figure A3.6, Appendix3, section A3.7) to maintain the maximum relative humidity of 98% with temperature variations from 50 to 80 °C. The details of pellet preparation, electrode setup, impedance measurement parameters, calculations of proton conductivity and activation energy are given in the Appendix3, Section A3.7-A3.7. To check the long-term stability of this proton conducting material, the pellet sample was held in the most humidified elevated temperature for 48 hours and the impedance spectra were recorded after a constant time interval. The conductivity values at different temperatures were calculated from their corresponding Nyquist plots of impedance spectra after fitting with the most resemble equivalent circuit (Figure 3.2a).

For the construction of Nyquist plots, the real impedances (Z´) were plotted against imaginary impedances (Z´´) as shown in Figure 3.2a. The impedance spectra in the low frequency region are responsible for electrode-electrolyte contact resistance and the inter-grain resistance of the sample. The high frequency region impedance spectra, obtained from the contribution of the title material’s resistance, correspond to the actual proton conduction / transport. As the temperature increases, the respective proton conductivity values increase and reach to a maximum value of 3.30 × 10^{-1} at 80.5 °C (Figure 3.2b).

Stability of this POM based nano-blackberry material **$\{W_{72}Fe_{30}\}_{NB}$** was verified by proton conductivity measurement of the palletised sample at 80 $^{\circ}$C under relative humidity of 98% over a period of 72 hours. Each conductivity measurement data was recorded after an interval of 12 hours. The relevant Nyquist plots of impedance spectra show no significant change as shown in Figure 3.2c. Apart from doing the long-term stability during several cycles of proton conductivity measurements of the material, the

PXRD and FT-IR studies have been performed after the proton conductivity measurements, recorded at different temperatures (RH 98%) to check the robustness of the material. The title compound is found to be stable after proton conductivity measurement of each cycle, which is confirmed from FT-IR, PXRD, FESEM and EDX analysis as shown in, section A3.10, Appendix3. No notable changes were found in the spectra before and after the impedance measurement.

Activation energy (E_a) of proton conduction was calculated for **$\{W_{72}Fe_{30}\}_{NB}$** from the Arrhenius equation based on the proton conductivity measurement at different temperatures and at constant relative humidity (98%). From the least-squares fit of the Arrhenius plot, the activation energy (E_a) is calculated (section A3.9, Appendix3) and it is found to be 1.95 eV (>0.4 eV) (Figure 3.2d). This indicates that the vehicle mechanism is associated with this proton conduction across these nano-blackberries. The vehicular mechanism is the most common mechanism of the proton migration in aqueous systems where migration of proton occurs by the diffusion of charged “proton-carrier”, such as, H_3O^+.[55-57] The vehicular mechanism of diffusion-controlled proton conduction, shown by tungsten nano-blackberries can be justified by the presence of free protons (arising from acidic hydroxyl groups) throughout the interior of the nano-blackberries that are floating around the cluster as well as in the linking region of $\{W_{72}Fe_{30}\}$ clusters as shown in Figure 3.1**.**

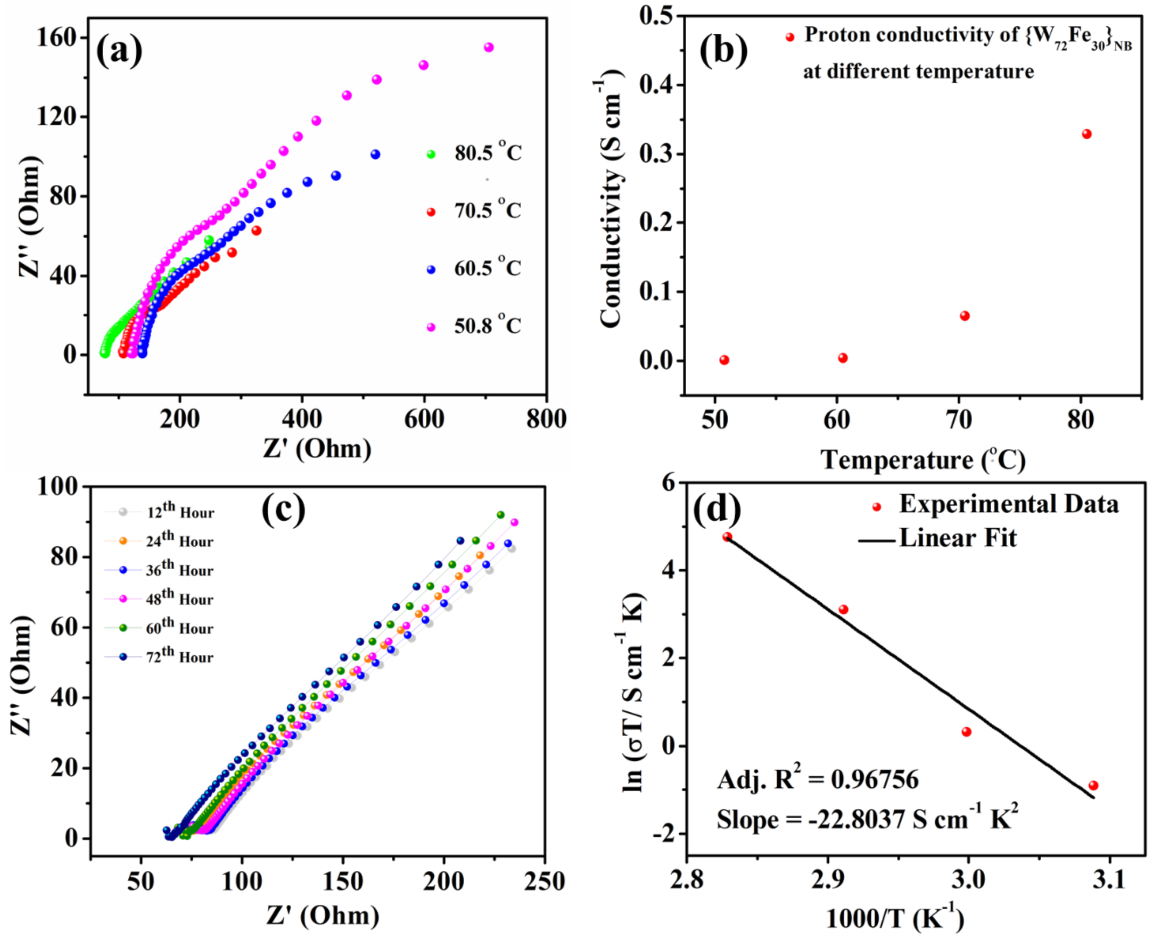

Figure 3.2. a) Nyquist plots of impedance spectra collected from 50.8 °C to 80.5 °C at 98% RH. (b) The variation of proton conductivity with change in temperature for **$\{W_{72}Fe_{30}\}_{NB}$** at a constant relative humidity (98% RH), (c) Nyquist plots of impedance spectra, recorded at each twelve hour time interval at 80 °C and 98% relative humidity (RH) over a total period of 72 hours for **$\{W_{72}Fe_{30}\}_{NB}$**. (d) Arrhenius plots of temperature dependence of proton conductivity of **$\{W_{72}Fe_{30}\}_{NB}$**.

The title material (tungsten nano-blackberries), super proton conductor, is considerably thermally stable, but it cannot be used directly in the fuel cells as the proton conductive electrolyte. This is because, a fuel cell needs a thin proton exchange membrane (PEM) for proton conduction from anode to cathode and this ‘nano-blackberries’ material per se lacks of ability to form a stable membrane. Thus, if this efficient proton conductive POM material is to be used in a fuel cell, it has to be processed / fabricated into a membrane. Indeed, “heteropoly acid” type POMs had been employed as “nanofillers to increase the proton conductivity of phosphoric acid (PA) doped polyethersulfone-polyvinylpyrrolidone (PES-PVP) polymer membranes for high temperature polymer electrolyte membrane fuel cells (HT-PEMFCs).[40,43] forming PWA/PES-PVP composite membrane for HT-PEMFCs. These proton exchange membrane fuel cells (PEMFCs) work at higher temperatures (more than 100 °C) offering enhancement of the electrodes' kinetics, the recovery of useful heat and better water management due to the formation of water in the vapor phase. But the main disadvantage of using heteropoly acid POMs as nanofillers is their high solubility in polar solvents like water. On the other hand, the 'tungsten nano-blackberries' material in the present work is not only stable at higher temperature but is also insoluble in water.

3.5. Fabrication and proton exchange membranes

Motivated by the obtained superior proton conductivity of as such **$\{W_{72}Fe_{30}\}$** nanoblackberries, we have further checked the processability of these polyoxometalates into a polymer supported matrix to fabricate superior proton conducting **polymer-POM** mixed matrix PEMs. We have chosen poly [2,2′-(m-phenylene)-5,5′-benzimidazole] (**m-PBI**) polymer as a matrix, because it is a rigid polymer with high-mechanical strength, thermal stability, and -chemical stability. **m-PBI** shows high proton conductivity in a fully anhydrous condition after phosphoric acid (PA) loading; thus PA-loaded m-PBI can be a potential membrane material for a fuel cell. Even then, one needs to employ a proton conductive material (having supramolecular interaction sites) as a nanofiller into this PA-loaded m-PBI membranes, because PBI-based membranes exhibit acid leaching at an elevated temperature, less PA doping level, low mechanical strength and low oxidative stability. In this context, the nanofillers (tungsten nano-blackberries in the present work) play an important role to obtain an efficient proton exchange membrane. The intermolecular supramolecular interactions (e.g., H-bonding interactions in the present study) between the nanofillers (having terminal and bridging oxo groups to accommodate hydrogen bonding in the present study) and the polymer (having N-H functionality, see Scheme 1) not only enhance the PA uptake, thereby enhances the proton conductivity but also it provides mechanical stability and reduces the acid leaching at the elevated temperatures. As mentioned in the experimental section (vide supra), we fabricated **2.5%$\{W_{72}Fe_{30}\}$@m-PBI**, **5%$\{W_{72}Fe_{30}\}$@m-PBI** and **50%$\{W_{72}Fe_{30}\}$@m-PBI** through the loading of **2.5 wt%**, **5 wt%** and **50 wt% $\{W_{72}Fe_{30}\}$** polyoxometalates homogeneous dispersion (with respect to m-PBI polymer wt. %) in dimethyl acetamide (DMAc) to 2 wt % **m-PBI** solution in DMAc.

3.5.1. PXRD Analysis

The powder X ray diffraction patterns of pristine **m-PBI, $\{W_{72}Fe_{30}\}$-2.5%** and **$\{W_{72}Fe_{30}\}$-5%** membranes are portrayed in the Figure 3.3. **$\{W_{72}Fe_{30}\}$** nanoblackberries clusters are amorphous in nature, analyzed from the observed broad halo in the 2θ region 25°- 35°.[17] Presence of broad halo was also observed for m-PBI in the 2θ range of 20°-30° due to the amorphous nature of the polymer.[38] In the **$\{W_{72}Fe_{30}\}$@m-PBI** MMMs, the presence of similar kind of broad halo was also observed with slight shift in the 2θ value towards the higher 2θ region when compared with the pristine m-PBI. Presence of strong donor-acceptor type H-bonding interaction between the -W=O and -Fe-O-H_2 functional groups of **$\{W_{72}Fe_{30}\}$** nanoclusters with the m-PBI imidazole 'N-H' groups resulted peak shifting into the fabricated MMMs.

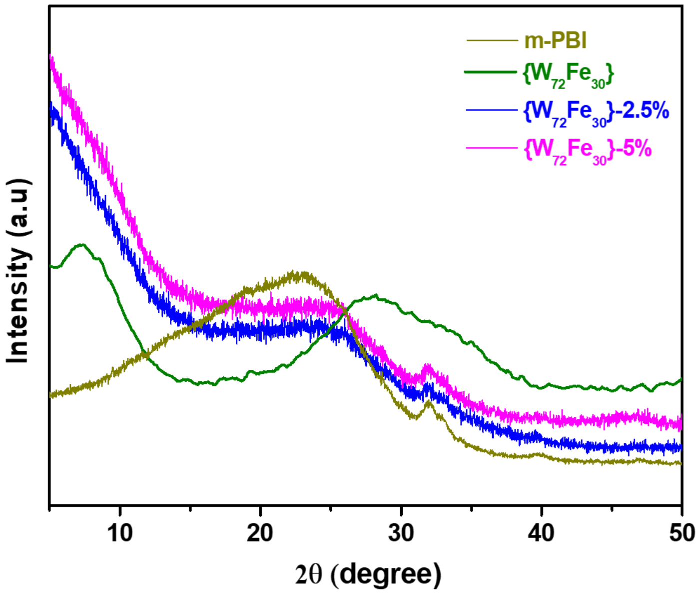

Figure 3.3. (a) PXRD patterns of m-PBI, $\{W_{72}Fe_{30}\}$, and the fabricated MMMs.

3.5.2. FT-IR Analysis

FT-IR spectra of **$\{W_{72}Fe_{30}\}$** nanoblackberries, **m-PBI, $\{W_{72}Fe_{30}\}$-2.5%** and **$\{W_{72}Fe_{30}\}$-5%** membranes are given in the [Figure 3.4 and Figure A3.11]. m-PBI exhibits three distinguishable broad peaks at 3415, 3143 and 3060 cm^{-1} which appears due to the non-hydrogen bonded free N-H groups, self-associated hydrogen bonded N-H groups and aromatic C-H stretching, respectively.[58,59] All the peaks associated with m-PBI are present in the polymer-POM composite MMMs. **$\{W_{72}Fe_{30}\}$** nanoclusters also exhibit a broad peak at 3060 cm^{-1} due to the presence of –OH functionalities inside and outside of the polyoxometalates clusters (Figure A3.11). In addition, a peak at 553 cm^{-1} was observed due to –Fe=O, peaks at 637, 728, 937 cm^{-1} signify the presence of –W=O functionalities, 1445 and 1540 cm^{-1} peaks are corresponding to –COO functionalities, and the peak at 1616 cm^{-1} was observed due to the presence of H_2O molecules inside the **$\{W_{72}Fe_{30}\}$** clusters (Figure 3.4).[17] All those peaks of **$\{W_{72}Fe_{30}\}_{NB}$** are appeared as new peaks in the fabricated MMMs at 562, 592, 644, 738 and 1412 cm^{-1} with noticeable peak shifting, and the intensity of the peaks increases with increasing **{$W_{72}Fe_{30}$}** loading from 2.5% to 5% in the membranes. The peak associated at 795 cm^{-1} in the m-PBI also resulted increased peak intensity in the **{$W_{72}Fe_{30}$}-5%** membrane signal by merging with the **{$W_{72}Fe_{30}$}** peaks. Also, significant spectral broadening was observed into the MMMs at (1020-1090) cm^{-1} and 1532 cm^{-1} (Figure 3.4). All such phenomenon are resulted due to the formation of strong donor-acceptor type H-bonding interfacial interaction between the –W=O, –Fe=O, –Fe-OH_2 and –COO, linkages present in the **{$W_{72}Fe_{30}$}** nanoclusters with the m-PBI imidazole 'N-H' groups (as schematically represented in Scheme A3.1). The FT-IR signals of **{$W_{72}Fe_{30}$}** polyoxometalates (Figure 3.4 & Figure A3.11 of Appendix3) merges with the m-PBI peaks, which governs generation of new peaks with positional shifting along with spectral broadening in the polymer-POM composites due to the proposed interaction pattern. Hence, both the PXRD and FT-IR analysis signifies the inference drawn from each other.

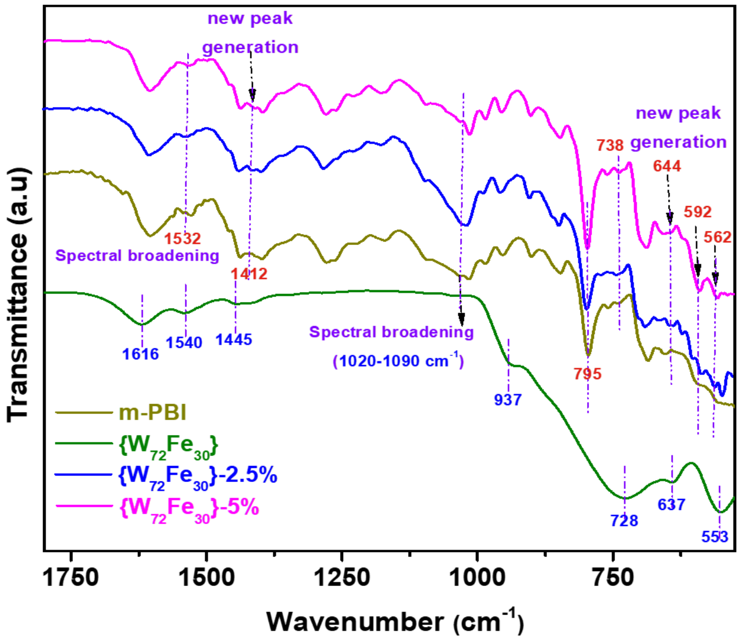

Figure 3.4. (a) ATR-FTIR spectra of m-PBI, {$W_{72}Fe_{30}$}, and the fabricated MMMs.

3.5.3. Morphology studies of the fabricated MMMs

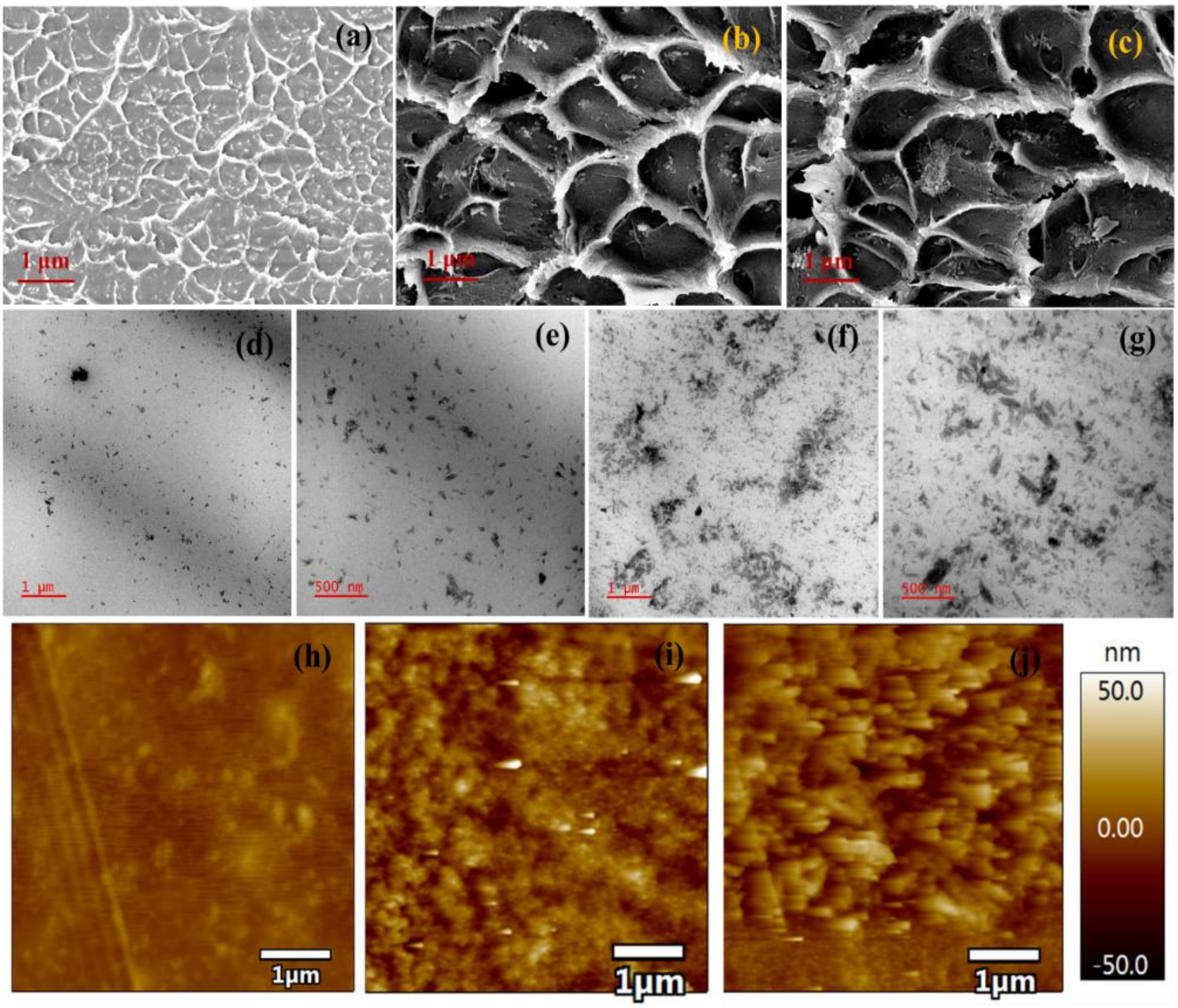

Figure 3.5. (a) FE-SEM cross-sectional image of pristine **m-PBI,** (b) **{$W_{72}Fe_{30}$}-2.5%** and (c) **{$W_{72}Fe_{30}$}-5%** membranes. (d, e) Surface TEM images of **{$W_{72}Fe_{30}$}-2.5%** membrane at different magnification. (f, g) Surface TEM images of **{$W_{72}Fe_{30}$}-5%** membrane at different magnification. (h) AFM surface topology of **m-PBI** (i) **{$W_{72}Fe_{30}$}-2.5%** and (j) **{$W_{72}Fe_{30}$}-5%** membrane.

3.5.3.1. FESEM analysis

The surface and cross-sectional morphology of the **{$W_{72}Fe_{30}$}-2.5%** and **{$W_{72}Fe_{30}$}-5%** membranes are completely altered when compared with pristine m-PBI membrane. m-PBI exhibits ripple-sponge like network structure with formation of small and homogeneous micro-cavities all over the matrix from the cryo-fractured cross-sectional FESEM analysis (Figure 3.5a-c). In contrast to m-PBI, in the **{$W_{72}Fe_{30}$}-2.5%** and **{$W_{72}Fe_{30}$}-5%** membranes, formation of larger triangular or square shaped crater-like fibrillar cavities were formed with homogeneous dispersion of **{$W_{72}Fe_{30}$}** clusters throughout the porous cross-sectional region (Figure 3.5b-c and Figure A3.12). The extensively altered morphology is a direct outcome of the strong interfacial H-bonding between the –W=O, –Fe=O and –Fe-OH_2 functionalities present in the POM cluster with the imidazole ‘N-H’ groups of m-PBI, which is responsible for significantly improved thermo-mechanical and tensile properties of the MMMs. The surface FESEM analysis of the **{$W_{72}Fe_{30}$}-2.5%** and **{$W_{72}Fe_{30}$}-5%** membranes also have been performed [see Appendix 3 Figure A3.13)], and the morphology exhibits homogeneous dispersion of polyoxometalates clusters throughout the membrane matrix with agglomeration and self-assembly of the fillers at certain areas. The FESEM EDX elemental analysis was also being recorded for the **{$W_{72}Fe_{30}$}-5%** membrane (Figure A3.14), which shows homogeneous dispersion of Carbon (C), Nitrogen (N), Oxygen (O), Tungsten (W), and Iron (Fe) all over the membrane surface. The homogeneous dispersion nature of the hydrophilic filler materials and the highly altered morphology resulted into the membranes surface and interfacial region responsible for superior proton conduction in the **polymer-POM** composite membranes.

3.5.3.2. TEM analysis

TEM analysis of the MMMs was also performed in order to further evaluate the dispersion nature of the polyoxometalates clusters into the m-PBI network (Figure 3.5d-g). **{$W_{72}Fe_{30}$}** clusters are dispersed homogeneously into the dense polymeric network also self-assembled agglomeration of nanoclusters was observed at certain places into the **{$W_{72}Fe_{30}$}-5%** membrane surface. At higher filler loading, two factors contribute significantly, (1) the –W=O, –Fe=O and –Fe-OH_2 functionalities present in the POM cluste forms H-bonding among themselves, which resulted in the self-assembly of fillers, (2) and H-bonding with the m-PBI functionalities, which generates network like structural anisotropy into the dense fibrillar polymer matrix. Therefore, these two factors contribute significantly towards the generation of an anisotropic structural self-assembled network into the composite MMMs surface.

3.5.3.3. AFM analysis

Furthermore, Atomic force microscopy (AFM) analysis was also performed to evaluate the 2D surface topology of the fabricated MMMs. AFM topology of the MMMs resulted in completely altered morphology compared to m-PBI with homogeneous dispersion of polyoxometalates clusters throughout the membrane surface [(5 x 5) μm] and the surface becomes increasingly rough with formation of bright and dark areas in the MMMs (Figure 3.5h-j), which is responsible for significantly increased surface roughness in the {W72Fe30}-(2.5% and -5%) membranes with respect to m-PBI (see Table A3.2). The three-dimensional (3D) AFM images and the associated height profiles of the membranes (see Figure A3.15a-c) also signifies the analogy made from the 2D surface topology, responsible for thermo-mechanical and tensile reinforcement in the MMMs.60

3.5.4. TGA analysis

The TGA plot of the **{$W_{72}Fe_{30}$}** clusters are given in the Appendix 3 Figure A3.4**,** where the initial weight loss is seen before 200 °C due to the evaporation of water molecules on the surface of the polyoxometalates cluster and due to the H-bonded bound water molecules present inside the **{$W_{72}Fe_{30}$}** cluster. The 2nd weight loss is observed beyond 600 °C due to the loss of acetate anions present in the cluster in the form of acetic acid.[17] The TGA plots of PA loaded m-PBI, {$W_{72}Fe_{30}$}-2.5% and {$W_{72}Fe_{30}$}-5% membranes are given in the Figure 3.6b and Figure A3.16 [zoomed TGA plot (50 °C - 200 °C)].

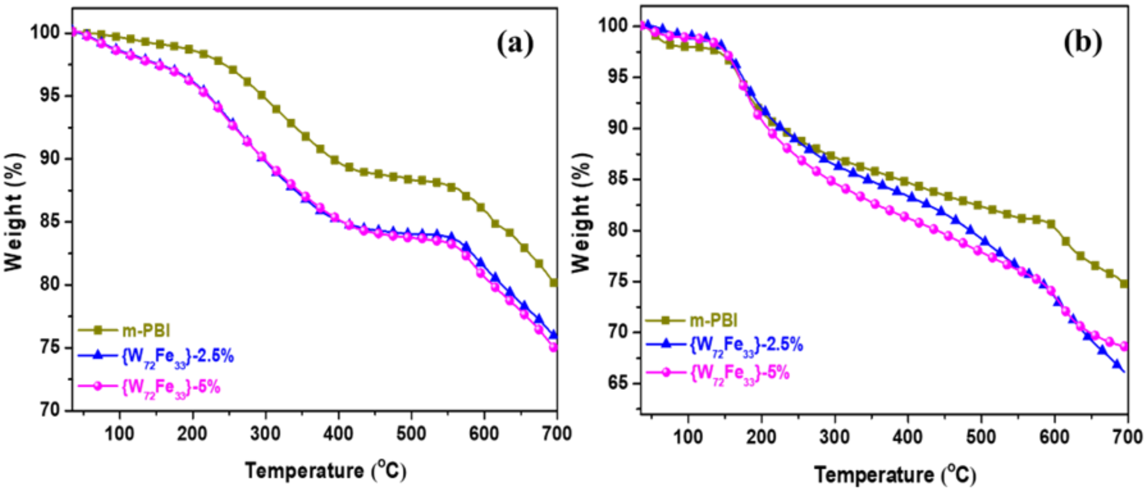

Figure 3.6. (a) TGA plots of dry **m-PBI, {$W_{72}Fe_{30}$}-2.5%** and **{$W_{72}Fe_{30}$}-5%** membranes. (b) TGA plots of PA doped **m-PBI, {$W_{72}Fe_{30}$}-2.5%** and **{$W_{72}Fe_{30}$}-5%** membranes.

We observed that the first weight loss in between temperature region 100 °C - 200 °C due to the evaporation of bound water molecules and surface absorbed moisture of the PA doped membranes,[61,62] followed by a gradual weight loss up to 550 °C due to the evaporation or polycondensation of PA impregnated in the membrane.[63] The final weight loss is seen after 550 °C due to the degradation of the main polymer backbone. An interesting observation is observed while comparing the thermal stability of the undoped and PA doped MMMs (Figure 3.6 and Figure A3.16). Unlike the undoped composites, thermal stability of the PA doped MMMs found to be superior over PA doped m-PBI in the temperature region between 50 °C - 200 °C. It is worth mentioning that PA boiling point is only 158 ºC, therefore, the superior thermal stability of the PA loaded MMMs even at 200 °C signifies superior PA retention into the membranes porous fibrillar interfacial region. Formation of extensive donor-acceptor type H-bonding between the of -W=O and -Fe-O-H_2 functionalities present in the {$W_{72}Fe_{30}$} clusters with the PA molecules are responsible for such exceptional thermal stability of the PA doped MMMs.

3.6. Water uptake, swelling ratio, PA loading and proton conductivity of the MMMs

The water uptake, PA doping level, swelling ratio in water and PA for all of the MMMs and pristine m-PBI are tabulated in Table 1 with detailed experimental procedures (see Appendix 3 Section A3.11.9). It has been observed that, incorporation of **{$W_{72}Fe_{30}$}** nanoblackberries into the m-PBI matrix resulted decrement in water uptake in the MMMs, and the capacity of water uptake follows inverse relationship with the increasing filler loading in the membranes. While, m-PBI displayed water uptake value of 9.04 wt%, the **{$W_{72}Fe_{30}$}-2.5%** and **{$W_{72}Fe_{30}$}-5%** membranes resulted water uptake of 6.85 wt% and 5.21 wt%, respectively. In the **Polymer-POM** membrane matrix, there is a significant donor-acceptor type H-bonding formation occurs between the m-PBI imidazole '–N=' groups with the polyoxometalates functionalities (Scheme A3.1), hence '–N=' atoms of PBI remains unavailable to form H-bonding with the free H_2O molecules, which resulted decrement in water uptake with increasing filler loading in the membranes.

3.7. Swelling ratio and PA loading

The swelling ratio (SWR) of the fabricated MMMs also follows inverse proportionality with increasing **{$W_{72}Fe_{30}$}** loading wt% in the composite membranes. The resulted SWR of **{$W_{72}Fe_{30}$}-2.5%** membrane in water and PA are 1.92 wt% and 15.93 wt%, respectively. While, for **{$W_{72}Fe_{30}$}-5%** membrane the SWR further decreased to 1.47 wt% and 13.62 wt% in water and PA, respectively. The obtained values of SWR found to be significantly lower than the SWR observed from **m-PBI** membrane in water (8.07 wt%) and PA (22.93 wt%). PXRD and FT-IR analysis have given evidences in favor of strong interfacial H-bonding inside the **Polymer-POM** composites which caused decreased SWR in the MMMs. PA doping level of the membranes is a significant parameter in order to evaluate the efficiency of proton conduction into the membrane matrix as higher PA doping level results formation of more labile proton conduction points into the membrane. m-PBI exhibits an expected PA doping level of 9.68 mol/PBI repeat unit which shows gradual increment with increasing polyoxometalates loading in the MMMs **(**Table 1.1**).** For example, the PA doping level of 13.80 and 16.19 mol/repeat unit are achieved for **$\{W_{72}Fe_{30}\}$-2.5%** and **$\{W_{72}Fe_{30}\}$-5%** membranes, respectively which is a synergistic effect of several factors. Firstly, the **$\{W_{72}Fe_{30}\}$** nanoclusters are consisting of –W=O, –Fe=O, -COO and $–Fe-OH_2$ functionalities which can form donor-acceptor type H-bonding interaction extensively with the PA molecules as shown in Scheme 3.2, hence with increasing POM loading PA doping level tends to increase in the MMMs. Secondly, the –W=O, –Fe=O, $–Fe-OH_2$ functionalities of the POM materials interact significantly with the '−N=' atom of the **PBI** imidazole to generate an ordered structure which resulted ordered space between the polymer chains in the MMMs responsible for significant PA impregnation into the membrane. Also, at higher filler loading PA molecules exert plasticizing effect and disrupt some of the existing H-bonding between the polyoxometalates clusters and m-PBI and form new H-bonding with the **Polymer-POM** composites, responsible for improved PA loading. And thirdly, at higher POM loading, the development of highly altered crater like thick fibrillar morphology, and the self-assembly of nanoblackberries into the dance polymeric network developed hydrophilic ion channels throughout the membrane matrix, responsible for large amount of PA incorporation into the interfacial region.

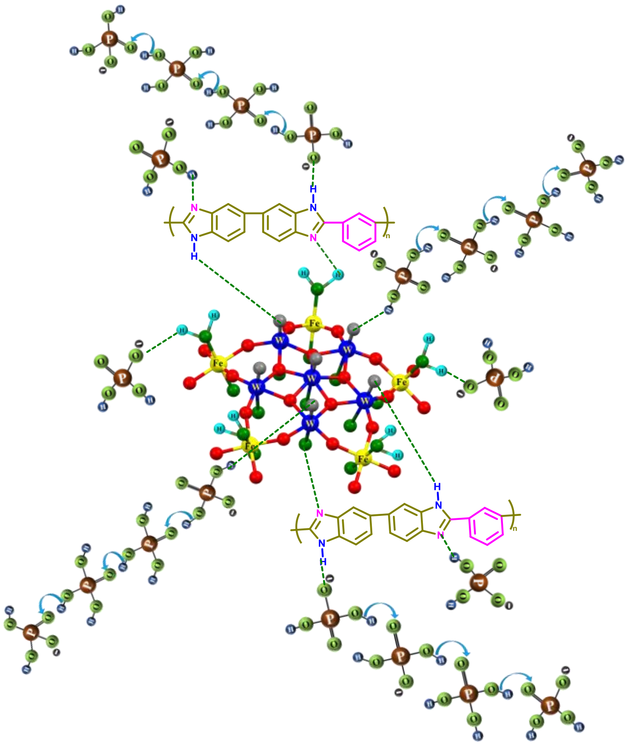

Scheme 3.2. Schematic representation of the interaction pattern in the PA doped **$\{W_{72}Fe_{30}\}$@m-PBI** MMMs with the PA molecules

Table 3.1. Water uptake, swelling ratio in water and PA, PA loading level of the **m-PBI, {$W_{72}Fe_{30}$}-2.5%** and **{$W_{72}Fe_{30}$}-5%** membranes [a]

Sample name	Water uptake (wt%)	Swelling ratio in water (%)	Swelling ratio in PA (%)	PA loading (no. of mol/PBI r.u)
m-PBI	9.04 (1.23)	8.07 (1.37)	22.93 (2.11)	9.68 (2.28)
{W72Fe30}-2.5%	6.85 (0.77)	1.92 (0.45)	15.93 (1.71)	13.80 (0.66)
{W72Fe30}-5%	5.21 (0.69)	1.47 (0.62)	13.62 (1.57)	16.19 (0.84)

[a] The number in the bracket represents the standard deviation value obtained from measurements.

3.8 Proton conductivity of the MMMs

Proton conductivity analysis has been performed for all the PA doped **m-PBI, {$W_{72}Fe_{30}$}-2.5%** and **{$W_{72}Fe_{30}$}-5%** membranes under an anhydrous environment between the temperature range of 30 °C – 160 °C, and the detailed experimental analysis procedure is given in the Appendix3 (Section A3.11.10). The obtained proton conductivity values of the MMMs were calculated from the experimentally generated Nyquist plots by fitting with the most relevant equivalent circuit (for details, see section 3.16, Figure A3.17 in Appendix3).

All the **{$W_{72}Fe_{30}$}** loaded PA doped MMMs displayed much improved proton conductivity when compared with PA doped pristine m-PBI, and the proton conductivity values of the polyoxometalates loaded MMMs follows proportionality with increasing filler loading into the membrane matrix. While, **m-PBI** resulted proton conductivity value of 0.056 S cm^{-1} at 160 °C under anhydrous condition, the obtained proton conductivity values of the **{$W_{72}Fe_{30}$}-2.5%** and **{$W_{72}Fe_{30}$}-5%** membranes are 0.126 S cm^{-1} and 0.159 S cm^{-1}, respectively, at 160 °C, under identical experimental condition (Figure 3.7, Table A3.3, Section A3.16).

Hence, the **{$W_{72}Fe_{30}$}-5%** membrane exhibits almost ~3-fold increment in proton conductivity compared with m-PBI. In the earlier section, we have discussed the significant contributing factors for improved PA doping levels in the MMMs. In the similar note, all such factors responsible for increased PA doping levels in the composite membranes efficiently contribute towards superior proton conduction in the MMMs. Hence, the improved PA doping level of **{$W_{72}Fe_{30}$}-5%** membrane (16.19 mol/ PBI repeat unit) over **{$W_{72}Fe_{30}$}-2.5%** membrane (13.80 mol/ PBI repeat unit) resulted much higher proton conductivity in the former one. In addition, the as such **{$W_{72}Fe_{30}$}** nanoclusters exhibit proton conductivity in the 10^{-1} S cm^{-1} order at 80 °C. Therefore, incorporating hydrophilic **{$W_{72}Fe_{30}$}** polyoxometalates into the PBI matrix enables more proton hopping sites throughout the polymer network under PA doped condition, responsible for a significant ~3-fold increased proton conductivity value in the MMMs. In addition, the highly altered morphology of the MMMs observed from FESEM, TEM and AFM analysis (Figure 3.5) contributes efficiently towards more PA uptake and retention into the membranes interfaces, which further facilitates increased proton conductivity. We have also fabricated a membrane **{$W_{72}Fe_{30}$}-7.5%** (with 7.5% POM loading), and measured the proton conductivity under identical experimental condition, and we are unable to get any proton conductivity for this membrane, as for this sample the significantly higher filler loading forms agglomeration of nanoclusters into the membrane matrix, throughout the composite matrix causing no proton conduction at all. This phenomenon of nanofillers agglomeration causing disruption of the proton conduction channel is observed by several researchers.[64] Hence, **{$W_{72}Fe_{30}$}-5%** filler loaded membranes found to be optimum loading of **{$W_{72}Fe_{30}$}** nanoclusters to fabricate efficient PBI based super proton conducting PEMs. To check the long-term efficiency of proton conduction in the membranes, isothermal proton conductivity of **m-PBI**, **{$W_{72}Fe_{30}$}-2.5%** and **{$W_{72}Fe_{30}$}-5%** membranes were performed at 160 °C for prolong 24 h and the detailed experimental procedure along with the observations obtained from the experiment is given in the Section A3.17 and A3.11.11, Figure A3.18 of Appendix3. All the MMMs demonstrated retention of proton conductivity without noticeable change at elevated temperature (160 °C) under prolong treatment. We have also fabricated **50% {$W_{72}Fe_{30}$}@m-PBI** composite membrane and measured its proton conductivity at different temperature conditions in aqueous medium at a RH of 98% with the help of two electrode system by sandwiching the membrane between two carbon wafers to make a pellet (see Nyquist plot in Figure A3.19, Appendix3). We have achieved a proton conductivity of 5.706×10^{-2} S cm^{-1} in aqueous condition (80 °C and 98% RH) without PA doping. For the first time we have reported this **50% {$W_{72}Fe_{30}$}@m-PBI** composite membrane and the importance is that the membrane shows proton conductivity in aqueous medium whereas the as such membrane of m-PBI didn't show any proton conduction in aqueous medium. This indicates that the proton transportation in aqueous medium is due to compound **$\{W_{72}Fe_{30}\}_{NB}$** which is 50% loaded into the membrane m-PBI, as we have discussed earlier the compound **$\{W_{72}Fe_{30}\}_{NB}$** itself acts as a shell, like a membrane allowing passive transportation of small cations through the shell.[15] All the conductivity values of **50% $\{W_{72}Fe_{30}\}$@m-PBI** composite membrane are shown in the Table A3.5 (Appendix 3).

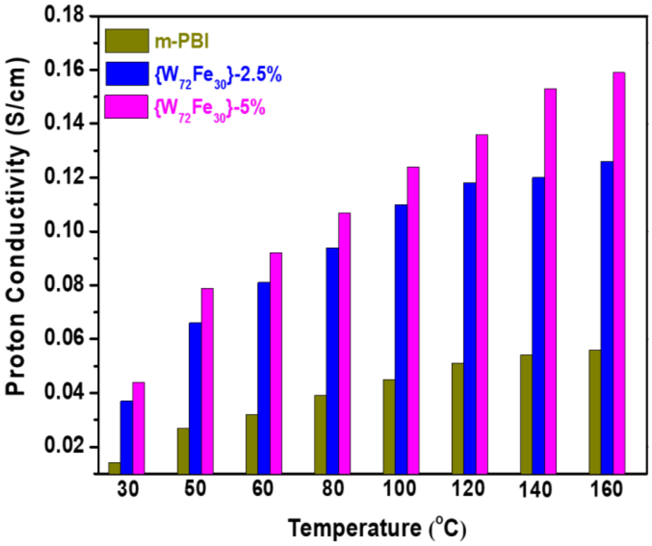

Figure 3.7. Proton conductivity values of **m-PBI, $\{W_{72}Fe_{30}\}$-2.5%** and **$\{W_{72}Fe_{30}\}$-5%** membranes.

3.9 Activation energy (E_a) calculations of the MMMs

The activation energy (E_a) values for all the membranes have been calculated from the temperature dependent Arrhenius plot, obtained from the proton conductivity of the membranes within the temperature range of 30 °C - 160 °C. The calculated E_a values for **m-PBI, $\{W_{72}Fe_{30}\}$-2.5%** and **$\{W_{72}Fe_{30}\}$-5%** membranes are ranges from 12.71-13.54 kJ/mol or ≈ (0.13-0.14) eV (Figure 3.8)**,** implies proton conduction in the MMMs predominately occurs through Grotthuss proton transport mechanism, which operated due to the extensive proton conduction network generation, resulted continuous proton hopping sites in the MMMs between the PA molecules with the **m-PBI** imidazole 'N-H' and the –W=O, –Fe=O, –Fe-OH_2 functionalities of the polyoxometalates clusters through continuous construction and destruction of H-bonding network inside the proton conduction channels.[15] Also, minor deviation of the Arrhenius plots from linearity indicates proton conduction partially operated via vehicular mechanism. Self-assembly of **$\{W_{72}Fe_{30}\}$** nanoclusters into the MMMs network causes self-diffusion of protons throughout the membrane matrix, which may have resulted partly operational vehicular mechanism.[60,64] The resulted E_a values of the MMMs found to be slightly less than m-PBI, resembles that POM clusters incorporation into the m-PBI network generated extensive proton conduction channels for more efficient pathway of proton conduction into the composite matrix, which resulted decreased E_a. Activation energy of the **50% $\{W_{72}Fe_{30}\}$@m-PBI** composite membrane without PA in aqueous medium has been measured and found to be 0.1845 eV (Figure A3.20, Appendix3) and hence in this case also the proton transport happens in the membrane by following the Grotthuss mechanism. It is to be noted that the **$\{W_{72}Fe_{30}\}$** nanoclusters proton conduction follows a vehicular mechanism with an activation energy 1.95 eV. Therefore, it is interesting to note that the activation energy barrier and the conduction mechanism of this nanocluster can be readily tuned by simply making a composite with m-PBI.

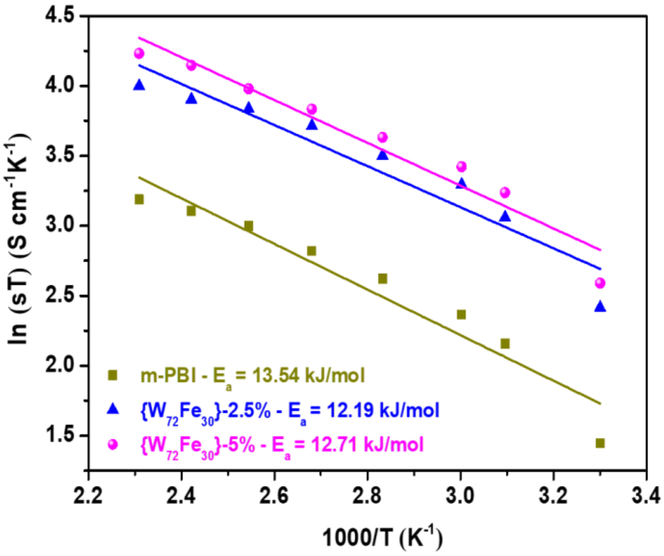

Figure 3.8. Arrhenius activation energy plot of the corresponding membranes.

3.10. Thermal transition and mechanical properties of the membranes

3.10.1. The temperature dependent storage modulus (E′) plots

The temperature dependent storage modulus (E′) plots (obtained from the DMA analysis) of the dry **m-PBI, $\{W_{72}Fe_{30}\}$-2.5%** and **$\{W_{72}Fe_{30}\}$-5%** membranes are represented in the Figure 3.9 and the corresponding storage moduli values of the membranes at 100 °C, 250 °C and 400 °C are tabulated in the Table S6. All the **$\{W_{72}Fe_{30}\}$** polyoxometalates loaded MMMs exhibited significantly improved storage modulus values when compared with m-PBI. But we have observed a slight decrement in storage modulus values with increasing POM loading from **-2.5%** to **-5%** in the MMMs, which might be resulted due to the plasticizing effect operated at higher filler loaded membranes.[65] In other words, beyond a certain wt% of filler loading, the reinforcement effect of the organic functionalities present in the polyoxometalates clusters is dominated by plasticizing effect. Therefore, the effective immobilization of the polymer chains occurs up to a certain threshold wt% concentration of **{W$_{72}$Fe$_{30}$}$_{NB}$** loading in the membrane matrix, beyond which (i.e. for **{W$_{72}$Fe$_{30}$}-5%** membrane) the dominance of plasticizing effect causes softening of the polymer chains, which resulted slightly decreased storage modulus. Hence, , the **{W$_{72}$Fe$_{30}$}-5%** membranes still resulted a huge 318 % and 282 % increment in (E′) at 100 °C and 400 °C, respectively, when compared to pristine m-PBI, indicates the suitability and superiority of the MMMs for high temperature PEM applications.

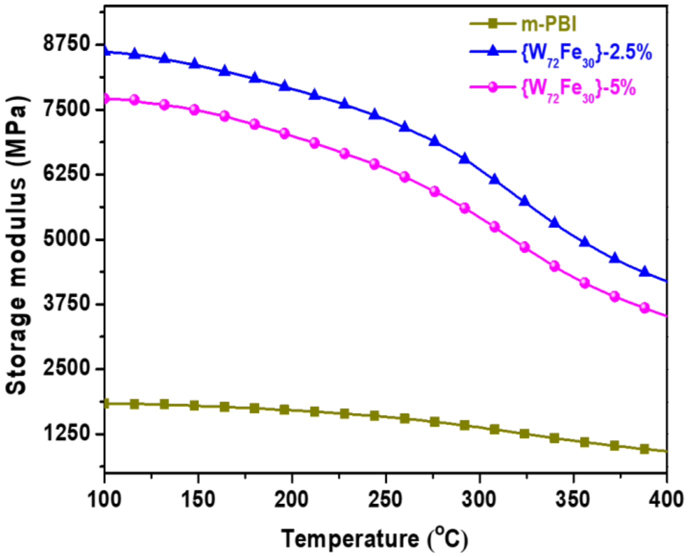

Figure 3.9. Temperature dependent storage modulus,

3.10.2. The temperature dependent Loss modulus and Tan δ plot

The temperature dependent Loss modulus and Tan δ plot (Figure 3.10a, b) of all the **{W$_{72}$Fe$_{30}$}** loaded MMMs showed a single relaxation peak and the temperature associated with the peak is abbreviated as the glass transition temperature (T_g).[66] The obtained T_g values, of the pristine m-PBI and the **{W$_{72}$Fe$_{30}$}$_{NB}$** loaded membranes range from 320 °C - 340 °C (Figure 3.10b), which matches well with the literature reports of PBI based PEMs.[38,60] The obtained T_g values of the composite membranes are almost similar with the T_g value of m-PBI, though from the Loss modulus plot we have observed slight decrement in T_g value for the **{W$_{72}$Fe$_{30}$}-5%** membrane, which might be due to the plasticizing effect in the **-5%** filler loaded membranes causing polymer chains softening.

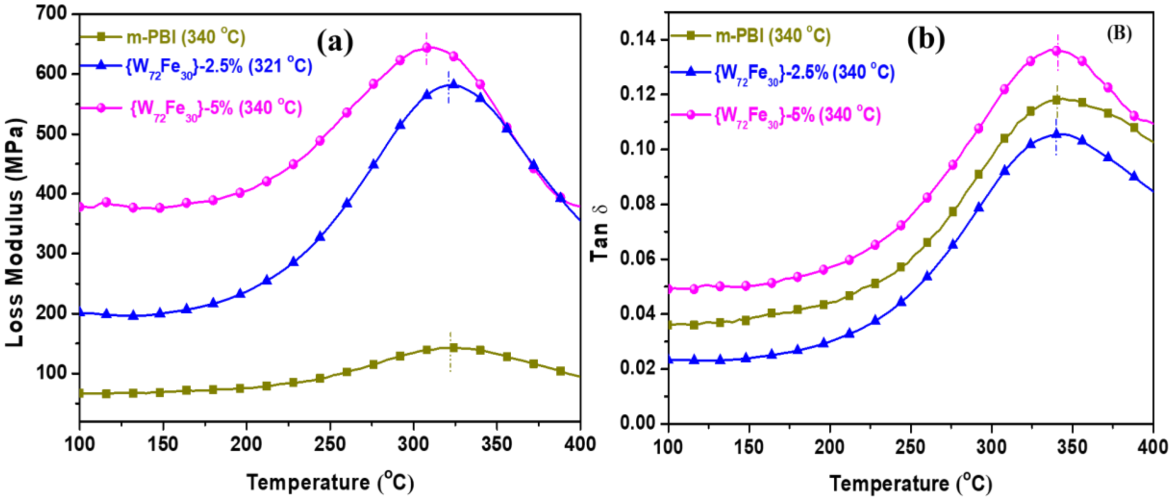

Figure 3.10. Temperature dependent (a) Loss modulus and (b) tan δ plots of **m-PBI, {$W_{72}Fe_{30}$}-2.5%** and **{$W_{72}Fe_{30}$}-5%** membranes obtained from DMA analysis (the obtained T_g values. from the Loss modulus and tan δ plots are given the bracket in the corresponsing Figures).

3.10.3. The stress-strain profiles

The stress-strain profiles of the PA doped **m-PBI, {$W_{72}Fe_{30}$}-2.5%** and **{$W_{72}Fe_{30}$}-5%** membranes were checked and are shown in Figure 3.11**.** The tensile stress (MPa) and elongation at break (%) values of all the membranes are tabulated in the Table A3.7**.** All the POM loaded composite PEMs showed superior stress-strain profile when compared with m-PBI owing to the strong reinforcement effect from the POM fillers. The tensile stress value of the membrane decreases along with increase in the elongation at break (%) value with increasing **{$W_{72}Fe_{30}$}** nanoclusters loading from -2.5% to -5% in the MMMs. Earlier we have observed highest PA loading level in the **{$W_{72}Fe_{30}$}-5%** membrane, and PA doping level follows proportionality with the filler loading. Hence, for **{$W_{72}Fe_{30}$}-5%** membrane, due to higher PA doping level PA molecules might exert plasticizing effect by disrupting some of the existing interfacial H-bonding present in the **Polymer-POM** composites and forms new H-bonding with the composite functionalities, which makes the polymer chain movement much flexible resulting decrement in tensile stress with significantly improved elongation at break value.

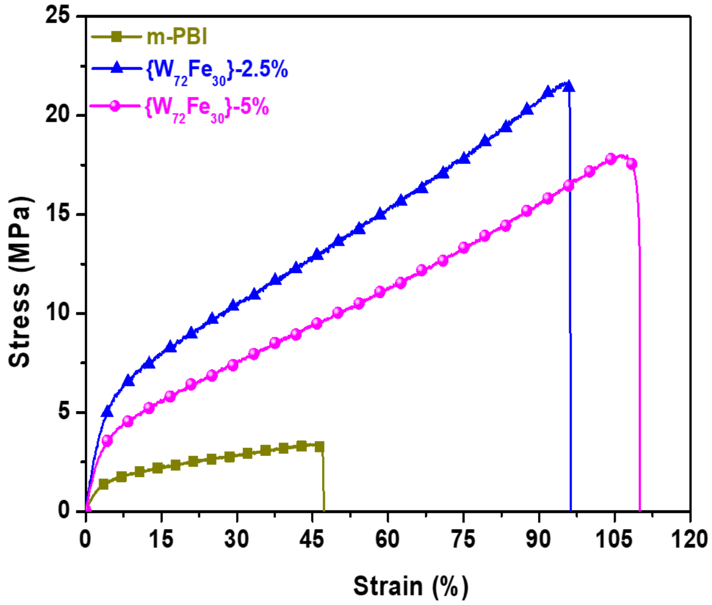

Figure 3.11. Temperature dependent stress-strain profile of PA loaded membranes.

3.11. PA leaching analysis of the PA doped MMMs

To evaluate the PA retention efficacy of the PA loaded **{$W_{72}Fe_{30}$}@m-PBI** membranes, PA leaching analysis of all the MMMs were performed and represented in Figure 3.12 along with the detailed experimental procedure (see **Section A3.11.12** in Appendix3). After each hour of analysis, the weight of the PA doped membranes was measured carefully and PA leaching was calculated from the weight loss ratio of PA present in the membrane (Figure 3.12).[67] m-PBI loses 44.41% PA during first hour of analysis, followed by 54.27% and 67.17% PA loss during the 2nd and 3rd hour of analysis, respectively, and hence resulted to be inefficient membrane for PA retention under saturated water vapour condition. In contrast to the previous observation, **{$W_{72}Fe_{30}$}** POM loaded membranes showed much higher PA retention, which was also increases with increasing **{$W_{72}Fe_{30}$}** filler loading. While **{$W_{72}Fe_{30}$}-2.5%** membrane leaches 25.20%, 30.17% and 35.31% PA after 1st, 2nd and 3rd hour of analysis, respectively, the high filler loaded sample leaches 25.56% and 29.56% PA after 1st, 2nd and 3rd hour of analysis, respectively. The presence of W=O and Fe-O-H_2 hydrophilic functionalities in the **{$W_{72}Fe_{30}$}** material form donor-acceptor type H-bonding interaction with PA, and with increasing filler loading the extent of H-bonding increases, which results more PA loading followed by more PA retention in the MMMs. Also, presence of porous thick fibrils in the membranes cross-section and homogenous dispersion of **{$W_{72}Fe_{30}$}$_{NB}$** all over the MMMs surface obtain from FESEM, hydrophilic-hydrophobic domain formation with increased surface roughness from AFM, and structural self-assembly of **{$W_{72}Fe_{30}$}** fillers into the dense polymer network from surface TEM analysis contributes significantly for improved PA retention. In addition, the increased thermal stability of the PA doped MMMs compared to PA doped m-PBI between 50 °C - 200 °C also indicates towards superior PA retention ability of the polymer-POM composites. The improved PA retention of **{$W_{72}Fe_{30}$}-5%** membrane over **{$W_{72}Fe_{30}$}-2.5%** is due to the higher PA doping level of the former one.

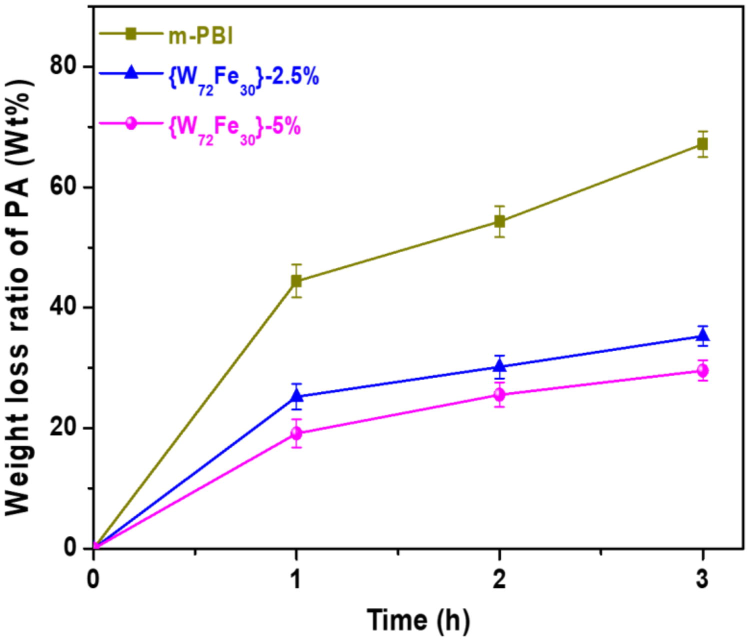

Figure 3.12. Time dependent PA retention study of the **m-PBI, {$W_{72}Fe_{30}$}-2.5%** and **{$W_{72}Fe_{30}$}-5%** membranes.

3.12. Comparison of the current results with literature reports

We have tried to evaluate a brief perspective by comparing our currently obtained results with the literature reports. We have compared the proton conductivity of the synthesized **{$W_{72}Fe_{30}$}** nanoblackberries with the other polyoxometalates based proton conductors in literature (see Appendix3 Section **A3.20**, Table A3.7), which signifies superior proton conductivity our synthesized **{$W_{72}Fe_{30}$}** compared to literature reports. To the best of our knowledge this will be the highest proton conductivity on POM based proton conductors reported in literature till date. Also, our fabricated MMMs **{$W_{72}Fe_{30}$}-2.5%** and **{$W_{72}Fe_{30}$}-5%** showed a superior ~3-fold proton conductivity increments with respect to bare m-PBI**.** Comparison with literature survey resembles the quality of our finding to develop superior **polymer-POM** based proton conductors.

3.13. Conclusions

In conclusion, we have explored the proton conductivity of the nanoclusters containing compound $\{W_{72}Fe_{30}\}_{NB}$, and we have achieved proton conductivity of 3.30×10^{-1} at 80 °C (98%RH). For the first time we have reported the highest proton conductivity among MOF (metal organic frameworks) and POM based compounds. As we cannot use this compound directly in the practical application, we have fabricated PA doped $\{W_{72}Fe_{30}\}$@m-PBI membranes in two different loading levels of $\{W_{72}Fe_{30}\}$ by weight: **2.5% $\{W_{72}Fe_{30}\}$@m-PBI** and **5.0% $\{W_{72}Fe_{30}\}$@m-PBI.** Both membranes have performed as efficient proton exchange membranes when doped with PA and they are having good tensile and thermo-mechanical properties with superior PA retention capacity. The proton conductivity of **2.5% $\{W_{72}Fe_{30}\}$+PA@m-PBI** and **5.0% $\{W_{72}Fe_{30}\}$+PA@m-PBI** membranes are 0.126 S cm^{-1} and 0.159 S cm^{-1}, respectively at 160 °C. We have also fabricated **50% $\{W_{72}Fe_{30}\}$@m-PBI** composite membrane and achieved a proton conductivity of 5.706×10^{-2} S cm^{-1} in aqueous condition (80 °C and 98% RH). Finally, the current work showed the synthesis and proton conductivity of **$\{W_{72}Fe_{30}\}$** and its importance as a nanofiller in MMMs which improved its performance as a proton exchange membrane.

3.14 References

1. Müller, A.; Sarkar, S.; Shah, S. Q. N.; Bogge, H.; Schmidtmann, M.; Sarkar, Sh.; Kögerler, P.; Hauptfleisch, B.; Trautwein, A. X.; Schunemann, V. Archimedean synthesis and magic numbers: ″sizing″ giant molybdenum-oxide-based molecular spheres of the Keplerate type. Angew. Chem. Int. Ed. 1999, 38, 3238-3241.
2. Todea, A. M.; Merca, A.; Bogge, H.; Glaser, T.; Pigga, J. M.; Langston, M. L. K.; Liu, T.; Prozorov, R.; Luban, M.; Schroder, C.; Casey, W. H.; Müller, A. Porous Capsules {(M)M5}12FeIII30 (M=MoVI, WVI): Sphere Surface Supramolecular Chemistry with 20 Ammonium Ions, Related Solution Properties, and Tuning of Magnetic Exchange Interactions. Angew. Chem. Int. Ed. 2010, 49, 514 –519.
3. Jung, J. K.; Procissi, D.; Vincent, R.; Suh, B. J.; Borsa, F.; Kogerler, P.; Schroder, C.; Luban, M. Proton NMR in the giant paramagnetic molecule {Mo72Fe30}. J. Appl. Phys, 2002, 91, 7388-7390.
4. Kuepper, K.; Derks, C.; Taubitz, C.; Prinz, M.; Joly, L.; Kappler, J. P.; Postnikov, A.; Yang, W.; Kuznetsova, T. V.; Wiedwald, U.; Ziemann, P.; Neumann, M. Electronic

structure and soft-X-ray-induced photoreduction studies of iron-based magnetic polyoxometalates of type {(M)M5}12FeIII30(M = MoVI, WVI). Dalton Trans. 2013, 42, 7924–7935.

5. Garlea, V. O.; Nagler, S. E.; Zarestky, J. L.; Stassis, C.; Vaknin, D.; Kögerler, P.; McMorrow, D. F.; Niedermayer, C.; Tennant, A.; Lake, B.; Qiu, Y.; Exler, M.; Schnack, J.; Luban, M. Probing spin frustration in high-symmetry magnetic nanomolecules by inelastic neutron scattering. Phys. Rev. B, 2006, 73, 024414.
6. Lago, J.; Micotti, E.; Corti, M. Low-energy spin dynamics in the giant Keplerate molecule Mo72Fe30%: A muon spin relaxation and 1H NMR investigation. Phys. Rev. B, 2007, 76, 064432.
7. Schröder, C. Multiple nearest-neighbor exchange model for the frustrated magnetic molecules {Mo72Fe30} and {Mo72Cr30}. Phys. Rev. B, 2008, 77, 224409.
8. Neuscamman, E.; Chan, G. K. Correlator product state study of molecular magnetism in the giant Keplerate Mo72Fe30. Phys. Rev. B, 2012, 86, 064402.
9. Schröder, C. Competing Spin Phases in Geometrically Frustrated Magnetic Molecules. Phys. Rev. Lett. 2005, 94, 017205.
10. Ostroushko, A. A.; Tonkushina, M. O.; Korotaev, V. Y.; Prokofeva, A. V.; Kutyashev, B.; Vazhenin, V. A.; Danilova,I. G.; Menshikov, S. Y. Stability of the Mo72Fe30 Polyoxometalate Buckyball in Solution. Russ. J. Inorg. Chem. 2012, 57, 1210–1213.
11. Fareghi-Alamdari, R.; Hafshejani, S. M.; Taghiyar, H.; Yadollahi, B.; Farsani, M. R. Recyclable, Green and Efficient Epoxidation of Olefins in Water with Hydrogen Peroxide Catalyzed by Polyoxometalate Nanocapsule. Catal. Commun. 2016, 78, 64-67.
12. Goss. K.; Kamra, A.; Spudat, C.; Meyer, C.; Kögerler, P.; Schneider, C. M. CVD growth of carbon nanotubes using molecular nanoclusters as catalyst. Phys. Status Solidi B 2009, 246, 2494–2497.
13. Liu, T.; Imber, B.; Diemann, E.; Liu, G.; Cokleski, K.; Li, H.; Chen, Z.; Müller, A. Deprotonations and Charges of Well-Defined {Mo72Fe30} Nanoacids Simply Stepwise Tuned by pH Allow Control/Variation of Related Self-Assembly Processes. J. Am. Chem. Soc. 2006, 128, 15914-15920.
14. Liu, T. Supramolecular Structures of Polyoxomolybdate-Based Giant Molecules in Aqueous Solution. J. Am. Chem. Soc. 2002, 124, 10942-10943.
15. Mishra, P. P.; Pigga, J.; Liu, T. Membranes Based on “Keplerate”-Type Polyoxometalates: Slow, Passive Cation Transportation and Creation of Water Microenvironment. J. Am. Chem. Soc. 2008, 130, 1548-1549.
16. Zhang, J.; Li, D.; Liu, G.; Glover, K, J.; Liu, Tianbo. Lag Periods During the Self-Assembly of {Mo72Fe30} Macroions: Connection to the Virus Capsid Formation Process. J. Am. Chem. Soc. 2009, 131, 15152-15159.

17. Kolli, H. K.; Jana, D.; Das, S. K. Nanoblackberries of {W72Fe33} and {Mo72Fe30}: Electrocatalytic Water Reduction. Inorg. Chem. 2021, 60, 15569–15582.
18. Mekala, R.; Supriya, S.; Das, S. K. Isolation of Blackberry-Shaped Nanoparticles of a Giant {Mo72Fe30} Cluster and Their Transformation to a Crystalline Nanoferric Molybdate. Inorg. Chem. 2016, 55, 12504−12507.
19. Mekala, R.; Supriya, S.; Das, S. K. Fate of a Giant {Mo72Fe30}-Type Polyoxometalate Cluster in an Aqueous Solution at Higher Temperature: Understanding Related Keplerate Chemistry, from Molecule to Material. Inorg. Chem. 2013, 52, 9708−9710.
20. Hickner, M. A.; Ghassemi, H.; Kim, Y. S.; Einsla, B. R.; McGrath, J. E. Alternative Polymer Systems for Proton Exchange Membranes (PEMs). Chem. Rev. 2004, 104, 4587–4611.
21. Elwan, H. A.; Mamlauk, M.; Scott, K. A review of proton exchange membranes based on protic ionic liquid/polymer blends for polymer electrolyte membrane fuel cells. J. Power Sources 2021, 484, 229197.
22. Escorihuela, J.; Mancilla, J. O.; Alexandrova, L.; Castillo, L. F. D.; Compañ, V. Recent Progress in the Development of Composite Membranes Based on Polybenzimidazole for High Temperature Proton Exchange Membrane (PEM) Fuel Cell Applications. Polymers 2020, 12, 1861.
23. Pan, M.; Pan, C.; Li, C.; Zhao, J. A review of membranes in proton exchange membrane fuel cells: Transport phenomena, performance and durability Renew. Sust. Energy Rev. 2021, 141, 110771.
24. Scofield, M. E.; Liu, H.; Wong, S. S. A Concise Guide to Sustainable PEMFCs: Recent Advances in Improving Both Oxygen Reduction Catalysts and Proton Exchange Membranes. Chem. Soc. Rev. 2015, 44, 5836−5860.
25. Liu, Y. R.; Chen, Y. Y.; Zhuang, Q.; Li, G. Recent advances in MOFs-based proton exchange membranes. Coord. Chem. Rev. 2022, 471, 214740.
26. Wu, L.; Zhang, Z.; Ran, J.; Zhou, D.; Li, C.; Xu, T. Advances in Proton-Exchange Membranes for Fuel Cells: An Overview on Proton Conductive Channels (PCCs). Phys. Chem. Chem. Phys. 2013, 15, 4870–4887.
27. Tandekar, K.; Singh, C.; Supriya, S. Proton Conductivity in {Mo72Fe30}-Type Keplerate. Eur. J. Inorg. Chem. 2021, 734–739.
28. Li, S.; Zhao, Y.; Knoll, S.; Liu, R.; Li, G.; Peng, Q.; Qiu, P.; He, D.; Streb, C.; Chen, X. High Proton-Conductivity in Covalently Linked Polyoxometalate-Organoboronic Acid-Polymers. Angew. Chem. Int. Ed. 2021, 60, 16953–16957.
29. Liu, Y.; Yang, X.; Miao, J.; Tang, Q.; Liu, S.; Shi, Z.; Liu, S. Polyoxometalate-functionalized metal–organic frameworks with improved water retention and uniform

proton-conducting pathways in three orthogonal directions. Chem. Commun. 2014, 50, 10023-10026.

30. Iwano, T.; Shitamatsu, K.; Ogiwara, N.; Okuno, M.; Kikukawa, Y.; Ikemoto, S.; Shirai, S.; Muratsugu, S.; Waddell, P. G.; Errington, R. J.; Sadakane, M.; Uchida, S. Ultrahigh Proton Conduction via Extended Hydrogen-Bonding Network in a Preyssler-Type Polyoxometalate-Based Framework Functionalized with a Lanthanide Ion. ACS Appl. Mater. Interfaces 2021, 13, 19138-19147.
31. Wang, X.; Mao, W.; Song, Y.; Meng, F.; Hu, X.; Liu, B.; Su, Z. Hourglass-Type Polyoxometalate-Based Crystalline Material as an Efficient Proton-Conducting Solid Electrolyte. Inorg. Chem. 2021, 60, 18912-18917.
32. Zhu, M.; Iwano, T.; Tan, M.; Akutsu, D.; Uchida, S.; Chen, G.; Fang, X. Macrocyclic Polyoxometalates: Selective Polyanion Binding and Ultrahigh Proton Conduction. Angew. Chem. Int. Ed. 2022, 61, 1-5.
33. Escorihuela, J.; Narducci, R.; Compañ, V.; Costantino, F. Proton Conductivity of Composite Polyelectrolyte Membranes with Metal-Organic Frameworks for Fuel Cell Applications. Adv. Mater. Interfaces 2019, 6, 1801146.
34. Li, A-L.; Gao, Q.; Xu, J.; Bu, X-H. Proton-conductive metal-organic frameworks: Recent advances and Perspectives. Coord. Chem. Rev. 2017, 344, 54–82.
35. Li, D.; Tan, X. L.; Chen, L. L.; Liu, X. Y.; Li, Y. M.; Dang, D. B.; Bai, Y. Four Dawson POM-based inorganic-organic supramolecular compounds for proton conduction, electrochemical and photocatalytic activity. J. Solid State Chem. 2022, 305, 122694.
36. Basu, O.; Mukhopadhyay, S.; Laha, S.; Das, S. K. Defect Engineering in a Metal−Organic Framework System to Achieve Super-Protonic Conductivity. Chem. Mater. 2022, 34, 6734−6743.
37. Sannigrahi, A.; Arunbabu, D.; Murali Sankar, R.; Jana, T. Aggregation Behavior of Polybenzimidazole in Aprotic Polar Solvent. Macromolecules 2007, 40, 2844–2851.
38. Hazarika, M.; Jana, T. Proton Exchange Membrane Developed from Novel Blends of Polybenzimidazole and Poly(Vinyl-1,2,4-Triazole). ACS Appl. Mater. Interfaces 2012, 4, 5256–5265.
39. Zhang, S.; Lu, Y.; Sun, X. W.; Li, Z.; Dang, T. Y.; Zhang, Z.; Tian, H. R.; Liu, S. X. Purely inorganic frameworks based on polyoxometalate clusters with abundant phosphate groups: single-crystal to single-crystal structural transformation and remarkable proton conduction. Chem. Commun. 2020, 56, 391-394.
40. Nimir, W.; Al-Othman, A.; Tawalbeh, M.; Makky, A. A.; Ali, A.; Maleh, H. K.; Karimi, F.; Karaman, C. Approaches towards the development of heteropolyacid-based high temperature membranes for PEM fuel cells. Int. J. Hydrog. Energy. 2023, 48, 6638-6656.

41. Lu, S.; Xu, X.; Zhang, J.; Peng, S.; Liang, D.; Wang, H.; Xiang, Y. A Selfanchored Phosphotungstic Acid Hybrid Proton Exchange Membrane Achieved via One-Step Synthesis. Adv. Energy Mater. 2014, 4, 140084.
42. Zhai, S.; Song, H.; Jia, X.; Yang, K.; Feng, M.; He, S.; Lin, J. Fabrication of water-insoluble phosphotungstic acid-carbon nitride nanohybrids for promoting proton transport of nanocomposite proton exchange membranes. J. Power Sources, 2021, 506, 230195.
43. Zhang, J.; Chen, S.; Bai, H.; Lu, S.; Xiang, Y.; Jiang, S. P. Effects of phosphotungstic acid on performance of phosphoric acid doped polyethersulfonepolyvinylpyrrolidone membranes for high temperature fuel cells. Int. J. Hydrog. Energy, 2021, 46, 11104 - 11114.
44. Motz, A. R.; Kuo, M. -C.; Horan, J. L.; Yadav, R.; Seifert, S.; Pandey, T. P.; Galioto,S.; Yang, Y.; Dale, N. V.; Hamrocke, S. J.; Herring, A. M. Heteropoly acid functionalized fluoroelastomer with outstanding chemical durability and performance for vehicular fuel cells. Energy Environ. Sci., 2018, 11, 1499-1509.
45. Nakamura, O.; Kodama, T.; Ogino, I.; Miyake, Y. High-Conductivity Solid Proton Conductors: Dodecamolybdophosphoric Acid And Dodecatungstophosphoric Acid Crystals. Chemistry Letters, 1979, 17-18.
46. Martinelli, A.; Otero-Mato, J. M.; Garaga, M. N.; Elamin, K.; Rahman, S. M. H.; Zwanziger, J. W.; Zwanziger, U. W.; Varela, L. M. A New Solid-State Proton Conductor: The Salt Hydrate Based on Imidazolium and 12-Tungstophosphate. J. Am. Chem. Soc. 2021, 143, 13895-13907.
47. Li, S.; Zhao, Y.; Knoll, S.; Liu, R.; Li, G.; Peng, Q.; Qiu, P.; He, D.; Streb, C.; Chen, X. High Proton-Conductivity in Covalently Linked Polyoxometalate Organoboronic Acid-Polymers. Angew. Chem. Int. Ed. 2021, 60, 16953-16957.
48. Li, Z.; Lin, L. D.; Yu, H.; Li, X. X.; Zheng. S. T. All-Inorganic Ionic Porous Material Based on Giant Spherical Polyoxometalates Containing Core-Shell K6@K36-Water Cage. Angew. Chem. Int. Ed. 2018, 57, 15777-15781.
49. Yang, P.; Alsufyani, M.; Emwas, A. H.; Chen, C.; Khashab, N. M. Lewis Acid Guests in a {P8W48} Archetypal Polyoxotungstate Host: Enhanced Proton Conductivity via Metal-Oxo Cluster within Cluster Assemblies. Angew. Chem. Int. Ed. 2018, 57, 13046-13051.
50. Yang, F.; Xu, G.; Dou, Y.; Wang, B.; Zhang, H.; Li, H. W. R.; Chen. B. A flexible metal–organic framework with a high density of sulfonic acid sites for proton conduction. Nat. Energy, 2017, 2, 877-883.
51. Elahi, S. M.; Chand, S.; Deng, W. H.; Pal, A.; Das, M. C. Polycarboxylate-Templated Coordination Polymers: Role of Templates for Superprotonic Conductivities of up to 10-1 S cm-1. Angew. Chem. Int. Ed. 2018, 57, 6662-6666.

52. Mukhopadhyay, S.; Debgupta, J.; Singh, C.; Sarkar, R.; Basu, O.; Das, S. K. Designing UiO-66-Based Superprotonic Conductor with the Highest Metal−Organic Framework Based Proton Conductivity. ACS Appl. Mater. Interfaces 2019, 11, 13423-13432.
53. Li, X. M.; Dong, L. Z.; Li, S. L.; Xu, G.; Liu, J.; Zhang, F. M.; Lu, L. S.; Lan, Y. Q. Synergistic Conductivity Effect in a Proton Sources-Coupled Metal−Organic Framework. ACS Energy Lett. 2017, 2, 2313-2318.
54. Basu, O.; Mukhopadhyay, S.; Laha, S.; Das, S. K. Defect Engineering in a Metal−Organic Framework System to Achieve Super-Protonic Conductivity. Chem. Mater. 2022, 34, 6734-6743.
55. Kreuer, K. D. Proton Conductivity: Materials and Applications. Chem. Mater. 1996, 8, 610-641.
56. Shigematsu, A.; Yamada, T.; Kitagawa, H. Wide Control of Proton Conductivity in Porous Coordination Polymers. J. Am. Chem. Soc. 2011, 133, 2034-2036.
57. Shimizu, G. K. H.; Taylor, J. M.; Kim, S. Chemistry. Proton conduction with metal-organic frameworks. Science 2013, 341, 354-355.
58. Singha, S.; Jana, T.; Modestra, J. A.; Naresh Kumar, A.; Mohan, S. V. Highly Efficient Sulfonated Polybenzimidazole as a Proton Exchange Membrane for Microbial Fuel Cells. J. Power Sources 2016, 317, 143–152.
59. Hazarika, M.; Jana, T. Novel Proton Exchange Membrane for Fuel Cell Developed from Blends of Polybenzimidazole with Fluorinated Polymer. Eur. Polym. J. 2013, 49, 1564–1576.
60. Basu, O.; Das, A.; Jana, T.; Das, S. K. Design of Flexible Metal − Organic Framework-Based Superprotonic Conductors and Their Fabrication with a Polymer into Proton Exchange Membranes. ACS Appl. Energy Mater. 2022, DOI: 10.1021/acsaem.2c02972.
61. Jouanneau, J.; Mercier, R.; Gonon, L.; Gebel, G. Synthesis of Sulfonated Polybenzimidazoles from Functionalized Monomers: Preparation of Ionic Conducting Membranes. Macromolecules 2007, 40, 983–990.
62. Lee, S.; Nam, K.-H.; Seo, K.; Kim, G.; Han, H. Phase Inversion-Induced Porous Polybenzimidazole Fuel Cell Membranes: An Efficient Architecture for High-Temperature Water-Free Proton Transport. Polymers 2020, 12, 1604.
63. Mukhopadhyay, S.; Das, A.; Jana, T.; Das, S. K. Fabricating a MOF Material with Polybenzimidazole into an Efficient Proton Exchange Membrane. ACS Appl. Energy Mater. 2020, 3, 7964-7977.
64. Escorihuela, J.; Sahuquillo, Ó.; García-Bernabé, A.; Giménez, E.; Compañ, V. Phosphoric Acid Doped Polybenzimidazole (PBI)/Zeolitic Imidazolate Framework Composite Membranes with Significantly Enhanced Proton Conductivity under Low Humidity Conditions. Nanomaterials 2018, 8, 775.

65. Gorre, A.; Das, A.; Jana, T. Mixed Matrix Composite PEM with Super Proton Conductivity Developed from Ionic Liquid Modified Silica Nanoparticle and Polybenzimidazole. J. Macromol. Sci. Part A Pure Appl. Chem. 2023, 60, 38-50.
66. Mukherjee, N.; Das, A.; Jana, T. Poly(N-Vinyl Triazole- b- N-Vinyl Imidazole) Grafted on MWCNTs as Nanofillers to Improve Proton Conducting Membranes. ACS Appl. Nano Mater. 2023, 6, 544-557.
67. Das, A.; Mukherjee, N.; Jana, T. Polymer-Grafted Graphene Oxide/Polybenzimidazole Nanocomposites for Efficient Proton-Conducting Membranes. ACS Appl. Nano Mater. 2023, 6, 6365-6379.

CHAPTER 4

Giant Polyoxometalate $\{W_{72}Fe_{30}\}$ in the form of Gel and Xerogel: Rheology and Proton Conduction

Overview

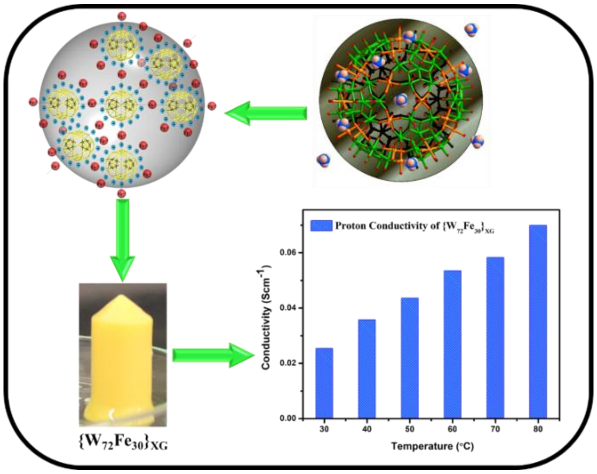

Polyoxometalate (POM) gel is quite well-known, but mostly with organic molecules. Pure inorganic POM gel is hardly known. When an aqueous solution of sodium tungstate is mixed with an aqueous solution of ferric chloride, an immediate precipitation is observed to be formed ─ the resulting suspension on stirring at room temperature for three hours followed by its centrifugation results in the formation of straw-color gel. The resulting gel has been characterized by rheological studies indicating that this is a soft gel. Linear visco elastic (LVE) region for the 24 hours data of this gel spans from 0.1 – 2.5%, when the storage modulus (G′) is 2674 Pa. The relevant yield stress (σ_y) value is found to be 82 Pa. As expected, when we apply more strain, the storage modulus gets decreased. Dehydration of this gel at room temperature brings about the corresponding xerogel, characterization of which confirms that the xerogel is a $\{W_{72}Fe_{30}\}$ type giant Keplerate-based POM compound $[Fe(H_2O)_6]_{14}[W_{72}Fe_{30}O_{252}(H_2O)_{72}(OH)_{60}]\cdot166H_2O$ (**$\{W_{72}Fe_{30}\}_{XG}$**) and the basic building unit of the gel must be $\{W_{72}Fe_{30}\}$ cluster unit. The xerogel is characterized with 60 hydroxyl groups per formula unit and these hydroxyl groups are acidic in nature. Interestingly, the title xerogel, **$\{W_{72}Fe_{30}\}_{XG}$**, an inexpensive metal-oxide-based material, exhibits proton conduction in the solid state. The material shows super proton conductivity of 6.99×10^{-2} S cm^{-1} at 80 ºC and 98% relative humidity. The activation energy (E_a) for the proton conduction is found to be 0.2 eV indicating that the Grotthuss mechanism is involved in the proton conduction.

4.1. Introduction

Polyoxometalates (POMs) are the large metal-oxo cluster containing compounds, that are widely explored in the areas of electrochemical water splitting, photo-induced water splitting, electronics, catalysis, nanotechnology and medicinal chemistry.[1-14] Among polyoxometalates, Keplerates $\{M_{72}Fe_{30}\}$ (M = Mo and W) have a unique structure as a giant spherical cluster with a wide range of applications. The well-known Keplerate compound $[Na_6(NH_4)_{20}\{Fe(H_2O)_6\}_2][\{W^{VI}_6O_{21}(SO_4)\}_{12}\{Fe(H_2O)\}_{30}(SO_4)_{13}(H_2O)_{34}]\cdot 200H_2O$ (**$\{W_{72}Fe_{30}\}_{Cryst}$**) was originally synthesized by Achim Müller group in the year 2010.[15] It has 12 pentagonal units $[(W)W_5O_{21}(H_2O)_6]^{6-}$, linked among these pentagons, by 30 Fe(III) monomeric $\{Fe^{III}O_5(H_2O)\}^{3+}$ linkers as shown in Figure 4.1.[15] Recently, we have isolated the amorphous $\{W_{72}Fe_{30}\}$ cluster containing compound $Fe_3[W_{72}Fe_{30}O_{252}(CH_3COO)_2(OH)_{25}(H_2O)_{103}]\cdot 180H_2O$ (**$\{W_{72}Fe_{30}\}_{NM}$**) in a one-pot synthesis by reaction of aqueous solution of sodium tungstate with ferric chloride in the presence of acetic acid.[16] The extra three Fe^{3+} ions, which are not part of the $\{W_{72}Fe_{30}\}$ cluster, plays an important role in maintaining the stability of the isolated compound (**$\{W_{72}Fe_{30}\}_{NM}$**. The $\{W_{72}Fe_{30}\}$ cluster is less explored in terms of its physical properties; there are only few reports that are related to its magnetic-, electronic- and catalytic-properties.[17,18] The catalysis includes electrocatalytic hydrogen evolution reaction (HER) by water reduction and selective oxidation of sulfides to sulfones using hydrogen peroxide as an oxidant.[16,18] In the present work, we have explored gel formation in a simple aqueous synthesis involving $\{W_{72}Fe_{30}\}$ cluster as a building unit without using any organic molecule.

A gel is a non-fluid 3D network that expands through a fluid phase.[19] If the fluid is having organic building block, then it is called as organogel.[20-22] If the fluid is water, then it is referred to as hydrogel.[20,23] Estroff and Hamilton have proposed a theory related to the gel formation on self-assembly of proteins during the tertiary structure formation from the pertinent building blocks.[24] Initially, the building blocks form the sub-nanosized aggregations and further they link to exhibit different morphologies like fibers, micelles, ribbons, etc. in nano- to micro-meter scales.[25] These self-assembling molecular gels (hydrogel and organogel) have recently gained enormous attention in the various fields, e.g., biosensing, self-cleaning membranes, catalysis, batteries and drug delivery.[23,26,27] Mostly, gel formation includes the self-assembly of a metal ion with an organic ligand. Pure inorganic gel is scarcely reported.[23] In inorganic chemistry, POM clusters have been introduced as building units for the formation of supramolecular gel because POM cluster units enhance the rate of formation of gels due to their oxygen-rich surface and charge on the cluster.[25]

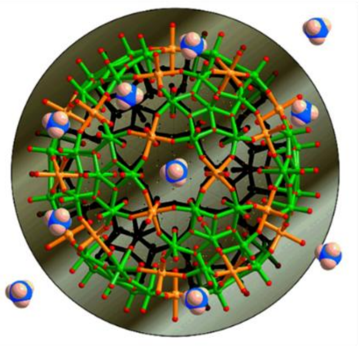

Figure 4.1. Ball and stick representation of $\{W_{72}Fe_{30}\}$ cluster containing compound.[15]

POM containing supramolecular gel materials have a vast number of applications in the field of lithium-ion batteries, supercapacitors, ink-free printing, switchable liquid separation and seawater desalination.[25,28-47] Polyoxovanadate-gels have shown applications as biosensors, battery electrodes and in the area of solar energy conversion.[2] Most of the POM gels are formed by the combination of 'POM anion and surfactant cation', 'POM anion and ionic-liquid cation', 'POM anion and zwitterion cation', 'POM anion and peptide cation', POM anion and organic macrocyclic cation', POM anion and organic polymer cation', etc.[25] In all these combinations, the cationic part is an organic molecule in its cationic form that counterbalances the negative charge of the POM anion. The gel-formation by a combination of a 'POM anion and a metal cation' (without an organic component) is hardly known,[23] which is desirable to obtain thermally stable xerogel materials. And a gel material formed from a giant POM cluster anion is not at all known.

In the present work, for the first time, we report a pure inorganic gel, formed from a giant POM cluster anion $\{W_{72}Fe_{30}\}$, popularly known as Keplerate anion, without using any commonly used organic moiety simply by mixing an aqueous solution of sodium tungstate with an aqueous solution of ferric chloride. This type of hydrogel formation is an unexplored area of contemporary materials research. We have dried the obtained hydrogel at an ambient condition by simple evaporation (a sol-gel technique)[19] to the corresponding xerogel and characterized the solid material (xerogel) by diverse spectral techniques including microscopy and elemental analyses to obtains its formula as $[Fe(H_2O)_6]_{14}[W_{72}Fe_{30}O_{252}(H_2O)_{72}(OH)_{60}]\cdot 166H_2O$ (**$\{W_{72}Fe_{30}\}_{XG}$**). The resulting xerogel is found to be a macroporous material as evidenced by microscopy. We have thus performed N_2 gas adsorption studies of this xerogel **$\{W_{72}Fe_{30}\}_{XG}$**. This is characterized with 60 hydroxyl groups per formula unit and this material is turned out to be acidic, evidenced from a simple pH experiment. Thus, this xerogel behaves like a solid inorganic acid having acidic hydroxyl groups. As expected, this xerogel material **$\{W_{72}Fe_{30}\}_{XG}$** exhibits proton conduction in its solid-state.

Solid materials exhibiting high proton conductivity has received considerable attention in recent times.[48-53] The gel materials (especially xerogels from hydrogels) are generally the good proton conducting materials as they have more number of pores filled with water molecules which can be used in the proton conduction.[54] It is known that Nafion is the well-known proton conducting electrolyte in the proton exchange membrane fuel cells (PEMFCs).[55-56] Although Nafion shows reasonable performance in the PEMFCs, its practical use is limited by its considerably poor performance at low humidity and at higher temperatures; Nafion is also considerably expensive.[55-57] These restrictions have made researchers develop other materials that could replace Nafion for efficient proton conduction in PEMFCs. Thus, both MOF (metal organic framework) and POM (polyoxometalate) containing compounds have parallelly been evolved as solid proton conducting materials.[58-61] In fact, $\{Mo_{132}\}$-Keplerate with diverse organic cations and $\{Mo_{72}Fe_{30}\}$-Keplerate itself ($[Mo_{72}Fe_{30}O_{252}(CH_3COO)_{12}\{Mo_2O_7(H_2O)\}_2\{H_2Mo_2O_8(H_2O)\}(H_2O)_{91}]\cdot 150H_2O$) have been explored as solid proton conductors.[62-63]

In this work, we have demonstrated that the xerogel material $[Fe(H_2O)_6]_{14}[W_{72}Fe_{30}O_{252}(H_2O)_{72}(OH)_{60}]\cdot 166H_2O$ (**$\{W_{72}Fe_{30}\}_{XG}$**) having large numbers of pores, lattice water molecules and -OH groups, exhibits excellent proton conductivity in its solid state (6.99×10^{-2} S cm^{-1} at 80 °C and RH 98%). There are various reports of xerogel materials, other than polyoxometalates, that show moderate to good proton conduction solid-state.[55, 64-70] To the best of our knowledge, this is the first report of hydrogel and corresponding xerogel materials that are obtained from a giant POM cluster, $\{W_{72}Fe_{30}\}$. This xerogel, **$\{W_{72}Fe_{30}\}_{XG}$**, that is turned out to be a microporous material, not only shows moderate N_2-adsorption behavior but also shows excellent proton conduction and moderate electrical conductivity. In a nut shell, we have reported here a macro-porous gel material of $\{W_{72}Fe_{30}\}$ giant polyoxometalate, obtained from a simple aqueous synthesis, that shows gas-adsorption, proton conductivity as well as electrical conductivity.

4.2. Experimental Section

4.2.1. Materials

All the chemicals were used as received without any further purification. Sodium tungstate ($Na_2WO_4.2H_2O$) was purchased from SRL chemicals and ferric chloride hexa hydrate ($FeCl_3.H_2O$) was purchased from sigma aldrich chemicals.

4.2.2 Synthesis of $\{W_{72}Fe_{30}\}_{Gel}$ – $[Fe(H_2O)_6]_{14}[W_{72}Fe_{30}O_{252}(H_2O)_{72}(OH)_{60}]\cdot 160H_2O$

An aqueous solution (25 mL) of $Na_2WO_4\cdot 2H_2O$ (4 g, 12.12 mmol) was made homogeneous solution under vigorous stirring condition and then another aqueous solution (5 mL) of $FeCl_3\cdot 6H_2O$ (3.402 g, 12.58 mmol) was added to it. Instantaneously, a yellow-colored precipitation was observed; the reaction mixture was stirred for 3 hours at room temperature and then it was centrifuged for 15 mins at 1200 rpm. The resulting solution was filtered off and the filtrate got transformed to a thick gel material after 24 hours (even after an immediate centrifugation and filtration, filtrate forms a thick gel after 24 hours). The resultant hydrogel **$\{W_{72}Fe_{30}\}_{HG}$** (mud brown color) was dried at room temperature and atmospheric pressure and then washed with distilled water to remove the crystallized sodium chloride on the surface of the xerogel. The washed xerogel was dried under vacuum desiccator to get a moisture free xerogel. Yield: 2.0 g. Infrared spectrum of the **$\{W_{72}Fe_{30}\}_{XG}$** compound shows the bands at 1619 (m, δ (H_2O)), 924 (m, $\bar{\upsilon}$(W=O)), 718 (s) and 552 cm^{-1} (m). The further characterizations of the compound have been discussed.

4.2.3 Methods

The instrumental details of the all the experiments are provided in appendix 1.

4.2.4 Rheology Studies

A strain-controlled rheometer of make Anton Parr, MCR 501 designed with a cone-plate measuring system with the cone angle of 0.5^o and a plate with the diameter of 25 mm have been used for the rheology studies. To the bottom plate of the rheometer, a Peltier temperature controller is attached to check the temperature difference with an accuracy of 0.1° C. The entire setup of the rheometer has been placed inside the hood to achieve the uniform temperature throughout the measurement. We have used 10 g of gel compound for each rheology studies. We have placed the sample on the sample holder position of the rheometer and then evenly spread the compound and then applied the pressure to start the measurement once the temperature reaches to 25 °C. All the measurements were carried out at a constant temperature of 25 °C. We have also carried out the measurement of G′ and G″ with respect to temperature.

4.3. Results and Discussion

4.3.1. Structural Analysis of $\{W_{72}Fe_{30}\}_{XG}$

Earlier, we have synthesized the nano-blackberries of both molybdenum $Na_2[Mo_{72}Fe_{30}O_{252}(CH_3COO)_4(OH)_{16}(H_2O)_{108}]\cdot 180H_2O$ (**$\{Mo_{72}Fe_{30}\}_{NM}$**) and tungsten $Fe_3[W_{72}Fe_{30}O_{252}(CH_3COO)_2(OH)_{25}(H_2O)_{103}]\cdot 180H_2O$ (**$\{W_{72}Fe_{30}\}_{NM}$**) in amorphous form.[16] Among these two nanomaterials, the formation of tungsten nano-blackberry material seems to be of high significance because of its enormous stability (even at higher temperatures) and its efficient electrocatalytic activity towards water reduction to molecular hydrogen. When we mix an aqueous solution of sodium tungstate solution with an aqueous solution of ferric chloride in the presence of acetic acid, we obtain tungsten nano-blackberry compound **$\{W_{72}Fe_{30}\}_{NM}$** after 15 minutes of mixing. But if the same reaction is carried out in the absence of acetic acid, we cannot isolate tungsten nanoblackberries **$\{W_{72}Fe_{30}\}_{NM}$**; instead we observe the formation of gel after 45 minutes of mixing the reaction mixture; after half an hour of stirring the aqueous reaction

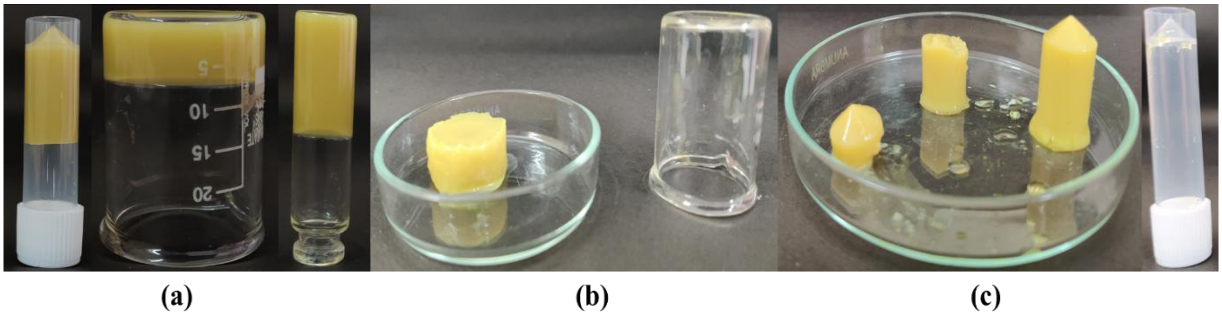

(a) (b) (c)

Figure 4.2. (a) Photographs of the gel materials in different shapes in inverted vials and beaker; (b) and (c) engraving the gel to make diverse shapes of the gel material using the beaker and vials.

mixture, a cloudy suspension is formed, which was centrifuged to get a clear solution; the clear solution on standing at room temperature leads to the formation of a gel as shown in Figure 4.2. Thus, acetic acid plays

an important role to the formation of nano-blackberries; $\{W_{72}Fe_{30}\}$ clusters (formed *in situ*) assemble through Fe^{3+} centers (through Coulombic interactions) resulting in the formation of a nano-blackberry as shown in Figure 4.3. Hence a nanoblackberry $Fe_3[W_{72}Fe_{30}O_{252}(CH_3COO)_2(OH)_{25}(H_2O)_{103}]\cdot 180H_2O$ (**$\{W_{72}Fe_{30}\}_{NM}$**) is nothing but a

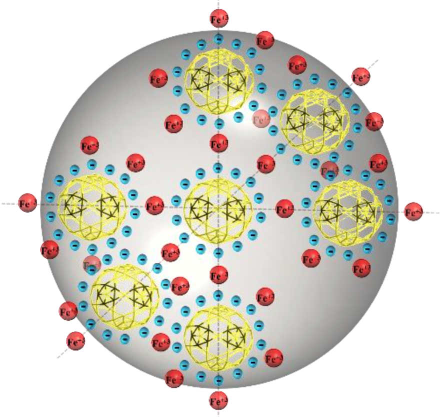

Figure 4.3. Schematic representation of compound **$\{W_{72}Fe_{30}\}_{NM}$** in which six 0.5 Fe^{3+} cations surrounding each cluster from six sides in three axes.[16]

supramolecular assembly of $\{W_{72}Fe_{30}\}$ clusters linked through Fe^{3+} centers. It seems that coordinated acetate anion in $\{W_{72}Fe_{30}\}$ cluster causes deprotonation of the iron-coordinated hydroxyl groups to make more negative charge density on each cluster surface. This facilitates the Coulombic attractive type of interactions between $\{W_{72}Fe_{30}\}$ clusters and Fe^{3+} centers resulting in the formation of nano-blackberries, **$\{W_{72}Fe_{30}\}_{NM}$**. On the other hand, when acetic acid is not present in this aqueous reaction mixture, $\{W_{72}Fe_{30}\}$ clusters (formed *in situ*) do not get assembled through Fe^{3+} (probably, the cluster surface attached hydroxyl groups do not get deprotonated due to the lack of acetate anion); instead an inorganic gel is formed due to the formation of a supramolecular hydrogen bonding network involving $\{W_{72}Fe_{30}\}^{42-}$ cluster anions and $14\{Fe(H_2O)_6\}^{3+}$ cations, whereby the network expands through fluid phase (water) resulting in a hydrogel $[Fe(H_2O)_6]_{14}[W_{72}Fe_{30}O_{252}(H_2O)_{72}(OH)_{60}]\cdot xH_2O$, which on dehydration (air dry at room temperature) forms the xerogel $[Fe(H_2O)_6]_{14}[W_{72}Fe_{30}O_{252}(H_2O)_{72}(OH)_{60}]\cdot 166H_2O$, where x>>>166. This xerogel is thoroughly characterized by diverse spectral techniques including elemental analyses (ICP) and microscopy (FESEM and HR-TEM) and formulated as $[Fe(H_2O)_6]_{14}[W_{72}Fe_{30}O_{252}(H_2O)_{72}(OH)_{60}]\cdot166H_2O$ (**$\{W_{72}Fe_{30}\}_{XG}$**). It can be assumed that the parent hydrogel and dehydrated xerogel would have same compositions except the water content. The 'tungsten nano-blackberries $Fe_3[W_{72}Fe_{30}O_{252}(CH_3COO)_2(OH)_{25}(H_2O)_{103}]\cdot180H_2O$ (**$\{W_{72}Fe_{30}\}_{NM}$**)' material (Figure 4.3) has already been reported by us and its characterization 'fingerprints', for example, IR and Raman spectral features have been used to characterize the xerogel in the present work.

4.3.2. FT-IR spectrum of $\{W_{72}Fe_{30}\}_{NM}$ and $\{W_{72}Fe_{30}\}_{XG}$

The main difference between the formulas of **$\{W_{72}Fe_{30}\}_{NM}$** and **$\{W_{72}Fe_{30}\}_{XG}$** is the presence of two acetate ligands per formula unit of **$\{W_{72}Fe_{30}\}_{NM}$** and the absence of any acetate in **$\{W_{72}Fe_{30}\}_{XG}$**. As shown in Figure 4.4, the IR spectra of **$\{W_{72}Fe_{30}\}_{XG}$** and **$\{W_{72}Fe_{30}\}_{NM}$** are comparable except the evidence of tiny features of carboxylate in the IR spectrum of **$\{W_{72}Fe_{30}\}_{NM}$**. This is consistent with their elemental analysis by EDX (Appendix4, Section A4.6 and A4.7).

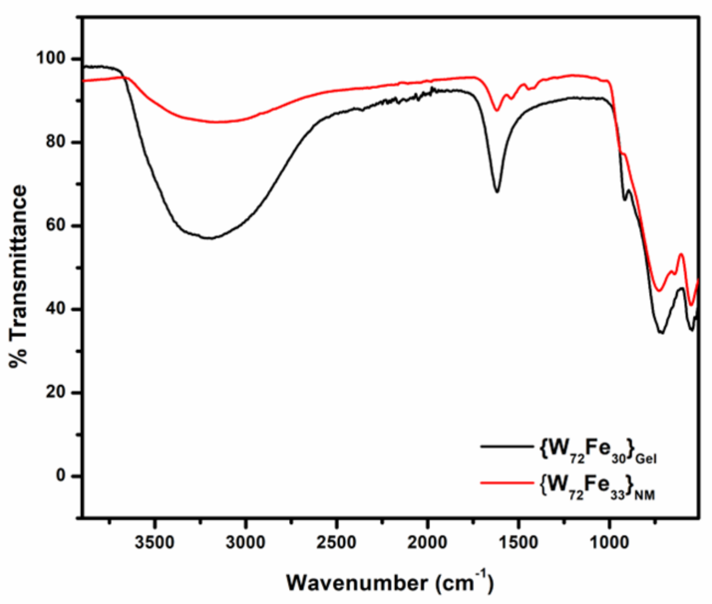

Figure 4.4. (a) FT-IR spectrum of **$\{W_{72}Fe_{30}\}_{XG}$** compound $[Fe(H_2O)_6]_{14}[W_{72}Fe_{30}O_{252}(H_2O)_{72}(OH)_{60}]\cdot166H_2O$, compared with that of the compound $Fe_3[W_{72}Fe_{30}O_{252}(CH_3COO)_2(OH)_{25}(H_2O)_{103}]\cdot180H_2O$ (**$\{W_{72}Fe_{30}\}_{NM}$**).

4.3.3. Raman spectrum of $\{W_{72}Fe_{30}\}_{NM}$ and $\{W_{72}Fe_{30}\}_{XG}$

The Raman spectra (Figure 4.5) of **$\{W_{72}Fe_{30}\}_{XG}$** and **$\{W_{72}Fe_{30}\}_{NM}$** are identical confirming the presence of $\{W_{72}Fe_{30}\}$ cluster cage in **$\{W_{72}Fe_{30}\}_{XG}$**, thereby the presence of $\{W_{72}Fe_{30}\}$ cluster in hydrogel in the present work. The Raman bands appear at 963 (W=O), 869, 760, 588, 439, 349 and 185 cm^{-1} in the Raman spectra of both gel and nano-blackberry compounds as shown in the Figure 4.5. ICP-OES metal analyses (Appendix4, Section A4.7) and thermogravimetric studies (vide infra) suggest that there are 44 iron atoms and 166 lattice water molecules per formula unit of the xerogel compound.

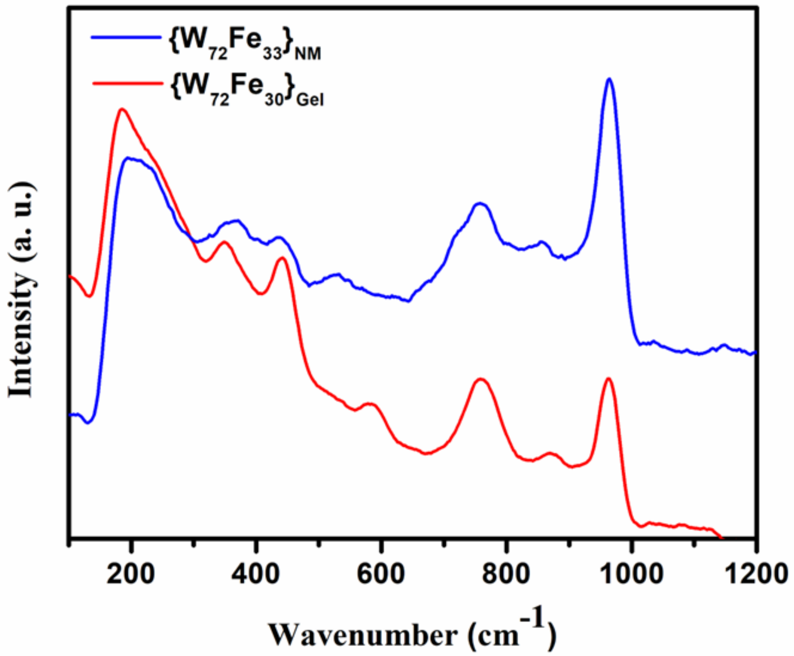

Figure 4.5. Raman spectrum of the compound **$\{W_{72}Fe_{30}\}_{XG}$** which is compared with that of **$\{W_{72}Fe_{30}\}_{NM}$**

We have already seen from IR- and Raman- spectral studies that $\{W_{72}Fe_{30}\}$ cluster is present in xerogel compound; thus 14 iron ions act as cations per formula unit of gel compound. Besides, ICP-OES analysis, we have also carried out the quantitative estimation of iron content of the xerogel compound by volumetric titration (the detailed calculations and relevant experimental details are given in Appendix4, Section A4.7). The obtained result is consistent with ICP-OES data, i.e., 44 iron atoms per formula. We have used 66 hydroxyl anions per formula unit to counterbalance the overall charge of the xerogel compound, $[Fe(H_2O)_6]_{14}$ $[W_{72}Fe_{30}O_{252}(H_2O)_{72}(OH)_{60}]\cdot166H_2O$ (**$\{W_{72}Fe_{30}\}_{XG}$**).

4.3.4. PXRD of $\{W_{72}Fe_{30}\}_{XG}$

The powder X-Ray diffraction (PXRD) plot (Figure 4.6) exhibits four broad features at 27.17°, 31.60°, 42.99° and 53.85° for the compound **$\{W_{72}Fe_{30}\}_{XG}$**, which clearly indicates that the xerogel compound is semi-crystalline in nature, which is consistent with TEM-SAED data (vide infra).

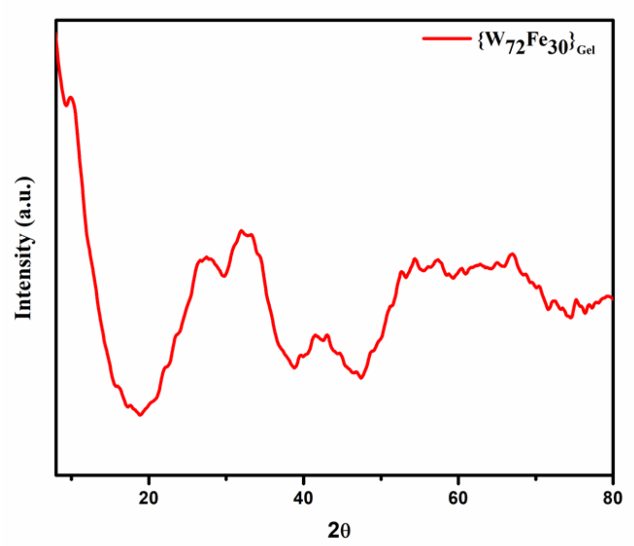

Figure 4.6. PXRD pattern of compound **$\{W_{72}Fe_{30}\}_{XG}$**

4.3.5. TGA of $\{W_{72}Fe_{30}\}_{XG}$

Figure 4.7 shows the thermogravimetric analysis plot of the compound **$\{W_{72}Fe_{30}\}_{XG}$**; there is a weight loss from 30°C to 260°C due to loss of lattice water molecules (observed - 16.46%; theoretical - 16.94%). Further, a weight loss from 260°C to 300°C is observed corresponding to the loss of coordinated water molecules. We have already seen that the xerogel in the present work is a semicrystalline material from PXRD studies. When a hydrogel goes to xerogel by dehydration (at room temperature), formation of pores is expected. Thus, the obtained xerogel, obtained in this work, was subjected to microscopic studies, namely FESEM and HR-TEM.

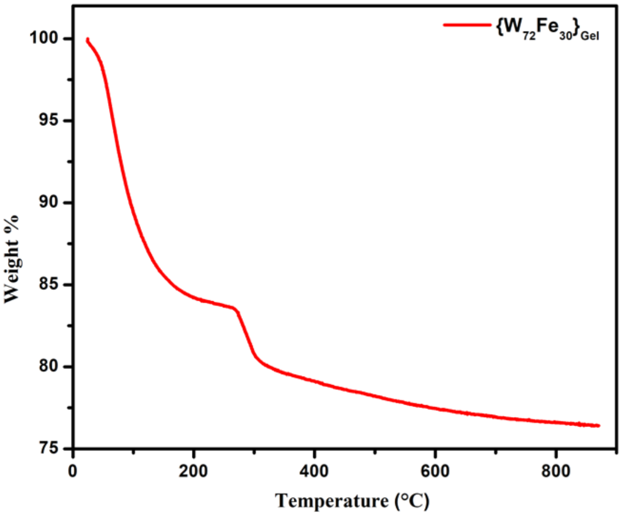

Figure 4.7. (d) thermogravimetric plot of the gel compound $\mathbf{\{W_{72}Fe_{30}\}_{XG}}$.

4.3.6. FESEM of $\{W_{72}Fe_{30}\}_{XG}$

The FESEM images of the xerogel, $\mathbf{\{W_{72}Fe_{30}\}_{XG}}$ is shown in Figure 4.8, which shows that the xerogel is porous in nature with the pore sizes ranging from 70 to 100 nm. This xerogel, as mentioned previously, is obtained by air drying the gel material at room temperature. If we take the pre-gel material (the dense viscous liquid state which is about to be transformed to gel) and dry at room temperature, the resulting solid shows the pore sizes in the range of 200 to 250 nm as found from FESEM (Appendix4 Section A4.5). This indicates that the pores of this porous material are dynamic in nature and the pore sizes can be changed on the application of an external stimulus.

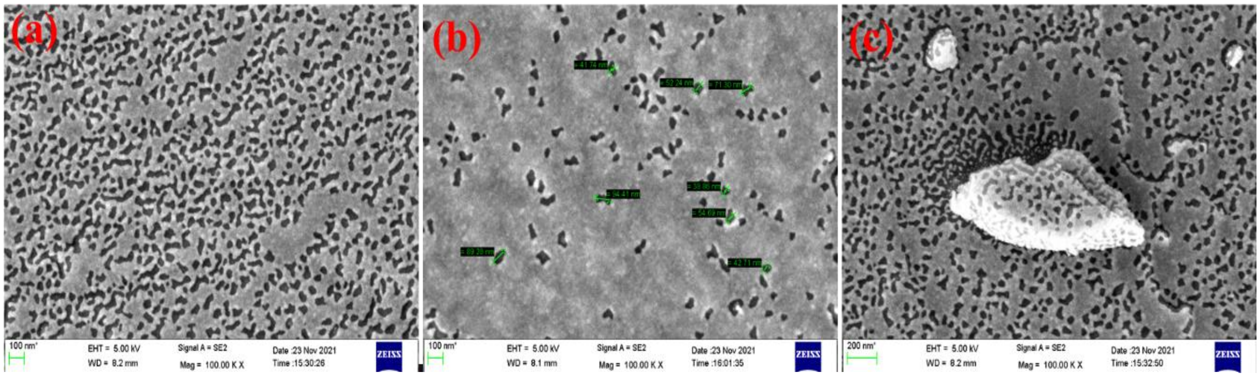

Figure 4.8. (a-c) FESEM images of the compound $[Fe(H_2O)_6]_{14}[W_{72}Fe_{30}O_{252}(H_2O)_{72}(OH)_{60}]\cdot166H_2O$ at different resolutions;

4.3.7. HR-TEM of $\{W_{72}Fe_{30}\}_{XG}$

This is reflected in the high resolution transmission electron microscopy (HR-TEM) images of **$\{W_{72}Fe_{30}\}_{XG}$** is shown in Figures 4.9a and 4.9b. The pore sizes get decreased when the same xerogel sample **$\{W_{72}Fe_{30}\}_{XG}$** is subjected to HR-TEM source energy. Indeed, the compound gets disintegrated at higher magnification of HR-TEM. We have already mentioned that the title xerogel is semicrystalline on the basis of PXRD studies. This is consistent with the selective area electron diffraction (SAED) pattern (Figure 4.9c) of compound **$\{W_{72}Fe_{30}\}_{XG}$** which shows diffraction when the compound is exposed to high electron beam environment, but there are less diffractions in the selective area electron diffraction (SAED) pattern. The porosity of this material has been corroborated by performing the gas adsorption studies of **$\{W_{72}Fe_{30}\}_{XG}$**. We found that the relevant BET surface area is 73.737 m^2g^{-1} (Appendix4, Section A4.9) and the average pore volume and pore width are 0.01925 cc/g and 2268 Å (around 200 nm), respectively. The pertinent adsorption isotherm shows that it is a type III macro-porous material. We have also performed the energy dispersive X-ray (EDX) spectroscopy for the **$\{W_{72}Fe_{30}\}_{XG}$** compound to know the surface composition; Figure A4.6 and A4.7 (Appendix4) shows the image of the selected surface area of **$\{W_{72}Fe_{30}\}_{Gel}$** including its EDX plot, histogram of the elemental composition and the elemental mapping analysis.

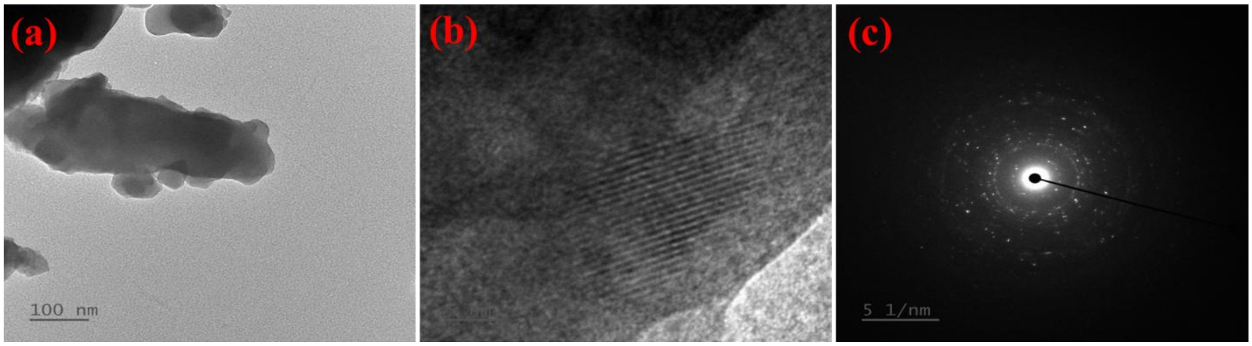

Figure 4.9. (a,b) HR-TEM images of the compound **$\{W_{72}Fe_{30}\}_{XG}$**; (c) SAED pattern of the compound **$\{W_{72}Fe_{30}\}_{XG}$**.

4.3.8. Rheology Studies

In the present work, we are dealing with a giant polyoxometalate-based gel material (Figure 4.2). In order to have a deeper insights on this gel formation and its mechanical strength, the rheology studies are performed on this gel compound (which upon drying at room temperature gives xerogel **$\{W_{72}Fe_{30}\}_{XG}$**). We have carried out the measurement of storage modulus (G′) and loss modulus (G″) with respect to the angular frequency and strain. From the Figures 4.10a and

4.10b, we clearly observe that G′ is always greater than G″ and also, with increase in time both the G′ and G″ have increased, which indicates that with time the gel becomes more and more solid, meaning thereby the mechanical strength of the gel material **{$W_{72}Fe_{30}$}$_{HG}$** increases with time. As shown in the Figures 4.10c and 4.10d (the plots of modulus versus strain), we have measured the amplitude sweep (strain %) values for the compound **{$W_{72}Fe_{30}$}$_{HG}$** at different time intervals and we found that the G′ remains constant in the range of 0.1-2.5% and the values of G″ are constant in the range of 0.1 - 5%. These ranges of 0.1-2.5% and 0.1 - 5% are called linear viscoelastic (LVE) ranges of G′ and G″, respectively. At the higher values of strain %, the G′ and G″ values gets dropped, which indicates a transition takes place from linear to non-linear viscoelastic region. We can see from Figure 4.10c, LVE for the 24 hours data ranges from 0.1 – 2.5%, where the G′ is 2674 Pa. Later, after this linear LVE, the G′ starts getting dropped on the application of higher strain / amplitude sweep. It is interesting to note that we have observed an unusual feature in this curve (kind of a hump) in the range of G′ 636 Pa to G′ 61 Pa at the applied strain range of 8% to 51%. This indicates a slight increase in the strain value in this particular range. This can be explained by the fact that the gel material in the present work is formed by the self-assembly of {$W_{72}Fe_{30}$} clusters and during this application of increasing strain in this range the self-assembly gets destructed, thereby consuming slightly more applied strain (energy). On further increase of strain i.e., beyond 50%, the cluster {$W_{72}Fe_{30}$}, i.e., the building unit gets deformed. We have calculated the G′ - G″ values to know the rigidity of the gel material **{$W_{72}Fe_{30}$}$_{HG}$** with respect to time. We have calculated G′ - G″ values at different time intervals. In general, the more is the value of G′ - G″, the mechanical strength is more. As shown in Table 4.1, we observe that our gel compound after 24 hours of formation shows the G′ - G″ value of 2055 Pa, which is highest when we compare the same with those of other relevant polyoxometalate based gels.[71-73] We have also measured the yield stress (σ_y) values for the compound **{$W_{72}Fe_{30}$}$_{HG}$** with the help of a plot of shear stress *versus* strain measurement and we have observed that the gel of the present work exhibits the elastic nature till 82 Pa of yield stress, beyond which, the gel will be in the free flow state (semi-liquid). We have also observed that yield stress values increase with increase in time as shown in the Table 4.1, which shows that the elastic nature of the gel material is increased with time. The thermal behavior of the gel **{$W_{72}Fe_{30}$}$_{HG}$** with respect to G′ and G″ has also been monitored at the temperature range of 20-50 °C as shown in the Figure 4.10e. We have observed that there is slow increase in the G′ and

G″ as we increase the temperature from 20-50 ºC and the G′ is always larger than G″ which proves that the compound is hydrogel, and it exhibits elastic nature throughout this temperature range. The gelation process has been monitored with time at a constant temperature of 25 ºC. We have measured G′ and G″ as a function of time as shown in the Figure 4.10f. We have noted that the values of both G′ and G″ increase with the time, but G′ increases more faster than G″ which says that the strength of the present gel material increases with an elastic behavior by transforming from liquid to viscoelastic solid. Thus, the whole rheology studies including frequency sweep and amplitude sweep (strain (%)) studies, establish that the obtained gel material **$\{W_{72}Fe_{30}\}_{HG}$** exhibits an elastic solid nature.

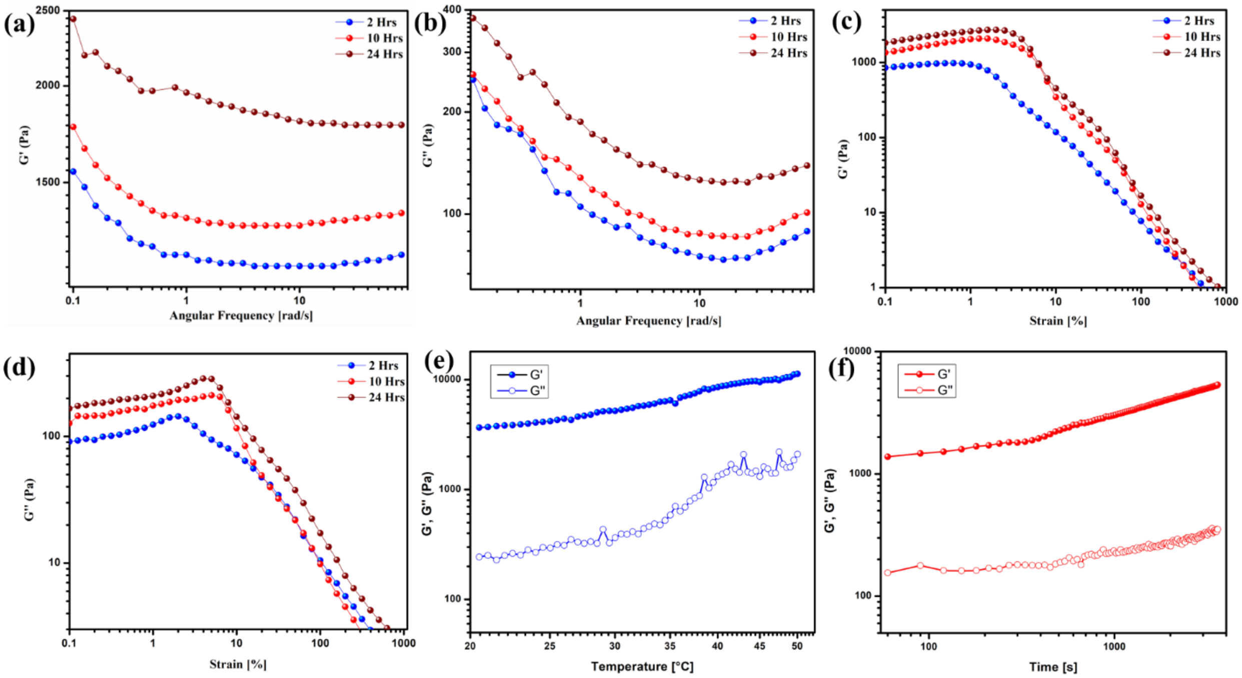

Figure 4.10. (a) Measurement of G′ with respect to angular frequency in the time span of two, ten and twenty-four hours of the compound **$\{W_{72}Fe_{30}\}_{HG}$**. (b) Measurement of G″ with respect to angular frequency in the time span of two, ten and twenty-four hours of the compound **$\{W_{72}Fe_{30}\}_{HG}$**. (c) Amplitude sweep measurement of the compound **$\{W_{72}Fe_{30}\}_{HG}$** with respect to G′ in the time span of two, ten and twenty-four hours. (d) Amplitude sweep measurement of the compound **$\{W_{72}Fe_{30}\}_{HG}$** with respect to G″ in the time span of two, ten and twenty-four hours. (e) Variation of G′ and G″ with respect to temperature. (f) Variation of G′ and G″ with respect to time.

Table 4.1: G′- G″ and Yield stress values for **$\{W_{72}Fe_{30}\}_{HG}$** with respect to time.

Time Interval (Hours)	G′-G″ (Pa)	Yield Stress (Pa)
2	1302	12.4
10	1514	63.3
24	2055	82

4.3.9. Proton Conductivity Studies

Proton conductivity(σ) was measured for the compound **$\{W_{72}Fe_{30}\}_{XG}$** with help of electrochemical impedance spectroscopy; the two electrode system has been used for the measurement. The compound is sandwiched between two carbon paper electrodes to form a pellet (Pellet preparation has been mentioned in the Appendix4 Section A4.11). A homemade setup has been used for the proton conductivity measurements (Appendix4 Section A4.11). Conductivity calculations were done from the Nyquist plot fitted with the suitable equivalent circuit (Appendix4 Section A4.11). Nyquist plots were constructed between the real part of impedance (Z') and imaginary part of impedance (Z"). Impedance spectra were recorded in the temperature range of 30 ºC to 80 ºC at a relative humidity (R.H.) of 98% (Appendix4 Section A4.11). The title xerogel **$\{W_{72}Fe_{30}\}_{XG}$** shows a relative increase in the proton conductivity with respect to increase in temperature (Figure 4.11a). At 80 ºC and 98% R.H., the compound **$\{W_{72}Fe_{30}\}_{XG}$** shows the higher proton conductivity of 6.99×10^{-2} S cm^{-1}. This value suggests that the title material **$\{W_{72}Fe_{30}\}_{XG}$** is one of the super proton conducting materials among the POM based proton conducting materials based on the relevant recent reports (Appendix4 Table A4.4). Even at lower temperature (30 ºC; 98% R.H.), the compound **$\{W_{72}Fe_{30}\}_{XG}$** shows proton conductivity of 2.54×10^{-2} S cm^{-1}. The relevant detailed calculations have been mentioned in the Appendix4 section A4.11. The impedance spectral data, obtained, were analyzed and fitted in the relevant circuit ((R1/Q1) + (R2/Q2) + Q3) to calculate the proton conductivity, where R1 and R2 are resistance and Q1, Q2 and Q3 are constant phase. The experimental data of impedance spectra, obtained, could be fitted with the above-mentioned circuit without any notable error (χ^2). Activation energy (E_a) for the proton conduction shown by the compound **$\{W_{72}Fe_{30}\}_{XG}$** was calculated from the proton conductivity values obtained at different temperatures (Figure 4.11a) and thereby an Arrhenius plot is constructed (Figure 4.11b). We have found that the activation energy (E_a) during proton conduction in the compound **$\{W_{72}Fe_{30}\}_{XG}$** is 0.2 eV and the linearity of the Arrhenius plot is well maintained as the proton conductivity as increased with increase in temperature from 30-80 ºC. The value of the activation energy indicates that the Grotthuss mechanism is involved in the proton conduction in the compound **$\{W_{72}Fe_{30}\}_{XG}$**. This can be supported by the logic that the mobile protons of the Fe(III)-OH_2 functionality of $\{W_{72}Fe_{30}\}$ cluster forms a hydrogen bonds with the water molecules present between the different clusters by forming the H_3O^+-H_2O system which helps in the migration of protons to achieve high conductivity values. Further, we have analyzed the stability of compound by recording the PXRD patterns of the pelletized compound after the EIS measurement (Appendix4 Section A4.12). During stability check, we have carried out the conductivity measurement with time at 80 ºC and relative humidity of 98%; we found that the compound is stable till 10 hours, beyond which pelletized compound started to deform and ooze out of the pellet which prevented us to carry on with the measurement. A prolonged exposure of the concerned xerogel compound **$\{W_{72}Fe_{30}\}_{XG}$** to higher temperature results in the material into complete dryness, as a result of which the proton networking channel in the compound gets disturbed which leads to break of conductivity chain. The mobile protons for the proton conduction in the compound **$\{W_{72}Fe_{30}\}_{XG}$** were generated from the acidic Fe(III)-OH_2 centers and lattice water molecules.[65] This is the first time we are reporting the formation of a gel material from a Keplerate type of POM $\{W_{72}Fe_{30}\}$ cluster containing compound that shows huge proton conductivity (6.99×10^{-2} S cm^{-1}) and low activation energy (0.2 eV).

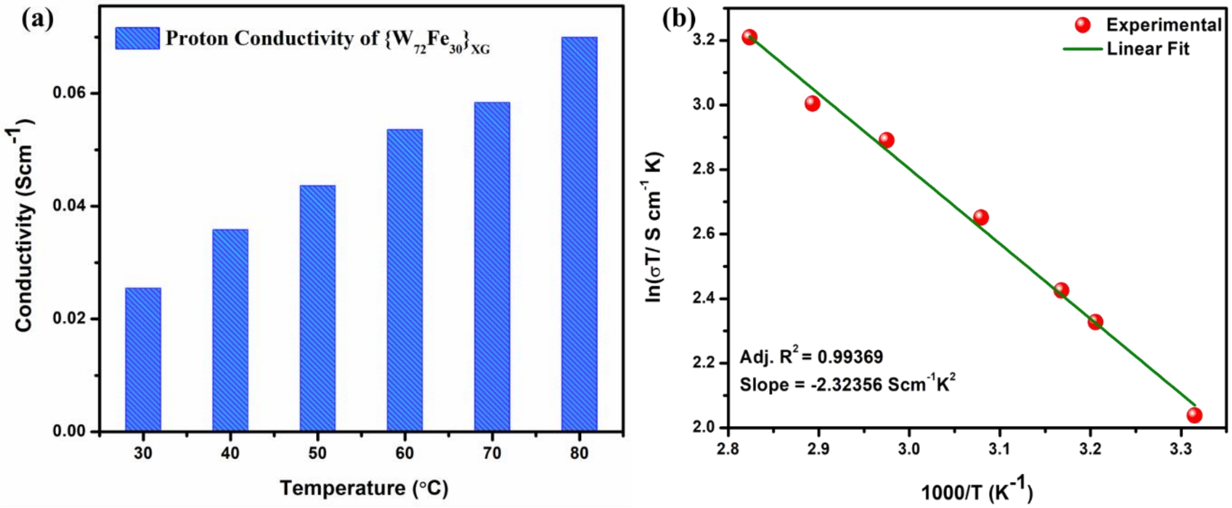

Figure 4.11. (a) the variation of proton conductivity with change in temperature for **$\{W_{72}Fe_{30}\}_{XG}$** at a constant relative humidity (98% RH) and (b) Arrhenius plot of proton conductivity for **$\{W_{72}Fe_{30}\}_{XG}$** at 98% RH.

4.3.10. Electrical Conductivity

In the present work, we have measured the electrical conductivity of the xerogel material **$\{W_{72}Fe_{30}\}_{XG}$**. This xerogel **$\{W_{72}Fe_{30}\}_{XG}$** has a good number of unpaired electrons (44×5 = 220) as it is having the 44 Fe(III) centers per formula unit of compound $[Fe(H_2O)_6]_{14}[W_{72}Fe_{30}O_{252}(H_2O)_{72}(OH)_{60}]\cdot160H_2O$ (assuming each iron center is high spin

Fe(III) center). Some of these electrons could be loosely bound to the nucleus, that can make the material

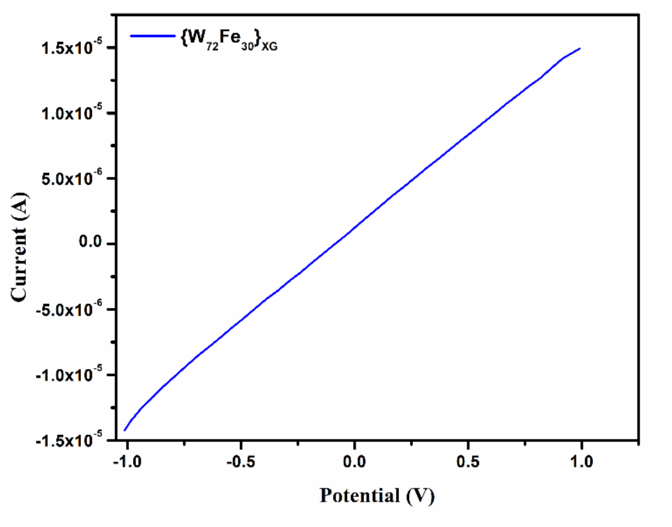

Figure 4.12. Current (I) vs. potential (V) plot of the compound **$\{W_{72}Fe_{30}\}_{XG}$**.

electrically conductive. This made us interested to measure the electrical conductivity of this xerogel **$\{W_{72}Fe_{30}\}_{XG}$**. Generally, the electrical conductivity is measured from the current (I) versus potential (V) curve to validate the behavior of the material for Ohm's law. From the figure 4.12, we can observe that when we have applied a potential (V) from -1.0 V to 1.0 V, the current of the corresponding compound is also increased with respect to potential, which clearly shows that the compound **$\{W_{72}Fe_{30}\}_{Gel}$** is following the Ohm's law. We have also calculated the electrical conductivity of the compound from the following equation.

$$\sigma = \frac{l}{RA} \text{ (where } A = \pi d^2/4 \text{)} \qquad \ldots\ldots\ \text{(eqn 1)}$$

Where, σ ($S\ cm^{-1}$) is electrical conductivity, A (cm^2) is the surface area and l is the length (cm) of the solid material, d (cm) is diameter of the cell and R is resistance for the xerogel. We have achieved an electrical conductivity of 2.43×10^{-5} S cm^{-1} for the compound **$\{W_{72}Fe_{30}\}_{XG}$** at the potential range of -1 V to 1 V. The detailed calculation of the conductivity is mentioned in the Appendix4 section A4.13.

4.4. Conclusion

In conclusion, a pure inorganic Keplerate hydrogel $\mathbf{\{W_{72}Fe_{30}\}_{HG}}$ without any organic moiety has been reported for the first time in the gel chemistry area of polyoxometalates (POMs). The gel material has been characterized by rheology studies indicating that it is gel with modest mechanical strength. The xerogel $\mathbf{\{W_{72}Fe_{30}\}_{XG}}$ has been characterized using various microscopic and spectroscopic techniques. FESEM images suggest that the compound is porous in nature. Further, the xerogel $\mathbf{\{W_{72}Fe_{30}\}_{XG}}$ exhibits a high proton conductivity of 6.99×10^{-2} S cm^{-1}. The porosity of this xerogel material has been established by gas adsorption studies. N_2 gas adsorption capacity of this title material is found to be 0.556 mmol/g. It is a rare example of POM compound that exhibits an electrical conductivity of $2.43x10^{-5}$ S cm^{-1} at applied potential 1 V. This xerogel $\mathbf{\{W_{72}Fe_{30}\}_{XG}}$ material has potential to be used as a nanofiller in an organic polymer matrix to make proton exchange membrane for fuel cell applications. This is under progress in our laboratory.

4.5. References

1. Tsunashima, R.; Richmond, C.; Cronin, L. Exploring the mobility of nanoscale polyoxometalates using gel electrophoresis. *Chem. Sci.,* **2012**, *3*, 343–348.
2. Seliverstov, A.; Rangus, M.; Hartmann, M.; Mitchell S. G.; Streb C. Instantaneous formation of polyoxometalate-based cerium vanadium oxide gels. *Inorg. Chem. Front.,* **2017**, *4*, 160–164.
3. Muller, A.; Peters, F.; Pope M. T.; Gatteschi, D. Polyoxometalates: Very Large Clusters Nanoscale Magnets. *Chem. Rev.,* **1998**, *98*, 239-271.
4. Hill, C. L. Introduction: Polyoxometalates Multicomponent Molecular Vehicles to Probe Fundamental Issues and Practical Problems. *Chem. Rev.,* **1998**, *98*, 1-2.
5. Hasenknopf, B. Polyoxometalates: introduction to a class of inorganic compounds and their biomedical applications. *Front. Biosci.,* **2005**, *10*, 275-287.
6. Liu, T. Hydrophilic Macroionic Solutions: What Happens When Soluble Ions Reach the Size of Nanometer Scale. *Langmuir,* **2010**, *26*, 9202-9213.
7. Long, D.-L.; Burkholder, E.; Cronin, L. Polyoxometalate clusters, nanostructures and materials: From self-assembly to designer materials and devices. *Chem. Soc. Rev.,* **2007**, *36*, 105-121.
8. Kortz, U.; Muller, A.; Slageren, J.; Schnack, J.; Dalal, N. S.; Dressel, M. Polyoxometalates: Fascinating structures, unique magnetic properties. *Coord. Chem. Rev.,* **2009**, *253*, 2315-2327.

9. Long, D.-L.; Tsunashima, R.; Cronin, L. Polyoxometalates: Building Blocks for Functional Nanoscale Systems. *Angew. Chem., Int. Ed.,* **2010**, *49*, 1736-1758.
10. Long, D.-L.; Cronin, L. Towards Polyoxometalate-Integrated Nanosystems. *Chem.–Eur. J.,* 2006, 12, 3698-3706.
11. Miras, H. N.; Cooper, G. J. T. Long, D.-L.; Bogge, H.; Muller, A.; Streb, C.; Cronin, L.; Unveiling the Transient Template in the Self-Assembly of a Molecular Oxide Nanowheel. *Science*, **2010**, *327*, 72-74.
12. Ziv, A.; Grego, A.; Kopilevich, S.; Zeiri, L.; Miro, P.; Bo, C.; Muller, A.; Weinstock, I. A. Flexible Pores of a Metal Oxide-Based Capsule Permit Entry of Comparatively Larger Organic Guests. *J. Am. Chem. Soc.*, **2009**, *131*, 6380-6382.
13. Noro, S.-I.; Tsunashima, R.; Kamiya, Y.; Uemura, K.; Kita, H.; Cronin, L.; Akutagawa, T.; Nakamura, T. Adsorption and Catalytic Properties of the Inner Nanospace of a Gigantic Ring-Shaped Polyoxometalate Cluster. *Angew. Chem., Int. Ed.,* **2009**, *48*, 8703-8706.
14. Long, D.-L.; Kogerler, P.; Cronin, L. Old Clusters with New Tricks: Engineering S···S Interactions and Novel Physical Properties in Sulfite-Based Dawson Clusters. *Angew. Chem., Int. Ed.,* **2004**, *43*, 1817-1820.
15. Todea, A. M.; Merca, A.; Bögge, H.; Glaser, T.; Pigga, J. M.; Langston, M. L. K.; Liu, T.; Prozorov, R.; Luban, M.; Schröder C.; Casey W. H.; Müller A. Porous Capsules $\{(M)M_5\}_{12}Fe^{III}_{30}$ ($M = Mo^{VI}, W^{VI}$): Sphere Surface Supramolecular Chemistry with 20 Ammonium Ions, Related Solution Properties, and Tuning of Magnetic Exchange Interactions. *Angew. Chem. Int. Ed.,* **2010**, *49*, 514 –519.
16. Kolli, H. K.; Jana, D.; Das, S. K. Nanoblackberries of $\{W_{72}Fe_{33}\}$ and $\{Mo_{72}Fe_{30}\}$: Electrocatalytic Water Reduction. *Inorg. Chem.,* 2021, *60*, 20, 15569–15582.
17. Kuepper, K.; Derks, C.; Taubitz, C.; Prinz, M.; Joly,L.; Kappler, J-P.; Postnikov, A.; Yang, W.; Kuznetsova,g T. V.; Wiedwald, U.; Ziemanna P.; Neumann M. Electronic structure and soft-X-ray-induced photoreduction studies of iron-based magnetic polyoxometalates of type $\{(M)M_5\}_{12}Fe^{III}_{30}$ ($M = Mo^{VI}, W^{VI}$). *Dalton Trans.* **2013**, *42,* 7924-7935.
18. Haddadi, H.; Korani, E. m.; Hafshejani S. M.; Farsani M. R. Highly Selective Oxidation of Sulfides to Sulfones by H_2O_2 Catalyzed by Porous Capsules. *J. Clust. Sci.* **2015**, *26*, 1913 –1922.
19. Danks, A. E.; Hall, S. R.; Schnepp, Z. The evolution of 'sol–gel' chemistry as a technique for materials synthesis. *Mater. Horiz.,* **2016**, *3*, 91—112.
20. Livage, J.; Lemerlen J. Transition Metal Oxide Gels and Colloids. *Ann. Rev. Mater. Sci.,* **1982**, *12*, 103-122.

21. Ross-Murphy S. B. Structure and rheology of gelatin gels: recent progress. *Polymer*, **1992**, *33*, 2622-2627.
22. Corriu, R. J. P.; Leclercq, D.; Lefèvre, P.; Mutin, P. M.; Vioux, A. Preparation of Monolithic Metal Oxide Gels by a Non-hydrolytic Sol-Gel Process. J. Mater. Chem., **1992**, *2*, 673-674.
23. Mondal, C.; Ganguly, M.; Pal, J.; Sahoo, R.; Sinhaa A. K.; Pal T. Pure inorganic gel: a new host with tremendous sorption capability. *Chem. Commun.*, **2013**, *49*, 9428-9430.
24. Estroff, L. A.; Hamilton, A. D. Water Gelation by Small Organic Molecules. *Chem. Rev.*, **2004**, *104*, 1201-1218.
25. Li, B.; Xuan, L.; Wu, L. Polyoxometalate-Containing Supramolecular Gels. *Macromol. Rapid Commun.*, **2022**, *43*, 2200019.
26. Dai, C.; Zhao, G.; You, Q.; Zhao, M. A Study on Environment-Friendly Polymer Gel for Water Shut-Off Treatments in Low-Temperature Reservoirs. *J. Appl. Polym. Sci.*, **2014**, 40154.
27. Livage, J. Redox Reactions in Transition Metal Oxide Gels. *J. Sol-Gel Sci. Technol.* **1993**, *1*, 21-33.
28. Meng, X.; Wang, H. N.; Zou, Y. H.; Wang, L. S.; Zhou, Z. Y. Polyoxometalate-based metallogels as anode materials for lithium-ion batteries. *Dalton Trans.*, **2019**, *48*, 10422-10426.
29. Li, W.; Yao, H.; Yan, K.; Zheng, G.; Liang, Z.; Chiang Y-M.; Cui Y. The synergetic effect of lithium polysulfide and lithium nitrate to prevent lithium dendrite growth. *Nat. Commun.* **2015**, *6*, 7436.
30. Yan, B.; He, C. Y.; Chen, S.; Xiang, L.; Gong, L.; Gu, Y. C.; Zeng, H. B. Nano confining Cation-π Interactions as a Modular Strategy to Construct Injectable Self-Healing Hydrogel. *CCS Chem.* **2022**, *4*, 2724–2737.
31. Wei, Z.; Yang, J. H.; Zhou, J.; Xu, F.; Zrinyi, M.; Dussault, P. H.; Osada, Y.; Chen, Y. M. Self-healing gels based on constitutional dynamic chemistry and their potential applications. *Chem. Soc. Rev.*, **2014**, *43*, 8114-8131.
32. Li, L.; Tu, Z.-M.; Hua, Y.; Li, X.-N.; Wang, H.-Y.; Zhang, H. A novel multifunction photochromic metal–organic framework for rapid ultraviolet light detection, amine-selective sensing and inkless and erasable prints. *Inorg. Chem. Front.*, **2019**, *6*, 3077-3082.
33. Ju, L.; Gao, W. B.; Zhang, J. Y.; Qin, T. Y.; Du, Z.; Sheng, L.; Zhang, S. X.-A. A new absorption/fluorescence dual-mode hydrochromic dye for water-jet printing and anti-counterfeiting applications. *J. Mater. Chem. C*, **2020**, *8*, 2806-2811.
34. Macharia, D. K.; Ahmed, S.; Zhu, B.; Liu, Z.; Wang, Z.; Mwasiagi, J. I.; Chen, Z.; Zhu, M. UV/NIR-Light-Triggered Rapid and Reversible Color Switching for Rewritable Smart Fabrics. *ACS Appl. Mater. Interfaces*, **2019**, *11*, 13370-13379.

35. Li, L.; Zou, Y. C.; Hua, Y.; Li, X. N.; Wang, Z. H.; Zhang, H. Polyoxometalate–viologen photochromic hybrids for rapid solar ultraviolet light detection, photoluminescence-based UV probing and inkless and erasable printing. *Dalton Trans.*, **2020**, *49*, 89-94.
36. Yi, T.; Sada, K.; Sugiyasu, K.; Hatano, T.; Shinkai, S. Photo-induced colour generation and colour erasing switched by the sol–gel phase transition. *Chem. Commun.*, **2003**, *344*.
37. Yang, Y. Q.; Guan, L.; Jiang, H. C.; Duan, L. J.; Gao, G. H. A rapidly responsive photochromic hydrogel with high mechanical strength for ink-free printing. *J. Mater. Chem. C*, **2018**, *6*, 7619-7625.
38. Yang, Y. Q.; Guan, L.; Gao, G. H. Low-Cost, Rapidly Responsive, Controllable, and Reversible Photochromic Hydrogel for Display and Storage. *ACS Appl. Mater., Interfaces*, **2018**, *10*, 13975-13984.
39. Feng, J. F.; Tan, M.; Zhang, S.; Li, B. J. Recent Advances of Porous Materials Based on Cyclodextrin. *Macromol. Rapid Commun.*, **2021**, *42*, 2100497.
40. Friess, F. V.; Hu, Q.; Mayer, J.; Gemmer, L.; Presser, V.; Balzer, B. N.; Gallei, M. Nanoporous Block Copolymer Membranes with Enhanced Solvent Resistance Via UV-Mediated Cross-Linking Strategies. *Macromol. Rapid Commun.* **2022**, *43*, 2100632.
41. Zhang, G. H.; Li, B. Y.; Zhou, Y.; Chen, X. F.; Li, B.; Lu, Z.-Y.;Wu, L. X. Processing supramolecular framework for free interconvertible liquid separation. *Nat. Commun.*, **2020**, *11*, 425.
42. Kong, X. P.; Wan, G. F.; Li, B.; Wu, L. X. Recent advances of polyoxometalates in multi-functional imaging and photothermal therapy. *J. Mater. Chem. B.* **2020**, *8*, 8189-8206.
43. Chen, Q.; Zhao, J.; Cheng, H. H.; Qu, L. T. Progress in 3D-Graphene Assemblies Preparation for Solar-Thermal Steam Generation and Water Treatment. *Acta Phys.-Chim. Sin.* **2022**, *38*, 2101020.
44. Zhang, S. M.; Lu, Q. C.; Yu, B.; Cheng, X. J.; Zhuang, J.;Wang, X. Polyoxometalates Facilitating Synthesis of Subnanometer Nanowires. *Adv. Funct. Mater.*, **2021**, *31*, 2100703.
45. Ponton, A.; Barboux-Doeuff, S.; Sanchez, C. Rheology of titanium oxide-based gels: determination of gelation time versus temperature. *Colloids Surfaces A Physicochem. Eng. Asp.*, **2000**, *162*, 177–192.
46. Weston, J. S.; Weston, J. H.; Grady, B. P. Rheological characterization of yield stress gels formed *via* electrostatic heteroaggregation of metal oxide nanoparticles. *Soft Matter*, **2017**, *13*, 6743-6755
47. Sanchez, C. Optical properties of transition metal oxide gels. *Proc. SPIE 1328, Sol-Gel Optics*, **1990**, DOI: 10.1117/12.22544.

48. Matsuda, A.; Kanzaki T.; Tadanaga, K.; Kogure, T.; Tatsumisago M.; Minami T. Sol-Gel Derived Porous Silica Gels Impregnated with Sulfuric Acid Pore Structure and Proton Conductivities at Medium Temperatures. *J. Electrochem. Soc.*, **2002**, *149*, E292-E297.
49. Wasiucionek, M.; Breiter, M. W. Ionic conductivity of silica gels and dynamic properties of their pore liquids studied by impedance spectroscopy and polarized-light spectrofluorimetry. Solid State Ionics. **2000**, *136–137*, 453–456.
50. Colomban, Ph. Latest Developments in Proton Conductors. *Ann. Chim. Sci. Mater.,***1999**, *24*, 1-18.
51. Bonnet, B.; Jones, D. J.; Roziere, J.; Tchicaya, L.; Alberti, G.; Casciola, M.; Massinelli, L.; Bauer, B.; Peraio, A.; Ramunni, E. Hybrid organic-inorganic membranes for a medium temperature fuel cell. *J. New Mater. Electrochem. Syst.*, **2000**, *3*, 87-92.
52. Štangar, U. L.; Grošelj, N.; Orel, B.; Colomban, Ph. Structure of and Interactions between P/SiWA Keggin Nanocrystals Dispersed in an Organically Modified Electrolyte Membrane. *Chem. Mater.*, **2000**, *12*, 3745-3753.
53. Haile, S. M.; Boyesen, D. A.; Chisholm, C. R. I.; Merle, R. B. Solid acids as fuel cell electrolytes. *Nature* (London), **2001**, *410*, 910-913.
54. Tatsumisago, M.; Minami, T. Preparation of Proton-Conducting Amorphous Films Containing Dodecamolybdophosphoric Acid by the Sol—Gel Method. *J. Am. Ceram. Soc.*, **1989**, *72*, 484-486.
55. Colomer, M. T.; Anderson, M.A. High porocity silica xerogels prepared by particulate sol-gel route: pore structure and proton conductivity. *J. Non-Cryst. Solids.*, **2001**, *2-3*, 93-104.
56. Kreuer, K. D. On the development of proton conducting materials for technological applications. *Solid State Ionics*, **1997**, *97*, 1-15.
57. Sumner, J. J.; Creagar, S. E.; Ma, J. J.; Desmarteau, D. D. Proton Conductivity in Nafion® 117 and in a Novel Bis[(perfluoroalkyl)sulfonyl]imide Ionomer Membrane. *J. Electrochem. Soc.*, **1998**, *145*, 107.
58. Phang, W. J.; Jo, H.; Lee, W. R.; Song, J. H.; Yoo, K.; Kim, B.; Hong, C. S. Superprotonic Conductivity of a UiO-66 Framework Functionalized with Sulfonic Acid Groups by Facile Postsynthetic Oxidation. *Angew. Chem. Int. Ed.* **2015**, *54*, 5142-5146.
59. Zhai, Q. G.; Mao, C.; Zhao, X.; Lin, Q.; Bu, F.; Chen, X.; Bu, X.; Feng, P. Cooperative Crystallization of Heterometallic Indium–Chromium Metal–Organic Polyhedra and Their Fast Proton Conductivity. *Angew. Chem., Int. Ed.* **2015**, *54*, 7886-7890.
60. Wu, X.; Wu, Q. A typical solid high-protonic conductor: A kind of vanadium-substituted heteropoly acid $H_5PW_{10}V_2O_{40}\cdot15H_2O$. *Materials Letters* **2021**, *302*, article No.130372.

61. Li, D.; Tan, X. L.; Chen, L. L.; Liu, X. Y.; Li, Y. M.; Dang, D. B.; Bai, Y. Four Dawson POM-based inorganic-organic supramolecular compounds for proton conduction, electrochemical and photocatalytic activity. *Journal of Solid State Chemistry*, **2022**, *305*, article No.122694.
62. Tandekar, K.; Singh, C.; Supriya S. Proton Conductivity in {$Mo_{72}Fe_{30}$}-Type Keplerate. **2021**, 734-739.
63. Liu, W.–J.; Dong, L.–Z.; Li, R.–H.; Chen, Y.–J.; Sun, S.–N.; Li, S.–L.; Lan, Y.–Q. Different Protonic Species Affecting Proton Conductivity in Hollow Spherelike Polyoxometalates. *ACS Appl. Mater. Interfaces*. **2019**, *11*, 7030–7036.
64. Nishiwaki, S.; Tadanaga, K.; Tatsumisago, M.; Minami, T. Preparation and Proton Conductivity of Surfactant-Templated Mesoporous Silica Gels Impregnated with Protonic Acids. *J. Am. Ceram. Soc.*, **2000**, *83*, 3004–3008.
65. Matsuda, A.; Honjo, H.; Tatsumisago, M.; Minami, T. Electric Double-Layer Capacitors Using $HClO_4^-$ Doped Silica Gels as a Solid Electrolyte. *Solid State Ionics*, **1998**, *113–115*, 97–102.
66. Tatsumisago, M.; Minami, T. Preparation of Proton-Conducting Amorphous Films Containing Dodecamolybdophosphoric Acid by the Sol–Gel Method, *J. Am. Ceram. Soc.*, **1989**, *72*, 484–86.
67. Tatsumisago, M.; Sakai, Y.; Honjo, H.; Minami, T. Proton Conduction of Acid/Salt Doped Silica Gels. *J. Ceram. Soc. Jpn.*, **1995**, *103*, 189–190.
68. Tatsumisago, M.; Honjo, H.; Sakai, Y.; Minami, T. Proton-Conducting Silica Gel Films Doped with a Variety of Electrolytes. *Solid State Ionics*, **1994**, *74*, 105–108.
69. Hirata, K.; Matsuda, A.; Hirata, T.; Tatsumisago, M.; Minami, T. Preparation and Characterization of Highly Proton-Conductive Composites Composed of SiO_2– P_2O_5 Gel and Styrene–Ethylene–Butylene–Styrene Elastomer. *J. Sol-Gel Sci. Technol.*, **2000**, *17*, 61–69.
70. Li, L.; He, L.; Wang, B.; Ge, P.; Jing, L.; Liu, H.; Gong, C.; Zhang, B.; Zhang J.; Bu W. Secondary dialkylammonium salt/crown ether [2] pseudorotaxanes as nanostructured platforms for proton transport. *Chem. Commun.*, **2018**, *54*, 8092-8095.
71. Li, B.; Xuan, L.; Wu, L. Polyoxometalate-Containing Supramolecular Gels. *Macromol. Rapid Commun.* **2022**, 2200019.
72. Li, L.; He, L.; Wang, B.; Ge, P.; Jing, L.; Liu, H.; Gong, C.; Zhang, B.; Zhang, J.; Bu, W. Secondary dialkylammonium salt/crown ether [2]pseudorotaxanes as nanostructured platforms for proton transport. *Chem. Commun.*, **2018**, *54*, 8092—8095.
73. Liu, Q.; Wang, X. Polyoxometalate Clusters: Sub-nanometer Building Blocks for Construction of Advanced Materials. *Matter*, **2020**, *2*, 816–841.

CHAPTER 5

Mechanochemical and Aerial KI Oxidation Mediated by a Giant $\{Mo_{72}Fe_{30}\}$ Polyoxometalate

Overview

The giant polyoxometalate cluster of the Keplerate compound $[Mo_{72}Fe_{30}O_{252}(CH_3COO)_{12}\{Mo_2O_7(H_2O)\}_2\{H_2Mo_2O_8(H_2O)\}(H_2O)_{91}]\cdot150\ H_2O$ (**$\{Mo_{72}Fe_{30}\}$**) is known to be characterized with 72 cage Mo^{VI}-centers and 30 high spin Fe^{III} centers. When this yellow colored Keplerate compound is grinded with KI (potassium iodide) solid in a mortar pestle in solid state, the color of the solid mixture becomes olive green, which turns back into yellow-orange, when this green-color solid mixture is exposed to air for few hours. It turns out that KI gets oxidized by **$\{Mo_{72}Fe_{30}\}$** in solid state with the formation of iodine (I_2) in the solid reaction mixture and in turn, the $\{Mo_{72}Fe_{30}\}$ cluster get reduced with the formation of $\{Mo_{72}Fe_{30}\}^{15-}$, retaining the $\{Mo_{72}Fe_{30}\}$ cluster cage without any destruction. When this green-colored reduced solid reaction mixture is exposed to air, the aerial oxygen oxidizes the reduced $\{Mo_{72}Fe_{30}\}^{15-}$ cluster regenerating the parent oxidized state of $\{Mo_{72}Fe_{30}\}$ resulting in the formation of potassium superoxide (KO_2) in the orange-yellow solid reaction mixture. The molecular iodine (I_2) formed in the solid reaction mixture is extracted with chloroform ($CHCl_3$). Thus, the overall reaction cycle can be described as a mechanochemical aerial KI oxidation mediated by the Keplerate (**$\{Mo_{72}Fe_{30}\}$**).

5.1. Introduction

Polyoxometalates (POMs) are the anionic clusters consisting of early transition metals with highest oxidation states.[1-3] These have gained an enormous attention in the field of materials chemistry and medicinal chemistry due to their high charge, photochromic properties, nano dimension and rich electrochemical properties.[2,4-17] Among POMs, giant clusters $\{(M^{VI})M^{VI}_5\}_{12}\{Mo^V_2\}_{30}$ ($\equiv\{M^{VI}_{72}Mo^V_{60}\}$) and $\{(M^{VI})M^{VI}_5\}_{12}\{M'\}_{30}$ (M = Mo or W; M' = VO^{2+}, Fe^{3+} or Cr^{3+}) represent giant metal oxide-based Nano-capsules, also called Keplerates, that have attracted huge attention because of their structural beauty and importance in diverse areas of research, e.g., biological sciences, molecular physics, magnetochemistry, materials science, chemical science and mathematics.[18-31] Among these Keplerates, **$\{Mo_{72}Fe_{30}\}$** cluster is of immense interest, which has been reflected in the following facts. **$\{Mo_{72}Fe_{30}\}$** cluster containing compound $[Mo_{72}Fe_{30}O_{252}(CH_3COO)_{12}\{Mo_2O_7(H_2O)\}_2\{H_2Mo_2O_8(H_2O)\}(H_2O)_{91}]\cdot150\ H_2O$ (**1**) was discovered in the year of 1999 by Müller and co-workers and around 130 original research articles got published until today only on this compound in a wide range of journals: from chemistry to physics through materials science.[5-8,32] It has unique properties like nano-encapsulation, surface supramolecular chemistry and magnetic properties, that have been explored, but still it is less explored compared to other polyoxometalates.[2,25,33] POMs have distinct applications like sensing and catalysis which involves the redox activity (reversible) by changing their electronic states without any disintegration.[34-40] POMs related to Dawson and Keggin have been explored much more in terms of their redox properties compared to the redox properties of Keplerates.[41-44] The icosahedral molecule {**$Mo_{72}Fe_{30}$**} has 72 molybdenum polyhedra that are organized into sets of 12 pentagonal $[(Mo)Mo_5O_{21}(H_2O)_6]^{6-}$ units separated from one another by 30 $\{Fe^{III}O_6\}$ linkers. Each of these linkers exposes a single terminal Fe^{III}-OH_2 functional group projecting outwards from the surface of the {**$Mo_{72}Fe_{30}$**} cage.[32] Inside this nano-capsule, there are 12 additional water molecules bound to 12 Fe^{III} centers. The remaining 18 Fe^{III} linkers are bridged to molybdate (two of $[Mo_2O_7(H_2O)]$ type and one of $[H_2Mo_2O_8(H_2O)]$ type) or to acetate ligands. The {**$Mo_{72}Fe_{30}$**} cluster having 30 high spin Fe^{III}

centers, thereby having 150 unpaired electrons, is considered to be a unique magnetic object and a considerable number of reports has appeared that describe diverse levels of magnetism of this nano-sized molecular magnet.[45-51] Besides its magnetism, its supramolecular chemistry is also remarkable.[20,25] Liu and co-workers have shown that the clusters of {**$Mo_{72}Fe_{30}$**} self-assemble in an aqueous solution into blackberry type supramolecular structures.[52-53] Later, Liu, Müller and their co-workers demonstrated that the **{$Mo_{72}Fe_{30}$}** cluster acts as a nano-sized inorganic weak acid in dilute aqueous solution that can deprotonate differently depending on the pH, which allows to form “nanoparticles” of varying sizes.[52-53] Thus, the nano-capsule {**$Mo_{72}Fe_{30}$**} has been explored extensively as far as magnetism and (solution) supramolecular chemistry are concerned. The catalytic application of this cluster containing compound is also briefly mentioned.[54-56] Recently, we have reported its electrocatalytic behavior towards the hydrogen evolution reaction.[57] When an inorganic substance (compound **1**) has proved its distinctive importance in the areas of chemistry, physics, materials science and biological sciences within 23 years of its discovery, its solid-state reactions (more specifically, mechano-chemical reactions) have not been explored. Generally, the solid-state transformations accelerated by heat, substrate induced interfacial reactions, light and mechanochemical force.[58-72] We wished to perform a mechanochemical reaction, mediated by **{$Mo_{72}Fe_{30}$}** cluster, because its outer surface is characterized 30 Fe^{3+} centers, each ligating 30 water molecules directing outwards from the surface of the {$Mo_{72}Fe_{30}$} cage and 72 Mo^{VI} centers each having a terminal Mo=O group. Keeping the fact in mind that each {Fe^{III}-OH_2} motif has electron pulling tendency towards iron center (as expressed by its acidic nature), they have potential to undergo redox reactions in the solid state; in other words, the cluster cage can be reduced by oxidizing a substrate. When compound **1** (**{$Mo_{72}Fe_{30}$}**) cluster containing compound) is mechanically

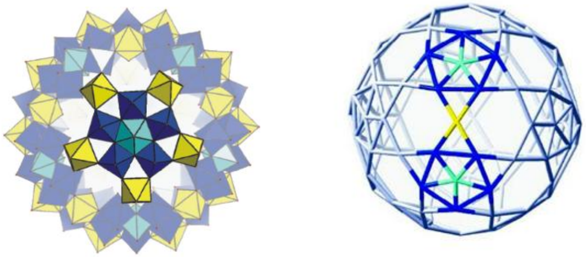

Figure 5.1. Left: polyhedral representation of {**$Mo_{72}Fe_{30}$**}; right: stick presentation of {**$Mo_{72}Fe_{30}$**}.[32]

ground with KI in a mortar pestle in the solid state, it results in the formation of iodine (KI oxidation, eqn. 1). Surprisingly this reaction does not take place in solution state!

$$\mathbf{2\ \{Mo_{72}Fe^{III}{}_{30}\} + 30\ e^{-} \rightarrow 2\ \{Mo_{72}Fe^{II}{}_{30}\}^{15-}}$$

$$\mathbf{30\ KI - 30\ e^{-} \rightarrow 15\ I_2 + 30\ K^{+}}$$

$$\mathbf{2\ \{Mo_{72}Fe_{30}\} + 30\ KI \rightarrow 15\ I_2 + 2\{Mo_{72}Fe_{30}\}^{15-} + 30\ K^{+}} \quad \text{(eqn. 1)}$$

5.2. Experimental Section

5.2.1. Materials

Chemicals were purchased in AR grade and utilized as received. Sodium molybdate ($Na_2MoO_4.2H_2O$) and glacial acetic acid were purchased from SRL chemicals and ferric chloride ($FeCl_3 \cdot 6H_2O$) from Sigma Aldrich, India, potassium iodide from TCI chemicals and HPLC grade chloroform from Fischer scientific limited.

5.2.2. Synthesis of Compound 1 ({$Mo_{72}Fe_{30}$}) – [$Mo_{72}Fe_{30}O_{252}(CH_3COO)_{12}[Mo_2O_7(H_2O)]_2[H_2Mo_2O_8(H_2O)](H_2O)_{91}$] ·150 H_2O

To a stirred solution of $FeCl_3 \cdot 6H_2O$ (1.1 g, 4.1 mmol) and $CH_3COONa \cdot 3H_2O$ (1.1 g, 8.1 mmol) in 75 mL of H_2O, 1.4 g of Mo_{132} [$(NH_4)_{42}\{Mo_{132}O_{372}(CH_3COO)_{30}(H_2O)_{72}\}$. Ca. 300 H_2O. Ca. 10 CH_3COONH_4] was added to it. The resulting mixture was stirred for 24 hours. After acidification with 1 mL HCl and 2.0 g of NaCl is added to it, the stirred reaction mixture was heated to 90 ± 95°C and then filtered hot. The yellow filtrate was cooled to room temperature, and a yellow, rhombic crystals of compound **1** formed over a time period of 2 ± 3 days. The crystals were collected by filtration, washed twice with water (to remove the NaCl), and then dried in air. Yield: 0.5 ± 0.6 g. Characteristic IR bands for **1** (KBr pellet): nÄ .1624 (m, d(H2O)), 1534 (m, nas(COO)), 1416 (s-m, ns(COO)), 959 (m, n(Mo.O)), 854 (m), 736 (s), 619 (m), 537 (s).

5.2.3. Mechanochemical reaction of Compound 1 with Potassium Iodide (KI)

A series of mechanochemical reactions were performed at different molar ratios of **{$Mo_{72}Fe_{30}$}** to KI ranging from 1: 30 and 1: 15.

5.2.3.1. {$Mo_{72}Fe_{30}$} 1: 30 (KI) ratio

200 mg (0.0107 mmol) of **{$Mo_{72}Fe_{30}$},** compound **1** and 54 mg (0.32 mmol) of KI were taken in mortar and grinded together using pestle resulting in the formation of dark green color solid. The solid so obtained was treated with 15 mL of $CHCl_3$ in order to extract Iodine and subsequently the reaction mixture was stirred for 5 hours whereby the $CHCl_3$ medium turns into deep purple color. It was then filtered and the amount of iodine was estimated from the filtrate by spectrophotometric analysis. Chloroform solutions of various iodine concentrations were made and a calibration curve was obtained using UV-Visible spectrophotometer (Appendix5).

5.2.3.2. {$Mo_{72}Fe_{30}$} 1: 15 (KI) ratio

Compound 3 has been synthesized following the same procedure as for compound 2 except that the amount of KI taken was 27 mg (0.16mmol)

5.2.4. Methods

The instrumental details of the all the experiments are provided in appendix 1.

5.2.5. Electrochemical studies

We have performed most of the electrochemical studies with the help of an electrochemical cell with three-electrode system which has glassy carbon as the working electrode and Pt as the reference and counter-electrode. The electrolyte used was dry acetonitrile by using tetrabutylammonium perchlorate as a supporting electrolyte under inert condition (nitrogen atmosphere). The electrochemical measurements were carried out in a heterogeneous manner for the insoluble compounds by taking the sample and preparing a homogenous suspension. The sample is prepared by taking 8.0 mg of crystalline compounds and 2.0 mg of carbon black powder in a 2.0 mL of ethanol and water mixture (3:2) solution. After sonicating the suspension mixture for 30 minutes, we added 20 µL of 5 weight% nafion to the sonicated suspension and then the mixture was sonicated for further 30 minutes to get complete homogeneous suspension / ink. On the glassy carbon electrode which is having a geometrical area of 0.07 (cm^2), 10 µL of the sample mixture / homogeneous suspension ink was coated and this way 40 µg of the sample was actually coated on the surface of the working electrode and the same amount of sample was used for whole electrochemical measurements. Ag/AgCl electrode was used as a reference electrode and all the electrode potentials in the measurements were transformed to RHE scale with the help of the following relation. E (NHE) = E (Ag/AgCl) + 0.204 + 0.059 pH. Usually, the cyclic voltametric measurements were carried out at a scan rate of 100 mVs^{-1} and iR corrections were manually fixed after finishing all the measurements.

5.3. Results and Discussion

Synthesis of compound **1** was performed by following a reported procedure that resulted in isolation of yellow-colored rhombic crystals within 2-3 days after the reaction of $FeCl_3.2H_2O$ solution with $[NH_4]_{42}[\{Mo_{132}O_{372}(CH_3COO)_{30}(H_2O)_{72}\}$. Ca. 300 H_2O. Ca. 10 $CH_3COONH_4]$ (**1**) in the presence of sodium acetate.[32] We have also carried out the basic characterizations of the compound **1** like FTIR, Raman, PXRD, FESEM and UV-visible spectroscopy. A mechano-chemical reaction (eqn 1) has been carried out at ambient condition mediated by **$\{Mo_{72}Fe_{30}\}$** cluster containing compound **1** which leads to oxidation of KI to produce I_2. It is logical to know the proportion of the reactants of this KI oxidation reaction, because a **$\{Mo_{72}Fe_{30}\}$** cluster has 30 Fe- and 72 Mo-centers in their highest oxidation states. Thus, we performed a series of mechano-chemical reactions by grinding a

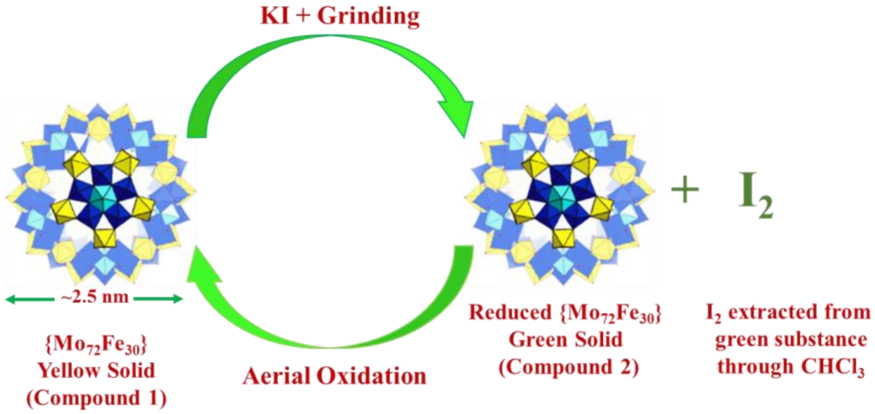

Scheme 5.1. A schematic representation of reversible aerial KI oxidation mediated by **$\{Mo_{72}Fe_{30}\}$** Keplerate.

constant amount of compound **1** **$\{Mo_{72}Fe_{30}\}$** crystals (Figure 5.2a) with varying amounts of KI powder. In each case we observe, during grinding, that the yellow **$\{Mo_{72}Fe_{30}\}$** solid (Figures 5.2a & 2b) turns into green solid (compound **2**) (Figure 5.2c) instantaneously. Here potassium iodide acts as a reducing agent; the formation of green solid (compound **2**) from compound **1** indicates the reduction of **{$Mo_{72}Fe_{30}$}** cluster in compound **1** and potassium iodide self-oxidized to produce iodine. When we carry out same reaction in solution state by dissolving **{$Mo_{72}Fe_{30}$}** cluster containing compound **1** in water followed by adding KI aqueous solution, we do not find any color change and we do not find any iodine formation in solution state reaction. After each batch of mechano-chemical reaction, the compound **2** (green solid) in solid-reaction mixture is treated with $CHCl_3$ solvent to extract iodine (Figure 5.2d). The purple-pink $CHCl_3$ solution (iodine extract, Figure 5.2d), obtained from each mechanochemical reaction batch, is subjected to spectrophotometric study to determine the amount of iodine formed (a calibration plot was plotted using known concentrations of iodine, Appendix5, section A5.2). From these iodine estimation experiments, we found that, one equivalent of **{$Mo_{72}Fe_{30}$}** cluster containing compound **1** reacts with fifteen equivalents of KI to produce 7.5 equivalents of iodine (eqn. 1). In order to check the recyclability of the mechanochemical KI oxidation, it is necessary to regenerate

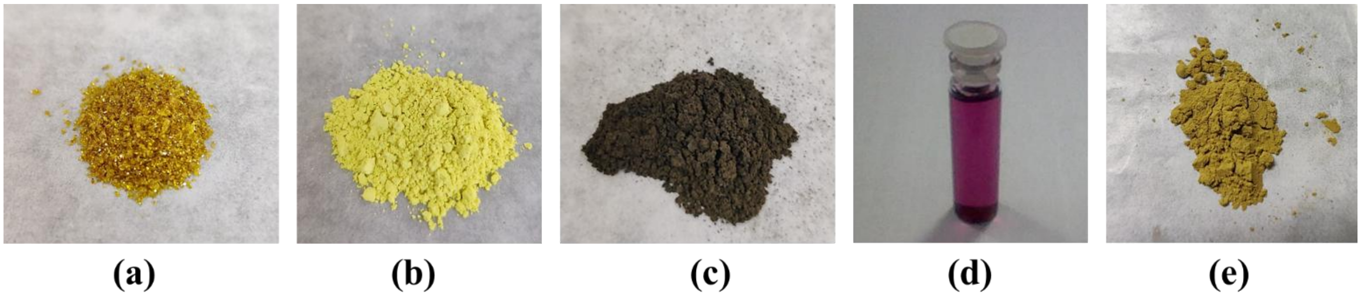

Figure 5.2. Pictures of (a) as synthesized **{$Mo_{72}Fe_{30}$}** (in its crystals form), (b) as synthesized **{$Mo_{72}Fe_{30}$}** (in its powder form), (c) green solid obtained by grinding **{$Mo_{72}Fe_{30}$}** with KI, (d) $CHCl_3$ extract (iodine solution) of this green solid, (e) regenerated **{$Mo_{72}Fe_{30}$}** compound.

{**$Mo_{72}Fe_{30}$**} after one cycle of KI oxidation. It is observed that the material right after iodine extraction is not as active as parent {**$Mo_{72}Fe_{30}$**} compound towards mechanochemical oxidation of KI. Thus, the material right after iodine extraction is heated in a conventional oven at 70 °C for 3 hours followed by its exposure to water vapor for 24 hours. Apart from this, the regeneration of compound **1** involves oxidation of the reduced cluster **{$Mo_{72}Fe_{30}$}$^{15-}$** (compound **2**) by aerial molecular oxygen (eqn. 2) to its original form (yellow solid). The regenerated {**$Mo_{72}Fe_{30}$**} (compound **3**) (Figure 5.2e) behaves same way as parent {**$Mo_{72}Fe_{30}$**} compound does towards KI oxidation in the mechanochemical reaction. Thus, regeneration of {$\mathbf{Mo_{72}Fe_{30}}$} compound involves oxidation of the reduced cluster {$Mo_{72}Fe_{30}$}$^{15-}$ by aerial molecular oxygen (eqn. 2). As a result, superoxide is expectedly formed in the solid reaction mixture. We have seen that mechanochemical KI oxidation mediated by {$\mathbf{Mo_{72}Fe_{30}}$} needs 15 KI per {$\mathbf{Mo_{72}Fe_{30}}$} cluster, thereby meaning that each cluster is reduced by 15 electrons per cycle of mechanochemical KI oxidation.

$$\mathbf{2\{Mo_{72}Fe_{30}\}^{15-} + 30\ K^{+} + 15\ O_2 \rightarrow 2\{Mo_{72}Fe_{30}\} + 30\ KO_2}\ \text{(eqn. 2)}$$

Diverse spectroscopic studies have been performed on the compound **1**, compound **2** and compound **3** to know the performance of the reversible redox cycles carried out for the {$\mathbf{Mo_{72}Fe_{30}}$} cluster containing compound.

5.3.1. IR spectrum of Compound 1,2 & 3

IR spectra (Figure 5.3) displays the characteristic peaks at 1619 (m, δ (H_2O)), 1526 (m, ν_{as} (COO)), 1420 ν_s (s-m, (COO)), 963 (m, ν (Mo=O)), 845 (m), 740 (s), 623 (m), 541 (s) for the compound **3** which is regenerated from the compound **1** by reaction with KI. The peaks of the regenerated compound **3** match almost one to one with the peaks of parent compound **1** (IR peaks of compound **1**: 1624, 1534, 1416, 959, 854, 736, 619, 537 cm^{-1}). The green colored compound **2** is supposed to be a mixture of reduced cluster **{$\mathbf{Mo_{72}Fe_{30}}$}$^{\mathbf{15-}}$** , in-situ formed molecular iodine (I_2) and excess KI used in the mechanochemical reaction. Thus the IR spectrum of green solid mixture (compound **3**) shows the characteristic IR peaks of compound **1** with some amount shift of the IR peak-positions (because it is the reduced cluster **{$\mathbf{Mo_{72}Fe_{30}}$}$^{\mathbf{15-}}$**) and some additional peaks (for example, peaks at 1747 cm^{-1} and 1219 cm^{-1}) that come from excess KI and molecular iodine formed in the mechanochemical reaction as shown in Figure 5.3.

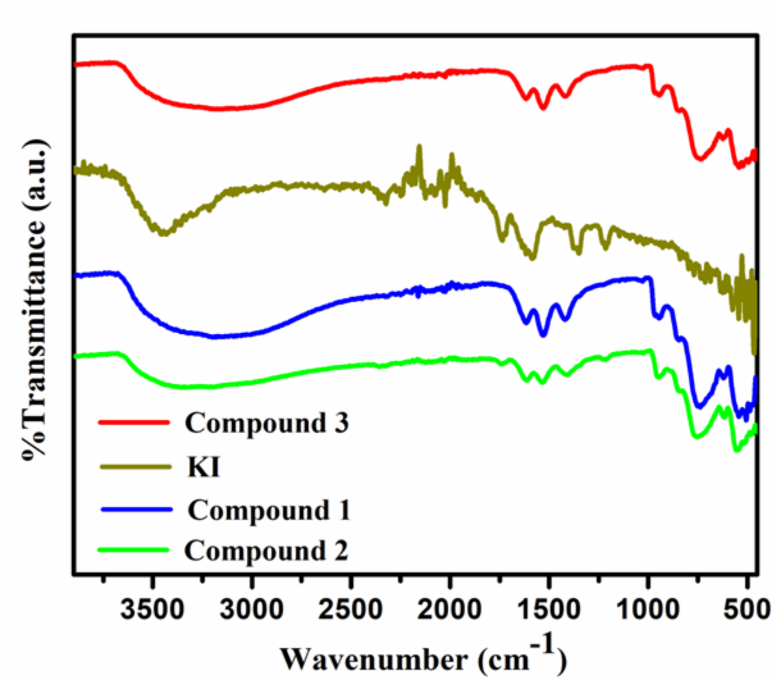

Figure 5.3. Compared FT-IR spectrum of compound **1, 2** and **3**.

5.3.2. PXRD spectrum of Compound 1,2 & 3

Figure 5.4 presents powder X-ray diffraction (PXRD) patterns of {$\mathbf{Mo_{72}Fe_{30}}$} cluster containing compound **1** as such, KI-grinded **{$\mathbf{Mo_{72}Fe_{30}}$}** cluster containing compound (compound **2**), solid KI as such and the solid reaction mixture after iodine extraction (compound **3**). It is evident from Figure 5.4 that, the molecular structure of {$\mathbf{Mo_{72}Fe_{30}}$} along with its crystal packing remains same even after its reduction by grinding with solid KI with the formation of iodine. Some of the un-reacted KI is present in the mechanochemical reaction mixture, as observed by comparing the powder X-ray diffraction pattern of KI grinded {$\mathbf{Mo_{72}Fe_{30}}$} reaction mixture with those of {$\mathbf{Mo_{72}Fe_{30}}$} compound itself and KI itself (Figure 5.4). The crystallinity of the compound **1** is maintained even after undergoing to reduction and oxidation reactions.

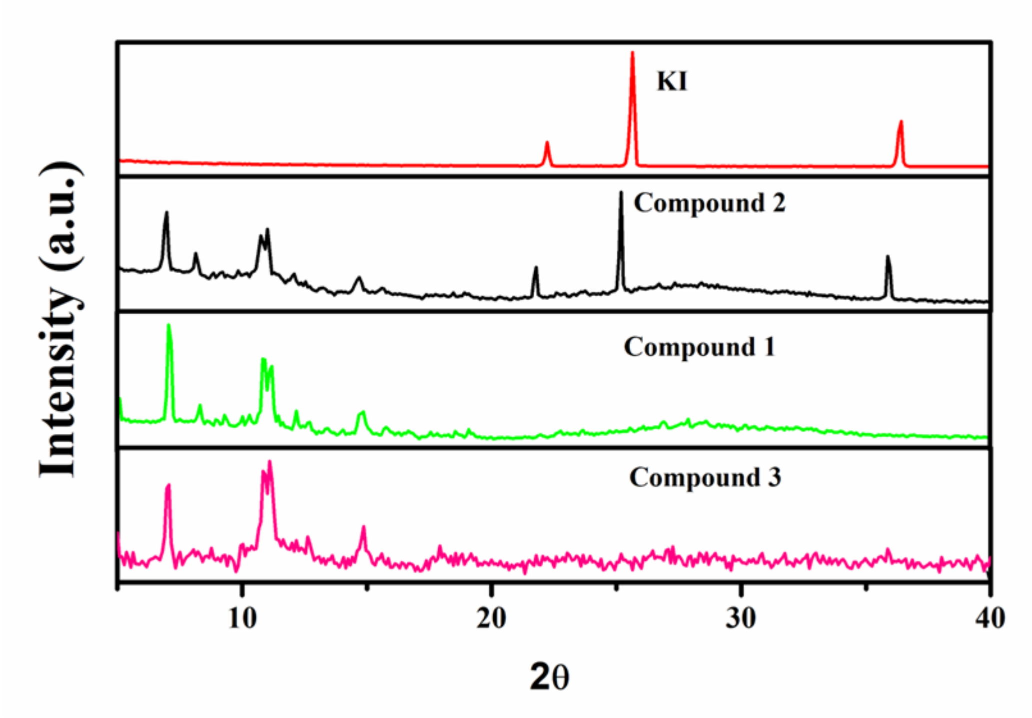

Figure 5.4. Compared PXRD spectrum of compound **1, 2** and **3**.

5.3.3. Solid-state DRS spectrum of Compound 1,2 & 3

The solid-state diffused reflectance spectra are recorded for the compounds **1** and **2** and after the Kulbelka-Munk conversion, the spectral data are displayed in the Figure 5.5. As shown in Figure 5.5, the overall spectral features of compounds **1** and **2** are similar except the fact that there are some extra features at around 500 to 650 nm in the electronic spectrum of compound **2** and the charge transfer transition in the region of 300 to 500 nm is resolved in the case of compound **2**. In this study, compound 2 is nothing but a solid reaction mixture that contains mainly reduced cluster $\{\mathbf{Mo_{72}Fe_{30}}\}^{15-}$ along with unreacted KI and some amount of iodine. The reduced cluster $\{\mathbf{Mo_{72}Fe_{30}}\}^{15-}$ is formed by the reduction of oxidized $\{Mo_{72}Fe_{30}\}$ by I^-, when, in principle, both Mo(VI) and Fe(III) centers can be reduced. Among Fe(III) and Mo(VI) centers, Fe(III) center is more prone to be reduced than Mo(VI) center, because Fe(III) has acidic water coordinated to it. Even Fe(III) gets reduced first, there can be interatomic electron transfer forming Mo(V) center. There is an EPR spectral evidence of the formation of Mo(V) center (vide infra). The feature at around 500 to 650 nm in the electronic spectrum of compound **2** can be attributed d-d transition arising from Fe(II) / Mo(V) center or from both. The broad feature in the region of 300 to 500 nm for both compounds **1** and **2** is due to oxygen to metals (molybdenum and iron) charge transfer transitions and the reduction of Fe(III) and Mo(VI) centers in compound **2** causes the resolution of the charge transfer transition in the region of 300 to 500 nm in the electronic spectrum of compound **2**.

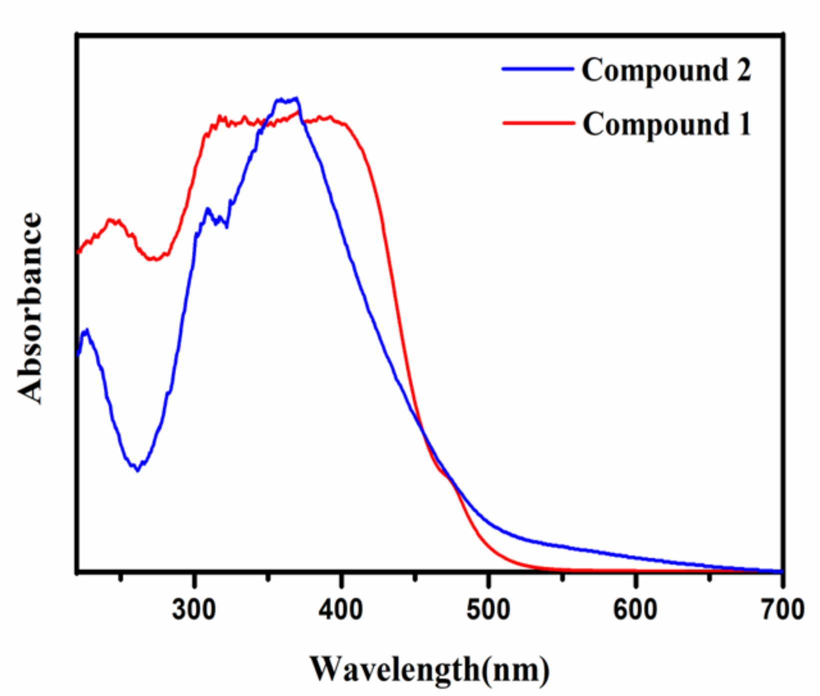

Figure 5.5. Compared solid-state DRS spectrum of compound **1** and **2**.

5.3.4. Raman spectrum of Compound 1,2 & 3

The Raman spectra for the parent compound **1**, reduced compound **2** and **3** (regenerated to parent compound) have been recorded and shown in the Figure 5.6. Raman signals of compounds **1**, **2** and **3** are almost identical to each other, indicating that {$Mo_{72}Fe_{30}$} cluster cage is retained (does not disintegrate) during the solid-state redox cycle.

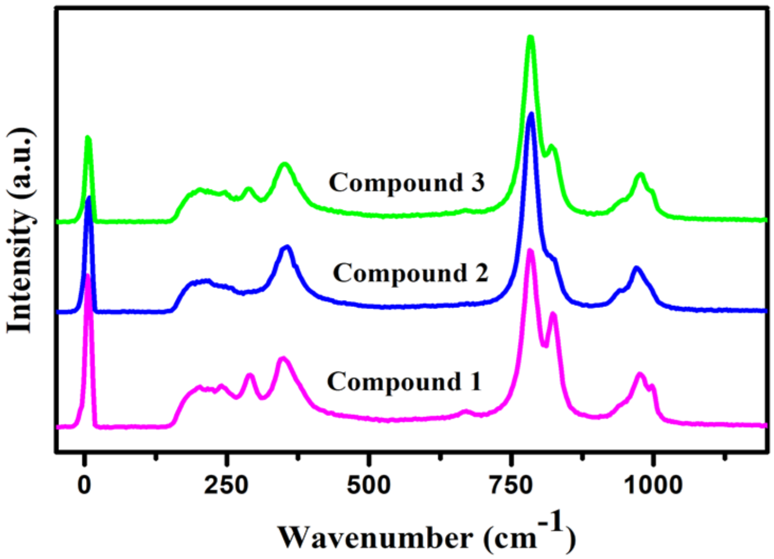

Figure 5.6. Compared Raman spectrum of compound **1,2** and **3**.

5.3.5. EPR spectroscopic studies of Compound 1,2 & 3

In this mechanochemical solid-state redox cycle, the regeneration step can be explained by oxidation of reduced cluster {$\mathbf{Mo_{72}Fe_{30}}$}$^{15-}$ by aerial oxygen (eqn. 2), whereby the molecular oxygen (from air) gets oxidized to super oxide. The reduction of Mo(VI) center to Mo(V) center and formation of superoxide (one-electron-reduced O_2 molecule) by the reduced cluster {$\mathbf{Mo_{72}Fe_{30}}$}$^{15-}$ can be monitored by EPR spectral studies. The EPR spectroscopic studies were carried out for the compound **1**, **2** and **3** at 4K. When we grind the compound **1** (fully oxidized cluster) with KI (white solid) in a mortar pestle, it turned into a green colored solid mixture. This was immediately subjected to EPR spectroscopy at 4K (liquid helium). A broad feature, which comes for any Fe(III) species, appeared with the appearance of a tiny peak at g = 1.96. This can be assigned to Mo(V) formed in the solid reaction mixture with the formation of reduced {$Mo_{72}Fe_{30}$} cluster, which we characterized as {$\mathbf{Mo_{72}Fe_{30}}$}$^{15-}$ in the present work. This reduced

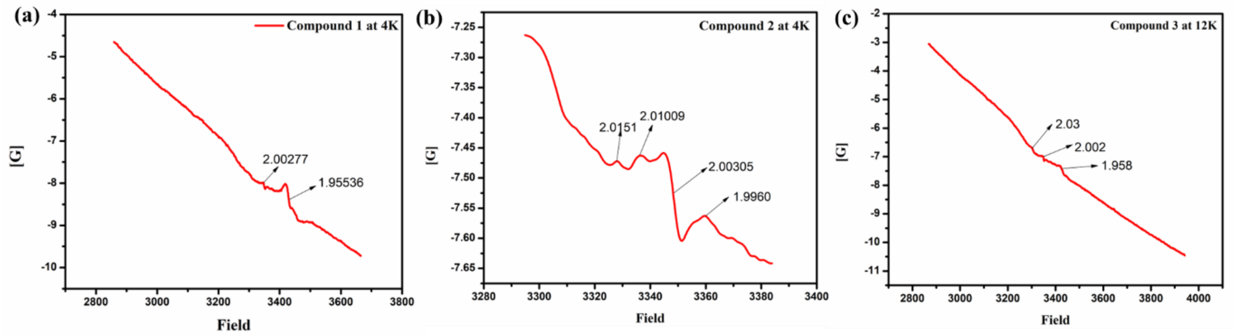

Figure 5.7. (a) EPR spectrum of green solid reaction mixture after 15 minutes of grinding compound **1** with solid KI in a portal pestle; (b) EPR spectrum of yellow-green solid reaction mixture after 30-40 minutes of grinding compound **1** with solid KI; (c) EPR spectrum of yellow colored solid reaction mixture after 5-6 hours of grinding compound **1** with solid KI in a portal pestle.

species reacts with molecular oxygen from air and forms superoxide. Figure 5.7a displays the EPR plot of the green solid reaction mixture after 15 minutes of grinding, which shows a tiny peak at g = 2.00277 for potassium superoxide (KO_2) formed in the solid reaction mixture along with the clearly visible signal for Mo(V) at g =1.96. With time the superoxide peak becomes more prominent as shown in Figure 5.7b, which shows a rhombic feature of superoxide with g_1 = 2.1051, g_2 = 2.0101 and g_3 = 2.0031 and Mo(V) signal gradually diminishes. After 5-6 hours of aerial oxygen exposure, the green reaction mixture becomes yellow colored solid which shows diminishing phase superoxide and Mo(V) as shown Figure 5.7c Thus, this time-dependent EPR spectral studies support the regeneration stage of compound **3** from compound **2**.

5.3.6. Aerial Oxidation Studies Compound 2 & 3

We performed some experiments to know whether the aerial oxygen is the actual oxidant for this regeneration of parent compound **1** (or compound **3**) from compound **2** and to know the time required for the compound **2** to get into aerial oxidation to convert into compound **3**. We have placed one part of the grinded sample *i.e.*, compound **2** in an inert condition (glove box) and we placed the second part of the same sample in an ambient atmospheric condition. We observed that in a week time the compound **2** (green color) converted completely to yellow-colored compound **3** in an atmospheric condition, whereas the green color of the sample placed in an inert condition (glove box) has been intact as shown in Figure 5.8a and 5.8c. We characterized the both samples with the help of solid-state diffused reflectance spectroscopy (DRS) as shown in the Figure 5.8a and 5.8b. We observed that the absorbance peaks for the freshly prepared compound **2** (grinded green solid reaction mixture) match one to one with DRS peaks of sample placed in an inert condition (glove box), whereas the sample placed in the atmospheric condition has been oxidized to form compound **1** (or compound **3**) whose absorption spectrum matches well with that of parent compound **1** as shown in Figure 5.8a and 5.8b respectively.

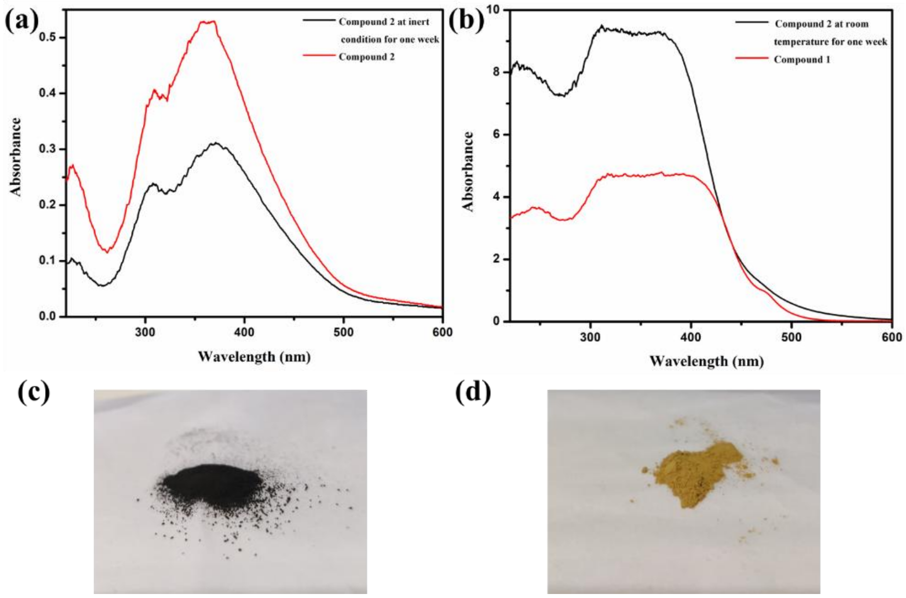

Figure 5.8. (a) Solid state UV-visible diffuse reflectance spectrum (DRS) of compound **2** kept in an inert condition, compared with the diffuse reflectance spectrum of freshly grinded green solid reaction mixture; (b) DRS of regenerated compound **1** (or **3**) brought about by keeping the green solid reaction mixture at an ambient atmospheric condition, compared with DRS of parent compound **1**; (c, d) pictures of compound **2** kept in an inert condition and in an ambient atmospheric condition, respectively.

5.3.7. Room temperature magnetic moment measurements of Compound 1 & 3

We have carried out the room temperature magnetic moment measurements for the both the compounds **1** and **2**; the resultant magnetic moment values are 11.266 BM and 6.657 BM respectively. It can be seen that the room temperature magnetic moment of compound **2** is considerably less than that of compound **1**. This is consistent with the fact that the parent compound **1** contains 30 Fe(III) octahedral centers per formula unit and all 30 Fe(III) centers are in high spin states (oxo ligands), whereas, in compound **2**, some of these Fe(III) ions get reduced to Fe(II), which would be low spin d^6 system, naturally affecting on the magnetic moment by diminishing its value from 11.266 BM to 6.657 BM.

5.3.8. Mechanochemical reactions of {$Mo_{72}Fe_{30}$}

We have performed a series of mechanochemical reactions at different molar ratios of **{$Mo_{72}Fe_{30}$}** to KI ranging from 1: 30 and 1: 15. To know the amount (concentration) of iodine released from the reaction mixture we have carried out the spectrophotometric measurements for the extracted iodine from the reaction mixture. Chloroform solutions of various known concentrations of Iodine solutions were made and a calibration curve was obtained using UV-Visible spectrophotometer as shown in the Figure A5.4a (Appendix5 Section A5.4. The absorption spectra of 1: 30 and 1: 15 concentrated **{$Mo_{72}Fe_{30}$}** and KI grinded sample as shown in the Figure 5.9. From the spectra it is well known that the absorbance of 1: 30 sample is more when compared with the 1: 15 sample. With the help of these iodine estimation experiments, we found that, one equivalent of {$Mo_{72}Fe_{30}$} cluster containing compound **1** reacts with fifteen equivalents of KI to produce 7.5 equivalents of iodine (eqn. 1). When we carry out the same reaction in solution state by dissolving {**$Mo_{72}Fe_{30}$**} cluster containing compound in water followed by adding KI aqueous solution, we do not find any color change; thus, we do not find any iodine formation in solution state.

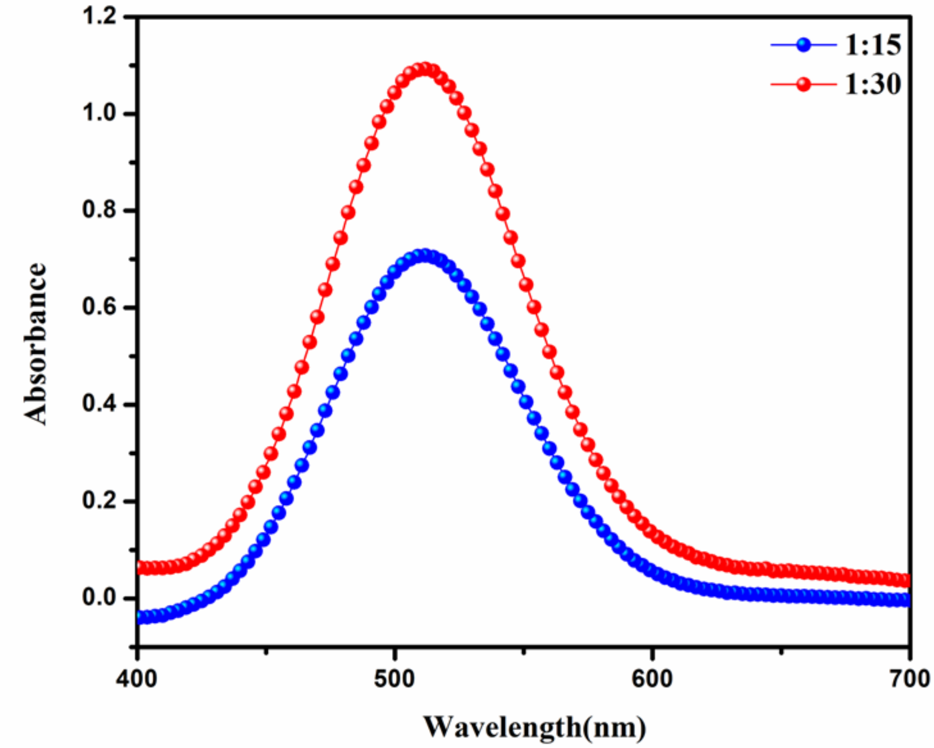

Figure 5.9. (a) UV-visible spectrum (solution state) for compound **2** in two different loadings 1:30 and 1:15.

5.3.9. Electrochemical Studies of Compound 1 & 2

We have carried out the electrochemical studies for the compound **1** and compound **2**. But we know that both the compounds **1** and **2** are water soluble, but the iodine produced in the compound **2** is insoluble in water. Due to this reason, we could not perform the homogeneous electrochemical studies. We have opted for the non-aqueous electrochemical studies for both the compounds. We have performed a cyclic voltammograms (CVs) of compound **1** and **2** (Figure 5.10) in acetonitrile medium by using tetrabutylammonium perchlorate as a supporting electrolyte under inert condition (nitrogen atmosphere). By comparing the CVs of both compounds, we can clearly observe that the compound **1** undergoes the electrocatalytic reduction which may involve Fe^{3+}/Fe^{2+}, Fe^{2+}/Fe^{+} and Mo^{6+}/Mo^{5+} couples and we also observe the corresponding oxidation peaks in the anodic side (Figure 5.10). On the other hand, in the case reduced compound **2**, we observe similar feature along with a sharp oxidation in the anodic window that can be corresponded to KI (present in excess) oxidation to molecular iodine. So, the electrochemical studies also support that the $\{Mo_{72}Fe_{30}\}$ cluster remains intact during this solid-state redox cycle involving aerial KI oxidation.

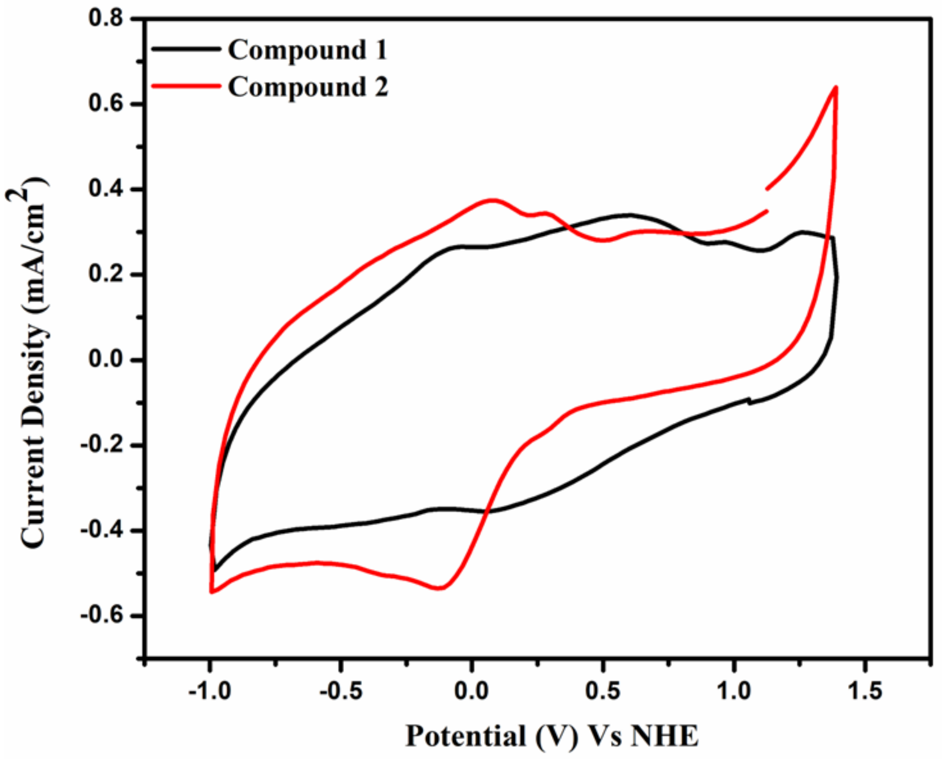

Figure 5.10. Cyclic voltammograms of compound **1** and **2** in acetonitrile (tetrabutylammonium perchlorate has been used as an electrolyte).

5.4. Conclusions

Crystalline compound **1** which has an icosahedral structure with a basic unit **{$Mo_{72}Fe_{30}$}** cluster have been well explored in the many application fields, but its reversible redox conversion through mechanochemical and aerial KI oxidation is not been reported till now. In the present work, we have demonstrated that the Fe^{III} containing cluster **{$Mo_{72}Fe_{30}$}** easily undergoes reduction by oxidizing KI to produce I_2 involving the reduction of Fe(III) to Fe(II) followed by intramolecular electron transfer from Fe(II) center to Mo(VI) centers with the formation Mo(V) centers. The reduced **{$Mo_{72}Fe_{30}$}$^{15-}$** cluster can react with aerial oxygen to form superoxide with the regeneration of parent oxidized **{$Mo_{72}Fe_{30}$}** compound. Thus, the whole cycle can be described as mechanochemical solid state aerial KI oxidation mediated by giant **{$Mo_{72}Fe_{30}$}** type POM. Therefore, the compound parent compound **1** has a potential towards solid state catalysis through mechanochemical reactions which is a new and interesting field to work with Keplerate type giant polyoxometalates.

5.5. References:

1. Pope, M.T.; Yamase, T. Polyoxometalate Chemistry for Nano-composite Design, Kluwer Academic/Plenum Publishers, New York, **2002**.
2. Müller, A.; Gouzreh, P. From linking of metal-oxide building blocks in a dynamic library to giant clusters with unique properties and towards adaptive chemistry. *Chem. Soc. Rev.,* **2012**, *41*, 7431–7463.
3. Tandekar, K.; Naulakha, P.; Supriya S. Reversible redox activity of {$Mo_{72}Fe_{30}$} nano-polyoxometalate cluster in three crystalline forms. *Inorganica Chimica Acta*, **2020**, *511*, 119729.
4. Xu, L.; Wang, E.B.; Li, Z.; Kurth, D.G.; Du, X.G.; Zhang, H.Y.; Qin, C. Preparation and nonlinear optical properties of ultrathin composite films containing both a polyoxometalate anion and a binuclear phthalocyanine. New J. Chem., **2002**, *26*, 782–786.
5. Coronado, E.; Giménez-Saiz, C.; Gómez-García, C.J. Recent advances in polyoxometalate-containing molecular conductors. *Coord. Chem. Rev.*, **2005**, *249*, 1776–1796.
6. Coronado, E.; Curreli, S.; Giménez-Saiz, C.; Gómez-García, C. J.; Roth, J. A new BEDT-TTF salt and polypyrrole films containing the chiral polyoxometalate $[H_4Co_2Mo_{10}O_{38}]^{6-}$. *Synth. Met.*, **2005**, *154*, 241–244.
7. Long, D.-L.; Burkholder, E.; Cronin, L. Polyoxometalate clusters, nanostructures and materials: From self-assembly to designer materials and devices. Chem. Soc. Rev., **2007**, *36*, 105-121.

8. Long, D.-L.; Tsunashima, R.; Cronin, L.; Polyoxometalates: Building Blocks for Functional Nanoscale Systems. *Angew. Chem., Int. Ed.,* **2010**, *49*, 1736-1758.
9. Nomiya, K.; Torrii, H.; Hasegawa, T.; Nemoto, Y.; Nomura, K.; Hashino, K.; Uchida, M.; Kato, Y.; Shimizu, K.; Oda, M. Insulin mimetic effect of a tungstate cluster. Effect of oral administration of homo-polyoxotungstates and vanadium-substituted polyoxotungstates on blood glucose level of STZ mice. *J. Inorg. Biochem.,* **2001**, *86*, 657–667.
10. Ma, H. Y.; Peng, J.; Han, Z. G.; Yu, X.; Dong, B. X. A novel biological active multilayer film based on polyoxometalate with pendant support-ligand. *J. Solid State Chem.,* **2005**, *178*, 3735–3739.
11. Hasenknopf, B.; Polyoxometalates: introduction to a class of inorganic compounds and their biomedical applications. *Front. Biosci.,* **2005**, *10*, 275-287.
12. Yamase, T. Anti-tumor, -viral, and -bacterial activities of polyoxometalates for realizing an inorganic drug J. Mater. Chem. **2005**, *15*, 4773–4782.
13. Yanagie, H.; Ogata, A.; Mitsui, S.; Hisa, T.; Yamase, T.; Eriguchi, M. Anticancer activity of polyoxomolybdate. Biomed. Pharmacother., **2006**, *60* 349–352.
14. Mitsui, S.; Ogata, A.; Yanagie, H.; Kasano, H.; Hisa, T.; Yamase, T.; Eriguchi, M. *Biomed. Pharmacother.,* **2006,** *60*, 353–358.
15. Dan, K.; Yamase, T.; Prevention of the interaction between HVEM, herpes virus entry mediator, and gD, HSV envelope protein, by a Keggin polyoxotungstate, PM-19. *Biomed. Pharmacother.,* **2006,** *60*, 169–173.
16. Shigeta, S.; Mori, S.; Yamase, T.; Yamamoto, N.; Yamamoto, N. Anti-RNA virus activity of polyoxometalates. *Biomed. Pharmacother.,* **2006,** *60*, 211–219.
17. Inoue, Suzuki, M.; T.; Fujita, Y.; Oda, M.; Matsumoto, N.; Yamase, T. Enhancement of antibacterial activity of β-lactam antibiotics by $[P_2W_{18}O_{62}]^{6-}$, $[SiMo_{12}O_{40}]^{4-}$, and $[PTi_2W_{10}O_{40}]_{7-}$ against methicillin-resistant and vancomycin-resistant *Staphylococcus aureus*. *Inorg. Biochem.,* **2006**, *100* 1225–1233.
18. Müller, A.; Krickemeyer, E.; Bögge, H.; Schmidtmann, M.; Peters, F. Organizational Forms of Matter: An Inorganic Super Fullerene and Keplerate Based on Molybdenum Oxide. Angew. Chem. Int. Ed., **1998**, *37*, 3359–3363
19. Müller, A.; Kö gerler, P.; Dress, A. W. M. Giant metal-oxide-based spheres and their topology: from pentagonal building blocks to Keplerates and unusyual spin systems. *Coord. Chem. Rev.,* **2001**, *222*, 193−218.
20. Müller, A.; Das, S. K.; Kö gerler, P.; Bögge, H.; Schmidtmann, M.; Trautwein, A. X.; Schünemann, V.; Krickemeyer, E.; Preetz, W. A new type of supramolecular compound:

molybdenum-oxide-based composites consisting of magnetic nanocapsules with encapsulated Keggin-ion electron reservoirs cross-linked to a two-dimensional network. *Angew. Chem., Int. Ed.*, **2000**, *39*, 3413−3417.

21. Fu, Z.-D.; Koegerler, P.; Ruecker, U.; Su, Y.; Mittal, R.; Brueckel, T. An approach to the magnetic ground state of the molecular magnet {$Mo_{72}Fe_{30}$}. *New J. Phys.,* **2010**, *12,* 083044 (1-15).
22. Pigga, J. M.; Liu, T. Determination of the effective charge density of pH responsive Keplerate polyoxometalate clusters by means of agarose gel electrophoresis. *Eur. J. Inorg. Chem.,* **2013**, *2013*, 1854−1858.
23. Kögerler, P.; Tsukerblat, B.; Müller, A. Structure-related frustrated magnetism of nanosized polyoxometalates: aesthetics and properties in harmony. *Dalton Trans*., **2010**, *39*, 21−36.
24. Müller, A.; Todea, A. M.; van Slageren, J.; Dressel, M.; Bögge, H.; Schmidtmann, M.; Luban, M.; Engelhardt, L.; Rusu, M. Triangular geometrical and magnetic motifs uniquely linked on a spherical capsule surface. *Angew. Chem., Int. Ed.,* **2005**, *44*, 3857−3861.
25. Todea, A. M.; Merca, A.; Bögge, H.; Glaser, T.; Pigga, J. M.; Langston, M. L. K.; Liu, T.; Prozorov, R.; Luban, M.; Schröder, C.; Casey, W. H.; Müller, A. Porous capsules $\{(M)M_5\}_{12}Fe^{III}_{30}$ (M = Mo^{VI}, W^{VI}): sphere surface supramolecular chemistry with 20 ammonium ions, related solution properties, and tuning of magnetic exchange interactions. *Angew. Chem., Int. Ed.,* **2010**, *49*, 514−519.
26. Zhang, J.; Li, D.; Liu, G.; Glover, K. J.; Liu, T. Lag periods during the self-assembly of {Mo72Fe30} macroions: connection to the virus capsid formation process. *J. Am. Chem. Soc.,* **2009**, *131*, 15152−15159.
27. Mishra, P. P.; Pigga, J.; Liu, T. Membranes based on ″Keplerate″- type polyoxometalates: slow, passive cation transportation and creation of water microenvironment. *J. Am. Chem. Soc.,* **2008**, *130*, 1548−1549.
28. Liu, G.; Liu, T. Strong attraction among the fully hydrophilic {$Mo_{72}Fe_{30}$} macro-anions. *J. Am. Chem. Soc.,* **2005**, *127*, 6942−6943.
29. Liu, G.; Liu, T. Thermodynamic properties of the unique self-assembly of {$Mo_{72}Fe_{30}$} inorganic macro-ions in salt-free and salt containing aqueous solutions. *Langmuir,* **2005**, *21*, 2713−2720.
30. Botar, B.; Ellern, A.; Hermann, R.; Koegerler, P. Electronic control of spin coupling in Keplerate-type polyoxomolybdates. *Angew. Chem., Int. Ed.,* **2009**, *48*, 9080−9083.
31. Veen, S. J.; Kegel, W. K. Structural instability of shell-like assemblies of a Keplerate-type polyoxometalate induced by ionic strength. *J. Phys. Chem. B,* **2009**, *113*, 15137−15140.
32. Müller, A.; Sarkar, S.; Shah, S. Q. N.; Bogge, H.; Schmidtmann, M.; Sarkar, Sh.; Kögerler, P.; Hauptfleisch, B.; Trautwein, A. X.; Schunemann, V. Archimedean synthesis and magic numbers:

"sizing" giant molybdenum-oxide-based molecular spheres of the Keplerate type. *Angew. Chem. Int. Ed.* **1999,** *38*, 3238-3241.

33. Todea, A. M.; Al-Karawi, A. J. M.; Glaser, T.; Walleck, S.; Chamoreau, L. M.; Thouvenot, R.; Gouzerh, P.; Müller, A. Encapsulation of Keggin-type anions in reduced molybdenum–iron-type Keplerates as a general phenomenon. *Inorg. Chim. Acta*. **2012**, *389*, 107-111.
34. Kozhevnikov, I. V. Catalysis by Heteropoly Acids and Multicomponent Polyoxometalates in Liquid-Phase Reactions. *Chem. Rev.* **1998**, *98*, 171–198.
35. Sadakane, M.; Steckhan, E. Electrochemical Properties of Polyoxometalates as Electrocatalysts. *Chem. Rev.* **1998**, *98*, 219–237.
36. Katsoulis, D. E. A Survey of Applications of Polyoxometalates. *Chem. Rev.* **1998**, *98*, 359–387.
37. Mizuno, N.; Yamaguchi, K.; Kamata, K. Epoxidation of olefins with hydrogen peroxide catalyzed by polyoxometalates *Coord. Chem. Rev.* **2005**, *249*,1944–1956.
38. Hill, C. L.; Progress and challenges in polyoxometalate-based catalysis and catalytic materials chemistry. *J. Mol. Catal. A: Chem.* **2007**, *262*, 2–6.
39. Mizuno, N.; Kamata, K. Catalytic oxidation of hydrocarbons with hydrogen peroxide by vanadium-based polyoxometalates. *Coord. Chem. Rev.* **2011**, *255*, 2358–2370.
40. Wang, S. S.; Yang, G. Y. Recent Advances in Polyoxometalate-Catalyzed Reactions. *Chem. Rev.* **2015**, *115*, 4893–4962.
41. Keita, B.; Mbomekalle, I. M.; Nadjo, L. Redox behaviours and electrocatalytic properties of copper within Dawson structure-derived sandwich heteropolyanions $[Cu_4(H_2O)_2(X_2W_{15}O_{56})_2]^{16-}$ (X=P or As). *Electrochem. Commun.* **2003**, *5*, 830–837.
42. Song, I. K.; Barteau, M. A. Redox properties of Keggin-type heteropolyacid (HPA) catalysts: effect of counter-cation, heteroatom, and polyatom substitution. *J. Mol. Catal. A Chem.* **2004**, *212*, 229–236.
43. Park, D. R.; Song, J. H.; Lee, S. H.; Song, S. H.; Kim, H.; Jung, J. C.; Song, I. K. Redox properties of $H_3PMo_xW_{12-x}O_{40}$ and $H_6P_2Mo_xW_{18-x}O_{62}$ heteropolyacid catalysts and their catalytic activity for benzyl alcohol oxidation. *Appl. Catal. A* **2008**, *349*, 222–228.
44. Park, D. R.; Park, S.; Bang, Y.; Song, I. K. Redox properties and oxidation catalysis of group 5 metal (V, Nb, Ta)-containing Keggin and Wells–Dawson heteropolyacid (HPA) catalysts. *Appl. Catal. A* **2010**, *373*, 201–207.
45. Jung, J. K.; Procissi, D.; Vincent, R.; Suh, B. J.; Borsa, F.; Kogerler, P.; Schroder, C.; Luban, M. Proton NMR in the giant paramagnetic molecule $\{Mo_{72}Fe_{30}\}$. *Journal of Applied Physics,* **2002,** *91*, 7388-7390.

46. Kuepper, K.; Derks, C.; Taubitz, C.; Prinz, M.; Joly, L.; Kappler, J. P.; Postnikov, A.; Yang, W.; Kuznetsova, T. V.; Wiedwald, U.; Ziemann, P.; Neumann, M. Electronic structure and soft-X-ray-induced photoreduction studies of iron-based magnetic polyoxometalates of type $\{(M)M_5\}_{12}Fe^{III}_{30}(M = Mo^{VI}, W^{VI})$. *Dalton Trans.*, **2013**, *42*, 7924–7935.
47. Garlea, V. O.; Nagler, S. E.; Zarestky, J. L.; Stassis, C.; Vaknin, D.; Kögerler, P.; McMorrow, D. F.; Niedermayer, C.; Tennant, A.; Lake, B.; Qiu, Y.; Exler, M.; Schnack, J.; Luban, M. Probing spin frustration in high-symmetry magnetic nanomolecules by inelastic neutron scattering. *Physical Review B,* **2006**, *73*, 024414.
48. Lago, J.; Micotti, E.; Corti, M. Low-energy spin dynamics in the giant Keplerate molecule $Mo_{72}Fe_{30}$%: A muon spin relaxation and ^{1}H NMR investigation. *Physical Review B*, **2007**, *76*, 064432.
49. Schröder, C. Multiple nearest-neighbor exchange model for the frustrated magnetic molecules $\{Mo_{72}Fe_{30}\}$ and $\{Mo_{72}Cr_{30}\}$. *Physical Review B,* **2008**, *77,* 224409.
50. Neuscamman, E.; Chan, G. K. Correlator product state study of molecular magnetism in the giant Keplerate $Mo_{72}Fe_{30}$. *Physical Review B,* **2012**, *86*, 064402.
51. Schröder, C. Competing Spin Phases in Geometrically Frustrated Magnetic Molecules. *PRL.* **2005**, *94*, 017205.
52. Liu, T.; Imber, B.; Diemann, E.; Liu, G.; Cokleski, K.; Li, H.; Chen, Z.; Müller, A. Deprotonations and Charges of Well-Defined $\{Mo_{72}Fe_{30}\}$ Nanoacids Simply Stepwise Tuned by pH Allow Control/Variation of Related Self-Assembly Processes. *J. Am. Chem. Soc.* **2006**, *128*, 15914-15920.
53. Liu, T. Supramolecular Structures of Polyoxomolybdate-Based Giant Molecules in Aqueous Solution. *J. Am. Chem. Soc.* **2002**, *124*, 10942-10943.
54. Garazhian, Z.; Rezaeifard, A.; Jafarpour, M.; Farrokhi, A. $\{Mo_{72}Fe_{30}\}$ Nanoclusters for the Visible-Light-Driven Photocatalytic Degradation of Organic Dyes. *ACS Appl. Nano Mater*. **2020**, *3*, 648−657.
55. Mokhtari, R.; Rezaeifard, A.; Jafarpour, M.; Farrokhi, A. Visible-light driven catalase-like activity of blackberry-shaped $\{Mo_{72}Fe_{30}\}$ nanovesicles: combined kinetic and mechanistic studies. *Catal. Sci. Technol*., **2018**, *8*, 4645-4656.
56. Garazhian, Z.; Rezaeifard, A.; Jafarpour, M. A nanoscopic icosahedral $\{Mo_{72}Fe_{30}\}$ cluster catalyzes the aerobic synthesis of benzimidazoles. *RSC Adv.,* **2019**, *9*, 34854-34861.
57. Kolli, H. K.; Jana, D.; Das, S. K. Nano-blackberries of $\{W_{72}Fe_{33}\}$ and $\{Mo_{72}Fe_{30}\}$: Electrocatalytic Water Reduction. *Inorg. Chem.* **2021**, *60*, 15569–15582.

58. Takaoka, K.; Kawano, M.; Tominaga, M.; Fujita, M. In Situ Observation of a Reversible Single-Crystal-to-Single-Crystal Apical-Ligand-Exchange Reaction in a Hydrogen-Bonded 2D Coordination Network. *Angew. Chem., Int. Ed.* **2005**, *44*, 2151-2154.
59. Hu, C.; Englert, U. Crystal-to-Crystal Transformation from a Chain Polymer to a Two-Dimensional Network at Low Temperatures. *Angew. Chem., Int. Ed.* **2005**, *44*, 2281-2283.
60. Toh, N. L.; Nagarathinam, M.; Vittal, J. J. Topochemical Photodimerization in the Coordination Polymer $[\{(CF_3CO_2)(\mu\text{-}O_2CCH_3)Zn\}2(\mu\text{-bpe})_2]_n$ through Single-Crystal to Single-Crystal Transformation. *Angew. Chem., Int. Ed.* **2005**, *44*, 2237-2241.
61. Papaefstathiou, G. S.; Zhong, Z.; Geng, L.; MacGillivray, L. R. Coordination-Driven Self-Assembly Directs a Single-Crystal-to-Single-Crystal Transformation that Exhibits Photocontrolled Fluorescence. *J. Am. Chem. Soc.* **2004**, *126*, 9158-9159.
62. Suh, M. P.; Ko, W. J.; Choi, H. J. A Metal−Organic Bilayer Open Framework with a Dynamic Component: Single-Crystal-to-Single-Crystal Transformations. *J. Am. Chem. Soc.* **2002**, *124*, 10976-10977.
63. Choi, H. J.; Suh, M. P. Dynamic and Redox Active Pillared Bilayer Open Framework: Single-Crystal-to-Single-Crystal Transformations upon Guest Removal, Guest Exchange, and Framework Oxidation. *J. Am. Chem. Soc.* **2004**, *126*, 15844-15851.
64. Hanson, K.; Calin, N.; Bugaris, D.; Scancella, M.; Sevov, S. C. Reversible Repositioning of Zinc Atoms within Single Crystals of a Zinc Polycarboxylate with an Open-Framework Structure. *J. Am. Chem. Soc.* **2004**, *126*, 10502-10503.
65. Maji, T. K.; Uemura, K.; Chang, H. -C.; Matsuda, R.; Kitagawa, S. Expanding and Shrinking Porous Modulation Based on Pillared-Layer Coordination Polymers Showing Selective Guest Adsorption. *Angew. Chem. Int. Ed.* **2004**, *43*, 3269-3272.
66. Lee, E. Y.; Suh, M. P. A Robust Porous Material Constructed of Linear Coordination Polymer Chains: Reversible Single-Crystal to Single-Crystal Transformations upon Dehydration and Rehydration. *Angew. Chem. Int. Ed.* **2004**, *116*, 2858-2861.
67. Takamizawa, S.; Nakata, E.; Yokoyama, H.; Mochizuki, K.; Mori, W. Carbon Dioxide Inclusion Phases of a Transformable 1D Coordination Polymer Host $[Rh_2(O_2CPh)_4(pyz)]_n$. *Angew. Chem. Int. Ed.* **2003**, *42*, 4331-4334.
68. Takamizawa, S.; Nakata, E.; Saito, T. Single-Crystal Adsorbents: A New Observation Field for Light Aggregates. *Angew. Chem. Int. Ed.* **2004**, *43*, 1368-1371.
69. 74 Chu, Q.; Swenson, D. C.; MacGillivray, L. R. A Single-Crystal-to-Single-Crystal Transformation Mediated by Argentophilic Forces Converts a Finite Metal Complex into an Infinite Coordination Network. *Angew. Chem. Int. Ed.* **2005**, *44*, 3569-3572.

70. Sabbani, S.; Das, S. K. Reversible solid to solid transformation in a crystalline state gas–solid reaction under ambient conditions: Fe–N(pyridine) bond formation at the expense of Fe–OH_2 bond breaking and vice versa. *CrystEngComm*, **2015**, *17*, 8850-8857.
71. Fernindez-Berth, J.; Reguera, E. Mechanochemical reactions in alkali halide pressed disks. *Solid State Ionics*, **1996**, *93*, 139-146.
72. Tandekar, K.; Mishra, N. K.; Sabbani, S. Solvent mediated reversible solid state photochromism of {Mo72Fe30} Keplerate. *Dalton Trans.*, **2021**, *50*, 6146-6151.
73. Anderson, W. L.; Stucki, J. W. Effect of Structural Fe^{2+} on Visible Absorption Spectra of Nontronite Suspensions. *Developments in Sedimentology*, **1979**, *27*, 75-83.
74. Ostroushko, A. A.; Tonkushima, M. O.; Safronov, A. P.; Korotaev, V. Yu.; Vazhenin, V. A.; Kolosov, V. Yu.; Martynova, N. A.; Kutashev, I. B.; Bogdanov, S. G.; Pirogov, A. N.; Grzhegorzhevskii, K. B.; Prokof'eva, A. V. Study of the stability of solid polyoxometalate $Mo_{72}Fe_{30}$ with a buckyball structure. *Russ. J. Inorg. Chem.* **2012**, *57*, 858–863.
75. Zhang, H.; Duan, L.; Lan, Y.; Wang, E.; Hu, C. Synthesis, Crystal Structure, and Photochromism of Novel Two-Dimensional Supramolecular Networks Based on Keggin-Type Polyoxoanion and Lanthanide Coordination Cations. *Inorg. Chem.* **2003**, *42*, 8053–8058.
76. Odom, B.; Hanneke, D.; D'Urso, B.; Gabrielse, G. New Measurement of the Electron Magnetic Moment Using a One-Electron Quantum Cyclotron. *Phys. Rev. Lett.* **2006**, *97*, 030801.

==

CHAPTER 6

Concluding Remarks and Future Scope

Chapter 6

6.1. Concluding Remarks

This thesis, entitled “**$\{M_{72}Fe_{30}\}$ (M=Mo, W) Polyoxometalates: Electrocatalysis, Proton Conductivity, Gelation and Mechanochemistry**” describes the isolation of Keplerate compounds into amorphous form by self-assembling process. We have demonstrated the applications of these materials by using as a heterogeneous electrocatalyst for hydrogen evolution reaction (HER) by water reduction of and as the proton conducting material for fuel cell applications. Both these events are important in achieving renewable energy to replace usage of the fossil fuels. The gist of this has been discussed in the introductory note (**chapter 1**) of this thesis.

Chapter 2 demonstrates the isolation and characterization of tungsten nano-blackberries **$\{W_{72}Fe_{30}\}_{NM}$** focusing a new light of assembling $\{W_{72}Fe_{30}\}$ clusters through Fe^{3+} ions. For the first time, we have shown a meaningful application of these nano-blackberries in the direction of generating sustainable energy. We have successfully synthesized the nano-blackberries of tungsten analogue $Fe_3[W_{72}Fe_{30}O_{252}(CH_3COO)_2(OH)_{25}(H_2O)_{103}]\cdot180H_2O$ (**$\{W_{72}Fe_{30}\}_{NM}$**). The self-assembled material of nano-blackberries of (**$\{W_{72}Fe_{30}\}_{NM}$**) has been characterized by diverse spectral studies including FT-IR, Raman spectroscopy, elemental analysis including ICP metal analysis and CHN analysis, volumetric analysis (for iron), microscopy techniques, DLS and Zeta potential measurements. We have found that extra three iron ions, that are present per $\{W_{72}Fe_{30}\}$ cluster in the compound **$\{W_{72}Fe_{30}\}_{NM}$** as linker of assembly, offer an enormous amount of rigidity / thermal stability of compound **$\{W_{72}Fe_{30}\}_{NM}$** when compared to its molybdenum analogue $Na_2[Mo_{72}Fe_{30}O_{252}(CH_3COO)_4(OH)_{16}(H_2O)_{108}]\cdot180H_2O$ (**$\{Mo_{72}Fe_{30}\}_{NM}$**), a kinetically labile substance, which on heating at 60-70°C degrades to $Fe_2(MoO_4)_3$. We have explored the electrocatalytic activity of the compounds **$\{Mo_{72}Fe_{30}\}_{NM}$** and **$\{W_{72}Fe_{30}\}_{NM}$** for hydrogen evolution reaction (HER) by water reduction. In a comparative kinetic study, the relevant turnover frequencies (TOFs) of $\{$**$W_{72}Fe_{30}$**$\}_{NM}$ and $\{$**$Mo_{72}Fe_{30}$**$\}_{NM}$ ($\sim0.72s^{-1}$ and $\sim0.45s^{-1}$, respectively) and the overpotential values of $\{$**$W_{72}Fe_{33}$**$\}_{NM}$ and $\{$**$Mo_{72}Fe_{30}$**$\}_{NM}$ (527 mV and 767 mV, respectively) show that $\{$**$W_{72}Fe_{30}$**$\}_{NM}$ performs better than $\{$**$Mo_{72}Fe_{30}$**$\}_{NM}$ in terms of their catalytic activity.

Chapter 3, we have explored the proton conductivity of the nanoclusters containing compound **$\{W_{72}Fe_{30}\}_{NB}$**, and we have achieved proton conductivity of 3.30×10^{-1} at 80 °C (98%RH). For the first time we have reported the highest proton conductivity among MOF (metal organic frameworks) and POM based compounds. As we cannot use this compound directly in the practical application, we have fabricated PA doped **$\{W_{72}Fe_{30}\}$@m-PBI** membranes in two different loading levels of $\{W_{72}Fe_{30}\}$ by weight: **2.5% $\{W_{72}Fe_{30}\}$@m-PBI** and **5.0% $\{W_{72}Fe_{30}\}$@m-PBI**. Both membranes have performed as efficient proton exchange membranes when doped with PA and they are having good tensile and thermo-mechanical properties with superior PA retention capacity. The proton conductivity of 2.5% $\{W_{72}Fe_{30}\}$+PA@m-PBI and 5.0% $\{W_{72}Fe_{30}\}$+PA@m-PBI membranes are 0.126 S cm^{-1} and 0.159 S cm^{-1}, respectively at 160 °C. We have also fabricated 50% $\{W_{72}Fe_{30}\}$@m-PBI composite membrane and achieved a proton conductivity of 5.706×10^{-2} S cm^{-1} in aqueous condition (80 °C and 98% RH). Overall, this work has demonstrated that an expensive metal-oxide based material can be obtained in gram quantity in an easy straight forward aqueous synthesis and this material shows super protonic conductivity; we have also shown that this metal-oxide material can be used as nano-filler into a versatile polymer membrane resulting in the fabrication of proton exchange membranes for fuel cell applications.

In **Chapter 4**, a pure inorganic Keplerate hydrogel **$\{W_{72}Fe_{30}\}_{HG}$** without any organic moiety has been reported for the first time in the gel chemistry area of polyoxometalates (POMs). The gel material has been characterized by rheology studies indicating that it is a gel with modest mechanical strength. The xerogel **$\{W_{72}Fe_{30}\}_{XG}$** has been characterized using various microscopic and spectroscopic techniques. FESEM images suggest that the compound is porous in nature. Further, the xerogel **$\{W_{72}Fe_{30}\}_{XG}$** exhibits a high proton conductivity of 6.99×10^{-2} S cm^{-1}. The porosity of this xerogel material has been established by gas adsorption studies. N_2 gas adsorption capacity of this title material is found to be 0.556 mmol/g. It is a rare example of POM compound that exhibits an electrical conductivity of 2.43×10^{-5} S cm^{-1} at applied potential 1 V. This xerogel **$\{W_{72}Fe_{30}\}_{XG}$** material has potential to be used as a nanofiller in an organic polymer matrix to make proton exchange membrane for fuel cell applications. This is under progress in our laboratory.

Finally, in the **Chapter 5**, Crystalline compound **$\{Mo_{72}Fe_{30}\}$** which has icosahedral structure with a basic unit **$\{Mo_{72}Fe_{30}\}$** cluster have been well explored in the many application fields, but its reversible redox conversion through mechanochemical reaction is not known until now. In this work, we have demonstrated a mechanochemical solid state reversible reaction that involves grinding of solid KI with solid **{$Mo_{72}Fe_{30}$}** crystalline compound resulting in KI oxidation to molecular iodine and reduction of **{$Mo_{72}Fe_{30}$}** cluster. The reduced cluster, in turn, gets oxidizred by aerial oxygen to regenerate parent oxidized **{$Mo_{72}Fe_{30}$}** compound with the formation potassium superoxide (KO_2) in the resulting solid reaction mixture. This this cycle can be described as mechanochemical aerial KI oxidation mediated by **{$Mo_{72}Fe_{30}$}** cluster. The formation of intermediate Mo(V) state of the **{$Mo_{72}Fe_{30}$}** cluster and the formation of KO_2 can be corroborated by EPR spectroscopy. Therefore, the compound **{$Mo_{72}Fe_{30}$}** has a potential towards solid state catalysis through mechanochemical reactions which is an interesting field to work with Keplerate type giant polyoxometalates.

To conclude, in this thesis work, we have synthesized water insoluble Keplerate compounds (mainly related to {$W_{72}Fe_{30}$} and {$Mo_{72}Fe_{30}$} clusters) and used as an electrocatalyst for HER and also showed the proton conductivity of the {$W_{72}Fe_{30}$} cluster containing compound. We have synthesized {$W_{72}Fe_{30}$} and {$Mo_{72}Fe_{30}$} in their amorphous forms through one pot synthesis with easily available laboratory chemicals. These two amorphous compounds exhibited the electrochemical activity towards hydrogen evolution reaction; we have also used {$W_{72}Fe_{30}$} cluster containing compound as a nanofiller in proton transport membrane when it exhibits the super proton conductivity. As we have observed that the crystalline forms of these cluster containing compounds are water soluble and we observed the electrodeposition has happened during the electrochemical activity studies. Thus, by synthesizing the water insoluble Keplerate compounds, one can easily study their electrocatalytic activity and proton conductivity.

6.2. Future Scope

In future, we would like to synthesize a Keplerate {$W_{72}Cr_{30}$} cluster containing compound which is not reported till now, either in crystalline or amorphous form. This will allow us to study and analyze its properties and applications.

We believe that the proposed Keplerate {$W_{72}Cr_{30}$} cluster containing compound will also plays an important role in exhibiting the catalytic activity. We know that, there are many reports on Keplerates which mainly focused on the study of their magnetic properties, selective catalytic properties and biomedical applications. So, we would like to focus on the synthesis of {$W_{72}Cr_{30}$} cluster containing compound (both in amorphous and crystalline form) and we would like to explore its electrochemical properties towards the catalytic reduction of water to molecular hydrogen.

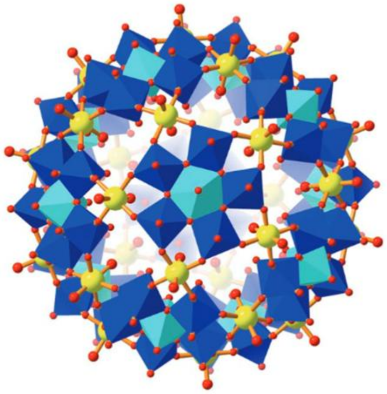

$\mathbf{W_{72}Cr_{30}}$

Figure 6.1. Imaginary structure of {$W_{72}Cr_{30}$} adapted from the structure of {$Mo_{72}Fe_{30}$}.

In the current thesis work, we have shown that the **{$W_{72}Fe_{30}$}$_{NB}$** is a superprotonic conductor because of the presence of hydroxyl groups which can be easily deprotonated and can be made the material proton conductive. There are other Keplerate materials like $Mo_{75}V_{20}$, Mo_{102}, $Mo_{72}V_{30}$, $Mo_{72}Cr_{30}$, $W_{72}Mo_{60}$, $W_{72}V_{30}$ which are not yet explored in studying their electrochemical properties to know their catalytic activity towards water reduction and water oxidation reactions and also as a proton conductor. All these known compounds have oxygen rich surfaces which can easily form a hydrogen bonding with water for proton conduction. The aim will be to make the amorphous forms of these Keplerate materials to make them water insoluble, so that heterogeneous electrocatalysis and proton conductivity can be studied.

Keplerate materials left behind due to the lack of processability. One can make the practical usage of Keplerate based proton conductors in Fuel cell preparation as a proton exchange membrane with the support of a polymer like m-PBI with **{$W_{72}Fe_{30}$}$_{NB}$** (**Chapter 3**). Such type of membranes are useful in improving the functional properties and proton conduction in fuel cell. These materials have high potential to replace the widely used proton exchange membrane Nafion.

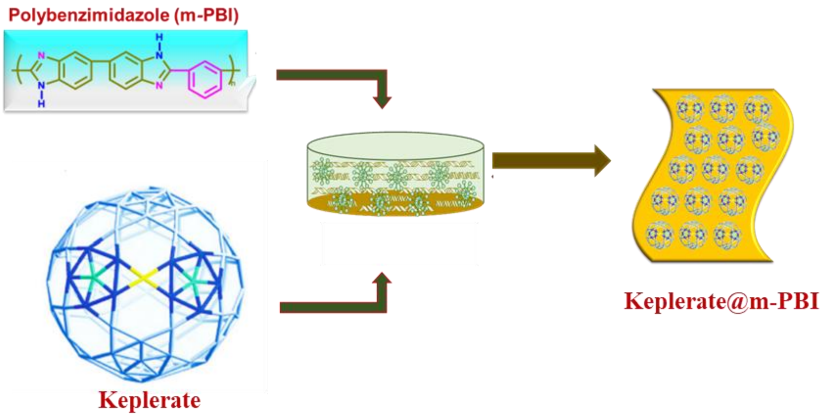

Scheme 6.1. Synthesis of m-PBI polymer supported membranes using Keplerates as nanofillers.

APPENDIX 1

Instrumental Details of Physical Characterizations

Fourier transformed – infrared (FT-IR) spectra was obtained by an iD7 ATR Thermo Fisher Scientific-Nicolet iS5 instrument. Directly the powdered sample was exposed to IR radiation by putting it on sample holder.

Raman Spectral Analysis was performed by a WITec model Alpha 300 R Raman microscope was used for recording the Raman spectra. A 633 nm laser was used as the excitation source. The laser intensity was maintained constant for all the samples.

Thermogravimetric Analysis (TGA) were performed in PerkinElmer-STA 6000 analyzer and TGA-GCMS was conducted in PerkinElmer Gas chromatograph Clarus® 580 and Mass spectrometer Clarus® SQ 8 S.

Powder X-ray diffractions (PXRD) patterns were recorded on a Bruker D8-Advance diffractometer by using graphite monochromated CuKα1 (1.5406Å) and Kα_2 (1.55439Å) radiation.

Inductively coupled plasma - optical emission spectrometry (ICP-OES) was used to estimate the amount of W, Mo, Fe and Na present in the $\{W_{72}Fe_{30}\}$ and $\{Mo_{72}Fe_{30}\}$ cluster containing compounds. An ICP-OES Varian 720-ES instrument was used.

The tensile strength measurement (stress-strain profile) of all the PA doped m-PBI PA doped Polymer-POM MMMs was obtained from universal testing machine (UTM, INSTRON-5965). 50 mm × 10 mm × 0.02 mm size PA doped films were used for this experiment. For each sample, at least three times measurements were tested in the machine to check the reproducibility. Stress-strain profile (tensile stress and elongation at break values) of the PA doped m-PBI and PA loaded nanocomposite MMMs were evaluated from the stress vs strain plot.

Field emission scanning electron microscopy (FESEM) measurement along with energy dispersive X-ray (EDX) were recorded on a Carl Zeiss model ultra 55 microscope whereas EDX spectrum was performed using oxford instruments X-Max^N SDD (50mm^2) system and INCA analysis software.

Transmission electron microscopy (TEM) images were recorded in an FEI Tecnai G^2 S-Twin microscope with an accelerating voltage of 200 kV. The selected area electron diffraction patterns (SAED) were recorded with the help of Gatan Inc CCD camera and GATAN digital microgram software.

Diffuse reflectance (DRS) UV-spectroscopy studies have been carried out on UV-2600 Shimadzu UV-Visible spectrophotometer to measure absorbance of the $\{W_{72}Fe_{30}\}$ and $\{Mo_{72}Fe_{30}\}$ cluster containing compounds.

Zeta potential measurement was carried out in Horiba SZ-100 to know the stability of nanoparticles of $\{W_{72}Fe_{30}\}$ and $\{Mo_{72}Fe_{30}\}$ cluster containing compounds.

Electrochemical Measurements were carried out with the help of Zahner Zanium electrochemical work station operated with Thales software. Whereas the membrane samples were studied using Auto lab Impedance analyser (PGSTAT302N) instrument.

Mechanical properties of m-PBI and **Polymer-POM** mixed matrix membranes were studied by using a dynamic mechanical analyser (DMA model Q-800). The loaded membranes dimensions were around 30 mm × 7 mm × 0.01 mm (L × W × T) and clamped on the films tension clamp of the pre-calibrated instrument. The samples were annealed at 400 °C for 15 minutes and then scanned from 100 °C to 400 °C with heating rate 4 °C/min. The storage modulus (E') and tan δ values were measured at a constant linear frequency 10 Hz with constant preloaded force of 0.01N.

Volumetric titration for the estimation of iron percent present in the compound $\{W_{72}Fe_{30}\}$ and $\{Mo_{72}Fe_{30}\}$ cluster containing compounds, in support with the ICP-OES analysis.

Dynamic light scattering (DLS) measurements has been carried out for the $\{W_{72}Fe_{30}\}$ and $\{Mo_{72}Fe_{30}\}$ cluster containing compounds dispersed in water, were performed using a Horiba SZ-100.

Dynamic vapour sorption (DVS) analysis of the samples $\{W_{72}Fe_{30}\}_{NM}$ and $\{W_{72}Fe_{30}\}_{XG}$ were performed on a TA Q5000 SA instrument, at a temperature of 25 ºC and under N_2 atmosphere.

N_2 gas sorption analysis were performed on the Quantachrome Autosorb IQ2 instrument. All the samples were degassed at 100 °C under vacuum for 24 hours, prior to N_2 sorption analysis. The temperature was maintained at 77 K during the experiment by a liquid nitrogen bath.

Rheology studies were carried out with help of strain-controlled rheometer (MCR 501, Anton Paar) at a temperature of 25 °C.

The inherent viscosity (I.V.) of the poly **2,2′-(m-phenylene)-5,5′-benzimidazole** (**m-PBI**) polymer was measured at 30 °C in water bath with the help of Cannon (model F725) capillary dilution viscometer and the I.V. values are calculated from the flow time data. A solution of m-PBI in H_2SO_4 was used for the viscosity measurement. The concentration of the m-PBI solution in H_2SO_4 is 0.2 g/dL. The obtained I.V. value of the synthesised **m-PBI** is 1.02 dL/g.

APPENDIX 2

Supporting data for chapter 2

Table of Contents

Section A2.1. Physical characterizations

As such synthesized compounds were characterized by FT-IR, powder X-ray diffraction, FESEM, thermogravimetric analysis (TGA), dynamic light scattering (DLS) studies and UV-visible diffused reflectance spectroscopy (DRS), inductively coupled plasmon optical emission spectroscopy (ICP-OES) and electrochemistry.

Fourier transformed – infrared spectra was obtained by an iD7 ATR thermo Fisher Scientific-Nicolet iS5 instrument. Directly the powdered sample was exposed to IR radiation by putting it on sample holder. TGA analysis were performed in PerkinElmer-STA 6000 analyzer and TGA-GCMS were conducted in PerkinElmer Gas chromatograph Clarus® 580 and Mass spectrometer Clarus® SQ 8 S. Diffuse reflectance (DRS) UV-spectroscopy studies have been carried out on UV-2600 Shimadzu UV-Visible spectrophotometer. Zeta potential measurement was carried out in Horiba scientific nano particle analyzer SZ-100. Dynamic Light Scattering (DLS) studies are carried out in Zetasizer nano S90 (Malvern Instruments, Germany) operating at 4mW He-Ne laser with 633nm wavelength at room temperature with the help of Malvern Zetasizer software. Field emission scanning electron microscopy (FESEM) measurement along with energy dispersive X-ray (EDX) was recorded on a Carl Zeiss model ultra 55 microscope whereas EDX spectrum was performed using oxford instruments X-Max^N SDD (50mm^2) system and INCA analysis software. Transmission electron microscopy (TEM) images were recorded in an FEI Tecnai G^2 S-Twin microscope with an accelerating voltage of 200 kV. The selected area electron diffraction patterns (SAED) were recorded with the help of Gatan Inc CCD camera and GATAN digital microgram software. All the electrochemical measurements were carried out with the help of Zahner Zanium electrochemical work station operated with Thales software.

Section A2.2. Synthesis, material and procedures.

The synthetic procedures were mentioned in the main text (article) and all the chemicals were taken as reagent grade, there was no further purification of the chemicals.

Section A2.3. Raman spectral analysis of $\{Mo_{72}Fe_{30}\}_{NM}$

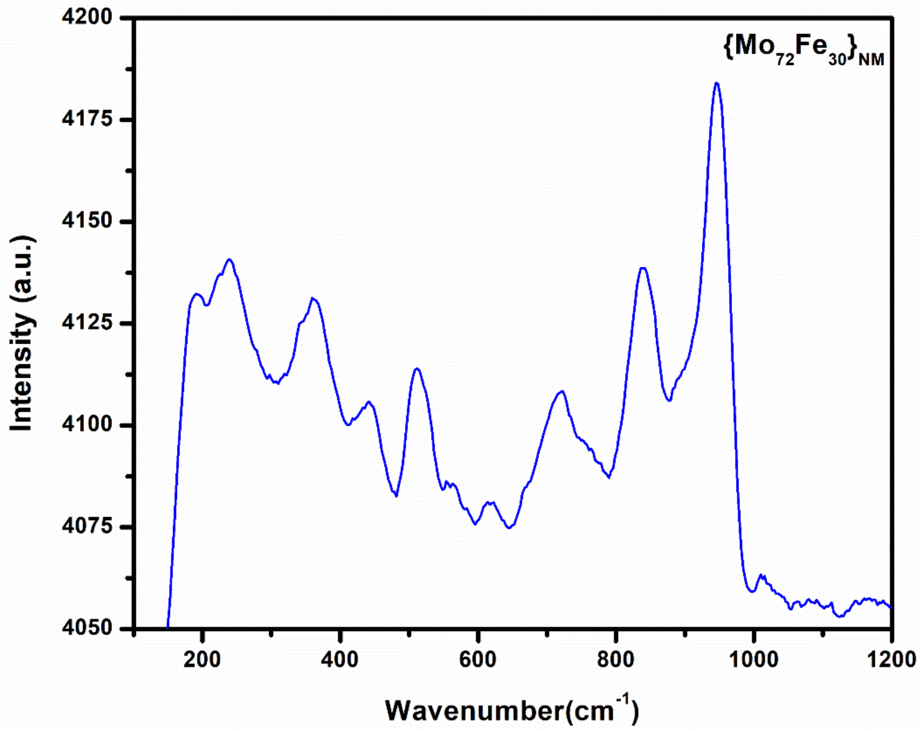

Figure A2.1. Raman spectrum of isolated amorphous $\mathbf{\{Mo_{72}Fe_{30}\}_{NM}}$ compound.

The solid-state Raman spectrum recorded using 632 nm laser excitation, compound **$\{Mo_{72}Fe_{30}\}_{NM}$** shows the characteristic bands at 946, 841, 722, 511, 442, 359 and 238 cm^{-1} as shown in Figure A2.1.

Section A2.4. PXRD pattern of $\{Mo_{72}Fe_{30}\}_{NM}$

The PXRD pattern of the as synthesized $\{Mo_{72}Fe_{30}\}$ cluster showing broad peak (Figure A2.2a) clearly indicates that is amorphous in nature. The molybdenum nano-blackberries, $Na_2[Mo_{72}Fe_{30}O_{252}(CH_3COO)_4(OH)_{16}(H_2O)_{108}]\cdot 180\ H_2O$ (**$\{Mo_{72}Fe_{30}\}_{NM}$**), upon heating in oven at 70^0C for 42 hrs, undergoes solid to solid transformation resulting in the formation of $Fe_2(MoO_4)_3$ as we have shown in the PXRD (Figure A2.2b); it shows sharp peaks which is completely in crystalline state. We have also refluxed the compound **$\{Mo_{72}Fe_{30}\}_{NM}$** in 50mL water at 100^0C for one hour, it has been transformed to crystalline form of ferric molybdate as shown in Figure A2.2c. When we have heated the compound **$\{W_{72}Fe_{33}\}_{NM}$** in muffle furnace at 200^0C for 2 hrs, the compound remains intact without transforming to ferric tungstate as shown in the PXRD pattern (Figure A2.2e) it exhibits a broad peak as before in Figure A2.2d which indicates that **$\{W_{72}Fe_{33}\}_{NM}$** is still in amorphous nature. Even, when the compound **$\{W_{72}Fe_{33}\}_{NM}$** was refluxed in 50mL water at 100^0C for six hours, it remained intact as it is showing the broad peak in PXRD (Figure A2.2f).

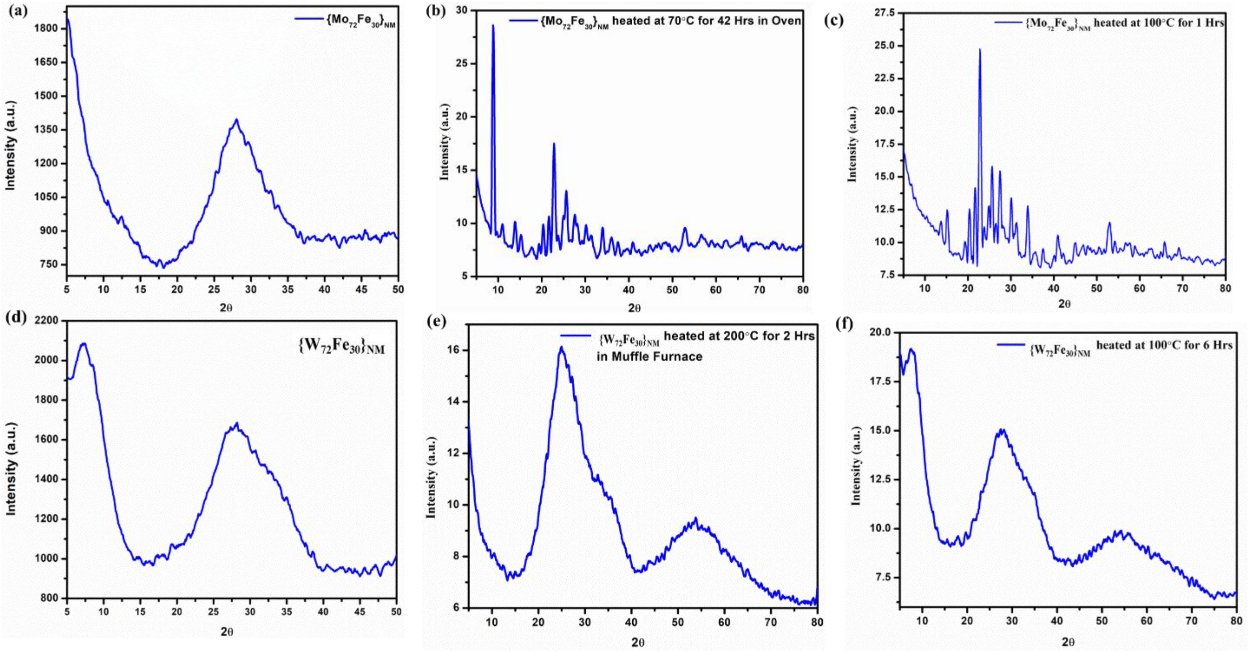

Figure A2.2. PXRD patterns of the (a) amorphous **$\{Mo_{72}Fe_{30}\}_{NM}$** compound, (b) **$\{Mo_{72}Fe_{30}\}_{NM}$** heated at 70^0C for 42 hrs in oven, (c) **$\{Mo_{72}Fe_{30}\}_{NM}$** heated at 100^0C for 1 hrs in 50mL water, (d) amorphous **$\{W_{72}Fe_{30}\}_{NM}$** compound, (e) **$\{W_{72}Fe_{30}\}_{NM}$** heated at 200^0C for 2 hrs in muffle furnace, (f) **$\{W_{72}Fe_{30}\}_{NM}$** heated at 100^0C for 6 hrs in 50mL water.

Section A2.5. Thermo gravimetric analysis- GCMS of $\{W_{72}Fe_{30}\}_{NM}$ and $\{Mo_{72}Fe_{30}\}_{NM}$

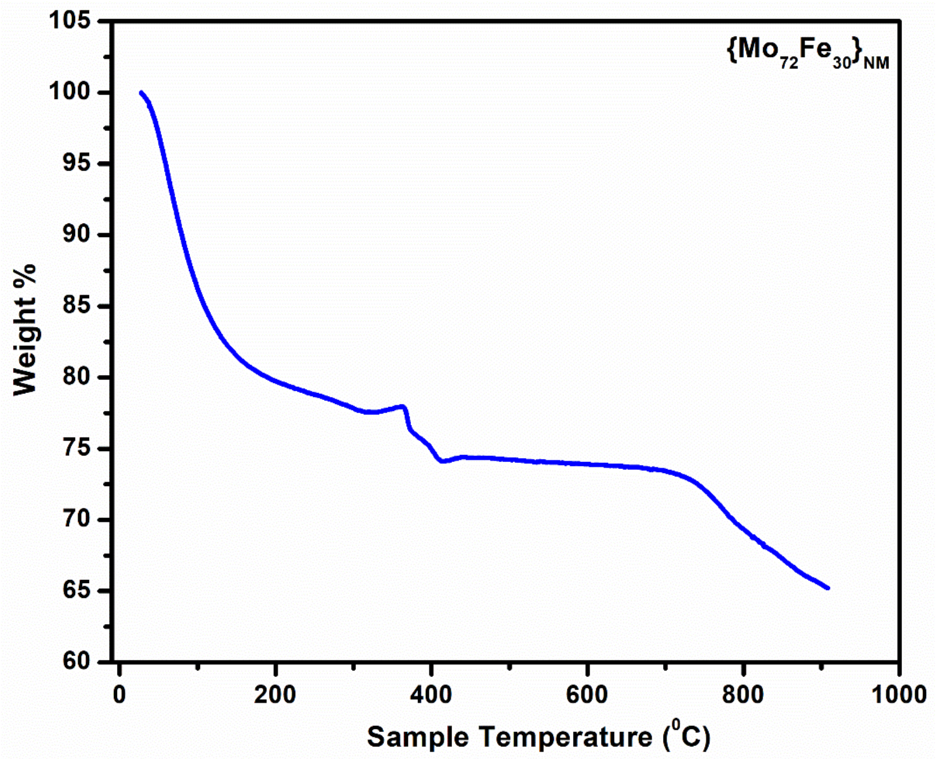

Figure A2.3. Thermogravimetric plot of the amorphous **$\{Mo_{72}Fe_{30}\}_{NM}$** compound.

TGA plot of the compound **$\{Mo_{72}Fe_{30}\}_{NM}$** clearly shows that below and around 100 ºC temperature, it loses the water molecules as shown in Figure A2.3 and it is thermally less stable when compared to **$\{W_{72}Fe_{30}\}_{NM}$** compound as shown in the Figure A2.4c. We have also carried out the TGA-GCMS analysis for the compound **$\{W_{72}Fe_{30}\}_{NM}$** to conform the presence of acetate ligands in the cluster and we have obtained a clear mass spectrum of the compound **$\{W_{72}Fe_{30}\}_{NM}$** as shown in the Figure A2.4.

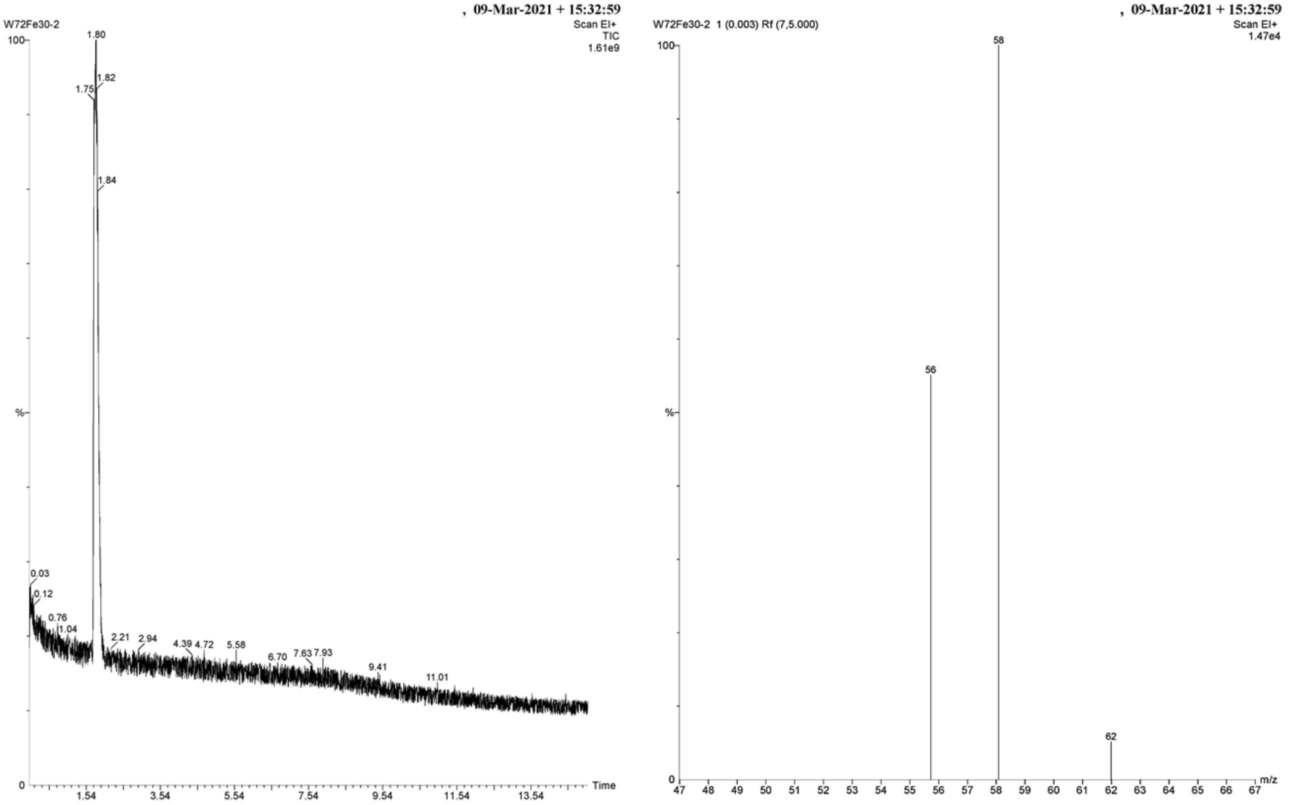

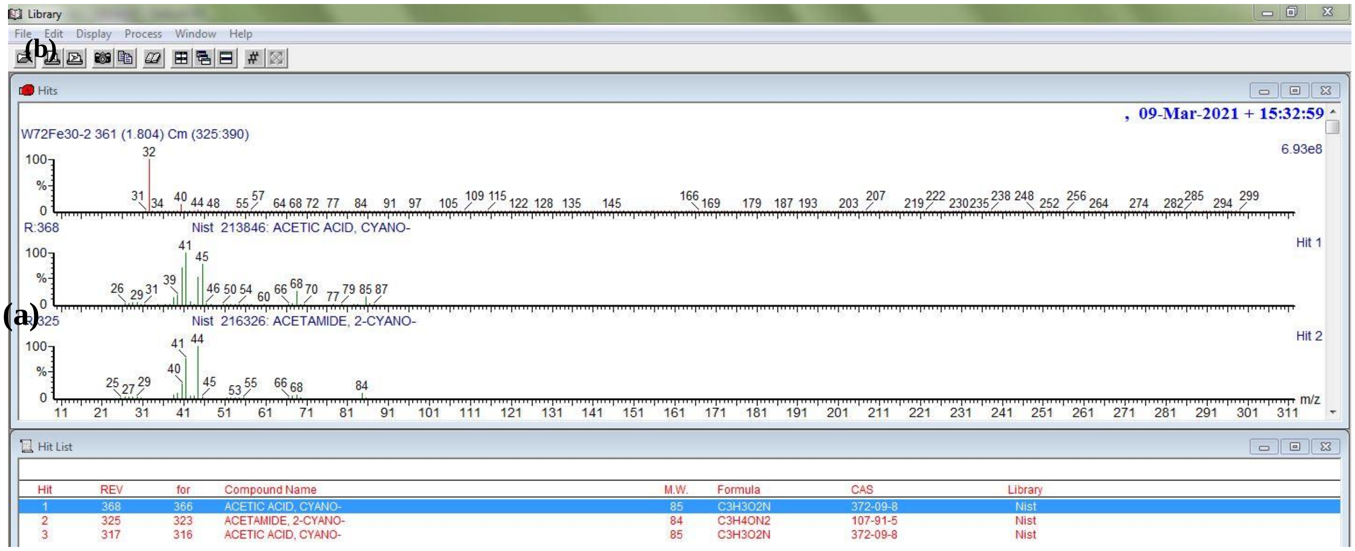

Hit	REV	for	Compound Name	M.W.	Formula	CAS	Library
1	368	366	ACETIC ACID, CYANO-	85	C3H3O2N	372-09-8	Nist
2	325	323	ACETAMIDE, 2-CYANO-	84	C3H4ON2	107-91-5	Nist
3	317	316	ACETIC ACID, CYANO-	85	C3H3O2N	372-09-8	Nist

Figure A2.4. Thermogravimetric Analysis – Gas Chromatograph Mass Spectrometric studies of the compound **$\{W_{72}Fe_{30}\}_{NM}$**, (a) chromatogram of **$\{W_{72}Fe_{30}\}_{NM}$**, (b) spectrum of **$\{W_{72}Fe_{30}\}_{NM}$** and (c) Library search of the acquired spectrum of the compound **$\{W_{72}Fe_{30}\}_{NM}$**.

Section A2.6. UV-visible spectral analysis of $\{W_{72}Fe_{30}\}_{NM}$ and $\{Mo_{72}Fe_{30}\}_{NM}$

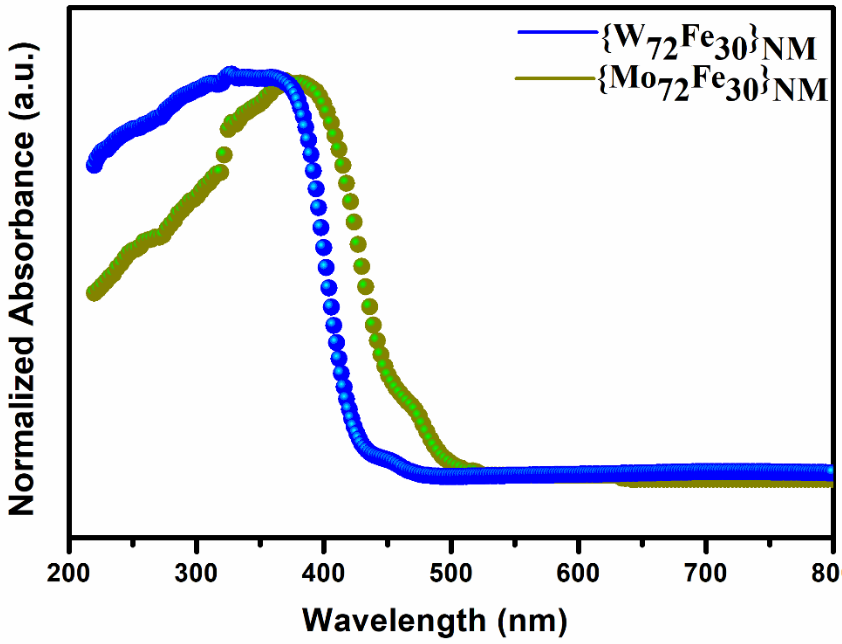

(a) **(b)**

Figure A2.5. Kubelka-Munk converted solid state diffused reflectance electronic spectra (DRS) of the compounds **$\{Mo_{72}Fe_{30}\}_{NM}$** and **$\{W_{72}Fe_{30}\}_{NM}$**.

The solid state diffused reflectance spectra of the compounds **$\{Mo_{72}Fe_{30}\}_{NM}$** and **$\{W_{72}Fe_{30}\}_{NM}$** shows absorption peaks at 381 nm and 361 nm respectively after the Kubalka-Munk conversion as displayed in the Figure A2.5.

Section A2.7. FESEM and HR-TEM analysis of {$Mo_{72}Fe_{30}$}$_{NM}$

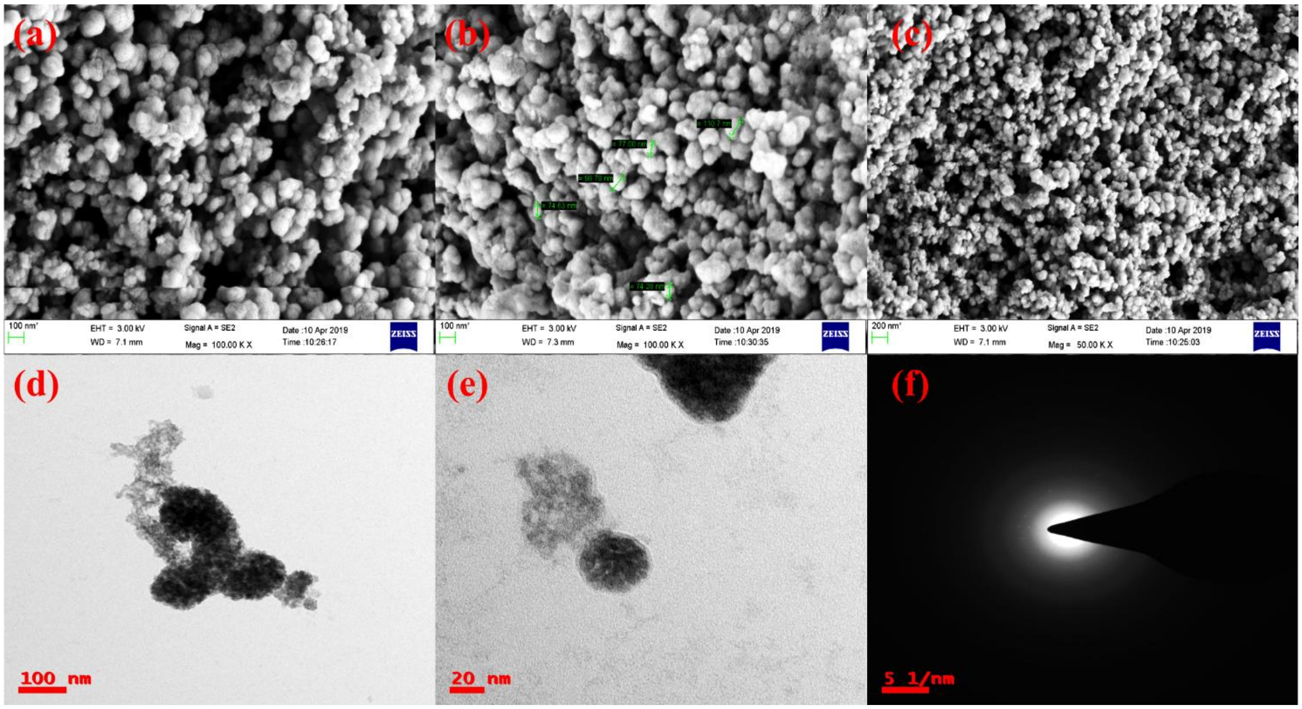

Figure A2.6. (a-c) FESEM images of the compound **{$Mo_{72}Fe_{30}$}$_{NM}$** at different resolutions; (d,e) HR-TEM images of the cluster **{$Mo_{72}Fe_{30}$}$_{NM}$** containing compound; (f) SAED pattern of the cluster **{$Mo_{72}Fe_{30}$}$_{NM}$** containing compound.

The FESEM images of the compound **{$Mo_{72}Fe_{30}$}$_{NM}$** has been taken on the carbon tape and coated with gold. Figures A2.6a, A2.6b and A2.6c clearly show that {$Mo_{72}Fe_{30}$} cluster containing compound **{$Mo_{72}Fe_{30}$}$_{NM}$** aggregates to form blackberry like nanovesicles which have pores on the surface. These nanoparticles have a particle around 50-100 nm as shown in Figure S6b. For the high-resolution transmission electron microscopy (HR-TEM) studies, the compound was suspended in water and coated on the copper grid. HR-TEM images of the compound **{$Mo_{72}Fe_{30}$}$_{NM}$** as shown in the Figure A2.6d and A2.6e are well in agreement with the FESEM images. The selective area electron diffraction (SAED) studies support the PXRD pattern, that the compound **{$Mo_{72}Fe_{30}$}$_{NM}$** was in amorphous nature as there was no diffraction pattern as shown in the Figure A2.6f.

Section A2.8. Energy-dispersive X-ray (EDX) analysis of $\{W_{72}Fe_{30}\}_{NM}$

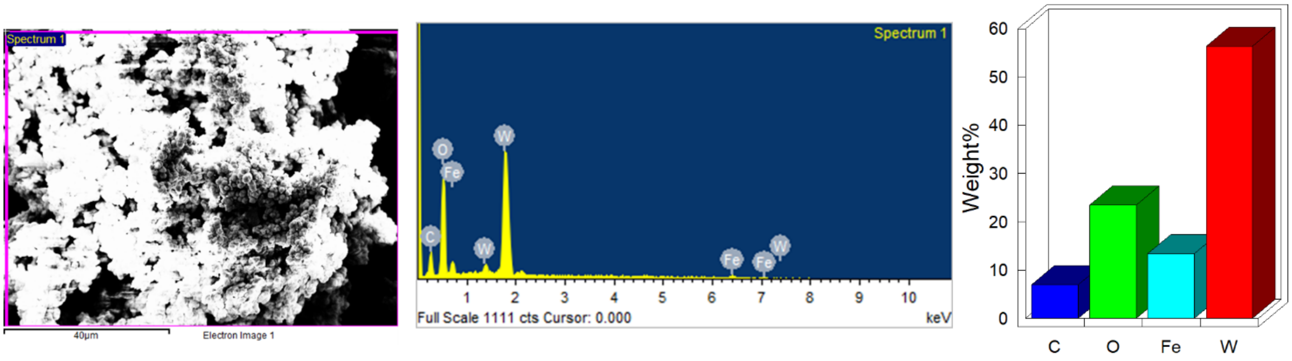

(a) **(b)** **(c)**

FigureA.2.7. (a) Selected surface area of the cluster **$\{W_{72}Fe_{30}\}_{NM}$** for the EDX analysis; (b) EDX spectrum for the cluster **$\{W_{72}Fe_{30}\}_{NM}$**; (c) histogram of the elemental composition on the selected surface of the cluster **$\{W_{72}Fe_{30}\}_{NM}$**.

Energy dispersive X-ray (EDX) spectroscopy was performed for the **$\{W_{72}Fe_{30}\}_{NM}$** compound to find out the composition on the surface of the $\{W_{72}Fe_{33}\}$ cluster. Figure A2.7a and A2.7b shows the image of the selected surface area of the compound **$\{W_{72}Fe_{33}\}_{NM}$** including its EDX analysis carried out and its EDX plot. The elemental composition can be seen in the Figure A2.7c in the form of histograms and it can also be seen in the Table A2.1 which are experimentally recorded with the help of EDX spectroscopy. The clear elemental composition of the compound **$\{W_{72}Fe_{30}\}_{NM}$** from EDX spectroscopy is displayed in the Table A2.1 and EDX-elemental mapping images of the compound **$\{W_{72}Fe_{30}\}_{NM}$** are shown in Figure A2.8.

Element	**Weight %**	**Atomic %**
Tungsten (W)	58.89	13.31
Iron (Fe)	12.70	9.45
Oxygen (O)	23.79	61.77
Carbon (C)	4.40	15.21

Table A2.1. Elemental composition of the compound **$\{W_{72}Fe_{30}\}_{NM}$** from EDX spectroscopic analysis.

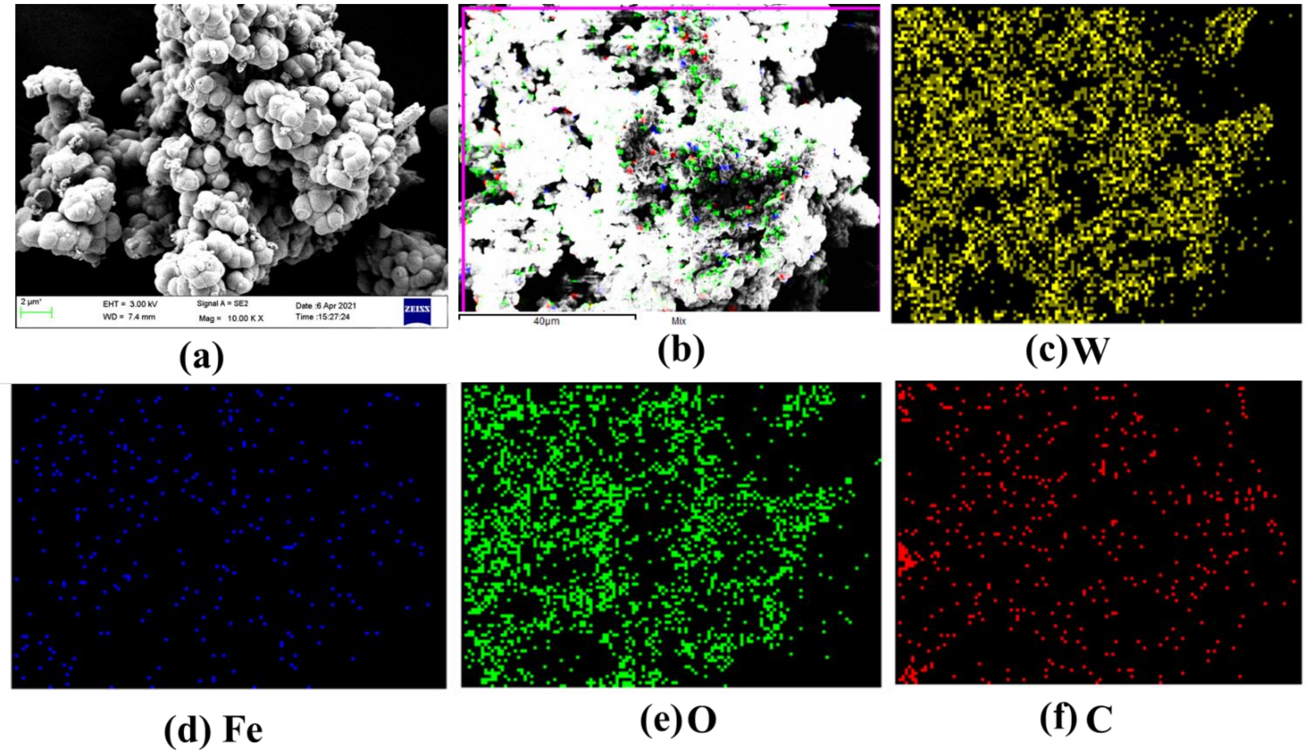

Figure A2.8. (a) FESEM image of the compound **$\{W_{72}Fe_{30}\}_{NM}$**; (b) selected surface area of the cluster **$\{W_{72}Fe_{30}\}_{NM}$** for the EDX- elemental mapping analysis; (c), (d), (e) and (f) displays the elemental abundance of tungsten, iron, oxygen and carbon present in the compound **$\{W_{72}Fe_{3}\}_{NM}$**. The sample is coated on a carbon tape.

Section A2.9. Elemental analysis of $\{W_{72}Fe_{30}\}_{NM}$ and $\{Mo_{72}Fe_{30}\}_{NM}$ from ICP-OES analysis

Sample Name	**Elements**	**Na**	**Fe**	**Mo/W**
$\{Mo_{72}Fe_{30}\}_{NM}$	Calculated	0.25%	9.12%	37.62% (Mo)
	Observed	0.04%	8.33%	36.80% (Mo)
$\{W_{72}Fe_{30}\}_{NM}$	Calculated	-----	7.46%	53.49% (W)
	Observed	<0.01%	7.83%	51.08% (W)

Table A2.2. Comparison of metal elemental composition of the compounds **$\{Mo_{72}Fe_{30}\}_{NM}$** and **$\{W_{72}Fe_{30}\}_{NM}$**, results from ICP-OES analysis and theoretically obtained metal compositions respectively.

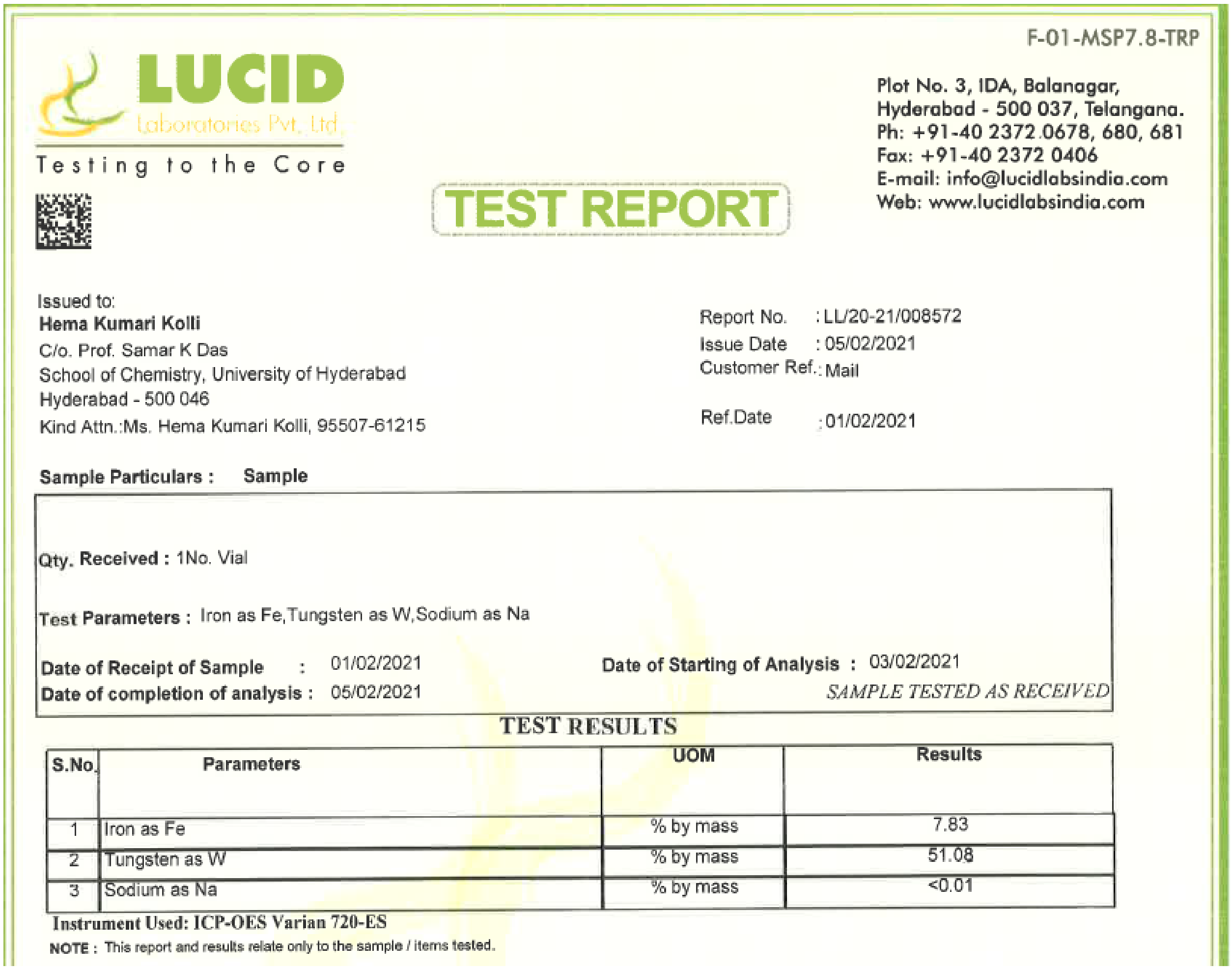

F-01-MSP7.8-TRP

LUCID
Laboratories Pvt. Ltd.
Testing to the Core

Plot No. 3, IDA, Balanagar,
Hyderabad - 500 037, Telangana.
Ph: +91-40 2372 0678, 680, 681
Fax: +91-40 2372 0406
E-mail: info@lucidlabsindia.com
Web: www.lucidlabsindia.com

TEST REPORT

Issued to:
Hema Kumari Kolli
C/o. Prof. Samar K Das
School of Chemistry, University of Hyderabad
Hyderabad - 500 046
Kind Attn.:Ms. Hema Kumari Kolli, 95507-61215

Report No. : LL/20-21/008572
Issue Date : 05/02/2021
Customer Ref.: Mail

Ref.Date : 01/02/2021

Sample Particulars : **Sample**

Qty. Received : 1No. Vial

Test Parameters : Iron as Fe,Tungsten as W,Sodium as Na

Date of Receipt of Sample : 01/02/2021
Date of Starting of Analysis : 03/02/2021
Date of completion of analysis : 05/02/2021

SAMPLE TESTED AS RECEIVED

TEST RESULTS

S.No.	**Parameters**	**UOM**	**Results**
1	Iron as Fe	% by mass	7.83
2	Tungsten as W	% by mass	51.08
3	Sodium as Na	% by mass	<0.01

Instrument Used: ICP-OES Varian 720-ES

NOTE : This report and results relate only to the sample / items tested.

Figure A2.9. Results of ICP-OES analysis of the compound $\mathbf{\{W_{72}Fe_{30}\}_{NM}}$ that gives the metal proportion present in the compound.

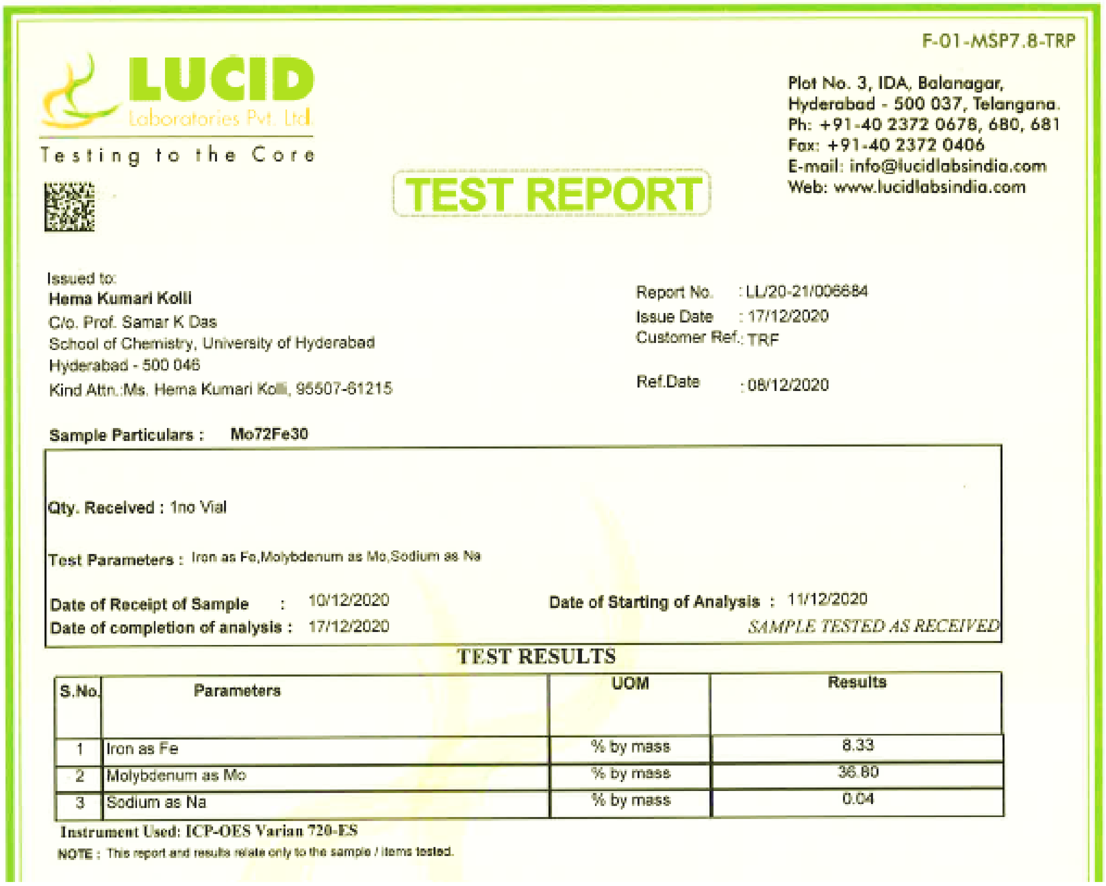

F-01-MSP7.8-TRP

LUCID
Laboratories Pvt. Ltd.
Testing to the Core

TEST REPORT

Plot No. 3, IDA, Balanagar,
Hyderabad - 500 037, Telangana.
Ph: +91-40 2372 0678, 680, 681
Fax: +91-40 2372 0406
E-mail: info@lucidlabsindia.com
Web: www.lucidlabsindia.com

Issued to:
Hema Kumari Kolli
C/o. Prof. Samar K Das
School of Chemistry, University of Hyderabad
Hyderabad - 500 046
Kind Attn.:Ms. Hema Kumari Kolli, 95507-61215

Report No. : LL/20-21/006684
Issue Date : 17/12/2020
Customer Ref.: TRF
Ref.Date : 08/12/2020

Sample Particulars : Mo72Fe30

Qty. Received : 1no Vial

Test Parameters : Iron as Fe,Molybdenum as Mo,Sodium as Na

Date of Receipt of Sample : 10/12/2020
Date of Starting of Analysis : 11/12/2020
Date of completion of analysis : 17/12/2020

SAMPLE TESTED AS RECEIVED

TEST RESULTS

S.No.	Parameters	UOM	Results
1	Iron as Fe	% by mass	8.33
2	Molybdenum as Mo	% by mass	36.80
3	Sodium as Na	% by mass	0.04

Instrument Used: ICP-OES Varian 720-ES

NOTE : This report and results relate only to the sample / items tested.

Figure A2.10. Results of ICP-OES analysis of the compound **$\{Mo_{72}Fe_{30}\}_{NM}$** that gives the metal proportion present in the compound.

Section A2.10. Carbon and hydrogen analysis of $\{W_{72}Fe_{30}\}_{NM}$ and $\{Mo_{72}Fe_{30}\}_{NM}$

Sample Name	Elements	Carbon	Hydrogen
$\{Mo_{72}Fe_{30}\}_{NM}$	Calculated	0.52%	3.31%
	Observed	0.62%	2.55%
$\{W_{72}Fe_{30}\}_{NM}$	Calculated	0.19%	2.41%
	Observed	Not Detected	1.58%

Table A2.3. Comparison of carbon and hydrogen elemental composition of the compounds **$\{Mo_{72}Fe_{30}\}_{NM}$** and **$\{W_{72}Fe_{30}\}_{NM}$**, results from elemental analysis and theoretically obtained compositions respectively.

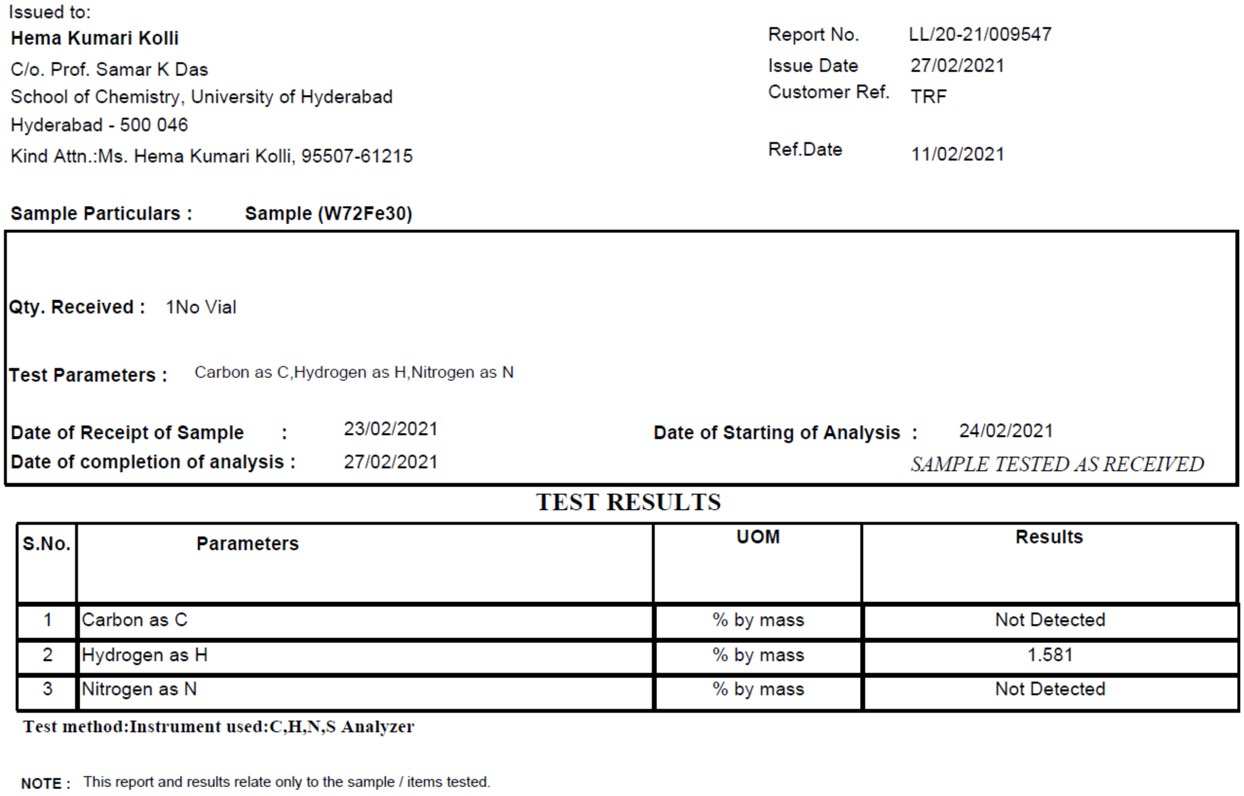

Issued to:
Hema Kumari Kolli
C/o. Prof. Samar K Das
School of Chemistry, University of Hyderabad
Hyderabad - 500 046
Kind Attn.:Ms. Hema Kumari Kolli, 95507-61215

Report No. LL/20-21/009547
Issue Date 27/02/2021
Customer Ref. TRF
Ref.Date 11/02/2021

Sample Particulars : **Sample (W72Fe30)**

Qty. Received : 1No Vial

Test Parameters : Carbon as C,Hydrogen as H,Nitrogen as N

Date of Receipt of Sample : 23/02/2021
Date of Starting of Analysis : 24/02/2021
Date of completion of analysis : 27/02/2021
SAMPLE TESTED AS RECEIVED

TEST RESULTS

S.No.	Parameters	UOM	Results
1	Carbon as C	% by mass	Not Detected
2	Hydrogen as H	% by mass	1.581
3	Nitrogen as N	% by mass	Not Detected

Test method:Instrument used:C,H,N,S Analyzer

NOTE : This report and results relate only to the sample / items tested.

Figure A2.11. Results of CHNS elemental analysis of the compound **$\{W_{72}Fe_{30}\}_{NM}$** that gives the carbon and hydrogen proportion present in the compound.

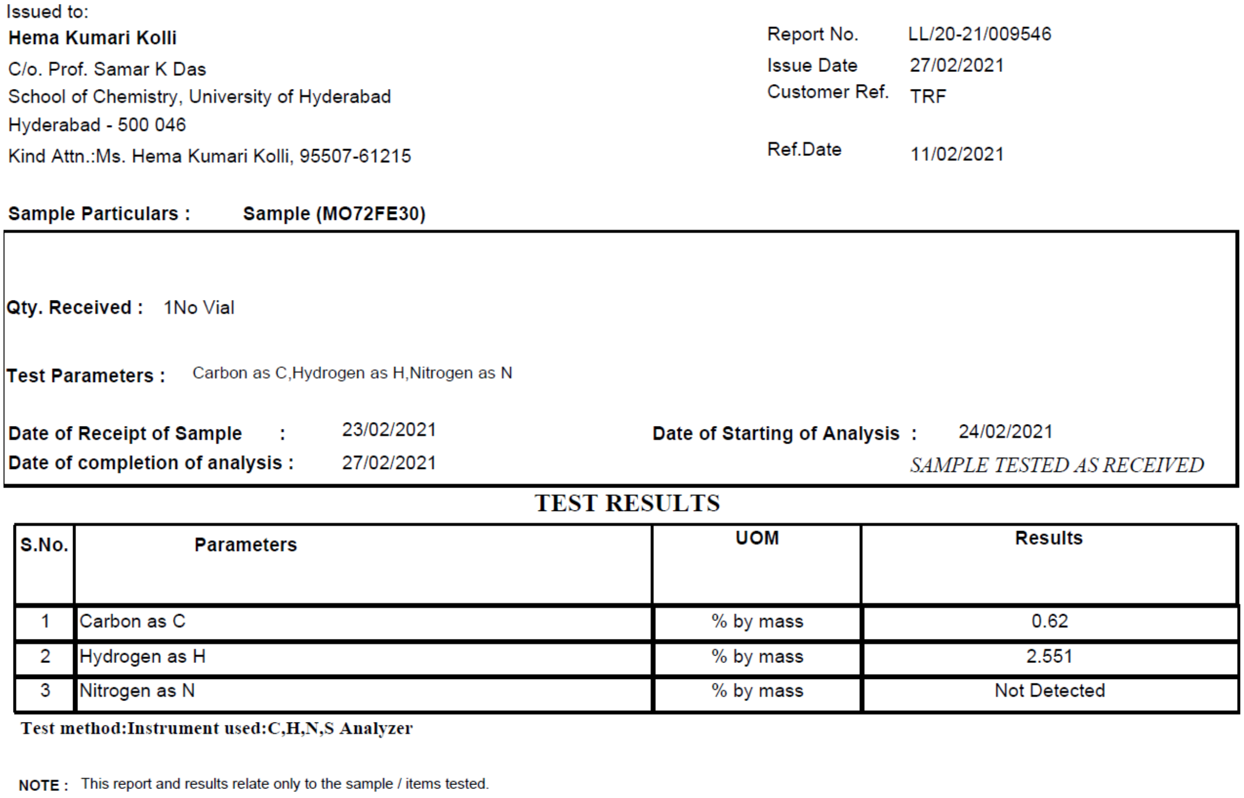

Issued to:
Hema Kumari Kolli
C/o. Prof. Samar K Das
School of Chemistry, University of Hyderabad
Hyderabad - 500 046
Kind Attn.:Ms. Hema Kumari Kolli, 95507-61215

Report No. LL/20-21/009546
Issue Date 27/02/2021
Customer Ref. TRF
Ref.Date 11/02/2021

Sample Particulars : **Sample (MO72FE30)**

Qty. Received : 1No Vial

Test Parameters : Carbon as C,Hydrogen as H,Nitrogen as N

Date of Receipt of Sample : 23/02/2021
Date of Starting of Analysis : 24/02/2021
Date of completion of analysis : 27/02/2021
SAMPLE TESTED AS RECEIVED

TEST RESULTS

S.No.	Parameters	UOM	Results
1	Carbon as C	% by mass	0.62
2	Hydrogen as H	% by mass	2.551
3	Nitrogen as N	% by mass	Not Detected

Test method:Instrument used:C,H,N,S Analyzer

NOTE : This report and results relate only to the sample / items tested.

Figure A2.12. Results of CHNS elemental analysis of the compound **{$Mo_{72}Fe_{30}$}$_{NM}$** that gives the carbon and hydrogen proportion present in the compound.

Carbon and hydrogen analyses of compounds **{$Mo_{72}Fe_{30}$}$_{NM}$** and **{$W_{72}Fe_{30}$}$_{NM}$** showing carbon analysis as 0.62 % (theoretical value 0.52%) and hydrogen analysis as 2.55% (theoretical value 3.31%) consistent with four acetate anions and 180 water molecules for the compound **{$Mo_{72}Fe_{30}$}$_{NM}$** as shown in the Figure A2.12 and Table A2.3**,** whereas for the compound **{$W_{72}Fe_{30}$}$_{NM}$** , it does not show any carbon, because less amount of carbon is present which was not able to be detected (theoretical value 0.19%) and hydrogen analysis as 1.58% (theoretical value 2.41%) consistent with two acetate anions and 180 water molecules as shown in the Figure A2.11 and Table A2.3. In order to conform the presence of acetate ligands in the compound **{$W_{72}Fe_{30}$}$_{NM}$,** we have carried out the TGA-GCMS for the sample as shown in the Figure A2.4.

Section S11. Zeta potential measurement of {$W_{72}Fe_{30}$}$_{NM}$ and {$Mo_{72}Fe_{30}$}$_{NM}$

For this analysis the compound was suspended in water and sonicated for 20 minutes for the uniform dispersion. Both the compounds **{$W_{72}Fe_{30}$}$_{NM}$** and **{$Mo_{72}Fe_{30}$}$_{NM}$** has been proved that they are negatively charged on the surface of the nanoparticles that was proved by the zeta potential studies as shown in the Figure A2.13 and A2.14 giving the values around -34.6 mV and -16.1 mV respectively.

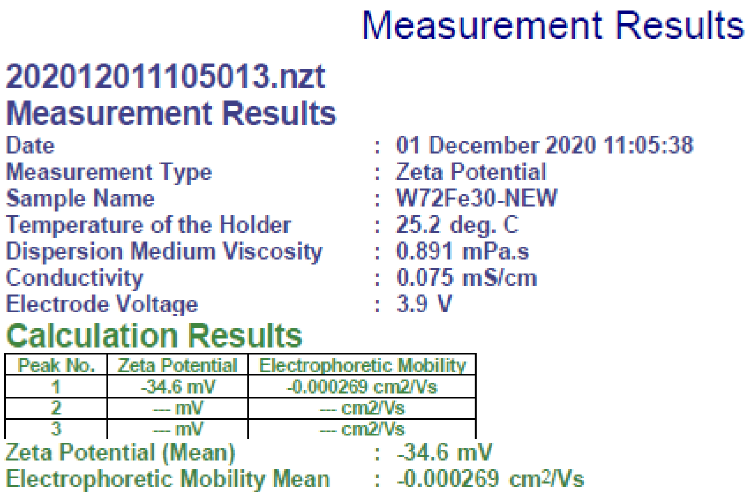

Measurement Results

202012011105013.nzt

Measurement Results

Date	: 01 December 2020 11:05:38
Measurement Type	: Zeta Potential
Sample Name	: W72Fe30-NEW
Temperature of the Holder	: 25.2 deg. C
Dispersion Medium Viscosity	: 0.891 mPa.s
Conductivity	: 0.075 mS/cm
Electrode Voltage	: 3.9 V

Calculation Results

Peak No.	Zeta Potential	Electrophoretic Mobility
1	-34.6 mV	-0.000269 cm2/Vs
2	--- mV	--- cm2/Vs
3	--- mV	--- cm2/Vs

Zeta Potential (Mean)	: -34.6 mV
Electrophoretic Mobility Mean	: -0.000269 cm2/Vs

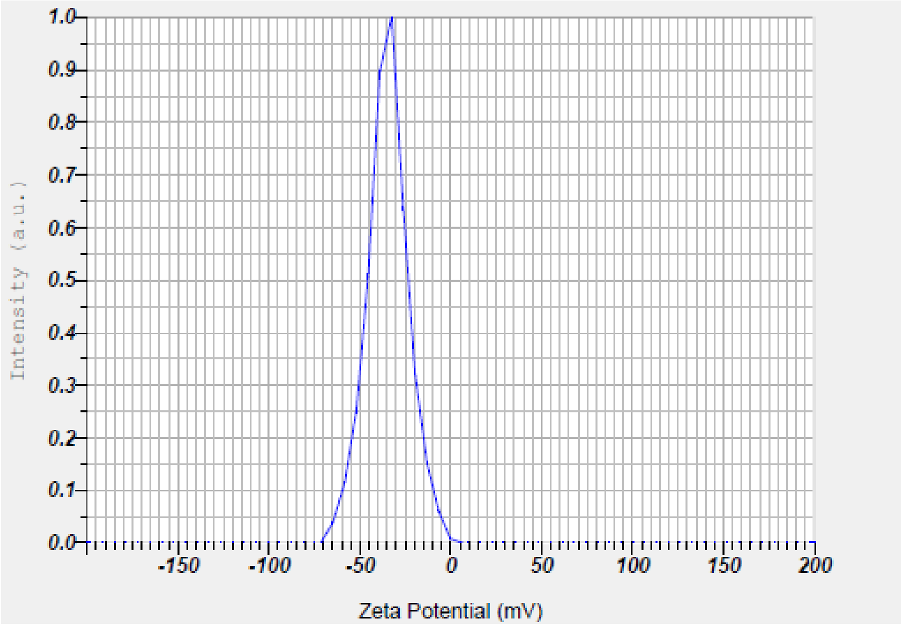

Figure A2.**13.** Zeta potential phase plot of $\{\mathbf{W_{72}Fe_{30}}\}_{\mathbf{NM}}$.

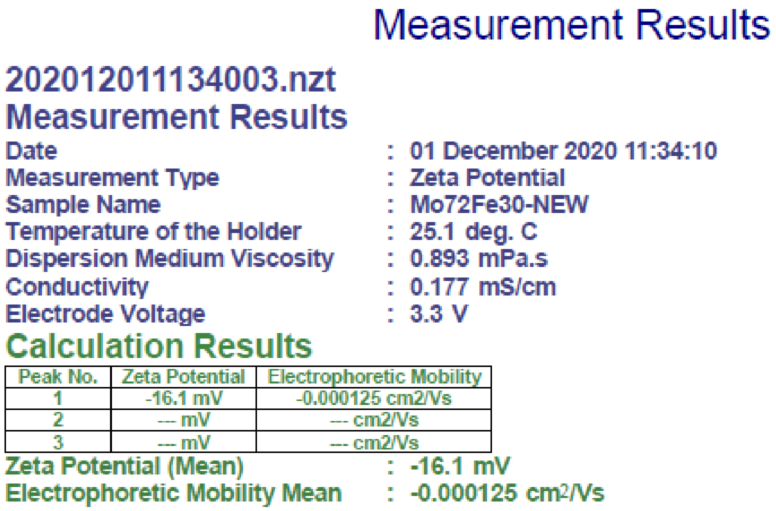

Measurement Results

202012011134003.nzt
Measurement Results

Date : 01 December 2020 11:34:10
Measurement Type : Zeta Potential
Sample Name : Mo72Fe30-NEW
Temperature of the Holder : 25.1 deg. C
Dispersion Medium Viscosity : 0.893 mPa.s
Conductivity : 0.177 mS/cm
Electrode Voltage : 3.3 V

Calculation Results

Peak No.	Zeta Potential	Electrophoretic Mobility
1	-16.1 mV	-0.000125 cm2/Vs
2	--- mV	--- cm2/Vs
3	--- mV	--- cm2/Vs

Zeta Potential (Mean) : -16.1 mV
Electrophoretic Mobility Mean : -0.000125 cm2/Vs

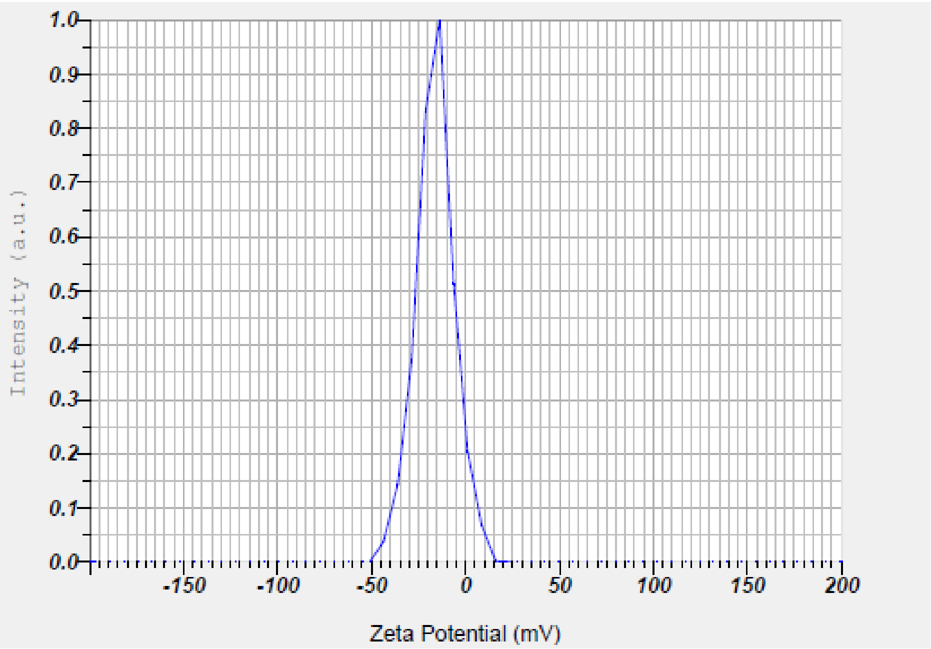

Figure A2.**14.** Zeta potential phase plot of **$\{Mo_{72}Fe_{30}\}_{NM}$**.

Section A2.**12. Dynamic light scattering (DLS) studies of $\{W_{72}Fe_{30}\}_{NM}$ and $\{Mo_{72}Fe_{30}\}_{NM}$.**

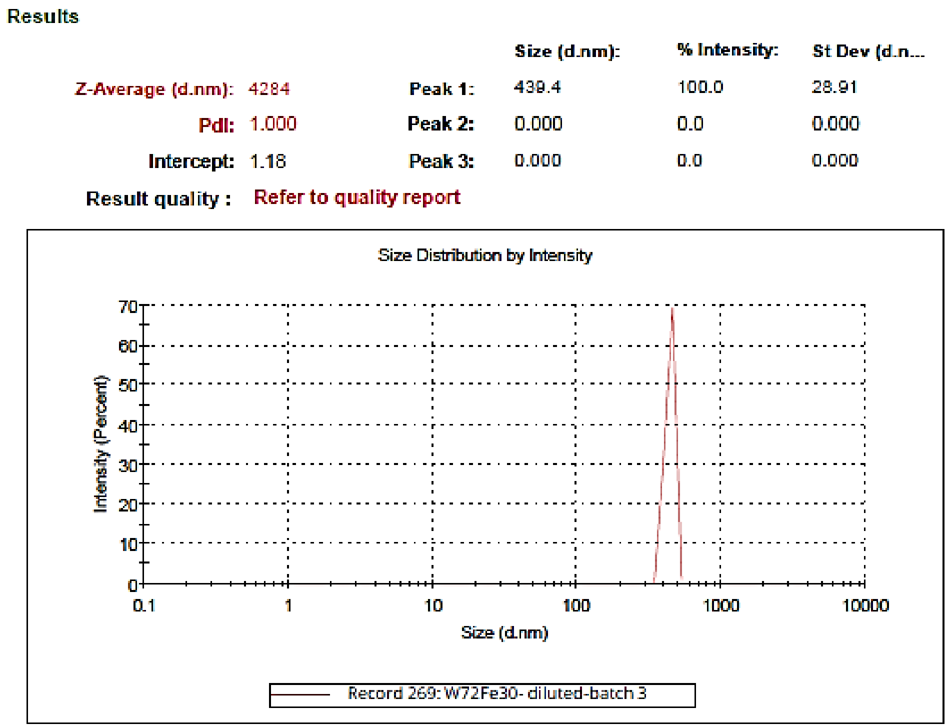

Results

			Size (d.nm):	% Intensity:	St Dev (d.n...
Z-Average (d.nm):	4284	Peak 1:	439.4	100.0	28.91
PdI:	1.000	Peak 2:	0.000	0.0	0.000
Intercept:	1.18	Peak 3:	0.000	0.0	0.000

Result quality : Refer to quality report

Figure A2.15. Size distribution plot from DLS of the compound **{$W_{72}Fe_{30}$}$_{NM}$** (Compound was suspended in water and then sonicated for 20 minutes).

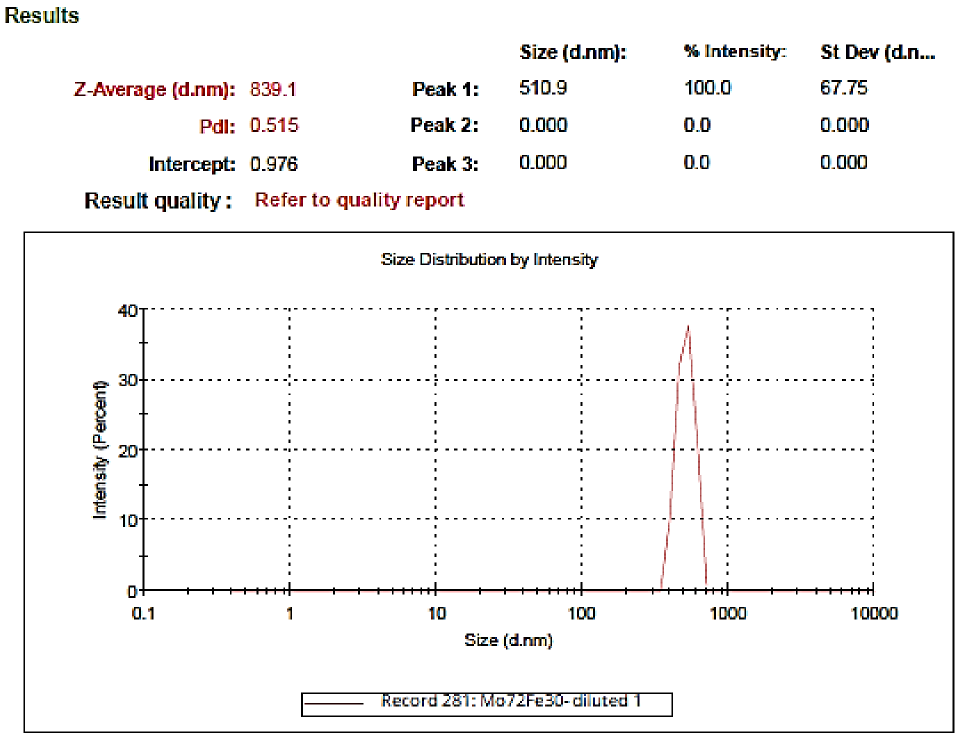

Results

			Size (d.nm):	% Intensity:	St Dev (d.n...
Z-Average (d.nm):	839.1	Peak 1:	510.9	100.0	67.75
PdI:	0.515	Peak 2:	0.000	0.0	0.000
Intercept:	0.976	Peak 3:	0.000	0.0	0.000

Result quality : Refer to quality report

FigureA.2.16. Size distribution plot from DLS of the compound **{$Mo_{72}Fe_{30}$}$_{NM}$** (compound was suspended in water and then sonicated for 20 minutes).

Section A2.13. Gas adsorption studies.

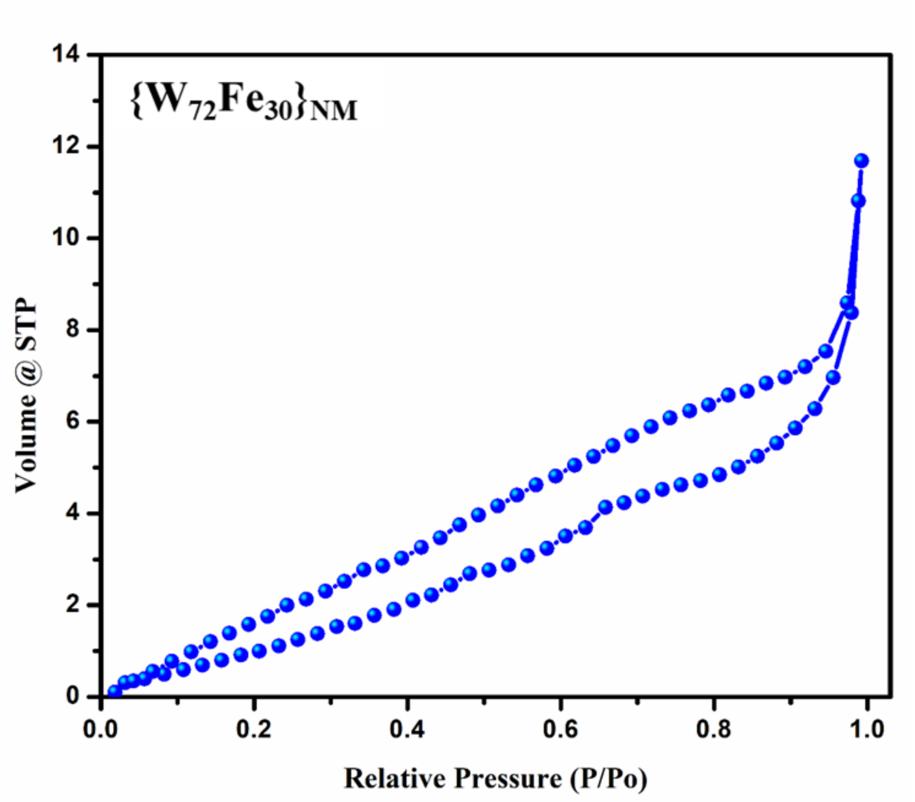

Figure A2.17. Gas adsorption isotherm of the amorphous compound **{$W_{72}Fe_{30}$}$_{NM}$**.

Surface porosity of the amorphous compound **{$W_{72}Fe_{30}$}$_{NM}$** is measured by nitrogen gas adsorption study. Initially, the sample was degassed at 120º C for 2 hrs under reduced pressure and then we have measured the adsorption isotherm with nitrogen gas using liquid nitrogen bath. According to the BET classification, the observed shape of the nitrogen adsorption isotherm belongs to TYPE III as shown in Figure A2.17. The BET surface area for the compound **{$W_{72}Fe_{30}$}$_{NM}$** is 5.345 m^2g^{-1}. The average pore volume and average pore width of the material **{$W_{72}Fe_{30}$}$_{NM}$** are 0.0117 cc/g and 43.95 Å (around 4 nm) respectively. According to the results, it is observed that the nature of adsorption isotherm for this material is type III macroporous material.

Section A2.14. Electrocatalytic hydrogen evolution

Quantitative hydrogen evolution experiment.

Bulk electrolysis was carried out for the both **{$Mo_{72}Fe_{30}$}$_{NM}$** and **{$W_{72}Fe_{30}$}$_{NM}$** compounds respectively at a constant current density of 1 mA/cm^2 for a period of 5 h with the help of two electrode system in a home built electrolysis setup. Fluorinated tin oxide (FTO) glass substrate of surface area 0.6 cm^2 was used as a working electrode (anode) where the measured amount of sample coated on the surface of the FTO glass substrate whereas a large platinum wire was used as a counter electrode (cathode) and 0.1M Na_2SO_4 solution of pH 2.5 was used as an electrolyte. The loading of the catalyst on the FTO glass substrate was 0.2 mg/cm^2. The hydrogen bubbles evolved at the FTO electrode during the electrolysis where gradually collected in a graduated tube of home-built electrolysis setup as shown in Figure A2.18 which is initially filled with an electrolyte and slowly it has been displaced with these hydrogen gas bubbles. The oxygen gas which was evolved at the counter electrode could not mix up with the hydrogen gas evolved at working electrode because the setup was built in such a way that gas evolved in the cathodic chamber could not enter into the anodic chamber. The two chambers were separated from each other by an inverted glass tube and a small window has been kept open between them to maintain the electrical continuity.[1]

(a) (b) (c)

Figure A2.18. Home built electrolysis setup for quantitative determination of gas evolved, used to calculate the Faradic efficiency of the compounds **$\{Mo_{72}Fe_{30}\}_{NM}$** and **$\{W_{72}Fe_{30}\}_{NM}$**.

Calculation of Faradaic Efficiency of $\{Mo_{72}Fe_{30}\}_{NM}$:

The amount hydrogen evolved from the above quantitative measurement in bulk electrolysis at constant current for a time period of 5 h under 1 atm pressure is 0.14 mL/hour.

As we know 22.4 liters is equal to 1 mol, so that 1 mL = (1/22400) mol = 4.464 x 10^{-5} mol.

Thus, the amount of hydrogen evolved in 1 hour = 0.14 x (4.464 x 10^{-5}) mol = 6.25 x 10^{-6} mol.

Whereas the ideal number of moles the hydrogen gas to be evolved is

$$H_2\text{ (ideal)} = \frac{\text{Q (total charge employed)}}{\text{n (no. of electrons required for the chemical change) x 1 Farad}}$$

Where n is 2 for hydrogen evolution reaction as it is a two-electron process and we have employed current of 600µA.

We know that, $$\text{Current (i)} = \frac{dQ}{dt}$$

Here, H_2 (ideal) for 1 h = (0.6 x 10^{-3} x 3600)/(2 x 96500) mol = 11.19 x 10^{-6} mol.

Therefore, the formula for Faradaic Efficiency is

$$\text{Faradaic Efficiency} = \frac{\text{Moles of Hydrogen Evolved by experiment}}{\text{Moles of Hydrogen Evolved by ideal}} \text{ x } 100$$

Finally, Faradaic Efficiency of **$\{Mo_{72}Fe_{30}\}_{NM}$** = {(6.25 x 10^{-6})/(11.19 x 10^{-6})} x 100 = **55.85%**

Calculation of Faradaic efficiency of $\{W_{72}Fe_{30}\}_{NM}$:

The amount hydrogen evolved from the above quantitative measurement in bulk electrolysis at constant current for a time period of 5 h under 1 atm pressure is 0.18 mL/hour.

As we know 22.4 liters is equal to 1 mol, so that 1 mL = (1/22400) mol = 4.464 x 10^{-5} mol.

Thus, the amount of hydrogen evolved in 1 hour = 0.18 x (4.464 x 10^{-5}) mol = 8.04 x 10^{-6} mol.

Whereas the ideal number of moles the hydrogen gas to be evolved is

$$H_2\text{ (ideal)} = \frac{\text{Q (total charge employed)}}{\text{n (no. of electrons required for the chemical change) x 1 Farad}}$$

Where n is 2 for Hydrogen Evolution reaction as it is a two-electron process and we have employed current of 600µA.

We know that, $$\text{Current (i)} = \frac{dQ}{dt}$$

Here, H_2 (ideal) for 1 h = $(0.6 \times 10^{-3} \times 3600)/(2 \times 96500)$ mol = 11.19×10^{-6} mol.

Therefore, the formula for Faradaic Efficiency is

$$\text{Faradaic Efficiency} = \frac{\text{Moles of Hydrogen Evolved by experiment}}{\text{Moles of Hydrogen Evolved by ideal}} \times 100$$

Finally, Faradaic Efficiency of $\mathbf{\{W_{72}Fe_{30}\}_{NM}}$ = $\{(8.04 \times 10^{-6})/(11.19 \times 10^{-6})\} \times 100$ = **71.85%**

Section A2.15. Gas chromatography (GC) of hydrogen which was evolved electrochemically from the clusters $\{W_{72}Fe_{30}\}_{NM}$ and $\{Mo_{72}Fe_{30}\}_{NM}$

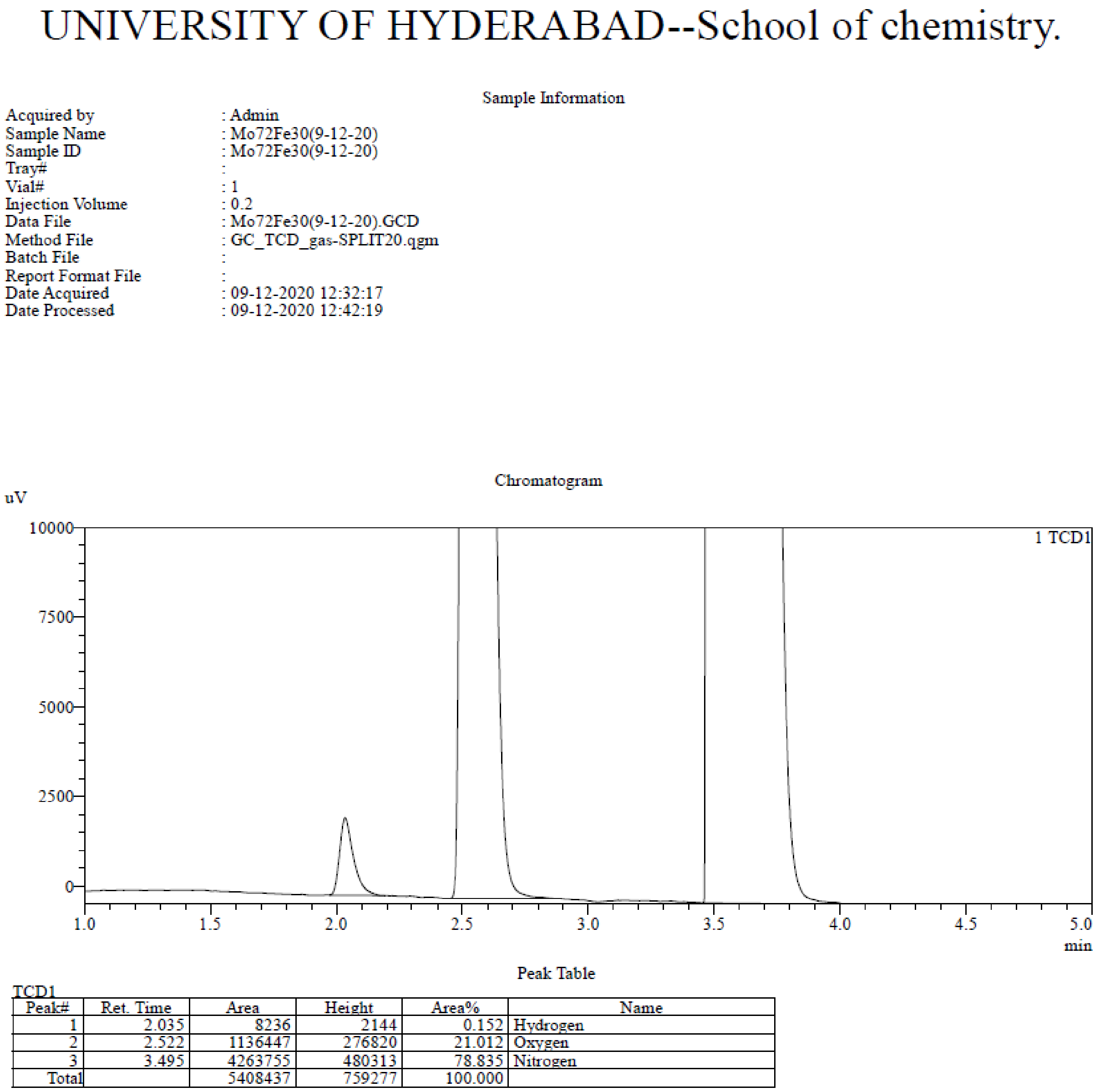

UNIVERSITY OF HYDERABAD--School of chemistry.

Sample Information

Acquired by : Admin
Sample Name : Mo72Fe30(9-12-20)
Sample ID : Mo72Fe30(9-12-20)
Tray# :
Vial# : 1
Injection Volume : 0.2
Data File : Mo72Fe30(9-12-20).GCD
Method File : GC_TCD_gas-SPLIT20.qgm
Batch File :
Report Format File :
Date Acquired : 09-12-2020 12:32:17
Date Processed : 09-12-2020 12:42:19

Chromatogram

Peak Table

TCD1

Peak#	Ret. Time	Area	Height	Area%	Name
1	2.035	8236	2144	0.152	Hydrogen
2	2.522	1136447	276820	21.012	Oxygen
3	3.495	4263755	480313	78.835	Nitrogen
Total		5408437	759277	100.000	

Figure A2.19. Gas chromatogram of the gas sample evolved during the electrolysis of the compound **$\{Mo_{72}Fe_{30}\}_{NM}$** which clearly indicates that the hydrogen gas was collected at the headspace of the home built setup.

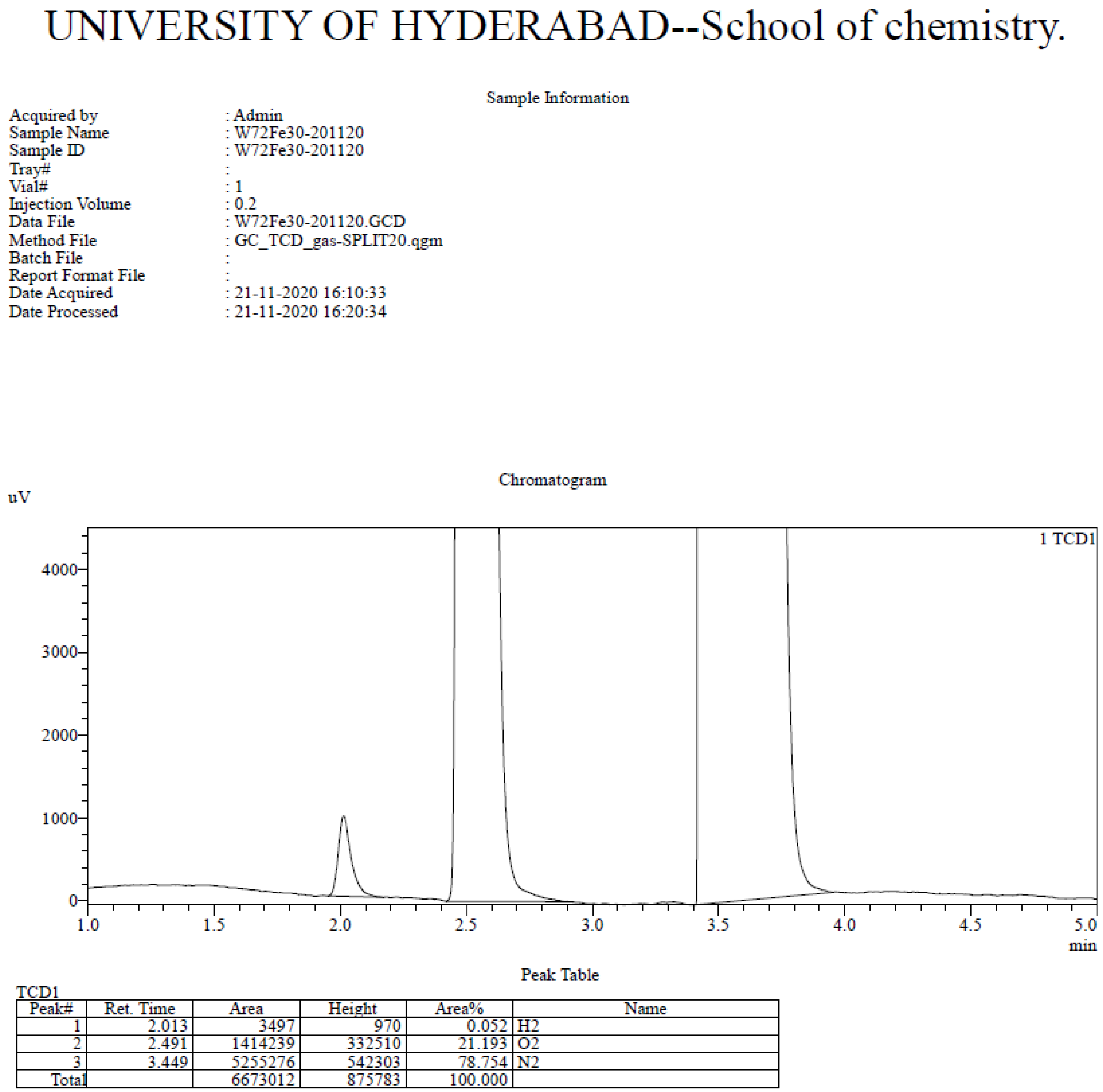

UNIVERSITY OF HYDERABAD--School of chemistry.

Sample Information

Acquired by	: Admin
Sample Name	: W72Fe30-201120
Sample ID	: W72Fe30-201120
Tray#	:
Vial#	: 1
Injection Volume	: 0.2
Data File	: W72Fe30-201120.GCD
Method File	: GC_TCD_gas-SPLIT20.qgm
Batch File	:
Report Format File	:
Date Acquired	: 21-11-2020 16:10:33
Date Processed	: 21-11-2020 16:20:34

Chromatogram

Peak Table

TCD1

Peak#	Ret. Time	Area	Height	Area%	Name
1	2.013	3497	970	0.052	H2
2	2.491	1414239	332510	21.193	O2
3	3.449	5255276	542303	78.754	N2
Total		6673012	875783	100.000	

Figure A2.20. Gas chromatogram of the gas sample evolved during the electrolysis of the compound **$\{W_{72}Fe_{30}\}_{NM}$** which clearly indicates that the hydrogen gas was collected at the headspace of the home built setup.

Section A2.16. TOF calculation[2]

TOF of both electrocatalyst **$\{W_{72}Fe_{30}\}_{NM}$** and **$\{Mo_{72}Fe_{30}\}_{NM}$** can be calculated from the equation, TOF = (I/2mF), where I, m and F correspond to current (in A), number of active sites (in mole) and Faraday constant (in C mol^{-1}) and the value two signifies that number of electrons required to generate one hydrogen molecule from two protons. The number of active sites can be calculated from the equation, m = (Q/2F), where, Q corresponds to charge (in A s) and the value two signifies that both the electrocatalyst involve in two electrons reduction for HER. Now, the resulting formula for TOF calculation can be written as, TOF = (I/Q). The current can be calculated from chronoamperometric measurement and charge can be calculated by integrating current versus time plot, obtained from CV recorded under non-catalytic condition (in THF medium, Tetrabutylammonium perchlorate as supporting electrolyte and glassy carbon as working electrode).

TOF of $\{Mo_{72}Fe_{30}\}_{NM}$: From the chronoamperometric measurement of **$\{Mo_{72}Fe_{30}\}_{NM}$**, the current value was observed to be – 5.5995 x 10^{-5} A (Figure 5c). The charge was calculated by integrating current versus time plot (within the potential range -0.5655V to -1.1080V) generated from CV, recorded under non-catalytic condition and calculated charge value was observed to be -1.231 x 10^{-4} A s [Figure A2.21 (a)]. Now,

$$\text{TOF} = (-5.5995 \times 10^{-5})\ \text{A} / (-1.231 \times 10^{-4})\ \text{A s}$$
$$= 0.45\ s^{-1}$$

TOF of $\{W_{72}Fe_{30}\}_{NM}$: From the Chronoamperometric measurement of **$\{W_{72}Fe_{30}\}_{NM}$**, the current value was observed to be – 8.6042 x 10^{-5} A (Figure 5d). The charge was calculated by integrating current versus time plot (within the potential range -0.5655V to -1.1080V) generated from CV, recorded under non-catalytic condition and calculated charge value was observed to be -1.189 x 10^{-4} A s [Figure A2.21 (b)]. Now,

$$\text{TOF} = (-8.6042 \times 10^{-5})\ \text{A} / (-1.189 \times 10^{-4})\ \text{A s}$$
$$= 0.72\ s^{-1}$$

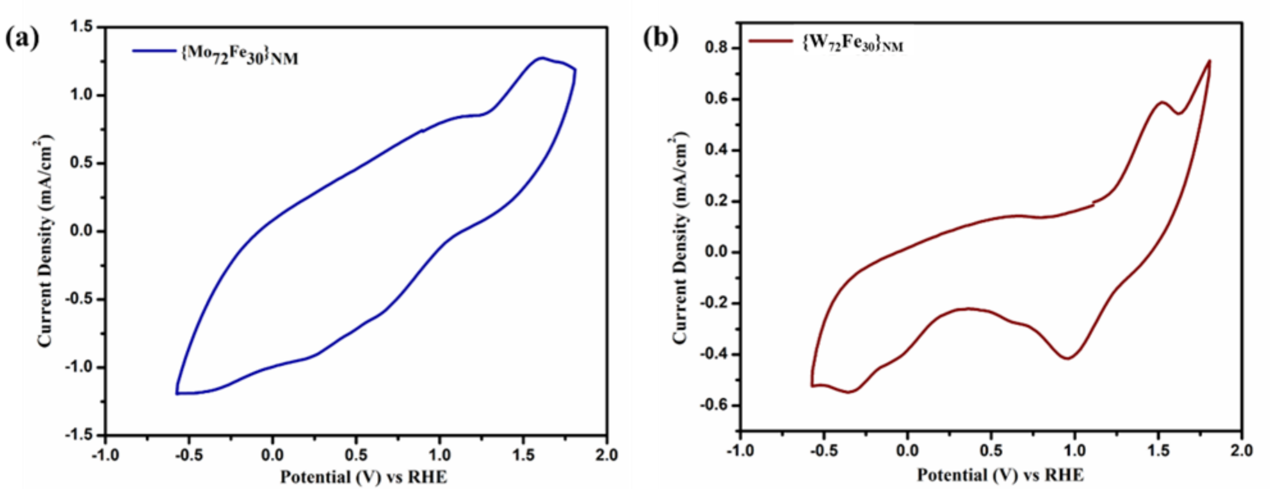

Figure A2.21. (a) CV of **$\{Mo_{72}Fe_{30}\}_{NM}$** in THF (tetrabutylammonium perchlorate as supporting electrolyte) on glassy carbon electrode. (b) CV of **$\{W_{72}Fe_{30}\}_{NM}$** in THF (tetrabutylammonium perchlorate as supporting electrolyte) on glassy carbon electrode.

Section A2.17. PCET calculation[3]

For a half cell reaction where both protons and electrons are involved,

$$Ox + mH^{+} + ne^{-} \longrightarrow Red(H)_{m}^{(m-n)+} \quad \ldots\ldots\ldots\ldots\ldots\ldots\ldots \text{(i)}$$

The Nernst equation can be written as,

$$E = E^{0} + (0.059m/n)*pH \quad \ldots\ldots\ldots\ldots\ldots\ldots\ldots\ldots\ldots\ldots\ldots \text{(ii)}$$

The slope (0.059m/n) can be obtained from the potential (E) and pH plot using the linear equation (ii)

In case of $\{Mo_{72}Fe_{30}\}_{NM}$, the slope from the plot of potential versus pH was observed to be 373 mV/pH (Figure 8c). Since, Muller and their co-workers reported that guest-free $\{Mo_{72}Fe_{30}\}$-type polyoxometalate (POM) cluster involved in electrochemical reduction by two electrons, the value of “n” should be two.[4] Now,

$$(0.059m/n) = 373 \times 10^{-3}$$

$$\text{So, } m = (373 \times 10^{-3} \times 2)/0.059 = 13$$

It was calculated from observed slope value that **$\{Mo_{72}Fe_{30}\}_{NM}$** involves in HER via proton-coupled electron transfer where thirteen protons and two electrons ($13H^{+}$ and $2e^{-}$) were involved.

In case of $\{W_{72}Fe_{30}\}_{NM}$, the slope from the plot of potential versus pH was observed to be 324 mV/pH (Figure 8d). Since, Muller and their co-workers reported that guest-free $\{Mo_{72}Fe_{30}\}$-type polyoxometalate (POM) cluster involved in electrochemical reduction by two electrons, the value of "n" should be two.[4] Now,

$$(0.059m/n) = 324 \times 10^{-3}$$

$$\text{So, } m = (324 \times 10^{-3} \times 2)/0.059$$

$$m = 11$$

It was calculated from observed slope value that **$\{W_{72}Fe_{30}\}_{NM}$** involves in HER via proton-coupled electron transfer where eleven protons and two electrons ($11H^+$ and $2e^-$) were involved.

Section A2.18. Characterization of sample coated on the electrode and electrolyte after electrochemical analysis

The stability studies has been carried out to the samples **$\{Mo_{72}Fe_{30}\}_{NM}$** and **$\{W_{72}Fe_{30}\}_{NM}$** with the help of FESEM and EDX-elemental mapping for the coated samples and ICP-OES studies for the electrolyte samples after chronoamperometric measurement. The sample was prepared by taking 8mg of compound and 2mg of carbon black powder were mixed in a 2 mL of ethanol and water mixture solution. On the glassy carbon electrode which is having a geometrical area of 0.0706 (cm^2), the sample mixture of 10 μL was coated on the surface of the glassy carbon electrode. After the chronoamperometric measurement at onset potential of -1.0V for 2h, the electrolyte was tested with the ICP-OES analysis and Mo, Fe and W, Fe was found very less quantity in the case of **$\{Mo_{72}Fe_{30}\}_{NM}$** and **$\{W_{72}Fe_{30}\}_{NM}$** sample electrolyte respectively. It is observed that **$\{Mo_{72}Fe_{30}\}_{NM}$** and **$\{W_{72}Fe_{30}\}_{NM}$** compounds have very negligible leaching into the electrolytic solution during the chronoamperometric measurement.

ICP-OES analysis of electrolytic solution after chronoamperometric studies:

Results of ICP-OES for the electrolytic solution display very negligible quantity of sample leaching into electrolytic solution after chronoamperometric measurement. The reports were shown in the Figure A2.22 and A2.23.

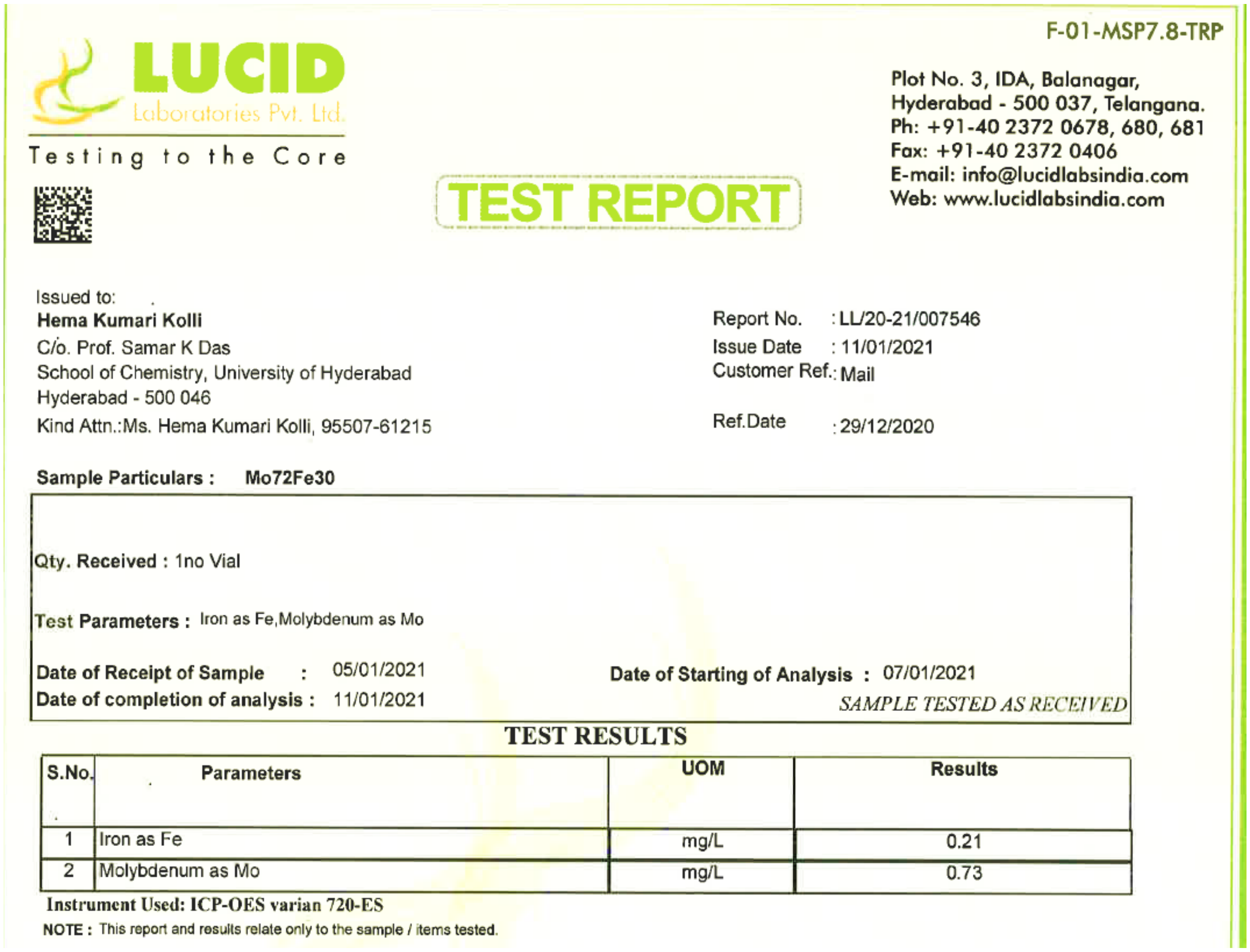

F-01-MSP7.8-TRP

LUCID
Laboratories Pvt. Ltd.
Testing to the Core

Plot No. 3, IDA, Balanagar,
Hyderabad - 500 037, Telangana.
Ph: +91-40 2372 0678, 680, 681
Fax: +91-40 2372 0406
E-mail: info@lucidlabsindia.com
Web: www.lucidlabsindia.com

TEST REPORT

Issued to:
Hema Kumari Kolli
C/o. Prof. Samar K Das
School of Chemistry, University of Hyderabad
Hyderabad - 500 046
Kind Attn.:Ms. Hema Kumari Kolli, 95507-61215

Report No. : LL/20-21/007546
Issue Date : 11/01/2021
Customer Ref.: Mail
Ref.Date : 29/12/2020

Sample Particulars : Mo72Fe30

Qty. Received : 1no Vial

Test Parameters : Iron as Fe,Molybdenum as Mo

Date of Receipt of Sample : 05/01/2021
Date of completion of analysis : 11/01/2021
Date of Starting of Analysis : 07/01/2021

SAMPLE TESTED AS RECEIVED

TEST RESULTS

S.No.	Parameters	UOM	Results
1	Iron as Fe	mg/L	0.21
2	Molybdenum as Mo	mg/L	0.73

Instrument Used: ICP-OES varian 720-ES

NOTE : This report and results relate only to the sample / items tested.

Figure A2.22. Results of ICP-OES analysis of the electrolytic solution of the compound **$\{Mo_{72}Fe_{30}\}_{NM}$** after chronoamperometric measurement for 2 hrs that gives the metal proportion present in the electrolyte.

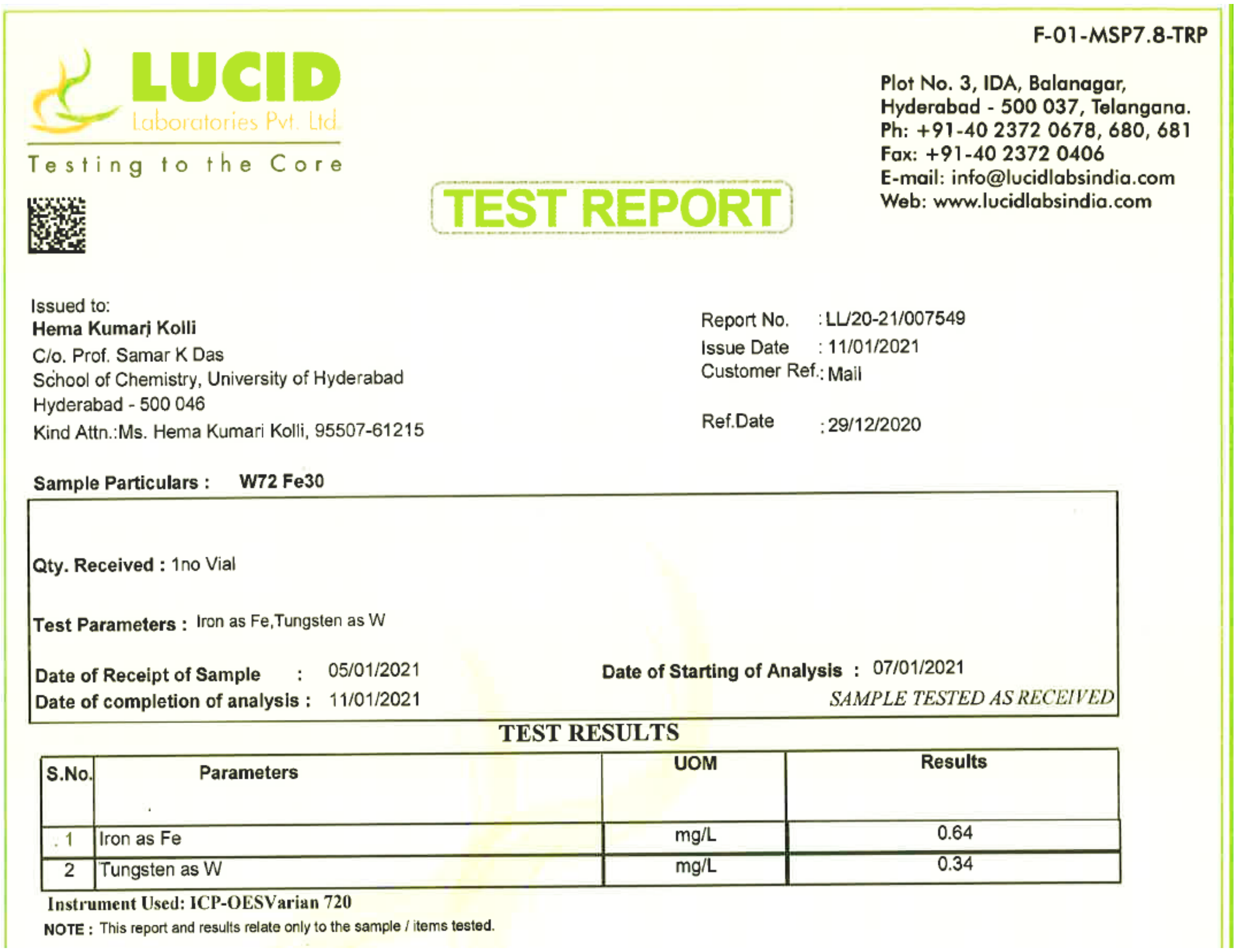

F-01-MSP7.8-TRP

LUCID
Laboratories Pvt. Ltd.
Testing to the Core

Plot No. 3, IDA, Balanagar,
Hyderabad - 500 037, Telangana.
Ph: +91-40 2372 0678, 680, 681
Fax: +91-40 2372 0406
E-mail: info@lucidlabsindia.com
Web: www.lucidlabsindia.com

TEST REPORT

Issued to:
Hema Kumari Kolli
C/o. Prof. Samar K Das
School of Chemistry, University of Hyderabad
Hyderabad - 500 046
Kind Attn.:Ms. Hema Kumari Kolli, 95507-61215

Report No. : LL/20-21/007549
Issue Date : 11/01/2021
Customer Ref.: Mail
Ref.Date : 29/12/2020

Sample Particulars : **W72 Fe30**

Qty. Received : 1no Vial

Test Parameters : Iron as Fe,Tungsten as W

Date of Receipt of Sample : 05/01/2021
Date of Starting of Analysis : 07/01/2021
Date of completion of analysis : 11/01/2021

SAMPLE TESTED AS RECEIVED

TEST RESULTS

S.No.	Parameters	UOM	Results
1	Iron as Fe	mg/L	0.64
2	Tungsten as W	mg/L	0.34

Instrument Used: ICP-OESVarian 720

NOTE : This report and results relate only to the sample / items tested.

Figure A2.23. Results of ICP-OES analysis of the electrolytic solution of the compound **$\{W_{72}Fe_{30}\}_{NM}$** after chronoamperometric measurement for 2 hrs that gives the metal proportion present in the electrolyte.

On the other hand, we have checked the stability of the catalysts with help of chronoamperometric measurements for 2 hrs by coating the sample on a carbon paper. We have analyzed the samples before and after the chronoamperometric measurement with the support of FESEM and EDX-elemental mapping as shown in the Figure A2.24, Figure A2.25, Figure A2.26 and Figure A2.27 by coating the same quantity of prepared sample i.e., 60uL before and after the chronoamperometric measurement.

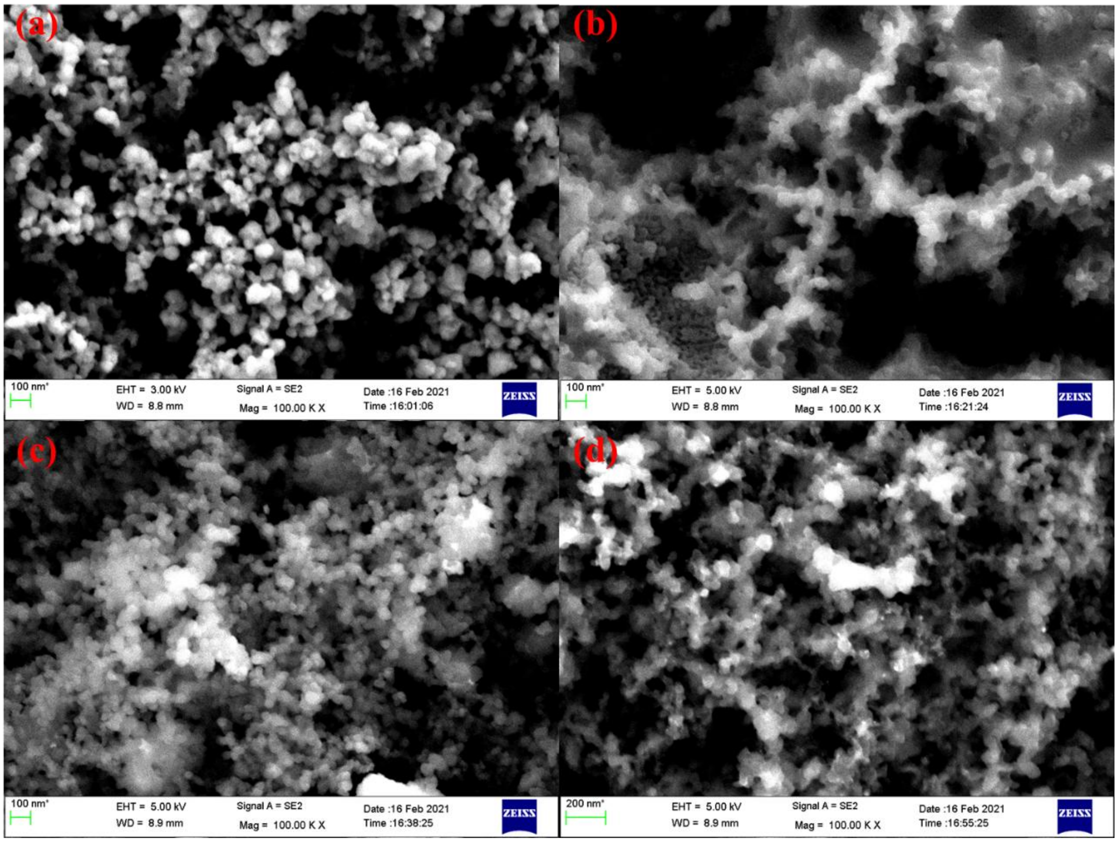

Figure A2.24. (a) and (b) are FESEM images of compound **$\{Mo_{72}Fe_{30}\}_{NM}$** before and after chronoamperometric measurement, whereas (c) and (d) are related to compound **$\{W_{72}Fe_{30}\}_{NM}$** before and after the chronoamperometric measurement, we have coated sample on carbon paper which is the working electrode.

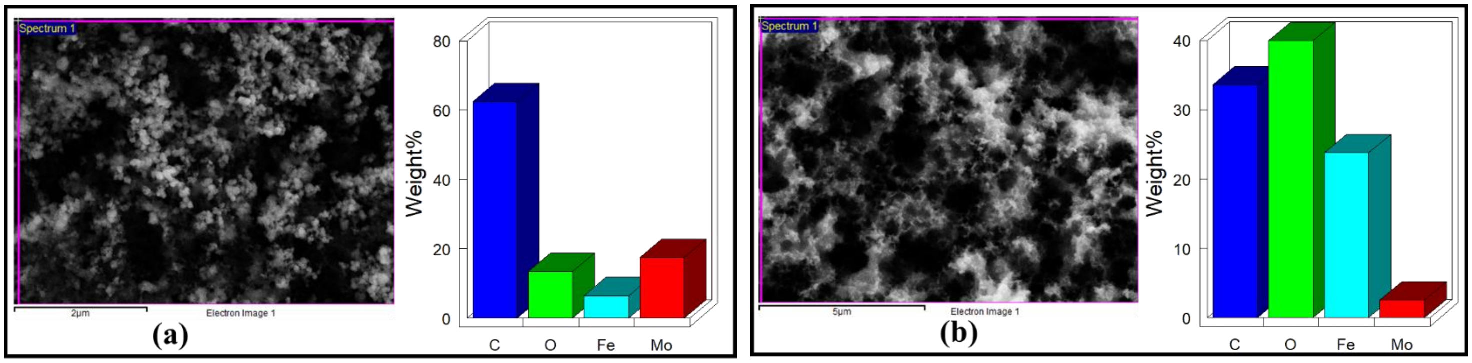

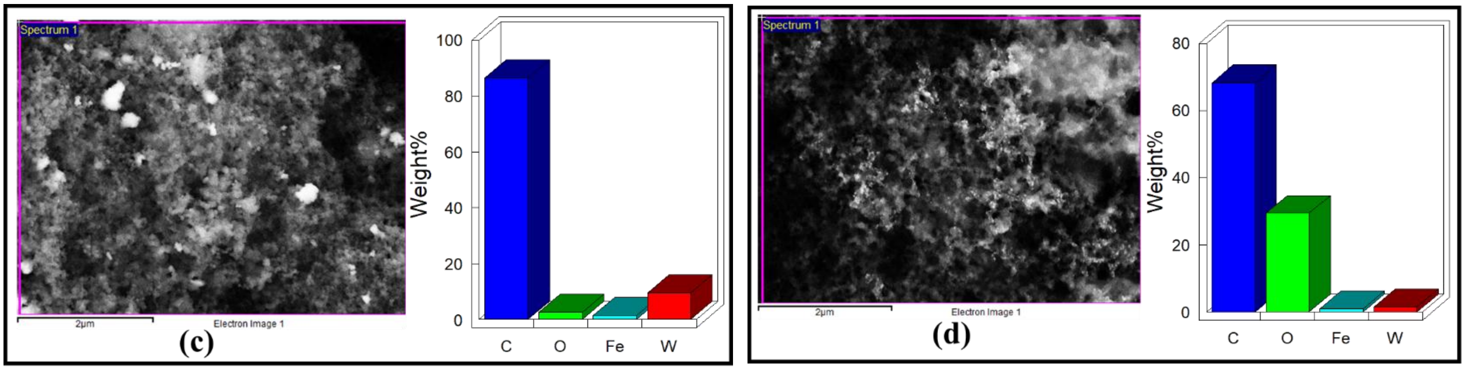

Figure A2.25. EDX-elemental analysis of compounds **$\{Mo_{72}Fe_{30}\}_{NM}$** and **$\{W_{72}Fe_{30}\}_{NM}$** mixed with carbon black and coated on the carbon paper (working electrode) before and after the chronoamperometric measurement, (a) and (b) are before and after measurement of the catalyst **$\{Mo_{72}Fe_{30}\}_{NM}$** whereas (c) and (d) are related to before and after measurement of catalyst **$\{W_{72}Fe_{30}\}_{NM}$** (chronoamperometric measurement in 0.1M Na_2SO_4 solution).

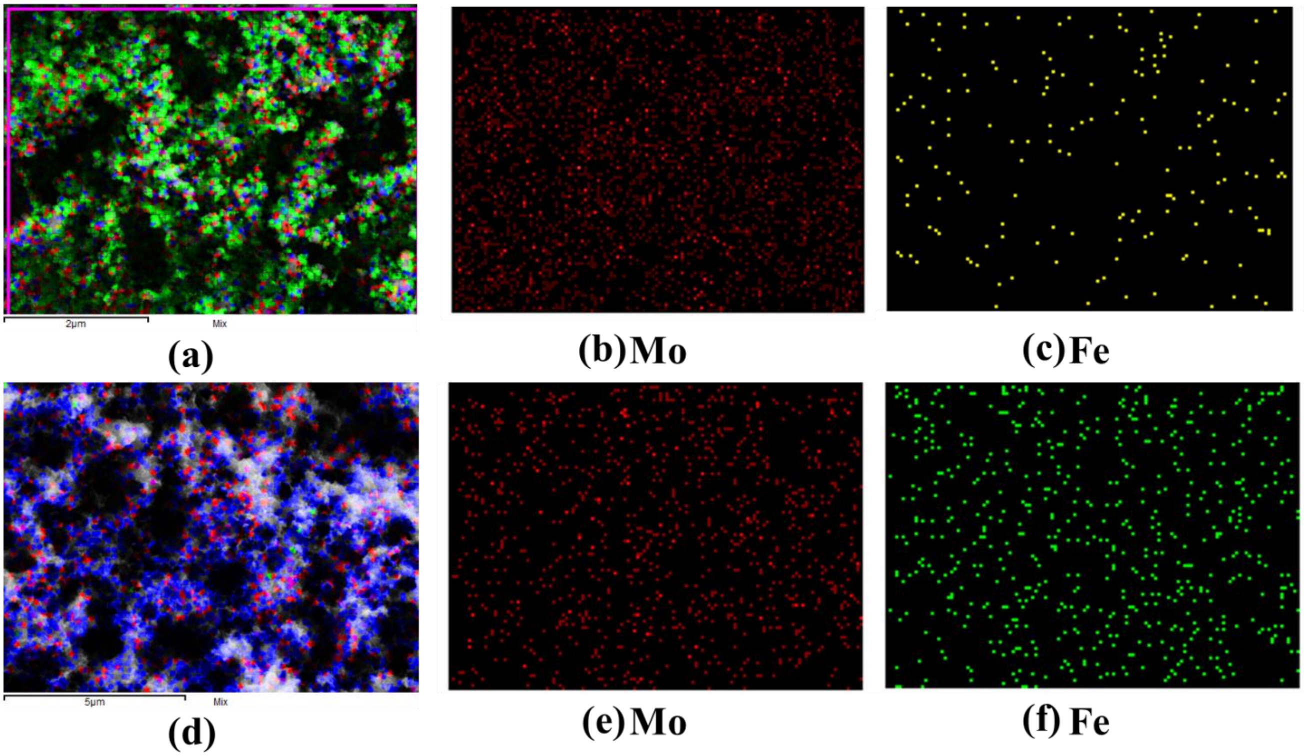

(a) (b)Mo (c)Fe

(d) (e)Mo (f) Fe

Figure A2.26. EDX-elemental mapping comparison of the carbon mixed sample **$\{Mo_{72}Fe_{30}\}_{NM}$** coated on carbon paper before and after the chronoamperometric measurement, (a), (b) and (c) are before and (d), (e) and (f) are after chronoamperometric measurement for 2 hrs in 0.1M Na_2SO_4 solution.

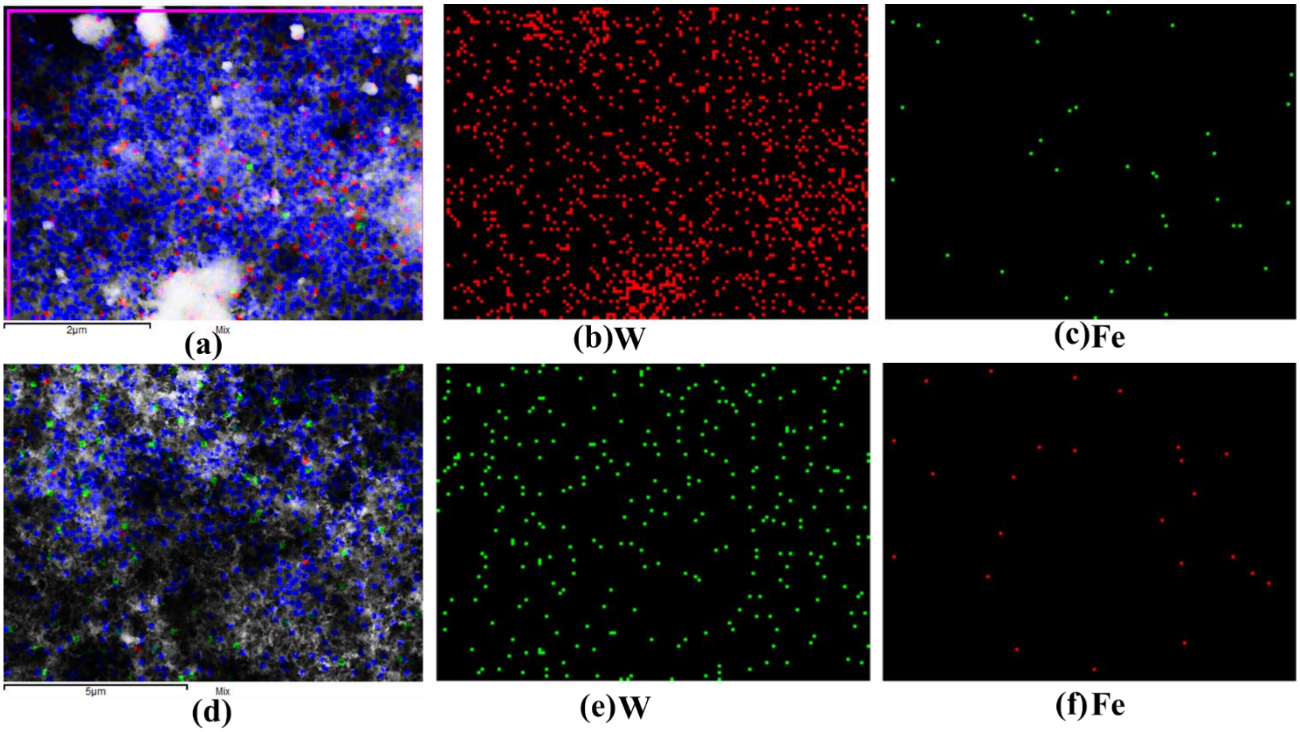

FigureA2.27. EDX-elemental mapping comparison of the carbon mixed sample **$\{W_{72}Fe_{30}\}_{NM}$** coated on carbon paper before and after the chronoamperometric measurement, (a), (b) and (c) are before and (d), (e) and (f) are after chronoamperometric measurement for 2 hrs in 0.1M Na_2SO_4 solution.

Section A2.19. Controlled experiments for the formation of compounds $\{Mo_{72}Fe_{30}\}_{NM}$ and $\{W_{72}Fe_{30}\}_{NM}$

An aqueous solution (20 mL) of $[Mo_{72}Fe_{30}O_{252}(CH_3COO)_{12}\{Mo_2O_7(H_2O)\}_2\{H_2Mo_2O_8(H_2O)\}(H_2O)_{91}] \cdot 150\ H_2O$ **$\{Mo_{72}Fe_{30}\}_{cryst}$** (400 mg) was acidified with 10 mL of glacial acetic acid; under vigorous stirring condition, another aqueous solution (5 mL) of $FeCl_3{\cdot}6H_2O$ (200 mg) was added to it. A yellow-colored precipitation was observed; the reaction mixture was stirred for fifteen minutes at room temperature and the resulting precipitate was filtered off and washed with water thoroughly and dried the compound at room temperature. Similarly, aqueous solution (20 mL) of $[Na_6(NH_4)_{20}\{Fe(H_2O)_6\}_2][\{W^{VI}_6O_{21}(SO_4)\}_{12}\{Fe(H_2O)\}_{30}(SO_4)_{13}(H_2O)_{34}] \cdot 200H_2O$ (**$\{W_{72}Fe_{30}\}_{cryst}$**) (400 mg) was acidified with 10 mL of glacial acetic acid; under vigorous stirring condition, another aqueous solution (5 mL) of $FeCl_3{\cdot}6H_2O$ (200 mg) was added to it. After ten minutes again 15mL more glacial acetic acid is added to the above mixture. Precipitate formation was observed; the reaction mixture was stirred for fifteen minutes at room temperature and the resulting precipitate was filtered off and washed with water thoroughly and dried the compound at room temperature.

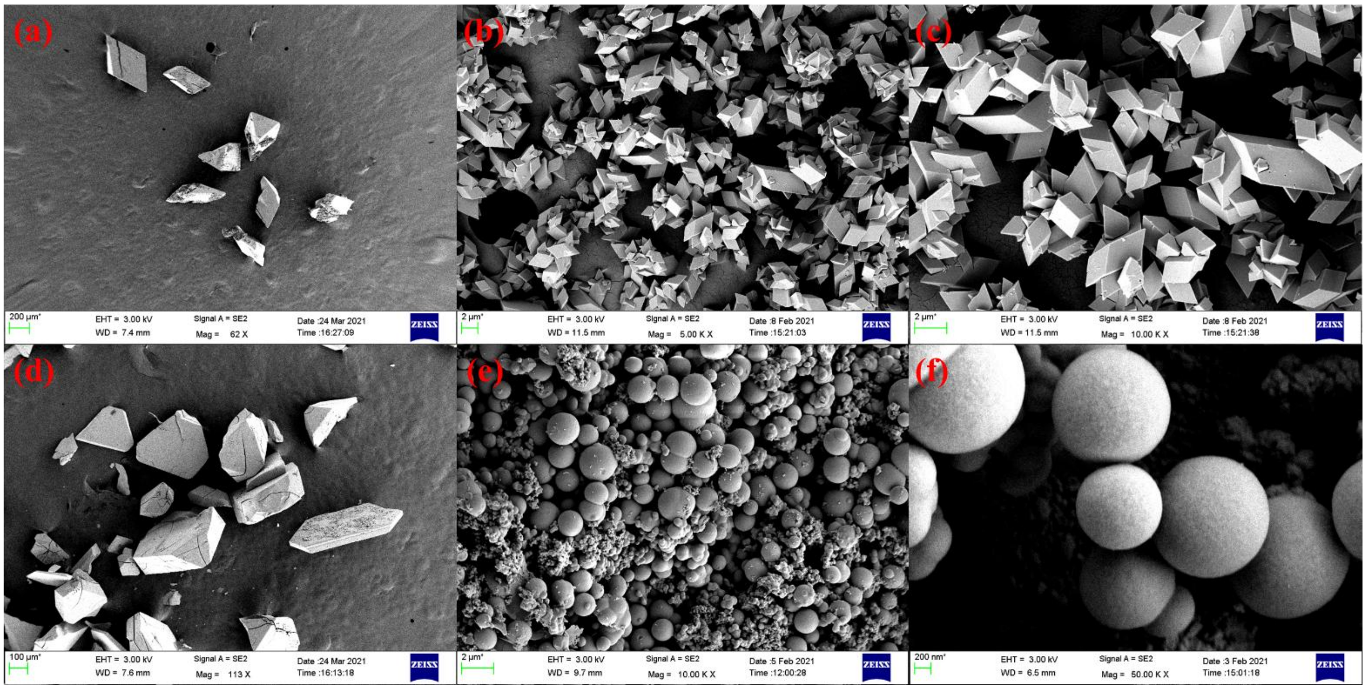

Figure A2.28. FESEM images (a) is related to **$\{Mo_{72}Fe_{30}\}_{cryst}$** before controlled experiment (b) and (c) are related **$\{Mo_{72}Fe_{30}\}_{cryst}$** compound after the controlled experiment and (d) is image of **$\{W_{72}Fe_{30}\}_{cryst}$** before controlled experiment (e) and (f) for **$\{W_{72}Fe_{30}\}_{cryst}$** after the controlled experiment.

FT-IR spectral analysis of $\{W_{72}Fe_{30}\}_{cryst}$.

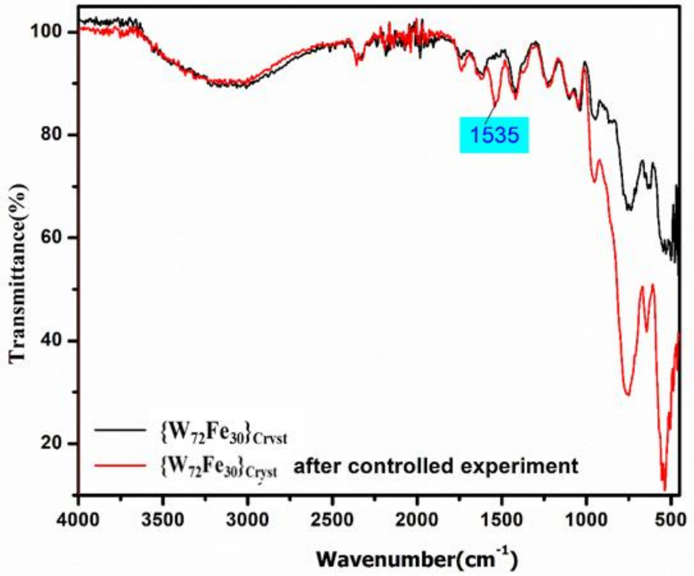

Figure A2.29. FT-IR spectrum of **$\{W_{72}Fe_{30}\}_{cryst}$** cluster containing compound which is compared with the same compound after controlled experiment.

From the FESEM images of the compounds **$\{Mo_{72}Fe_{30}\}_{cryst}$** and **$\{W_{72}Fe_{30}\}_{cryst}$** before and after carrying out the reaction clearly shows that **$\{Mo_{72}Fe_{30}\}_{cryst}$** compound did not undergo any reaction, it was same as before which is clearly seen in the FESEM images in Figure A2.28a, A2.28b and A2.28c. Whereas in the compound **$\{W_{72}Fe_{30}\}_{cryst}$** before the reaction it was completely in crystalline in nature as shown in the Figure A2.28d but when we have checked with the precipitate formed during the reaction as formed a aggregation of spheres of the compound **$\{W_{72}Fe_{30}\}_{cryst}$** as shown in the Figure A2.28e and A2.28f; it clearly supports our proposal of Fe ion as linker that plays a crucial role in the formation of these-micro-spheres in the compound **$\{W_{72}Fe_{30}\}_{NM}$**.

Section A2.20. Volumetric titration for the estimation of Iron content in the compound

Suspend around 500 mg of compound (**$\{Mo_{72}Fe_{30}\}_{NM}$** or **$\{W_{72}Fe_{30}\}_{NM}$**) in 10ml of distilled water. Add 1 M NaOH solution to the above uniformly mixed solution till it gives brick red color solution and stir it for 10 minutes. Filter the mixture and wash the residue thoroughly with water till tungsten completely removed from it (Test the filtrate solution by adding concentrated hydrochloric acid if it gives white precipitate tungsten is still remains in the residue, if not residue is free of tungsten). Dissolve the residue in the 10-15 mL of warm concentrated hydrochloric acid and makeup the solution to 20 mL by adding water and then heat the solution at 60^{o}C for 10 minutes. Add stannous chloride solution when the mixture is hot, color changes from yellow to pale green and excess 2-3 drops of stannous chloride is added. Solution is cooled down to room temperature and then add 10 mL mercuric chloride solution, makeup the solution to 150 mL with water and add 10 mL of Zimmermann Reinhardt solution to it. Now titrate the solution against 0.1 N $KMnO_4$ solution till it gives the pink color (end point).

Normality of $KMnO_4$ solution = 0.1047 N

$$\textbf{Amount of Iron present in the compound} = \frac{\textbf{Molecular weight of Iron x Volume of } KMnO_4 \textbf{ titrated x Normality of } KMnO_4}{1000}$$

$$\textbf{Percentage of Iron present in the compound} = \frac{\textbf{Amount of Iron present in the compound}}{\textbf{Total amount of compound taken}} \times 100$$

Percentage of iron present in $\{W_{72}Fe_{30}\}_{NM}$ compound:

Amount of Iron present in the **{$W_{72}Fe_{30}$}$_{NM}$** compound = {56x7.2x0.1047}/1000 = 0.04224 gms.

Percentage of Iron present in the **{$W_{72}Fe_{30}$}$_{NM}$** compound = {0.04224/0.5506}x100 = **7.672 %**.

Percentage of iron present in {$Mo_{72}Fe_{30}$}$_{NM}$ compound:

Amount of Iron present in the **{$Mo_{72}Fe_{30}$}$_{NM}$** compound = {56x8.1x0.1047}/1000=0.04752 gms.

Percentage of Iron present in the **{$Mo_{72}Fe_{30}$}$_{NM}$** compound = {0.04752/0.5110}x100 = **9.3 %**.

Section A2.21. An attempt to perform homogeneous electrocatalytic water reduction by using the crystalline substances {$Mo_{72}Fe_{30}$}$_{cryst}$ and {$W_{72}Fe_{30}$}$_{cryst}$ as catalysts

We then attempted to perform homogeneous electrocatalytic water reduction by using the crystalline substances $[Mo_{72}Fe_{30}O_{252}(CH_3COO)_{12}\{Mo_2O_7(H_2O)\}_2\ \{H_2Mo_2O_8(H_2O)\}(H_2O)_{91}]\cdot 150H_2O$ (**{$Mo_{72}Fe_{30}$}$_{cryst}$**) and $[Na_6(NH_4)_{20}\{Fe(H_2O)_6\}_2][\{W^{VI}{}_6O_{21}(SO_4)\}_{12}\ \{Fe(H_2O)\}_{30}(SO_4)_{13}(H_2O)_{34}]\cdot 200H_2O$ (**{$W_{72}Fe_{30}$}$_{cryst}$**) as catalysts in the same aqueous medium condition, which we used for heterogeneous electrocatalysis of water using amorphous nano-blackberry materials **{$Mo_{72}Fe_{30}$}$_{NM}$** and **{$W_{72}Fe_{30}$}$_{NM}$** as catalysts. But our attempts to perform homogeneous electrocatalysis of water using **{$Mo_{72}Fe_{30}$}$_{cryst}$** and **{$W_{72}Fe_{30}$}$_{cryst}$** as catalysts were without success. The first and foremost criterion of a true homogeneous electrocatalysis is: there should not be any electrodeposition on the working electrode. When we performed electrocatalysis in an aqueous solution of the crystalline compound **{$Mo_{72}Fe_{30}$}$_{cryst}$** or **{$W_{72}Fe_{30}$}$_{cryst}$**, it does not act as a true electrocatalyst because it gets electrochemically deposited on the working electrode which we proved by doing controlled experiments as described below. **{$Mo_{72}Fe_{30}$}$_{cryst}$** and **{$W_{72}Fe_{30}$}$_{cryst}$** as electrocatalysts were dissolved separately as homogeneous solutions in two different electrochemical cells. Multiple CV cycles (200 cycles) have been performed using GC and carbon paper as working electrodes. When the same working electrodes, that were used for (200) multiple CV cycles in homogeneous solutions (0.1 M Na_2SO_4 at pH 2.5) of **{$Mo_{72}Fe_{30}$}$_{cryst}$** or **{$W_{72}Fe_{30}$}$_{cryst}$**, are used again in fresh electrolyte (0.1 M Na_2SO_4 at pH 2.5) solutions separately without dissolving the respective catalysts, comparatively high catalytic currents for HER were observed due to electrodeposition on working electrodes as shown in Figure A2.30 (below). Under the same conditions, the electrodepositions on carbon paper working electrodes were established by FESEM images and relevant EDX analyses after multiple CV cycles (200 cycles) in both the cases of **{$Mo_{72}Fe_{30}$}$_{cryst}$** and **{$W_{72}Fe_{30}$}$_{cryst}$** (Figure A2.31).

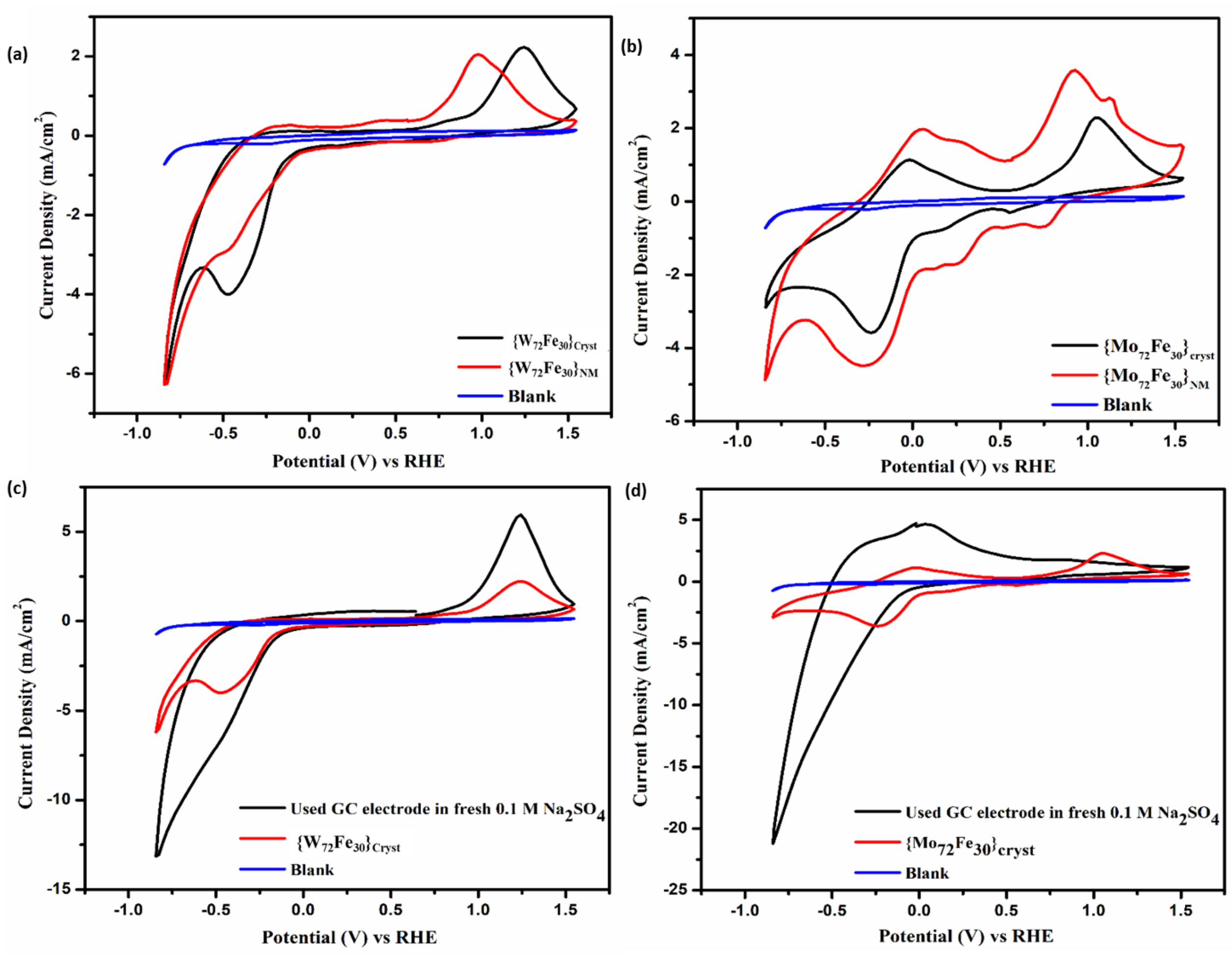

Figure A2.30. Cyclic voltammograms (CVs): performed in 0.1 M Na_2SO_4 at pH 2.5. (a) CV of blank GC (blue line); CV of 0.5 mM of **{$W_{72}Fe_{30}$}$_{cryst}$** (black line); CV of **{$W_{72}Fe_{30}$}$_{NM}$** (red line). (b) CV of blank GC (blue line); 0.5 mM of **{$Mo_{72}Fe_{30}$}$_{cryst}$** (black line); CV of **{$Mo_{72}Fe_{30}$}$_{NM}$** in (red line). (c) CV of blank GC (blue line); CV of 0.5 mM of **{$W_{72}Fe_{30}$}$_{cryst}$** (red line); CV of GC electrode after 200 CV cycles in **fresh 0.1M Na_2SO_4 at pH 2.5** (black line). (d) CV of blank (blue line); CV of 0.5 mM of **{$Mo_{72}Fe_{30}$}$_{cryst}$** (red line); CV of GC electrode after 200 CV cycles in fresh 0.1M Na_2SO_4 at pH 2.5 (black line).

It has already been mentioned that homogeneous electrocatalysis cannot be performed if the dissolved catalyst gets deposited under electrochemical condition, because in this case the dissolved crystalline compound does not work as a true catalyst. This restricts us to compare the electrocatalysis of our nano-blackberries **{$Mo_{72}Fe_{30}$}$_{NM}$** and **{$W_{72}Fe_{30}$}$_{NM}$** with that of their crystalline analogues **{$Mo_{72}Fe_{30}$}$_{cryst}$** and **{$W_{72}Fe_{30}$}$_{cryst}$**. In the present work, the nano-materials **{$Mo_{72}Fe_{30}$}$_{NM}$** and **{$W_{72}Fe_{30}$}$_{NM}$** act as true (heterogeneous) electrocatalysts, that are stable at least for two hours.

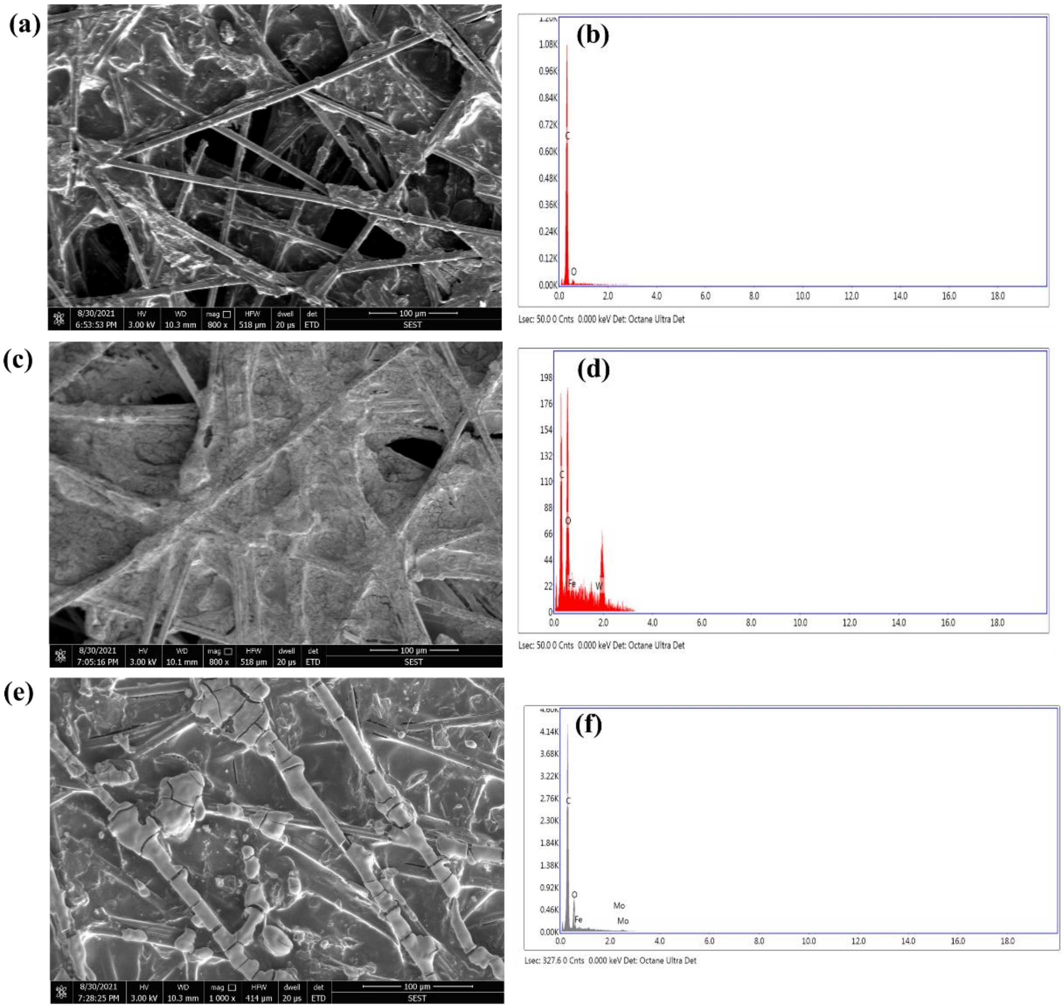

Figure A2.31. (a) and (b) FESEM image and EDX analysis of blank carbon paper respectively, (c) and (d) FESEM image and EDX analysis of carbon paper after multiple CV cycles (200 cycles) of 0.5 mM **$\{W_{72}Fe_{30}\}_{cryst}$** in 0.1 M Na_2SO_4 at pH 2.5 respectively, (e) and (f) FESEM image and EDX analysis of carbon paper after multiple CV cycles (200 cycles) of 0.5 mM **$\{Mo_{72}Fe_{30}\}_{cryst}$** in 0.1 M Na_2SO_4 at pH 2.5 respectively.

Section A2.22. Possible functional site for the HER: whether it is tungsten or iron

In order to investigate the possible functional site of **$\{W_{72}Fe_{30}\}_{NM}$** for the HER, we have performed the cyclic voltammograms (CVs) of **$\{W_{72}Fe_{30}\}_{NM}$** (Figure A2.32(a), below) and $FeCl_3.6H_2O$ (Figure A2.32(b), below) in THF medium (using tetrabutylammonium perchlorate as an supporting electrolyte) under inert condition (nitrogen atmosphere). By comparing CVs of both compounds, the redox couples A'_4/A_4, A'_3/A_3 and A'_2/A_2 appeared in CV of **$\{W_{72}Fe_{30}\}_{NM}$** (Figure S32(a), below) can tentatively be assigned as follows: A'_4/A_4 corresponds to Fe^{4+}/Fe^{3+} couple, A'_3/A_3 corresponds to Fe^{3+}/Fe^{2+} couple and A'_2/A_2 corresponds to W^{6+}/W^{5+} couple. The peak A_1 can be considered as formation of Fe^+ from Fe^{2+} and the corresponding Fe^{2+} from Fe^+ has been not observed in the CV. Thus, this peak A_1 (Fe^+) can be considered responsible for water reduction of hydrogen, because this (A_1, Fe^+) is very prone to convert to Fe^{2+} but response of Fe^{2+} formation is not there in the CV. From the Figure S32(b) (below), it has been observed that the redox peak of B_1 and B_2, generated from the $FeCl_3.6H_2O$, are resembled to the redox peak of A_1 and A_3 of **$\{W_{72}Fe_{30}\}_{NM}$** respectively. This observation clearly indicates that the functional site of the compound **$\{W_{72}Fe_{30}\}_{NM}$** is iron not the tungsten. Therefore, Fe^+ center is the most probable functional site for the HER.

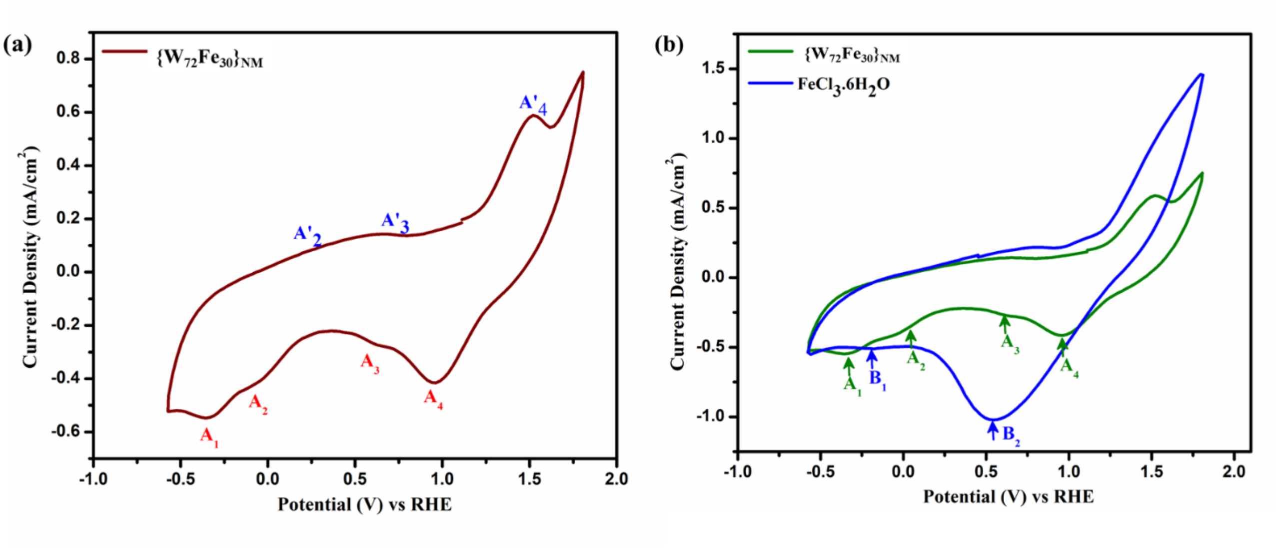

Figure A2.32. (a) CV of **$\{W_{72}Fe_{30}\}_{NM}$** in THF (tetrabutylammonium perchlorate as an supporting electrolyte); (b) CVs of **$\{W_{72}Fe_{30}\}_{NM}$** (green line) and $FeCl_3.6H_2O$ (blue line) in THF (tetrabutylammonium perchlorate as an supporting electrolyte).

Reference:

1. Mukhopadhyay, S.; Debgupta, J.; Singh, C.; Kar, A.; Das, S. K. A Keggin Polyoxometalate Shows Water Oxidation Activity at Neutral pH: POM@ZIF-8, an Efficient and Robust Electrocatalyst. *Angew. Chem. Int. Ed.* **2018**, *57*, 1918 –1923.

2. Mahmood, J.; Li, F.; Jung, S. M.; Okyay, M. S.; Ahmad, I.; Kim, S. J.; Park, N.; Jeong, H. Y.; Baek, J. B. An efficient and pH-universal ruthenium-based catalyst for the hydrogen evolution reaction. *Nature Nanotechnology*, **2017**, *12*, 441-447.

3. Weinberg, D. R.; Gagliardi, C. J.; Hull, J. F.; Murphy, C. F.; Kent, C. A.; Westlake, B. C.; Paul, A.; Ess, D. H.; McCafferty, D. G.; Meyer, T. J. Proton-Coupled Electron Transfer. *Chem. Rev.* **2012**, *112*, 4016−4093.
4. Todea, A. M.; Szakacs, J.; Konar, S.; Bogge, H.; Crans, D. C.; Glaser, T.; Rousseliere, H.; Thouvenot, R.; Gouzerh, P.; Muller, A. Reduced Molybenum-Oxide-Based Core–Shell Hybrids: “Blue” Electrons Are Delocalized on the Shell. *Chem. Eur. J.* **2011**, *17*, 6635 – 6642.

==

APPENDIX 3

Supporting data for chapter 3

Table of Contents

Section A3.1. Physical characterizations of $\{W_{72}Fe_{30}\}_{NB}$

As such synthesized compound was characterized by FT-IR, powder X-ray diffraction, FESEM, thermogravimetric analysis (TGA) and proton conductivity.

Fourier transformed – infrared spectra was obtained by an iD7 ATR thermo Fisher Scientific-Nicolet iS5 instrument. Directly the powdered sample was exposed to IR radiation by putting it on sample holder. TGA analysis were performed in PerkinElmer-STA 6000 analyzer and TGA-GCMS were conducted in PerkinElmer Gas chromatograph Clarus® 580 and Mass spectrometer Clarus® SQ 8 S. Field emission scanning electron microscopy (FESEM) measurement along with energy dispersive X-ray (EDX) was recorded on a Carl Zeiss model ultra 55 microscope, whereas EDX spectrum was performed using oxford instruments X-Max^N SDD (50mm^2) system and INCA analysis software. Transmission electron microscopy (TEM) images were recorded in an FEI Tecnai G^2 S-Twin microscope with an accelerating voltage of 200 kV. The selected area electron diffraction patterns (SAED) were recorded with the help of Gatan Inc CCD camera and GATAN digital microgram software. All the impedence measurements were carried out with the help of Zahner Zanium electrochemical work station operated with Thales software.

Section A3.2. FT-IR and PXRD analysis of {W$_{72}$Fe$_{30}$}$_{NB}$.

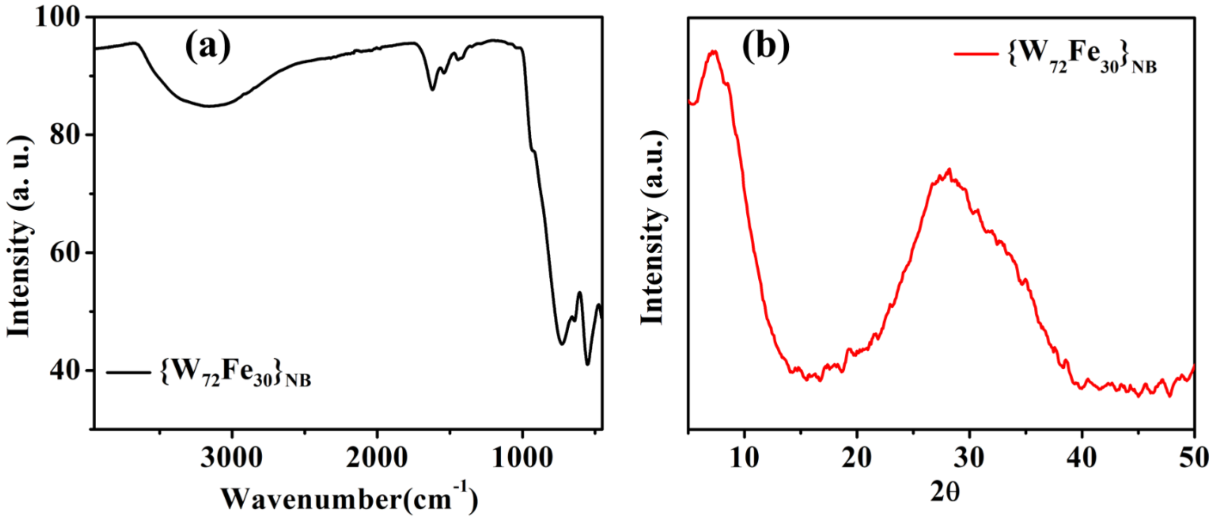

Figure A3.1. (a)FT-IR spectra of **{W$_{72}$Fe$_{30}$}$_{NB}$**. (b) PXRD analysis of **{W$_{72}$Fe$_{30}$}$_{NB}$**.

The FT-IR spectra recorded for the compound **{W$_{72}$Fe$_{30}$}$_{NB}$** shows the characteristic bands at 1616 (m, δ (H_2O)), 1546 (m, $\bar{\upsilon}_{as}$(COO)), 1450 (s-m, $\bar{\upsilon}_s$(COO)), 937 (m, $\bar{\upsilon}$ (W=O)), 728 (s), 637 (m), 553 cm^{-1} (m) as shown in Figure A3.1(a). The PXRD data clearly shows that the compound **{W$_{72}$Fe$_{30}$}$_{NB}$** is in amorphous nature as shown in the Figure A3.1(b)

Section A3.3. Raman spectral analysis of $\{W_{72}Fe_{30}\}_{NB}$.

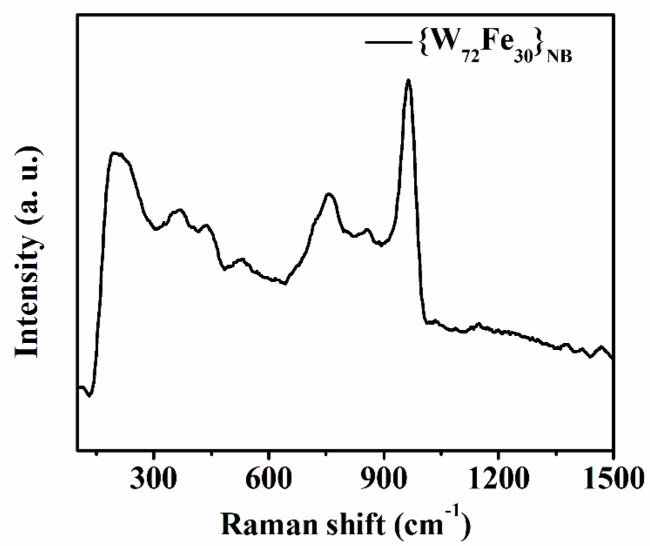

Figure A3.2. Raman spectrum of isolated amorphous $\{W_{72}Fe_{30}\}_{NB}$ compound.

The Raman spectrum of the compound $\{W_{72}Fe_{30}\}_{NB}$ recorded using 632 nm laser excitation, the characteristic bands shows at 965 (W=O), 856, 756, 528, 437, 364 and 202 cm^{-1} as shown in Figure A3.2.

Section A3.4. Thermogravimetric analysis of $\{W_{72}Fe_{30}\}_{NB}$.

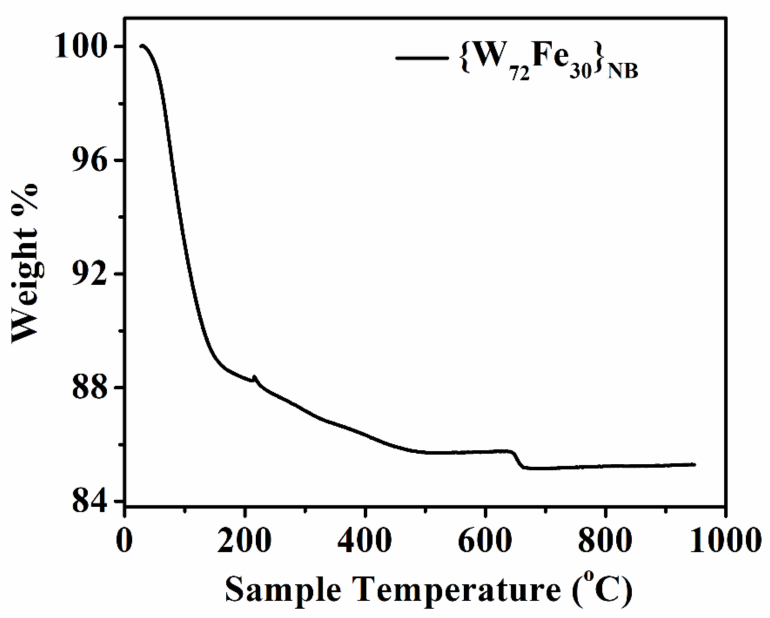

Figure A3.3. Thermogravimetric plot of the amorphous $\{W_{72}Fe_{30}\}_{NB}$ compound.

TGA plot of the compound $\{W_{72}Fe_{30}\}_{NB}$ clearly shows that the compound is stable till 600 °C and the temperature below and around 100 °C, it loses the water molecules as shown in Figure A3.3.

Section A3.5. FESEM analysis of $\{W_{72}Fe_{30}\}_{NB}$.

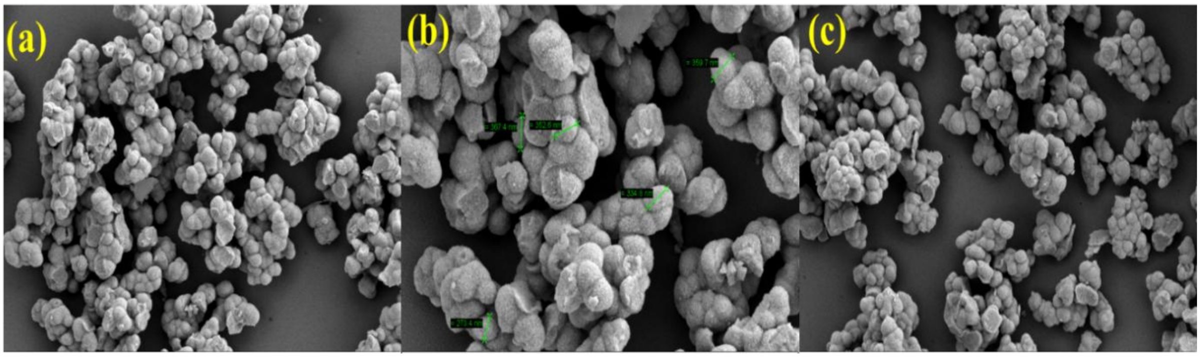

Figure A3.4. (a-c) FESEM images of the compound $\{W_{72}Fe_{30}\}_{NB}$ at different resolutions.

The FESEM images of the compound $\{W_{72}Fe_{30}\}_{NB}$ has been taken on the carbon tape and coated with gold. Figures A3.4a, A3.4b and A3.4c clearly show that $\{W_{72}Fe_{30}\}$ cluster containing compound $\{W_{72}Fe_{30}\}_{NB}$ aggregates to form blackberry like nanovesicles which have pores on the surface. These nanoparticles have a particle size around 300-500 nm as shown in Figure A3.4b.

Section A3.6 Water Sorption Analysis of $\{W_{72}Fe_{30}\}_{NB}$

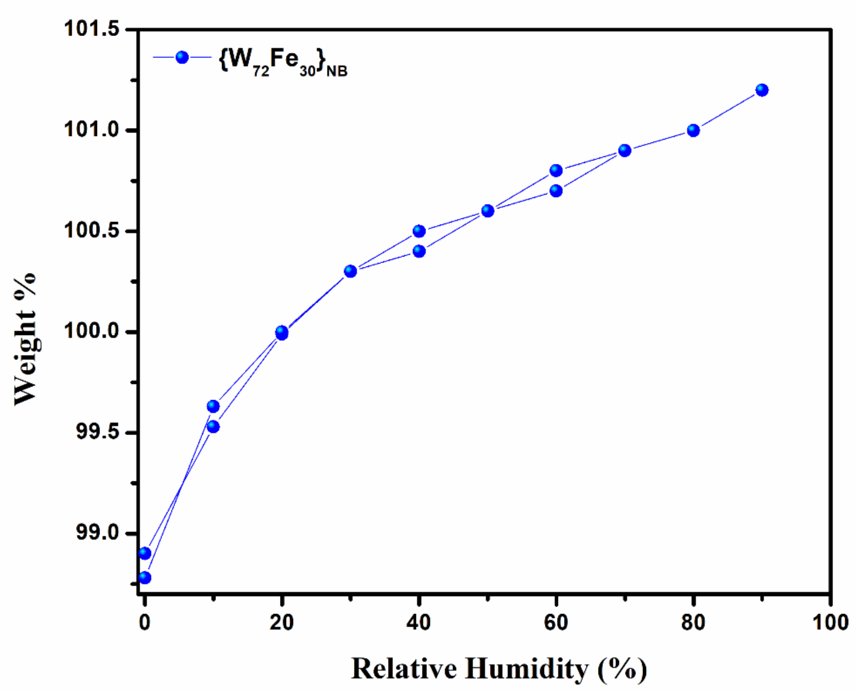

Figure A3.5. Water sorption isotherm of the compound $\{W_{72}Fe_{30}\}_{NB}$.

The water sorptivity of the compound $\{W_{72}Fe_{30}\}_{NB}$ is measured up to a relative humidity of 90% and the experiment is conducted at room temperature i.e. 25 °C by taking the known amount of sample. The water sorption is measured by increasing the relative humidity up to 90% and measures the amount of water sorption has taken place in the compound. From the above data it has been shown that 0.01185 g of water has been adsorbed per 1 g of sample as shown in the Figure A3.5.

Section A3.7. AC impedance measurement of $\{W_{72}Fe_{30}\}_{NB}$

(a) General methodology and set up of measurement

The proton conductivity of **$\{W_{72}Fe_{30}\}_{NB}$** was measured by alternating current (ac) impedance spectroscopy using a two electrode setup. The powdered samples were sandwiched between two carbon papers and pressed to discs under a pressure of 3-ton cm^{-2} for 2 min. Carbon papers are used to lower the contact resistance between the electrodes and to reduce the possibility of anomaly comes from the in homogeneity of the sample surface. Measurements were carried out over the frequency range of 1 Hz to 1 MHz with the input voltage amplitude of 5 mV. A homemade setup is used to maintain the humidity and temperature. In this set-up, a 5 L conical flask is partially filled with 2 L distilled water and kept over a heating source to heat water as shown in the figure A3.6. A digital thermometer is fitted parallelly with electrode set-up through the Teflon lid to check the temperature. A small hole is there on the Teflon lid to release the excess pressure generated inside the conical from water vapour. The whole setup is then heated to generate enough humidity (RH 98%) and the desired temperature. Before recording each data, the system was kept at constant temperature for 4 hours to achieve the equilibrium environment.

Figure A3.6. Picture of the home-made setup for proton conductivity measurement.

Impedance spectra were recorded for **$\{W_{72}Fe_{30}\}_{NB}$** during temperature variation at constant relative humidity (98%). To check the long-term stability of **$\{W_{72}Fe_{30}\}_{NB}$**, the sample was kept in the maximum humidified condition i.e., at 98% relative humidity and at 80 °C temperature for 48 hours period and the data were taken after each 12 hours' time interval. Bulk conductivities were calculated by fitting the Nyquist plots of impedance spectra with the most suitable electrical equivalent circuit.

To calculate the proton conductivity of the compound, the experimentally obtained impedance spectral data were fitted with the most relevant electrical circuit ((R1/Q1) + (R2/Q2) + Q3.

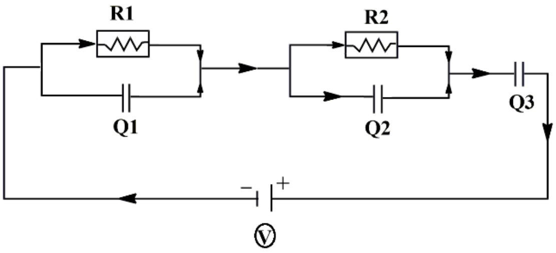

This circuit consists of three major components those are connected in a series such as, Z1 contains (R1/Q1) that indicates the impedance of the electrolyte, Z2 consist of (R2/Q2) indicates the resistance of the electrode-electrolyte interface and Q3 is a constant phase element that accounts for the low frequency region of the Nyquist plot of impedance spectrum.

Here R1 represents the bulk resistance of the pellet, is our prime interest from which conductivities were calculated and R2 accounts for the charge transfer resistance between the electrodes and the pellet electrolyte which is not related to the conductivity of the electrolyte. It depends mainly on the particle size of the material.

Thus, while determining the proton conductivity of the palletised sample from R1, the area of the cross section and thickness of the pellet are considered as unity.

Here we provided the values of R1, and R2 by fitting the experimentally obtained data points along the curve generated by the equivalent circuit mentioned above. The accuracy of the fitting was measured by the factor χ^2.

Table A3.1. Table of fitting parameters to determine proton conductivity of {$W_{72}Fe_{30}$}$_{NB}$ in various temperatures:

Temp. (°C)	Software	Value of R1(Ω)	Conductivity (Scm^{-1})	χ^2 value
80.5	EC-Lab V10.21	0.377	0.330	1.496×10^{-3}
70.5	EC-Lab V10.21	1.92	0.0648	4.851×10^{-3}
60.5	EC-Lab V10.21	29.82	0.00415	5.426×10^{-3}
50.8	EC-Lab V10.21	99.48	0.00125	6.019×10^{-3}

Section A3.8. Calculation of proton conductivity from the R1 value for {$W_{72}Fe_{30}$}$_{NB}$ at 80.5 °C (all other proton conductivity values were calculated using similar method:

Value of R1 =**0.377 Ω**.

Now we know, Conductance **(L) = (1/R) = σ** × **(A/d)** ……. Eqn (1)

Thus, conductivity **(σ) = (L)** × **d/A = (1/R)** × **(d/A)** …….. Eqn (2)

Where R is resistance of sample; σ is conductivity of the sample;

d = thickness of pellet = 0.165 cm.

A = area of cross section of pellet = 1.326 cm^2.

Putting the value R1 =**0.377 Ω**, in Eqn (2) we get the conductivity of **{$W_{72}Fe_{30}$}$_{NB}$** at 80.5 °C.

Conductivity of **{$W_{72}Fe_{30}$}$_{NB}$** at 80.5 °C is $(\sigma)_{80.5\,°C}$ = $\mathbf{0.330 \times 10^{-1}}$ Scm^{-1}.

All the conductivity data for **{$W_{72}Fe_{30}$}$_{NB}$** were calculated using similar data fitting and similar calculations.

Section A3.9. Activation energy calculation

Activation energy (E_a) of proton conductivity was calculated for **{$W_{72}Fe_{30}$}$_{NB}$** from its proton conductivity values at various temperatures. Derived plot was constructed between ln(σT) and 1000/T for **{$W_{72}Fe_{30}$}$_{NB}$**. Activation energy of proton conductivity was calculated from the slope of the plot with the help of Arrhenius equation. Detailed calculation is given below.

Calculation of activation energy

From Arrhenius Equation, $\sigma T = \sigma_0 \times \exp(-E_a/RT)$ ……… Eqn. (3)

Where, σ = conductivity of the sample, i.e., here proton conductivity;

σ_0 = Pre-exponential factor, E_a = Activation energy of proton conduction;

R= Ideal gas constant;

T= Temperature in Kelvin scale.

Eqn. (3) can be restructured as $\ln(\sigma T) = \ln\sigma_0 - (E_a/RT)$

It can be written as $\ln(\sigma T) = \ln\sigma_0 + (-E_a/(1000\times R))(1000/T)$ … Eqn. (4)

Eqn. (4) also represents the straight-line plot obtained between $\ln(\sigma T)$ and. 1000/T

Thus, Slope (m) = $(-E_a/1000\times R) = 22.8037\ \mathrm{Scm^{-1}K^{2}}$.

Activation energy of **$\{W_{72}Fe_{30}\}_{NB}$, E_a** = 189.584 kJ/mole = 1.952 eV.

Section A3.10. Characterization of the compound $\{W_{72}Fe_{30}\}_{NB}$ after EIS measurement

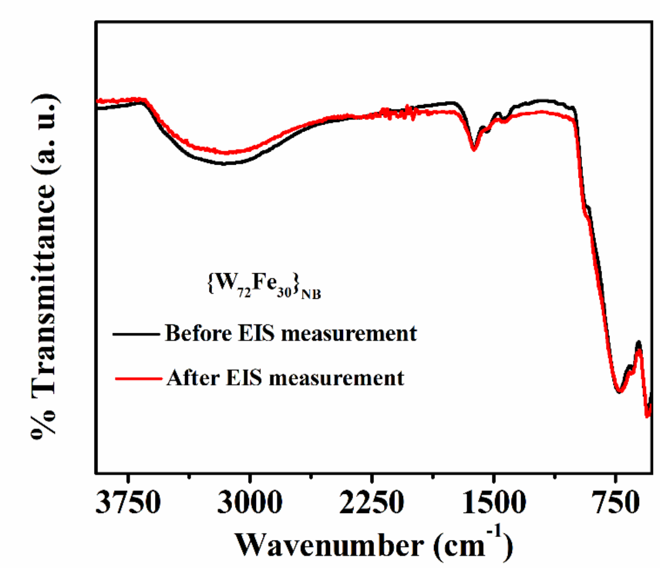

Figure A3.7. FT-IR spectra of **$\{W_{72}Fe_{30}\}_{NB}$** before and after EIS measurement with temperature variation at 98% RH.

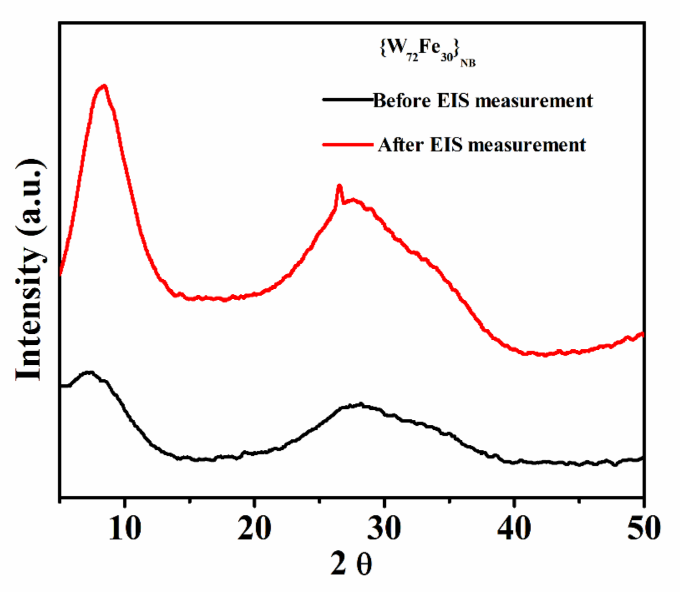

Figure A3.8. PXRDs of **$\{W_{72}Fe_{30}\}_{NB}$** before and after EIS measurement with temperature variation at 98% RH.

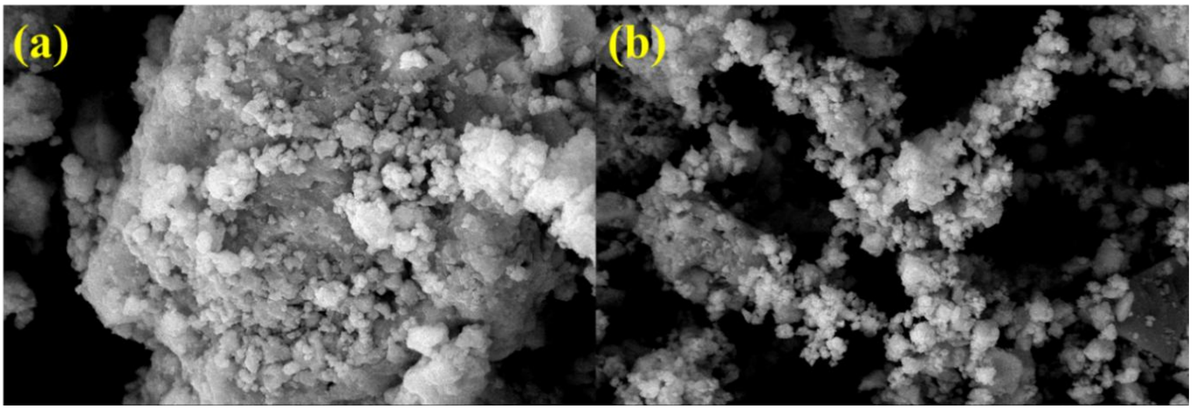

Figure A3.9. FESEM images of **$\{W_{72}Fe_{30}\}_{NB}$** at different resolutions after EIS measurement with temperature variation at 98% RH.

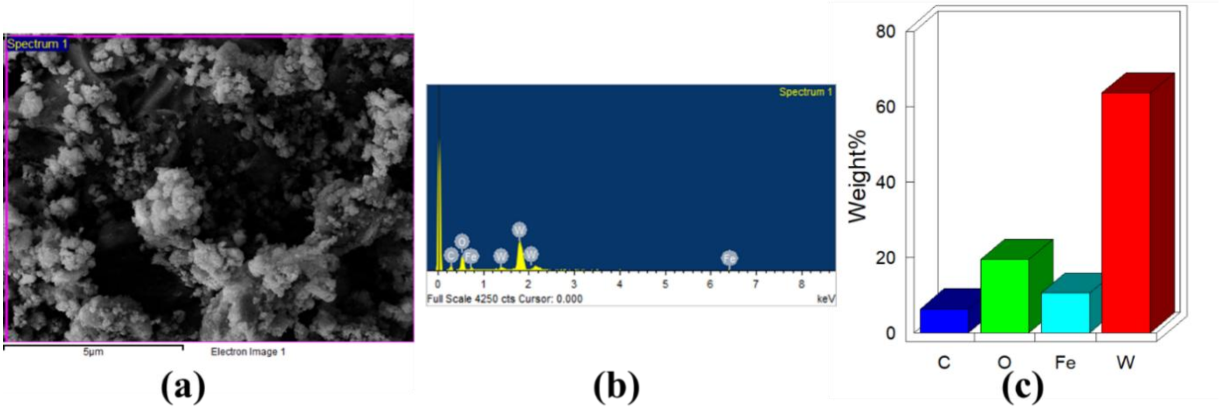

(a) (b) (c)

Figure A3.10 (a-c). EDX analysis of **$\{W_{72}Fe_{30}\}_{NB}$** after EIS measurement with temperature variation at 98% RH.

Section A3.11. Instrumental details of physical characterizations of MMMs

A3.11.1- The inherent viscosity (I.V.) of the poly **2,2′-(m-phenylene)-5,5′-benzimidazole** (**m-PBI**) polymer was measured at 30 °C in water bath with the help of Cannon (model F725) capillary dilution viscometer and the I.V. values are calculated from the flow time data. A solution of m-PBI in H_2SO_4 was used for the viscosity measurement. The concentration of the m-PBI solution in H_2SO_4 is 0.2 g/dL. The obtained I.V. value of the synthesised **m-PBI** is 1.02 dL/g.

A3.11.2 - The powder x-ray diffraction patterns of m-PBI, and **$\{W_{72}Fe_{30}\}_{NB}$** polyoxometalates loaded composite membranes were recorded on D8 Advance Bruker diffractometer 2θ range (5^o-50^o). The diffraction patterns were analyzed using Bruker DIFFRAC plus EVA software.

A3.11.3 - Fourier transformed - infrared (FT-IR) spectra of the **$\{W_{72}Fe_{30}\}_{NB}$** loaded MMMs were recorded on an iD7 ATR Thermo Fisher Scientific-Nicolet iS5 instrument. The membrane samples were directly put on the sample holder to record the spectra.

A3.11.4 - Field Emission Scanning Electron Microscopy (FESEM) and Atomic Force Microscopy (AFM)

The surface morphology of the pristine m-PBI, **$\{W_{72}Fe_{30}\}$-2.5%** and **$\{W_{72}Fe_{30}\}$-5%** membranes were evaluated by using a field emission scanning electron microscope (FESEM) (Model: Zeiss Merlin Compact). The FESEM cross section morphology of the membrane samples were done by breaking the membranes in liquid nitrogen medium. Samples were gold coated before imaging in FESEM. AFM surface topology and 3D AFM images of the membranes were captured by Atomic probe Microscope Model: NT-MDT Solve-Probe & Oxford Asylum.

A3.11.5 - TEM analysis of mixed matrix membranes

Transmission electron microscopy (TEM) studies were conducted on JEOL (JEM Model No. F200) TEM machine at an accelerating voltage of 200 kV. The samples were prepared by placing a drop of dimethyl acetamide (DMAc) dispersed m-PBI, **$\{W_{72}Fe_{30}\}$-2.5%** and **$\{W_{72}Fe_{30}\}$-5%** membranes solution on carbon coated copper (200 mesh) grids.

A3.11.6 - Thermogravimetric analysis (TGA) of undoped pristine m-PBI, **$\{W_{72}Fe_{30}\}$-2.5%** and **$\{W_{72}Fe_{30}\}$-5%** MMMs and its PA doped membranes were carried out on a TGA (TGA Q500, TA Instruments, USA) instrument operated in a temperature range from 35 °C to 700 °C with a scanning rate of 10°C / min under nitrogen gas flow. We have kept all the membrane samples at 100 °C isothermally for 30 minutes before measurement to evaporate excess water from the MOF loaded composite membranes. After that we have cooled the samples, allow them to achieve RT and start our measurement.

A3.11.7 - Mechanical properties of m-PBI and **Polymer-POM** mixed matrix membranes were studied by using a dynamic mechanical analyser (DMA model Q-800). The loaded membranes dimensions were around 30 mm × 7 mm × 0.01 mm (L × W × T) and clamped on the films tension clamp of the pre-calibrated instrument. The samples were annealed at 400 °C for 15 minutes and then scanned from 100 °C to 400 °C with heating rate 4 °C/min. The storage modulus (E') and tan δ values were measured at a constant linear frequency 10 Hz with constant preloaded force of 0.01N.

A3.11.8 - The tensile strength measurement (stress-strain profile) of the entire PA doped m-PBI PA doped Polymer-POM MMMs was obtained from universal testing machine (UTM, INSTRON-5965). 50 mm × 10 mm × 0.02 mm size PA doped films were used for this experiment. For each sample, at least three times measurements were tested in the machine to check the reproducibility. Stress-strain profile (tensile stress and elongation at break values) of the PA doped m-PBI and PA loaded nanocomposite MMMs were evaluated from the stress vs strain plot.

A3.11.9 - PA doping level, swelling ratio, water uptake of the MMMs

Three similar size pieces of the m-PBI, **{$W_{72}Fe_{30}$}** loaded **(-2.5%** and **-5%)** MMMs made from DMAc were immersed in phosphoric acid for 5 days. After that the doped membranes were soaked and wiped with filter paper and transferred to 50 ml water then titrated against 0.1 N sodium hydroxide (NaOH) by using an Autotitrator (Model Metrohm702). The phosphoric acid content was calculated as the number of PA moles per PBI repeat unit. The length, thickness and width of the dried membranes were measured before dipping in phosphoric acid and after 5 days of the dipping.

Swelling ratio of the membranes were calculated from the following equation.

$$\%\text{Swelling Ratio} = \frac{L_w - L_d}{L_d} \times 100\% \qquad (1)$$

Where, L_w, and L_d are the length of the wet membranes and dry membranes, respectively.

Similarly, the water uptake and swelling ratio in water for **m-PBI** and the fabricated MMMs were obtained by immersing the membranes in water for 5 days. The length, thickness and width of the dried membranes were measured before dipping in water. After 5 days, the membranes were removed from water bath and quickly wiped to remove surface water from the membranes and again the length, thickness and width of the wet membranes were measured. Water uptake was calculated from the following equation.

$$\%\text{Water Uptake} = \frac{W_w - W_d}{W_d} \times 100\% \qquad (2)$$

Where, W_w is wet membrane weight and W_d, is dry membrane weight, respectively.

Similarly, swelling ratio in water was measured using equivalent equation like equation (1).

A3.11.10 - Proton conductivity

Proton conductivity was carried out by four probe impedance analysis by using Auto lab Impedance analyser (PGSTAT302N) over a frequency range from 1 Hz to 100 KHz. The phosphoric acid doped **m-PBI, {$W_{72}Fe_{30}$}-2.5%** and **{$W_{72}Fe_{30}$}-5%** membranes were cut in rectangular shape, and then kept sandwiched between two Teflon plates with four platinum electrodes. Two outer electrodes (1.5 cm apart) supply current to the cell, while the two inner electrodes 0.5 cm apart on opposite sides of the membrane measure the potential drop. At first, the surface PA of the membranes were wiped out carefully and fitted into conductivity cell. Then, the whole conductivity cell set up was kept in a vacuum oven to measure the temperature dependence of proton conduction. The conductivity cell was placed in a vacuum oven at 100 °C for 2h to avoid the conduction due to the presence of water molecules. After that, the conductivity cell was cooled to room temperature in a vacuum desiccator and then before going to conductivity measurement, the cell was taken out to keep the sample dry. The conductivities of the membranes were measured from room temperature to 160 °C at intervals of 20 °C. At every temperature jump, the sample was kept for 30 minutes to attain isothermal equilibrium and then measurements were recorded. The conductivities of the membranes were calculated from the following equation:

$$\sigma = \frac{D}{RBL} \qquad (3)$$

Where, D is the distance between the electrodes (here it is 0.5 cm), B is the thickness of the membrane, L is the width of the membrane and R is the bulk resistance obtained from the Nyquist plot.

A3.11.11 - Isothermal proton conductivity

The membranes were isothermally kept at 160 °C for 24 h. Under this condition, the conductivity of **{$W_{72}Fe_{30}$}-2.5%** and **{$W_{72}Fe_{30}$}-5%** composite membranes and pristine **m-PBI** membrane were measured for every 2 h up to 24 h. We exclude night time measurement (8 h gap) and kept the cell in equilibrium for overnight at isothermal condition (160 °C). Further measurement of proton conductivity was performed next morning up-to 24 h, no notable change in proton conductivity of the membranes was observed after prolong treatment.

A3.11.12 - Acid retention test

The acid leaching test was performed for PA doped m-PBI, **$\{W_{72}Fe_{30}\}$-2.5%** and **$\{W_{72}Fe_{30}\}$-5%** membranes according to the previous reports. The doped membranes were taken out from the phosphoric acid bath medium and excess phosphoric acid was removed by wiping with a tissue paper. The membranes were then placed under the vapour condition at 100 °C for a period of three hours and the weight of the membrane (W_t) after every one hour was recorded after removing the leached acid from the membrane. The weight loss ratio of acid in the membranes was calculated by using the following formula:

$$\mathrm{R} = \frac{W_o - W_t}{W_a} \times 100\ \% \qquad (4)$$

Where, W_o is weight of the PA doped membranes at the initial time of zero hour, W_t is the weight of the PA membrane after leaching at different times (t) and W_a is the original weight of PA present in the membranes calculated from the PA doping level of the membranes.

Section A3.12 Donor-acceptor type H-bonding in the Polymer-POM composite network

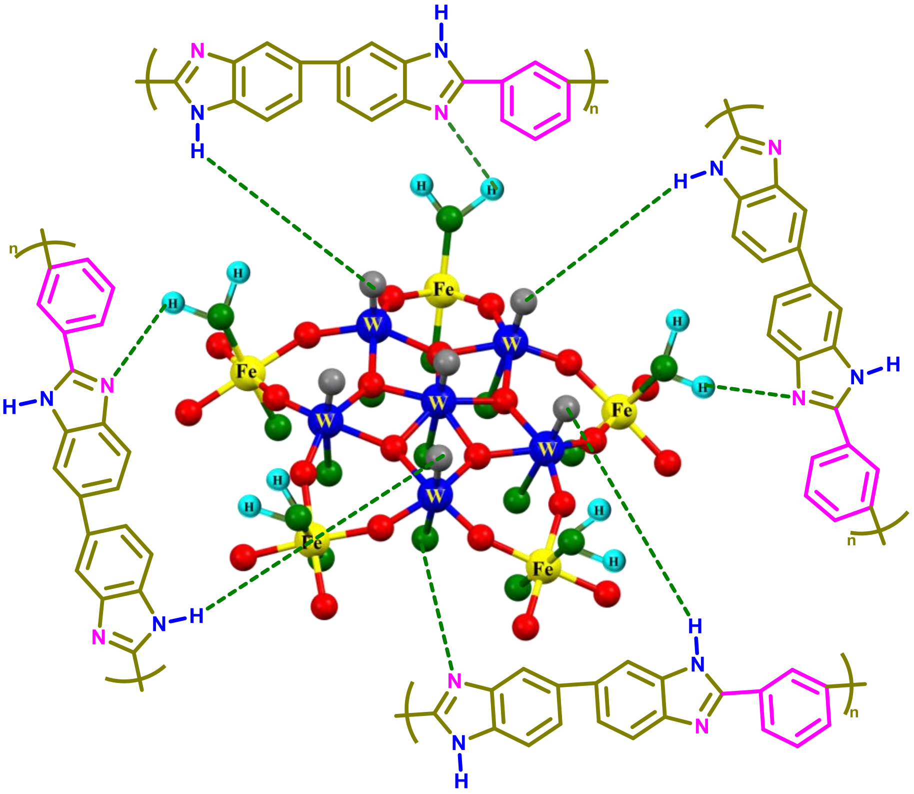

Scheme A3.1 (a) Schematic representation of interfacial H-bonding donor-acceptor type interaction between the **$\{W_{72}Fe_{30}\}$** clusters and the **m-PBI** polymers.

A3.13- FT-IR analysis of $\{W_{72}Fe_{30}\}$ loaded MMMs

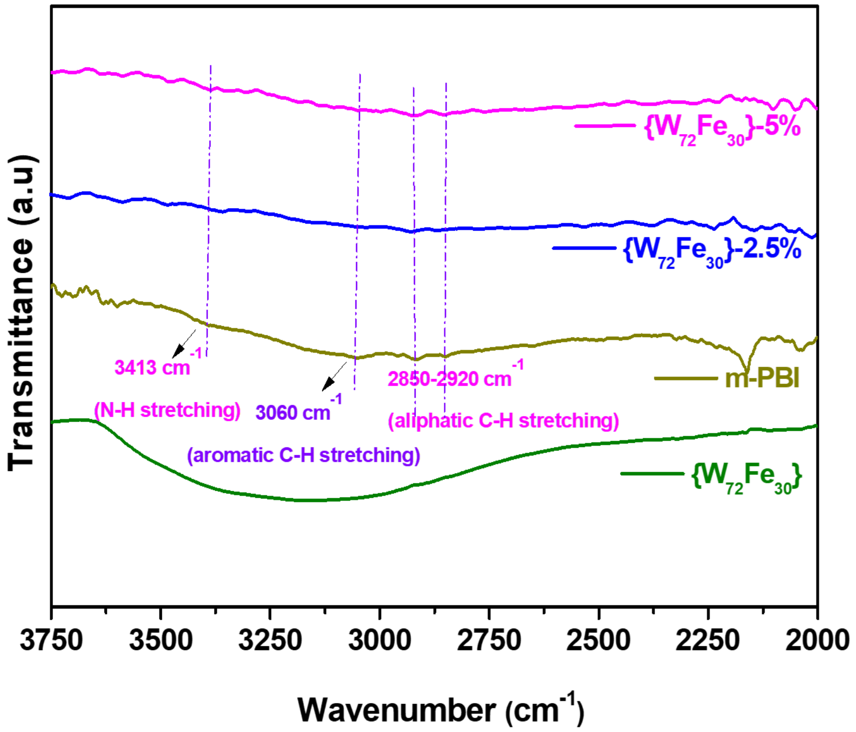

Figure A3.11. FT-IR spectra of the m-PBI, **$\{W_{72}Fe_{30}\}_{NB}$, $\{W_{72}Fe_{30}\}$-2.5%** and **$\{W_{72}Fe_{30}\}$-5%** membranes.

A3.14 - Morphology of the $\{W_{72}Fe_{30}\}$ loaded MMMs

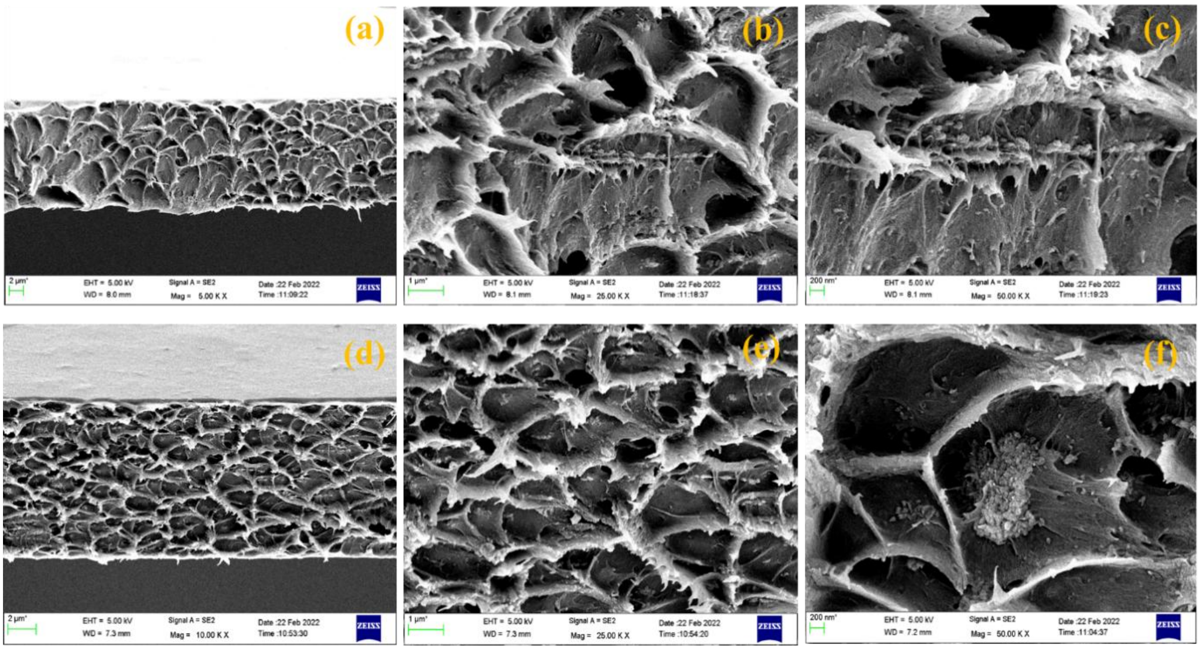

Figure A3.12. (a-c) Cross-sectional FESEM morphology of the **{$W_{72}Fe_{30}$}-2.5%** membrane at different magnification. (d-f) Cross-sectional FESEM morphology of the **{$W_{72}Fe_{30}$}-5%** membrane at different magnification.

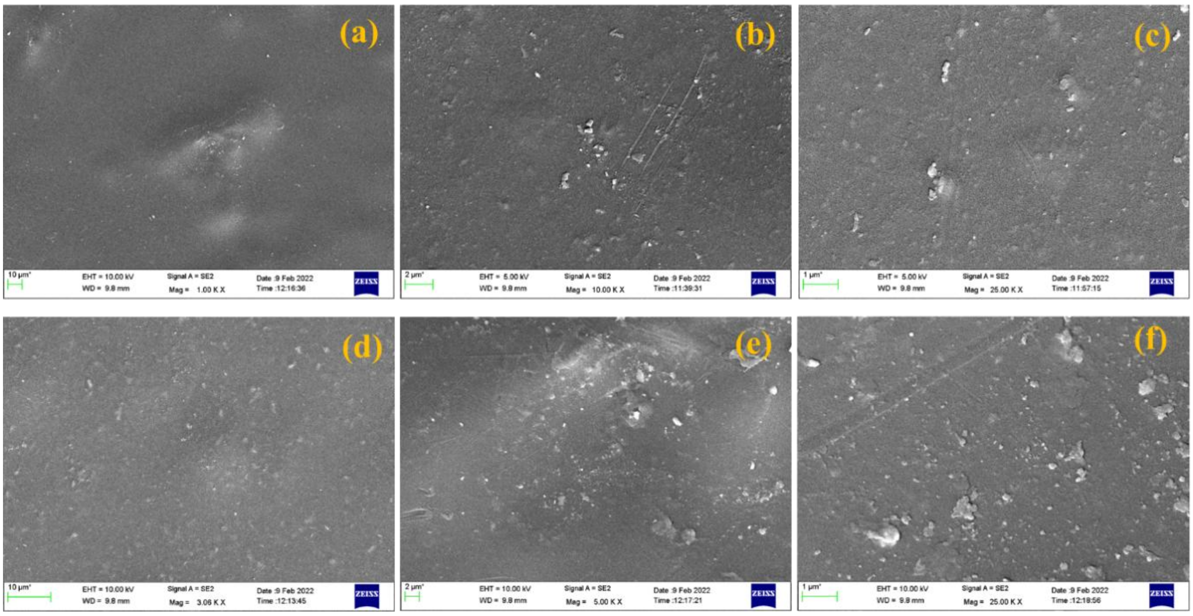

Figure A3.13. (a-c) Surface FESEM morphology of the **{$W_{72}Fe_{30}$}-2.5%** membrane at different magnification, and (d-f) Surface FESEM morphology of the **{$W_{72}Fe_{30}$}-5%** membrane, at different magnification.

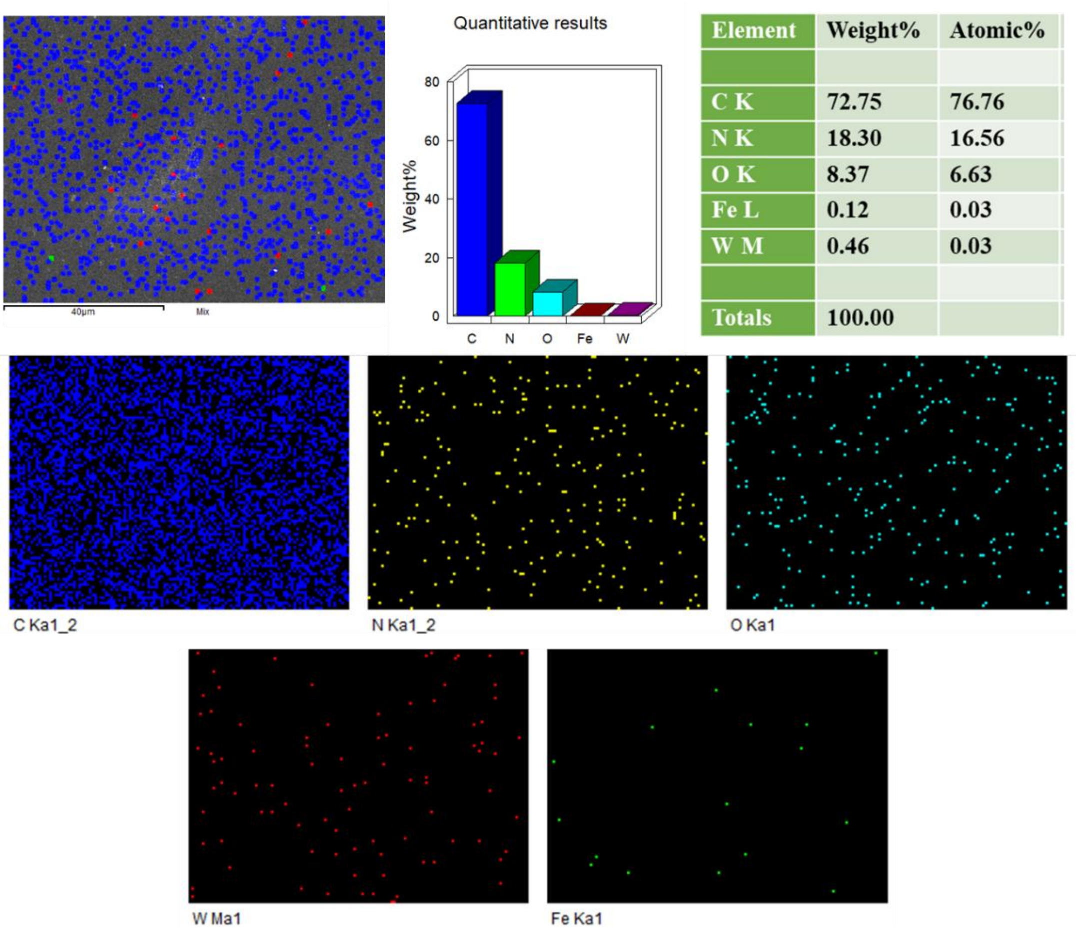

Element	Weight%	Atomic%
C K	72.75	76.76
N K	18.30	16.56
O K	8.37	6.63
Fe L	0.12	0.03
W M	0.46	0.03
Totals	100.00	

Figure A3.14. FESEM EDX and elemental analysis with elemental mapping of the **$\{W_{72}Fe_{30}\}$-5%** membrane surface.

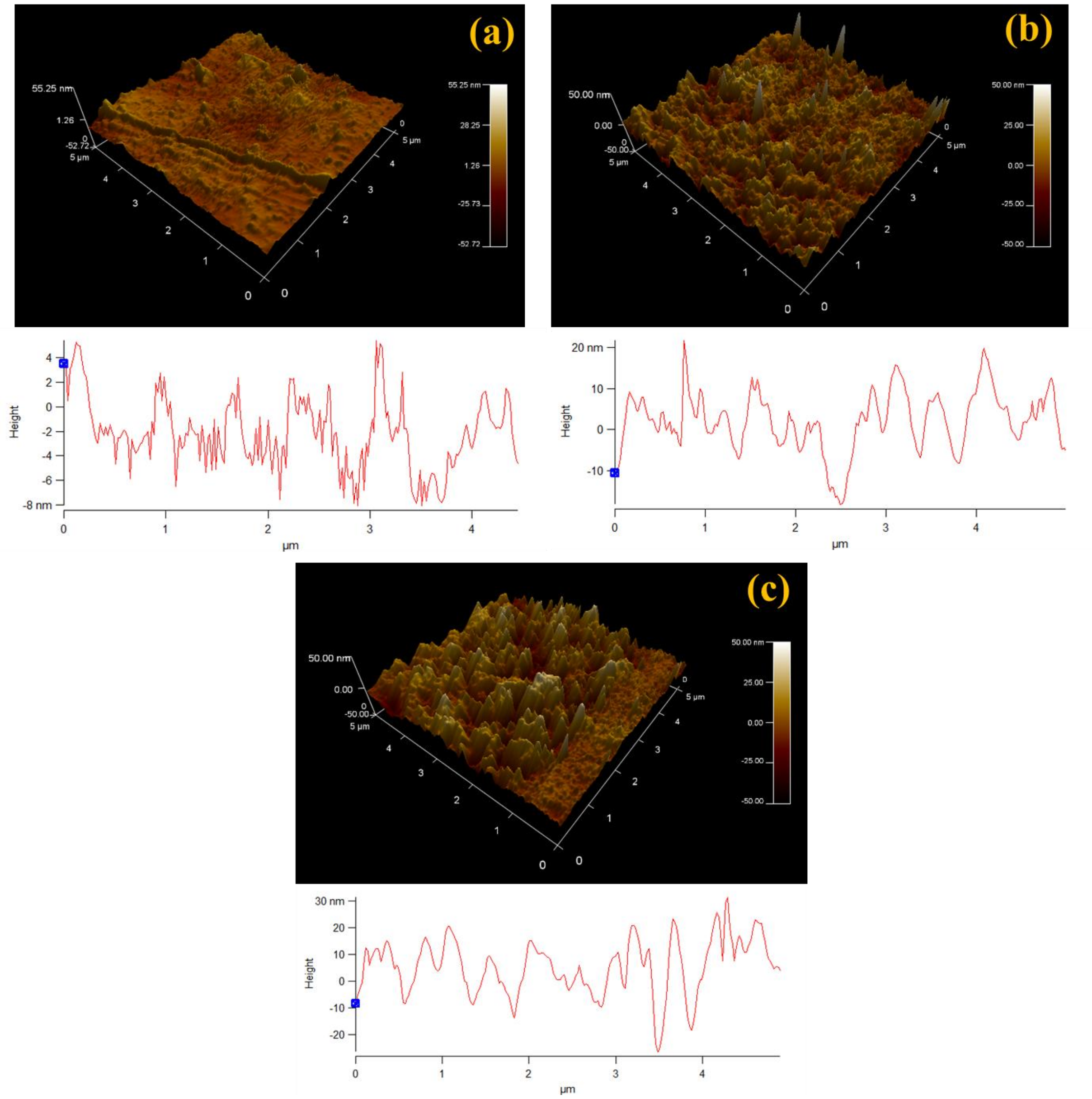

Figure A3.15. (a) AFM 3D images of the surface morphology of m-PBI, **(b) {$W_{72}Fe_{30}$}-2.5%** and **(c) {$W_{72}Fe_{30}$}-5%** membranes in addition with the corresponding height profiles of the mentioned MMMs along a straight line, respectively.

Table A3.2. Surface roughness of the **Polymer-POM** MMMs in a comparison with m-PBI.

Sample	Root mean square roughness (S_q) (nm)
m-PBI	4.782
{$W_{72}Fe_{30}$}-2.5%	7.878
{$W_{72}Fe_{30}$}-5%	9.788

A3.15 - Thermogravimetric analysis (TGA) of the PA doped membranes

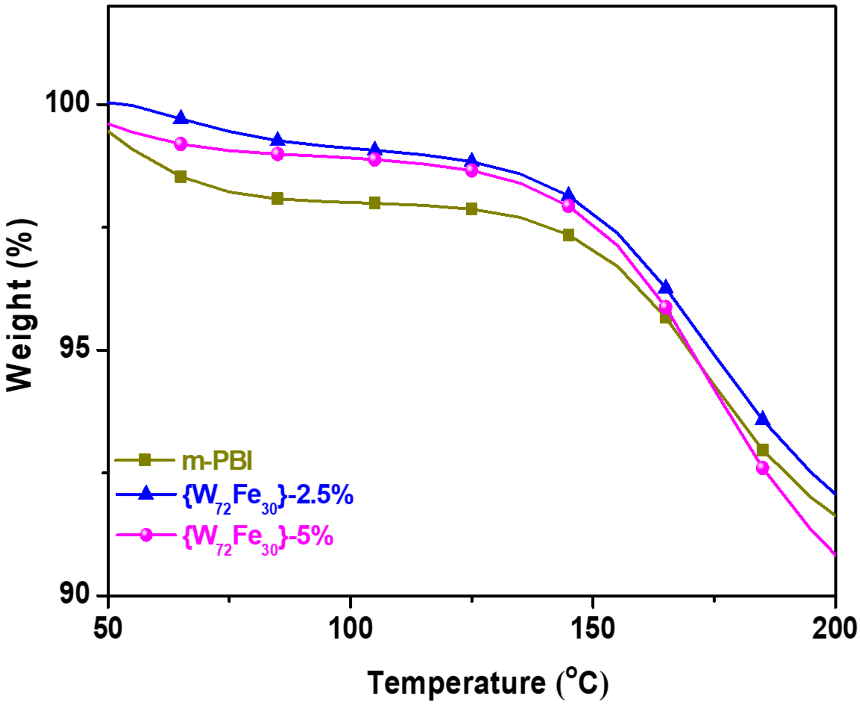

Figure A3.16. Zoomed TGA plots (50 ºC - 200 ºC) of PA doped m-PBI, **{$W_{72}Fe_{30}$}-2.5%** and **{$W_{72}Fe_{30}$}-5%** membranes.

Section A3.16 - Calculation of proton conductivity from Impedance spectra by fitting with equivalent circuit:

Equivalent circuit

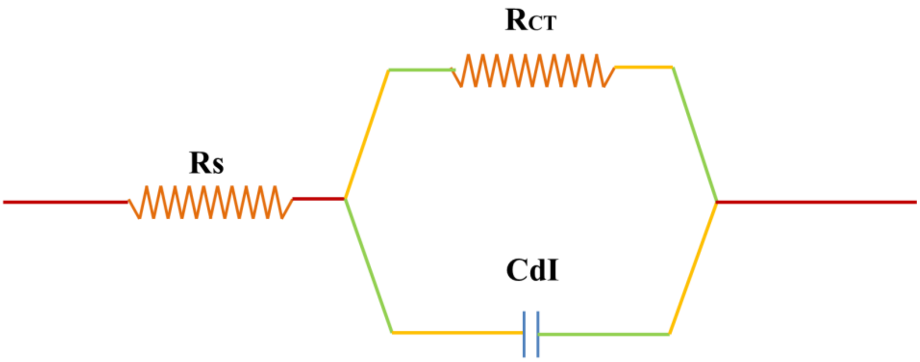

Impedance data were fitted to the most suitable equivalent circuit mentioned above with the help of EC-Lab software. The equivalent circuit is composed of three major components connected to each other in series. The bulk resistance (R_S) connected in series with a parallel combination of charge transfer resistance (R_{CT}) and a capacitor (CdI). Here R_S accounts for the bulk resistance of the membrane while R_{CT} represents the charge transfer resistance existing between the electrodes and the membrane electrolyte. Here, it should be noted that, charge transfer resistance R_{CT} is not associated with the conductivity of the electrolyte. Instead R_S is the crucial factor which quantifies the resistance of the bulk electrolyte. The bulk resistance of electrolyte i.e., R_S is of our primary interest as it represents conductivity of the membrane. R_S depends on (a) intrinsic conductivity of the PA loaded membrane sample (b) thickness of the membrane and (c) area of cross section of the membrane. Thus, to determine the proton conductivity of the membrane sample from the R_S value both of the other two factors (*i.e.,* area of cross section and thickness of membrane) should be taken into consideration.

Here we provide the values of R_S, and R_{CT} by fitting the experimentally obtained data points along the curve generated by the equivalent circuit mentioned above.

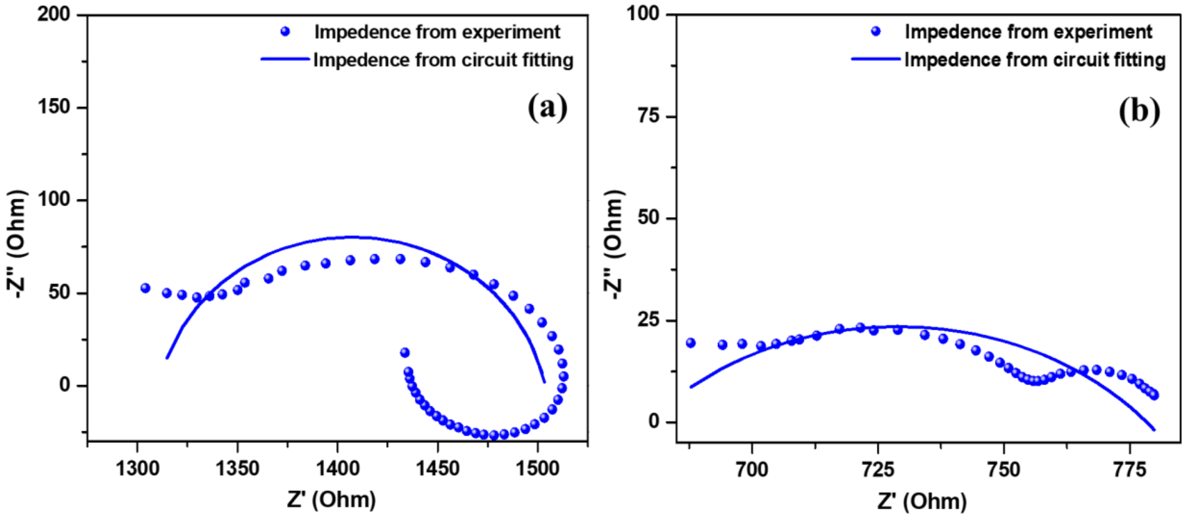

Figure A3.17. (a) Nyquist plot of **{$W_{72}Fe_{30}$}-2.5%** and **(b) {$W_{72}Fe_{30}$}-5%** membrane after equivalent circuit fitting at 160 °C.

Table A3.3. Fitting parameters to determine proton conductivity of **{$W_{72}Fe_{30}$}-2.5%** membrane in various temperatures**: Membrane thickness = 0.002 cm** or **0.02 mm.**

Temperature (°C)	**Value of R_S (Ohm)**	**Conductivity (Scm^{-1})**
30 °C	4508.9	0.037
50 °C	2512.6	0.066
60 °C	2055.2	0.081

80 °C	1775.9	0.094
100 °C	1505.9	0.110
120 °C	1405.1	0.118
140 °C	1381.9	0.120
160 °C	1314.9	0.126

Table A3.4. Fitting parameters to determine proton conductivity of **$\{W_{72}Fe_{30}\}$-5%** composite membrane in various temperatures**: Membrane thickness =0.003 cm** or **0.03 mm.**

Temperature (°C)	**Value of R_S (Ohm)**	**Conductivity (Scm^{-1})**
30 °C	2509.5	0.044
50 °C	1408.7	0.078
60 °C	1206.1	0.092
80 °C	1037.1	0.107
100 °C	894.24	0.124
120 °C	813.40	0.136
140 °C	724.80	0.153
160 °C	695.64	0.159

Section A3.17 - Isothermal proton conductivity of $\{W_{72}Fe_{30}\}$ loaded MMMs at 160 °C.

Isothermal proton conductivities of the m-PBI, **$\{W_{72}Fe_{30}\}$-2.5%** and **$\{W_{72}Fe_{30}\}$-5%** membranes were also measured to check the MMMs long term proton conductivity retention under elevated temperature. The membranes were isothermally kept at 160 °C for 24 h and the conductivity of individual membrane was measured for every 2 h interval up to 24 h. We observed an initial minor decrement in the proton conductivity values within the first 2-4 h of analysis. After the initial period, proton conductivities of the membranes found to be stable up to the entire experimental time range (24 h). Hydrophilic **$\{W_{72}Fe_{30}\}$** polyoxometalates loaded MMMs resulted prior retention of proton conductivity when compared to m-PBI. Generation of extensive donor-acceptor type H-bonding interaction between the –Fe=O, -W=O, and –Fe-OH_2 with the m-PBI imidazole 'N-H' groups, resulted formation of ordered structure into the composites network along with altered morphology, responsible for enhanced thermal, dimensional and thermo-mechanical stability of the membranes followed by retention of proton conductivity under prolong isothermal environment at elevated temperature (160 °C).

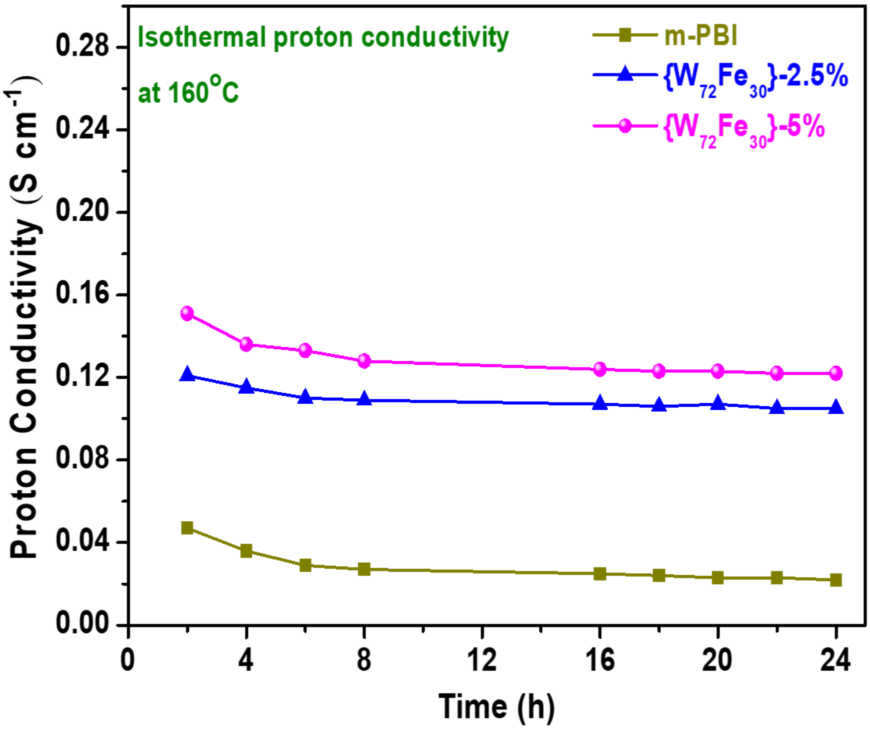

Figure A3.18. Isothermal proton conductivity of PA doped **m-PBI, $\{W_{72}Fe_{30}\}$-2.5%** and **$\{W_{72}Fe_{30}\}$-5%** membranes at 160 °C for 24 h.

Section A3.18 - AC impedance measurement of 50% $\{W_{72}Fe_{30}\}$@m-PBI composite membrane in aqueous medium.

Table A3.5. Table of fitting parameters to determine proton conductivity of 50% $\{W_{72}Fe_{30}\}$@m-PBI at various temperatures in aqueous medium:

Temp. (°C)	Software	Value of R1(Ω)	Conductivity (Scm^{-1})	χ^2 value
80	EC-Lab V10.21	0.944	0.0570	3.771×10^{-3}
70	EC-Lab V10.21	1.115	0.0583	1.074×10^{-3}
60	EC-Lab V10.21	1.338	0.0402	0.278×10^{-3}
50	EC-Lab V10.21	1.507	0.0357	0.453×10^{-3}
40	EC-Lab V10.21	26.58	0.0020	3.054×10^{-3}
30	EC-Lab V10.21	32.36	0.0016	6.078×10^{-3}

To calculate the proton conductivity of the **50% $\{W_{72}Fe_{30}\}$@m-PBI**, the experimentally obtained impedance spectral data were fitted with the same electrical circuit ((R1/Q1) + (R2/Q2) + Q3 which we have used for the compound **$\{W_{72}Fe_{30}\}_{NM}$**.

Calculation of proton conductivity from the R1 value for 50% {$W_{72}Fe_{30}$}@m-PBI at 80 °C:

Value of R1 =**0.9448 Ω**.

Now we know, Conductance **(L) = (1/R) = σ × (A/d)** ……. Eqn (1)

Thus, conductivity **(σ) = (L) × d/A = (1/R) × (d/A)** …….. Eqn (2)

d = thickness of pellet = 0.083 cm.

A = area of cross section of pellet = 1.4 cm^2.

Putting the value R1 =**0.9448 Ω**, in Eqn (2) we get the conductivity of **50% {$W_{72}Fe_{30}$}@m-PBI** at 80 °C.

Conductivity of **50% {$W_{72}Fe_{30}$}@m-PBI** at 80 °C is **(σ)** $_{80\,°C}$ = **5.706 × 10^{-2}** Scm^{-1}.

All the conductivity data **50% {$W_{72}Fe_{30}$}@m-PBI** were calculated using similar data fitting and similar calculations.

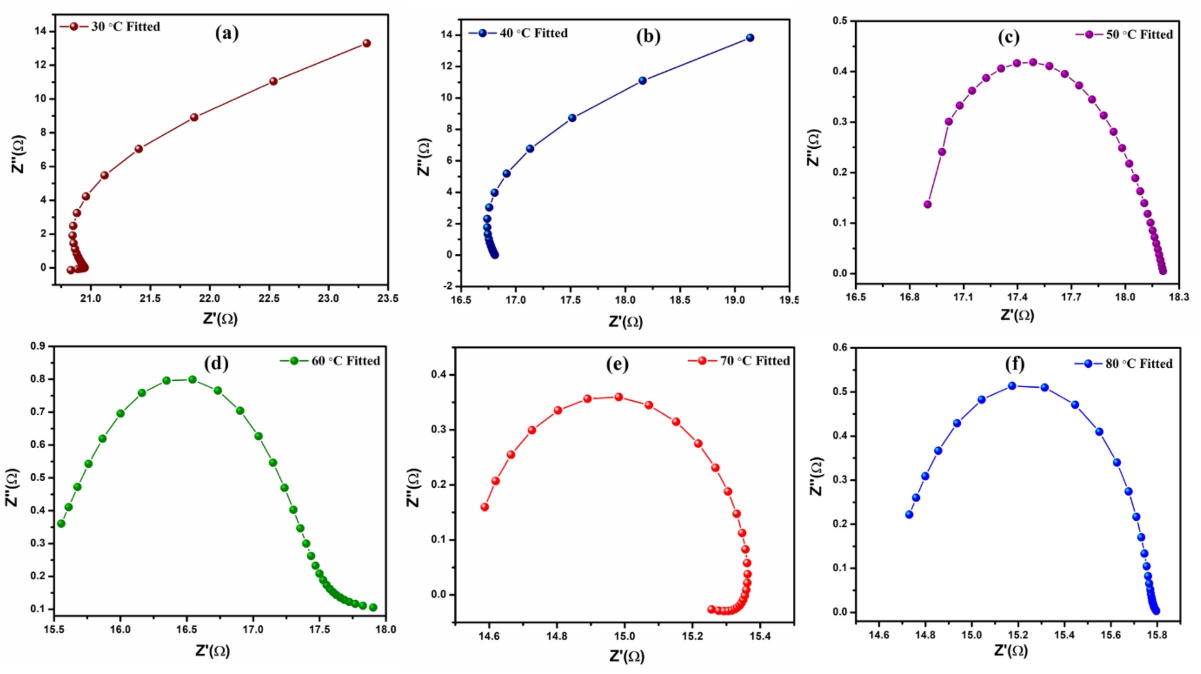

Figure A3.19. (a-f) Nyquist plots of impedance spectra collected from 30 °C to 80 °C at 98% RH for the compound **50% {$W_{72}Fe_{30}$}@m-PBI**.

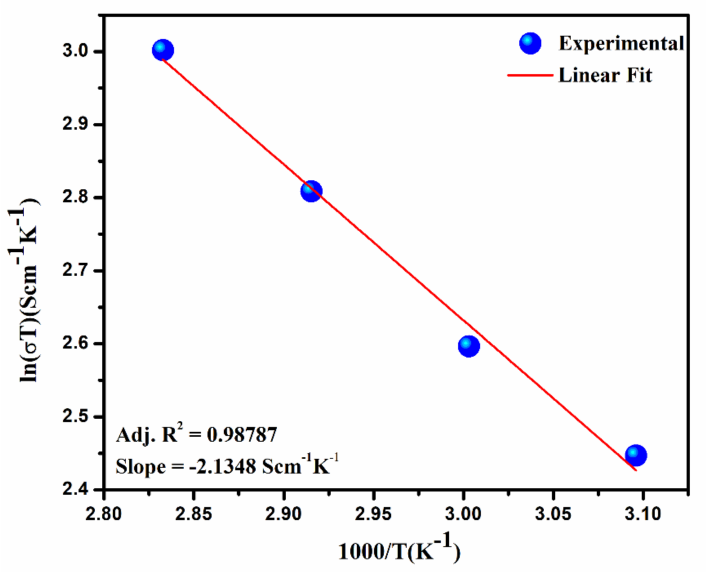

Figure A3.20. (a) Arrhenius plots of temperature dependence of proton conductivity of **50% $\{W_{72}Fe_{30}\}$@m-PBI**.

Calculation of activation energy:

From Arrhenius Equation, Eqn. (4) $\ln(\sigma T) = \ln\sigma_0 + (-E_a/(1000\times R))(1000/T)$

It also represents the straight-line plot obtained between $\ln(\sigma T)$ and $1000/T$

Thus, Slope (m) = $(-E_a/1000\times R) = 2.1348\ Scm^{-1}K^{2}$.

Activation energy of **50% $\{W_{72}Fe_{30}\}$@m-PBI**, **(E_a)** = 189.584 kJ/mole = 0.1845 eV.

A3.19 – Storage modulus values [E′ (MPa)] obtained from DMA, tensile stress values (MPa) and Elongation at break (%) values obtained from UTM analysis

Table S6. Temperature dependent storage modulus of the **m-PBI@$\{W_{72}Fe_{30}\}$** membranes obtained from DMA analysis.

Sample	E′ (MPa) at 100 °C	% of increase	E′ (MPa) at 250 °C	% of increase	E′ (MPa) at 400 °C	% of increase
m-PBI	1844		1577		921	
$\{W_{72}Fe_{33}\}$-2.5%	8616	367.24	7281	361.69	4194	355.37
$\{W_{72}Fe_{33}\}$-5%	7711	318.16	6335	301.71	3525	282.73

Table A3.7. Tensile Stress and Elongation at Break Values of m-PBI, **$\{W_{72}Fe_{30}\}$-2.5%** and **$\{W_{72}Fe_{30}\}$-5%** Composite Membranes

Sample	**Tensile stress at break (MPa)**	**Elongation at break (%)**
m-PBI	3.28	47
$\{W_{72}Fe_{30}\}$-2.5%	21.66	95
$\{W_{72}Fe_{30}\}$-5%	18.00	110

Section A3.20 A brief literature Survey of **$\{W_{72}Fe_{30}\}$** based proton conductors

Table A3.7. Table of various reported POM based proton conductors and their conductivity

S.No.	**Compound**	**Conductivity (S cm^{-1})**	**Activation Energy (eV)**	**Conditions**	**Reference**
0	**$\{W_{72}Fe_{30}\}_{NB}$**	**3.30×10^{-1}**	**1.952**	**80 °C, 98% RH**	**This work**
1	$\{Mo_{72}Fe_{30}\}$	1.85×10^{-3}	0.24	<57 °C, 50% RH	2
2	Mo_{240}	1.03×10^{-1}	0.24	80 °C, 98% RH	3
3	$HImMo_{132}$	4.98×10^{-2}	0.51	60 °C, 98% RH	4
4	$HMeIm\text{-}Mo_{132}$	2.1×10^{-2}	0.44	60 °C, 98% RH	4
5	$NbO_2(OH)PW_{12}$	7.25×10^{-3}	0.39	77 °C, 98% RH	5
6	$NaH_{15}\{[P_2W_{15}Nb_3O_{62}]_2(4PBA)_2((4PBA)_2O)\}\cdot 53H_2O$	1.59×10^{-1}	0.66	90 °C, 98% RH	6
7	$H_{14}[Na_6(H_2O)_{12}]_4[K_{42}Ge_8W_{72}O_{272}(H_2O)_{60}]\cdot$solvent	6.8×10^{-2}	0.52	85 °C, 98% RH	7
8	$[Cu_{12}(BTC)_8(H_2O)_{12}][H_3PW_{12}O_{40}]nH_2O$	4.76×10^{-5}	0.41	90 °C, 70% RH	8
9	$\{Na_7[(nBu)_4N]_{17}\}[Zn(P_3Mo_6O_{29})_2]_2\cdot$solvent	1.04×10^{-2}	0.22	80 °C, 75% RH	9
10	$K_{11}Eu[P_5W_{30}O_{110}K]\cdot 30H_2O$	1.0×10^{-2}	0.26	95 °C, 90% RH	10
11	$K_5H_6Eu[P_5W_{30}O_{110}K]\cdot 0.032PAA3000\cdot 30H_2O$	1.2×10^{-2}	0.48	95 °C, 90% RH	10
12	$H_{13}(HIm)_4K_2Na_4(H_2O)_9[Sb^{III}{}_9Sb^{V}Sm_3O_{14}{}^{-}(H_2O)_3][(SbW_9O_{33})_3(PW_9O_{34})]\cdot 26H_2O$	1.64×10^{-2}	0.54	85 °C, 98% RH	11
13	$(H_2bimb)_3[Zn_3(H_6P_4Mo_6O_{31})_2]$	4.54×10^{-3}	0.46	85 °C, 98% RH	12
14	$K_8H_4[Bi(H_2O)P_5W_{30}O_{110}]\cdot 0.03PAA5000\cdot 19H_2O$	8.5×10^{-3}	0.16	95 °C, 75% RH	13

15	$K_{13.0}H_{1.0}[Na(H_2O)P_5W_{30}O_{110}]\cdot 0.03PAA5000\cdot 20H_2O$	1.7×10^{-3}	0.40	65 °C, 75% RH	14
16	$H[Ce(H_2O)_4]_2[Mn^{V1}_3O_{38}]\cdot 9NMP\cdot 17H_2O$	4.68×10^{-3}	0.45	61 °C, 97% RH	15
17	$H[La(H_2O)_4]_2[Mn^{V1}_3O_{38}]\cdot 9NMP\cdot 17H_2O$	3.46×10^{-3}	0.48	61 °C, 97% RH	15
18	$[La_{10}Ni_{48}W_{140}Sb_{16}P_{12}O_{568}(OH)_{24}(H_2O)_{20}]^{86-}$	2.05×10^{-2}	0.22	22 °C, 100% RH	16
19	$\{(NH_4)_{13}[Mo_{28}^{V}Mo_{126}^{VI}O_{456}H_{34}(H_2O)_{70}]Cl_{17}(ClO_4)_{14}\cdot mH_2O\ (m\approx 240)\}_n$ (3D-$\{Mo_{154}\}_n$)	1.1×10^{-2}	0.264	22 °C, 100% RH	17
20	$H_5PW_{10}V_2O_{40}\cdot 15H_2O$	1.27×10^{-2}	0.263	18 °C, 80% RH	18
21	$C_{108}H_{36}Cu_{24}N_{48}O_{116}PMo_4V_8$	8.03×10^{-3}	0.96	70 °C , 98% RH	19
22	$H_2[Cu_2OL_3(H_2O)_2][Ce(L)(H_2O)_3(PW_{11}O_{39})]\cdot 17H_2O$	3.175×10^{-4}	0.456	85 °C, 98% RH	20
23	$((TEAH)_7K_2H_9\{P_2W_{18}\}\subset\{Mo_{24}Fe_{12}\}\cdot 116H_2O)$	5.9×10^{-3}	0.28	95 °C, 90% RH	21
24	$((TEAH)_{14}Na_{10}K_8H_8\{P_5W_{30}\}_2\subset\{Mo_{22}Fe_8\}\cdot 50H_2O)$	1.7×10^{-2}	0.31	95 °C, 90% RH	21
25	$[Cu(H_2bibb)_2(H_2O)_3(\alpha P_2W_{18}O_{62})]\cdot 10.5H_2O$	2.52×10^{-4}	0.42	85 °C, 98% RH	22
26	(TMA)KNa-$Mo_{16}S_{16}Se_8$	1.2×10^{-2}	0.77	55 °C, 97% RH	23
27	$H_3PW_{12}O_{40}\cdot 29H2O$	1.7×10^{-1}	0.14	25 °C, 80±5% RH	24
28	$H_3PMo_{12}O_{40}\cdot 29H2O$	1.8×10^{-1}	0.16	25 °C, 80±5% RH	24

References:

1. Kolli, H. K.; Jana, D.; Das, S. K. Nanoblackberries of $\{W_{72}Fe_{33}\}$ and $\{Mo_{72}Fe_{30}\}$: Electrocatalytic Water Reduction. *Inorg. Chem.* **2021**, *60*, 15569–15582.
2. Tandekar, K.; Singh, C.; Supriya, S. Proton Conductivity in $\{Mo_{72}Fe_{30}\}$-Type Keplerate. *Eur. J. Inorg. Chem.* **2021**, 734–739.
3. Lin, J.; Li, N.; Yang, S.; Jia, M.; Liu, J.; Li, X. M.; An, L.; Tian, Q.; Dong, L. Z.; Lan, Y. Q. Self-Assembly of Giant Mo_{240} Hollow Opening Dodecahedra. *J. Am. Chem. Soc.* **2020**, *142*, 13982–13988.
4. Liu, W. J.; Dong, L. Z.; Li, R. H.; Chen, Y. J.; Sun, S. N.; Li, S. L.; Lan, Y. Q. Different Protonic Species on Affecting Proton-Conductivity in Hollow Sphere-Like Polyoxometalates. *ACS Appl. Mater. Interfaces* **2019**, *11*, 7030–7036.
5. Wang, Y. D.; Wang, J. X.; Wei, M. J.; Liu, B. L.; Zang, H. Y.; Tan, H. Q.; Wang, Y. H.; Li, Y. G. Niobium Oxyhydroxide-Polyoxometalate Composite as an Efficient Proton-Conducting Solid Electrolyte. *ChemElectroChem* **2018**, *5*, 1–6.
6. Li, S.; Zhao, Y.; Knoll, S.; Liu, R.; Li, G.; Peng, Q.; Qiu, P.; He, D.; Streb, C.; Chen, X. High Proton-Conductivity in Covalently Linked Polyoxometalate-Organoboronic Acid-Polymers. *Angew. Chem. Int. Ed.* **2021**, *60*, 16953 –16957.
7. Li, Z.; Lin, L. D.; Yu, H.; Li, X. X.; Zheng, S. T. All-Inorganic Ionic Porous Material Based on Giant Spherical Polyoxometalates Containing Core-Shell $K_6@K_{36}$-Water Cage. *Angew. Chem.* **2018**, *130*, 16003 –16007.
8. Liu, Y.; Yang, X.; Miao, J.; Tang, Q.; Liu, S.; Shi, Z.; Liu, S. Polyoxometalate-functionalized metal–organic frameworks with improved water retention and uniform proton-conducting pathways in three orthogonal directions. *Chem. Commun.* **2014**, *50*, 10023-10026.
9. Gao, Q.; Wang, X. L.; Xu, J.; Bu, X. H. The First Demonstration of the Gyroid in a Polyoxometalate-Based Open Framework with High Proton Conductivity. *Chem. Eur. J.* **2016**, *22*, 9082-9086.
10. Iwano, T.; Shitamatsu, K.; Ogiwara, N.; Okuno, M.; Kikukawa, Y.; Ikemoto, S.; Shirai, S.; Muratsugu, S.; Waddell, P. G.; Errington, R. J.; Sadakane, M.; Uchida, S. Ultrahigh Proton Conduction via Extended Hydrogen-Bonding Network in a Preyssler-Type Polyoxometalate-Based Framework Functionalized with a Lanthanide Ion. *ACS Appl. Mater. Interfaces* **2021**, *13*, 19138-19147.

11. Xiao, H. P.; Zhang, R. T.; Li, Z.; Xie, Y. F.; Wang, M.; Ye, Y. D.; Sun, C.; Sun, Y. Q.; Li, X. X.; Zheng, S. T. Organoamine-Directed Assembly of 5p−4f Heterometallic Cluster Substituted Polyoxometalates: Luminescence and Proton Conduction Properties. *Inorg. Chem.* **2021**, *60*, 13718-13726.
12. Wang, X.; Mao, W.; Song, Y.; Meng, F.; Hu, X.; Liu, B.; Su, Z. Hourglass-Type Polyoxometalate-Based Crystalline Material as an Efficient Proton-Conducting Solid Electrolyte. *Inorg. Chem.* **2021**, *60*, 18912-18917.
13. Iwano, T.; Miyazawa, S.; Osuga, R.; Konda, J. N.; Honjo, K.; Kitao, T.; Uemura, T.; Uchida, S. Confinement of poly(allylamine) in Preyssler-type polyoxometalate and potassium ion framework for enhanced proton conductivity. *Commun. Chem.* **2019**, *2*, 1-8.
14. Niinomi, K.; Miyazawa, S.; Hibino, M.; Mizuno, N.; Uchida, S. High Proton Conduction in Crystalline Composites Based on Preyssler-Type Polyoxometalates and Polymers under Nonhumidified or Humidified Conditions. *Inorg. Chem.* **2017**, *56*, 15187-15193.
15. Wang, J. X.; Wang, Y. D.; Wei, M. J.; Tan, H. Q.; Wang, Y. H.; Zang, H. Y.; Li, Y. G. Inorganic open framework based on lanthanide ions and polyoxometalates with high proton conductivity. *Inorg. Chem. Front.* **2018**, *5*, 1213-1217.
16. Li, S. R.; Wang, H. Y.; Su, H. F.; Chen, H. J.; Du, M. H.; Long, L. S.; Kong, X. J.; Zheng, L. S. A Giant 3d-4f Polyoxometalate Super-Tetrahedron with High Proton Conductivity. *Small Methods* **2020**, *2000777*, 1-7.
17. Wang, H. Y.; Li, S. R.; Wang, X.; Long, L. S.; Kong, X. J.; Zheng, L. S. Enhanced proton conductivity of Mo_{154}-based porous inorganic framework. *Sci. China. Chem.* **2021**, *64*, 959-963.
18. Wu, X.; Wu, Q. A typical solid high-protonic conductor: A kind of vanadium-substituted heteropoly acid $H_5PW_{10}V_2O_{40}\cdot 15H_2O$. *Mater. Lett.* **2021**, *302*, article No.130372.
19. Xin, Y.; Zhou, Y.; Dong, L.; Wei, P.; Zou, X.; Zhang, F.; Li, G. One-pot self-assembly synthesis of $H_{3+x}PMo_{12-x}V_xO_{40}@[Cu_{6O}(TZI)_3(H_2O)_9(NO_3)_n]\cdot(H_2O)_{15}$ for enhanced proton conduction materials. *New J. Chem.* **2022**, *46*, 3909-3915.
20. Zhang, R. T.; Xiao, H. P.; Li, Z.; Wang, M.; Xie, Y. F.; Ye, Y. D.; Li, X. X.; Zheng, S. T. Two highly stable inorganic–organic hybrid 3D frameworks based on Cu–Ln incorporated polyoxometalates for selective dye removal and proton conduction. *CrystEngComm* **2021**, *23*, 2973-2981.

21. Zhu, M.; Iwano, T.; Tan, M.; Akutsu, D.; Uchida, S.; Chen, G.; Fang, X. Macrocyclic Polyoxometalates: Selective Polyanion Binding and Ultrahigh Proton Conduction. *Angew. Chem. Int. Ed.* **2022**, *61*, 1-5.
22. Li, D.; Tan, X. L.; Chen, L. L.; Liu, X. Y.; Li, Y. M.; Dang, D. B.; Bai, Y. Four Dawson POM-based inorganic-organic supramolecular compounds for proton conduction, electrochemical and photocatalytic activity. *J. Solid State Chem.* **2022**, *305*, 122694.
23. Zang, H. Y.; Chen, J. J.; Long, D. L.; Cronin, L.; Miras, H. N. Assembly of Thiometalate-Based {Mo_{16}} and {Mo_{36}} Composite Clusters Combining $[Mo_2O_2S_2]^{2+}$ Cations and Selenite Anions. *Adv. Mater.* **2013**, *25*, 6245-6249.
24. Nakamura, O.; Kodama, T.; Ogino, I.; Miyake, Y. High-Conductivity Solid Proton Conductors: Dodecamolybdophosphoric Acid and Dodecatungstophosphoric Acid Crystals. *Chem. Lett.* **1979**, 17-18.

APPENDIX 4

Supporting data for chapter 4

Table of Contents

Section A4.1. Physical characterizations

The synthesized compounds were characterized by FT-IR, Raman spectroscopy, powder X-ray diffraction, FESEM, HR-TEM, thermogravimetric analysis (TGA) and UV-visible diffused reflectance spectroscopy (DRS), inductively coupled plasmon optical emission spectroscopy (ICP-OES), rheology, proton conductivity and electrical conductivity.

FT-IR (Fourier transformed – infrared spectra) was recorded in iD7 ATR thermo Fisher Scientific-Nicolet iS5 instrument. The xerogel sample was exposed to IR radiation by keeping it on sample holder. Powder X-ray diffraction (PXRD) patterns were recorded on a Bruker D8-Advance diffractometer by using graphite monochromated $CuK\alpha1$ (1.5406Å) and $K\alpha_2$ (1.55439Å) radiation. Diffuse reflectance (DRS) UV-spectroscopy studies have been carried out on UV-2600 Shimadzu UV-Visible spectrophotometer. Field emission scanning electron microscopy (FESEM) measurement along with energy dispersive X-ray (EDX) was recorded on a Carl Zeiss model ultra 55 microscope whereas EDX spectrum was performed using oxford instruments X-Max^N SDD (50mm^2) system and INCA analysis software. Thermogravimetric analysis (TGA) analyses were performed in PerkinElmer-STA 6000 analyzer. Dynamic Vapour Sorption (DVS) studies were performed in TA Q5000 SA instrument. N_2 gas sorption studies were carried out on Quantachrome Autosorb IQ2 instrument. High Resolution Transmission electron microscopy (HR-TEM) images were recorded in an JEM-F200 microscope (JEOL) with an accelerating voltage of 200 kV. The selected area electron diffraction patterns (SAED) were recorded with the help of Gatan Inc CCD camera and GATAN digital microgram software. Zeta potential measurement was recorded in Horiba SZ-100. Rheology studies were carried out with help of strain-controlled rheometer (MCR 501, Anton Paar). All the proton and electrical conductivity measurements were carried out with the help of Zahner Zanium electrochemical workstation operated with Thales software. Details of the proton and electrical conductivity measurements are described below.

Section A4.2. Synthesis, material and procedures.

The synthetic procedures were mentioned in the main article and chemicals used are reagent grade, no further purification is required.

Section A4.3. Images of the compounds $\{W_{72}Fe_{30}\}_{HG}$.

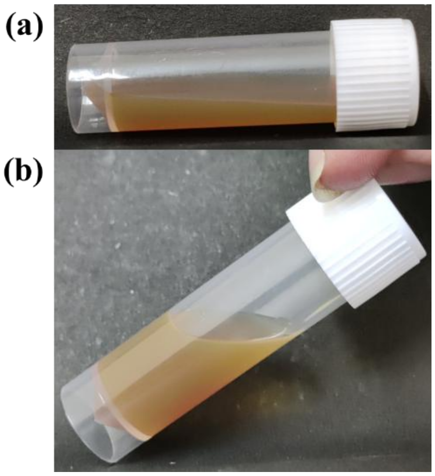

Figure A4.1. (a) and (b) are the pictures of the compound $\mathbf{\{W_{72}Fe_{30}\}_{HG}}$ before gel formation.

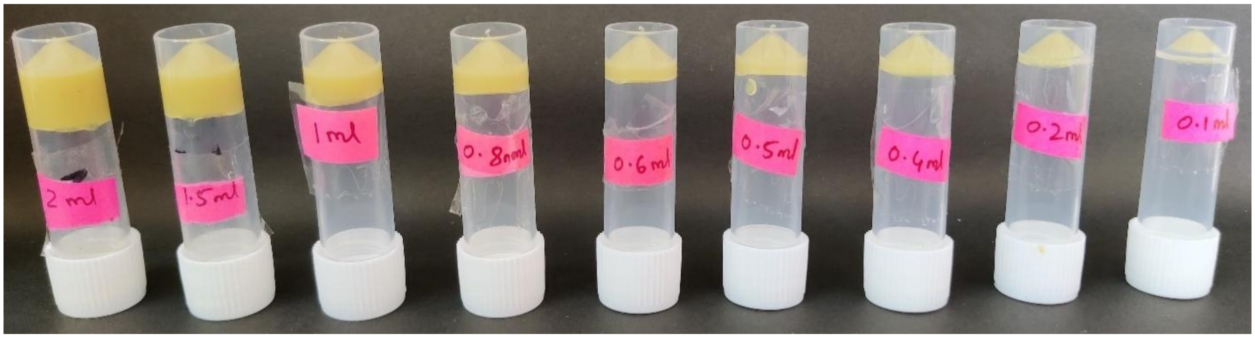

Figure A4.2. Pictures of the compound $\mathbf{\{W_{72}Fe_{30}\}_{HG}}$ after gel formation in the inverted vials of different volumes of the compound.

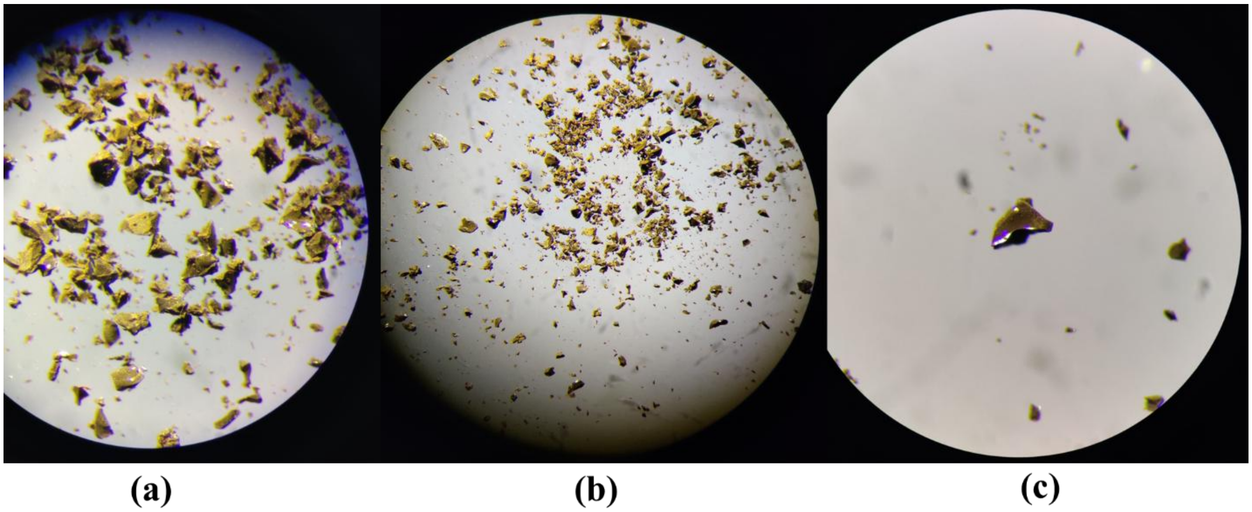

Figure A4.3. Pictures of the compound **$\{W_{72}Fe_{30}\}_{XG}$** under microscope after gel formation dried and washed with water.

Section A4.4. UV-visible spectral analysis of $\{W_{72}Fe_{30}\}_{Gel}$

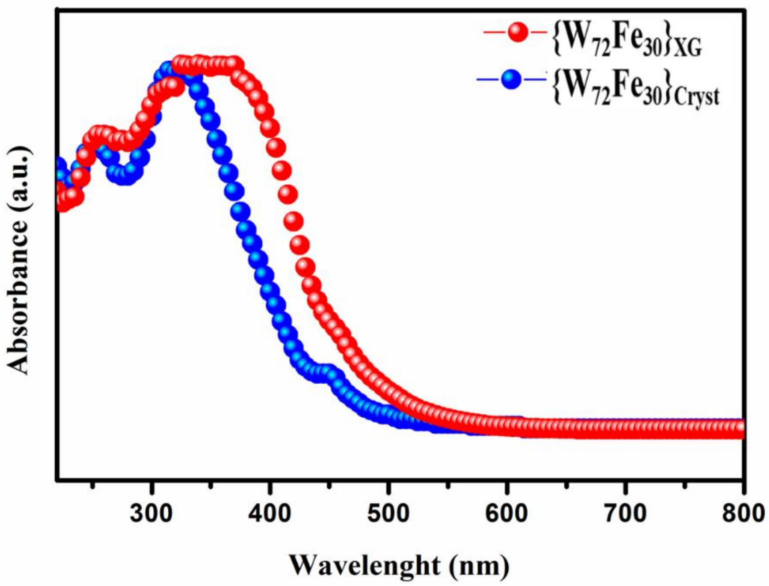

Figure A4.4. Kubelka-Munk converted solid state diffused reflectance electronic spectra (DRS) of the compounds **$\{W_{72}Fe_{30}\}_{Cryst}$** and **$\{W_{72}Fe_{30}\}_{XG}$**.

The solid state diffused reflectance spectra of the compounds **$\{W_{72}Fe_{30}\}_{Cryst}$** and **$\{W_{72}Fe_{30}\}_{XG}$** shows same absorption peaks at the wavelength of 450 nm, 340 and 250 nm respectively after the Kubalka-Munk conversion the absorbance spectrum is displayed in the Figure A4.4.

Section A4.5. FESEM analysis of $\{W_{72}Fe_{30}\}_{XG}$

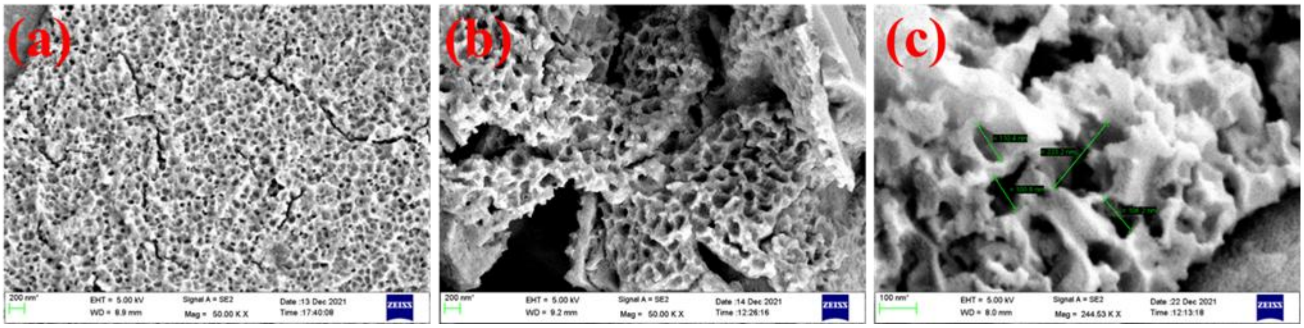

Figure A4.5. (a-c) FESEM images of the immediate dried gel after its formation (i.e. two hours) of compound $\{W_{72}Fe_{30}\}_{XG}$ at different resolutions.

The FESEM images of the compound $\{W_{72}Fe_{30}\}_{XG}$ has been taken on the carbon tape and coated with gold. The gel has been formed within two hours after that immediately it has been dried completely and then washed with water and then dried completely at room temperature. Figures **A4.**5a, **A4.**5b and **A4.**5c clearly show that $\{W_{72}Fe_{30}\}$ cluster containing compound $\{W_{72}Fe_{30}\}_{XG}$ is a porous material. These pores has a size around 200-300 nm as shown in Figure **A4.**5c.

Section A4.6. Energy-dispersive X-ray (EDX) analysis of $\{W_{72}Fe_{30}\}_{XG}$

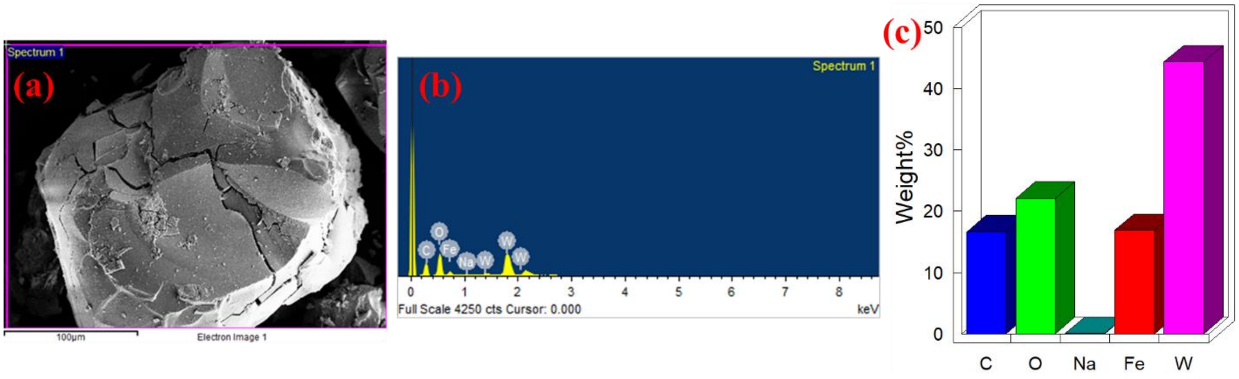

Figure A4.6. (a) Selected surface area of the compound $\{W_{72}Fe_{30}\}_{XG}$ for the EDX analysis; (b) EDX spectrum for the compound $\{W_{72}Fe_{30}\}_{XG}$; (c) histogram of the elemental composition on the selected surface of the compound $\{W_{72}Fe_{30}\}_{XG}$.

Energy dispersive X-ray (EDX) spectroscopy was taken for the compound $\{W_{72}Fe_{30}\}_{XG}$ to know the composition on the surface of the compound. The selected surface area of the compound $\{W_{72}Fe_{30}\}_{XG}$ including its EDX analysis and EDX plot has been shown in Figure **A4.**6a and **A4.**6b. In the Figure **A4.**6c, the elemental composition of the compound $\{W_{72}Fe_{30}\}_{XG}$ can be seen in the form of histograms and it also shown in the Table **A4.**1 which are experimentally recorded with the help of EDX spectroscopy. EDX-elemental mapping images of the compound **$\{W_{72}Fe_{30}\}_{XG}$** are shown in the Figure **A4.**7.

Table A4.1. Elemental composition of the compound **$\{W_{72}Fe_{30}\}_{XG}$** from EDX spectroscopic analysis.

Elements	**Weight %**	**Atomic %**
(Tungsten)W	44.35	7.29
(Iron)Fe	16.88	9.14
(Sodium)Na	0.04	0.06
(Oxygen)O	22.13	41.80
(Carbon)C	16.58	9.14

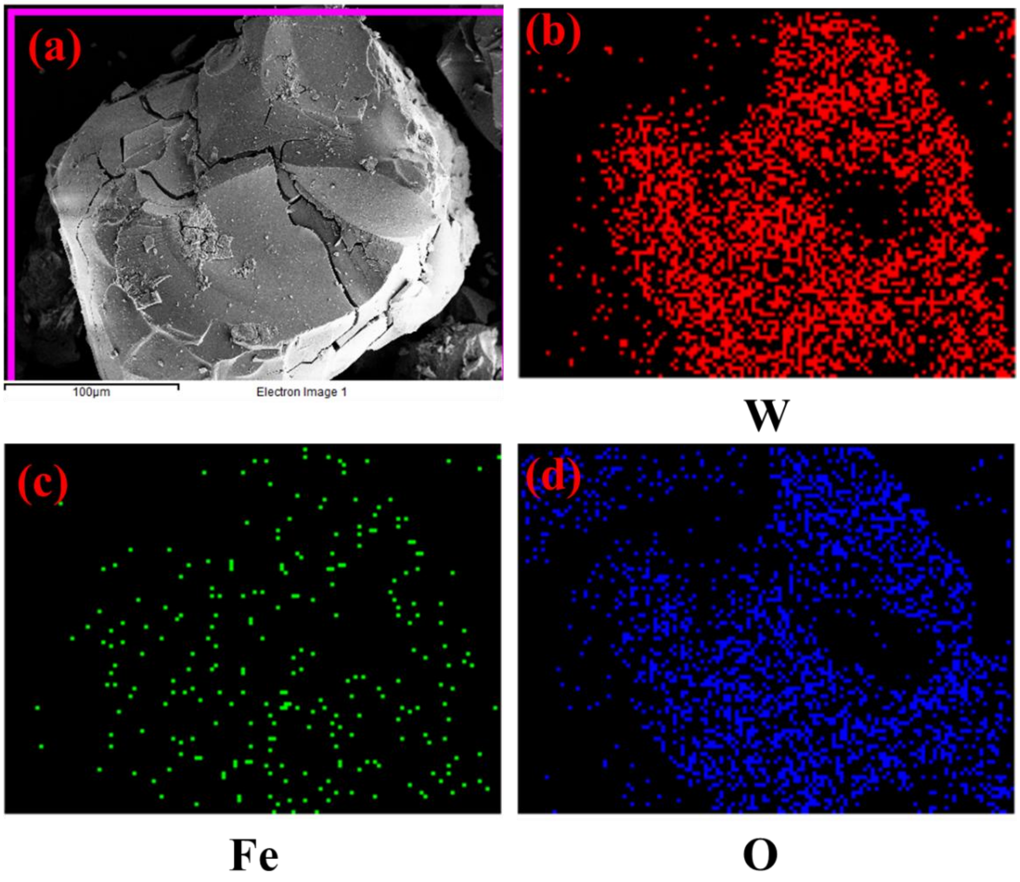

Figure A4.7. (a) FESEM image and selected surface area of the compound **$\{W_{72}Fe_{30}\}_{XG}$** for the EDX- elemental mapping analysis; (b), (c) and (d) displays the elemental abundance of tungsten, iron and oxygen present in the compound **$\{W_{72}Fe_{30}\}_{XG.}$** The sample is coated on a carbon tape.

Section A4.7. Elemental analysis of $\{W_{72}Fe_{30}\}_{XG}$ from ICP-OES analysis

Table A4.2. Comparison of metal elemental composition of the compound **$\{W_{72}Fe_{30}\}_{XG}$**, results from ICP-OES analysis and theoretically obtained metal compositions respectively.

Sample Name	Elements	Na	Fe	W
$\{W_{72}Fe_{30}\}_{XG}$	Calculated	-----	9.27%	49.87% (W)
	Observed	<0.03%	9.88%	47.75% (W)

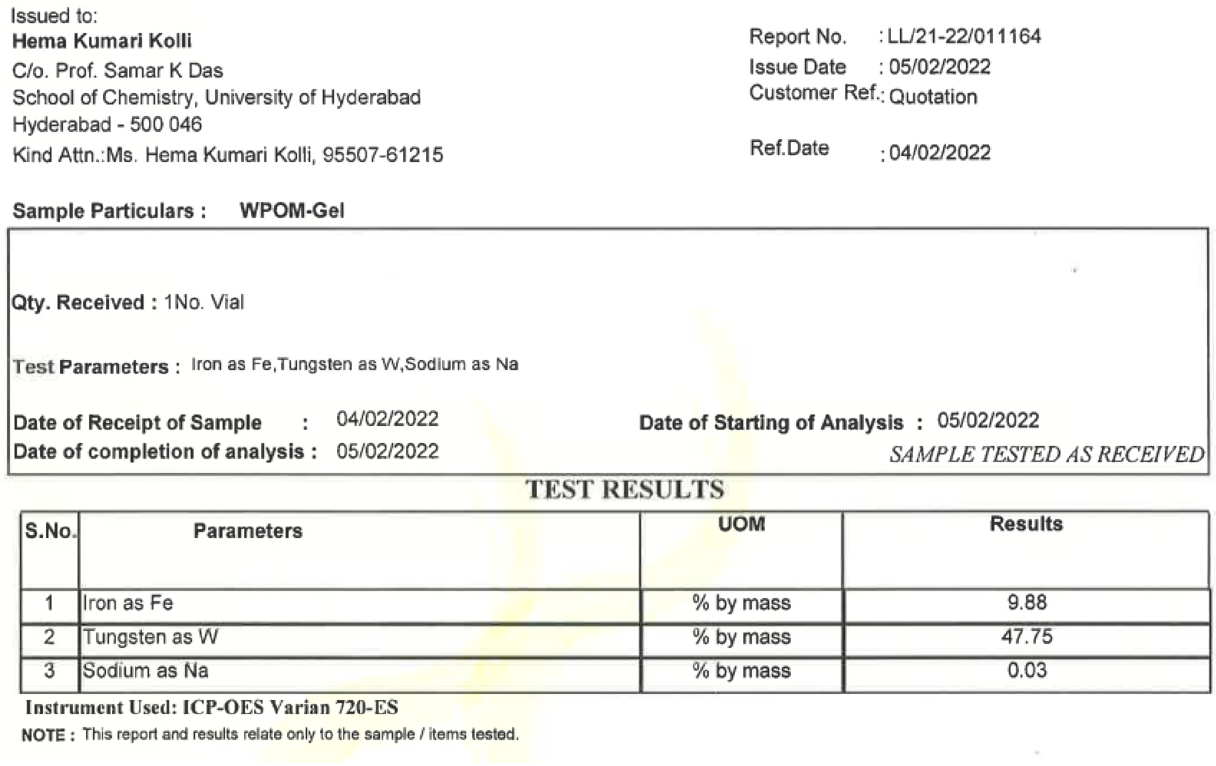

Issued to:
Hema Kumari Kolli
C/o. Prof. Samar K Das
School of Chemistry, University of Hyderabad
Hyderabad - 500 046
Kind Attn.:Ms. Hema Kumari Kolli, 95507-61215

Report No. : LL/21-22/011164
Issue Date : 05/02/2022
Customer Ref.: Quotation
Ref.Date : 04/02/2022

Sample Particulars : **WPOM-Gel**

Qty. Received : 1No. Vial

Test Parameters : Iron as Fe,Tungsten as W,Sodium as Na

Date of Receipt of Sample : 04/02/2022
Date of completion of analysis : 05/02/2022
Date of Starting of Analysis : 05/02/2022

SAMPLE TESTED AS RECEIVED

TEST RESULTS

S.No.	Parameters	UOM	Results
1	Iron as Fe	% by mass	9.88
2	Tungsten as W	% by mass	47.75
3	Sodium as Na	% by mass	0.03

Instrument Used: ICP-OES Varian 720-ES

NOTE : This report and results relate only to the sample / items tested.

Figure A4.8. Results of ICP-OES analysis of the compound **$\{W_{72}Fe_{30}\}_{XG}$** that gives the metal proportion present in the compound.

Section A4.8. Zeta potential measurement of the compound $\{W_{72}Fe_{30}\}_{XG}$

The compound was suspended in water and sonicated for 20 minutes to disperse uniformly. The compound **$\{W_{72}Fe_{30}\}_{XG}$** has been know that they are positively charged, that was proved by the zeta potential studies giving the value around 6.4 mV as shown in the Figure **A4.**9.

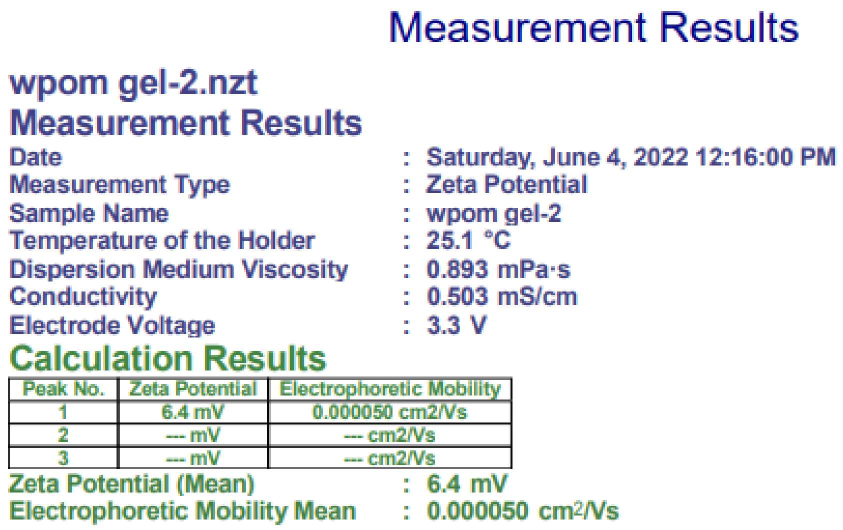

Measurement Results

wpom gel-2.nzt

Measurement Results

Date : Saturday, June 4, 2022 12:16:00 PM
Measurement Type : Zeta Potential
Sample Name : wpom gel-2
Temperature of the Holder : 25.1 °C
Dispersion Medium Viscosity : 0.893 mPa·s
Conductivity : 0.503 mS/cm
Electrode Voltage : 3.3 V

Calculation Results

Peak No.	Zeta Potential	Electrophoretic Mobility
1	6.4 mV	0.000050 cm2/Vs
2	--- mV	--- cm2/Vs
3	--- mV	--- cm2/Vs

Zeta Potential (Mean) : 6.4 mV
Electrophoretic Mobility Mean : 0.000050 cm2/Vs

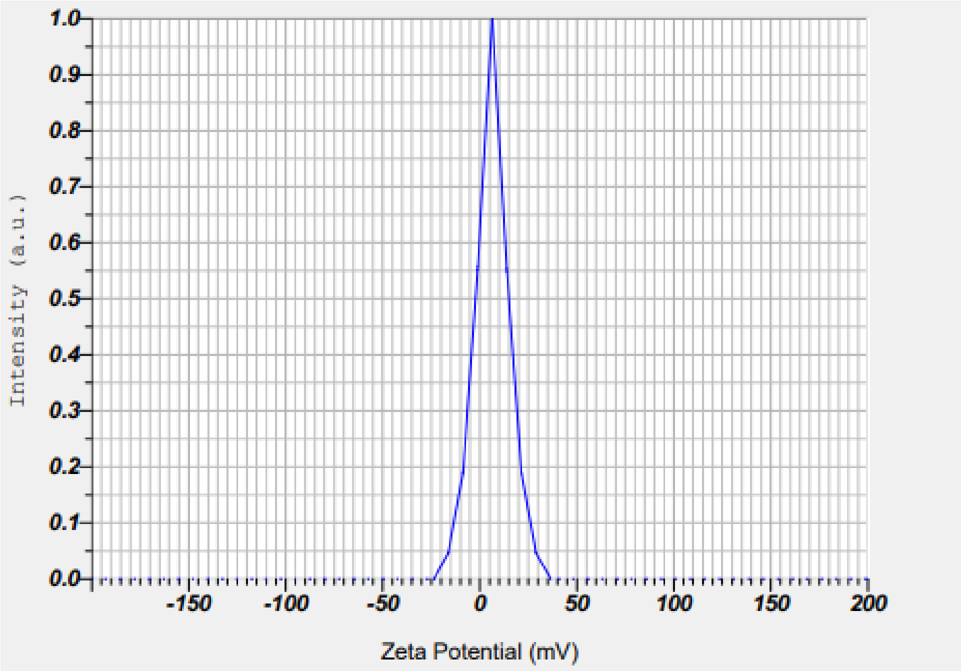

Figure A4.9. Zeta potential phase plot of **$\{W_{72}Fe_{30}\}_{XG}$**.

Section A4.9. Gas adsorption studies.

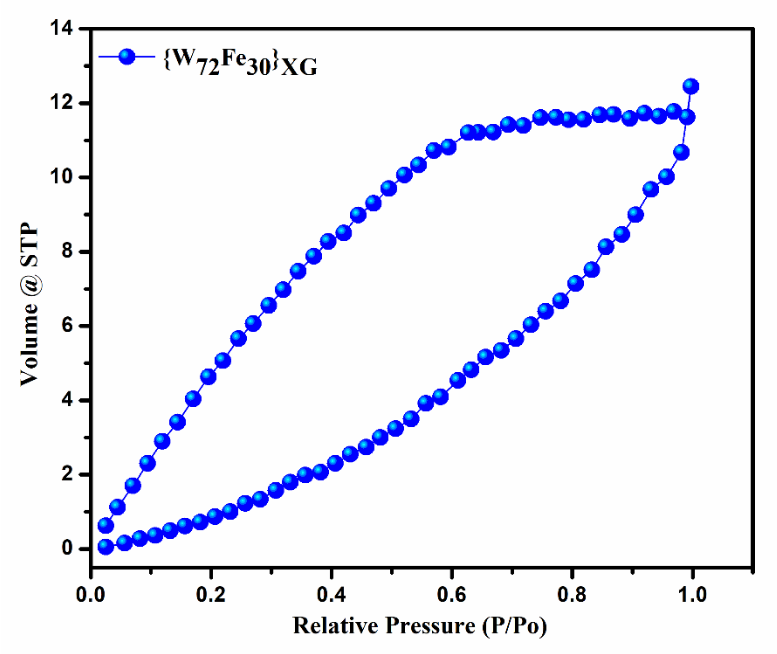

Figure A4.10. Gas adsorption isotherm of the gel compound **{W$_{72}$Fe$_{30}$}$_{XG}$**.

To know the surface porosity of the compound **{W$_{72}$Fe$_{30}$}$_{XG}$**, we have carried out the nitrogen gas adsorption studies. Initially, the sample was degassed at 100° C for 24 hrs under reduced pressure and then we have measured the adsorption isotherm with nitrogen gas using liquid nitrogen bath. As shown in Figure **A4.**10, TYPE III (according to BET classification) adsorption isotherm has been observed. The BET surface area for the compound **{W$_{72}$Fe$_{30}$}$_{XG}$** is 73.737 m^2g^{-1}. The material **{W$_{72}$Fe$_{30}$}$_{XG}$** has an average pore volume and pore width are 0.01925 cc/g and 2268 Å (around 200 nm) respectively. From the results, we have observed that the material has the nature of adsorption isotherm is type III macroporous material. Adsorption Capacity is 0.556 mmol/g.

Section A4.10. Dynamic Vapour Sorption Studies (DVS).

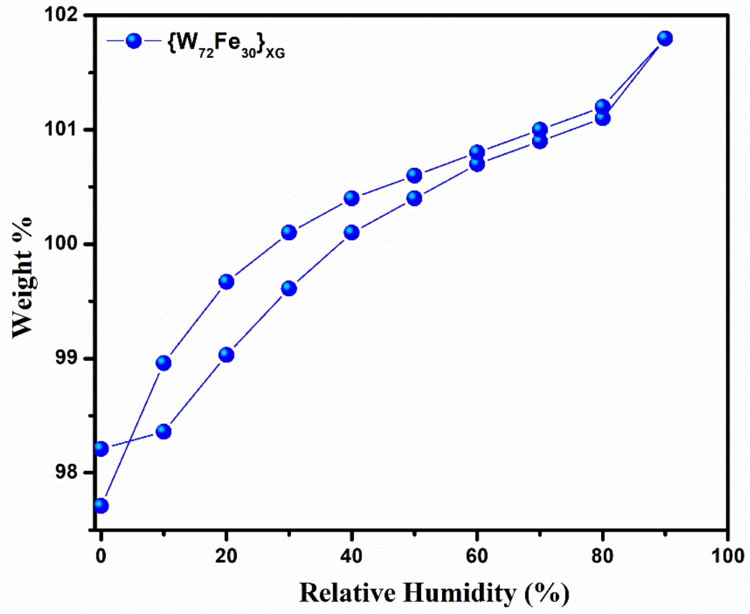

Figure A4.11. Water Up-take capacity of the compound **{$W_{72}Fe_{30}$}$_{XG}$** is determined from the DVS studies.

Initially, the compound **{$W_{72}Fe_{30}$}$_{XG}$** is activated at 100 ^{0}C for 4 hours. The water sorption for the compound **{$W_{72}Fe_{30}$}$_{XG}$** is measured by taking a known amount of sample and a temperature of 25 ^{0}C is maintained by increasing the relative humidity to 90%. We have observed that with the increase of relative humidity there is an increase in water uptake of the compound. As the compound is a gel material, so the water uptake is more.

Section A4.11. Electrochemical Impedance Spectroscopy Analysis (EIS).

Sample Preparation and setup for the measurement.

All the measurement were carried out by using Zahner Zanium electrochemical workstation operated with Thales software. Electrochemical Impedance was measured for the compound **{$W_{72}Fe_{30}$}$_{XG}$** with help of two electrode system in a parallel plate mode. The powdered compound **{$W_{72}Fe_{30}$}$_{XG}$** of 400mg is sandwiched between two carbon papers with the help of a custom-made pellet maker die (as shown in Figure **A4.**12) and kept under the hydraulic pressure of 3 ton for 3 min to make it in the form of pellet to avoid the airgaps in the material and after making the pellets we have carefully checked for breakage or crack on it. The carbon papers were used to decrease the contact resistance between the pellet and the electrode surface. Thickness of the pellet is measured with the help of a screw gauge and we have also measured the diameter of the pellets with the help of a scale and all the pellets have similar diameter as the pellet maker die is having the standard diameter. The pellet is placed between two metallic electrodes setup, it should be ensured that the two carbon papers are in contact with the two electrodes.

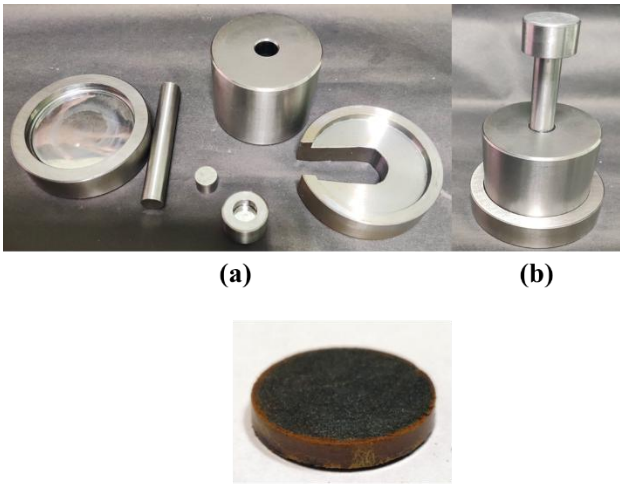

(a) **(b)**

(c)

Figure A4.12. Pellet maker die setup (a) Individual parts of the pellet maker (b) Assembly of parts together to make a pellet (c) Pellet of the compound $\{\mathbf{W_{72}Fe_{30}}\}_{\mathbf{XG}}$.

Then the electrode setup is placed in a homemade setup to carry out the proton conductivity measurements (as shown in Figure **A4.**13). The homemade setup consists of a conical flask of capacity 5 liters, 1-2 liters of distilled water inside the conical flask, a heater cum stirrer as a heating source and to heat the water uniformly and the two-electrode set up fitted (as shown in Figure **A4.**13) with a digital thermometer to monitor the temperature. The digital thermometer with a metallic tip has been adjusted to the length of the pellet position to measure the temperature at the pellet position. A Teflon lid holding the two-electrode setup and a digital thermometer is placed on the top of the conical flask containing water and then sealed with the Teflon tape and there is small hole on the Teflon lid to release the excess pressure due to water vapor inside the conical flask. The whole setup is placed on the heater and thereafter heated to the temperature to reach the required humidity of 98%. The setup was kept at a constant temperature for 2 hours to equilibrate before taking each measurement.

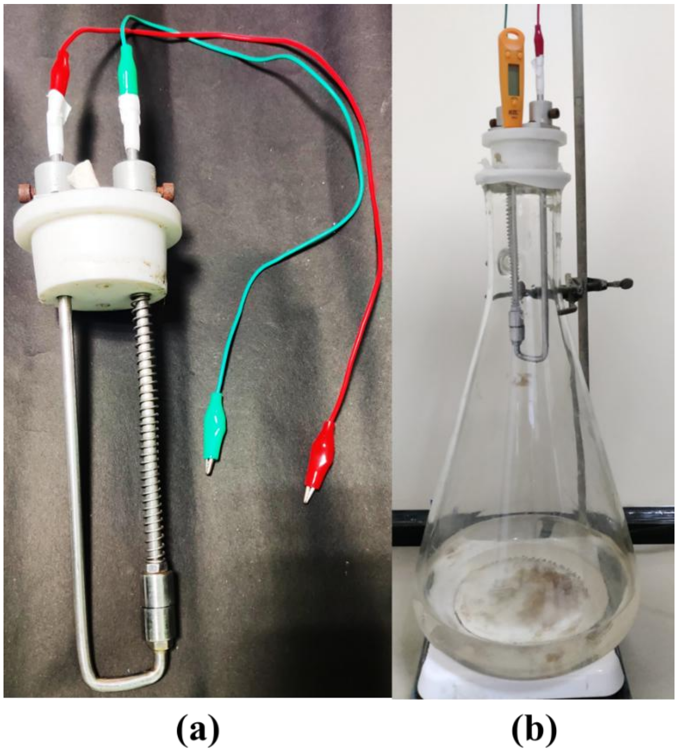

Figure A4.13. (a) Two electrode setup to perform the electrochemical impedance measurements (b) Picture of the home-made setup for carrying out the proton conductivity measurement.

Impedance spectra were recorded in the temperature range of 30 ºC to 80 ºC at a relative humidity of 98% and at a open circuit potential with the help of a sinusoidal signal of 5 mV amplitude with a frequency sweep from 1 Hz to 10^6 Hz.

Calculation of Proton Conductivity from Impedance Spectra.

Impedance spectra were recorded in the temperature range of 30 ºC to 80 ºC at a relative humidity of 98%. Conductivity calculations were done from the Nyquist plot fitted with the suitable equivalent circuit.

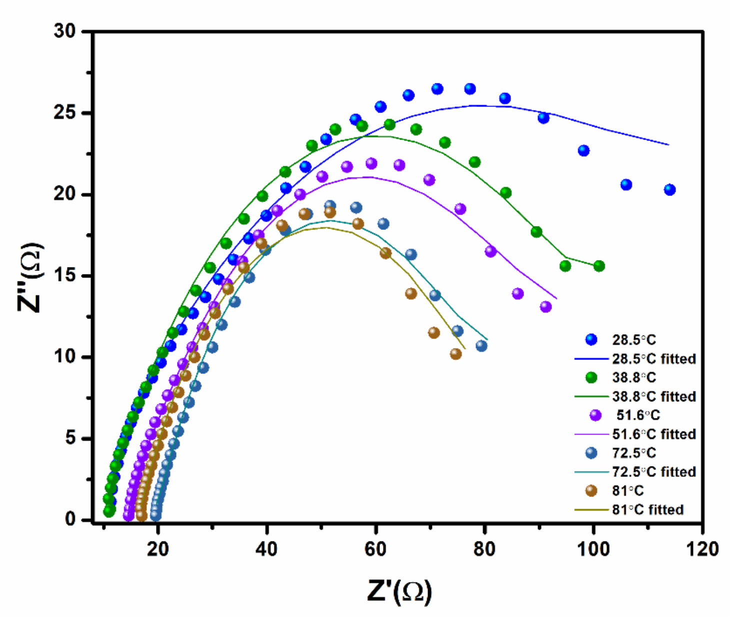

Figure A4.14 Nyquist plots of impedance measurement for the compound **$\{W_{72}Fe_{30}\}_{XG}$** at various temperatures and a relative humidity of 98% (Sphere indicates the experimental data points and thick line indicates the circuit fitted data points).

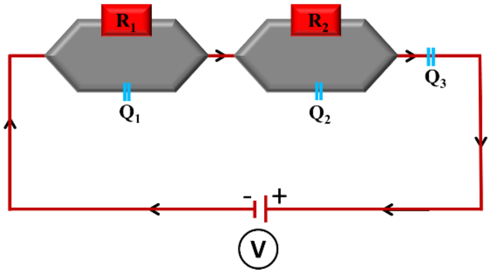

Nyquist plots were constructed between the real part of impedance (Z') and imaginary part of impedance (Z"). We have carried out the temperature-dependent proton conduction measurements for the compound **$\{W_{72}Fe_{30}\}_{XG}$** (Figure **A4.**14). Samples were put up at a constant relative humidity and temperature almost for four hours before collecting the data. The compound **$\{W_{72}Fe_{30}\}_{XG}$** shows a relative increase in the proton conductivity with respect to increase in temperature. The impedance spectral data obtained were analyzed and fitted in the relevant circuit to calculate the proton conductivity ((R_1/Q_1) + (R_2/Q_2) + Q_3), Where R_1 and R_2 are resistance and Q_1, Q_2 and Q_3 are constant phase. Here R1/Q1 is referred as Z_1 and R_2/Q_2 is referred as Z_2 and they are connected to each other in series. Z_1 is the pellet impedance, Z_2 is the impedance at electrode electrolyte junction and Q_3 is the constant phase element which refers to linear low frequency region of the Nyquist plot. In Z_1, R_1 and Q_1 are connected to each other in parallel mode and in Z_2 also R_2 and Q_2 are connected in parallel mode. Here R1 accounts for the bulk resistance of the compound **$\{W_{72}Fe_{30}\}_{XG}$**, where R_2 represents the inter grain proton conduction. The experimental data of impedance spectra obtained could be fitted with the above-mentioned circuit without any notable error (χ^2). **$\{W_{72}Fe_{30}\}_{XG}$** compound shows a proton conductivity (σ) of 6.99×10^{-2} S cm^{-1} at 80 ºC temperature with 98% relative humidity whereas at 30 ºC temperature proton conductivity (σ) of 2.54×10^{-2} S cm^{-1} with a relative humidity of 98%. This is the first time we are reporting the proton conductivity for the $\{W_{72}Fe_{30}\}$ cluster containing compound as a proton conductor.

Table A4.3: Table related to fitting parameters to determine the proton conductivity of the compound **$\{W_{72}Fe_{30}\}_{XG}$** at different temperatures.

Temperature (ºC)	**Software Used**	**Value of R1 (Ω)**	**Conductivity (Scm^{-1})**	**χ^2 Value**
28.5	EC-Lab V10.21	4.495	2.54×10^{-2}	9.66×10^{-3}
38.8	EC-Lab V10.21	3.486	3.28×10^{-2}	4.08×10^{-2}
42.5	EC-Lab V10.21	3.192	3.58×10^{-2}	2.24×10^{-2}
51.6	EC-Lab V10.21	2.62	4.36×10^{-2}	7.19×10^{-3}
63.0	EC-Lab V10.21	2.134	5.35×10^{-2}	4.96×10^{-3}
72.5	EC-Lab V10.21	1.959	5.83×10^{-2}	9.43×10^{-3}
81.0	EC-Lab V10.21	1.635	6.99×10^{-2}	8.62×10^{-3}

Calculation of proton conductivity from the R1 value for the compound $\{W_{72}Fe_{30}\}_{XG}$ at 80 °C with the help of the formula described below (all other proton conductivity values were calculated using similar method):

Value of **R1 =1.635 Ω**.

Now we know, Conductance **(L) = (1/R) = σ × (A/d)** ……. Eqn (1)

Thus, conductivity **(σ) = (L) × d/A = (1/R) × (d/A)** ……. Eqn (2)

Where R is resistance of sample; σ is conductivity of the sample;

d = thickness of pellet = **0.176 cm** for **$\{W_{72}Fe_{30}\}_{XG}$**.

A = area of cross section of pellet = **1.4 cm^2**.

Putting the value **R1 =1.635 Ω**, in Eqn (2) we get the conductivity of **$\{W_{72}Fe_{30}\}_{XG}$** at 80 °C.

Conductivity of **$\{W_{72}Fe_{30}\}_{XG}$** at 80 °C is (σ) 80 °C = 6.99×10^{-2} Scm^{-1}.

All the conductivity data for **$\{W_{72}Fe_{30}\}_{XG}$** was calculated using similar data fitting and similar calculations as shown in the table **A4.**3.

Activation energy (E_a) for the proton conduction of the compound **$\{W_{72}Fe_{30}\}_{XG}$** was calculated from the different temperature proton conductivity measurement. The detailed calculation has been mentioned below.

Activation Energy Calculation:

Activation energy (Ea) of proton conductivity was calculated for **$\{W_{72}Fe_{30}\}_{XG}$** from their proton conductivity values at different temperatures. Derived plot was drawn between ln(σT) and 1000/T for **$\{W_{72}Fe_{30}\}_{XG}$**. Activation energy of proton conductivity was calculated from the slope of the plot with the help of Arrhenius equation. Detailed calculation is given below.

From Arrhenius Equation,

$\Rightarrow \sigma T = \sigma_0 \times \exp(-E_a/RT)$

Where, σ = Proton conductivity of the sample; E_a = Activation energy of proton conduction;

R= Ideal gas constant; T= Temperature in Kelvin.

Above equation can be rewrite as

$\Rightarrow \ln(\sigma T) = \ln\sigma_0 - (E_a/RT)$

$\Rightarrow \ln(\sigma T) = \ln\sigma_0 + (-E_a/(1000\times R)(1000/T)$

Above equation also represents the straight-line plot obtained between ln(σT) and 1000/T.

Thus,

$\Rightarrow$ Slope (m) = $(-E_a/1000\times R) = 2.32356\ Scm^{-1}K^2$.

Activation energy of $\{W_{72}Fe_{30}\}_{XG,}$ (E_a) = 0.200 eV.

We have found that the activation energy (E_a) for the compound **$\{W_{72}Fe_{30}\}_{XG}$** is 0.2 eV. According to the measurement values the compound **$\{W_{72}Fe_{30}\}_{XG}$** follows a water-assisted Grotthuss mechanism for the proton conduction.

Section A4.12. Controlled experiment of compound {$W_{72}Fe_{30}$}$_{XG}$ after EIS measurements.

PXRD profile:

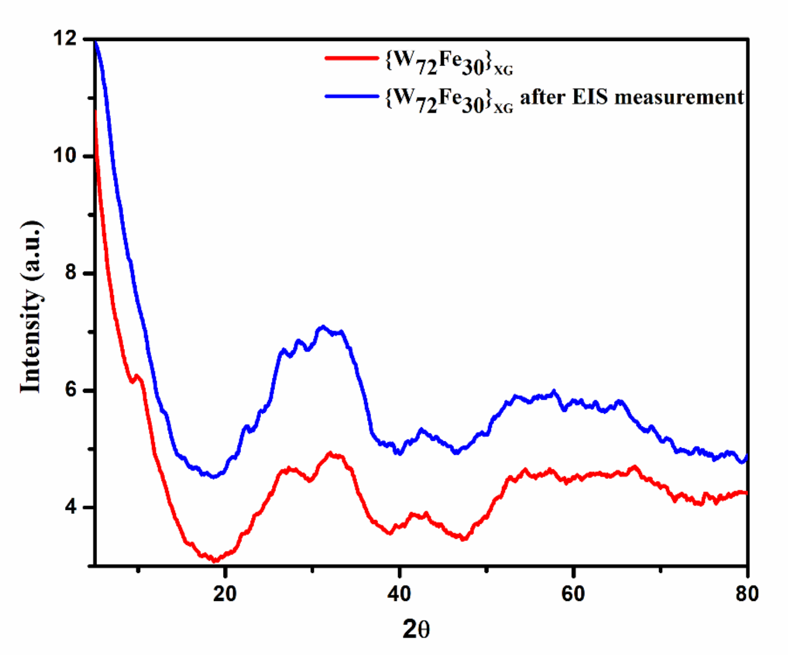

Figure A4.15. Powder X-ray diffraction analysis of the compound **{$W_{72}Fe_{30}$}$_{XG}$** before and after EIS measurement.

Section A4.13. Electrical Conductivity Study.

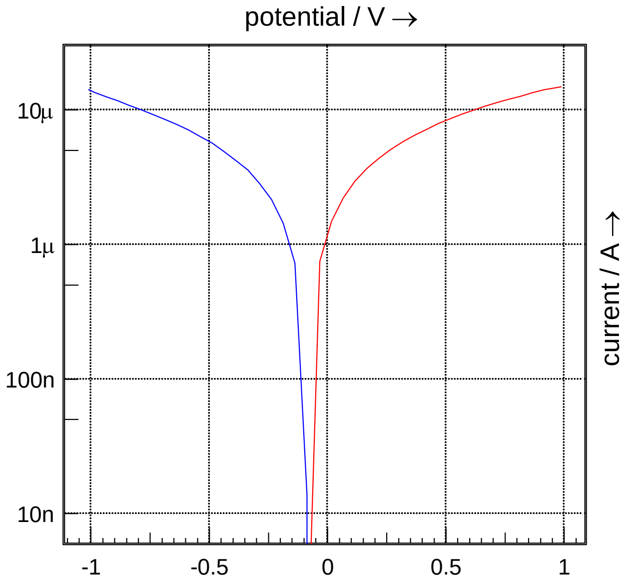

Figure A4.16. Electrical conductivity measurement (Potential vs. Current) of the compound **{$W_{72}Fe_{30}$}$_{XG}$** at a applied potential of -1V to 1V.

A two-electrode setup has been used for the electrical conductivity measurement of the compound $\mathbf{\{W_{72}Fe_{30}\}_{XG}}$. Approximately, 10 mg of finely grinded sample was taken in a cylindrical cell and we were ensured that two electrodes were in contact with the sample, so that when we could apply the electric current (dc current) that can pass through the sample from one metal electrode to another metal electrode of the setup. All the measurements were taken with the help of Zahner Zanium electrochemical workstation.

Calculation of Electrical Conductivity for the compound $\mathbf{\{W_{72}Fe_{30}\}_{XG}}$.

A two-electrode setup has been used for the electrical conductivity measurement of the compound $\mathbf{\{W_{72}Fe_{30}\}_{XG}}$. Approximately, 10 mg of finely grinded sample has been taken in a cylindrical cell and ensure that two electrodes are in contact with the sample, so that when we apply the electric current (dc current), it is allowed to pass through the sample from one metal electrode to another metal electrode of the setup. Electrical conductivity is calculated from the following equations 3 and 4 (Eqn. 3 and 4)

$$\sigma = \frac{l}{RA} \quad \text{.......... Eqn. 1}$$

$$R = \frac{V}{I} \quad \text{........... Eqn. 2}$$

Where, **σ** = Electrical conductivity

l = Length of the sample in the cylindrical cell = **0.06 cm**.

R = Resistance

A = Surface area of the cylindrical cell = $\pi d^2/4$ **= 0.04018 cm²**, where **d = 0.2262 cm**.

V = Applied potential (for compound $\mathbf{\{W_{72}Fe_{30}\}_{XG}}$**,** it is **1V**)

I = current (Observed Current for the compound $\mathbf{\{W_{72}Fe_{30}\}_{XG}}$ is **16.3μA**)

Electrical Conductivity of the compound $\mathbf{\{W_{72}Fe_{30}\}_{XG}}$ at a applied potential of 1V at room temperature is as follows.

$$\sigma = \frac{0.06}{6.134X10^{-4}X0.04018} \ \text{S cm}^{-1}$$

$$\sigma = 0.243X10^{-4} = 2.43X10^{-5} \text{ S cm}^{-1}$$

Electrical Conductivity of the compound $\mathbf{\{W_{72}Fe_{30}\}_{XG}}$ = $\mathbf{2.43X10^{-5}\ S\ cm^{-1}}$.

Section A4.14. Volumetric titration for the estimation of Iron content in the compound $\{W_{72}Fe_{30}\}_{XG}$.

Suspend around 500 mg of compound (**$\{W_{72}Fe_{30}\}_{XG}$**) in 10ml of distilled water. Add 1 M NaOH solution to the above uniformly mixed solution till it gives brick red color solution and stir it for 10 minutes. Filter the mixture and wash the residue thoroughly with water till tungsten completely removed from it (Test the filtrate solution by adding concentrated hydrochloric acid if it gives white precipitate tungsten is remains in the residue, if not residue is free of tungsten). Dissolve the residue in the 10-15 mL of warm concentrated hydrochloric acid and makeup the solution to 20 mL by adding water and then heat the solution at 60ºC for 10 minutes. Add stannous chloride solution when the mixture is hot, color changes from yellow to pale green and excess 2-3 drops of stannous chloride is added. Solution is cooled down to room temperature and then add 10 mL mercuric chloride solution, makeup the solution to 150 mL with water and add 10 mL of Zimmermann Reinhardt solution to it. Now titrate the solution against 0.1 N $KMnO_4$ solution till it gives the pink color (end point).

Normality of $KMnO_4$ solution = 0.1023 N

$$\textbf{Amount of Iron present in the compound} = \frac{\textbf{Molecular weight of Iron x Volume of } \mathbf{KMnO_4} \textbf{ titrated x Normality of } \mathbf{KMnO_4}}{\mathbf{1000}}$$

$$\textbf{Percentage of Iron present in the compound} = \frac{\textbf{Amount of Iron present in the compound}}{\textbf{Total amount of compound taken}} \times \mathbf{100}$$

Percentage of iron present in $\{W_{72}Fe_{30}\}_{XG}$ compound:

Amount of Iron present in the **$\{W_{72}Fe_{30}\}_{XG}$** compound = {56x9.0x0.1023}/1000 = 0.05155 gms.

Percentage of Iron present in the **$\{W_{72}Fe_{30}\}_{XG}$** compound = {0.05155/0.4506}x100 = **11.44 %**.

Section A4.15. Literature survey POM related proton conductors.

Table A4.4. Table of various reported POM based proton conductors and their conductivity.

S.No.	**Compound**	**Conductivity (S cm^{-1})**	**Activation Energy (eV)**	**Conditions**	**Reference**
0	**$\{W_{72}Fe_{30}\}_{XG}$**	**6.99×10^{-2}**	**0.2**	**80 ºC, 98% RH**	**This work**
1	$\{Mo_{72}Fe_{30}\}$	1.85×10^{-3}	0.24	<330K, 50% RH	1
2	Mo_{240}	1.03×10^{-1}	0.24	80 ºC, 98% RH	2
3	$HImMo_{132}$	4.98×10^{-2}	0.51	60 ºC, 98% RH	3
4	$HMeIm\text{-}Mo_{132}$	2.1×10^{-2}	0.44	60 ºC, 98% RH	3
5	$NbO_2(OH)PW_{12}$	7.25×10^{-3}	0.39	77 ºC, 98% RH	4
6	$H_{14}[Na_6(H_2O)_{12}]_4[K_{42}Ge_8W_{72}O_{272}(H_2O)_{60}]\cdot$solvent	6.8×10^{-2}	0.52	85 ºC, 98% RH	5
7	$[Cu_{12}(BTC)_8(H_2O)_{12}][H_3PW_{12}O_{40}]nH_2O$	4.76×10^{-5}	0.41	90 ºC, 70% RH	6
8	$K_{11}Eu[P_5W_{30}O_{110}K]\cdot 30H_2O$	1.0×10^{-2}	0.26	368K, 90% RH	7
9	$K_5H_6Eu[P_5W_{30}O_{110}K]\cdot 0.032PAA3000\cdot 30H_2O$	1.2×10^{-2}	0.48	368K, 90% RH	7
10	$K_8H_4[Bi(H_2O)P_5W_{30}O_{110}]\cdot 0.03PAA5000\cdot 19H_2O$	8.5×10^{-3}	0.16	368K, 75% RH	8
11	$K_{13.0}H_{1.0}[Na(H_2O)P_5W_{30}O_{110}]\cdot 0.03PAA5000\cdot 20H_2O$	1.7×10^{-3}	0.40	338K, 75% RH	9
12	$[La_{10}Ni_{48}W_{140}Sb_{16}P_{12}O_{568}(OH)_{24}(H_2O)_{20}]^{86-}$	2.05×10^{-2}	0.22	295K, 100% RH	10
13	$H_5PW_{10}V_2O_{40}\cdot 15H_2O$	1.27×10^{-2}	0.263	18 ºC, 80% RH	11
14	$H_2[Cu_2OL_3(H_2O)_2][Ce(L)(H_2O)_3(PW_{11}O_{39})]\cdot 17H_2O$	3.175×10^{-4}	0.456	85 ºC, 98% RH	12
15	$((TEAH)_7K_2H_9\{P_2W_{18}\}\subset\{Mo_{24}Fe_{12}\}\cdot 116H_2O)$	5.9×10^{-3}	0.28	368K, 90% RH	13
16	$((TEAH)_{14}Na_{10}K_8H_8\{P_5W_{30}\}_2\subset\{Mo_{22}Fe_8\}\cdot 50H_2O)$	1.7×10^{-2}	0.31	368K, 90% RH	13

17	$[Cu(H_2bibb)_2(H_2O)_3(\alpha P_2W_{18}O_{62})]\cdot 10.5H_2O$	2.52×10^{-4}	0.42	85 ºC, 98% RH	14
18	$H_3PW_{12}O_{40}\cdot$29H2O	1.7×10^{-1}	0.14	25 ºC, 80±5% RH	15

Section A4.16

References.

1. Tandekar, K.; Singh, C.; Supriya, S. Proton Conductivity in $\{Mo_{72}Fe_{30}\}$-Type Keplerate. *Eur. J. Inorg. Chem.* **2021**, 734–739.
2. Lin, J.; Li, N.; Yang, S.; Jia, M.; Liu, J.; Li, X. M.; An, L.; Tian, Q.; Dong, L. Z.; Lan, Y. Q. Self-Assembly of Giant Mo_{240} Hollow Opening Dodecahedra. *J. Am. Chem. Soc.* **2020**, *142*, 13982–13988.
3. Liu, W. J.; Dong, L. Z.; Li, R. H.; Chen, Y. J.; Sun, S. N.; Li, S. L.; Lan, Y. Q. Different Protonic Species on Affecting Proton-Conductivity in Hollow Sphere-Like Polyoxometalates. *ACS Appl. Mater. Interfaces* **2019**, *11*, 7030–7036
4. Wang, Y. D.; Wang, J. X.; Wei, M. J.; Liu, B. L.; Zang, H. Y.; Tan, H. Q.; Wang, Y. H.; Li, Y. G. Niobium Oxyhydroxide-Polyoxometalate Composite as an Efficient Proton-Conducting Solid Electrolyte. *ChemElectroChem* **2018**, *5*, 1–6.
5. Li, Z.; Lin, L. D.; Yu, H.; Li, X. X.; Zheng, S. T. All-Inorganic Ionic Porous Material Based on Giant Spherical Polyoxometalates Containing Core-Shell $K_6@K_{36}^{-}$Water Cage. *Angew. Chem.* **2018**, *130*, 16003 –16007.
6. Liu, Y.; Yang, X.; Miao, J.; Tang, Q.; Liu, S.; Shi, Z.; Liu, S. Polyoxometalate-functionalized metal–organic frameworks with improved water retention and uniform proton-conducting pathways in three orthogonal directions. *Chem. Commun.*, **2014**, *50*, 10023-10026.
7. Iwano, T.; Shitamatsu, K.; Ogiwara, N.; Okuno, M.; Kikukawa, Y.; Ikemoto, S.; Shirai, S.; Muratsugu, S.; Waddell, P. G.; Errington, R. J.; Sadakane, M.; Uchida, S. Ultrahigh Proton Conduction via Extended Hydrogen-Bonding Network in a Preyssler-Type Polyoxometalate-Based Framework Functionalized with a Lanthanide Ion. *ACS Appl. Mater. Interfaces* **2021**, *13*, 19138-19147.
8. Iwano, T.; Miyazawa, S.; Osuga, R.; Konda, J. N.; Honjo, K.; Kitao, T.; Uemura, T.; Uchida, S. Confinement of poly(allylamine) in Preyssler-type polyoxometalate and potassium ion framework for enhanced proton conductivity. *Communications Chemistry*, **2019**, *2*, 1-8.

9. Niinomi, K.; Miyazawa, S.; Hibino, M.; Mizuno, N.; Uchida, S. High Proton Conduction in Crystalline Composites Based on Preyssler-Type Polyoxometalates and Polymers under Nonhumidified or Humidified Conditions. *Inorg. Chem.* **2017**, *56*, 15187-15193.
10. Li, S. R.; Wang, H. Y.; Su, H. F.; Chen, H. J.; Du, M. H.; Long, L. S.; Kong, X. J.; Zheng, L. S. A Giant 3d-4f Polyoxometalate Super-Tetrahedron with High Proton Conductivity. *Small Methods* **2020**, *2000777*, 1-7.
11. Wu, X.; Wu, Q. A typical solid high-protonic conductor: A kind of vanadium-substituted heteropoly acid $H_5PW_{10}V_2O_{40}\cdot15H_2O$. *Materials Letters* **2021**, *302*, article No.130372.
12. Zhang, R. T.; Xiao, H. P.; Li, Z.; Wang, M.; Xie, Y. F.; Ye, Y. D.; Li, X. X.; Zheng, S. T. Two highly stable inorganic–organic hybrid 3D frameworks based on Cu–Ln incorporated polyoxometalates for selective dye removal and proton conduction. *CrystEngComm*, **2021**, *23*, 2973-2981.
13. Zhu, M.; Iwano, T.; Tan, M.; Akutsu, D.; Uchida, S.; Chen, G.; Fang, X. Macrocyclic Polyoxometalates: Selective Polyanion Binding and Ultrahigh Proton Conduction. *Angew. Chem. Int. Ed.* **2022**, *61*, 1-5.
14. Li, D.; Tan, X. L.; Chen, L. L.; Liu, X. Y.; Li, Y. M.; Dang, D. B.; Bai, Y. Four Dawson POM-based inorganic-organic supramolecular compounds for proton conduction, electrochemical and photocatalytic activity. *Journal of Solid State Chemistry*, **2022**, *305*, article No.122694.
15. Nakamura, O.; Kodama, T.; Ogino, I.; Miyake, Y. High-Conductivity Solid Proton Conductors: Dodecamolybdophosphoric Acid and Dodecatungstophosphoric Acid Crystals. *CHEMISTRY LETTERS*, **1979**, 17-18.

APPENDIX 5

Supporting data for chapter 5

Table of Contents

Section A5.1. Physical characterizations

The synthesized compounds were characterized by FT-IR, Raman spectroscopy, powder X-ray diffraction, FESEM, HR-TEM, thermogravimetric analysis (TGA) and UV-visible diffused reflectance spectroscopy (DRS), UV-visible spectroscopy and electrochemical studies. FT-IR (Fourier transformed – infrared spectra) was recorded in iD7 ATR thermo Fisher Scientific-Nicolet iS5 instrument. The samples were exposed to IR radiation by keeping it on sample holder. Powder X-ray diffraction (PXRD) patterns were recorded on a Bruker D8-Advance diffractometer by using graphite monochromated CuKα1 (1.5406Å) and $K\alpha_2$ (1.55439Å) radiation. Diffuse reflectance (DRS) UV-spectroscopy studies have been carried out on UV-2600 Shimadzu UV-Visible spectrophotometer. EPR spectra have been recorded using a JEOL JES–FA200 spectrometer in frozen DMSO at –140ºC. Electronic absorption studies have been carried out using a Cary 100 Bio UV–visible spectrophotometer at room temperature. Field emission scanning electron microscopy (FESEM) measurement along with energy dispersive X-ray (EDX) were recorded on a Carl Zeiss model ultra 55 Microscope whereas EDX spectrum was performed using oxford instruments X-Max^N SDD (50mm^2) system and INCA analysis software. Thermogravimetric analysis (TGA) analyses were performed in PerkinElmer-STA 6000 analyzer. High Resolution Transmission electron microscopy (HR-TEM) images were recorded in an JEM-F200 microscope (JEOL) with an accelerating voltage of 200 kV. All the electrochemical measurements were carried out with the help of Zahner Zanium electrochemical workstation operated with Thales software.

Section A5.2. Synthesis, material and procedures.

The synthetic procedures were mentioned in the main article and chemicals used are reagent grade, no further purification is required.

Section A5.3. Thermogravimetric analysis of compound 2.

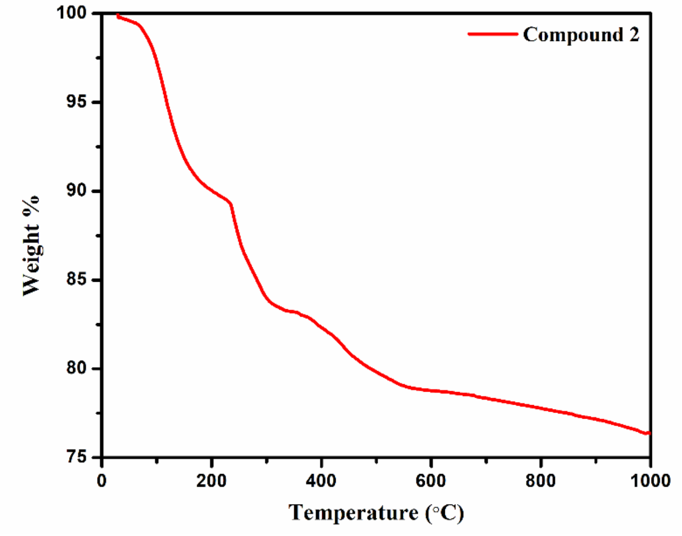

Figure A5.1. Thermogravimetric plot of the compound **2**.

TGA plot of the compound **2** clearly shows that below and around 100 ⁰C temperature, it loses the water molecules and I_2 present in it as shown in Figure A5.1 and then the cluster coordinated water molecules and acetate ligands lose has occurred at 200-400 ⁰C. Above 400 ⁰C temperature cluster starts deforming till 600 ⁰C.

Section A5.4. UV-visible spectral analysis.

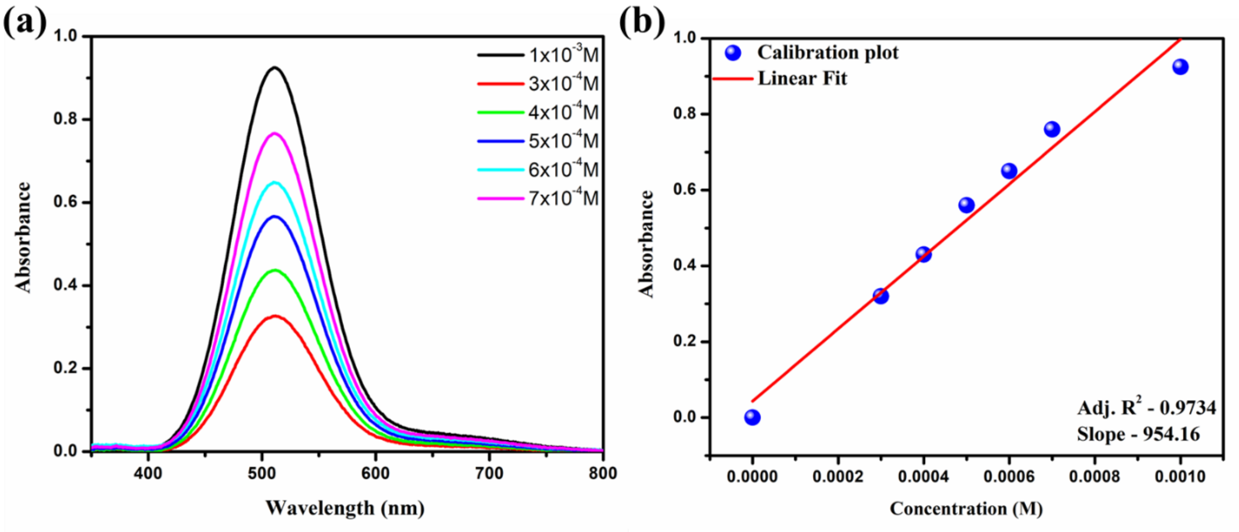

Figure A5.2. (a) Electronic absorption spectra of chloroform solutions of various Iodine concentrations; (b) calibration curve for the concentration Vs absorbance from UV-Visible spectrophotometer.

We have performed the UV-visible absorption spectral analysis for the chloroform solutions of various iodine concentrations as shown in the Figure A5.2a. We have recorded the spectra for the range of concentration from 0.0007 M to 0.001 M and obtained the absorbance range from 0.3 to 0.95. From this obtained range of absorbance, we have calculated the concentration of unknown iodine concentrated chloroform solution extracted from the compound **2** (as discussed in the main text) through the calibration curve plotted between concentration and absorbance as shown in the Figure A5.2b.

Section A5.5. FESEM analysis.

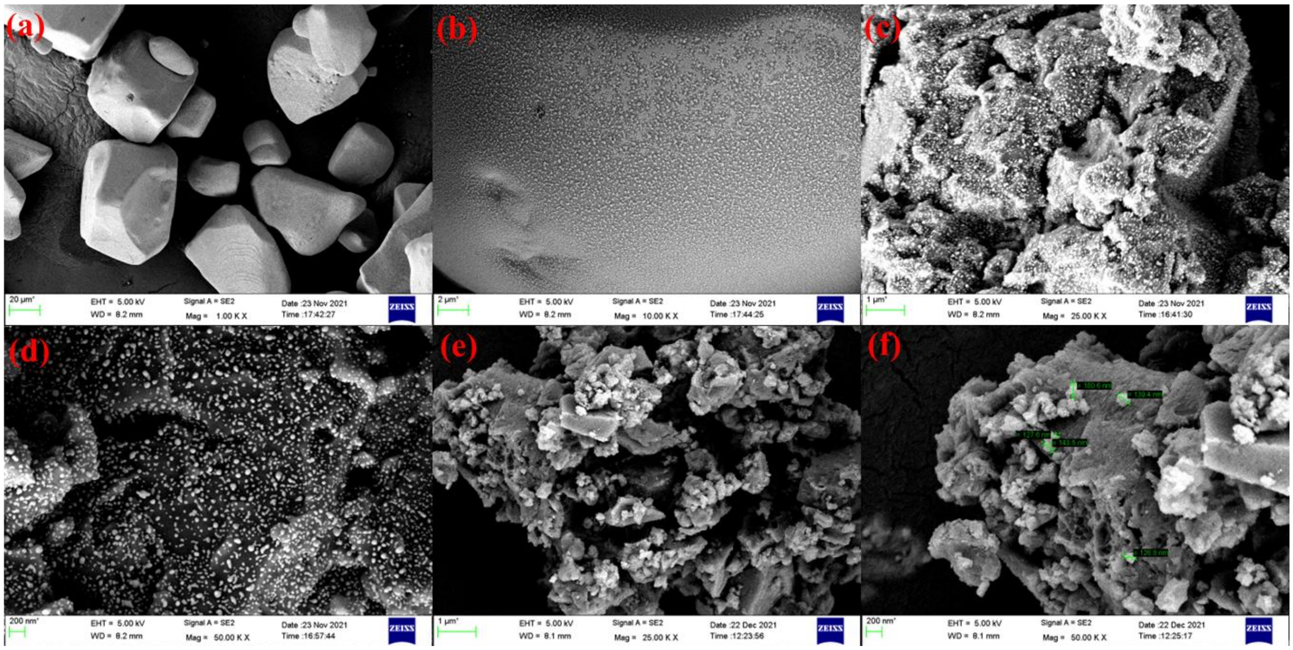

Figure A5.3. FESEM images of (a, b) KI; (c, d) compound **2**; (e, f) compound **3**.

The FESEM images of the samples has been taken on the carbon tape and coated with gold. As such KI has been taken for the analysis and we can observe a block type of structures of KI as shown in the Figure A5.3a and A5.3b. Compound **2**, immediately after grinding with KI has been recorded for the FESEM analysis as shown in the Figure A5.3c and A5.3d. We have observed a broken crystal images in the compound **3** as shown in the Figure A5.3e and A5.3f.

Section A5.6. Energy-dispersive X-ray (EDX) analysis.

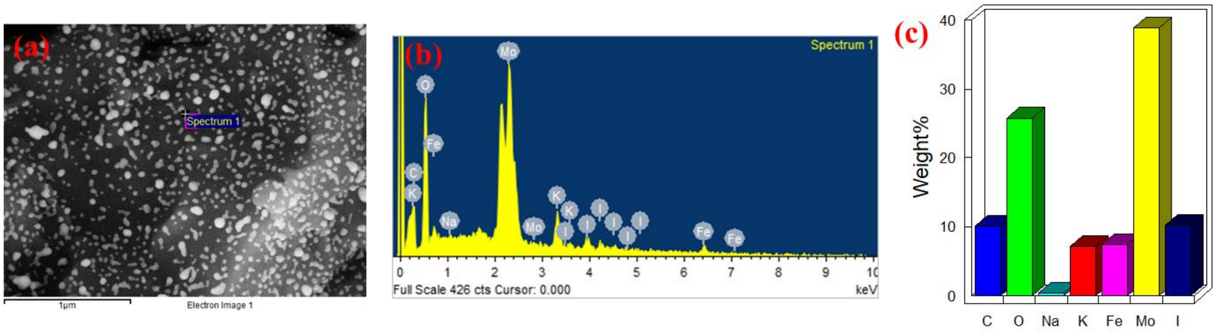

Figure A5.4. (a) Selected surface area of the compound **2** for the EDX analysis; (b) EDX spectrum for the compound **2**; (c) histogram of the elemental composition on the selected surface of the compound **2**.

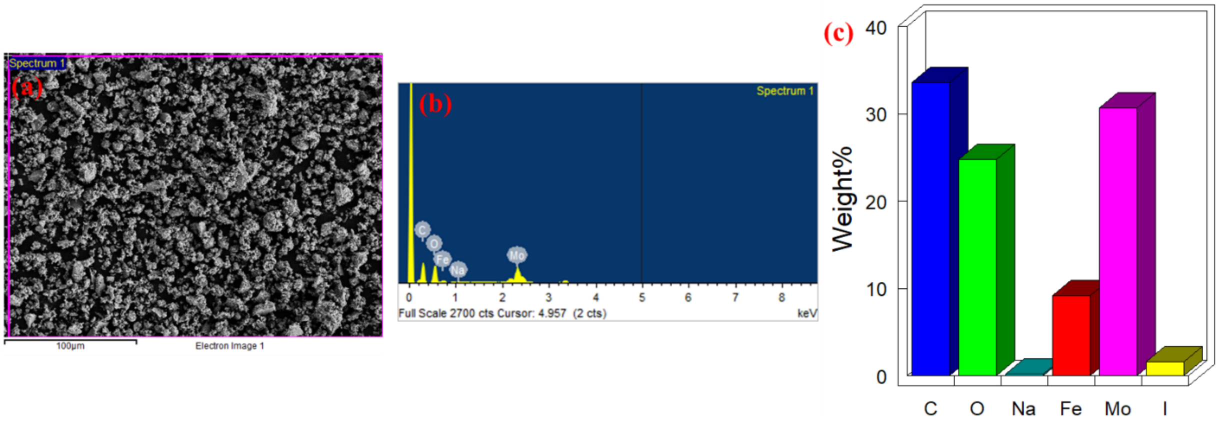

Figure A5.5. (a) Selected surface area of the compound **3** for the EDX analysis; (b) EDX spectrum for the compound **3**; (c) histogram of the elemental composition on the selected surface of the compound **3**.

Energy dispersive X-ray (EDX) spectroscopy was taken for the compound **2** and **3** to know the composition on the surface of the compound. The selected surface area of the compound **2** and **3** including its EDX analysis and EDX plot has been shown in Figure A5.4a, A5.4b and Figure A5.5a, A5.5b respectively. In the Figure S4c and S5c, the elemental composition of the compound **2** and **3** can be seen in the form of histograms and it also shown in the Table A5.1 and Table A5.2 which are experimentally recorded with the help of EDX spectroscopy.

Table A5.1. Elemental composition of the compound **2** from EDX spectroscopic analysis.

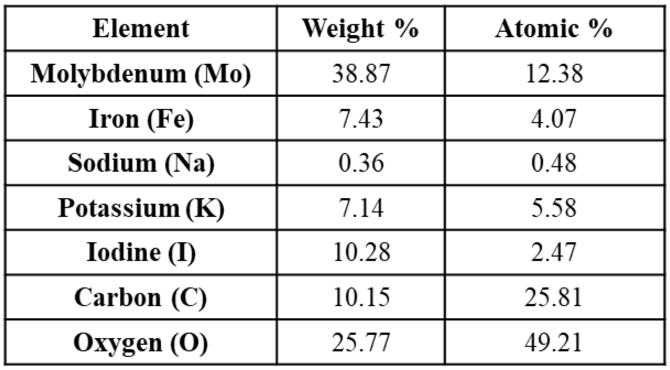

Element	Weight %	Atomic %
Molybdenum (Mo)	38.87	12.38
Iron (Fe)	7.43	4.07
Sodium (Na)	0.36	0.48
Potassium (K)	7.14	5.58
Iodine (I)	10.28	2.47
Carbon (C)	10.15	25.81
Oxygen (O)	25.77	49.21

Table A5.2. Elemental composition of the compound **3** from EDX spectroscopic analysis.

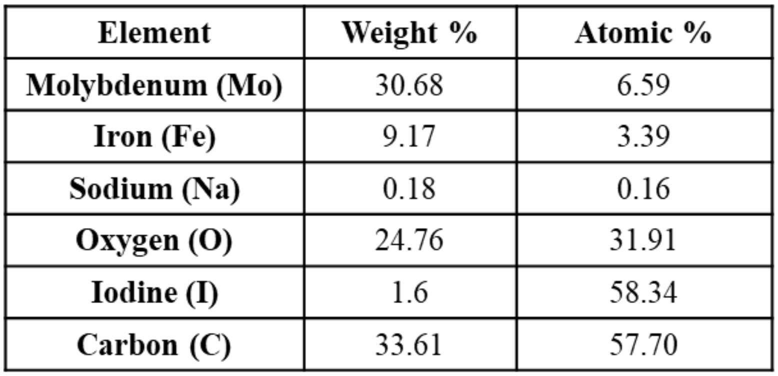

Element	Weight %	Atomic %
Molybdenum (Mo)	30.68	6.59
Iron (Fe)	9.17	3.39
Sodium (Na)	0.18	0.16
Oxygen (O)	24.76	31.91
Iodine (I)	1.6	58.34
Carbon (C)	33.61	57.70

Section A5.7. HR-TEM analysis of compound 2.

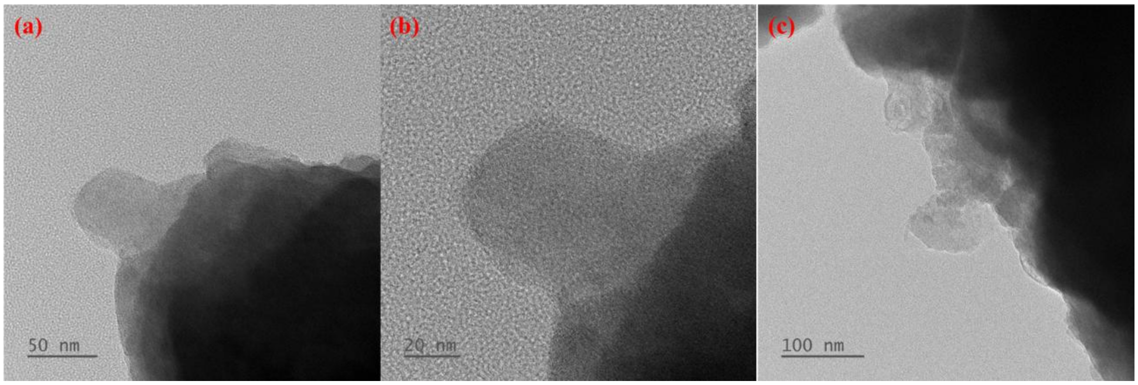

Figure A5.6. (a-c) HR-TEM analysis of compound **2** has been recorded at different magnification range.

We have performed the HR-TEM analysis for the compound **2** by coating the powdered sample on the copper grid and carried out the analysis as shown in the Figure A5**.**6a-c.

==

LIST OF PUBLICATIONS

1. **Nano-blackberries of {$W_{72}Fe_{33}$} and {$Mo_{72}Fe_{30}$}: Electrocatalytic Water Reduction.**
   Kolli, H. K.; Jana, D.; Das, S. K. *Inorg. Chem.* **2021**, *60*, 15569–15582.

2. **Efficient homogeneous electrocatalytic hydrogen evolution using a Ni-containing polyoxometalate catalyst.**
   Jana, D.; Kolli, H. K.; Sabnam, S.; Das, S. K. *Chem. Commun.*, **2021**, *57*, 9910-9913.

3. **Single Crystals of α-MoO_3-Intercalated {$Ni(H_2O)_6$}$^{2+}$ and Electrocatalytic Water Reduction: Toward a Class of Molybdenum Bronzes.**
   Jana, D.; Kolli, H. K.; Das, S. K. *Inorg. Chem.* **2022**, *61*, 3816–3820.

4. **$Co(OH)_2$ Intercalated in MoO_3 by Molecular Electrodeposition Resulting in a Conductive Material: A Molybdenum Bronze for Efficient Electrocatalytic Hydrogen Evolution.**
   Jana, D.; Kolli, H. K.; Das, S. K. *Chem. Mater.* **2023**, *35*, 3083–3094.

5. **Solid Nanoblackberries Exhibiting Super Proton Conductivity Fabricated as Proton Transport Membranes.**
   Saha, P.; Kolli, H. K.; Das, A.; Jana, T.; Das, S. K. Manuscript Under Preparation

6. **Giant Polyoxometalate {$W_{72}Fe_{30}$} in the form of Gel and Xerogel: Rheology and Proton Conduction**
   Kolli, H. K.; Jana, D.; Kumar, M. P.; Dhara, S.; Das, S. K. Manuscript Under Preparation

7. **Mechanochemical and Aerial KI Oxidation Mediated by a Giant {Mo72Fe30} Polyoxometalate**
   Kolli, H. K.; Jana, D.; Sabbani, S.; Das, S. K. Manuscript Under Preparation

LIST OF PRESENTATIONS

Oral presentation

1. **Nano-blackberries of {$W_{72}Fe_{33}$} and {$Mo_{72}Fe_{30}$}: Electrocatalytic Water Reduction.** Chemfest 2022 (In-house symposium) at School of Chemistry, University of Hyderabad, India, during 22-23 April 2022.

Poster presentation

1. **Chemistry of Giant [$Mo_{72}Fe_{30}$] Type Polyoxometalate Cluster Containing Compounds.** International conference on modern trends in inorganic chemistry (MTIC-XVIII) at IIT-Guwahati, India, during 11-13 December 2019.

2. **Nano-blackberries of {$W_{72}Fe_{33}$} and {$Mo_{72}Fe_{30}$}: Electrocatalytic Water Reduction.** Chemfest 2022 (In-house symposium) at School of Chemistry, University of Hyderabad, India, during 22-23 April 2022.

{M72Fe30} (M=Mo, W) Polyoxometalates: Electrocatalysis, Proton Conductivity, Gelation and Mechanochemistry

by Kolli Hema Kumari

Submission date: 25-May-2023 10:23AM (UTC+0530)
Submission ID: 2101377794
File name: Hema_Kumari.pdf (831.53K)
Word count: 33713
Character count: 180839

{M72Fe30} (M=Mo, W) Polyoxometalates: Electrocatalysis, Proton Conductivity, Gelation and Mechanochemistry

ORIGINALITY REPORT

31%	7%	29%	4%
SIMILARITY INDEX	INTERNET SOURCES	PUBLICATIONS	STUDENT PAPERS

PRIMARY SOURCES

1	Hema Kumari Kolli, Debu Jana, Samar K. Das. " Nanoblackberries of {W Fe } and {Mo Fe }: Electrocatalytic Water Reduction ", Inorganic Chemistry, 2021 Publication	19%
2	Sateesh Mulkapuri, Athira Ravi, Rajendar Nasani, Sathish Kumar Kurapati, Samar K. Das. "Barrel-Shaped-Polyoxometalates Exhibiting Electrocatalytic Water Reduction at Neutral pH: A Synergy Effect", Inorganic Chemistry, 2022 Publication	2%
3	Submitted to University of Hyderabad, Hyderabad Student Paper	2%
4	pubs.rsc.org Internet Source	1%
5	Subhabrata Mukhopadhyay, Anupam Das, Tushar Jana, Samar K. Das. "Fabricating a MOF Material with Polybenzimidazole into an	1%

S.K.Das

Prof. Samar K. Das
School of Chemistry
University of Hyderabad
Hyderabad-500 046., INDIA.
skdas@uohyd.ac.in

S.K.Das

Prof. Samar K. Das
School of Chemistry
University of Hyderabad
Hyderabad-500 046., INDIA.
skdas@uohyd.ac.in

S.K.Das

Prof. Samar K. Das
School of Chemistry
University of Hyderabad
Hyderabad-500 046., INDIA.
skdas@uohyd.ac.in

	Efficient Proton Exchange Membrane", ACS Applied Energy Materials, 2020 Publication	
6	www.researchgate.net Internet Source	<1 %
7	"All in One - Complete Issue: ChemInform 15/2010", ChemInform, 04/13/2010 Publication	<1 %
8	Subhabrata Mukhopadhyay, Joyashish Debgupta, Chandani Singh, Rudraditya Sarkar, Olivia Basu, Samar K. Das. "Designing UiO-66-Based Superprotonic Conductor with the Highest Metal–Organic Framework Based Proton Conductivity", ACS Applied Materials & Interfaces, 2019 Publication	<1 %
9	Anupam Das, Nilanjan Mukherjee, Tushar Jana. "Polymer-Grafted Graphene Oxide/Polybenzimidazole Nanocomposites for Efficient Proton-Conducting Membranes", ACS Applied Nano Materials, 2023 Publication	<1 %
10	Raju Mekala, Sabbani Supriya, Samar K. Das. " Isolation of Blackberry-Shaped Nanoparticles of a Giant {Mo Fe } Cluster and Their Transformation to a Crystalline Nanoferric Molybdate ", Inorganic Chemistry, 2016 Publication	<1 %

11	Kesar Tandekar, Pragya Naulakha, Sabbani Supriya. "Reversible redox activity of {Mo72Fe30} nano-polyoxometalate cluster in three crystalline forms", Inorganica Chimica Acta, 2020 Publication	<1 %
12	Raju Mekala, Sabbani Supriya, Samar K. Das. " Fate of a Giant {Mo Fe }-Type Polyoxometalate Cluster in an Aqueous Solution at Higher Temperature: Understanding Related Keplerate Chemistry, from Molecule to Material ", Inorganic Chemistry, 2013 Publication	<1 %
13	Edina Balogh, Ana Maria Todea, Achim Müller, William H. Casey. " Rates of Ligand Exchange between >Fe −OH Functional Groups on a Nanometer-Sized Aqueous Cluster and Bulk Solution ", Inorganic Chemistry, 2007 Publication	<1 %
14	www.science.gov Internet Source	<1 %
15	www.mdpi.com Internet Source	<1 %
16	Shyam Chand Pal, Debolina Mukherjee, Rupam Sahoo, Supriya Mondal, Madhab C. Das. "Proton-Conducting Hydrogen-Bonded	<1 %

Organic Frameworks", ACS Energy Letters, 2021
Publication

---

17 Submitted to Savitribai Phule Pune University <1%
Student Paper

---

18 Nilanjan Mukherjee, Anupam Das, Tushar Jana. " Poly(-vinyl triazole- - -vinyl imidazole) on MWCNTs as Nanofillers to Improve Proton Conducting Membranes ", ACS Applied Nano Materials, 2022 <1%
Publication

---

19 Subhabrata Mukhopadhyay, Anupam Das, Tushar Jana, Samar Kumar Das. "Fabricating a MOF Material with Polybenzimidazole into an Efficient Proton Exchange Membrane", ACS Applied Energy Materials, 2020 <1%
Publication

---

20 net.knigi-x.ru <1%
Internet Source

---

21 Shuvra Singha, Tushar Jana. "Structure and Properties of Polybenzimidazole/Silica Nanocomposite Electrolyte Membrane: Influence of Organic/Inorganic Interface", ACS Applied Materials & Interfaces, 2014 <1%
Publication

---

22 tel.archives-ouvertes.fr <1%
Internet Source

23	Lin Chen, Yongwen Ren, Faying Fan, Tianyuan Wu, Zhe Wang, Yaojian Zhang, Jingwen Zhao, Guanglei Cui. "Artificial frameworks towards ion-channel construction in proton exchange membranes", Journal of Power Sources, 2023 Publication	<1%
24	Kelly A. Perry, Karren L. More, E. Andrew Payzant, Roberta A. Meisner, Bobby G. Sumpter, Brian C. Benicewicz. " A comparative study of phosphoric acid-doped -PBI membranes ", Journal of Polymer Science Part B: Polymer Physics, 2014 Publication	<1%
25	Samai, Suman, and Kumar Biradha. "Chemical and Mechano Responsive Metal–Organic Gels of Bis(benzimidazole)-Based Ligands with Cd(II) and Cu(II) Halide Salts: Self Sustainability and Gas and Dye Sorptions", Chemistry of Materials, 2012. Publication	<1%
26	Shuvra Singha, Tushar Jana. "Effect of composition on the properties of PEM based on polybenzimidazole and poly(vinylidene fluoride) blends", Polymer, 2014 Publication	<1%
27	Marco Bugnola, Kaiji Shen, Eynat Haviv, Ronny Neumann. "Reductive Electrochemical Activation of Molecular Oxygen Catalyzed by	<1%

an Iron-Tungstate Oxide Capsule: Reactivity Studies Consistent with Compound I Type Oxidants", ACS Catalysis, 2020
Publication

---

28 Padmaja P. Mishra, Joe Pigga, Tianbo Liu. "Membranes Based on “Keplerate”-Type Polyoxometalates: Slow, Passive Cation Transportation and Creation of Water Microenvironment", Journal of the American Chemical Society, 2008
Publication
<1%

---

29 Balakondareddy Sana, Tushar Jana. "Polybenzimidazole composite with acidic surfactant like molecules: A unique approach to develop PEM for fuel cell", European Polymer Journal, 2016
Publication
<1%

---

30 daneshyari.com
Internet Source
<1%

---

31 Muller, A.. "Cross-linking nanostructured spherical capsules as building units by crystal engineering: related chemistry", Solid State Sciences, 20001201
Publication
<1%

---

32 polen.itu.edu.tr
Internet Source
<1%

33	P. Muthuraja, S. Prakash, V.M. Shanmugam, S. Radhakrsihnan, P. Manisankar. "Novel perovskite structured calcium titanate-PBI composite membranes for high-temperature PEM fuel cells: Synthesis and characterizations", International Journal of Hydrogen Energy, 2018 Publication	<1 %
34	edoc.unibas.ch Internet Source	<1 %
35	ir.kluniversity.in Internet Source	<1 %
36	link.springer.com Internet Source	<1 %
37	edepositireland.ie Internet Source	<1 %
38	etd.ohiolink.edu Internet Source	<1 %
39	www.freepatentsonline.com Internet Source	<1 %
40	High Temperature Polymer Electrolyte Membrane Fuel Cells, 2016. Publication	<1 %
41	repositorio.uam.es Internet Source	<1 %

42	unsworks.unsw.edu.au Internet Source	<1 %
43	Haikun Guo, Minghao Zeng, Xiang Li, Haibo He, Lixin Wu, Haolong Li. "Multifunctional Enhancement of Proton-Conductive, Stretchable, and Adhesive Performance in Hybrid Polymer Electrolytes by Polyoxometalate Nanoclusters", ACS Applied Materials & Interfaces, 2021 Publication	<1 %
44	Maria K. Daletou, Joannis Kallitsis, Stylianos G. Neophytides. "Chapter 6 6 Materials, Proton Conductivity and Electrocatalysis in High-Temperature PEM Fuel Cells", Springer Science and Business Media LLC, 2011 Publication	<1 %
45	Submitted to Seoul National University Student Paper	<1 %
46	baadalsg.inflibnet.ac.in Internet Source	<1 %
47	vdoc.pub Internet Source	<1 %
48	Das, S.K.. "Synthesis and performance evaluation of a polymer mesh supported proton exchange membrane for fuel cell	<1 %

applications", Journal of Membrane Science, 20100315
Publication

---

49 Dirk Volkmer, Alexander Du Chesne, Dirk G. Kurth, Heimo Schnablegger, Pit Lehmann, Michael J. Koop, Achim Müller. " Toward Nanodevices: Synthesis and Characterization of the Nanoporous Surfactant-Encapsulated Keplerate (DODA) (NH) [(H O) ⊂Mo O (CH COO) (H O)] ", Journal of the American Chemical Society, 2000 <1%
Publication

---

50 Tianbo Liu, Brandon Imber, Ekkehard Diemann, Guang Liu, Katrina Cokleski, Huilin Li, Zhiqiang Chen, Achim Müller. " Deprotonations and Charges of Well-Defined {Mo Fe } Nanoacids Simply Stepwise Tuned by pH Allow Control/Variation of Related Self-Assembly Processes ", Journal of the American Chemical Society, 2006 <1%
Publication

---

51 Ana Maria Todea. "Porous Capsules {(M)M5}12FeIII30 (M=MoVI, WVI): Sphere Surface Supramolecular Chemistry with 20 Ammonium Ions, Related Solution Properties, and Tuning of Magnetic Exchange Interactions", Angewandte Chemie, 12/09/2009 <1%
Publication

52	Arnulf Jäger-Waldau. "Chapter 459 Photovoltaics, Status of", Springer Science and Business Media LLC, 2012 Publication	<1 %
53	cris.bgu.ac.il Internet Source	<1 %
54	Bao Li, Luyun Xuan, Lixin Wu. "Polyoxometalate ‐ Containing Supramolecular Gels", Macromolecular Rapid Communications, 2022 Publication	<1 %
55	Shuvra Singha, Tushar Jana. "Influence of interfacial interactions on the properties of polybenzimidazole/clay nanocomposite electrolyte membrane", Polymer, 2016 Publication	<1 %
56	doras.dcu.ie Internet Source	<1 %
57	nlistsp.inflibnet.ac.in Internet Source	<1 %

Exclude quotes	On	Exclude matches	< 14 words
Exclude bibliography	On		